UNIVERSITÀ DI PISA

Scuola di Dottorato in Ingegneria "Leonardo da Vinci"

Corso di Dottorato di Ricerca in
SICUREZZA NUCLEARE E INDUSTRIALE

Tesi di Dottorato di Ricerca

Experimental and Computational Analysis of Condensation Phenomena for the Thermal-hydraulic Analysis of LWRs Containments

Autore:

Matteo Bucci

Relatori:

Prof. Walter Ambrosini

Ing. Nicola Forgione

Ing. Jean-Paul Magnaud

Prof. Francesco Oriolo

Prof. Sandro Paci

Ing. Etienne Studer

Anno 2009

Summary

This PhD research aims at improving the understanding of condensation phenomena of interest for the safety analysis of nuclear reactor containments. Particular attention if focused on the effect related to the possible presence of hydrogen, which could be released in the containment atmosphere during a loss of coolant accident with loss of core cooling and fuel pin clad oxidation.

The way steam condensation phenomena have been investigated in this work is multiple: theoretical, experimental and numerical analyses have been carried out.

A theoretical analysis of steam condensation is firstly proposed to clarify fundamental issues related to the modelling of diffusion phenomena in multicomponent mixtures.

Experimental data available by the CONAN and COPAIN separate effect test facilities were analyzed. Further experimental activities have been performed, aimed at collecting specific data concerning the effect induced by the presence of a noncondensable gas lighter than steam .

Three different condensation models are proposed, basing on the two main strategies adopted for wall condensation modelling in CFD codes: a fine approach based on the detailed resolution of the concentration, temperature and velocity gradients near the condensing wall and a less expensive approach adopting coarser discretization in the proximity of the condensing wall, based on the heat and mass transfer analogy. The HMTDM^{MSD} and the HMTDM^{EBD} approaches are proposed based on the first strategy, but different diffusion models. The HMTAM model is a fast running model based on the heat and mass transfer analogy.

The capabilities of several turbulence models in reproducing turbulent transpiration phenomena have been formerly evaluated. A first stage consisted in analyzing the capabilities of turbulence models to reproduce nondimensional velocity profiles in the presence of pure turbulent mass and momentum transfer. A second stage consisted in a numerical analysis of suction effects induced by condensation.

The condensation models have been finally applied to the modelling of the CONAN and COPAIN steam-air and steam-air-helium tests. An extensive comparison with local and integral experimental data is proposed.

A theoretical and numerical analysis is finally proposed, aimed at assessing to what extent helium is an appropriate substitute for hydrogen.

Concluding remarks are drawn and future activities are suggested, either under the experimental than the numerical point of view.

Acknowledgements

Al prof. Ambrosini ed al Dott. Forgione, al prof. Oriolo ed al prof. Paci, per i numerosi consigli e la loro inesauribile disponibilità, i miei piú sentiti ringraziamenti. Un generoso ringraziamento anche a tutti i ragazzi con cui ho avuto la fortuna di lavorare in dipartimento. Su tutti, e gli altri non me ne vogliano, un caloroso grazie a Medhat.

Un sentito grazie é rivolto anche a tutti i miei colleghi ed amici. In particolare ringrazio Etienne e Jean-Paul per le loro numerose consulenze, scientifiche e non, e per aver accettato di essere miei relatori "ester(n)i". Un ringraziamento speciale anche a Mitia, Paolo ed Enrico per il loro prezioso contributo e soprattutto per la loro amicizia. Un caloroso grazie ad Ema per la sua insostituibile presenza nei momenti di divertimento e non.

Un grazie speciale alla mia famiglia e a chi mi vuole molto più che bene.

A Mattia,
che non si arrese.

Contents

List of symbols

Symbol		Units
Latin letters		
A	Favre's suction parameter	$[-]$
A_f	Ackerman factor	$[-]$
B	Transpiration parameter	$[-]$
B_m	Mass transfer driving force	$[-]$
C	Molar concentration	$mole.m^{-3}$
Cp	Specific heat at constant pressure	$m^2.s^{-2}.K^{-1}$
D	Molecular diffusivity	$m^2.s^{-1}$
$\mathbb{D}$	Multicomponent mass transfer diffusivity	$m^2.s^{-1}$
$\mathbf{d}$	Diffusion driving force vector	m^{-1}
f_i	Friction coefficient	$[-]$
$\vec{f}$	Body force per unit mass	$m.s^{-2}$
$\vec{F}$	Force per unit mass	$m.s^{-2}$
F	Stefan suction factor	$[-]$
G_s	Entropy source	$J.kg^{-1}.K^{-1}.m^{-3}.s$
g	Gravity acceleration	$m.s^{-2}$
h	Heat transfer coefficient	$W.m^{-2}.K^{-1}$
h_m	Mass transfer coefficient	$kg.m^{-2}.s^{-1}$
$\hbar$	Enthalpy	$J.kg^{-1}$
$[\mathbb{I}]$	Identity matrix	$[-]$
$\vec{j}$	Diffusion mass flux vector	$kg.m^{-2}.s^{-1}$
$\vec{j}^*$	Diffusion molar flux vector	$mole.m^{-2}.s^{-1}$
k	Thermal conductivity	$kg.m.s^{-3}.K^{-1}$
K_m	Mass transfer coefficient	$m.s^{-1}$
l_m	Mixing length	m
M	Molar weight	$kg.mole^{-1}$
M_f	Kays & Moffat factor	$[-]$
$\vec{\dot{m}}''$	Mass flux vector	$kg.m^{-2}.s^{-1}$
$\vec{\dot{n}}''$	Molar flux vector	$mole.m^{-2}.s^{-1}$
P	Absolute pressure	Pa
$\vec{\dot{q}}''$	Heat flux	$W.m^{-2}$
R	Perfect gas constant ($= 8.313$)	$J.mole^{-1}.K^{-1}$

Symbol		Units
(con'd)		
S	Source term	$[-].m^{-3}$
$\mathbb{S}$	Rate of strain	s^{-1}
s	Entropy	$J.kg^{-1}.K^{-1}$
T	Temperature	K
t	Time	s
$\hat{u}$	Internal energy	$J.kg^{-1}$
$\vec{U}$	Velocity vector	$m.s^{-1}$
u	Velocity component	$m.s^{-1}$
U^+	Nondimensional velocity	$[-]$
U^*	Shear velocity	$m.s^{-1}$
v	Velocity component	$m.s^{-1}$
w	Velocity component	$m.s^{-1}$
x	Space coordinate	m
X	Molar fraction	$[-]$
y	Space coordinate	m
y^+	Nondimensional distance	m
Y	Mass fraction	$[-]$
Greek letters		
α	Thermal diffusivity	$m^2.s^{-1}$
χ	Helium-to-noncondensable gas ratio	$[-]$
δx	Cell thickness	m
ε	Turbulence kinetic energy dissipation	$m^{-2}.s^{-3}$
κ	Turbulence kinetic energy	$m^{-2}.s^{-2}$
ϕ	Generic scalar quantity	$[\phi]$
μ	Dynamic viscosity	$kg.m^{-1}.s^{-1}$
ν	Kinematic viscosity	$m^2.s^{-1}$
ω	Specific dissipation rate of κ	s^{-1}
π	Cauchy stress	Pa
ρ	Density	$kg.m^{-3}$
$\vec{\sigma}$	Entropy flux vector	$J.kg^{-1}.K^{-1}.m^{-2}.s$
τ	Shear stress	Pa

Subscripts

a	Refer to air
$b, bulk$	Refer to bulk conditions
c	Refer to the near-the-wall cell
ch	Refer to channel
f	Refer to film quantities
m	Refer to mixture
h	Refer to enthalpy
he	Refer to helium
i	Refer to the i species or to the interface
j	Refer to the j species
k	Refer to the k species
l	Refer to liquid
nc	Refer to noncondensables
0	Refer to stagnation conditions
q	Refer to momentum
s	Refer to sensible heat
sat	Refer to saturation conditions
t	Refer to turbulence
v	Refer to vapor
$w, wall$	Refer to wall conditions
∞	Refer to undisturbed conditions
$\perp$	Orthogonal to the condensing surface
$\parallel$	Parallel to the condensing surface

Superscripts

v	Refer to saturated steam enthalpy
l	Refer to saturated liquid enthalpy
lat	Refer to steam latent heat

Dimensionless numbers

$Gr = \frac{l^3 \rho g \Delta\rho}{\mu^2}$	Grashof number
$Le = \frac{Pr}{Sc} = \frac{D}{\alpha}$	Lewis number
$Nu = \frac{hl}{\lambda}$	Nusselt number
$Pe = RePr$	Peclet number
$Pr = \frac{C_p \mu}{\lambda} = \frac{\nu}{\alpha}$	Prandtl number
$Re = \frac{\rho U l}{\mu}$	Reynolds number
$Ri = \frac{Gr}{Re^2}$	Richardson number
$Sc = \frac{\nu}{D}$	Schmidt number
$Sh = \frac{h_m l}{\rho D}$	Local mass Sherwood number

The length l is taken equal to x for nondimensional local numbers or equal to L for nondimensional average numbers.

Abbreviations

AIChE	American Institute for Chemical Engineering
ASME	American Society for Mechanical Engineering
CEA	Commissariat á l'ènèrgie atomique
CFD	Computational Fluid Dynamics
FZJ	Forschungszentrum Julich
FZK	Forschungszentrum Karlsruhe
HMTAM	Heat and Mass Transfer Analogy Method
HMTDM	Heat and Mass Transfer Diffusion Method
IRSN	Institut de Radioprotection et Sûrété Nucléaire
JSI	Joseph Stefan Institute
JRC	Joint Research Centre Institute for Energy
KTH	Kungliga Tekniska Högskolan (Royal Institute of Technology)
LP	Lumped Parameter
NRG	Nuclear Research and consultancy Group
NIST	National Institute of Standards and Technology
PCC	Passive Containment Condenser
PCCS	Passive Containment Cooling System
SARnet NoE	Severe Accident Research Network of Excellence
SBWR	Simplified Boiling Water Reactor
UNIPI	University of Pisa
UPM	Universitad Politécnica de Madrid

Chapter 1

Introduction

1.1 General background

Among the reactor safety issues for pressurized and boiling light water reactors (LWRs), those concerning the hypothetical event of loss of coolant accident (LOCA) are among the most important [2]. Indeed, the loss of coolant accident has been always considered a reference accident condition in reactor safety and it is therefore chosen as design-basis accident (DBA). As a consequence, major efforts in the field of nuclear safety analysis have been devoted in the last decades aimed at providing computational tools capable of predicting the development and the consequences of LOCAs.

Whatever is the postulated accident scenario, a crucial aspect concerns the integrity of the nuclear reactor containment. Indeed, due to the sharp release of water vapor from the primary loop, a huge amount of energy is rapidly transferred to the containment atmosphere, causing the containment pressure to rise.

To limit the pressure peak and to promote the subsequent decrease of the containment pressure, several safety features can be adopted, aimed at making the steam to condense as quickly as possible. Spray systems are an example of the safety systems employed since a long time in pressurized water reactors (PWR). In boiling water reactors (BWR), having often smaller containment buildings, suppression pools have been used, in which the steam released in the dry-well is partially condensed before reaching the containment wet-well. Major improvements in the design of the new generations of reactors included new safety systems involving the use of natural forces to provide containment cooling; these system are sometimes referred to as passive containment cooling systems (PCCS). Example of PCCS are the one equipped with passive condensers in the General Electric simplified boiling water reactor (SBWR) [3] or the containment system of the Westinghouse's advanced pressurized reactor (AP600 and AP1000) [4], where condensation occurs on the containment walls, externally cooled under free convection. Last but non least, the containment walls themselves represent an important surface of heat exchange with the external environment, concurring to enhance the performance of the safety features. Condensation on the containment walls is therefore an important heat sink and represents a fundamental intrinsic safety feature of nuclear reactor

containments.

However, condensation strongly affects other relevant phenomena, like the containment atmosphere mixing, which determine the distribution of noncondensable gases that may be delivered during severe accident scenarios, with main reference to hydrogen. Indeed, as demonstrated by the Three Miles Island accident in 1979, in case of loss of core cooling, due to fuel pin cladding oxidation by superheated steam a significant amount of hydrogen can be produced and released to the containment atmosphere. Hydrogen represents a very dangerous issue for containment safety, since it can locally reach flammability limits and cause a great release of energy, causing a further threat to containment integrity.

In this scenario, the role of safety features adopted for promoting steam condensation is not obvious. Condensation occurring on containment walls, as well as the safety features designed to reduce the peak in steam release can locally aid the hydrogen to concentrate, providing a dangerous effect instead of a positive one.

Clearly, the prediction of these phenomena is a fundamental task in the safety analysis of nuclear reactor containments. Many activities have been therefore performed in the last decades to improve the capability of computational tools in predicting condensation phenomena and the overall containment atmosphere behavior. On one hand, extensive experimental activities have been carried out [5, 6, 7, 1, 8]. On the other hand, more and more sophisticated computational models have been developed (see chapter 3).

The condensation models adopted in containment lumped parameters (LP) codes used empirical or semi-empirical closure laws for the balance equations, developed basing on experimental data, mostly detailing the overall behavior of condensing atmospheres. Despite of the satisfactory behavior reached by these codes in predicting average thermal-hydraulic quantities during a postulated scenario, the analysis of local three dimensional thermal-hydraulic phenomena like the interaction of heat and mass transfer phenomena with the containment atmosphere is clearly beyond their possibilities. In this aim, new frontiers were open by the availability of modern computational fluid dynamics (CFD) tools. Promoted by the availability of faster and faster computers, with everyday increasing memory size, a renewed interest emerged to develop and qualify CFD models for the analysis of downscaled tests or even full scale containment plant phenomena. Thus, a justified interest emerged also for building and operating new experimental facilities, conceived to produce more detailed experimental data aimed at supporting the development and the validation of these models.

Physical phenomena of interest for the thermal-hydraulic analysis of the reactor containment were therefore investigated at different scales. Indeed, experimental facilities can be distinguished as separate effect test (SET) facilities, coupled effect test (CET) facilities and integral effect test (IET) facilities. The demarcation between two different classes is not always clear and sometimes depends on the specific performed test.

SET facilities are aimed at performing in depth analyses focusing on a specific phenomenon. CONAN [8] and COPAIN [1], operated respectively by University of Pisa and CEA Grenoble are SET facilities aimed at studying condensation phenomena over vertical walls. The GAMELAN facility [9], operated by CEA Saclay is instead conceived to investigate the interaction between buoyant jets and atmosphere in free, confined and stratified configurations. CET facilities combine different physical phenomena, analyzing their mutual interac-

tions. Large scale facilities like MISTRA [5] or ThAI [6], operated respectively by CEA Saclay and Becker Technologies, are considered CET facilities. Interactions of condensation phenomena with the flow field and stratified atmospheres are typical situations investigated by these facilities.

In similarity with experimental facilities, CFD models can be categorized depending on the detail to be achieved in the description of physical phenomena. Models capable of providing an accurate description of a specific physical phenomenon are usually developed and validated basing on the analysis of experimental data available by SET facilities. These models, whose application to large scale facilities is hard to attain, are mostly conceived to improve the understanding of the phenomenon and are very useful to support the development of simplified models, conceived for dealing with larger time and length scales, typical of CET and IET facilities.

When dealing with wall condensation, different approaches can be identified (see Tab. 1.1). A first approach consists in modelling wall condensation basing on the first principles of molecular diffusion. This approach consists in the integration of the different balance equations through the boundary layer and relies on the capability of the selected turbulence model to provide an accurate description of the turbulence phenomena near the condensation interface. A second, coarser approach consists in estimating the condensation rates by appropriate correlations and treating the near the wall turbulence by wall functions. This approach, attainable also for large scale modelling, is typical of containment field codes like TONUS [5] or GASFLOW [10], estimating the mass transfer coefficient by correlations based on the heat and mass transfer analogy.

1.2 Motivation for the present work

One of the main goals to be achieved by the adoption of CFD codes for containment safety analysis is the reduction of the uncertainties and therefore to increase the confidence in the safe design of a nuclear power plant (NPP). However, before a massive use of CFD codes can be considered advisable in nuclear safety applications, the evidence of their reliability must be provided. It is therefore necessary to demonstrate the capabilities of CFD tools in predicting fundamental and complex physical phenomena. In the aim to check the actual capabilities of these codes, benchmarking activities have been performed, based on the experimental data available by different experimental facilities. One of the most important benchmarks carried out in the field of condensation in the last decades is the International Standard Problem (ISP) 47 [11] promoted by the OECD (Organization for Economic Co-operation and Development), consisting of three different tests performed within the TOSQAN, the MISTRA and the ThAI facilities. At the conclusion of the ISP 47, the strengths and the weak points of the available CFD models were discussed and future follow up activities were proposed. Activities of interest were identified regarding the interaction between buoyant jets and stratified atmospheres and the effects produced by lighter than steam noncondensable gases on condensation phenomena and viceversa. Activities were mostly encouraged concerning detailed separate effect analyses, aimed at clarifying the fundamentals at the basis of the aforementioned phenomena.

Family	SET facilities	CET facilities
Aim	understanding of the phenomenon development and validation of models	interaction with different phenomena validation of models
Condensation modelling	molecular diffusion	correlations heat and mass transfer analogy
Near-wall turbulence	low-Re capabilities	wall functions
Facility	CONAN and COPAIN local measures: wall temperatures heat fluxes integral measures: condensation rates	MISTRA integral measures: mean wall temperatures condensation rates

Table 1.1: Experimental and modelling approaches in SET and CET facilities

An international program named SETH2 has been promoted by OECD making use of the Paul Scherrer Institute (PSI) PANDA facility [12] and the MISTRA facility. Relevant containment phenomena and separate effects are studied, including the interaction between buoyant jets and stratified atmosphere, natural convection, the effect of containment coolers, the effect of sprays.

Aim of this PhD thesis is to contribute to the understanding of wall condensation phenomena in steam-air and steam-air-helium mixtures. The subjet of steam condensation in the presence of different noncondensable species has been investigated under the theoretical, the experimental and the numerical points of view. The effects induced by noncondensable gases lighter than steam have been investigated by analyzing experimental data available by SET facilities and proposing further experimental data by the CONAN facility. CFD models have been developed for dealing with condensation at different length scales. Detailed models based on the first principles at the basis of molecular diffusion have been developed. Basing on the lesson learned by the analysis of the experimental data and the results of numerical simulations carried out by the detailed condensation models, a modification of a fast running model based on the heat and mass transfer analogy and developed in frame of the previous MSc thesis has been proposed, capable of dealing with different convection regimes and accounting for the presence of helium at different concentrations.

1.3 Thesis outline

This thesis is subdivided in ten chapters. Theoretical aspects are firstly treated, aiming at providing the background necessary to achieve a better understanding of the following chapters. An overview of CFD tools available for modelling condensation is therefore presented, identifying the main adopted strategies and their strength and weak points. Then, the analysis of the condensation tests available by the COPAIN and the CONAN facilities is proposed, aimed at improving the understanding of the available experimental data. The modelling of turbulent multicomponent diffusion phenomena is therefore treated and different CFD models are proposed. The different models are applied to the CONAN and COPAIN tests and the results are discussed. Finally, a theoretical and numerical comparison between helium and hydrogen is proposed, clarifying the possible differences between the two species and the suitability of helium as substitute of hydrogen in condensation tests.

More specifically, in chapter 2, an analysis of the governing equations that describe the thermal-hydraulic behavior of a multicomponent mixture is proposed, most of all focusing on the species balance equations. The theoretical bases of the diffusion phenomena in multicomponent mixtures are revised and two different diffusion models are developed. A simple model consists in defining the diffusion mass flux of a species in analogy with the diffusion mass fluxes in pure binary mixtures, by defining an approximate diffusion coefficient, also known as effective binary diffusivity (EBD). Though useful for practical purpose, the EBD model does not assure the mixture continuity equation to be intrinsically satisfied. A second model is therefore proposed, basing on the principles of irreversible thermodynamics, in which the diffusion mass fluxes of the different species are coupled and the mixture continuity equation is satisfied by definition. Two different approaches to model condensation phenomena are

therefore proposed: a first approach relying on the principles of molecular diffusion phenomena, intrinsically accounted for in the species balance equations and a second approach based on the analogy between heat and mass transfer.

A review is reported in chapter 3, aimed at analyzing the current capabilities of the modern CFD tools developed within the SARnet network of excellence in simulating wall condensation phenomena, with particular interest to those applications concerning the analysis of the nuclear reactor containment thermal-hydraulics. After illustrating the main studies performed since the beginning of the 20th century and the main activities carried out since the eighties in the nuclear safety field, an analysis of the current computational tools developed for modeling wall condensation phenomena is performed. The result of a research activity carried out in the frame of the SARnet network of excellence and coordinated by the University of Pisa is also presented. An in-depth review of the available models is proposed, together with the results of a benchmark exercise proposed to assess and compare their behavior. Basing on the results of the literature review and the benchmark exercise, the needs for future developments of the models are discussed to be pursued in this PhD research.

In chapters 4 and 5, experimental data available by CONAN and COPAIN are analyzed, respectively for condensation in steam-air and steam-air-helium mixtures. After proposing a detailed description of the facilities and of the operating procedures, the main results of previous analyses are summarized and discussed. A new methodology is therefore proposed, aimed at solving the pending questions on the interpretation of experimental data. The effects of buoyancy are investigated and mixed convection phenomena are highlighted. Steam-air-helium mixtures were investigated by COPAIN at different free stream velocities but parametrical analysis on the helium concentration was performed for a few cases. On the contrary, several helium concentrations have been analyzed by CONAN in tests having high free stream velocities. In the aim to clarify the effect of helium, as a noncondensable gas lighter than steam, new experiments have been performed within the CONAN facility at low free stream velocities. Remarkable effects on the convection regimes were observed, depending on the helium concentration in bulk. Buoyancy aided and buoyancy opposed regimes were experienced, as well as flow reversal phenomena occurring when the helium concentration is very important.

The modelling of turbulent wall condensation phenomena is treated in chapter 6. An overview of the different turbulence modelling strategies is offered. The incompressible and the compressible RANS (*Reynolds Averaged Navier-Stokes*) equations for multicomponent mixtures are presented, together with the *Boussinesq* and the *gradient-diffusion* hypotheses. The effect of turbulence on the diffusion of chemical species is analyzed. Two different CFD diffusion models are proposed on the basis of the theoretical analysis performed in chapter 2: a simplified model based on the *effective binary diffusivity* approximation and another model derived on the basis of the principles of irreversible thermodynamics. Three different condensation models are therefore proposed, basing on the two main strategies adopted for wall condensation modelling in CFD codes: a fine approach based on the resolution of the concentration, the temperature and the velocity gradients near the condensing wall and a less expensive approach adopting coarser discretization in the proximity of the condensing wall, basing on the heat and mass transfer analogy to estimate the condensation mass transfer rates.

Turbulence modelling is a keypoint in the modelling of wall condensation phenomena. In chapter 7, the capabilities of different turbulence models are therefore analyzed. The lack of experimental data concerning the characteristics of turbulence in condensation phenomena is a negative point for the validation of turbulence models, mostly conceived to deal with other flow phenomenologies than transpirating boundary layers. Thus, to assess the capabilities of the different turbulence models and the different low-Reynolds strategies, a route was proposed accounting for different phenomena of interest. A first stage allowed analyzing the capabilities of turbulence models to reproduce nondimensional velocity profiles in the presence of pure mass and momentum transfer, basing on the experimental data by Favre [13]. A second stage concerned the analysis of suction effects induced by condensation, in the light of different correlations proposed in literature to quantify its impact on the Sherwood number, the Nusselt number and the friction coefficient.

The different condensation models and the selected turbulence models are finally applied to the modelling of the COPAIN and CONAN tests. Results are illustrated and discussed in chapter 8. A comparison is shown between experimental measurements and calculated values. A comparison with local experimental data is preferred for more detailed models adopting a fine resolution of the near-wall condensing boundary layer. A comparison with available average quantities like heat flux or condensation rate is also proposed, either for diffusion based models than for the less detailed model based on the heat and mass transfer analogy.

A comparison between helium and hydrogen is finally proposed. The suitability of helium as a substitute for hydrogen is checked in chapter 9, illustrating the main differences expected in condensation phenomena, for the different convection regimes. Theoretical remarks are supported by parametrical scoping calculations.

In chapter 10, final conclusions and recommendations for future work are summarized.

Chapter 2

Theoretical analysis of condensation phenomena in multicomponent mixtures

This chapter is aimed at analyzing the governing equations that describe the thermal-hydraulic behavior of a multicomponent mixture. In the first part of the chapter, the theoretical bases of the diffusion phenomena in multicomponent mixture are revised and different diffusion models are proposed. Condensation is a diffusion process in which a condensable species diffuses towards a cold interface. This phenomenon is described by appropriate boundary conditions applied in the mathematical problem, which can be expressed basing on two different approaches. A first approach relies on the first principles of diffusion phenomena intrinsically accounted for in the species balance equations. A second approach is based on the analogy between heat and mass transfer.

2.1 The species and the continuity equations

A common approach to deal with multicomponent mixtures is here reported, as also proposed by Bird [14] or Taylor and Khristna [15].

A single phase multicomponent mixture is considered, including n different chemical species. The molar concentration of the mixture C is defined as the number of moles of the mixture per unit volume. A fraction X_i of these moles, called *molar fraction*, belongs to the i-th species, whose partial molar concentration is thus given by

$$C_i = X_i \, C \tag{2.1}$$

The mass concentration, or density, of the mixture is instead defined as the mass of the mixture per unit volume. Part of this mass is associated to the i-th species, whose contribution is proportional to its molar concentration and its molar weight. The partial species density is thus given by

$$\rho_i = C_i \, M_i \tag{2.2}$$

Finally, the density ρ of the mixture is the sum of the n species partial densities

$$\rho = \sum_{i=1}^{n} \rho_i \tag{2.3}$$

The ratio of the species density to the mixture density is known as *mass fraction* Y_i. For both mass and molar fractions, the following properties are clearly applicable:

$$\sum_{i=1}^{n} Y_i = 1 \tag{2.4}$$

$$\sum_{i=1}^{n} X_i = 1 \tag{2.5}$$

The mixture average molar weight is finally defined by

$$M = \frac{\rho}{C} = \frac{\sum_{i=1}^{n} \rho_i}{C} = \frac{\sum_{i=1}^{n} M_i \; C_i}{C} = \sum_{i=1}^{n} X_i \; M_i \tag{2.6}$$

as a function of molar fractions or, alternatively

$$M = \frac{\rho}{C} = \frac{\rho}{\sum_{i=1}^{n} C_i} = \frac{\rho}{\sum_{i=1}^{n} \frac{\rho_i}{M_i}} = \frac{1}{\sum_{i=1}^{n} Y_i / M_i} \tag{2.7}$$

as function of mass fractions. Let us consider an independent reference frame. The simplest continuity equation that describes the behavior of the i-th species is given by

$$\frac{\partial \rho_i}{\partial t} + \nabla \cdot \left(\rho_i \vec{U}_i \right) = S_i \tag{2.8}$$

where $\vec{U}_i$ is the velocity of the species in the absolute reference frame and S_i is the volumetric mass source term. The sum of the n independent equations of the single species allows writing the conservation equation of the mixture

$$\sum_{i=1}^{n} \frac{\partial \rho_i}{\partial t} + \sum_{i=1}^{n} \nabla \cdot \left(\rho_i \vec{U}_i \right) = \sum_{i=1}^{n} S_i \tag{2.9}$$

that can be further modified for the linearity property of the derivative operators

$$\frac{\partial \left(\sum_{i=1}^{n} \rho_i \right)}{\partial t} + \nabla \cdot \left(\sum_{i=1}^{n} \rho_i \vec{U}_i \right) = \sum_{i=1}^{n} S_i \tag{2.10}$$

Introducing the mixture density defined by Eq. (2.3) and assuming that, for the Lavoisier's law of conservation of mass, the source terms cancel each other, the Eq. (2.10) can be finally written as

$$\frac{\partial \rho}{\partial t} + \nabla \cdot \left(\rho \vec{U}_m \right) = 0 \tag{2.11}$$

where the term $\vec{U}_m$ is the mixture average velocity in the *mass reference frame*, defined as

$$\vec{U}_m = \sum_{i=1}^{n} Y_i \vec{U}_i \tag{2.12}$$

A similar reasoning can be proposed in terms of molar concentrations. In this case, the mole conservation equation of a species can be written as

$$\frac{\partial C_i}{\partial t} + \nabla \cdot \left(C_i \vec{U}_i \right) = S_i^* \tag{2.13}$$

Summing the n equations of the species and introducing the molar concentration of the mixture, the moles conservation equation can be finally written as

$$\frac{\partial C}{\partial t} + \nabla \cdot \left(C \vec{U}_m^* \right) = S^* \tag{2.14}$$

where the term $\vec{U}_m^*$ is the mixture average velocity in the *molar reference frame*

$$\vec{U}_m^* = \sum_{i=1}^{n} X_i \vec{U}_i \tag{2.15}$$

The term S^* is the volumetric molar source term of the mixture that, in the presence of chemical reactions, contrarily to the corresponding volumetric mass source term, can be different from zero. The mixture average velocity in the mass reference frame $\vec{U}_m$ and the mixture average velocity in the molar reference frame $\vec{U}_m^*$ are not equal in general. Just in the hypothetical case in which every chemical species has the same molecular weight the two velocities would be identical. Clearly, the two velocities are very similar in mixtures having a dominating species[1] and traces of the others.

For both the molar and the mass approach, the actual species velocity $\vec{U}_i$ can be decomposed in an average mixture velocity and a diffusion velocity. The diffusion velocity of the i-th species in the *mass reference frame* is thus given by

$$\vec{U}_{di} = \vec{U}_i - \vec{U}_m = \frac{\vec{j}_i}{\rho_i} \tag{2.16}$$

and the analogous diffusion velocity in the *molar reference frame* by

$$\vec{U}_{di}^* = \vec{U}_i - \vec{U}_m^* = \frac{\vec{j}_i^*}{C_i} \tag{2.17}$$

where the diffusion mass flux in the *mass reference frame* $\vec{j}_i$ and the diffusion molar flux in the *molar reference frame* $\vec{j}_i^*$ have been introduced, for which the following properties are obviously applicable:

$$\sum_{i=1}^{n} \vec{j}_i = 0 \tag{2.18}$$

$$\sum_{i=1}^{n} \vec{j}_i^* = 0 \tag{2.19}$$

[1] in terms of mass and molar fraction

Finally, the mass and the mole conservation equations of the generic i-th species can be written as

$$\frac{\partial \rho_i}{\partial t} + \nabla \cdot \left(\rho_i \vec{U}_m \right) = -\nabla \cdot \vec{j}_i + S_i \tag{2.20}$$

$$\frac{\partial C_i}{\partial t} + \nabla \cdot \left(C_i \vec{U}_m^* \right) = -\nabla \cdot \vec{j}_i^* + S_i^* \tag{2.21}$$

If mass and molar fraction are preferred to partial densities and concentrations, it is

$$\frac{\partial \rho Y_i}{\partial t} + \nabla \cdot \left(Y_i \rho \vec{U}_m \right) = -\nabla \cdot \vec{j}_i + S_i \tag{2.22}$$

$$\frac{\partial C X_i}{\partial t} + \nabla \cdot \left(X_i C \vec{U}_m^* \right) = -\nabla \cdot \vec{j}_i^* + S_i^* \tag{2.23}$$

Whatever is the adopted point of view, the set of the n species equation or the mixture continuity equation and $n-1$ species equations constitutes a mathematical system of n equations in $4n$ unknowns:

- 1 mixture density (or molar concentration);
- $n-1$ species mass fractions (or molar fractions);
- $3(n-1)$ components of the diffusion mass fluxes;
- 3 components of the mixture average velocity.

Once the momentum balance equations and the energy balance equations are added, the set of equations would include $n+4$ equations and $4n+2$ unknown: pressure and energy are introduced. A further equation is the equation of state of the mixture, correlating the thermodynamic unknowns already included. The missing $3(n-1)$ equations are those correlating the components of the diffusion fluxes to the other aforementioned unknowns. In the following paragraph 2.2, the simple case of diffusion in binary mixtures is addressed. In paragraph 2.3, an analysis of diffusion phenomena in multicomponent mixtures is instead performed and different diffusion models are proposed.

2.2 Diffusion mass fluxes in binary mixtures

The common way of estimating diffusion mass fluxes in binary mixture is adopting the *Fick's law* [16]. In a binary mixture, the diffusion mass flux is proportional to the gradient of the selected species via a diffusion coefficient between the two concerned chemical species[2]. In a mixture of species a and b the diffusion mass flux of the a species is therefore given by

$$\vec{j}_a = -\rho D_{ab} \nabla Y_a \tag{2.24}$$

and that of the b species

$$\vec{j}_b = -\rho D_{ba} \nabla Y_b \tag{2.25}$$

The equality of D_{ab} and D_{ba} allows verifying the condition (2.18). Indeed, the diffusion coefficients introduced in the Eqs. (2.24) and (2.25) are the actual

[2]Mechanical diffusion induced by pressure or selective external forces and thermal diffusion (Soret effect) are neglected

binary diffusion coefficient of the pair a b. This coefficient can be estimated by appropriate experiments or theoretically. For ideal gases, for instance, the Chapman and Enskog correlation is often adopted, based on kinetic theory of gases [17]. The overall mass flux of the a species, defined as

$$\vec{\dot{m}''}_a = \rho_a \vec{U}_a = Y_a \rho \left(\vec{U}_m + \vec{U}_{da} \right) \tag{2.26}$$

consists of the diffusion term and the term of entrainment due to average mixture motion

$$\vec{\dot{m}''}_a = \underbrace{Y_a \vec{\dot{m}''}}_{entrainment} + \underbrace{\vec{j}_a}_{diffusion} = Y_a \sum_{k=a,b} \vec{\dot{m}''}_k + \vec{j}_a \tag{2.27}$$

An analogous reasoning can be formulated in terms of diffusion molar fraction and molar fluxes. Similarly to diffusion mass fluxes, the diffusion molar fluxes of the a species is defined by

$$\vec{j}_a^* = -CD_{ab} \nabla X_a \tag{2.28}$$

and that of the b species

$$\vec{j}_b^* = -CD_{ba} \nabla X_b \tag{2.29}$$

The corresponding molar flux for the a species is given by

$$\vec{\dot{n}''}_a = X_a \vec{\dot{n}''} + \vec{j}_a = X_a \sum_{k=a,b} \vec{\dot{n}''}_k + \vec{j}_a^* \tag{2.30}$$

In multicomponent mixtures we deal with the difficult task to propose a correlation for mass diffusion coefficients. Two main solutions are advisable: a simple solution based on the effective binary diffusion approximation; a second, more complicated method consisting in a full multicomponent diffusion model developed on the basis of the principles of irreversible thermodynamics.

In the following paragraph 2.3, an accurate description of the more sophisticated full multicomponent diffusion theory is provided. The alternative and simpler effective binary diffusion approximation method will be detailed later in paragraph 2.4.

2.3 Full multicomponent diffusion matrix model

In this paragraph, the development of a diffusion model for multicomponent mixture is detailed. The model is developed based on the first principles of the irreversible thermodynamics. Molecular diffusion is in fact one of the irreversible processes responsible of entropy production.

The outline of the present paragraph are illustrated in the following.

Basing on the estimation of the entropy generation rate, general formulations are proposed in paragraph 2.3.1 for the diffusion mass fluxes of the different species and the heat flux;

The diffusion mass fluxes can be also expressed in the form of a *generalized Fick's law* for multicomponent mixtures, as shown in paragraph 2.3.2. The formulation of the diffusion mass fluxes proposed by the *generalized Fick's law* is very attractive, however the knowledge of the *multicomponent mass transfer coefficients* is required;

In this aim, in the paragraphs 2.3.3 and 2.3.4 it is shown how, for ideal gases, the *multicomponent mass transfer coefficients* can be estimated on the basis of the actual binary diffusion coefficient of a pair of gases in a pure binary mixture. For this purpose, a technique for inverting the *generalized Fick's law* to obtain the *Maxwell-Stefan equations* is presented in paragraph 2.3.3. The correlations that link the *multicomponent mass transfer coefficients* adopted in the *generalized Fick's law* and the multicomponent *Maxwell-Stefan diffusion coefficients* are therefore detailed in paragraph 2.3.4. Since the *Maxwell-Stefan diffusion coefficients* in a mixture of ideal gases are equal to the *actual binary diffusion coefficient* in a pure binary mixture [18], the *multicomponent mass transfer coefficients* adopted in the *generalized Fick's law* can be finally expressed as a function of known quantities.

An analysis of the driving forces promoting the diffusion phenomena is therefore proposed in paragraph 2.3.5 and the final formulation for the driving force in ideal gas mixtures is presented in paragraph 2.3.6. Finally, the correlations defining the *multicomponent diffusion mass fluxes* in mixtures of ideal gases are obtained.

2.3.1 The generalized formulation of irreversible thermodynamics

The most general formulation of the diffusion flux can be obtained on the basis of irreversible thermodynamics. The aim of the irreversible thermodynamics is the extension of the classical thermodynamics to include systems in which irreversible phenomena occur. The main hypothesis at the basis of the theory is that for system *not too far from equilibrium conditions* the postulate of *local equilibrium* of the classical thermodynamics can be extended to irreversible processes in which *departures from local equilibrium are sufficiently small that all thermodynamic state quantities may be defined locally by the same relations as for system at equilibrium* [15]. In addition to the latter principle, known as *quasi equilibrium postulate*, and those of equilibrium thermodynamics, the irreversible thermodynamics makes use of three further postulates listed below [14]:

- *linearity postulate*: all fluxes in the system may be written as linear relations involving all the forces;
- *Curie's postulate*: no coupling of fluxes or forces occurs if the difference in tensorial order of flux and force is an odd number;
- *Onsager's reciprocal relations*: in absence of magnetic field the matrix of phenomenological coefficients in the flux-force relations is symmetric.

The meaning of these postulates will be clarified later in the chapter, when they are recalled.

The basis for the development of a formulation for diffusion mass fluxes in multicomponent mixtures is the entropy balance equation. The entropy balance equation of a non reacting system can be written as [19]

$$\rho \frac{Ds}{Dt} = -\nabla \cdot \vec{\sigma} + G_s \tag{2.31}$$

where s is the specific entropy, $\vec{\sigma}$ is the entropy-flux vector and G_s is the rate of entropy production per unit volume.

Based on the *quasi-equilibrium postulate*, the equation

$$d\hat{u} = Tds - Pd\hat{v} + \sum_{i=1}^{n} \hat{g}_i dY_i \tag{2.32}$$

where the internal energy $\hat{u}$, the mass specific volume $\hat{v}$ and the partial Gibbs specific enthalpy $\hat{g}_i$ have been introduced, can be extended to systems not far from equilibrium in which diffusion phenomena occur. In particular, this relation can be applied to a fluid element in motion with a velocity $\vec{U}_m$. Changing the differentials with material derivatives we get

$$\frac{D\hat{u}}{Dt} = T\frac{Ds}{Dt} - P\frac{D\hat{v}}{Dt} + \sum_{i=1}^{n} \hat{g}_i \frac{DY_i}{Dt} \tag{2.33}$$

from which the material derivative of entropy can be resumed to be substituted in the entropy balance equation

$$\frac{Ds}{Dt} = \frac{1}{T}\Big[\frac{D\hat{u}}{Dt} + P\frac{D\hat{v}}{Dt} - \sum_{i=1}^{n} \hat{g}_i \frac{DY_i}{Dt}\Big] \tag{2.34}$$

The entropy balance of Eq. (2.31) can be thus changed to

$$\frac{\rho}{T}\Big[\frac{D\hat{u}}{Dt} + P\frac{D\hat{v}}{Dt} - \sum_{i=1}^{n} \hat{g}_i \frac{DY_i}{Dt}\Big] = -\nabla \cdot \vec{\sigma} + G_s \tag{2.35}$$

The material derivative are substituted according to the three following relationship based on the conservation equations:

- the material derivative of the specific volume.

$$\frac{D\hat{v}}{Dt} = -\frac{1}{\rho^2}\frac{D\rho}{Dt} = \frac{1}{\rho}\left(\nabla \cdot \vec{U}_m\right) = \hat{v}\left(\nabla \cdot \vec{U}_m\right) \tag{2.36}$$

- the material derivative of the species mass fraction, obtained by substituting the mixture continuity equation in the species equation

$$\frac{DY_i}{Dt} = -\frac{1}{\rho}\Big[\nabla \cdot \vec{j}_i - S_i\Big] \tag{2.37}$$

- the material derivative of the internal energy [14]

$$\frac{D\hat{u}}{Dt} = -\frac{1}{\rho}\Big[\nabla \cdot \vec{\dot{q}''} + \vec{\vec{\pi}} : \nabla\vec{U}_m - \sum_{i=1}^{n} \vec{j}_i \cdot \vec{f}_i\Big] \tag{2.38}$$

  where $-\vec{\vec{\pi}}$ is the Cauchy tensor and the terms $\vec{f}_i$ are the specific body forces per unit mass. The Cauchy tensor is defined as

$$-\vec{\vec{\pi}} = \vec{\vec{\tau}} - P\mathbb{I} \tag{2.39}$$

  with

$$\vec{\vec{\tau}} = \mu\left(\nabla\vec{U}_m + \nabla^T\vec{U}_m\right) - \frac{2}{3}\mu\left(\nabla \cdot \vec{U}_m\right)[\mathbb{I}] \tag{2.40}$$

The balance equation of entropy can thus be rewritten as

$$\begin{aligned}\frac{1}{T}\Big[-\nabla\cdot\vec{\dot{q}''}-\vec{\vec{\pi}}:\nabla\vec{U}_m \quad &+P\left(\nabla\cdot\vec{U}_m\right)+\sum_{i=1}^{n}\hat{g}_i\nabla\cdot\vec{j}_i \\ &-\sum_{i=1}^{n}\hat{g}_iS_i+\sum_{i=1}^{n}\vec{j}_i\cdot\vec{f}_i\Big]=-\nabla\cdot\vec{\sigma}+G_s\end{aligned} \tag{2.41}$$

Making use of the following relationships

$$\frac{1}{T}\nabla\cdot\vec{\dot{q}''}=\nabla\cdot\left(\vec{\dot{q}''}\frac{1}{T}\right)+\vec{\dot{q}''}\cdot\left(\nabla T\frac{1}{T^2}\right) \tag{2.42}$$

$$\frac{\hat{g}_i}{T}\nabla\cdot\vec{j}_i=\nabla\cdot\left(\vec{j}_i\frac{\hat{g}_i}{T}\right)-\vec{j}_i\cdot\nabla\frac{\hat{g}_i}{T} \tag{2.43}$$

$$\begin{aligned}-\pi:\nabla\vec{U}_m+P\left(\nabla\cdot\vec{U}_m\right) \quad &=+\vec{\vec{\tau}}:\nabla\vec{U}_m \\ &-P[\mathbb{I}]:\nabla\vec{U}_m+P\left(\nabla\cdot\vec{U}_m\right)=+\vec{\vec{\tau}}:\nabla\vec{U}_m\end{aligned} \tag{2.44}$$

a further modification of Eq. (2.41) is possible separating flux vector terms and volumetric source terms

$$\begin{aligned}-\nabla\cdot\Big[\frac{\vec{\dot{q}''}}{T}-\sum_{i=1}^{n}\frac{\hat{g}_i\vec{j}_j}{T}\Big] \quad &+\Big[-\vec{\dot{q}''}\cdot\frac{\nabla T}{T^2}+\frac{1}{T}\left(\vec{\vec{\tau}}:\nabla\vec{U}_m\right) \\ &-\frac{1}{T}\sum_{i=1}^{n}\hat{g}_iS_i-\sum_{i=1}^{n}\vec{j}_i\cdot\Big[\nabla\frac{\hat{g}_i}{T}-\frac{\vec{f}_i}{T}\Big]\Big]=-\nabla\cdot\vec{\sigma}+G_s\end{aligned} \tag{2.45}$$

The analogy between the left and the right members of Eq. (2.45) suggests concluding that

$$\vec{\sigma}=\frac{1}{T}\Big[\vec{\dot{q}''}-\sum_{i=1}^{n}\hat{g}_i\vec{j}_i\Big] \tag{2.46}$$

$$G_s=-\vec{\dot{q}''}\cdot\frac{\nabla T}{T^2}+\frac{1}{T}\left(\vec{\vec{\tau}}:\nabla\vec{U}_m\right)-\frac{1}{T}\sum_{i=1}^{n}\hat{g}_iS_i-\sum_{i=1}^{n}\vec{j}_i\cdot\Big[\nabla\frac{\hat{g}_i}{T}-\frac{\vec{f}_i}{T}\Big] \tag{2.47}$$

Moreover, the heat flux $\vec{\dot{q}''}$ can be split into two terms

$$\vec{\dot{q}''}=\vec{\dot{q}''}_{\hbar}+\sum_{i=1}^{n}\hbar_i\vec{j}_i \tag{2.48}$$

isolating the interdiffusional convection term (the second one) from the overall heat transfer. The entropy generation rate can therefore be expressed as

$$G_s=\frac{1}{T}\big[-\vec{\dot{q}''}_{\hbar}\cdot\nabla\ln T+\vec{\vec{\tau}}:\nabla\vec{U}_m-\sum_{i=1}^{n}\hat{g}_iS_i-\sum_{i=1}^{n}\vec{j}_i\cdot\frac{CRT}{\rho_i}\mathbf{d}_i\big] \tag{2.49}$$

where the *generalized driving force* $\mathbf{d}_i$ has been introduced by

$$\frac{CRT}{\rho_i}\mathbf{d}_i=T\nabla\frac{\hat{g}_i}{T}-\vec{f}_i+\hbar_i\nabla\ln T \tag{2.50}$$

The entropy generation rate is therefore given by the product of the different fluxes and the corresponding driving forces:

- entropy production by heat transfer

$$\frac{1}{T}\left[-\dot{\vec{q}}''_{\hbar}\cdot\nabla\ln T\right] \tag{2.51}$$

- entropy production by viscous dissipation

$$\frac{1}{T}\left[+\vec{\bar{\tau}}:\nabla\vec{U}_m\right] \tag{2.52}$$

- entropy production associated to volumetric source terms of the involved chemical species

$$\frac{1}{T}\left[-\sum_{i=1}^{n}\hat{g}_i S_i\right] \tag{2.53}$$

- entropy production by molecular diffusion

$$\frac{1}{T}\left[-\sum_{i=1}^{n}\vec{j}_i\cdot\frac{CRT}{\rho_i}\mathbf{d}_i\right] \tag{2.54}$$

In particular, the entropy production by molecular diffusion is given by the product of the diffusion mass fluxes $\vec{j}_i$ and the corresponding diffusion *generalized driving force* $\mathbf{d}_i$. Moreover, since $\sum_{i=1}^{n}\vec{j}_i = 0$ every arbitrary vector added to the diffusion driving force expressed by Eq. (2.50) will not change the diffusion entropy production term. The vector we add is

$$-\frac{\nabla P}{\rho}+\sum_{k=1}^{n}Y_k\vec{f}_k \tag{2.55}$$

which is a vanishing vector under steady mechanical equilibrium conditions, that is, the pressure gradients are balanced by external body forces. The complete formulation of the diffusion *generalized driving force* $\mathbf{d}_i$ is therefore obtained by

$$\frac{CRT}{\rho_i}\mathbf{d}_i = T\nabla\frac{\hat{g}_i}{T}-\vec{f}_i+\hbar_i\nabla\ln T-\frac{\nabla P}{\rho}+\sum_{k=1}^{n}Y_k\vec{f}_k \tag{2.56}$$

and the following properties can be found satisfied

$$\sum_{i=1}^{n}\mathbf{d}_i = 0 \tag{2.57}$$

In fact, in multicomponent mixtures, the Gibbs-Duhem equation can be written as follows [20]

$$\sum_{i=1}^{n} \rho_i \nabla \frac{\hat{g}_i}{T} - \frac{\nabla P}{T} + \sum_{i=1}^{n} \rho_i \hbar_i \frac{\nabla \ln T}{T} = 0 \tag{2.58}$$

Multiplying Eq. (2.56) times ρ_i and summing the n driving forces we get

$$\sum_{i=1}^{n} CRT\mathbf{d}_i = \sum_{i=1}^{n} \rho_i T \nabla \frac{\hat{g}_i}{T} - \sum_{i=1}^{n} \rho_i \vec{f}_i + \sum_{i=1}^{n} \rho_i \hbar_i \nabla \ln T - \sum_{i=1}^{n} \rho_i \frac{\nabla P}{\rho} + \sum_{i=1}^{n} \rho_i \sum_{k=1}^{n} Y_k \vec{f}_k \tag{2.59}$$

Due to the Gibbs-Duhem equation

$$\sum_{i=1}^{n} \rho_i T \nabla \frac{\hat{g}_i}{T} - \nabla P + \sum_{i=1}^{n} \rho_i \hbar_i \nabla \ln T = 0 \tag{2.60}$$

Moreover, it is

$$\sum_{i=1}^{n} \rho_i \vec{f}_i = \sum_{i=1}^{n} \rho_i \sum_{k=1}^{n} Y_k \vec{f}_k \tag{2.61}$$

and therefore we can conclude

$$\sum_{i=1}^{n} CRT\mathbf{d}_i = 0 \tag{2.62}$$

Due to the *linearity postulate* each flux can be expressed as a linear function of the different driving forces involved in the process of entropy production. However, according to *Curie's postulate*, only driving forces having a tensorial order that differs of an even number with the considered flux are concerned. The heat flux $\vec{q}''_{\hbar}$ and the n diffusion mass fluxes $\vec{j}_i$ are therefore linearly depending on ∇T and the n diffusion driving forces $\mathbf{d}_i$

$$\vec{q}''_{\hbar} = -a_{00} \nabla \ln T - \sum_{k=1}^{n} a_{0k} \frac{CRT}{\rho_k} \mathbf{d}_k \tag{2.63}$$

$$\vec{j}_i = -a_{i0} \nabla \ln T - \sum_{k=1}^{n} a_{ik} \frac{CRT}{\rho_k} \mathbf{d}_k \quad \forall i = 1, ..., n \tag{2.64}$$

where the *phenomenological coefficients* a_{00}, a_{i0}, a_{0k}, a_{ik} have been introduced, which, according to the *Onsager's reciprocal relations* are found to satisfy the relationship $a_{i0} = a_{0i}$ and $a_{ik} = a_{ki}$. Moreover, the same coefficients satisfy the relation

$$\sum_{k=1}^{n} a_{ik} = 0 \tag{2.65}$$

In fact, let us define a modified driving force Q_k by

$$Q_k = \frac{CRT}{\rho_k}\mathbf{d}_k \tag{2.66}$$

then, Eq. (2.64) can be rewritten as

$$\vec{j}_i = -a_{i0}\nabla \ln T - \sum_{k=1}^{n} a_{ik}Q_k \tag{2.67}$$

that becomes

$$\vec{j}_i = -a_{i0}\nabla \ln T - \sum_{\substack{k=1\\k\neq j}}^{n} a_{ik}Q_k - a_{ij}Q_j \tag{2.68}$$

when the j-th term is extracted from the summation. Since it must be

$$\sum_{i=1}^{n} \vec{j}_i = 0 \tag{2.69}$$

it follows that

$$\sum_{i=1}^{n} \vec{j}_i = -\sum_{i=1}^{n} a_{i0}\nabla \ln T - \sum_{i=1}^{n} a_{ij}Q_j - \sum_{i=1}^{n}\sum_{\substack{k=1\\k\neq j}}^{n} a_{ik}Q_k = 0 \tag{2.70}$$

Nevertheless, as a consequence of Eq. (2.69), the following relationship is also satisfied

$$\sum_{i=1}^{n} \vec{j}_i \cdot Q_i = \sum_{i=1}^{n} \vec{j}_i \cdot (Q_i - Q_j) \tag{2.71}$$

and according to the *linearity postulate* and the *Curie's postulate*, the diffusion mass flux could also be expressed by

$$\vec{j}_i = -a_{i0}\nabla \ln T - \sum_{\substack{k=1\\k\neq j}}^{n} a_{ik}\,(Q_k - Q_j) \tag{2.72}$$

In this case, summing the n diffusion mass fluxes, we get

$$\sum_{i=1}^{n} \vec{j}_i = -\sum_{i=1}^{n} a_{i0}\nabla \ln T - \sum_{i=1}^{n}\sum_{\substack{k=1\\k\neq j}}^{n} a_{ik}\,(Q_k - Q_j) = 0 \tag{2.73}$$

Subtracting Eq. (2.73) to Eq. (2.70), the following equivalence is obtained

$$-\sum_{i=1}^{n} a_{ij}Q_j - \sum_{i=1}^{n}\sum_{\substack{k=1\\k\neq j}}^{n} a_{ik}Q_k = -\sum_{i=1}^{n}\sum_{\substack{k=1\\k\neq j}}^{n} a_{ik}\,(Q_k - Q_j) \tag{2.74}$$

that is

$$-\sum_{i=1}^{n} a_{ij} = \sum_{i=1}^{n}\sum_{\substack{k=1\\k\neq j}}^{n} a_{ik} \tag{2.75}$$

Eq. (2.75) is satisfied if

$$-a_{ij} = \sum_{\substack{k=1\\k\neq j}}^{n} a_{ik} \tag{2.76}$$

that means

$$\sum_{k=1}^{n} a_{ik} = 0 \tag{2.77}$$

and, as a consequence

$$\sum_{k=1}^{n} a_{i0} = 0 \tag{2.78}$$

In fact, summing the n diffusion mass fluxes represented in the form of Eq. (2.67), we get

$$\sum_{i=1}^{n} \vec{j}_i = -\sum_{i=1}^{n} a_{i0} \nabla \ln T - \sum_{i=1}^{n} \sum_{k=1}^{n} a_{ik} Q_k = 0 \tag{2.79}$$

that is

$$\sum_{i=1}^{n} \vec{j}_i = -\sum_{i=1}^{n} a_{i0} \nabla \ln T - \sum_{k=1}^{n} Q_k \sum_{i=1}^{n} a_{ik} = 0 \tag{2.80}$$

Finally, substituting Eq. (2.77) in Eq. (2.80), we get

$$\sum_{i=1}^{n} a_{i0} = 0 \tag{2.81}$$

The diffusion mass fluxes and the heat flux given respectively by Eqs. (2.64) and Eq. (2.63) are therefore known once the phenomenological coefficients will be known. For practical purpose, however, as detailed in the following paragraph, Eqs. (2.64) and Eq. (2.63) are usually turned to obtain the so called *generalized Fick's law*, where the phenomenological coefficients will be replaced by the *multicomponent mass transfer coefficients*.

2.3.2 The generalized Fick's law

The a_{i0} phenomenological coefficients are usually called *thermal diffusion coefficients* and are usually written as D_i^T, for which the following property is obviously applicable

$$\sum_{i=1}^{n} D_i^T = 0 \tag{2.82}$$

Similarly, an interesting choice consists in defining the *multicomponent mass*

transfer coefficients as[3]

$$\mathbb{D}_{ij} = \frac{CRTa_{ij}}{\rho\ \rho_j} \tag{2.89}$$

for which the following properties are found to be applicable:

$$\mathbb{D}_{ij}Y_j = \frac{CRT}{\rho\ \rho_j}a_{ij}Y_j = \frac{CRT}{\rho\ \rho_i}a_{ji}Y_i = \mathbb{D}_{ji}Y_i \tag{2.90}$$

and

$$\sum_{i=1}^{n}\mathbb{D}_{ij} = \sum_{i=1}^{n}\frac{CRT}{\rho\ \rho_j}a_{ij} = \frac{CRT}{\rho\ \rho_j}\sum_{i=1}^{n}a_{ij} = 0 \tag{2.91}$$

or

$$\sum_{j=1}^{n}\mathbb{D}_{ij}Y_j = \sum_{j=1}^{n}\frac{CRT}{\rho\ \rho_j}a_{ij}Y_j = \frac{CRT}{\rho^2}\sum_{j=1}^{n}a_{ij} = 0 \tag{2.92}$$

In fact, substituting the terms 2.89 in Eqs. (2.64), the diffusion mass fluxes can be written as[4]

$$\vec{j}_i = -\rho\sum_{j=1}^{n}\mathbb{D}_{ij}\mathbf{d}_j - D_i^T\nabla\ln T \tag{2.95}$$

[3]Similar choices were proposed by Curtiss and Hirschfelder [21] and Curtiss [22]. In the first work [21] the so called *Zero-Diagonal-Diffusivity-Definition* (ZD) was proposed, where the multicomponent diffusion coefficients given by

$$\mathbb{D}_{ij}^{ZD} = \frac{CRT}{\rho}\left(\frac{a_{ij}}{\rho_j} + \sum_{\substack{k=1\\k\neq i}}^{n}\frac{a_{ik}}{\rho_i}\right) \tag{2.83}$$

for which the following properties are applied

$$\mathbb{D}_{ii}^{ZD} = 0 \tag{2.84}$$

$$\sum_{i=1}^{n}\left(\mathbb{D}_{ij}^{ZD} - \mathbb{D}_{ik}^{ZD}\right) = 0 \tag{2.85}$$

The *Symmetric-Definition* (SD) is instead introduced in the second work [22], where the diffusion coefficients are defined as

$$\mathbb{D}_{ij}^{SD} = \frac{CRTa_{ij}}{\rho_i\ \rho_j} \tag{2.86}$$

for which the following properties are applied

$$\mathbb{D}_{ij}^{SD} = \mathbb{D}_{ji}^{SD} \tag{2.87}$$

$$\sum_{i=1}^{n}Y_i\mathbb{D}_{ij}^{SD} = 0 \tag{2.88}$$

[4]Alternatively, adopting the *Zero-Diagonal-Diffusivity-Definition* (see Eq. (2.83)) we would have

$$\vec{j}_i = -\rho\sum_{j=1}^{n}\mathbb{D}_{ij}^{ZD}\mathbf{d}_j - D_i^T\nabla\ln T \tag{2.93}$$

where we would avoid that the diagonal terms $\mathbb{D}_{ii}^{ZD}$ of the matrix are zero. On the other hand, adopting the *Symmetric-Definition* (see Eq. (2.86)) we would have

$$\vec{j}_i = -Y_i\rho\sum_{j=1}^{n}\mathbb{D}_{ij}^{SD}\mathbf{d}_j - D_i^T\nabla\ln T \tag{2.94}$$

where we would avoid the presence of the mass fraction of the i-th species multiplying the diffusion mass fluxes $\rho\sum_{j=1}^{n}\mathbb{D}_{ij}^{SD}\mathbf{d}_j$.

also known as *generalized Fick's law*, that, as proposed by Taylor and Khristna [15], can be written in a usefull matrix form as

$$\mathbf{j} = -\rho\ [\mathbb{D}]\mathbf{d} - \mathbf{D}^T \nabla \ln T \tag{2.96}$$

where $\mathbf{j}$ is the vector of the diffusion mass fluxes $\vec{j}_i$ and $\mathbf{d}$ is the vector of the driving forces

$$\mathbf{j} = (\vec{j}_1, \vec{j}_2, \vec{j}_3, ..., \vec{j}_n) \tag{2.97}$$

$$\mathbf{d} = (\mathbf{d}_1, \mathbf{d}_2, \mathbf{d}_3, ..., \mathbf{d}_n) \tag{2.98}$$

The vector $\mathbf{D}^T$ is the thermal diffusion coefficients vector

$$\mathbf{D}^T = (D_1^T, D_2^T, D_3^T, ..., D_n^T) \tag{2.99}$$

The *multicomponent mass transfer coefficient matrix* $[\mathbb{D}]$ is instead given by

$$[\mathbb{D}] = \begin{pmatrix} \mathbb{D}_{11} & \mathbb{D}_{12} & \dots & \mathbb{D}_{1n} \\ \mathbb{D}_{21} & \mathbb{D}_{22} & \dots & \mathbb{D}_{2n} \\ \vdots & \vdots & \ddots & \vdots \\ \mathbb{D}_{n1} & \mathbb{D}_{n2} & \dots & \mathbb{D}_{nn} \end{pmatrix} \tag{2.100}$$

Once the $\mathbb{D}_{ij}$ are known, the generalized Fick's law will allow calculating the diffusion mass fluxes.

The estimation of these coefficients can be experimental. However, in some particular cases, a formulation can be found, correlating the multicomponent mass transfer coefficients to the actual binary diffusion coefficient of two species in a pure binary mixture. In the next paragraphs 2.3.3 and 2.3.4 it will be shown how to do that.

2.3.3 The generalized Maxwell-Stefan equations

In this paragraph, a technique for inverting the *generalized Fick's law* to obtain the *Maxwell-Stefan equations* is presented[5] In this aim, further diffusion coefficients are introduced, known as *Maxwell-Stefan diffusion coefficients* $\mathcal{D}_{ik}$. Let us define a modified diffusion velocity $\vec{U}_i^\dagger$ as

$$\vec{U}_i^\dagger = \frac{\vec{j}_i + D_i^T \nabla \ln T}{\rho_i} = -\frac{\rho}{\rho_i} \sum_{j=1}^{n} \mathbb{D}_{ij} \mathbf{d}_j \tag{2.101}$$

The same modified diffusion velocity can be written for the k species and subtracted to the previous Eq. (2.101), multiplied by $X_i X_k / \mathcal{D}_{ik}$, to obtain

$$\frac{X_i X_k}{\mathcal{D}_{ik}} \left(\vec{U}_i^\dagger - \vec{U}_k^\dagger \right) = -\frac{X_i X_k}{\mathcal{D}_{ik}} \sum_{j=1}^{n} \left(\frac{\mathbb{D}_{ij}}{Y_i} - \frac{\mathbb{D}_{kj}}{Y_k} \right) \mathbf{d}_j \tag{2.102}$$

Next, the sum on k is performed

$$\sum_{\substack{k=1 \\ k \neq i}}^{n} \frac{X_i X_k}{\mathcal{D}_{ik}} \left(\vec{U}_i^\dagger - \vec{U}_k^\dagger \right) = -\sum_{\substack{k=1 \\ k \neq i}}^{n} \frac{X_i X_k}{\mathcal{D}_{ik}} \sum_{j=1}^{n} \left(\frac{\mathbb{D}_{ij}}{Y_i} - \frac{\mathbb{D}_{kj}}{Y_k} \right) \mathbf{d}_j \tag{2.103}$$

[5] This technique is inspired by the work Merk [23], where the *Zero-Diagonal-Diffusivity-Definition* (see Eq. (2.83)) was adopted

that can be turned to

$$\sum_{\substack{k=1\\k\neq i}}^{n} \frac{X_i X_k}{\mathcal{D}_{ik}} \left(\vec{U}_i^{\dagger} - \vec{U}_k^{\dagger}\right) = -\sum_{j=1}^{n} \sum_{\substack{k=1\\k\neq i}}^{n} \frac{X_i X_k}{\mathcal{D}_{ik}} \left(\frac{\mathbb{D}_{ij}}{Y_i} - \frac{\mathbb{D}_{kj}}{Y_k}\right) \mathbf{d}_j \tag{2.104}$$

It will be assumed that

$$\sum_{\substack{k=1\\k\neq i}}^{n} \frac{X_i X_k}{\mathcal{D}_{ik}} \left(\frac{\mathbb{D}_{ij}}{Y_i} - \frac{\mathbb{D}_{kj}}{Y_k}\right) = -\delta_{ij} + Y_i \tag{2.105}$$

In Eq. (2.105) it is assumed tentatively that

$$\sum_{\substack{k=1\\k\neq i}}^{n} \frac{X_i X_k}{\mathcal{D}_{ik}} \left(\frac{\mathbb{D}_{ij}}{Y_i} - \frac{\mathbb{D}_{kj}}{Y_k}\right) = -\delta_{ij} - Y_i \tag{2.106}$$

Indeed, it can be verified that the one proposed is a possible solution. Multiplying both terms times Y_j and summing on the j terms we get

$$\sum_{j=1}^{n} \sum_{\substack{k=1\\k\neq i}}^{n} \frac{X_i X_k}{\mathcal{D}_{ik}} \left(Y_j \frac{\mathbb{D}_{ij}}{Y_i} - Y_j \frac{\mathbb{D}_{kj}}{Y_k}\right) = \sum_{j=1}^{n} \left(-\delta_{ij} Y_j + Y_i Y_j\right) \tag{2.107}$$

that gives

$$\sum_{\substack{k=1\\k\neq i}}^{n} \frac{X_i X_k}{\mathcal{D}_{ik}} \sum_{j=1}^{n} \left(Y_j \frac{\mathbb{D}_{ij}}{Y_i} - Y_j \frac{\mathbb{D}_{kj}}{Y_k}\right) = 0 \tag{2.108}$$

thanks to Eq. (2.92) the identity $0 = 0$ is thus satisfied.

therefore obtaining

$$\sum_{\substack{k=1\\k\neq i}}^{n} \frac{X_i X_k}{\mathcal{D}_{ik}} \left(\vec{U}_i^{\dagger} - \vec{U}_k^{\dagger}\right) = -\sum_{j=1}^{n} \left(-\delta_{ij} + Y_i\right) \mathbf{d}_j \tag{2.109}$$

Since the n driving forces sum to zero, we get finally

$$\sum_{\substack{k=1\\k\neq i}}^{n} \frac{X_i X_k}{\mathcal{D}_{ik}} \left(\vec{U}_i^{\dagger} - \vec{U}_k^{\dagger}\right) = \mathbf{d}_i \tag{2.110}$$

Substituting the definition of modified diffusion velocity 2.101 into Eq. (2.110), the *Maxwell-Stefan generalized equations* are obtained.

$$\sum_{\substack{k=1\\k\neq i}}^{n} \frac{X_i X_k}{\mathcal{D}_{ik}} \left(\frac{\vec{j}_k}{\rho_k} - \frac{\vec{j}_i}{\rho_i}\right) = \mathbf{d}_i - \sum_{\substack{k=1\\k\neq i}}^{n} \frac{X_i X_k}{\mathcal{D}_{ik}} \left(\frac{D_k^T}{\rho_k} - \frac{D_i^T}{\rho_i}\right) \nabla \ln T \tag{2.111}$$

2.3.4 The multicomponent mass transfer coefficients

The previous Eqs. (2.95) and (2.111) represent the two most important formulation for the mass flux relations in multicomponent mixtures. The two formulations propose a different point of view of the same phenomenon, as shown in the previous paragraph 2.3.3.

Which is the best formulation, it depends on the context. For instance, the *generalized Fick's law* is more suitable for our purposes; however the *multicomponent mass transfer coefficient* of Eq. (2.95) are composition dependent and relies on the definition of the *phenomenological coefficients*.

In this paragraph, the common root of the two models will be put in evidence by proposing a correlation that links the *multicomponent mass transfer coefficients* adopted in the *generalized Fick's law* to the *Maxwell-Stefan diffusion coefficients*. Since the Maxwell-Stefan coefficients, in some cases, can be easily correlated to the actual binary diffusion coefficients, a method is here developed to express the multicomponent mass transfer coefficient as a function of the mixture composition and the actual binary diffusion coefficients. In particular, in mixtures of ideal gases, the Maxwell-Stefan diffusion coefficients are equal to the actual binary diffusion coefficient of a pair in a pure binary mixture:

$$\mathcal{D}_{ik} = D_{ik} \tag{2.112}$$

Indeed, once the correlation that links the *multicomponent mass transfer coefficients* to the *Maxwell-Stefan diffusion coefficients* is known, the generalized Fick's law will be usefully applicable.

Let us therefore consider a mixture of ideal gases and multiply Eq. (2.111) times the molar concentration and split the different terms to obtain

$$\begin{aligned} &\sum_{\substack{k=1\\k\neq i}}^{n} \frac{X_i \vec{j}_k}{D_{ik} M_k} - \sum_{\substack{k=1\\k\neq i}}^{n} \frac{X_k \vec{j}_i}{D_{ik} M_i} + \\ &\nabla \ln T \Big[\sum_{\substack{k=1\\k\neq i}}^{n} \frac{X_i D_k^T}{D_{ik} M_k} - \sum_{\substack{k=1\\k\neq i}}^{n} \frac{X_k D_i^T}{D_{ik} M_i} \Big] = C \mathbf{d}_i \end{aligned} \tag{2.113}$$

The different terms are then regrouped as follows

$$\sum_{\substack{k=1\\k\neq i}}^{n} \frac{X_i (\vec{j}_k + D_k^T \nabla \ln T)}{D_{ik} M_k} - \sum_{\substack{k=1\\k\neq i}}^{n} \frac{X_k (\vec{j}_i + D_i^T \nabla \ln T)}{D_{ik} M_i} = C \mathbf{d}_i \tag{2.114}$$

The n term is then extracted from the summation

$$\begin{aligned} &\sum_{\substack{k=1\\k\neq i}}^{n-1} \frac{X_i (\vec{j}_k + D_k^T \nabla \ln T)}{D_{ik} M_k} + \frac{X_i (\vec{j}_n + D_n^T \nabla \ln T)}{D_{in} M_n} - \\ &(\vec{j}_i + D_i^T \nabla \ln T) \sum_{\substack{k=1\\k\neq i}}^{n} \frac{X_k}{D_{ik} M_i} = C \mathbf{d}_i \end{aligned} \tag{2.115}$$

According to Eq. (2.18) and Eq. (2.78), the $\vec{j}_n$ and the D_n^T terms can be written as the sum of the other $n-1$ terms to obtain

$$\begin{aligned} &\sum_{\substack{k=1\\k\neq i}}^{n-1} \frac{X_i (\vec{j}_k + D_k^T \nabla \ln T)}{D_{ik} M_k} - \sum_{k=1}^{n-1} \frac{X_i (\vec{j}_k + D_k^T \nabla \ln T)}{D_{in} M_n} \\ &- \sum_{\substack{k=1\\k\neq i}}^{n} \frac{X_k (\vec{j}_i + D_i^T \nabla \ln T)}{D_{ik} M_i} = C \mathbf{d}_i \end{aligned} \tag{2.116}$$

and therefore, extracting the i-th term from the summation we get

$$\begin{aligned}&\sum_{\substack{k=1\\k\neq i}}^{n-1}\frac{X_i(\vec{j}_k+D_k^T\nabla\ln T)}{D_{ik}M_k}-\sum_{\substack{k=1\\k\neq i}}^{n-1}\frac{X_i(\vec{j}_k+D_k^T\nabla\ln T)}{D_{in}M_n}-\\&\frac{X_i(\vec{j}_i+D_i^T\nabla\ln T)}{D_{in}M_n}-\sum_{\substack{k=1\\k\neq i}}^{n}\frac{X_k(\vec{j}_i+D_i^T\nabla\ln T)}{D_{ik}M_i}=C\mathbf{d}_i\end{aligned}\tag{2.117}$$

Finally, the different terms are regrouped to obtain

$$\begin{aligned}&(\vec{j}_i+D_i^T\nabla\ln T)\Big[-\Big(\frac{X_i}{D_{in}M_n}+\sum_{\substack{k=1\\k\neq i}}^{n}\frac{X_k}{D_{ik}M_i}\Big)\Big]+\\&\sum_{\substack{k=1\\k\neq i}}^{n-1}(\vec{j}_k+D_k^T\nabla\ln T)\Big[X_i\Big(\frac{1}{D_{ik}M_k}-\frac{1}{D_{in}M_n}\Big)\Big]=C\mathbf{d}_i\end{aligned}\tag{2.118}$$

Once we define

$$A_{ii}=-M\Big(\frac{X_i}{D_{in}M_n}+\sum_{\substack{k=1\\k\neq i}}^{n}\frac{X_k}{D_{ik}M_i}\Big)\tag{2.119}$$

and

$$A_{ik}=X_iM\Big(\frac{1}{D_{ik}M_k}-\frac{1}{D_{in}M_n}\Big)\tag{2.120}$$

the diffusion mass flux can be written as

$$A_{ii}(\vec{j}_i+D_i^T\nabla\ln T)+\sum_{\substack{k=1\\k\neq i}}^{n-1}A_{ik}(\vec{j}_k+D_k^T\nabla\ln T)=\rho\mathbf{d}_i\tag{2.121}$$

that can be further rewritten in the useful matrix form as follows

$$[A]\ \Big(\ \mathbf{j}+\mathbf{D}^T\nabla\ln T\ \Big)=\rho\mathbf{d}\tag{2.122}$$

Multiplying times the inverse of the A matrix we finally obtain

$$\mathbf{j}=\rho\ [A]^{-1}\mathbf{d}-\mathbf{D}^T\nabla\ln T\tag{2.123}$$

It is therefore immediate to conclude that the *multicomponent mass transfer coefficient matrix* introduced in the *generalized Fick's law* (see Eq. (2.96)) can be estimated on the basis of the pure binary mixture coefficients by

$$[\mathbb{D}]=-[A]^{-1}\tag{2.124}$$

It is well remarked that, according to Eq. (2.124), since the terms A_{in} are zero and so are corresponding term of the inverse matrix $[A]^{-1}$, the n-th column of the diffusion matrix is also zero.

2.3.5 The generalized driving force

In this paragraph, the *generalized driving force* introduces by Eq. (2.56) is modified to obtain a more usefull formulation, which will be later specialized in paragraph 2.3.6 for the case of ideal gases.

In Eq. (2.56) the *generalized driving force* for diffusion phenomena was defined in the following form

$$CRT\mathbf{d}_i = \rho_i T\nabla\frac{\hat{g}_i}{T} - \rho_i\vec{f_i} + \rho_i\hbar_i\nabla\ln T - \rho_i\frac{\nabla P}{\rho} + \rho_i\sum_{k=1}^{n}Y_k\vec{f_k} \tag{2.125}$$

The quantities $\hat{g}_i$, $\hbar_i$ and P are functions of the state of the fluid components and can be described by the temperature, the pressure and a set of $n-1$ molar fractions, at each position and at each time. Let us define the activity a_i of a chemical species as

$$\hat{g}_i = \hat{g}_i^0 + \frac{RT}{M_i}\ln a_i \tag{2.126}$$

The quantity $\hat{g}_i^0$ is a function only of the temperature and it is defined at a standard state. The activity is a function of temperature, pressure and $n-1$ molar fractions. Basing on Eq. (2.126), the driving force can be rewritten as

$$CRT\mathbf{d}_i = C_iRT\nabla\ln a_i + \rho_i(\hbar_i - \hbar_i^0)\nabla\ln T - Y_i\nabla P - \rho_i\Big(\vec{f_i} - \sum_{k=1}^{n}Y_k\vec{f_k}\Big) \tag{2.127}$$

In fact, the terms $T\nabla\left(\frac{\hat{g}_i}{T}\right)$ in which Eq. (2.126) is hanged, becomes

$$\begin{aligned} T\nabla\left(\tfrac{\hat{g}_i}{T}\right) = T\nabla\left(\tfrac{\hat{g}_i^0}{T}\right) + \tfrac{RT}{M_i}\nabla\ln a_i \quad &= \nabla\hat{g}_i^0 - \hat{g}_i^0\nabla T + \tfrac{RT}{M_i}\nabla\ln a_i \\ &= -(Ts_i^0 + \hat{g}_i^0)\nabla\ln T + \tfrac{RT}{M_i}\nabla\ln a_i \\ &= -\hbar_i^0\nabla\ln T + \tfrac{RT}{M_i}\nabla\ln a_i \end{aligned} \tag{2.128}$$

where the relation

$$\begin{aligned} \nabla\hat{g}_i^0 = \tfrac{d\hat{g}_i^0}{dT}\nabla T \quad &= \tfrac{d(\hbar_i^0 - Ts_i^0)}{dT}\nabla T \\ &= \left[\tfrac{d\hat{u}_i^0}{dT} + \tfrac{d(P^0\hat{v}_i)}{dT} - T\tfrac{ds_i^0}{dT} - s_i^0\right]\nabla T \\ &= \left[T\tfrac{ds_i^0}{dt} - P^0\tfrac{d\hat{v}_i}{dt} + \tfrac{d(P^0\hat{v}_i)}{dT} - T\tfrac{ds_i^0}{dT} - s_i^0\right]\nabla T \\ &= \left[\hat{v}_i\tfrac{dp^0}{dT} - s_i^0\right]\nabla T \\ &= -s_i^0\nabla T \end{aligned} \tag{2.129}$$

has been introduced.

The Eq. (2.127) can be put in a different form by considering the activity a_i to be a function of temperature, pressure and $n-1$ species molar fractions. The term $C_iRT\nabla\ln a_i$ can be thus linearized as

$$\begin{aligned} C_iRT\nabla\ln a_i = C_iRT\textstyle\sum_{k=1}^{n-1}\left(\tfrac{\partial\ln a_i}{\partial X_k}\right)_{T,P,X\neq X_k}\nabla X_k \\ +C_iRT\left(\tfrac{\partial\ln a_i}{\partial P}\right)_{T,X}\nabla P + C_iRT\left(\tfrac{\partial\ln a_i}{\partial T}\right)_{P,X}\nabla T \end{aligned} \tag{2.130}$$

The partial derivative with respect to pressure and temperature are equal to

$$\frac{\partial \ln a_i}{\partial P} = \frac{M_i \hat{v}_i}{RT} \tag{2.131}$$

$$\begin{aligned}
\tfrac{\partial \ln a_i}{\partial P} &= \tfrac{M_i}{RT}\tfrac{\partial \hat{g}_i}{\partial P} = \tfrac{M_i}{RT}\tfrac{\partial(\hbar_i - T s_i)}{\partial P} \\
&= \tfrac{M_i}{RT}\tfrac{\partial(\hat{u}_i + P\hat{v}_i - T s_i)}{\partial P} \\
&= \tfrac{M_i}{RT}\left(T\tfrac{\partial s_i}{\partial P} - P\tfrac{\partial \hat{v}_i}{\partial P} + \hat{v}_i + P\tfrac{\partial \hat{v}_i}{\partial P} - T\tfrac{\partial s_i}{\partial P}\right) \\
&= \tfrac{M_i \hat{v}_i}{RT}
\end{aligned} \tag{2.132}$$

and

$$\frac{\partial \ln a_i}{\partial T} = -(\hbar_i - \hbar_i^0)\frac{M_i}{RT^2} \tag{2.133}$$

$$\begin{aligned}
\tfrac{\partial \ln a_i}{\partial T} &= \tfrac{M_i}{RT}\left[\tfrac{\partial \hat{g}_i - \hat{g}_i^0}{\partial T} - (\hat{g}_i - \hat{g}_i^0)\tfrac{\partial \ln T}{\partial T}\right] \\
&= \tfrac{M_i}{RT}\left[\tfrac{\partial \hat{g}_i - \hat{g}_i^0}{\partial T} - \tfrac{\hat{g}_i - \hat{g}_i^0}{T}\right] \\
&= \tfrac{M_i}{RT}\left[\tfrac{\partial \hbar_i}{\partial T} - T\tfrac{\partial s_i}{\partial T} - \tfrac{\partial \hbar_i^0}{\partial T} + T\tfrac{\partial s_i^0}{\partial T} - \tfrac{\hbar_i - \hbar_i^0}{T}\right] \\
&= \tfrac{M_i}{RT}\left[\tfrac{\partial \hat{u}_i}{\partial T} + \tfrac{\partial P\hat{v}_i}{\partial T} - T\tfrac{\partial s_i}{\partial T} - \tfrac{\partial \hat{u}_i^0}{\partial T} - \tfrac{\partial P\hat{v}_i^0}{\partial T} + T\tfrac{\partial s_i^0}{\partial T} - \tfrac{\hbar_i - \hbar_i^0}{T}\right] \\
&= -(\hbar_i - \hbar_i^0)\tfrac{M_i}{RT^2}
\end{aligned} \tag{2.134}$$

Substituting Eqs. (2.131) and (2.133) we finally get

$$\begin{aligned}
C_i RT\nabla \ln a_i = C_i RT \sum_{k=1}^{n-1}\left(\frac{\partial \ln a_i}{\partial X_k}\right)_{T,P,X\neq X_k}\nabla X_k \\
+C_i M_i \hat{v}_i \nabla P - C_i\left(\hbar_i - \hbar_i^0\right)\nabla \ln T
\end{aligned} \tag{2.135}$$

that can be substituted in Eq. (2.127) to obtain the final form of the *generalized driving force*

$$\begin{aligned}
CRT\mathbf{d}_i = C_i RT \sum_{k=1}^{n-1}\left(\frac{\partial \ln a_i}{\partial X_k}\right)_{T,P,X\neq X_k}\nabla X_k \\
+(C_i M_i \hat{v}_i - Y_i)\nabla P - \rho_i\left(\vec{f}_i - \sum_{k=1}^{n} Y_k \vec{f}_k\right)
\end{aligned} \tag{2.136}$$

2.3.6 The diffusion mass fluxes in mixtures of ideal gases

In mixtures of ideal gases, Eq. (2.136) can be further simplified. For ideal gases it is in fact [14]

$$\sum_{k=1}^{n-1}\left(\frac{\partial \ln a_i}{\partial X_k}\right)_{T,P,X\neq X_k}\nabla X_k = \nabla \ln X_i \tag{2.137}$$

Moreover, introducing the ideal gas equation of state

$$P = CRT \tag{2.138}$$

the driving force for a mixture of ideal gas can be finally written as

$$\mathbf{d}_i = \nabla X_i + (X_i - Y_i)\nabla \ln P - \frac{\rho_i}{P}\Big(\vec{f_i} - \sum_{k=1}^{n} Y_k \vec{f_k}\Big) \tag{2.139}$$

where the different contributions due to mechanical diffusion are recognized at the right hand member, from left to right: concentration diffusion, pressure diffusion and forced diffusion. The final formulation for the diffusion mass flux in a mixture of ideal gases is thus given by

$$\begin{aligned} A_{ii}(\vec{j_i} + D_i^T \nabla \ln T) \quad &+ \textstyle\sum_{k=1,k\neq i}^{n-1} A_{ik}(\vec{j_k} + D_k^T \nabla \ln T) \\ &= \rho\Big[\nabla X_i + (X_i - Y_i)\nabla \ln P - \tfrac{\rho_i}{P}\Big(\vec{f_i} - \textstyle\sum_{k=1}^{n} Y_k \vec{f_k}\Big)\Big] \end{aligned} \tag{2.140}$$

Whenever pressure and forced diffusion can be neglected, the simplified formulation written in matrix form is

$$[A]\ \Big(\ \mathbf{j} + \mathbf{D}^T \nabla \ln T\ \Big) = \rho \nabla \mathbf{X} \tag{2.141}$$

A finishing touch consist in expressing the molar fraction gradient as a function of the mass fraction gradients. This is relatively easy in ideal gases mixtures. For ideal gas mixture is in fact

$$\nabla X_i = -\Big[M\Big(\frac{X_i}{M_n} + \frac{1 - X_i}{M_i}\Big)\Big]\nabla Y_i - \sum_{\substack{k=1 \\ k\neq i}}^{n-1}\Big[X_i M\Big(\frac{1}{M_k} - \frac{1}{M_n}\Big)\Big]\nabla Y_k \tag{2.142}$$

Let us rewrite the steam mass fraction in the mixture as

$$Y_i = \frac{X_i M_i}{M} = \frac{X_i M_i}{\left(\sum_{k=1}^{n} Y_k / M_k\right)^{-1}} \tag{2.143}$$

The gradient of the mass fraction of the i species is given by

$$\nabla Y_i = \frac{M_i}{M}\nabla X_i + X_i M_i \sum_{k=1}^{n} \frac{\nabla Y_k}{M_k} \tag{2.144}$$

that can be turned to obtain

$$\nabla X_i = \frac{M}{M_i}\nabla Y_i - X_i M \sum_{k=1}^{n} \frac{\nabla Y_k}{M_k} \tag{2.145}$$

Next, we extract the n and the i species from summation

$$\nabla X_i = \frac{M}{M_i}\nabla Y_i - X_i M \left[\sum_{\substack{k=1 \\ k\neq i}}^{n-1} \frac{\nabla Y_k}{M_k} + \frac{\nabla Y_i}{M_i} + \frac{\nabla Y_n}{M_n}\right] \tag{2.146}$$

Since mass fractions sum to one, the gradients sum to zero; the ∇Y_n can be thus expressed as the sum of the previous $n-1$ mass fractions gradients

$$\nabla X_i = \frac{M}{M_i}\nabla Y_i - X_i M \left[\sum_{\substack{k=1 \\ k\neq i}}^{n-1} \frac{\nabla Y_k}{M_k} + \frac{\nabla Y_i}{M_i} - \frac{\sum_{k=1}^{n-1} \nabla Y_k}{M_n}\right] \tag{2.147}$$

Next the i species is extracted from summation

$$\nabla X_i = \frac{M}{M_i}\nabla Y_i - X_i M \left[\sum_{\substack{k=1 \\ k\neq i}}^{n-1} \frac{\nabla Y_k}{M_k} - \frac{\sum_{k=1}^{n-1} \nabla Y_k}{M_n} + \frac{\nabla Y_i}{M_i} - \frac{\nabla Y_i}{M_n}\right] \tag{2.148}$$

that can be rearranged to obtain Eq. 2.142

that in matrix form can be written as

$$\nabla \mathbf{X} = -[R]\nabla \mathbf{Y} \tag{2.149}$$

where the terms of the $[R]$ matrix are given by

$$R_{ii} = \left[M\left(\frac{X_i}{M_n} + \frac{1 - X_i}{M_i}\right)\right] \tag{2.150}$$

$$R_{ik} = \left[X_i M\left(\frac{1}{M_k} - \frac{1}{M_n}\right)\right] \tag{2.151}$$

The diffusion mass flux can be finally written as

$$\mathbf{j} = -\rho\ [\mathbb{D}]\nabla \mathbf{Y} - \mathbf{D}^T \nabla \ln T \tag{2.152}$$

where

$$[\mathbb{D}] = [A]^{-1}[R] \tag{2.153}$$

2.4 The effective binary diffusion coefficient

Instead of using Eq. (2.152), a simpler method exists for evaluating diffusion mass fluxes in multicomponent mixtures based on the *effective binary diffusivity approximation*. In analogy with the relationship for the mass flux in binary mixtures (2.30), the species molar flux in a multicomponent mixture can be written as:

$$\vec{\dot{n}''}_i = \vec{j}_i^* + X_i \sum_{k=1}^{n} \vec{\dot{n}''}_k = -CD_{im}^* \nabla X_i + X_i \sum_{k=1}^{n} \vec{\dot{n}''}_k \tag{2.154}$$

where the diffusion coefficient D_{im}^* of the species in the mixture is introduced. By projecting the Eq. (2.154) on an arbitrary direction $\vec{a}$, this coefficient can be resumed from the same Eq. (2.154) in the following form

$$\frac{1}{CD_{im}^*} = \frac{-\nabla X_i \cdot \vec{a}}{\left(\vec{\dot{n}''}_i - X_i \sum_{k=1}^{n} \vec{\dot{n}''}_k\right) \cdot \vec{a}} \tag{2.155}$$

The In a mixture of ideal gases, according to Eq. (2.111), the ∇X_i term can be replaced by

$$\nabla X_i = \sum_{\substack{k=1 \\ k \neq i}}^{n} \frac{X_i X_k}{D_{ik}} \left(\frac{\vec{j}_k}{\rho_k} - \frac{\vec{j}_i}{\rho_i}\right) = \sum_{\substack{k=1 \\ k \neq i}}^{n} \frac{X_i X_k}{D_{ik}} \left(\frac{\vec{j}_k^*}{C_k} - \frac{\vec{j}_i^*}{C_i}\right) \tag{2.156}$$

in which, for the sake of simplicity, thermal diffusion effects have been omitted. By substituting Eq. (2.156) in Eq. (2.155), after some mathematical manipulations we get

$$\frac{1}{CD_{im}^*} = \frac{\sum_{j=1}^{n} (1/CD_{ij})(X_j \vec{\dot{n}''}_i - x_i \vec{\dot{n}''}_j) \cdot \vec{a}}{\left(\vec{\dot{n}''}_i - X_i \sum_{k=1}^{n} \vec{\dot{n}''}_k\right) \cdot \vec{a}} \tag{2.157}$$

Owing to its dependence on molar fluxes, Eq. (2.157) is not very useful; however, in some particular cases, it reduces to a simpler form which can be easily employed. First of all, for a binary system, it is immediate to verify that, as expected

$$\frac{1}{D_{im}^*} = \frac{1}{D_{ab}} \tag{2.158}$$

Moreover, in a multicomponent mixture in which a species diffuses in a quasi-homogeneous mixture, that is the velocities V_j are zero or equal for all species different from the i-th, it can be verified that the molar effective binary diffusivity D_{im}^* is given by:

$$\frac{1 - X_i}{D_{im}^*} = \sum_{\substack{j=1 \\ j \neq i}} \frac{X_j}{D_{ij}} \tag{2.159}$$

The formulation of the Effective Binary Diffusivity approximation in terms of mass fluxes is similar. The species mass flux in a multicomponent mixture can be written as:

$$\vec{\dot{m}''}_i = \vec{j}_i + Y_i \sum_{k=1}^{n} \vec{\dot{m}''}_k = -\rho D_{im} \nabla Y_i + Y_i \sum_{k=1}^{n} \vec{\dot{m}''}_k \tag{2.160}$$

and then

$$\frac{1}{\rho D_{im}} = \frac{-\nabla Y_i \cdot \vec{a}}{\left(\vec{\dot{m}''}_i - Y_i \sum_{k=1}^{n} \vec{\dot{m}''}_k\right) \cdot \vec{a}} \tag{2.161}$$

After some mathematical passages, it's possible to turn the equation 2.161 into the following

$$\frac{1}{C D_{im}} = \frac{\left(-\nabla X_i + \frac{X_i \nabla \bar{M}}{\bar{M}}\right) \cdot \vec{a}}{\left(\vec{\dot{m}''}_i - X_i \sum_{k=1}^{n} \vec{\dot{m}''}_k\right) \cdot \vec{a}} \tag{2.162}$$

Then, it can easily be seen that:

$$D_{im} = D^*_{im} \frac{1}{1 - \frac{\nabla \bar{M} \cdot \vec{a}}{\bar{M}} \frac{X_i}{\nabla X_i \cdot \vec{a}}} \tag{2.163}$$

Under particular circumstances, the effective binary mass diffusivity and the molar one are equal or, at least, very similar. In particular, if the species molecular weights are very similar, as well as if the i-th component is present but in traces, while having a strong concentration gradient, the multiplication term in Eq. (2.163) tends to unity; in such a situation, the relationship (2.159) held also for the equivalent binary mass diffusivity:

$$\frac{1 - X_i}{D_{im}} = \sum_{\substack{j=1 \\ j \neq i}} \frac{X_j}{D_{ij}} \tag{2.164}$$

Obviously, where applicable, the introduction of an effective binary diffusion coefficient, like the one proposed in Eq. (2.159) or (2.164) simplifies remarkably the modelling of multispecies diffusion, with respect to the mathematical formulation derived in the full multicomponent theories. It should be anyway remarked that, due to the mathematical relationship of the diffusion coefficients, the sum of the diffusion fluxes cannot be found equal zero in the mixture, introducing a systematic error in the balance equations.

$$\sum_{i=1}^{n} \vec{j}_i = \sum_{i=1}^{n} -\rho D_{im} \nabla Y_i \neq 0 \tag{2.165}$$

Not always this error can be considered negligible.

2.5 Momentum and energy balance equations

To complete the set of equations describing the behavior of a multicomponent mixture the momentum balance equations and the energy balance equations are added

$$\frac{\partial \rho \vec{U}_m}{\partial t} + \nabla \cdot (\rho \vec{U}_m \vec{U}_m) = \nabla \cdot \vec{\bar{\tau}} - \nabla P + \rho \vec{g} + S_q \tag{2.166}$$

where the mixture average velocity in the mass reference frame is used and the average mixture density. The shear stress tensor for a newtonian fluid is given by

$$\vec{\bar{\tau}}_{xy} = \mu \Big(\frac{\partial u}{\partial y} + \frac{\partial v}{\partial x} \Big) - \frac{2}{3} \mu \left(\nabla \cdot \vec{U}_m \right) \delta_{xy} \tag{2.167}$$

The momentum balance equations for a single species or a multicomponent mixture are very similar. The main difference consists in the evaluation of the mixture viscosity. Indeed, a formulation usually adopted for estimating dynamic viscosity in multicomponent mixtures of non polar fluids is the well known *Wilke's law* [24]

$$\mu = \sum_{i=1}^{n} \frac{X_i \mu_i}{\sum_{k=1}^{n} X_k \Phi_{ik}} \tag{2.168}$$

where the Φ_{ik} Wilke's coefficients are given by

$$\Phi_{ik} = \frac{\left[1 + \left(\frac{\mu_i}{\mu_k}\right)^{\frac{1}{2}} \left(\frac{M_k}{M_i}\right)^{\frac{1}{4}}\right]^2}{\left[8\left(1 + \frac{M_i}{M_k}\right)\right]^{\frac{1}{2}}} \tag{2.169}$$

The multicomponent thermodynamic energy balance equation is

$$\frac{\partial \rho \hbar}{\partial t} + \nabla \cdot (\rho \vec{U}_m \hbar) = -\nabla \cdot \vec{\dot{q}''} + S_h \tag{2.170}$$

where the viscous dissipation term is neglected and the mixture average $\hbar$ are obtained as the mass weighted average of the enthalpies of the single species

$$\hbar = \sum_{i=1}^{n} Y_i \hbar_i \tag{2.171}$$

In ideal gases, the single species specific enthalpy can be usually defined as

$$\hbar_i(T) = \hbar_i^0 + \int_{T_0}^{T} Cp(\tilde{T}) d\tilde{T} \tag{2.172}$$

where T_0 is the reference temperature. The main difference between the single species energy balance equation and the multicomponent energy balance equation consists in the heat flux term $\vec{\dot{q}''}$. This is simply given by the products of the thermal conductivity and the temperature gradient in the single species mixtures. Indeed, in the case of multicomponent mixtures there are additional terms due to species diffusion. According to Eqs. (2.48) and (2.63), the heat flux in a multicomponent mixture is given by

$$\vec{\dot{q}''} = \vec{\dot{q}''}_{\hbar} + \sum_{k=1}^{n} \vec{j}_k \hbar_k = -a_{00} \nabla \ln T - \sum_{k=1}^{n} a_{0k} \frac{CRT}{\rho_k} \mathbf{d}_k + \sum_{k=1}^{n} \vec{j}_k \hbar_k \tag{2.173}$$

Substituting the driving forces expressed by the Maxwell-Stefan equations (2.111) in Eq. (2.173), the heat flux can be written as

$$\begin{aligned} \vec{\dot{q}''} = &-\Big[a_{00} + \sum_{j=1}^{n}\sum_{k=1}^{n} \frac{CRT}{\rho_j} D_j^T \frac{X_j X_k}{D_{jk}} \Big(\frac{D_k^T}{\rho_k} - \frac{D_j^T}{\rho_j}\Big)\Big] \nabla \ln T \\ &- \sum_{j=1}^{n}\sum_{k=1}^{n} \frac{CRT}{\rho_j} D_j^T \frac{X_j X_k}{D_{jk}} \Big(\frac{\vec{j}_k}{\rho_k} - \frac{\vec{j}_j}{\rho_j}\Big) + \sum_{k=1}^{n} \vec{j}_k \hbar_k \end{aligned} \tag{2.174}$$

the coefficient of $\nabla \ln T$ is, by common agreement, taken to be the thermal conductivity times the temperature [20]. Adopting this assumption the energy flux can be finally written as

$$\vec{\dot{q}''} = -k\nabla T - \sum_{j=1}^{n}\sum_{k=1}^{n} \frac{CRT}{\rho_j} D_j^T \frac{X_j X_k}{D_{jk}} \left(\frac{\vec{j}_k}{\rho_k} - \frac{\vec{j}_j}{\rho_j} \right) + \sum_{k=1}^{n} \vec{j}_k \hbar_k \tag{2.175}$$

The heat flux vector is therefore written as the sum of three different contributions: the conductive heat flux, the contribution originating from the Dufour effect, containing both diffusion fluxes and thermal diffusion coefficients, and the interdiffusional convection terms, containing diffusion fluxes. The interdiffusional convection terms are generally important in diffusing systems, whereas the Dufour effect term is usually small and can be neglected in the most cases. Finally, the energy balance equation for a multicomponent mixture is written as

$$\frac{\partial \rho \hbar}{\partial t} + \nabla \cdot (\rho \vec{U}_m \hbar) = \nabla \cdot \left(k\nabla T - \sum_{k=1}^{n} \vec{j}_k \hbar_k \right) + S_h \tag{2.176}$$

The energy balance equations for a single species or a multicomponent mixture are thus very similar. A further difference consists in the evaluation of the thermal conductivity. The Wilke's law is also used for estimating the thermal conductivity in multicomponent mixtures

$$k = \sum_{i=1}^{n} \frac{X_i \; k_i}{\sum_{k=1}^{n} X_k \Phi_{ik}} \tag{2.177}$$

where the Φ_{ik} Wilke's coefficients are given by Eq. 2.168.

2.6 Diffusion phenomena in the presence of a condensable species

Given a multicomponent mixture with a condensing species v and $n-1$ non-condensable gases, let us assume that each gas behaves as an ideal gas. In the absence of volumetric source terms, the set of equations describing the behavior of the mixture includes the mixture continuity equation, $n-1$ species equations, including the condensing species, the momentum balance equations and energy balance equations

$$\frac{\partial \rho}{\partial t} + \nabla \cdot \left(\rho \vec{U}_m \right) = 0 \tag{2.178}$$

$$\frac{\partial Y_i \rho}{\partial t} + \nabla \cdot \left(Y_i \rho \vec{U}_m \right) = -\nabla \cdot \vec{j}_i \quad \forall i = 1.....n-1 \tag{2.179}$$

$$\frac{\partial \rho \vec{U}_m}{\partial t} + \nabla \cdot (\rho \vec{U}_m \vec{U}_m) = \nabla \cdot \vec{\vec{\tau}} - \nabla P + \rho \vec{g} + S_q \tag{2.180}$$

$$\frac{\partial \rho \hbar}{\partial t} + \nabla \cdot (\rho \vec{U}_m \hbar) = \nabla \cdot \left(k\nabla T - \sum_{k=1}^{n} \vec{j}_k \hbar_k \right) \tag{2.181}$$

where the diffusion mass fluxes are given by

$$[\mathbb{D}] = D_{im} [\mathbb{I}] \tag{2.182}$$

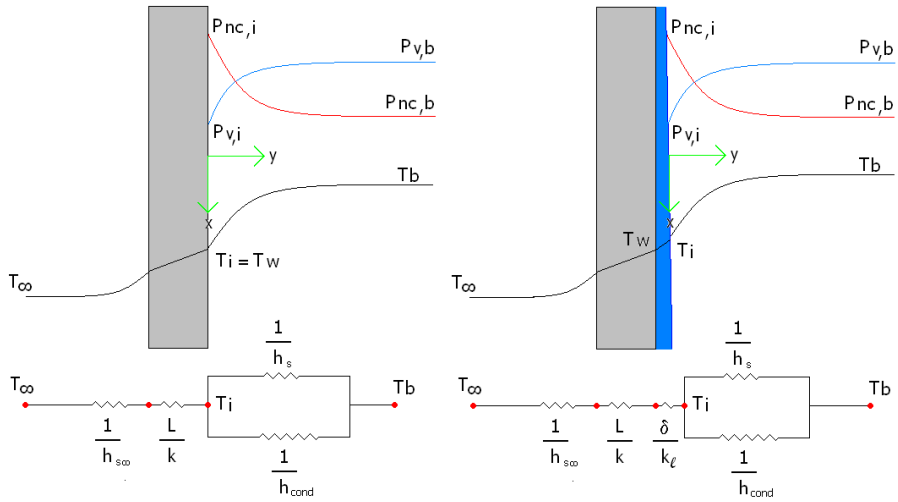

Figure 2.1: Sketch of temperature and concentration profiles in the condensing boundary layer with (right) and without (left) condensate liquid film (steam is assumed in saturation conditions $T_b = T_s at(P_{v,b})$)

when the simplified effective binary diffusion model is adopted, or

$$[\mathbb{D}] = [A]^{-1}[R] \tag{2.183}$$

when it is used the full multicomponent diffusion model.

Given the appropriate set of balance equations, condensation over surface is accounted by means of appropriate boundary conditions. In this paragraph, these boundary conditions are derived based on the first principles governing the diffusion phenomena. In the following paragraph it is detailed how these can be imposed adopting the heat and mass transfer analogy.

In the presence of a multicomponent mixture of noncondensable gases and a condensing vapor, condensation occurs over a cold wall, whose temperature is lower than the saturation temperature of the vapor corresponding to its partial pressure in bulk. Due to phase change, the concentration of the condensing species is reduced at the wall causing further bulk vapor to diffuse towards the condensation interface (see Fig. 2.1).

Vapor diffusing towards the cold interface entrains noncondensable species that, owing to the non permeability of the phase change interface, accumulates in the proximity of it. A large build-up of noncondensable gases establishes, reducing the mobility of the condensing species and thus increasing the resistance to heat and mass transfer. At the condensing interface, the steam partial pressure is linked to the temperature, since phase change can be assumed to occur in saturation conditions. The partial pressure of the noncondensable gases is given by[6]

$$P_{nc,i} = P - P_{v,sat}(T_i) \tag{2.184}$$

[6]In the following equations, up to the end of this chapter, the i subscript will refer to interface and not to the i-th species

and, in ideal mixture of ideal gases, the ratio between the partial pressure and the absolute pressure defines the molar fraction of the species

$$X_{v,i} = \frac{P_{v,sat}}{P} \tag{2.185}$$

$$X_{nc,i} = \frac{P_{nc,sat}}{P} \tag{2.186}$$

In this scenario the partial pressure of noncondensables at the interface is higher than the partial pressure in bulk. A counter-diffusion establishes in the direction orthogonal to the interface, consequence of the non permeability conditions at the interface

$$\dot{m}''_{nc,i} = Y_{nc,i}\dot{m}''_i + \vec{j}_{nc,i} = 0 \tag{2.187}$$

where the terms $\dot{m}''_{nc,i}$ and $\vec{j}_{nc,i}$ are mass fluxes and diffusion mass fluxes in the direction orthogonal to the condensing interface. Being $\dot{m}''_{k,i} = 0$, $\forall k \neq v$, it follows that the condensation mass flux of vapor is given by

$$\dot{m}''_{v,i} = \frac{j_{v,i}}{1 - Y_{v,i}} \tag{2.188}$$

Moreover, since

$$\dot{m}''_{v,i} = \rho_{v,i} v_{v,i} = \rho_i v_{m,i} \tag{2.189}$$

at the condensing interface, the average mixture velocity orthogonal to the wall $v_{m,i}$ is given by

$$v_{m,i} = \frac{\dot{m}''_{v,i}}{\rho_i} = \frac{j_{v,i}}{\rho_i(1 - Y_{v,i})} \tag{2.190}$$

where $j_{v,i}$ is calculated according to the selected diffusion model previously described, whatever it is. In a multicomponent mixture of ideal gases with a condensing species, a condensation interface is thus completely defined once are provided the condensing temperature, that is also the vapor partial pressure, the average mixture velocity $v_{m,i}$ and the non permeability conditions expressed by Eq. (2.187) of the noncondensable species. Actually, the main difficulty consists on defining the interface temperature. Whenever it is not directly assigned with a so called *first kind* or *Dirichlet* boundary condition, this is a function of the overall heat flux and the overall thermal resistance themselves (see Fig. 2.1). In this case, a boundary condition called of the *third kind* is applied. The presence of the liquid film just adds an additional thermal resistance, much smaller than the resistance due to the noncondensable build-up at interface.

2.7 The analogy between heat and mass transfer

In similarity with the Newton's law for heat transfer in which the heat transfer coefficient is defined as

$$h_s = \frac{\dot{q}''_i}{T_i - T_b} \tag{2.191}$$

in mass transfer problems a mass transfer coefficient for condensing vapors can be proposed as follows

$$h_m = \frac{j_{v,i}}{Y_{v,i} - Y_{v,b}} \tag{2.192}$$

Substituting Eq. (2.188) in Eq. (2.192) the condensation mass flux can be written as

$$\dot{m}''_{v,i} = h_m \frac{Y_{v,i} - Y_{v,b}}{1 - Y_{v,i}} = h_m B_m \tag{2.193}$$

where the term B_m is given the name of *macroscopical driving force*, to distinguish it from the *driving force* introduced in the analysis of multicomponent diffusion in paragraph 2.3. The average mixture velocity at the interface can be written as

$$v_{m,i} = \frac{\dot{m}''_{v,i}}{\rho_i} = \frac{h_m B_m}{\rho_i} \tag{2.194}$$

The characterization of the condensing interface reduces therefore to evaluate the mass transfer coefficient h_m. In this aim, two main approaches are possible: a first approach relies on empirical correlations based on experimental data, whereas a second approach is based on the analogy between the heat and mass transfer phenomena.

For the sake of simplicity, let us consider a binary mixture of a noncondensable gas and a condensing vapor. In steady-state conditions, the set of equations that describe the diffusion phenomena of the condensable species includes the continuity equation of the mixture, the balance equation of momentum, the continuity equation of a chemical species, e.g. the condensing one in our case, and the appropriate boundary conditions. The two-dimensional boundary layer equations for an incompressible newtonian fluid in laminar flow, are listed below

$$\frac{\partial u}{\partial x} + \frac{\partial v}{\partial y} = 0 \tag{2.195}$$

$$u\frac{\partial u}{\partial x} + v\frac{\partial u}{\partial y} = \nu\frac{\partial^2 u}{\partial^2 y} + \begin{cases} -\frac{1}{\rho}\frac{dP}{dx} + g_x & \textit{forced convection} \\ g_x \beta_m (Y_v - Y_{v,b}) & \textit{natural convection} \end{cases} \tag{2.196}$$

where it is introduced

$$\beta_m = -\frac{1}{\rho}\Big(\frac{\partial \rho}{\partial Y_v}\Big)_{P,T} \tag{2.197}$$

and

$$u\frac{\partial Y_v}{\partial x} + v\frac{\partial Y_v}{\partial y} = D_{vm}\frac{\partial^2 Y_v}{\partial^2 y} \tag{2.198}$$

Both the natural convection than the forced convection formulation of the momentum balance equations are proposed, in which the effects of buoyancy are only accounted for by the differences of vapor mass fractions. The set of boundary conditions to be imposed at the condensing interface is given by

$$\begin{cases} Y_v(y \to \infty) & = Y_{v,b} \\ Y_v(y = 0) & = Y_{v,i} \\ v_{m,i}(y = 0) & = \frac{\dot{m}''_{v,i}}{\rho_i} \end{cases} \tag{2.199}$$

The analogous equations that describe the corresponding pure heat transfer problem are instead

$$\frac{\partial u}{\partial x} + \frac{\partial v}{\partial y} = 0 \tag{2.200}$$

$$u\frac{\partial u}{\partial x}+v\frac{\partial u}{\partial y}=\nu\frac{\partial^2 u}{\partial^2 y}+\begin{cases}-\frac{1}{\rho}\frac{dP}{dx}+g_x & \textit{forced convection}\\ g_x\beta_T(T-T_b) & \textit{natural convection}\end{cases} \tag{2.201}$$

where it is introduced

$$\beta_T=-\frac{1}{\rho}\Big(\frac{\partial\rho}{\partial T}\Big)_P \tag{2.202}$$

and

$$u\frac{\partial T}{\partial x}+v\frac{\partial T}{\partial y}=\alpha\frac{\partial^2 T}{\partial^2 y} \tag{2.203}$$

Both the natural convection and the forced convection formulation of the momentum balance equations are proposed, in which the effects of buoyancy are only accounted for by the differences of temperature. The set of boundary conditions to be imposed at the condensing interface is given by

$$\begin{cases}T(y\to\infty) & =T_b\\ T(y=0) & =T_i\\ v_{m,i}(y=0) & =0\end{cases} \tag{2.204}$$

We are therefore dealing with two sets of equation that are very similar and that reduce to be the same when the thermal and molecular diffusivities are similar $Le\sim 1$ and also are buoyancy forces in the natural convection regimes. Indeed, the most important difference consists in the boundary condition on the orthogonal velocity. The analogy between the two set of equations is therefore restricted to the case with very low condensation rates, where the orthogonal velocity could be reasonably negligible. Under the aforementioned hypothesis, the heat and mass transfer analogy consists in establishing a formal correspondence between the pure heat transfer coefficient h_s and the mass transfer coefficient at low mass transfer rate $h_{m,0}$. In this aim, the correlations expressing the Nusselt number, Nu, as a function of the Reynolds, Re, the Grashof, Gr, and the Prandtl, Pr, number can be applied also for expressing the Sherwood number, Sh_0, at low mass transfer rate, where the Prandtl number is substituted by the Schmidt number Sc and the Grashof number by the modified Grashof number.

$$Nu=f(Re,Gr,Pr,\texttt{geometry})\Longrightarrow Sh_0=f(Re,Gr_m,Sc,\texttt{geometry}) \tag{2.205}$$

2.7.1 The Stefan factor

In order to extend the validity of the heat and mass transfer analogy to cases at higher condensation rate, a correction should be introduced, accounting for the *transpiration effects* induced by condensation on the species boundary layers. This correction factor, known as *suction factor* accounts for the modification induced by condensation on the species boundary layer. In particular, *suction* causes the boundary layer to be thinner, improving the characteristic of the mass transfer. On the other hand, in the case of evaporation, the species boundary layers are thickened and the mass transfer characteristics are reduced. This phenomenon, opposed to *suction*, is known as *blowing*.

The *suction factor* can be evaluated by analyzing the so called *Stefan's problem*. This problem involves a one dimensional stagnant layer of thickness δ_m

with a condensing species, described by the following set of equations and boundary conditions

$$\frac{d(\rho v)}{dy} = 0 \tag{2.206}$$

$$\frac{d(\rho v Y_v)}{dy} - \rho D_{vm} \frac{d^2 Y_v}{dy^2} = 0 \tag{2.207}$$

with

$$\begin{cases} Y_v(y \to \infty) & = Y_{v,b} \\ Y_v(y = 0) & = Y_{v,i} \\ v_{m,i}(y = 0) & = \frac{\dot{m}''_{v,i}}{\rho_i} \end{cases} \tag{2.208}$$

Under the assumption of uniform density and molecular diffusivities through the stagnant layer, the solution of the mathematical problem is given by

$$Y_v(y) = Y_{v,i} + (Y_{v,b} - Y_{v,i}) \frac{e^{\frac{\dot{m}''_{v,i} y}{\rho D_{vm}}} - 1}{e^{\frac{\dot{m}''_{v,i} \delta_m}{\rho D_{vm}}} - 1} \tag{2.209}$$

Substituting Eq. (2.209) in the definition of mass transfer coefficient (2.192) we get

$$h_m = \frac{\dot{m}''_{v,i}}{e^{\frac{\dot{m}''_{v,i} \delta_m}{\rho D_{vm}}} - 1} \tag{2.210}$$

Since

$$h_{m,0} = \lim_{\dot{m}''_{v,i} \to 0} h_m = \frac{\rho D_{vm}}{\delta_m} \tag{2.211}$$

the previous Ed. (2.210) can be rewritten as

$$h_m = \frac{\dot{m}''_{v,i}}{e^{\frac{\dot{m}''_{v,i}}{h_{m,0}}} - 1} \tag{2.212}$$

Being from Eq. (2.193)

$$\frac{\dot{m}''_{v,i}}{h_m} = B_m \tag{2.213}$$

it follows that

$$e^{\frac{\dot{m}''_{v,i}}{h_{m,0}}} - 1 = B_m \tag{2.214}$$

and therefore

$$\dot{m}''_{v,i} = h_{m,0} \ln(1 + B_m) \tag{2.215}$$

It is immediate to conclude that

$$h_m = h_{m,0} \frac{\ln(1 + B_m)}{B_m} = h_{m,0} \frac{\Phi_m}{e^{\Phi_m} - 1} = h_{m,0} F \tag{2.216}$$

where the *Stefan suction factor* F is introduced as

$$F = \frac{\Phi_m}{e^{\Phi_m} - 1} \tag{2.217}$$

Multiplying the F factor times the driving force we get

$$B_m \; F = B_m \frac{\ln\left(1+B_m\right)}{B_m} = \ln\frac{1-Y_{v,b}}{1-Y_{v,i}} = \ln\frac{Y_{nc,b}}{Y_{nc,i}} \tag{2.218}$$

The boundary condition introduced by Eq. 2.194 can therefore be rewritten as

$$v_{m,i} = \frac{\dot{m}''_{v,i}}{\rho_i} = \frac{h_m B_m}{\rho_i} = \frac{h_{m,0} F B_m}{\rho_i} = \frac{h_{m,0} \ln\frac{Y_{nc,b}}{Y_{nc,i}}}{\rho_i} \tag{2.219}$$

with $h_{m,0}$ given by

$$h_{m,0} = \frac{\rho_f D_{vm,f} Sh_{0,l}}{l} \tag{2.220}$$

where l is the characteristic length scale of the considered problem.

Basing on the distinction between mass transfer coefficient at low mass transfer rate and mass transfer coefficient at higher mass transfer rate we distinguish a *corrected Sherwood number* Sh_0, linked to the corresponding Nusselt number via the heat and mass transfer analogy expressed by Eq. (2.205), and an *actual Sherwood number* that is obtained by multiplying the previous one be the Stefan suction factor F.

$$Sh_{0,l} = \frac{\dfrac{\dot{m}''_{v,i}}{\ln\frac{Y_{nc,b}}{Y_{nc,i}}}x}{\rho_f D_f} \tag{2.221}$$

$$Sh_l = \frac{h_m l}{\rho_f D_f} = \frac{\frac{\dot{m}''_{v,i}}{B_m} l}{\rho_f D_f} \tag{2.222}$$

2.7.2 The Ackermann and the Moffat factors

In similarity with the concentration boundary layers, temperature and velocity profiles are also affected by transpiration effects. To account for suction effects on the momentum and the heat transfer coefficient two further coefficients must be introduced. The Ackermann coefficient [25] is conceived to correct the heat transfer coefficient estimated by the available correlation for pure heat transfer

$$h_s = h_{s,0} A_f \tag{2.223}$$

where the $h_{s,0}$ coefficient corresponds to pure heat transfer cases. In analogy with the Stefan factor defined by Eq. (2.217), the Ackermann factor A_f is defined by

$$A_f = \frac{\Phi_t}{e^{\Phi_t} - 1} \tag{2.224}$$

where

$$\Phi_t = \frac{\dot{m}''_{v,i} Cp_{v,i}}{h_{s,0}} \tag{2.225}$$

A coefficient M_f is proposed by Kays & Moffat [26] to correct the friction coefficient of the pure momentum or momentum and heat transfer cases

$$f_i = f_{i,0} M_f \tag{2.226}$$

where $f_{i,0}$ is the friction coefficient in the absence of mass transfer. The Kays & Moffat coefficient [26] is given by

$$M_f = \frac{\ln(1+\Phi_v)}{\Phi_v} \tag{2.227}$$

where

$$\Phi_v = \frac{\dot{m}''_{v,i}}{\rho_b u_{m,b}(f_{i,0}/2)} \tag{2.228}$$

When we deal with condensation phenomena, the interface local mass transfer is a negative quantity. This means that, all the correction factors introduced are larger than one. This effect, known as suction, causes the simultaneous increasing of mass, heat and friction coefficients. On the other hand, in the case of evaporation, the interface local mass flux is positive. The proposed correction coefficients are therefore less than one. This is the case of blowing: mass transfer, heat transfer and friction coefficients are simultaneously reduced.

2.8 Concluding remarks

This chapter was aimed at analyzing the diffusion phenomena occurring in condensing multicomponent mixtures under the theoretical point of view.

The governing equations that describe the behavior of a multicomponent mixture of ideal gases were revised in detail.

Two different diffusion models were proposed. A first model was deduced on the basis of the irreversible thermodynamics principles. A second simplified model is based on the approximation of effective binary diffusivity.

The boundary conditions describing condensation phenomena over a cold surface have been analyzed. A first approach consists on assigning appropriate boundary conditions basing on the mathematical resolution of the diffusion fluxes near the condensing interface. This allows to evaluate the average mixture velocity at the condensing interface once the mass fraction of the condensing species is known and non permeability conditions of the noncondensable species are imposed. A second approach, based on the analogy between heat and mass transfer, allows assigning the interface mixture velocity basing on the bulk and the interface properties via empirical, semi-empirical or theoretical correlation aimed at estimating the heat transfer coefficient in pure heat transfer cases.

Chapter 3

Overview of CFD models for condensation

This chapter is aimed at analyzing the current capabilities of the modern CFD tools in simulating wall condensation phenomena, with particular interest to those applications concerning the analysis of the nuclear reactor containment thermal-hydraulics.

In the first part of the chapter, a review of some fundamental studies performed about condensation phenomena since the beginning of the 20th century is performed.

The second part is aimed at analyzing the state-of-art of the current CFD tools. After illustrating the main studies performed since the eighties in the nuclear safety field, an analysis of the current computational tools developed for modeling wall condensation phenomena is performed. In this context, the result of a research activity carried out in the frame of the SARnet network of excellence and coordinated by the University of Pisa is presented. An in-depth description of the available models is proposed, together with the results of a benchmark exercise proposed to assess and compare their behavior.

Based on the analysis of the literature review and the results of the proposed benchmark problems, the needs for future improvements and development are discussed with the aim to identify the main goals of this PhD research.

3.1 Fundamental studies on condensation

Since the beginning of the 20th century, both experimental and theoretical studies on condensation in presence of noncondensable gases were carried out extensively.

In a time when modern calculators were not available, the mathematical and numerical instruments developed during the previous centuries, not only but also in the field of fluid mechanics, allowed performing fruitful analyses of the mass transfer phenomena involved in wall condensation. The similarity method, originally applied by Blasius in the solution of the laminar boundary layer equations was adapted for solving the more complex condensing boundary layer problem. Together with studies based on the analytical solution of the

mathematical problem, a more physical approach developed, analyzing condensation in analogy with the momentum and the heat transfer phenomena.

Here, a chronological review of the main studies that contributed to improve the knowledge on condensation is reported. Analytical studies are reported first, followed by an overview of the different forms of the heat and mass transfer analogy.

The first, pioneering analytical work on condensation was reported in 1916 by Nusselt [27], who formulated the problem of pure vapor condensation in terms of simple forces and heat balance within the condensate film, neglecting the effects of inertia forces and energy convection. For the gravity driven laminar flows, where a laminar boundary layer arises from natural convection or forced laminar flows, the governing partial differential equations admit a similarity solution and the resulting ordinary differential equations may be integrated either analytically or numerically. Owing to this reason, since the 50s, extensive studies have been performed in the field of laminar condensation. In 1956, Rohsenow [28, 29] improved the Nusselt theory including energy convection in the heat balance, but neglecting inertia forces and noncondensables. In 1959, Sparrow and Gregg [30] included both energy convection and inertia forces of the condensate film. In 1961, Koh et Al. [31] considered the mutual inertia forces between the liquid film and the condensing vapor. Analysis of vapors condensation in pure forced convection regime were also performed by Cess [32] and Koh [33]. Despite the fact that exact similarity solutions are not possible in combined free and forced convection regime, introducing several approximations, Rohsenow [28], Chung [34] and Shekriladze [35] analyzed forced convection condensation also in presence of body force. Jacobs instead, analyzed the combined convection regime by an approximate integral method [36].

The presence of a second or a third noncondensable chemical species was omitted in the Nusselt model and the further studies that were also conceived for pure vapor condensation. Anyway, since the beginning of the century it was clear that even small amounts of noncondensable in the bulk vapor could cause a large reduction of the mass transfer rates. Dated back in 1929, the work by Othmer [37] is one of the most representative among the different experimental studies performed at the beginning of the 20th century. The effects induced by the presence of a small noncondensable amount were demonstrated. Even a small amount of noncondensable gas in the bulk of vapor was proven to cause a large build-up of the noncondensable gas at the condensing interface, thus reducing the mass transfer properties of the vapor. In 1964 Sparrow and Lin [38] analyzed buoyancy driven condensation in presence of a noncondensable gas, adopting the similarity method for solving the mass, the species, the energy and the momentum balance equations. It was clearly shown and confirmed by comparison with experimental data that the presence of a noncondensable gas is the dominating contribution in the degradation of transfer coefficients and that the various other processes in the vapor are by no means of equal importance. Minkowycz and Sparrow [39] improved the model including the effect of variable properties, interfacial resistance, superheating and thermal diffusion. The results confirmed that a small bulk concentration of the noncondensable gas can have a decisive effect on the heat transfer rate and that others are second order effects. The effect of a noncondensable gas in a forced convection laminar boundary layer was firstly explored in 1967 by Sparrow et Al. [40]. It emerged that in forced convection regime the degradation due to the presence of non-

condensable gases is less relevant than in buoyancy driven condensation. The presence of interfacial resistance was also examined, revealing negligible effects on heat transfer. The effect of steam superheating, with respect to saturation conditions, was analyzed by Minkowycz and Sparrow [41] in the forced convection : comparisons between forced convection and buoyancy driven convection regimes indicated that the latter was much more sensitive to superheating. Fujii and Uehara [42] in 1972 and Felicione and Seban [43] in 1973 proposed an analysis of buoyancy driven condensation phenomena in binary mixtures with an initial free stream velocity. Felicione and Seban solved the boundary layer equations with the integral approach. Both similarity and integral methods were found to give very similar results. The influence of free stream velocity was remarked, resulting in improved mass transfer rates. Owing to this fact, in 1973, Al-Diwany and Rose [44] proposed an experimental study of laminar free convection condensation. Very special attention was paid to avoid forced convection contribution in heat and mass transfer. The agreement of the self-similar boundary layer solutions developed for free buoyancy and the new experimental data improved.

Up to the beginning of the seventies, analytical studies based on the similarity method concerned exclusively laminar flows. In the case of turbulent flows a similarity analysis is less likely and there is the additional problem of providing a model for turbulence transport processes.

It was in this phase that the computational fluid dynamics methods were first applied in condensation modeling. The first applications of computational fluid dynamics (CFD) to wall condensation modeling is dated at the beginning of the seventies. In 1972, the finite difference numerical solution a forced flow laminar condensation problem was presented by Denny and Josionis [45]. The governing conservation equation in the vapor phase were solved numerically, confirming the conclusions drawn by Sparrow et Al. [40]. The numerical solution of a turbulent forced convection mass transfer problem was performed in 1974 by Jones and Renz [46], proposing a comparison with the database of Dallmeyer [47].

Stated the importance of the CFD techniques, that will be extensively treated later, it's remarked that fundamental studies in the field on turbulent condensation had been possible since the beginning of the century by another powerful approach. As mentioned, the heat and mass transfer analogy was developed for analyzing vapor condensation in the presence of noncondensable gases, based on the common root of the physical phenomena of momentum, heat and mass transfer.

Since the proposal of Reynolds's analogy between heat and momentum transfer [48] and its extension proposed by Colburn to more general conditions [49], the analogy has been applied with success in the prediction of other transport phenomena involving laminar or turbulent diffusion. The analogy between the heat transfer and the mass transfer phenomena concerning a chemical species absorbed or emitted at a surface was proposed for the first time in the pioneering works of Chilton and Colburn [50, 51].

The analysis of the available literature has allowed identifying two main categories of approaches: those based on mass, in which the driving force is expressed in terms of species mass fractions, and those based on mole, proposing similar relationship for the driving force, but expressed in terms of partial pressures or molar fractions [52]. Whatever the adopted approach, mass transfer problems are solved by introducing an appropriate transfer coefficient, in analogy with

the definition usually adopted for heat transfer. The mass transfer rate is then defined as the product of the mass transfer coefficient times a driving force, according to the definition proposed in Newton's law for the sensible heat transfer. In the original formulation of the Chilton and Colburn heat and mass transfer analogy [51], the condensation driving force was expressed in terms of steam partial pressures. Other formulations of the analogy based on the original idea of Chilton and Colburn were proposed in the following years, adopting different choices. Spalding [53] and Lienhard [54] casted the analogy in terms of mass fractions, expressing the condensation driving force as a function of the noncondensables mass fractions. Bird [55] adopted a molar approach, expressing the driving force in terms of noncondensables molar fractions. Based on the original model of Chilton and Colburn [51], Kreith [56], Collier [57] and Butterworth and Hewitt [58] proposed formulations of the analogy in which the condensation driving force is a function of the noncondensables partial pressures.

Later on, the heat and mass transfer analogy was widely employed in the analysis of the nuclear reactor containment thermal-hydraulics. On the contrary, the boundary layer solutions, although insightful from a theoretical point of view were not adopted due to their complexity. The following paragraph draws an outline of the main experimental and numerical activities performed within the nuclear community since the beginning of the eighties. A connection is here made evident between the fundamental research on condensation and the research applied to nuclear safety analysis.

3.2 Condensation modeling in safety analysis

Doubtless, condensation in presence of noncondensable gases is a relevant contributor to reactor containment atmosphere behavior, owing to its influence in the evolution of several design basis and severe accidents. In fact, the high efficiency involved by this heat transfer mechanism makes the heat sinks available within the containment atmosphere very effective in limiting the maximum pressure achieved after a loss of coolant accident (LOCA). Several safety features have been conceived to promote energy and mass exchange with the steam expected to be released in the containment atmosphere during a LOCA. Spray systems are an example of the safety systems employed since a long time in the pressurized water reactors. Major improvements in the design of the new generations of reactors included new safety systems involving the use of natural forces to provide containment cooling. These system are sometimes referred to as passive containment cooling systems (PCCS). An example of PCCS are the passive condensers of the General Electric simplified boiling water reactor (SBWR) [3] or the containment system of the Westinghouse's advanced pressurized reactor (AP600) [4], where condensation occurs on the containment walls externally cooled under free convection. Condensation on the containment walls, is definitely an important heat sink and represents a fundamental intrinsic safety feature of nuclear reactor containments. Moreover, condensation strongly affects other relevant phenomena, like the containment atmosphere mixing, which determine the distribution of noncondensable gases that may be delivered during severe accident scenarios, hydrogen in particular. Many activities have been performed in the last decades to investigate this phenomenon and to improve the capability to predict the atmosphere behavior inside the containment. On

one hand, an extensive experimental activity has been carried out. On the other hand, more and more sophisticated computational models have been developed.

Two pioneering works addressing condensation at large scales, such as reactor containment were proposed by Uchida [59] and Tagami [60] that estimated the average heat transfer coefficient on the basis of the ratio between the noncondensables and the steam density in an enclosure. Anyway, these correlations, largely adopted in the first accident analysis, were proven to be too simplicistic, missing fundamental variables such as pressure, temperature and bulk velocity that are of primary importance in a condensing scenario [61, 62]. With the advent of the new passive safety features of the SBWR and the AP600 there was a change in the potential conditions within the reactor containment. A renewed interest emerged in performing new experiments aimed at confirming the PCCS capabilities. Two main situations were addressed experimentally, representative of condensation on the containment walls and within the tubes of the PCCS condensers. Large scale experiments were also performed to evaluate the performance of the entire containment cooling system of the AP600. These test gave general information on pressure, temperature and containment response. Dehbi [63, 64] conducted experimental works in free convection regimes. Different correlations were developed accounting for different pressures, mass fractions of vapor, noncondensables and light noncondensable gases. Huhtiniemi [65, 66] considered the effect of surface orientation and bulk velocity in a small scale rectangular facility. On the same facility, Pernsteiner et Al. [67] studied the effect of light gas addition. To bridge the gap between the large time varying simulation of an accident and the smaller separate effects studies, an experimental study addressing conditions similar to those expected during an accident in the AP600, was conducted by Anderson et Al. [68] in a scaled containment geometry. To support the design of the passive containment condensers (PCC) and steam generator (GV), experiments measuring local condensation heat transfer from steam-air mixtures in vertical tubes were carried out by Vierow et Al. [69], Ogg [70], Siddique et Al. [71, 72] and Kageyama [73]. Kuhn et Al. addressed also the case of steam-helium mixtures [74, 75] with improved local measurement techniques.

The first adopted models accounting for condensation phenomena in accident analysis lumped parameter (LP) codes [76] used empirical correlations like those of Uchida [59] and Tagami [60]. A step forward in the modeling of condensation was the introduction of models proposing a more mechanistic representation of the phenomenon, generally based on the heat and mass transfer analogy. In 1983, Corradini [77] proposed a formulation of the analogy for evaluating the average mass transfer coefficient in a configuration representative of the nuclear reactor containment under accidental conditions. The model was validated against the steady-state Uchida [59] and Tagami [60] correlations. The effect of liquid film waviness was also addressed [78]. The model, modified and implemented in a two-dimensional code, was applied in the simulation of the integral Carolinas Virginia Tube Reactor CVTR test [78] and the Huhtiniemi separate effect condensation tests [65, 66]. Another innovative formulation of the analogy between heat and mass transfer was proposed by Peterson et Al. [79] in 1993. In the Peterson's diffusion layer model (DLM), the mass transfer problem is converted to an equivalent heat transfer one; the equivalent condensation heat transfer coefficient is directly introduced and the driving force is taken as a temperature difference. The model was originally applied to the prediction

of condensation phenomena in vertical tubes with a noncondensable gas representative of the PCC [80]. The validation of the model was performed against the classical correlations available in literature for heat transfer and against the experimental data of Ogg [70], Siddique et Al. [71, 72], Kageyama [73] and Kuhn et Al. [74, 75]. The agreement with the Uchida correlation was also checked [62]. Recently, a modified version has been proposed to take into account the presence of a multicomponent noncondensables mixture [81]. The model of Peterson was also tested by Herranz et Al. against the Vierow experimental data [82] and, in a variant improved to deal with larger gas to wall temperature difference [83], against the experimental database of Anderson et Al. [68] and Dehbi [64].

3.3 CFD tools for containment analysis

Despite of the activities performed in the last decades in the field of LP code development and validation, a renewed interest emerged at the end of the nineties, promoted by the availability of the new faster and faster computers. New frontiers were open by the opportunity to develop and qualify models using the CFD techniques in the analysis of downscaled tests or even full scale containment plant phenomena. This justified the interest for additional experimental studies about condensation aimed at better supporting development and validation activities in the field of CFD.

New experimental facilities have been built in the aim to produce more detailed experimental data, useful to improve the modeling capabilities of the new computer codes in the analysis of containment thermal-hydraulics. Several research programs have been carried out, including condensation among the different involved phenomena of interest.

CONAN [8] and COPAIN [1] are separate effect facilities purposely conceived to address wall condensation phenomena in different convection regimes. CONAN is operated by UNIPI and COPAIN by CEA Grenoble. Up to now, most tests have been performed within internal research programs. However, in the frame of this doctoral thesis, CONAN tests on steam condensation in presence of air have been released in the form of a benchmark problem [84] within the partners of the SARnet network of excellence on severe accidents (www.sar-net.org) .

Since the end of the nineties, the large scale MISTRA facility [5] has been operated by CEA Saclay. High quality experimental data have been gathered, representative of the thermal-hydraulic conditions of a nuclear reactor containment after a postulated loss of coolant accident. The MICOCO benchmark [85] and the International Standard Problem 47 (ISP47) have been proposed addressing condensation. In particular, the ISP47 promoted by OECD was aimed to collect experimental data for computer codes development and validation, covering important and still uncertain phenomena for containment thermal-hydraulics such as wall condensation, natural circulation, atmosphere stratification, turbulent diffusion as well as interaction between them [11]. The ISP47 MISTRA test mainly focused on the interaction of physical phenomena such as condensation and stratification, turbulence and buoyancy [5]. A smaller scale facility, TOSQAN, operated at IRSN Saclay, was also included in the ISP47 program, providing more detailed information about specific phenomena [7]. The validation of computer codes in multidimensional and compartmented geometry

was instead proposed against the ThAI database [6]. Condensation phenomena were analyzed both with steam-air and steam-air-helium mixtures. As a result of the code assessment, the following three phenomena appeared to be the major issues: condensation, light gas density stratification, and jet injection.

Other facilities have been operated, in which condensation was analyzed as a concurring phenomenon. Among them, the PHEBUS facility [86] operated at IRSN Cadarache is an integral facility incorporating a downscaled representation of the reactor core, the primary circuit including the steam generator, and the containment. Among the different tests performed within PHEBUS, the PHEBUS FP international program included condensation as one of the different involved phenomena [86].

The objective to be reached by these activities, both experimental than numerical has been a greater reliability in the prediction of plant phenomena, owing to more fundamental and mechanistic approaches than adopted in lumped parameter codes, whose limitations in simulating containment flow patterns and atmosphere mixing are clear from first principles and experience of use as well.

Despite of the extensive numerical studies performed up to now, the development of CFD codes suitable for the simulation of condensation in nuclear reactor containments represents still a challenging step for the complexity of the addressed phenomena and the demanding nature of these techniques in relation to the request of computational resources. The need for more coordinate and efficient efforts emerged within the main institutions involved in the development of CFD code for containment analysis. In the frame of the SARnet Network of Excellence, in particular, the need was felt for assessing the status of condensation models adopted in CFD codes relevant for nuclear reactor applications.

The next section summarizes the result of a research activity carried out in the frame of the SARnet network of excellence and coordinated by the University of Pisa. The state of the art of the modeling capabilities of the different available models have been firstly analyzed. After performing a review of the models, appropriate benchmark problems were proposed to assess and compare their behavior. A first step of the benchmark (identified as the 0-th step) was aimed at comparing code responses among each other and with applicable correlations in the application to a classical problem of condensation on a flat plate; the reference geometrical and operating conditions for this step were selected as an idealization of those typical in the CONAN experimental facility, operated at the University of Pisa. Then, the Step-1 of the activity involved addressing experimental data from the CONAN facility at different steam mass fractions and velocities and the comparison of the measured condensation rates and of local heat fluxes with code results.

3.4 Models Overview

In the aim to provide a clearer perspective about the use of the various wall condensation models, an analysis of the different models available in literature has been performed. This work consisted in gathering contribution from the main institutions involved worldwide in the development of the field code for the safety analysis of the reactor containment.

The diffusion phenomena of a chemical species in a carrier medium is usually

treated by commercial CFD codes by means of the Fick's diffusion law, possibly extended to multicomponent mixture by an appropriate definition of the species diffusion coefficient. Despite of the capability of these codes to deal with multicomponent transport, wall condensation models are generally not available. Fortunately, most of these codes allows assigning explicit source terms by which it is possible to implement user-defined mass transfer models. Thus, wall condensation phenomena can be modeled by means of volumetric sinks of mass and enthalpy applied in the near-wall cells. Whatever the methodology adopted to evaluate the condensation mass flux $\dot{m}''$, the volumetric source terms of mass and energy are usually defined in the form

$$S_m = \frac{\dot{m}''}{2\triangle_c} \tag{3.1}$$

$$S_h = S_m \hbar \tag{3.2}$$

where the term $2\triangle_c$ is the thickness of the cell where the source term is applied. Energy source terms are built on the basis of the mass sinks and according to the reference scale used for enthalpy by the different codes. At least in principle, source terms should be associated to every transported quantity. Momentum source terms, as well as turbulence source terms should be then applied in order to satisfy the balance equations. The available models usually neglect these sources, but sometimes this could not be an appropriate choice. In chapter 7, an analysis is proposed, investigating the effect of the different momentum source terms.

Research codes, at least in principle, can treat condensation in a different way. The CASTEM model [87], for instance, consists in imposing the average mixture velocity at the condensing interface and an non permeability condition for the noncondensable species.

In both cases, condensation velocity or volumetric sources can be evaluated in different ways:

- by means of fine discretization, usually based on diffusion laws;
- by means of coarse discretization, by defining a mass transfer coefficient:
    1. on the basis of semi-empirical correlations
    2. on the basis of the analogy between heat and mass transfer

The models based on a diffusion approach are capable to evaluate heat and mass transfer rates on the basis of concentration and temperature distributions in the near wall region, without requiring any specific closure law. These models require a very fine space discretization close to the wall, since the accuracy of the simulation depends in fact on the thickness of the cells next to the condensing wall. Thus, while meeting the turbulence model requirements, the thinner are these cells, the better the diffusion flux are evaluated.

The models based on an explicit formulation of the analogy between heat and mass transfer evaluate the mass transfer rates on the basis of bulk and interfacial concentrations, temperatures and properties. Clearly, these models reduce the computational efforts, by the use of coarser meshes. However, for complex geometries and not well defined phenomenologies, there is a fundamental ambiguity in choosing a mass transfer correlation and in defining the bulk

properties on whose basis the mass transfer coefficient should be calculated. Moreover, appropriate wall functions would be required to deal with transpiration effect, that are not accounted for by standard logarithmic wall functions. Nevertheless, there is a limited use of the information which can be provided by CFD. Various forms of the analogy are usually proposed in the different condensation models. In the aim to provide a clearer perspective about their use in engineering applications, Ambrosini et al. [88, 52] proposed a review of the different formulations, proposing a unified treatment based on the generalization of the Peterson's approach [79]. The application of the different formulations to the analysis of an extensive database for wall condensation and evaporation phenomena [52] allowed assessing that the related quantitative differences are limited, at least in the case of air-steam mixtures.

In the following section, a detailed description of the main presently available models for condensation phenomena is proposed. The description of the models is mainly focused on the details of the mass transfer and the turbulence models. Jointly, the description of the main work performed as validation activity of the models is also reported.

3.4.1 Condensation models based on a detailed near-wall treatment

Models in commercial CFD codes

Most of the CFD models conceived for fine modeling of the wall condensation phenomena are based on the Fickian diffusion principles. Similar models have been proposed and validated by the University of Pisa, NRG, FZJ and KTH [89]. According to the Fick's law, the steam mass flux at the condensing interface, assumed impermeable to noncondensable gases, is given by (see chapter 2):

$$\vec{\dot{m}''}_{v,i} = -\rho_i D_{vm,i} \frac{\nabla Y_{v,i}}{1 - Y_{v,i}} \tag{3.3}$$

To achieve an accurate representation of the mass fraction gradients, near-wall cells must be sufficiently small to make possible to assume a linear behavior of the concentration profiles. The steam mass fraction gradient can thus be approximated as a finite difference ratio:

$$\nabla Y_{v,i} \sim \frac{Y_{v,c} - Y_{v,i}}{\triangle_c} \tag{3.4}$$

Whenever considered, in these models the presence of the liquid film is simulated by mean of a pseudo-temperature imposed at the boundary of the computational domain, based on a 0D film model that computes iteratively the interface temperature on the basis of the imposed wall temperature and the calculated heat flux. The liquid film interface with the condensing mixture can be then approximated with the condensing wall:

$$\nabla Y_{v,w} = \frac{Y_{v,c} - Y_{v,w}}{\triangle_c} \tag{3.5}$$

A fundamental difference in the models consists in choice to define the mixture density and the steam diffusion coefficient to use for calculating the con-

densation mass flux. University of Pisa and KTH calculate the interface values on the basis of the interface temperature and the mixture composition [89]:

$$\dot{m}'' = -\rho_i D_{vm,i} \frac{Y_{v,c} - Y_{v,i}}{\triangle_c} \tag{3.6}$$

NRG [89] approximates the interface values with the values calculated by the code in the cells beside the condensing wall

$$\dot{m}'' = -\rho_c D_{vm,c} \frac{Y_{v,c} - Y_{v,i}}{\triangle_c} \tag{3.7}$$

FZJ [89] approximates the interface density with that of the first cell and calculates the diffusion coefficient at the film temperature, given by the average of the interface and the bulk temperature.

$$\dot{m}'' = -\rho_c D_{vm,f} \frac{Y_{v,c} - Y_{v,i}}{\triangle_c} \tag{3.8}$$

Clearly, the difference between the University of Pisa/KTH and the NRG approach is increasingly negligible for finer and finer near-wall meshes. This does not happen in the case of the diffusion coefficient adopted by FZJ, whose diffusion coefficient is naively evaluated at the average temperature between the condensing interface and the bulk.

One of the keypoints of the diffusion based models is the modelling of turbulence. Different models have been tried, also depending on the adopted CFD code. University of Pisa (FLUENT) used the RNG $\kappa - \varepsilon$ model with an appropriate two layer treatment to deal with the near-wall turbulence. FZJ (CFX) usually preferred the SST model by Menter, consisting in combining the $\kappa - \varepsilon$ model in the bulk region and the $\kappa - \omega$ in the near-wall region. In addition to SST other models have also been used by NRG: the standard $\kappa - \varepsilon$ models with a two-layer treatment for the near-wall turbulence (labelled $\kappa - \varepsilon$ in Fig. 3.1), low-Re $\kappa - \varepsilon$ models and the low-Re $\kappa - \omega$ model (labelled $\kappa - \omega$ in Fig. 3.1). All turbulence models require the nondimensional distance from the wall y^+ of the first cell to be inferior to 1. Provided that the requirements on y^+ are verified, the turbulence kinetic energy κ and its dissipations ε are 0 in the cell. Additional source terms are thus unuseful. However, the turbulence kinetic energy specific dissipation rate ω is maximum. In this case, typical of the $\kappa - \omega$ and the SST model, negative mass sources result in an increased specific dissipation rate and a sensible deformation of the boundary layer. Provided that condensation affects the near-wall turbulence, the solution adopted by NRG is to assign source terms that allow conserving the specific dissipation rate:

$$S_\omega = S_m \omega_c \tag{3.9}$$

Considering the size of the near-wall cells, sources linked to the momentum balance equations are omitted in the most models. It is supposed that the parallel and the orthogonal velocity components in these cells are small enough to not modify remarkably momentum and as a consequence temperature and concentration profiles, but the accuracy of this assumption is not clearly proven.

NRG validated his condensation model against the Huhtiniemi database, also performing a sensitivity analysis of the condensation rate y^+ at the first wall mesh for different turbulence models (see Fig. 3.1), the ISP47 tests performed

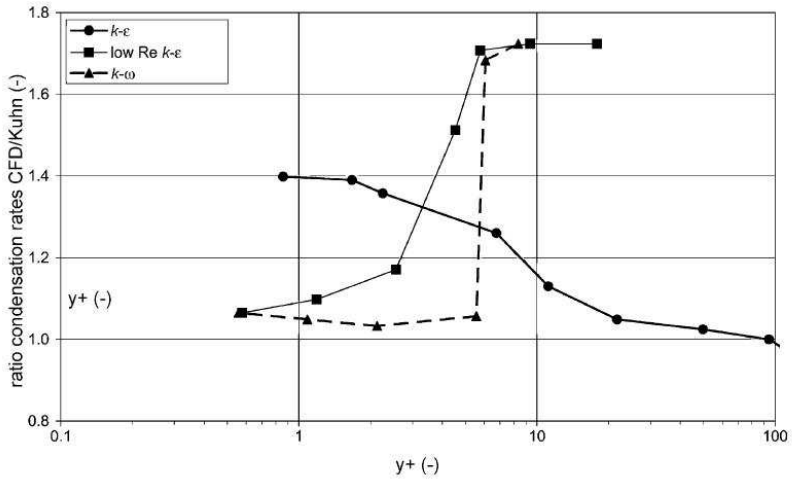

Figure 3.1: NRG model - Example of the influence of y^+ at the first wall mesh on the calculation of the condensation rate in one of the Huhtiniemi tests (Fig. from [90])

within TOSQAN, MISTRA and ThAI and the FPT-0 and the FPT-1 tests performed within PHEBUS [90] (see Fig. 3.2).

The mass transfer model of UNIPI, named HMTDM, was previously applied in the simulation of film evaporation cooling tests performed in EFFE facility for the study of the cooling capability of the AP600 PCCS [91]. The validation of the model has been performed also against the experimental database of CONAN of steam condensation in presence of air [8, 92] (see Fig. 3.3) and the phase A of the TOSQAN test performed in the frame of the ISP47 [93] (see Fig. 3.4).

KTH checked their model against the Uchida, the Tagami and the Dehbi correlation (see Fig. 3.5).

Condensation models based on a detailed near-wall treatment in research CFD code

The CASTEM code, developed by CEA, is a multipurpose research code that uses a finite element discretization method. The flow solver is based on an asymptotic model of the Navier-Stokes equation at the low Mach number regime, where the pressure field can be decomposed into a thermodynamic pressure and a fluctuating pressure responsible of the flow. A fully implicit algorithm is used for pressure velocity coupling.

In the CASTEM code, diffusion phenomena in binary mixture are treated by means of the Fick's diffusion law. Wall condensation phenomena in the presence of air are then simulated by a pure diffusive model that is integrated in the structure of the code by appropriate boundary conditions assigned to the momentum balance equations. The interface Stefan velocity, evaluated on the

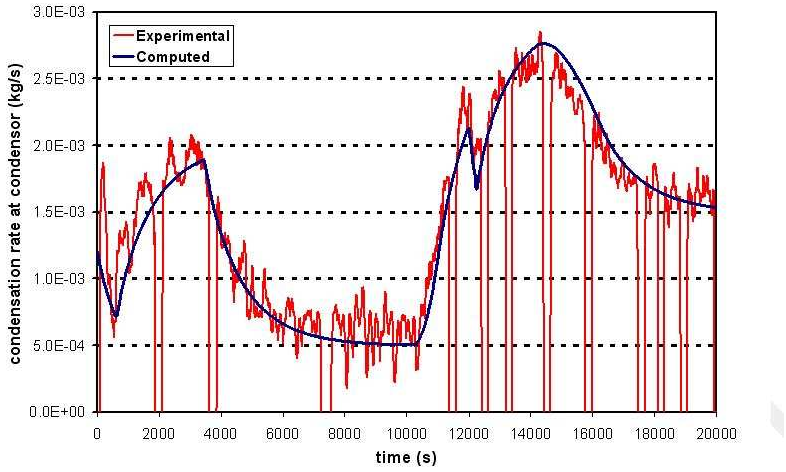

Figure 3.2: NRG model - Measured and predicted condensation rate in the PHEBUS FPT1 test (Fig. from [89])

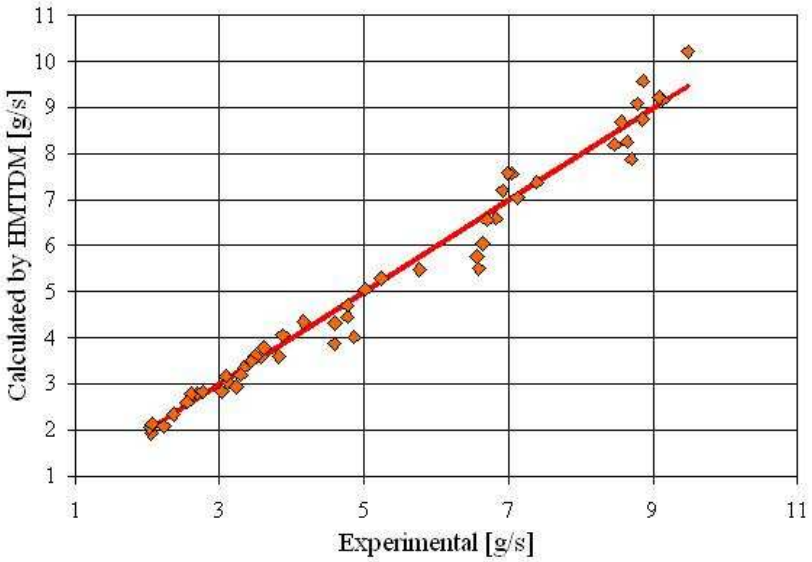

Figure 3.3: UNIPI/HMTDM model - Measured and predicted condensation rates for steam-air tests performed within the CONAN facility (Fig. from [89])

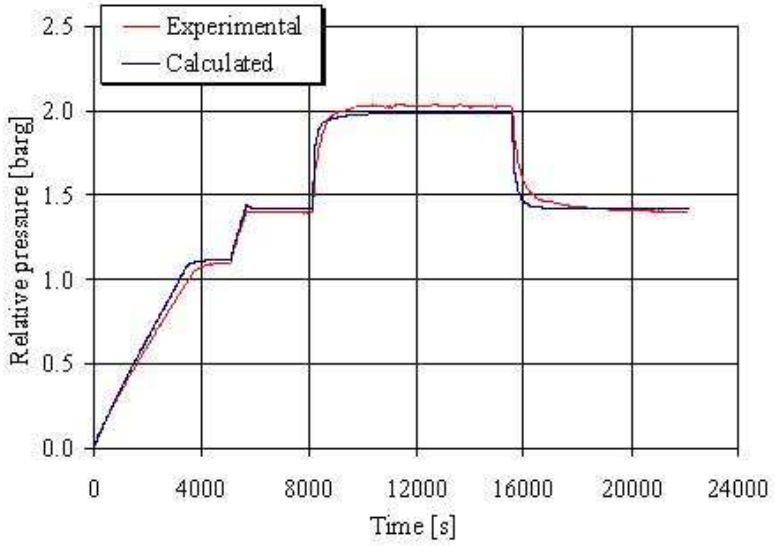

Figure 3.4: UNIPI/HMTDM model - Measured and predicted condensation rate in the ISP47 TOSQAN test (Phase A) (Fig. from [89])

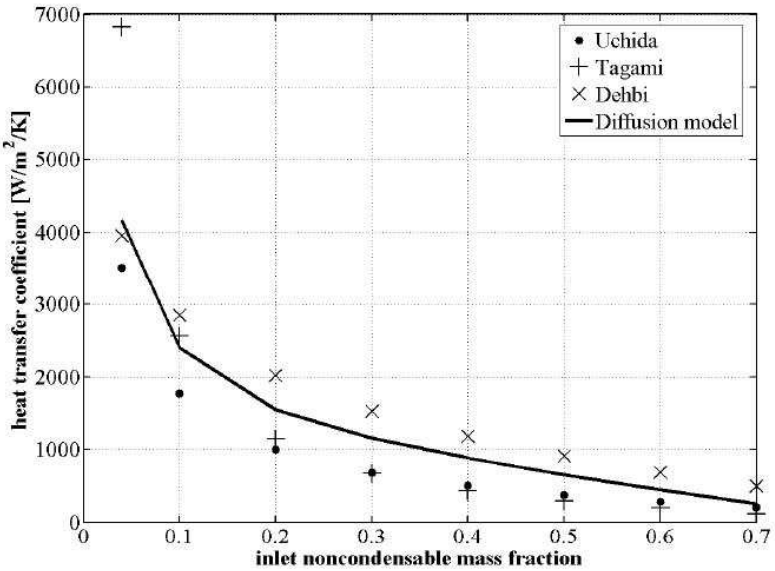

Figure 3.5: KTH model - Influence of noncondensable mass fraction on the average heat transfer coefficient (Fig. from [89])

basis of the Fick's diffusion law and assigned to the condensing wall is given by:

$$u_{\vec{stef},i} = \frac{\dot{\vec{m}}''}{\rho_i} = -D_{va,i}\frac{\nabla Y_{v,i}}{1 - Y_{v,i}}$$

The air flux is imposed equal zero all over the condensation surface. The presence of the liquid film is neglected; the condensation temperature, corresponding to the temperature at the interface between the liquid film and the gas mixture is then assumed to be the wall temperature. The assumption of ideal gas behavior of the steam is taken, so that the steam molar fraction is given by the ratio of the steam partial pressure and the mixture absolute pressure. To deal with turbulence modeling in channels, a mixing length model is used, in which the mixing length parameter depends on the distance from the walls:

$$l_m = y_w\left(1 - 2\frac{y_w}{W_{ch}}\right) \tag{3.10}$$

The Reynolds turbulence number based on the mixing length is then given by

$$Re_t = \frac{\rho u l_m}{\mu} \tag{3.11}$$

where u is the centerline velocity and

$$\mu_t = \Big(Re_t - C^2\Big)\frac{\mu}{C^2} \tag{3.12}$$

is the turbulence viscosity. The C constant is tuned on the basis of nondimensional velocity profiles predicted in pure heat transfer cases. Turbulent Prandtl and Schmidt number are assumed equal to 0.9 all over the domain.

3.4.2 Other condensation models based on a detailed near-wall treatment

Condensation modeling based on the Nusselt theory

A mass transfer model has been proposed by UJV for fine modeling of condensation phenomena, based on Nusselt of the filmwise condensation. The liquid film is taken into account with a 0D model that allows assigning its equivalent resistance and the velocity at the interface with the gas mixture.

Steady state simulations are performed with a pseudo-transient time scheme. The algorithm includes an internal iteration loop, aimed to calculate the appropriate liquid film structure, compatible with the condensation mass flow rate.

At a certain time step, the solution is converged with an assigned condensation mass flow rate and a corresponding film structure of thickness δ_{old}. The profile of the liquid film resumed from the previous time step is the first tentative profile δ_l for the time step to be solved.

Given the liquid film thickness δ_l, the condensation heat transfer that crosses the condensate film is taken equal to

$$\dot{q}_w'' = h_{c,l}\Big(T_{sat}(P_{v,c}) - T_w\Big) \tag{3.13}$$

where $T_{sat}(P_{v,c})$ is the saturation temperature corresponding to the partial pressure of the steam in the near-wall cell that in the approximation of UJV, for small cells in the near-wall layer, is similar to the interface temperature. The heat transfer coefficient through the liquid film is given by

$$h_{c,l} = \frac{k_l}{\delta_l} \tag{3.14}$$

with δ limited in order to avoid $h_{c,l} > 20000 W.m^{-2}.K^{-1}$.

According to the Nusselt theory, in a downward condensing mixture, the velocity profiles of a laminar liquid film are self similar, depending on the distance y from the wall:

$$u_l = \frac{1}{\mu_l}\rho_l g \delta_l^2 \left[\frac{y}{\delta_l} - \frac{1}{2}\left(\frac{y}{\delta_l}\right)^2\right] \tag{3.15}$$

The corresponding condensate film flow rate (per unit depth) from the control volume with film thickness δ_l to the downstream control volume is then given by:

$$\dot{M}_{l,out} = \rho_l \int_0^{\delta_l} u_l dy = \frac{1}{3\mu_l}\rho_l^2 g \delta_{l,out}^3 \tag{3.16}$$

In the same way, the condensate mass flow rate from the upward control volume is given by:

$$\dot{M}_{l,in} = \rho_{l,in} \int_0^{\delta_{l,in}} u_{l,in} dy = \frac{1}{3\mu_{l,in}}\rho_{l,in}^2 g \delta_{l,in}^3 \tag{3.17}$$

It is assumed that the condensate is cooled down from the saturation temperature $T_{sat}(P_v, c)$ at the interface to the mean temperature of the liquid film, according to the following relationship:

$$T_{sat}(P_{v,c}) - T_f = \frac{3}{8}\Big(T_{sat}(P_{v,c}) - T_w\Big) \tag{3.18}$$

The resulting condensation mass flux is then estimated by:

$$\dot{m}'' = \frac{\dot{q}_w''}{\hbar^{lat}(T_{sat}(P_{v,c})) + Cp_l\Big(T_{sat}(P_{v,c}) - T_f\Big)} \tag{3.19}$$

The mass balance over an arbitrary near-wall volume can be then written as:

$$\frac{\delta M}{\delta t} = \dot{M}_{l,in} - \dot{M}_{l,out} + \dot{m}'' \tag{3.20}$$

substituting equations (3.16) and (3.18) in equation (3.19), the updated value of the liquid film is given by

$$\delta_{new} = \delta_{old} + \frac{g\triangle t}{3\mu_l \triangle x}\rho_l\Big(\delta_{l,in}^3 - \delta_{l,out}^3\Big) + \frac{\triangle t}{\rho_l}\frac{V_{cell}}{A_{cell}}\dot{m}'' \tag{3.21}$$

At each internal iteration, the new film thickness δ_{new} replaces δ_l and all the internal iteration loop is repeated until all quantities and the $\delta_{l,in}$ profile are converged. Once convergence is reached the volumetric source terms of the

external loop are updated. The steam volumetric source is then obtained by substituting the condensation mass flux obtained by Eq. (3.19) in Eq. (3.1).

The presence of the condensing film is also accounted for thanks to a moving wall boundary condition. On the surface of the domain corresponding to the condensing wall a sliding velocity is imposed equal to

$$u_w = \frac{1}{2\mu_l}\rho_l g \delta_l^2 \tag{3.22}$$

A realizable $\kappa - \varepsilon$ models is employed, coupled with special wall functions conceived to deal with transpiration effects, named *Enhanced Wall Treatment* in the Fluent code.

The model was checked against the test N1 performed in the Russian facility EREC BCEQ, related to the behavior of bubble condensers during large break LOCAs [94].

Condensation modeling based on the stagnant layer theory

Based on the theory of the stagnant layer, VTT and JRC condensation models are implemented respectively in the Fluent and the CFX code. The VTT and JRC model combines a condensation model based on the stagnant layer theory and the heat and mass transfer analogy, conceived in principle to be use for relatively coarse near-wall discretizations, with a turbulence model having low-Re capabilities.

The molar fluxes of a non-condensable gas and a vapor through a plane at a distance y from the condensing interface are given by the following pair of differential equations

$$\dot{n}_a^{''} = \dot{n}^{''} X_a + j_a^* = \dot{n}^{''} X_a - C\ D_{av} \frac{dX_a}{dy} = 0 \tag{3.23}$$

$$\dot{n}_v^{''} = \dot{n}^{''} X_v + j_v^* = \dot{n}^{''} X_v - C\ D_{av} \frac{dX_v}{dy} \tag{3.24}$$

Because there is no net flow of the non-condensable gas through the plane, the two equations can be reduced to

$$\dot{n}_v^{''} = -C\ D_{av} \frac{dX_v}{dy} \left(\frac{1}{1 - X_v} + 1 \right) \tag{3.25}$$

The integration of Eq. (3.25) from the condensing interface $y = 0$ to the edge of the boundary layer $y = \delta$ allows calculating the molar flux of vapor passing through the interface. Assuming that the molar concentration and the diffusion coefficient are constant in the diffusion layer, the molar flux of steam is given by

$$\dot{n}_v^{''} = -\frac{C\ D_{av}}{\delta_n}\ \ln \frac{1 - X_{v,i}}{1 - X_{v,\delta}} \tag{3.26}$$

where δ_n refers to the thickness of the stagnant layer. In a turbulent boundary layer, the diffusivity becomes the turbulent diffusivity and this can be included in a turbulent mass transfer coefficient h_m, which is defined as

$$h_m = \frac{M_v\ D_{av}\ \rho}{M\ \delta_n} \tag{3.27}$$

The vapor molar flux can be therefore reversed to a mass flux

$$\dot{m}_v^{''} = -h_m \ \ln \frac{1 - X_{v,i}}{1 - X_{v,\delta}} \tag{3.28}$$

The mass transfer coefficient h_m is here evaluated by the analogy between heat and mass transfer. The molar fraction at the interface is determined from the partial pressure of the vapor assuming saturation at the interface temperature. The vapor at the edge of the boundary layer has the same properties than the bulk and may be a super-saturated vapor. Only the dry part of the vapor will form the concentration gradient which drives the condensation flux, therefore, only the molar fraction of dry vapor must be used to determine the mass flux of vapor in bulk.

$$X_{v,\delta} = min\Big[X_{v,\delta}; X_{v,sat}(T_b)\Big] \tag{3.29}$$

It is also assumed that the water droplets suspended in the vapor are not transported to the interface, but merely act as a reservoir for the production of dry vapor to counter the depletion in the boundary layer by condensation.

The mass flux of vapor crossing the interface contributes to the transfer of heat through two mechanisms: the convection of sensible heat from the gas into the film and the release of latent heat due to the phase change. Both mechanisms influence the interface temperature that, in turn, governs the saturation conditions at the interface. The vapor concentration gradient, and hence the mass flux, is dependent on the interface temperature and the interface temperature is itself dependent on the amount of heat deposited by the mass flux. Therefore, an iterative scheme is required to achieve compatibility between the interface temperature and the vapor mass flux. An energy balance on the liquid film interface gives the required equation to update the interface temperature for a given vapor mass flux:

$$T_i = \frac{T_w \ \frac{k_l}{\delta_l} + \Big(h_s - \dot{m}_v^{''} C_{p,b}\Big) - \dot{m}_v^{''} H_i^{lat}}{\frac{k_l}{\delta_l} + h_s - \vec{\dot{m}}^{''}{}_v C_{p,b}} \tag{3.30}$$

where the sensible heat transfer coefficient h_s from the gas phase to the liquid is known by appropriate heat transfer correlation. On the other hand, the determination of the effective heat transfer coefficient through the film requires the thickness δ_l of the liquid film to be known. If the liquid film is neglected, as in the case of the VTT model, the liquid film interface temperature reduces to the wall temperature. In the JRC model, the liquid film is instead accounted. An average film thickness is applied, determined by integrating of the Nusselt equation over the height of the vertical wall, with the simplifying assumption that the wall is vertical over its entire height. The Nusselt equation for the liquid film thickness is:

$$\delta_l = \left[\frac{4\mu_l k_l x(T_i - T_w)}{g \ \hbar_i^{lat} \rho_l(\rho_l - \rho_b)}\right]^{\frac{1}{4}} \tag{3.31}$$

Assuming the temperature change across the film to be of the order of 1 C, for a water liquid film eq. (3.31) reduces to

$$\delta_l = 0.0001 \ x^{\frac{1}{4}} \tag{3.32}$$

The integration over the height of the wall L, gives the average film thickness as

$$\delta_l = 0.00008\ L^{\frac{1}{4}} \tag{3.33}$$

Once the iterative procedure is converged on the steam molar flux and the interface temperature T_i the volumetric source terms are applied to the cells beside the condensing wall.

As already remarked, the VTT and JRC model combines a condensation model based permitting the use of relatively coarse discretization with a turbulence model having low-Re capabilities and therefore requiring a refined near-wall discretization. Actually, the computational cost of a model depends on the required resolution of the balance equations in the boundary layer. Since the governing equations are solved in detail in the near-wall region, it is not clear which is the advantage of introducing correlations via the heat and mass transfer analogy instead of solving the species mass flux at the condensing interface by the diffusion laws.

VVT implemented the model in the FLUENT code and applied it coupled with the standard $\kappa - \varepsilon$ model with enhanced wall treatment functions to the simulation of the ISP47 MISTRA test by VTT [95].

3.4.3 Coarse mesh condensation models based on the heat and mass transfer analogy

The UNIPI HMTAM condensation model

A condensation model for coarse meshes have been developed and validated at UNIPI, named HTMAM [96]. The mass transfer rate is obtained. The model is based on the analogy between heat and mass transfer cast in terms of mass fractions, as proposed in the formulation of Spalding [53]:

$$\dot{m}'' = Sh_0 \frac{\rho_c\ D_{v,c}}{l} ln \frac{Y_{n,b}}{Y_{n,w}} \tag{3.34}$$

where l is a characteristic length and the film properties are taken at the center of the first cell and the Sherwood number is evaluated on the basis of the Nusselt number in equivalent conditions of pure heat exchange

$$Nu_0 = f\Big(Re, Gr, Pr\Big) \Longrightarrow Sh_0 = f\Big(Re, Gr, Sc\Big) \tag{3.35}$$

The RNG $\kappa - \varepsilon$ model is used, coupled with a standard wall treatment approach for dealing with near-wall turbulence. Near-wall cells are thick enough to meet the requirement $60 < y^+ < 300$. The validation of the HTMAM model has been performed against the CONAN database of steam condensation with air (see Fig. 3.6) and the ISP47 TOSQAN test in presence of air and helium (see Fig. 3.7). The steady states of the ISP47 MISTRA test were also performed.

The CEA TONUS condensation model

TONUS is the name of a special application of the CASTEM code, purposely conceived to address thermal-hydraulic phenomena in the nuclear reactor containment; the TONUS condensation model is then purposely conceived for addressing condensation phenomena in turbulent natural convection, whose relevance is remarkable in a loss of coolant accident scenario. A condensation model

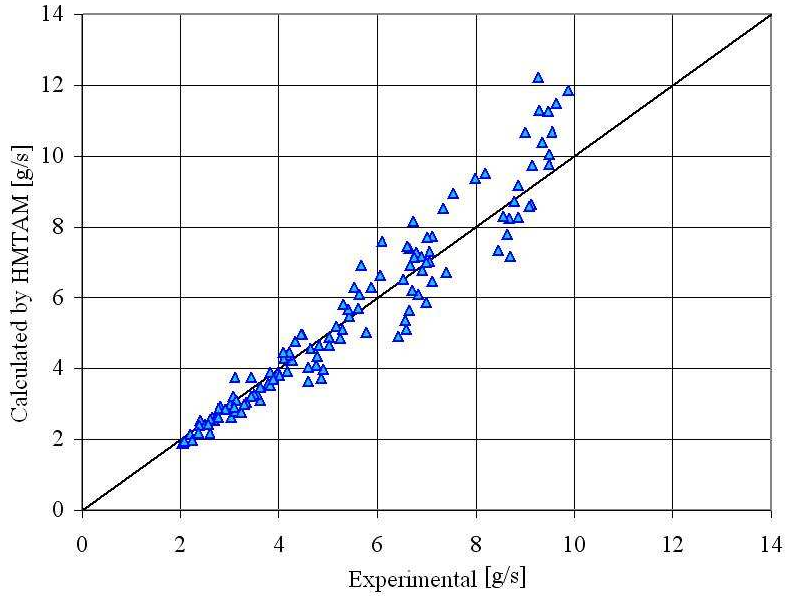

Figure 3.6: UNIPI/HMTAM model - Measured and predicted condensation rates for steam-air tests performed within the CONAN facility (Fig. from Bucci [96])

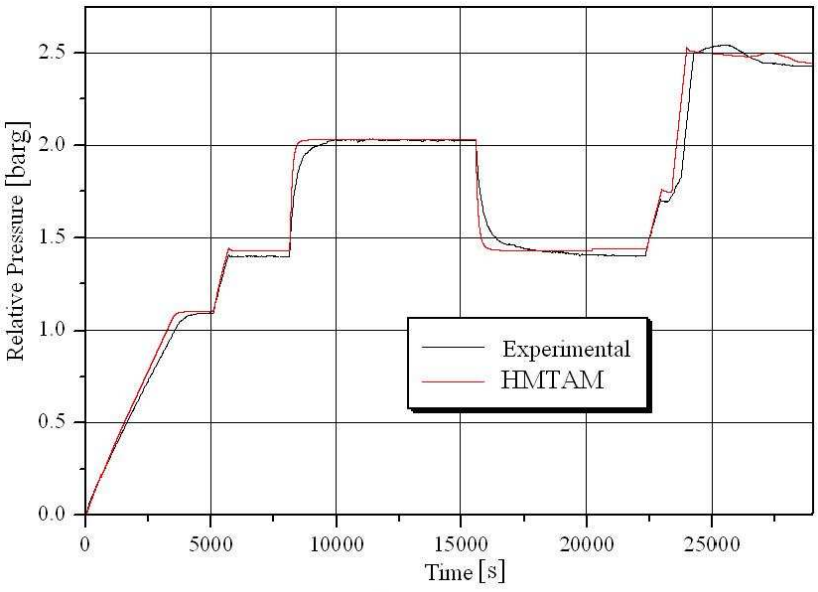

Figure 3.7: UNIPI/HMTAM model - Measured and predicted condensation rate in the ISP47 TOSQAN test (Fig. from Bucci [96])

based on the analogy between heat and mass transfer has been developed and validated by CEA in the frame of the TONUS project. Being TONUS conceived as a special CAST3M application, mass transfer is simulated in a similar way. However, mass flux is imposed at the interface, instead of the Stefan velocity (see Eq. (3.4.1)). The overall heat transfer flux is evaluated on the basis of the Chilton-Colburn analogy:

$$\dot{q}^{''} = h_{tot}(T_b - T_w) \tag{3.36}$$

where h_{tot} is the sum of the pure convective heat transfer coefficient and the condensation heat transfer coefficient:

$$h_{tot} = h_s + h_c \tag{3.37}$$

The convective heat transfer coefficient is obtained by the McAdams correlation

$$h_c = 0.13k\left[\frac{g}{\nu^2}\frac{|\rho_w - \rho_b|}{\rho_b}\right]^{1/3} \tag{3.38}$$

where Pr is assumed equal 1.

The condensation heat transfer is given by:

$$h_c = K_m\frac{H^v - H^l}{T_b - T_w}\alpha(\rho_b^v - \rho_w^v) \tag{3.39}$$

where

$$K_m = h_s\frac{D_{vm}^{2/3}\nu^{1/3}}{k}\left(\frac{1}{1 - Y_{v,i}}\right) \tag{3.40}$$

is the mass transfer coefficient in $[m/s]$. The mass flux is then given by:

$$\dot{m}^{''} = K_m\rho(Y_{v,i} - Y_{v,b}) \tag{3.41}$$

In TONUS, turbulence is modeled by a mixing length model. The characteristic length, above which the length scale are solved and below which the scales are modeled by a turbulent viscosity is usually assumed constant all over the computational domain. The turbulence viscosity is thus given by

$$\mu_t = l_m^2 S \tag{3.42}$$

where

$$S = \frac{1}{2}||\nabla\vec{U} + \nabla\vec{U}^T u|| \tag{3.43}$$

The TONUS code has been extensively applied to the simulation of a relevant database concerning condensation. The Huhtiniemi and the COPAIN tests have been simulated (see Fig. 3.8), as well as the PHEBUS FPT1 test, and the TOSQAN and the MISTRA tests performed in the frame of the ISP47. The modeling of other tests performed within MISTRA has also been performed in the frame of research activities by CEA.

3.4.4 Coarse mesh condensation modeling based on empirical correlations

A suitable approach for dealing with condensation in coarse mesh calculations is adopting experimental correlations to define the mass transfer coefficient.

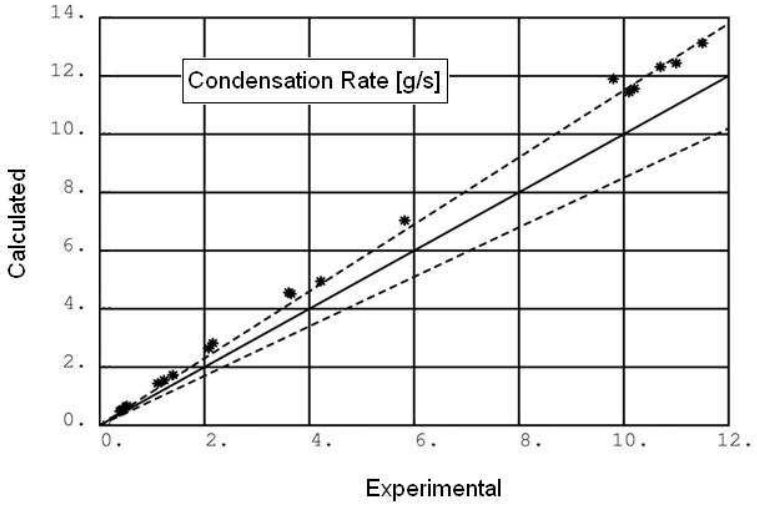

Figure 3.8: CEA TONUS model - Measured and predicted condensation rates for steam-air tests performed within the COPAIN facility (Fig. from Deri [97])

The JSI condensation model

In this aim, JSI adopted the Uchida correlation. In this case, the condensation mass flux is evaluated as follows:

$$\dot{m}'' = C_U \frac{\rho_{v,c}}{\rho_{nc,c}} \frac{T_c - T_w}{\hbar^{lat}} \tag{3.44}$$

where T_c is the near-wall cell temperature. Indeed, all physical variables, except T_w should be calculated in the bulk. In the model, for the sake of simplicity, bulk flow conditions are replaced by conditions in the cells contiguous to the condensing wall and thus the model is sensitive to their size. Actually, the cell size is limited by the requirement of the turbulence model and the near-wall modeling strategy. Wall functions are used requiring the nondimensional distance of the center of the near-wall cells Y_c^+ limited to 300, for which bulk conditions are hardly attained. An adjustable coefficient C_U is therefore used, tuned to achieve the right experimental pressure. Once attained the correct experimental pressure for a specific steady-state condition, the model is checked against the concentration profiles of the different involved chemical species. Clearly, the JSI model lack of generality. The TOSQAN and the ThAI ISP47 tests have been addressed [98, 99, 100, 101].

The UPM condensation model

The model proposed by UPM is based on the Terasaka correlation [102]. The model was selected between four different models adopting various forms of the heat and mass transfer analogy [103]. The Terasaka correlation accounts for the effects of degradation induced by noncondensable gases with respect to the pure vapor condensation. The model makes use of an experimental correlation

that multiplies the condensation heat flux predicted by the Nusselt theory in similar conditions to simulate the effect of heat transfer degradation due to noncondensable gases. It is:

$$\dot{q}_{cond}^{''} = f(Y_{nc})\ \dot{q}_{Nu}^{''} \tag{3.45}$$

where

$$f(Y_{nc}) = \Big[1\ -\ 0.964\ Y_{nc}\ +\ 4.989\ Y_{nc}^2\ -\ 4.135\ Y_{nc}^3\Big] \frac{1 - Y_{nc}}{1 + 15.48 Y_{nc}} \tag{3.46}$$

and the condensation mass flux is finally given by:

$$\dot{m}^{''} = \frac{\dot{q}_{cond}^{''}}{\hbar^{lat}} \tag{3.47}$$

The model has been tested against the MISTRA MICOCO test and the Dehbi database [103, 104].

3.4.5 Other coarse mesh condensation models

Coarse mesh condensation models based on wall functions

In the GASFLOW code [10], developed by FZK, turbulence modeling in the near-wall region is dealt with by wall functions. Based on velocity wall functions, the heat transfer coefficient is evaluated and the mass transfer is therefore deduced on the basis of the heat and mass transfer analogy.

The current wall function model for turbulent boundary layer is based on the Von Karman three layer model:

$$u^+(y^+) = \begin{cases} y^+ & y^+ \le 5 \\ 5 \ln y^+ - 3.05 & 5 < y^+ \le 30 \\ \frac{1}{\kappa} \ln y^+ + 5.5 & 30 < y^+ \end{cases} \tag{3.48}$$

where $\kappa = 0.4$ is the Von Karman constant.

Integrating the turbulent boundary layer equation, the convective heat transfer coefficient is obtained in the following form

$$\begin{aligned} \frac{h_s}{\rho\ C_p\ u^*} &= \left[\int_0^{y^+} dy^+ \left(\frac{1}{Pr_t}\frac{\nu_t}{\nu} + \frac{1}{Pr}\right)^{-1}\right]^{-1} \\ &= \left[\int_0^{y^+} dy^+ \left(\frac{1}{Pr_t}\Big(\nu^+ - 1\Big) + \frac{1}{Pr}\right)^{-1}\right]^{-1} \end{aligned} \tag{3.49}$$

where

$$\nu^+ = \frac{dy^+}{du^+} = \frac{\nu_t}{\nu} + 1 \tag{3.50}$$

According to the Von Karman profiles, the most general heat transfer functions for $y+ > 30$ are given by:

$$\frac{h_s}{\rho\ C_p\ u^*} =$$

$$\left[5Pr + \int_5^{30} dy^+ \left(\frac{1}{5Pr_t}\Big(y^+ - 5\Big) + \frac{1}{Pr}\right)^{-1} + \int_{30}^{y^+} dy^+ \left(\frac{1}{Pr_t}\Big(\kappa y^+ - 1\Big) + \frac{1}{Pr}\right)^{-1}\right]^{-1}$$

(3.51)

A modification of the FZK GASFLOW model is proposed by VEIKI. modified wall functions are used following:

$$u^+(Re_w) = \begin{cases} Re_w^{0.5} & 0 < Re_w \leq 25 \\ 3.20735\ \ln Re_w\ - 5.3239 & 25 < Re_w \leq 428.843 \\ 2.1875\ \ln Re_w\ - 0.8572 & 428.843 < Re_w \end{cases} \tag{3.52}$$

where the wall Reynolds number is defined as

$$Re_w = \frac{u\ y}{\nu} \tag{3.53}$$

Instead of integrating the turbulent thermal boundary layer, as proposed by FZK, the convective heat transfer coefficient is obtained via the Colburn Reynolds analogy between momentum and heat transfer

$$h_s = \frac{\rho\ C_p\ u^*}{u^+}\ Pr^{\frac{2}{3}} \tag{3.54}$$

Whatever is the adopted GASFLOW version, the mass transfer coefficient is hence obtained by the analogy between heat and mass transfer:

$$K_m = \frac{h_s}{\rho\ C_p}\ Le^{\frac{2}{3}} \tag{3.55}$$

The rates of heat transfer and condensation increase when the mass of steam becomes a relatively large fraction of the mass of the gas mixture. As the mass-transfer rate increases, the thermal and concentration boundary layers become thinner because of the suction effect of the condensation process. This reduction in the boundary layer thickness further increases the temperature and concentration gradients near the boundary and consequently increases the heat and mass-transfer coefficients. The opposite effect occurs at a surface where vaporization of a liquid film is taking place; hence, the heat and mass transfer coefficients decrease during these conditions. Correction factors [105, 25] can be used to determine the increase in the heat and mass transfer coefficients. The corrected heat-transfer coefficient then become

$$h_s^* = h_s\ \frac{\Phi_T}{e^{-\Phi_T} - 1} \tag{3.56}$$

where the factor Φ_t is given by:

$$\Phi_T = \frac{\dot{m}^{''} \; C^v_{p,w}}{h_s} \tag{3.57}$$

Following similar ideas as with the heat-transfer coefficient for relatively large steam mass fractions, the mass-transfer coefficient is corrected by

$$K^*_m = K_m \; \log \frac{R+1}{R} \tag{3.58}$$

where the flux ratio R is expressed

$$R = \frac{X_{v,w} - X_{v,b}}{1 - X_{v,w}} \tag{3.59}$$

Finally, it is:

$$\dot{m}^{''} = K^*_m \Big(\rho_{v,sat}(T_w) - \rho_{v,c} \Big) \tag{3.60}$$

and, consequently, the volumetric mass source term of steam, assigned to the near-wall cells is given by:

$$S_m = K_m \Big(\rho_{v,sat}(T_w) - \rho_{v,c} \Big) \frac{A_c}{V_c} \tag{3.61}$$

In the case of evaporation, for the situation where dryout of the mass transfer surface may occur, the liquid film totally evaporates leaving the surface dry, an alternative formulation of the surface mass transfer is

$$S_m = \frac{A_c}{V_c} \; min \left[K_m \Big(\rho_{v,sat}(T_w) - \rho_{v,c} \Big) \; ; \; \frac{\delta_l \rho_l}{2 \triangle t} \right] \tag{3.62}$$

where δ_l is the film thickness and $\triangle t$ is the computational time step in seconds. Note the sign of the equation: positive indicates vaporization of the liquid film, whereas negative means condensation. In the case of liquid film vaporization, at near dryout condition, only half of the available film is allowed to evaporate in a time step. This ensures that the model will not evaporate all of the liquid film in a single time step for this heat structure.

The capabilities of the GASFLOW model have been checked against an extensive set of condensation data comprehensive of the all ISP47 tests (see Fig. 3.9), the PHEBUS FPT0 and FPT1 tests.

3.5 The SARnet condensation benchmarks

An analysis of the models features, reported in the previous paragraph allowed identifying the main strategies adopted for the purpose of condensation modeling in CFD and the most relevant experiences by which the models capabilities have been checked. Most of the reported models were tested in the frame of the ISP47 program, highlighting some open issues, like the effect of helium addition, that are difficult to understand by analyzing integral tests in large scale facilities, like MISTRA and THAI [11].

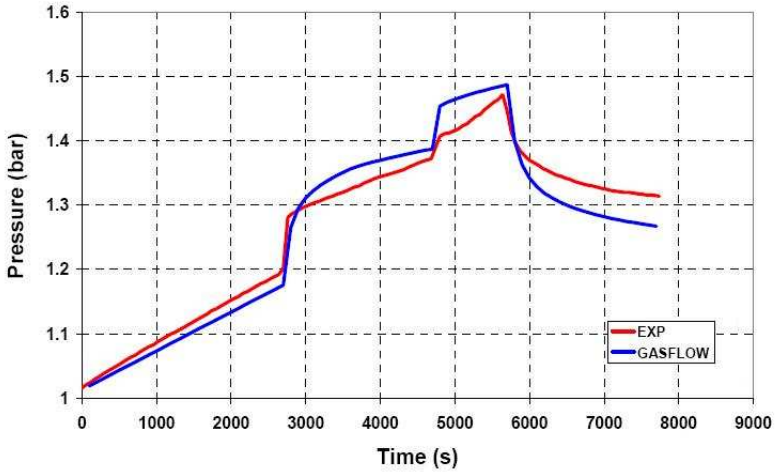

Figure 3.9: GASFLOW model - Measured and predicted pressure in the ISP47 ThAI test (Fig. from [89])

In this aim, the need for a dedicated and more detailed code improvement around these experimental conditions emerged in the frame of the SARnet NoE. As a first step towards a more in-depth understanding of the aforementioned complex phenomena, a benchmark exercise has been proposed to compare and validate the different available CFD models previously described in predicting heat and mass transfer during condensation in the presence of air as noncondensable gas. The activities were performed in two steps, proposing a 0th level problem and a 1st level one, addressing respectively idealized conditions and real experimental data. In the former case, a geometry similar to the one of the CONAN facility [8] was considered, assuming constant condensing surface temperature conditions that cannot be actually achieved in experiments; in this step, code results for heat and mass transfer were compared with engineering correlations credited to be applicable in the considered conditions. In the latter case, boundary conditions from CONAN experiments were provided to participants, requesting blind predictions of the overall condensation rate and of the local heat fluxes and surface temperatures, to be compared with available measurements.

3.5.1 The step 0: condensation on an isothermal flat plate

This first step of the benchmark exercise was conceived to have a first approach to the problem, to be subsequently dealt with on the basis of experimental data. The objective of the 0th Step was to compare code results with correlations considered applicable to the addressed problem. Reference was made to the 2D computational domain sketched in Fig. 3.10, to be used in two different ways:

- by pure convective heat transfer calculations (no steam condensation), capable to highlight the adequacy of the adopted turbulence models and of the selected numerical grids in reproducing the heat transfer trends

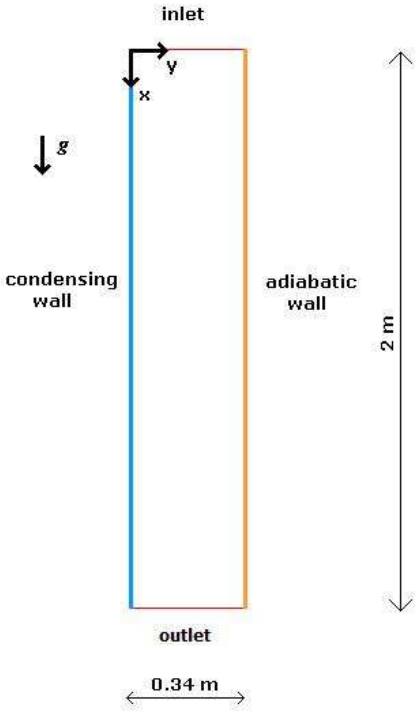

Figure 3.10: Geometrical configuration of the proposed computational domain for 0th Step

predicted at large values of the local Reynolds number by the correlation

$$Nu_x = 0.0296\ Re_x^{0.8} Pr^{0.33} \tag{3.63}$$

- by simultaneous heat and mass transfer calculations, whose results should be compared among each other and with the correlation drawn from the previous one by the application of the analogy between heat and mass transfer

$$Sh_{0,x} = 0.0296\ Re_x^{0.8} Sc^{0.33} \tag{3.64}$$

Equations (3.63) and (3.64) usually address external flow over a flat plate. These equations can be anyway applied to the proposed internal flow problem, being the channel sufficiently wide to avoid the interaction between the boundary layers that are established on the condensing wall and the adiabatic wall (see Fig. 3.10).

The models used for predicting condensation were first checked against a pure convective heat transfer case, in order to assess their capability in reproducing pure heat transfer phenomena, before addressing the more challenging heat and mass transfer. In this aim, participants were asked to calculated the local Nusselt number, according to the classical definition:

$$Nu_x = \frac{\dot{q}''\ x}{(T_i - T_b)\ k_i} \tag{3.65}$$

Test name	u_{inlet} $[m/s]$	T_{wall} $[K]$	T_{inlet} $[K]$	$Y_{v,inlet}$ [-]	P $[Pa]$
HT-30-3	3	303.15	363.15	0	101325
HT-30-6	6	303.15	363.15	0	101325
HT-60-3	3	333.15	363.15	0	101325
HT-60-6	6	333.15	363.15	0	101325
HMT-30-3	3	303.15	363.15	saturation	101325
HMT-30-6	6	303.15	363.15	saturation	101325
HMT-60-3	3	333.15	363.15	saturation	101325
HMT-60-6	6	333.15	363.15	saturation	101325

Table 3.1: Boundary conditions for the 0th step cases

Condensation adds a further challenge to the capabilities in modeling boundary layer phenomena, since temperature, velocity and concentration distributions are distorted by the presence of transversal flow. The modeling of steam condensation and the consistent modeling of species diffusion represent further code features to be assessed by comparison with available correlations. In this aim, participants in the benchmark were asked to calculate the Sherwood numbers as a function of the calculated mass fluxes

$$Sh_{0,x} = \frac{\dot{m}''}{\frac{\rho D}{x} \ln \frac{Y_{nc,b}}{Y_{nc,i}}} \tag{3.66}$$

coherently with the corrections for suction effects proposed on the basis of the solution of the Stefan's problem.

Table 3.1 summarizes the values of the relevant independent parameters in the proposed eight cases involving both pure heat transfer (HT cases) and heat and mass transfer (HMT cases).

The values of inlet velocity were selected in order to allow the analysis of computed data at sufficiently large Reynolds numbers, to assure that the forced convection correlations are applicable at least in the last part of the channel. The heat and mass transfer cases involved a saturated air and steam mixture at the assigned inlet temperature. The two values of temperature of the condensing wall, assumed to be uniform, represent actually gas-liquid interfacial values, since no falling film is considered at the wall; this assumption was introduced to avoid complications due to different modeling of the falling film by the Participants.

Ten organizations participated in this step of the Benchmark adopting different codes and models, as reported in Table 3.2.

As it can be noted from Figure 3.11 and 3.12, all the codes were reasonably successful in predicting the asymptotic trend of the correlation in the heat transfer cases; this testifies for an adequate representation of boundary layer phenomena with the adopted models and discretization. On the other hand, Figs. 3.13 and 3.14 show a greater degree of spread in the asymptotic power-law trends obtained by the different codes in the prediction of the Sherwood number; this spread is anyway limited, except in the case of predictions by JSI, which are out of range because of the use of a different definition of the dimensionless parameters and the adoption of the Uchida correlation for a forced convection case.

Organization	Code	Condensation and turbulence model
CEA	Cast3m	Fickian diffusion Buleev mixing length
FZJ	CFX 10.0	Fickian diffusion SST
FZK	GASFLOW 2.4	Heat and mass transfer analogy Standard $\kappa - \varepsilon$ + standard wall functions
JRC	CFX 10.0	Stagnant layer theory SST
JSI	CFX 4.4	Uchida Standard $\kappa - \varepsilon$ + standard wall functions
NRG	Fluent 6.3	Fickian diffusion Launder and Sharma low-Re $\kappa - \varepsilon$
UJV	Fluent 6.1	Nusselt theory Realizable $\kappa - \varepsilon$ + EWT functions
UNIPI	Fluent 6.1	Fickian diffusion RNG $\kappa - \varepsilon$ + EWT functions
VEIKI	GASFLOW 2.4	Heat and mass transfer analogy Standard $\kappa - \varepsilon$ + standard wall functions
VTT	Fluent 6.2	Stagnant layer theory Standard $\kappa - \varepsilon$ + EWT functions

Table 3.2: Participants and adopted models in the SARnet condensation benchmark

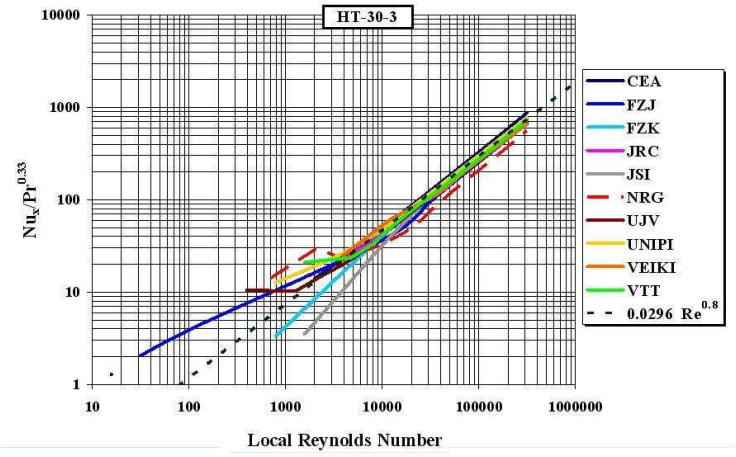

Figure 3.11: Results obtained for two heat transfer cases in the HT-30-3 case (Fig. from [106])

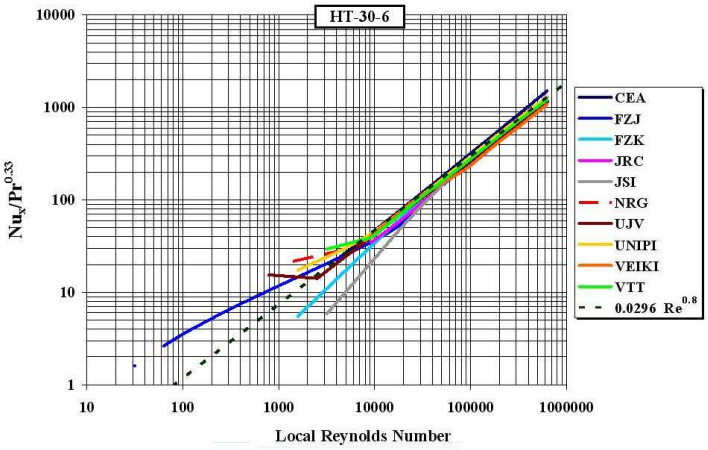

Figure 3.12: Results obtained for two heat transfer cases in the HT-30-6 case (Fig. from [106])

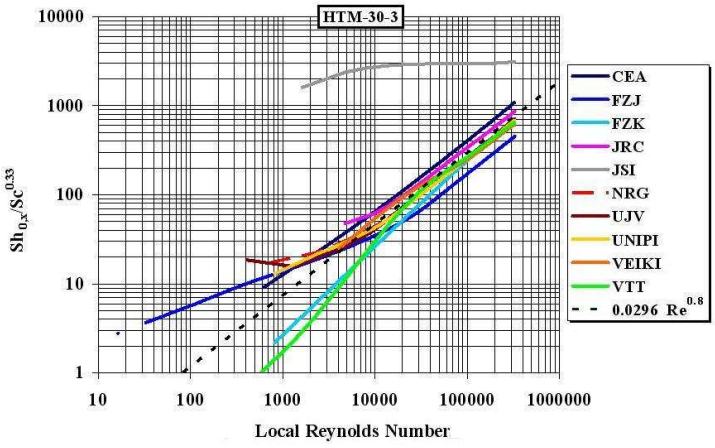

Figure 3.13: Results obtained for two heat transfer cases in the HMT-30-3 case (Fig. from [106])

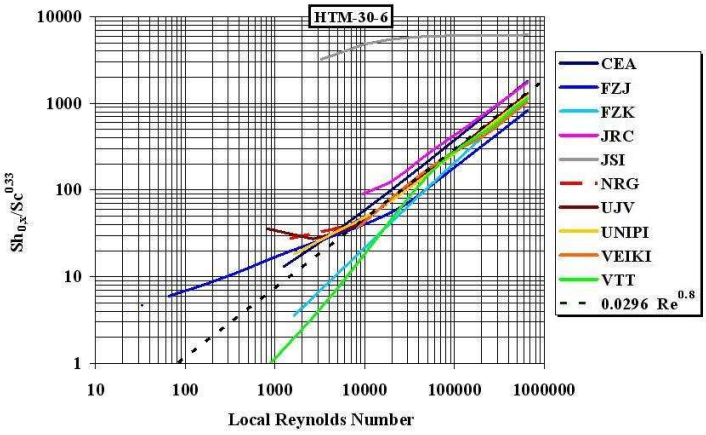

Figure 3.14: Results obtained for two heat transfer cases in the HMT-30-6 case (Fig. from [106])

3.5.2 The step 1: condensation in the CONAN experimental facility

The step 1 of the benchmark addressed experiments purposely performed in the CONAN experimental facility. To the purposes of the benchmark exercise, the test section can be represented as shown in Figure 3.15.

The facility includes a primary loop containing the test section, being a 2 m long square cross section channel (0.34 x 0.34 m). One of the sides of the test channel is made of a 4.5 cm thick aluminum plate cooled on the rear surface by secondary water flowing in a 5 mm deep rectangular channel. The primary steam and air mixture enters nearly at atmospheric pressure at the top of the channel in downward direction, with measured velocity, temperature and relative humidity. The lateral surfaces of the channel can be assumed to be adiabatic, except for the thick aluminum plate. A more detailed description of the CONAN facility will be provided in the next chapter.

Experimental data from five experimental tests were proposed to Participants. These data were related to operating conditions characterized by a nominal value of the secondary coolant close to 303.15 K, a steam generator power of 10 kW and mixture velocities from 1.5 to 3.5 m/s. In Figure 3.15, the data provided to Participants for each proposed experimental point are highlighted using the blue color, while the values to be provided were the distributions of plate surface temperatures and heat fluxes along the centerline and the total collected condensation rate.

On the basis of previous modelling experience at the University of Pisa, it was suggested to make use of a 2D computational domain addressing the channel middle plane orthogonal to the cooled plate and parallel to its longitudinal axis (see Fig. 3.15). Values of the turbulence intensity and of integral turbulence length scale were also suggested, leaving anyway to Participants the freedom to perform sensitivity analyses on these parameters on the basis of their engineering skills.

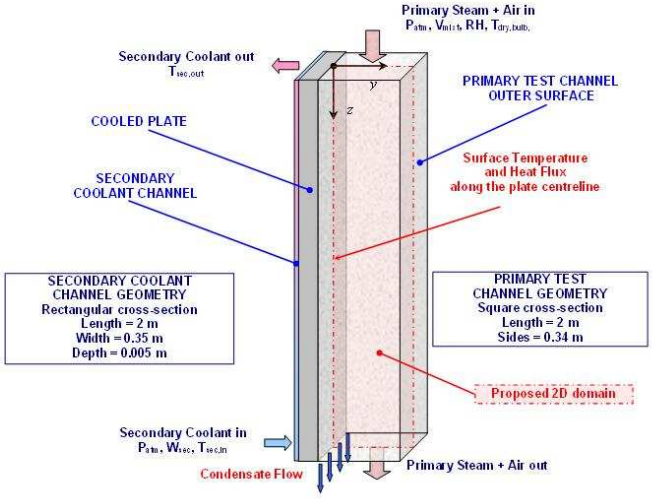

Figure 3.15: Sketch of the CONAN facility test section (Fig. from [84])

For dealing with condensing plate boundary conditions, the limited number of values of plate surface temperatures obtained from the measurements suggests that it is not advisable to assign any elaboration of such data in the form of interpolating functions. Previous experience at the University of Pisa showed that the use of the secondary coolant parameters and the heated plate conductivity to define appropriate 3rd kind boundary conditions at the rear of the plate surface is much more effective in providing less questionable input parameters to perform the calculations. In this regard, two different modelling strategies were suggested:

- simulating the heat conduction behavior of the 4.5 cm thick cooled aluminum plate by a conjugated heat transfer approach, imposing a linear trend of the secondary coolant temperature distribution and a suitable value of the heat transfer coefficient at the rear surface;
- considering an equivalent plate thermal resistance to be assigned in series with the convective one at the rear of the plate.

Since exploratory calculations previously performed at the University of Pisa showed only minor differences between the results of the two approaches, the choice between them was left to the Participants.

Nine organizations analyzed the proposed Step 1 data (CEA, FZJ, FZK, JRC Petten, JSI, NRG, UJV, UNIPI and VEIKI). The adopted models were basically the ones applied by the same organizations in the case of 0th Step. Most of the Participants simulated the cooled plate making use of an equivalent resistance (the second of the above described approaches), with the exception of the FZJ, CEA and UNIPI, that applied also the conjugated heat transfer approach.

The results obtained in terms of overall condensation rates are compared with experimental data in Figure 3.16.

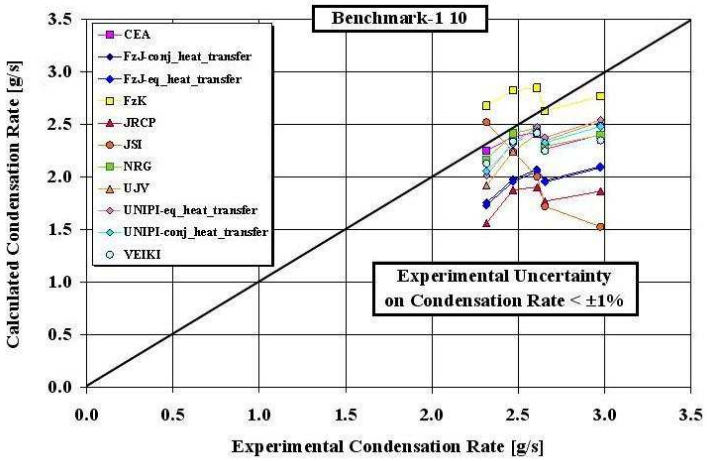

Figure 3.16: Calculated vs. experimental overall condensation rate predicted by participants for the step 1 exercise (Fig. from [84])

As it can be noted, there is a general tendency to underestimate the measured condensation rate. In particular, it can be noted that a group of models (adopted by CEA, NRG, UJV, UNIPI and VEIKI) provides very similar results, slightly underestimating the experimental data of condensation rate. The common qualitative trend of the discrepancies with respect to experimental values suggests also common reasons for this behavior. Systematic trends in relation to the effect of the slight degree of superheating existing in some conditions suggest a future specific analysis of the effect of this parameter.

The model by JSI, owing to the use of the Uchida correlation, seems not to catch the correct trend of condensation rate; in particular, since the experimental data involve different values of the ratio between steam and noncondensable gas density, being the most relevant parameter in the Uchida correlation, the obtained predictions are very sensitive to this ratio, disregarding other effects. Such discrepancies were completely within the expectations of JSI that adopted the Uchida correlation as a simple trial to estimate the error coming from the use of such a simplified formulation in the present conditions.

The effects of the assumptions made for heat transfer through the plate (conjugated heat transfer or equivalent plate thermal resistance) appears negligible. This can be noted comparing the results obtained by FZJ and UNIPI with the two approaches. The obvious reason for this behavior is the minor role of 2D heat conduction effects within the cooled plate.

The general underestimation of condensation rate seems to be the consequence of a systematic inadequacy in evaluating the heat flux distribution at channel inlet. This can be noted, for instance, in Figure 3.17 and Figure 3.18, reporting the data obtained by CEA and UJV. It can be noted, that the local heat flux is systematically underestimated by the calculations in the entrance region of the channel, where the codes predict a quicker extinction of the entrance effects with respect to the experiments. This behavior, not yet completely understood, has been the subject of subsequent sensitivity analyses performed by

changing the turbulence intensity and the integral length scale at the inlet as well as considering inlet velocity distributions different from the simple flat one suggested for the analysis. Nevertheless, it is apparent that the use of different turbulence models plays a role in this respect.

3.5.3 Final remarks on the condensation benchmarks

The two steps of the benchmarking activity allowed assessing the behavior of state-of-art condensation models adopted by the main institutions involved in the analysis of nuclear reactor thermal-hydraulics in the frame of SARnet. Though the proposed problems were related to forced convection condensation, which is often of lower interest for containment analyses with respect to free convection, the availability of the CONAN facility offered the opportunity to address in a systematic way the capabilities of codes in predicting experimentally observed behavior. Summarizing the relevant conclusions achieved up to now, it can be noted that:

- though at different extents, all the adopted CFD models are reasonably in agreement with the information at the basis of a well known correlation for forced convection heat transfer on a flat plate;
- even in the idealized case of condensation over an isothermal flat plate, most codes provided a reasonable prediction of the behavior expected on the basis of the analogy between heat and mass transfer, though in this case the spread in the obtained results around the correlation was larger;
- the application to actual experiments revealed more detail on the behavior of models, highlighting a general tendency to underestimate entrance effects; turbulence modeling in the development region near the inlet section can be the cause of this underestimation.
- some of the proposed models accounted the liquid film presence by an additional thermal resistance associated to the condensate layer. A comparison between condensation models adopting the liquid film modeling and others revealed that the resistance associated to the liquid film is negligible with respect to that due to the noncondensables build-up at the interface.

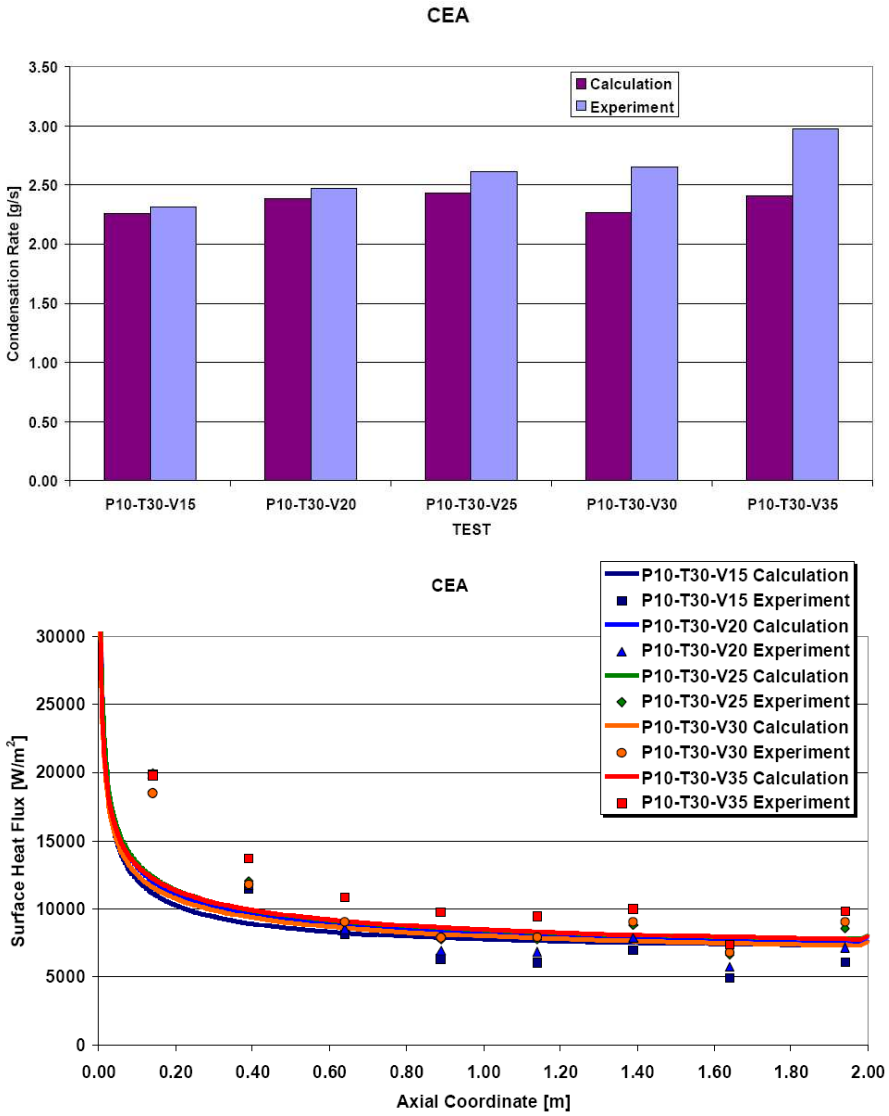

Figure 3.17: Sample comparison of calculated and experimental values of condensation rate and local heat flux (CEA data: Fig. from [84])

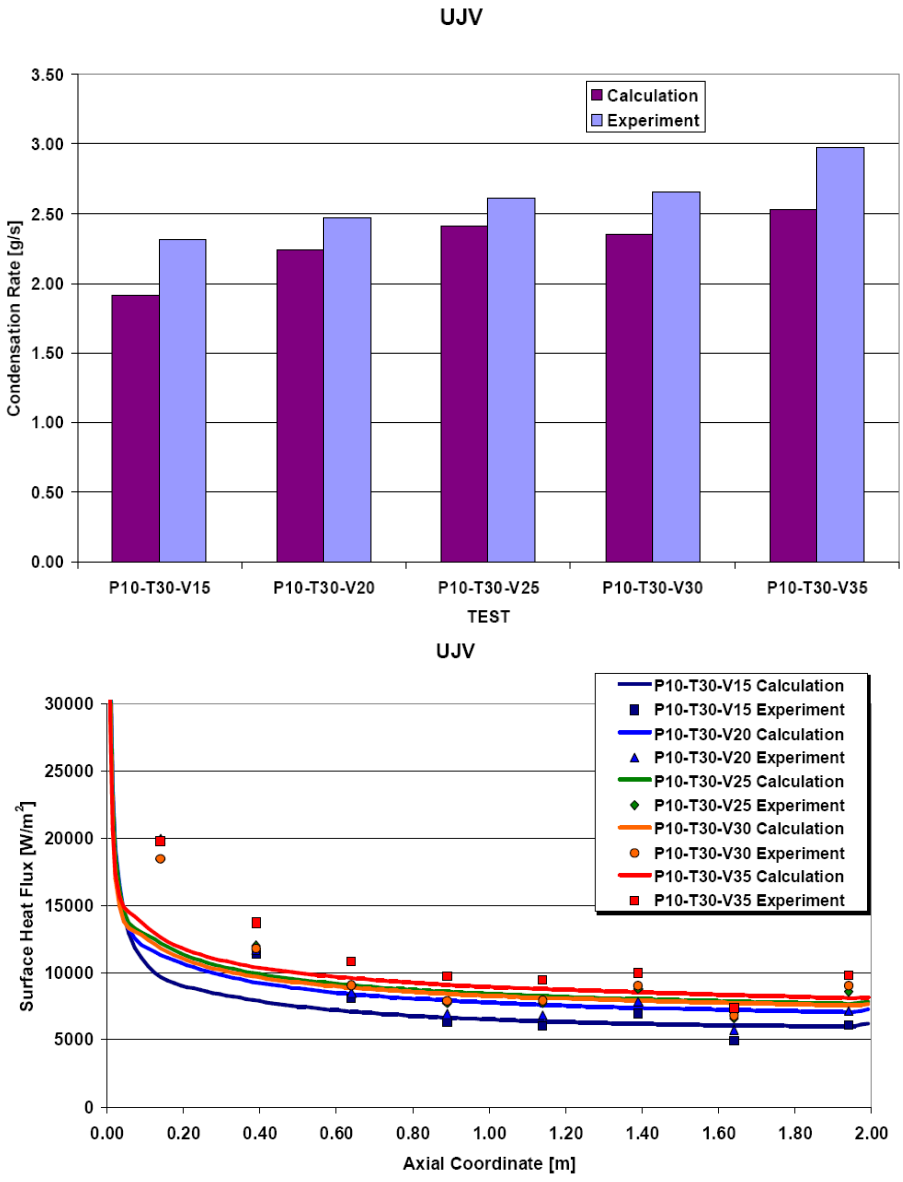

Figure 3.18: Sample comparison of calculated and experimental values of condensation rate and local heat flux (UJV data: Fig. from [84])

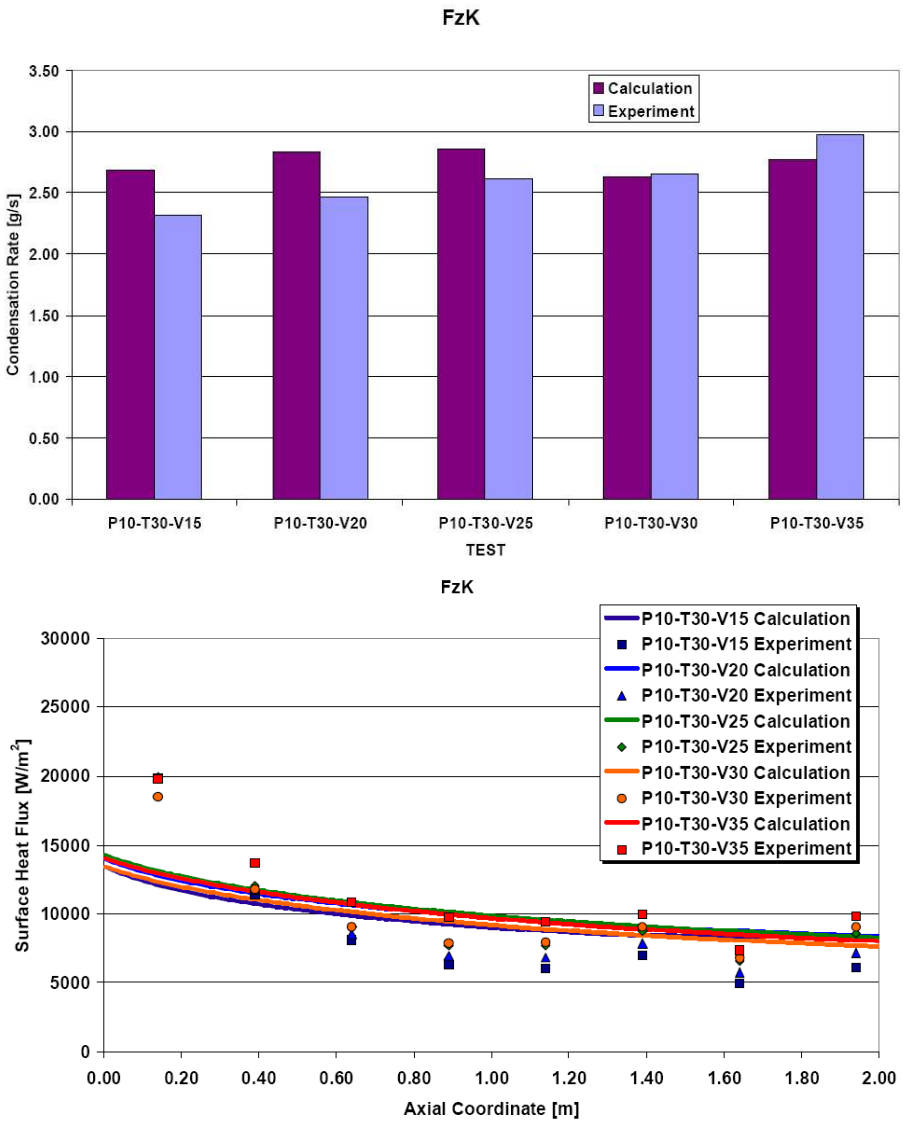

Figure 3.19: Sample comparison of calculated and experimental values of condensation rate and local heat flux (FZK data: Fig. from [84])

3.6 Concluding remarks

As resulting from the overview of available models, three main strategies are possible for modeling wall condensation phenomena. A first strategy is based on a detailed resolution of the flow and energy equations and relies on the capabilities of evaluating the concentration and the temperature gradient in the near-wall region. A second strategy is based on correlations, usually obtained via the analogy between heat and mass transfer, that allows coarser discretizations of the near-wall region to be employed and then faster computations possible. An innovative and possibly low-cost third strategy, out of the purposes of this research, should rely on dedicated wall functions that account for transpiration effects on momentum, heat and concentration boundary layers.

The present state-of-the-art in this field shows that a completely mechanistic approach to full scale plant or large experimental facilities requires huge computational resources, suggesting the need for introducing model simplifications. In this aim, the heat and mass transfer analogy constitutes the primary modelling approach for predicting condensation or evaporation in faster running, coarse mesh modeling. Indeed, most of the CFD models applied in the modeling of the ISP47 tests, relied on the heat and mass transfer analogy.

The models based on the analogy between heat and mass transfer evaluate the mass transfer rates on the basis of bulk and interfacial concentrations, temperatures and properties. Clearly, these models reduce the computational efforts, making possible the use of coarser meshes. However, for complex geometries and not well defined phenomenologies, there is a fundamental ambiguity in choosing a mass transfer correlation. For complex flow pattern, it is also unclear how to define the bulk properties on whose basis the mass transfer coefficient should be calculated. In the thermal-hydraulic conditions experienced in the MISTRA ISP47 tests, with mixed flow pattern and stratified atmosphere, the applicability of the heat and mass transfer analogy emerged to be unsuccesful [11]. The effects induced by a lighter than steam noncondensable gas were also really not reproduced.

Actually, the complications involved in the application of CFD to heat and mass transfer phenomena are bound to the usual difficulty in treating the near-wall region. This aspect, being a crucial one for many flows requiring an accurate representation of boundary layer phenomena, is even more relevant in the case of simultaneous heat and mass transfer, since fluid-dynamic, thermal and concentration boundary layers superimpose and affect each other; transversal motion due to suction or blowing adds a further phenomenon to be accurately represented. Models based on the analogy between heat and mass transfer clearly are lacking of the capabilities for capturing local transfer phenomena, for which it would be advisable to adopt mechanistic approaches coupled with turbulence models with low-Re capabilities. These local phenomena, combined with the entrainment phenomena associated to other flow structures, affect the overall behavior of the volume atmosphere, in particular by modifying the local concentration of the noncondensable species that, in turn, affects the mass transfer properties. CFD codes should improve their capability of such transient stratified flows. As remarked as a conclusion of the ISP47, reasons for the wrong behavior of some CFD models in such configurations are probably coming from momentum and diffusion transport [11]: if velocities and turbulent diffusion are not well calculated, such transient behavior involving the competition between

different phenomena (natural or weakly forced convection) cannot be calculated with a good accuracy. Turbulence modelling is probably the main reason for that.

To solve computational issues concerning vapor condensation in presence of noncondensable gases, detailed computational analysis of the phenomena are required. No further studies would be in fact fruitful without a deeper understanding of the phenomena experienced in presence of lighter than steam noncondensable gases [11]. Further investigations are therefore needed, and a dedicated and more detailed code improvement around these experimental conditions is recommended. Due to interacting phenomena, analysis and explanation of the condensation distribution are difficult in coupled or integral effect test facilities. Simplified analytical test cases and separate effect tests studies are instead interesting to enhance the current knowledge.

Stated that mechanistic models are hardly applicable to large scale analysis, they anyway constitute appropriate tools for in-depth investigation of the local phenomena affecting condensation in presence of noncondensable gases heavier and lighter than steam. The review about condensation modelling in CFD has been analyzed, concerning the different approaches employed to simulate wall condensation phenomena in CFD codes and, in particular, mechanistic models. The main features of the different models are illustrated, together with the status of validation for containment thermal-hydraulic analysis.

A first important step toward the understanding of local phenomena involved in wall condensation has been successfully completed in the frame of the SARnet NoE; activities were coordinated by UNIPI, also in the frame of this PhD research, proposing a Benchmark Problem in order to compare the different models and the different codes. The results of these activities, including a purely numerical stage and a comparison with the CONAN experimental data, allowed assessing the capabilities of the different models in reproducing forced convection condensation phenomena of binary mixtures in simple geometries.

The analysis of the benchmark results and of the available literature has allowed identifying weak-points in the analysis of the condensation phenomena. In particular, the need is felt for clarifying two main aspects that are the subject of this PhD research: the role of turbulence modelling in condensation phenomena and the effect of a noncondensable gas lighter than steam.

Many turbulence models have been used without a sufficient verification of their capabilities in dealing with mass transfer problems and, on the other hand, experimental data detailing the characteristics of turbulence in condensation phenomena are not easily available. The need for a more detailed analysis of condensation phenomena with helium was also felt in the analysis of the experiences available in medium and large scale facilities. The understanding of local phenomena requires small scale separate effects facilities. The available database, against which models can be validated, includes basically the experience of Pernsteiner [67] and the experiments with the French COPAIN facility [1], but experimental datapoints are advisable for a more extensive set of experimental conditions.

Chapter 4

Analysis of steam condensation tests in the presence of air

Separate effect test facilities are useful for providing detailed and accurate data on specific phenomena. COPAIN [1] and CONAN [8], in particular, are separate effect test facilities aimed at investigating condensation phenomena in presence of noncondensable gases for a wide range of operating conditions. Unlike in integral effect test facilities like MISTRA [5] or ThAI [6], more detailed data are available concerning the local behavior of condensation phenomena, not affected, as far as possible, by other concurring phenomena as stratification or recirculating flows. Stated that the final task of CFD tools concerns the modeling of all the simultaneous phenomena of interest for the thermal-hydraulic analysis of a nuclear reactor containment, these data are anyway very useful for the validation of CFD mass transfer models to be integrated in the containment field codes.

This chapter is aimed at reviewing the experimental data made available by the CONAN and the COPAIN separate effect facilities. Attention is focused on condensation tests in the presence of air. A description of the facilities and their main operating features is proposed, followed by a summary of the main conclusions of previous analyses of experimental data. Finally, a new analysis is presented, aimed at improving the understanding of condensation phenomena in the different convection regimes.

4.1 The COPAIN facility

COPAIN is a separate effect facility operated since 1998 by CEA Grenoble [1]. The experimental program has provided a database for a wide range of parameters (See Table 4.1). Tests on condensation have been carried out at different operating conditions; tests have been performed at different pressures, different velocities and different temperatures. Most tests concern condensation of superheated steam mixed with air; the effect of helium, as a substitute of hydrogen in experimental activities has been investigated in several cases. The

influence of a controlled liquid film flowing over the condensing surface has also been analyzed.

4.1.1 Main features of the COPAIN test section

The Copain test section consists of a rectangular cross section channel (0.6 m x 0.5 m), whose length is about 4 m. The condensing plate is 0.6 m wide and 2.0 m long. The rectangular channel is located inside a cylindrical vessel, part of a pressurized primary loop, by which is insulated from the external environment. A secondary loop provides the heat sink necessary to evacuate the heat transferred to the condensing plate (see Fig. 4.1).

The condensing plate is made of stainless steel, whose thickness is 25 mm.

A cooling loop is optimized for achieving an homogeneous temperature on the backside of the condensing plate. Within the condensing plate, twenty measures of temperature difference DT_j and 4 measures of temperature TF_i allow estimating the heat flux profile and the temperature on the condensing surface (see Fig. 4.2).

4.1.2 Operating procedure

A test is characterized by four independent operating conditions:

- operating pressure;
- mass (or molar) fractions of the noncondensable gases;
- average temperature (or superheating temperature of steam);
- desired average heat flux.

Each test consists in reaching a well defined steady-state obtained by setting the operating pressure, the mixture velocity and mixture temperature at the required values and regulating the secondary circuit temperature in order to achieve the desired heat flux. Labels are assigned to each test as follows:

PaaWbbFccMP_ddd

- aa : operating pressure in decimal of *bar*;
- bb : mass fraction of noncondensable gases;
- cc : desired average heat flux in kW/m^2;
- M : takes A for steam-air mixtures and B for steam-air-helium mixtures;
- P : always takes B (depends on the different kinds of condensing plates);
- ddd : number of the test.

The operating procedure is described as follows:

1. Once the operating conditions are selected, the mass of noncondensable gases to be injected into the primary system of the facility is calculated, aiming at achieving the desired mass or molar fractions during the test. The set-point temperature of the secondary system is also estimated by heat transfer correlations, on the basis of the desired operating heat flux and the average temperature of the condensing mixture.

Pressure $[bar]$	1.0 - 1.2 - 4.0 - 6.7
Noncondensable gas mass fractions [-]	0.1 - 0.3 - 0.4 - 0.5 - 0.88 - 1.0
Inlet Velocity $[m/s]$	0.1 - 0.3 - 0.5 - 1.0 - 2.0 - 3.0
Average Heat Flux $[kW/m^2]$	1 - 5 - 10 - 25
Steam Superheating $[K]$	10 - 20 - 40
Helium to Noncondensables Ratio [-]	0.0 - 0.1 - 0.4 - 1.0
Liquid Film Flow Rate $[\cdot\ \mathit{Inlet\ Flow\ Rate}]$	1 - 5 - 40

Table 4.1: Operating conditions of COPAIN [1]

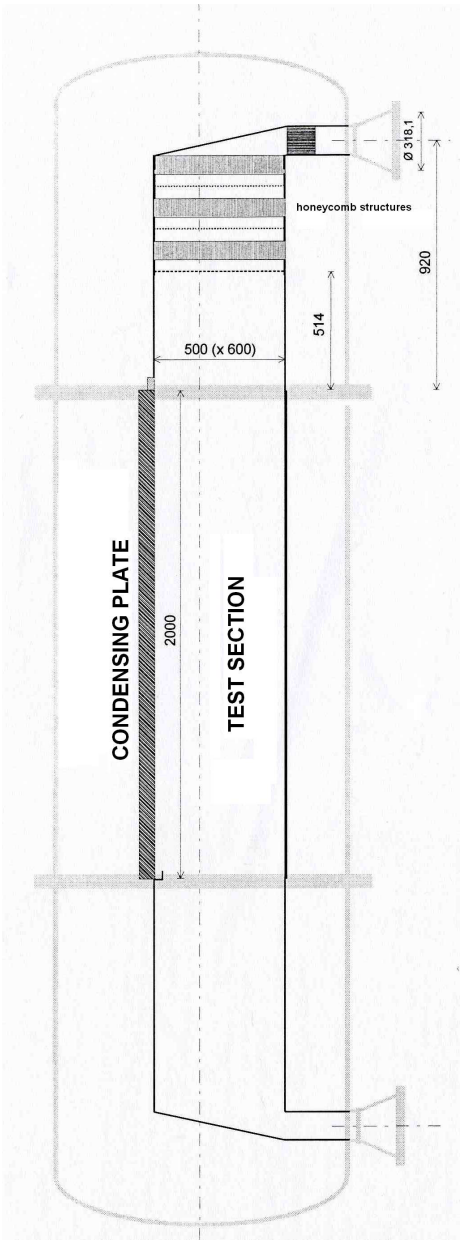

Figure 4.1: Test section of the COPAIN facility

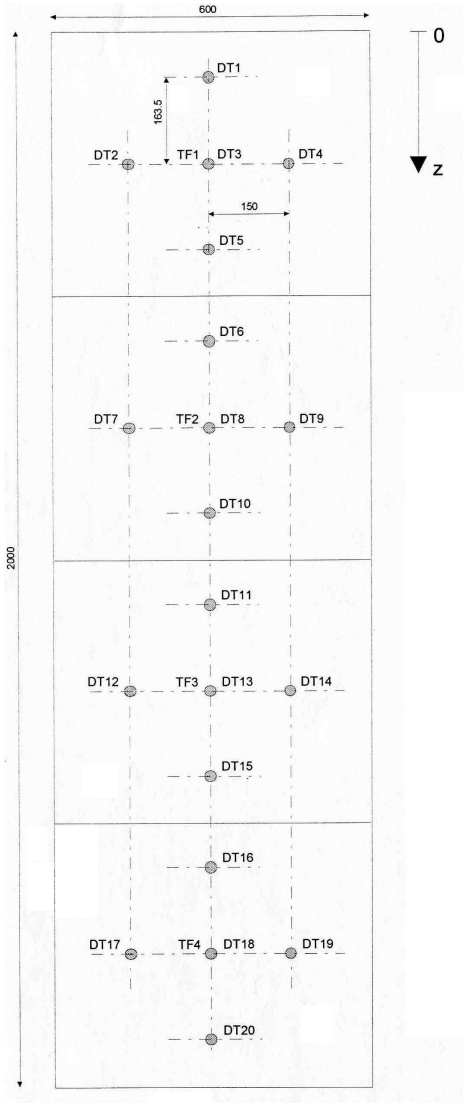

Figure 4.2: Layout of temperatures TF_i and temperature differences DT_j measurement points in the condensing plate

2. Filling of the primary system with the calculated amount of air at environment temperature.
3. Filling of the primary system with the calculated amount of helium, if any, at ambient (room) temperature.
4. Heating of the external walls of the facility.
5. Activation of the data acquisition system.
6. Activation of the heaters of the primary circuit (set-point temperature fixed equal to the selected operating temperature for the addressed test series).
7. Activation of the secondary cooling circuit (set-point temperature fixed to the calculated value).
8. Activation of the liquid film (if any).
9. Activation of the boiler (set-point pressure equal to the selected operating pressure for the concerned tests series).
10. Activation of the primary circuit blower.
11. Injection of steam into the primary circuit.
12. Regulation of the primary circuit temperature by heaters.
13. Stabilization of the primary circuit pressure and temperature to the selected operating values and regulation of the secondary cooling circuit temperature in order to get the desired heat flux on the condensing plate.

Once a steady-state is reached, measurement data are recorded with a frequency of 0.5 Hz during 15 minutes. To obtain another steady-state condition, the mixture flow rate is modified and the secondary circuit temperature is regulated to achieve, as far as possible, the same heat flux as before. Five different steady-state conditions are usually obtained for each test series by decreasing the inlet velocity, in order to investigate different convection regimes. To identify a specific steady-state, the number of the test and the number of the steady-state are necessary:

P_ddd_n

For each steady-state condition a set of boundary conditions are monitored and provided:

- P, *average pressure inside the test section* ($\pm$ 20 mbar): obtained as the average of the local pressure values measured in two different points of the test section;
- T_b, *average temperature inside the test section* ($\pm$ 0.6 K): average value between the temperatures at the inlet and the outlet sections. Inlet and outlet temperatures results to be very close, being the difference in the order of the experimental uncertainty.

- U_{inlet}, *inlet velocity* ($\pm$ 0.04 m/s): a flat profile is achieved at the inlet section by a honeycomb structure; the inlet velocity value is given by the ratio between mass flow rate and the cross section area of the test section.
- X_{nc} and Y_{nc}, *noncondensable molar and mass fraction*: the air density is evaluated by measuring the absolute pressure before and after feeding the primary system, at the environment temperature and still empty of steam. Helium is fed after air and the further pressure increase allows estimating the helium density. The number of moles of air and helium is thus known. Once the steady-state is reached, the knowledge of the average temperature and the thermodynamic pressure allow estimating the amount of steam, assumed to behave as a real gas. Boundary conditions are then provided in terms of mass and molar fractions for the noncondensable species. Moreover, the knowledge of the mixture composition and the average temperature allows calculating the saturation temperature T_{sat} corresponding to the steam partial pressure in the mixture.
- TP_e, *temperature on the secondary side of the condensing plate*: the secondary circuit is conceived to achieve an homogeneous temperature profile on the backside of the condensing plate. Four thermocouples TF_i are located inside the condensing plate at a distance of 24 mm from the condensing surface (1 mm from the back surface); the secondary side temperature TP_e is thus taken as one of the temperature measured in the lowest thermocouples TF_i, that means, with reference to Fig. 4.2, the temperatures TF_2, TF_3, TF_4.

4.1.3 Data processing procedure

Given the average temperature on the secondary side of the condensing plate TP_e, the local heat fluxes (see Fig. 4.3) are calculated from the 20 measurements of temperature difference DT_j by

$$\Phi_j = k\frac{DT_j}{e_p} = k\left(TP_e + 0.5DT_j\right)\frac{DT_j}{e_p} \tag{4.1}$$

whose uncertainty is estimated by the following relationship:

$$\delta\Phi_j = 0.06\Phi_j + 100\ W/m^2 \tag{4.2}$$

The local temperature on the condensing surface is thus estimated by:

$$TP_{s,j} = TP_e + DT_j\frac{e_p^{'}}{e_p} \tag{4.3}$$

Once the heat fluxes are known, to know the local mass fluxes it is necessary to separate the sensible heat transfer and the latent heat transfer contributions. If the assumption is done that the liquid film, if present, has negligible thickness and thus a negligible thermal resistance, the interface condensing temperature T_i can be assumed equal to the temperature estimated on the condensing wall TP_s [1].

[1] This assumption is justified also by the fact that at the low condensation rates typical of CONAN and COPAIN (less than 10 g/s) it is very difficult to obtain a continuous film instead of rivulets (see Fig. 4.4); on the other hand, whenever a film could be achieved, its thickness and the related heat transfer resistance would be very small.

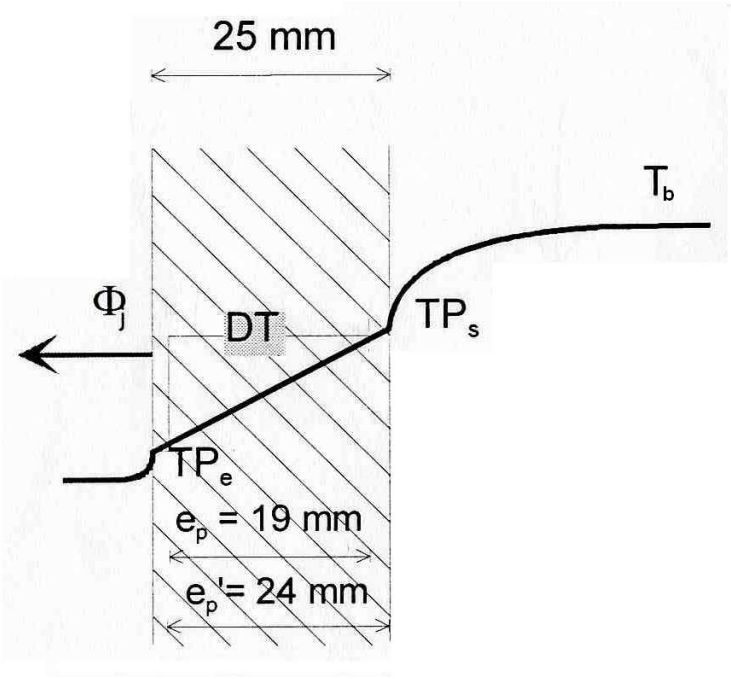

Figure 4.3: Sketch of temperature profile within the condensing plate

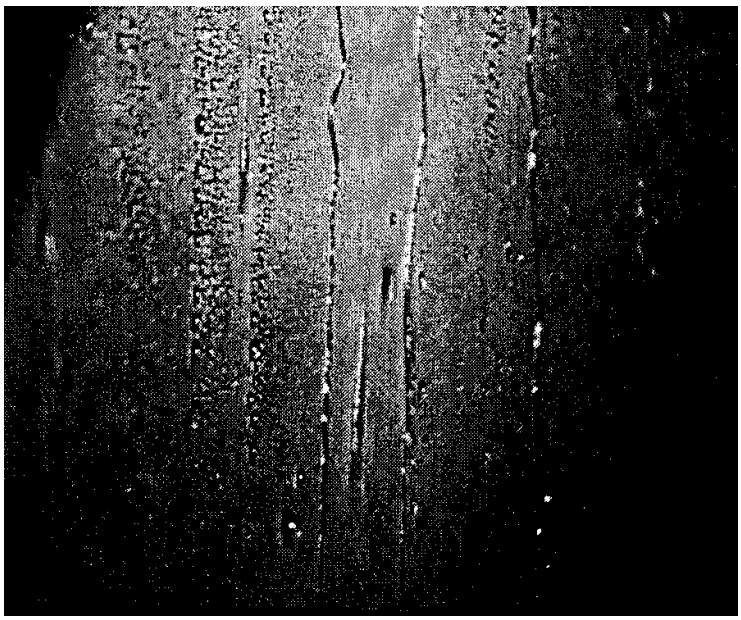

Figure 4.4: Picture of the COPAIN condensing plate during a test at high mass transfer rate and high velocity

$$\Phi_j = \underbrace{\Phi_{j,s}}_{sensible\ heat} + \underbrace{\hbar^{lat}\left(TP_{s,j}\right)\dot{m}_j^{''}}_{latent\ heat} \tag{4.4}$$

where $\Phi_{j,s}$ and $\dot{m}_j^{''}$ are respectively the sensible heat flux and mass flux corresponding to the point j. The ratio between the sensible heat flux and the condensation mass flux can be written as follows

$$\frac{\Phi_{j,s}}{\dot{m}_j^{''}} = \frac{h_s\left(TP_{s,j} - T_b\right)}{h_m B_m} = \frac{\frac{Nu_x k}{x_j}\left(TP_{s,j} - T_b\right)}{\frac{Sh_x \rho D}{x_j}\frac{\left(Y_{v,i_j} - Y_{v,b}\right)}{1 - Y_{v,i_j}}} \tag{4.5}$$

where Y_{v,i_j} is the steam mass fraction at the interface corresponding to the point j. Here, the analogy between heat and mass transfer is introduced

$$\frac{Nu_{0,x}}{Sh_{0,x}} = \left(\frac{Pr}{Sc}\right)^{\frac{1}{3}} \tag{4.6}$$

Assuming that suction influences species and energy transfer in the same way, that means the equality of the Stefan and the Ackerman coefficients (See paragraph 2), the analogy can be turned to obtain

$$\frac{Nu_{0,x}}{Sh_{0,x}} = \frac{Nu_x}{A}\frac{F}{Sh_x} = \frac{Nu_x}{Sh_x} = \left(\frac{Pr}{Sc}\right)^{\frac{1}{3}} \tag{4.7}$$

Substituting Eq. (4.7) in Eq. (4.5), after some mathematical manipulations, the ratio between average sensible heat flux and mass flux is given by

$$\frac{\Phi_{j,s}}{\dot{m}_j^{''}} = \frac{Cp\left(TP_{s,j} - T_b\right)}{\frac{\left(Y_{v,i_j} - Y_{v,b}\right)}{1 - Y_{v,i_j}}}\left(\frac{Sc}{Pr}\right)^{\frac{2}{3}} = \frac{Cp\left(TP_{s,j} - T_b\right)}{\frac{\left(Y_{v,i_j} - Y_{v,b}\right)}{1 - Y_{v,i_j}}} Le^{\frac{2}{3}} \tag{4.8}$$

The local sensible heat flux $\Phi_{j,s}$ and the local mass flux $\dot{m}_j^{''}$ are therefore obtained by solving Eqs. 4.4 and 4.8. The experimental local Sherwood Sh_x number is finally calculated by:

$$Sh_{x,j} = \frac{\dot{m}_j^{''} x_j}{\rho D B_m} = \frac{\dot{m}_j^{''} x_j}{\rho D}\frac{1 - Y_{v,i_j}}{Y_{v,i_j} - Y_{v,b}} \tag{4.9}$$

The corrected local Sherwood $Sh_{0,x}$ number, accounting for the suction effect, is then calculated by

$$Sh_{0,x,j} = \frac{\dot{m}_j^{''} x_j}{\rho D\ F\ B_m} = \frac{\dot{m}_j^{''} x_j}{\rho D}\frac{1}{\ln \frac{Y_{nc,b}}{Y_{nc,i_j}}} \tag{4.10}$$

where the suction factor F of Stefan is introduced. Similarly, the local Nusselt number is given by:

$$Nu_x = \frac{\Phi_{j,s} x_j}{\left(TP_{s,j} - T_b\right)\ k} \tag{4.11}$$

Data processing can be also performed in terms of average quantities. Once the local heat fluxes are available, the average heat flux is obtained by means of the following relationship

$$\bar{\Phi} = \frac{1}{S}\sum_{j=1}^{20} \Phi_j S_j \tag{4.12}$$

where S_j is the area of influence assigned to each local flux measurement Φ_j and S is the total condensing surface

$$S = \sum_{j=1}^{20} S_j \tag{4.13}$$

The average temperature on the condensing surface TP_s (see Fig. 4.3) is instead assumed equal to

$$TP_s = TP_e + DT\frac{e_p^{'}}{e_p} \tag{4.14}$$

where DT is the temperature difference associated to TP_e, respectively equal to DT_8, DT_{13} and DT_{18} for TP_e assigned equal to TF_2, TF_3 and TF_4 (see Fig. 4.2). The uncertainty on the temperature differences is estimated $\pm$ 1.0 K. To know the average mass flux the same procedure is followed than the local approach. Given the total average heat flux

$$\bar{\Phi} = \bar{\Phi_s} + \hbar^{lat}\left(T_i\right)\bar{\dot{m}''} \ , \tag{4.15}$$

the ratio between the sensible heat flux and the condensation mass flux can be written as follows

$$\frac{\bar{\Phi_s}}{\bar{\dot{m}''}} = \frac{h_s\left(TP_s - T_b\right)}{h_m\frac{\left(Y_{v,i}-Y_{v,b}\right)}{1-Y_{v,i}}} = \frac{\frac{Nu_L k}{L}\left(TP_s - T_b\right)}{\frac{Sh_L\rho D}{L}B_m} \tag{4.16}$$

Introducing the analogy between heat and mass transfer

$$\frac{Nu_{0,L}}{Sh_{0,L}} = \frac{Nu_L}{A}\frac{F}{Sh_L} = \frac{Nu_L}{Sh_L} = \left(\frac{Pr}{Sc}\right)^{\frac{1}{3}} \tag{4.17}$$

and substituting Eq. (4.17) in Eq. (4.16), the ratio between average sensible heat flux and mass flux is thus given by

$$\frac{\bar{\Phi_s}}{\bar{\dot{m}''}} = \frac{Cp\left(TP_s - T_b\right)}{\frac{\left(Y_{v,i}-Y_{v,b}\right)}{1-Y_{v,i}}}\left(\frac{Sc}{Pr}\right)^{\frac{2}{3}} = \frac{Cp\left(TP_s - T_b\right)}{\frac{\left(Y_{v,i}-Y_{v,b}\right)}{1-Y_{v,i}}}Le^{\frac{2}{3}} \tag{4.18}$$

The experimental average Sherwood numbers, Sh_L and $Sh_{0,L}$, are thus obtained by:

$$Sh_L = \frac{\bar{\dot{m}''}L}{\rho D B_m} = \frac{\bar{\dot{m}''}L}{\rho D}\frac{1-Y_{v,i}}{Y_{v,i}-Y_{v,b}} \tag{4.19}$$

$$Sh_{0,L} = \frac{\bar{\dot{m}''}L}{\rho D\ F\ B_m} = \frac{\bar{\dot{m}''}L}{\rho D}\frac{1}{\ln\frac{Y_{nc,b}}{Y_{nc,i}}} \tag{4.20}$$

The average Nusselt number is instead given by:

$$Nu_L = \frac{\bar{\Phi_s}L}{k\ \left(TP_s - T_b\right)} \tag{4.21}$$

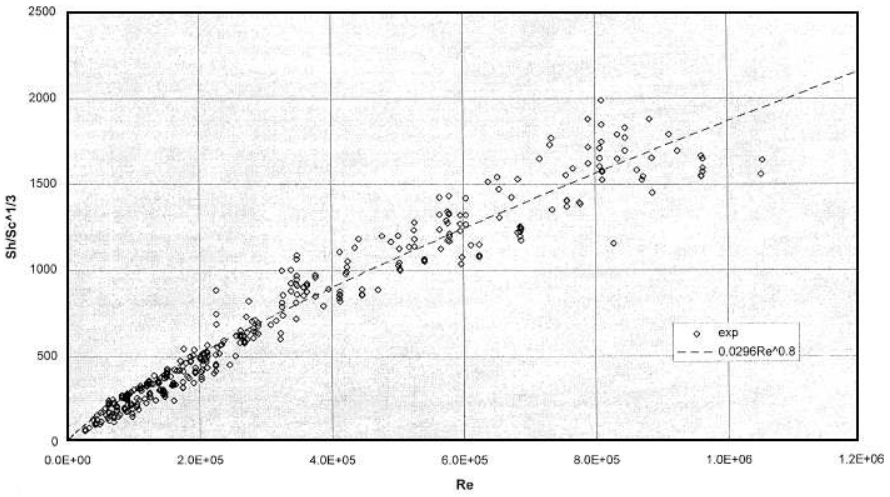

Figure 4.5: Comparison between the experimental Sherwood number Sh_x values and the Schlichting correlation for the high velocity cases(Fig. from Bazin [1])

4.1.4 Previous analyses of the COPAIN experimental data [1]

The experimental program of COPAIN provided a database for a wide range of parameters. In this paragraph, tests performed in presence of air are addressed; tests in presence of helium will be analyzed in chapter 5.

Experimental Sherwood numbers have been compared to the classical correlation for forced convection and natural convection conditions. Data corresponding to measurement points near the inlet section (within 0.5 m from the beginning of the condensing plate) have been discarded, in order to avoid misleading measures affected by entrance effects. In natural convection regime, the local formulation of the McAdams correlation [107] is adopted for comparison:

$$Sh_x = 0.13\ Gr_x^{1/3} Sc^{1/3} \tag{4.22}$$

The Schlichting correlation is instead proposed for forced convection:

$$Sh_x = 0.0296 Re_x^{0.8} Sc^{1/3} \tag{4.23}$$

In Fig. 4.5 and 4.6, the experimental Sherwood numbers are compared to the proposed correlation, respectively in the forced and the natural convection cases. The data corresponding to the highest inlet velocity (2.0 and 3.0 m/s) are found to be well fitted by the Schlichting correlation. In the natural convection cases, for lower velocities, the data are above the McAdams correlation. As a result of the analysis, an hybrid correlation is proposed by Bazin et al. [1] for all the convection regimes, in which the Sherwood number is defined as

$$Sh_x = max\left[0.0296 Re_x^{0.8} Sc^{1/3}; 0.13\ Gr_x^{1/3} Sc^{1/3}\right] \tag{4.24}$$

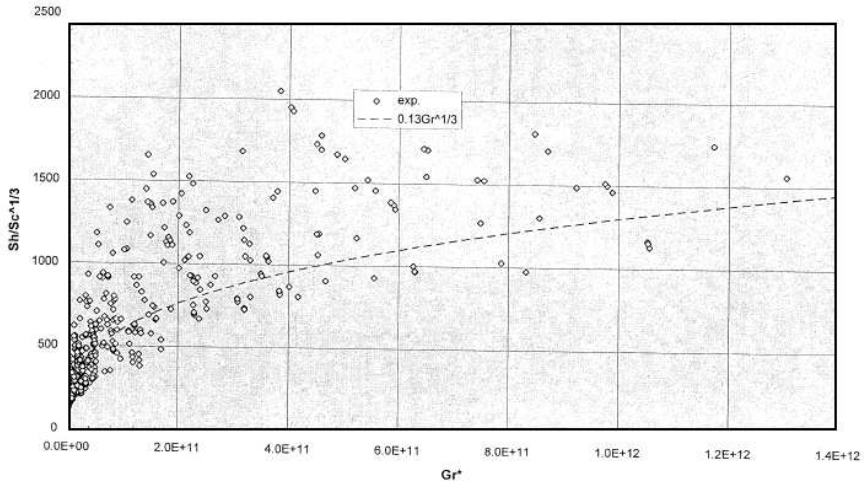

Figure 4.6: Comparison between the experimental Sherwood number Sh_x values and the McAdams correlation for the low velocity cases (Fig. from Bazin [1])

On the basis of the collected results, suction effects are found remarkable in the natural convection regime. In a first instance this is visible by comparing the experimental Sherwood number with the McAdams correlation (see Fig. 4.6). In the forced convection regime, for the same reasoning, suction effects seem not to appear and the use of suction correction factor seems not to be justified in these cases [1]. Pressure effects have been tested in the range between 1 and 6.7 bar. These effects are taken into account by physical properties and are therefore accounted by the Sherwood number. In Fig. 4.7, the ratio between the Sherwood number and the correlation 4.24 is proposed as a function of pressure. A slight increase of the ratio is shown with increasing pressure, that can be anyway justified by suction effects, being the higher pressure tests associated to higher steam mass fractions in the bulk [1]. The same reasoning formulated for pressure can be extended to superheating, whose effects are embedded in properties. Indeed, for a given mass fraction of steam, the effect of superheating consists in an improvement in the sensible heat transfer, whereas the latent heat transfer rate is basically uninfluenced (see Fig. 4.8). Basing on collected experimental data, conclusions were drawn concerning the most interesting issues to be explored in detail. Among them are of our interest the effect of suction and the effect of the body forces that affect the convection regime, most of all in the transition between forced and natural convection. In this extent, the interest emerged also for performing test with upward mixture velocity in the test section [1].

4.1.5 Local measurements

A purposely designed measurement device as been employed for temperature and mass fraction measurements in the boundary layer (See Fig. 4.9). Such a

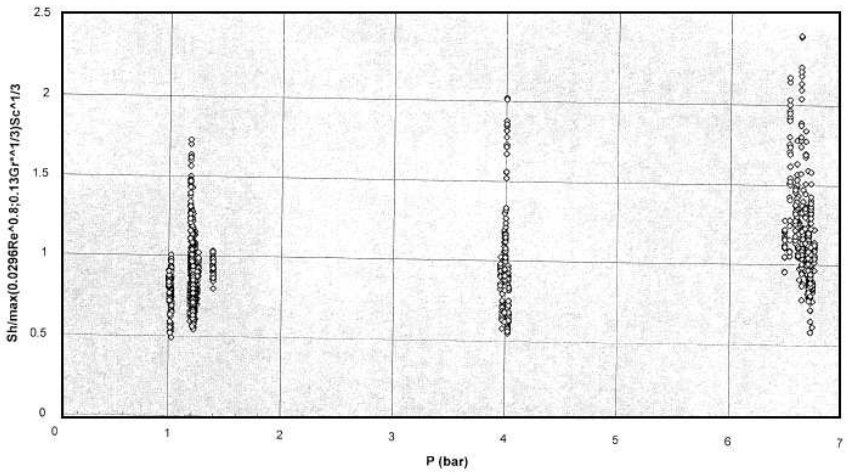

Figure 4.7: Influence of pressure on the Sherwood number Sh_x in the COPAIN tests (Fig. from Bazin [1])

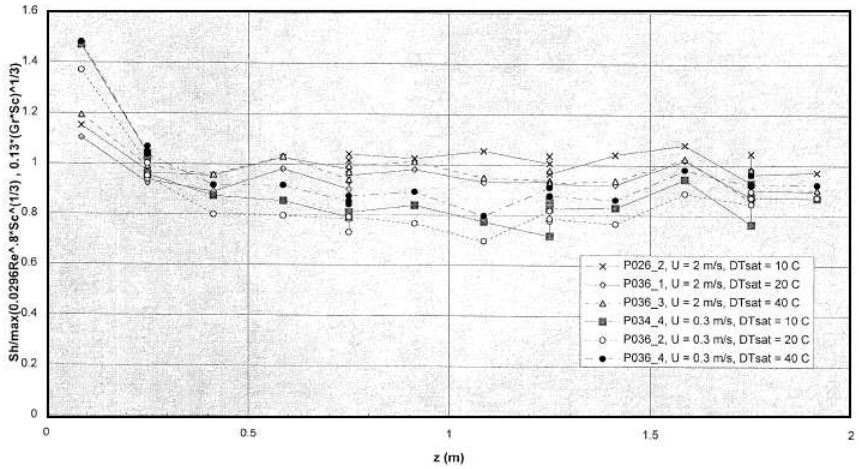

Figure 4.8: Influence of steam superheating on the Sherwood number Sh_x in the COPAIN tests (Fig. from Bazin [1])

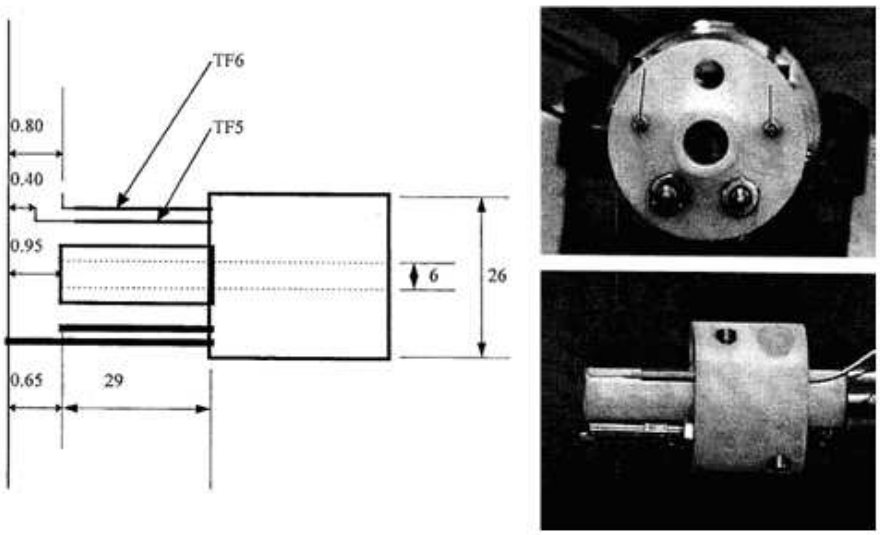

Figure 4.9: Details of the device used for local measurements of temperature and concentration (measures in mm)

device allows two different temperature measurements, named $TF5$ and $TF6$. A sampling line is also employed for sucking the gas mixture in the aim to measure the species concentration and resume the concentration profiles in the boundary layer . Once steady-state conditions are obtained, the local measurements device is advanced through the channel up to get in contact with the condensing wall. This allows setting the reference position of the thermocouples and the sampling line with an error of the order of 5 micrometers. The $TF5$ thermocouple is set at 0.4 mm from the condensing surface, the $TF6$ at 0.8 mm and the sampling line at 0.85 mm. The device is displaced progressively; about twenty measurements are recorded between the initial position and 200 mm from the condensing surface. The $TF5$ thermocouple that is the closest to the condensing wall is likely to be wet by water rivulets or droplets sliding on the condensing surface during the first phases of the procedure. If wet, the measured temperatures are lower than the dry thermocouples, due to water evaporation. This results in differences between the temperatures measured at the same distance from the condensing wall by $TF5$ and $TF6$, less likely to be wet (see Fig. 4.10). Another important remark concerns the intrusive nature of the concentration measurements. The velocity of aspiration at the entrance of the sampling line adopted for concentration measurements ranges from 0.02 m/s to 0.1 m/s [1]. These values are very high with respect to the velocity scales characteristic of condensation. Suction effects due to condensation are likely to be annealed by the aspiration in the sampling line, that causes the boundary layers to thicken, changing remarkably the characteristic of the condensing boundary layer.

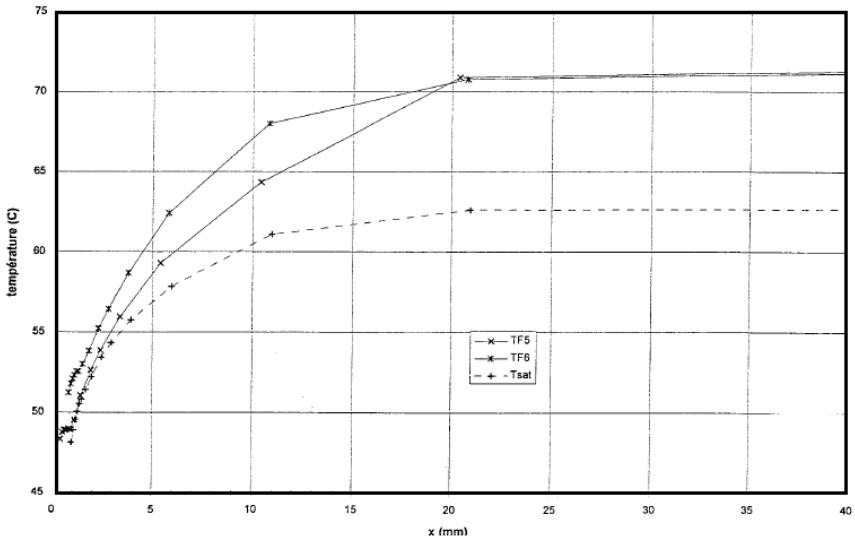

Figure 4.10: Local temperature measurements across the boundary layer in a COPAIN test

4.2 The CONAN facility

The CONAN facility (CONdensation with Aerosols and Noncondensable gases) is operated by the Department of Mechanical, Nuclear and Production Engineering of the University of Pisa [8]. The apparatus was conceived to collect data of steam condensation of interest for nuclear reactor containment thermal-hydraulic analysis. The facility consists of three different loops, primary, secondary and tertiary, which accomplish with the operating needs encountered in running the experiments (See Fig. 4.11):

- the primary loop, in which the mixture of steam and noncondensable gases circulates and partly condenses on a flat wall;
- the secondary loop, which provides the required cooling of the condensing plate by circulating water, whose temperature can be varied;
- the tertiary loop, which allows controlling the temperature of the cooling fluid (the water of the secondary loop).

Most tests concerned the condensation of steam in the presence of air and helium in forced convection regime (See Tab. 4.2). The facility has been exclusively operated at atmospheric pressure.

4.2.1 Main features of the CONAN facility

The primary loop contains the test section (See Fig. 4.12), consisting in a roughly 2 m long, 0.34 m side channel having square cross section, in which a

Steam generator power $[kW]$	10 - 15 - 20 - 25 - 30
Secondary coolant inlet temperature $[C]$	30 - 40 - 50 - 60 - 70
Inlet Velocity $[m/s]$	1.5 - 2.0 - 2.5 - 3.0 - 3.5
Secondary coolant flow rate $[kg/s]$	1
Steam Superheating $[K]$	< 5
Helium to Noncondensables Ratio [-]	0.0 to 1.0

Table 4.2: Nominal operating conditions of CONAN

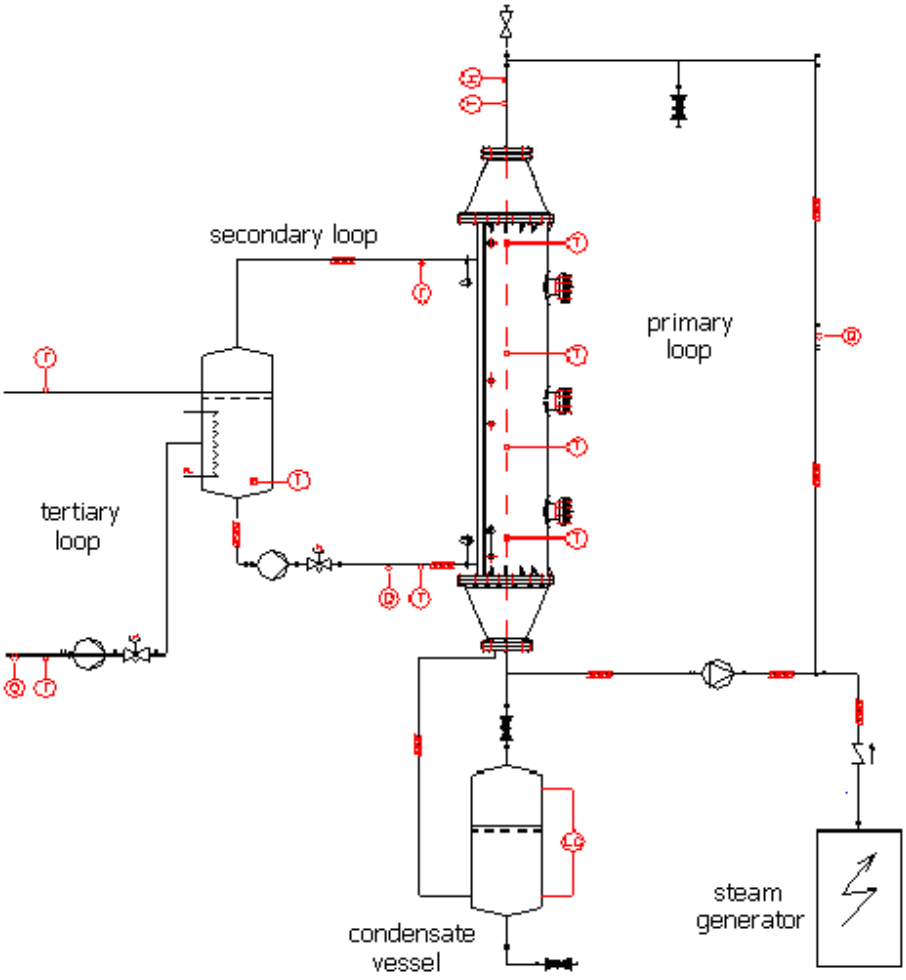

Figure 4.11: Layout of the CONAN facility

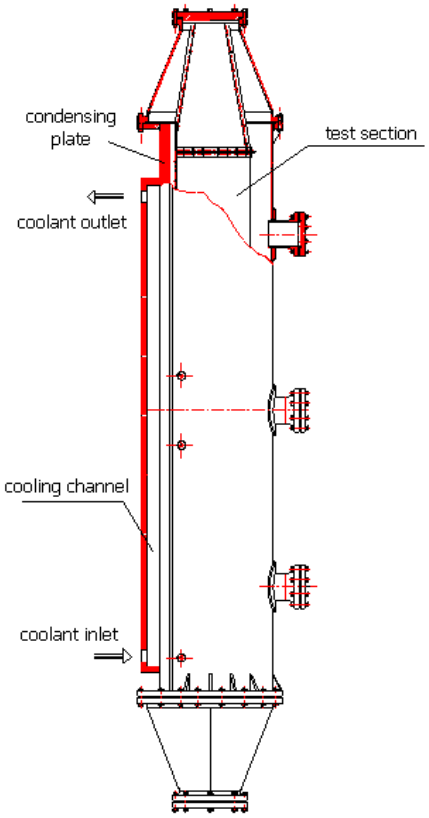

Figure 4.12: Test section of the CONAN facility

mixture of steam, air and helium is circulated. One of the lateral surfaces of the channel belongs to a 4.5 cm thick aluminum flat plate, cooled on the back side by the water of the secondary loop. Condensation occurs on the inner surface of the cooled plate and the related condensate flow is collected at the bottom of it by a gutter and routed by a small diameter piping to an external vessel; a relatively accurate estimate of the condensate flow is obtained by differential pressure measurement in this vessel (See Fig. 4.11). The other surfaces of the test section are insulated from the external environment, to avoid that condensation occurs over them. Variable area sections connect both the test section channel to the primary loop piping. The bottom part of the test section is connected to a variable speed blower for circulating the air-helium-steam mixture. Steam produced by a 60 kW electrical steam generator is injected in the bottom part of the primary loop via a tee junction. The uppermost part of the primary loop is presently connected to the external atmosphere via an open pipe, to maintain atmospheric pressure conditions. The secondary loop includes a 5 mm deep, 35 cm wide rectangular cooling channel located on the back side of the aluminum plate, two collectors and pipes for routing water at the outlet of the cooling channel to a mixing vessel, being a component common to the secondary and tertiary loop. The vessel is equipped with three heaters, having each one a power of 3 kW, for water warming up during the start up phase and water temperature control during operation. A pump located at the exit of the mixing vessel routes extracted water again to the secondary channel. The tertiary loop has the role of extracting cold water from a large reservoir available on the site, pumping it into the mixing vessel and extracting by free fall into an outlet pipe an equal flow of warm water, thus obtaining the required power extraction from the secondary loop.

4.2.2 Operating procedure

In the tests performed up to now, at atmospheric pressure, the main operating variables are:

- the steam generator power, controlled by an electronic equipment manually operated in the facility control room;
- the primary volumetric flow, adjusted to the prescribed values by varying the frequency of the electrical supply of the blower motor through an inverter driven by the related computer software;
- the air-helium percentages, obtained by injecting helium in the primary circuit up to the desired concentration;
- the secondary coolant temperature at the inlet of the cooling channel, controlled by changing the tertiary loop flow and the temperature set-point of the heaters in the mixing vessel;
- the secondary coolant flow rate.

Once the steam generator power and the primary flow are fixed and the secondary coolant flow and temperature are set to the prescribed values, the primary mixture temperature and concentration are automatically defined. In fact, starting with an initial noncondensables rich mixture, injection of steam

through the steam generator outlet line and spontaneous purging of the excess air through the pipe open to the atmosphere increases steam concentration up to the point in which the obtained conditions allow a condensation rate equal to the inlet steam flow, provided this does not exceed the maximum system condensing capabilities. On the other hand, whenever the injected steam flow is lower than the condensation rate, the internal atmosphere tends to shrink, sucking air from the open pipe and decreasing the steam fraction down to a new equilibrium condition. Steady-state conditions can be therefore stably achieved, thus letting investigating a wide range of operating conditions. Tests are labeled as follows:

Paa-Tbb-Vcc-Hee

- aa : steam generator power in kW;
- bb : secondary coolant temperature at the inlet of the cooling channel $[^{\circ}C]$;
- cc : inlet velocity in decimal of m/s;
- ee : molar fractions of helium in the noncondensable gas (if helium is not used, the label Hee is omitted);

In the following, the main steps of the operating procedure are summarized:

1. Heating up the water stored in the secondary loop. This is performed by three resistance heaters in the proper storage vessel. During this heating up phase, also the pump of this loop is running; the changes in the temperatures at the inlet and the outlet of the cooling section are measured and the temporal changes are displayed on the PC screen.
2. Activation of the primary circuit blower and the steam generator. This step aims at heating the primary circuit in order to minimize spurious condensation heat losses.
3. The flow rate is adjusted to achieve the desired inlet velocity in the test section.
4. The steam generator power is set to the desired operating value.
5. Filling of helium (if any). The amount of helium is monitored to achieve the desired ratio with air and it is continuously measured during the course of the test.
6. The pump in the tertiary loop is activated and controlled, in order to evacuate from the secondary loop the heat released by condensation in the primary loop. The heaters in the mixing vessel compensate small unbalances.

Data coming from the measuring system are continuously conditioned and acquired. Once steady-state conditions are reached, the available measures are recorded with a frequency of 0.5 Hz for periods of 600 seconds or more. The main measurements available in the facility are:

- temperature and relative humidity of the bulk mixture entering the test channel, estimated by temperature measurements through a dry bulb and a wet bulb thermal resistance, as indicated by Lioce [108];
- temperature of the bulk mixture at four locations along the channel, by calibrated K-type thermocouples;
- level in the condensate collecting tank;
- volumetric flow of the mixture in the primary circuit, measured by a *vortex* flow meter;
- temperature at different locations and depths along and in the thickness of the aluminum plate, by 1 mm Ktype thermocouples inserted in 1.1 mm holes drilled in the plate (See Fig. 4.13);
- temperature of the secondary coolant in the inlet and outlet collectors;
- flow rate of the secondary coolant, via a Coriolis type flowmeter;
- temperature of the tertiary coolant at the inlet and at the outlet of the mixing vessel;
- pressure in the primary vessel;
- helium mole fraction, obtained by conductivity measurement of the non-condensable air-steam mixture, after sampling the mixture at the inlet of the channel and condensing the steam.

4.2.3 Data processing procedure

Basing on the temperature measurements available within the condensing plate, the local heat fluxes are evaluated with a method similar to the one used for COPAIN. Unlike in COPAIN, temperature in the secondary side of the condensing wall is not uniform. Due to the nature of the secondary circuit, the same assumption cannot be extended in the case of CONAN. The temperature in the secondary side of the condensing wall is more likely to be increasing, countercurrent to the condensing mixture in the test section. Moreover, entrance effects are experienced to be a relevant phenomena, enhancing the heat and mass transfer in the first part of the channel. Both aspects result in a variable temperature profile on the condensing surface. Due to the local nature of heat flux and boundary conditions, an average analysis could be misleading in the case of CONAN, for which a local analysis of experimental data has been preferred.

Given the temperature values measured on the condensing plate, the local heat flux corresponding to a couple of thermocouples $TP_{e,j}$, $TP_{i,j}$ at a distance x_j from the inlet section is given by:

$$\Phi_j = k(T_{avg})\ \nabla T = k\Big(\frac{TP_{e,j} + TP_{i,j}}{2}\Big)\frac{TP_{e,j} - TP_{i,j}}{e_p} \tag{4.25}$$

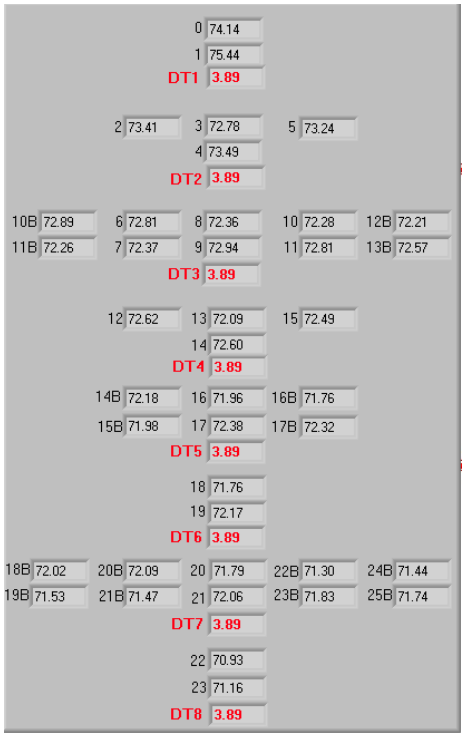

Figure 4.13: Layout of thermocouples within the condensing plate of CONAN

and the temperature on the condensing surface $T_{c,j}$ is estimated assuming a linear temperature profile across the aluminum plate

$$T_{c,j} = TP_{e,j} + (TP_{e,j} - TP_{i,j}) \frac{e_p^{'}}{e_p} \tag{4.26}$$

As in COPAIN, the assumption is done that the liquid film, if present, has negligible thickness[2]. The condensation temperature $T_{i,j}$ is then assigned to the wall temperature $T_{c,j}$. Once the local heat flux and the condensation temperature are known, the local condensation mass flux $\dot{m}_j^{''}$ is calculated by:

$$\dot{m}_j^{''} = \frac{\Phi_j - \Phi_{j,s}}{\hbar^{lat}(T_{i,j})} \tag{4.27}$$

where $\Phi_{j,s}$ is the sensible heat transfer, estimated on the basis of experimental correlations for pure heat transfer. The uncorrected and the corrected local Sherwood numbers are thus recovered as proposed in Eqs. 4.9 and 4.10 for COPAIN.

[2]It has been anyway proven that removing this assumption and accounting for the corresponding falling film thickness results in negligible changes in the obtained results.

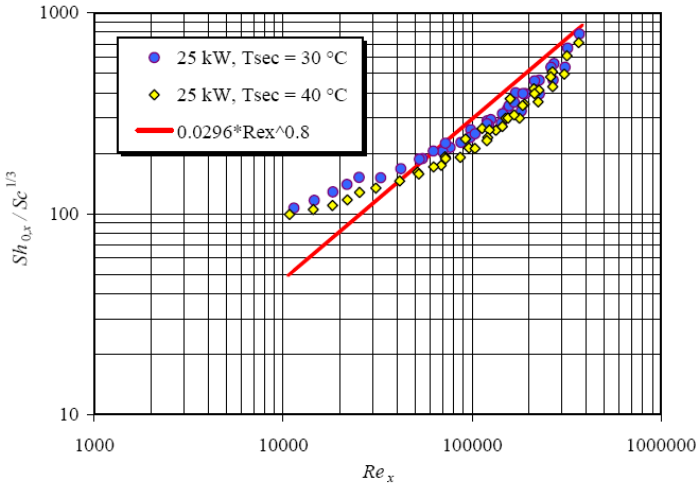

Figure 4.14: Effect of the secondary coolant inlet temperature (low temperature cases) in the prediction of the corrected Sherwood number Sh_{0x} (figure from Mogliani [92])

4.2.4 Main results of the previous air-steam condensation tests within CONAN

Two main experimental campaigns have been performed with the CONAN facility addressing wall condensation phenomena in presence of air. The first experimental campaign, detailed in the work of Konle [109], concerned condensation tests at high wall temperature. The operating secondary coolant inlet temperatures were 50, 60 and 70 $°C$. These tests were performed at all the operating steam generator powers and velocities presented in Tab. 4.2. A second experimental campaign, detailed in the work of Mogliani [92], was carried out repeating all the tests for different secondary coolant inlet temperatures: tests at 30 and 40 $°C$ of secondary coolant temperature were performed. Both experimental campaigns allowed drawing similar conclusions concerning the effect of the different operating conditions.

The effect of steam generator power and secondary coolant temperature in the prediction of suction effects were addressed. In Fig. 4.14 and 4.15 the influence of the secondary coolant temperature are analyzed at constant operating steam generator power. In both cases, with increasing temperature in the secondary side, the values of $Sh_{0x}/Sc^{1/3}$ tend generally to decrease for the same local Reynolds number. Moreover, there is a higher discrepancy of the data to values below the correlation line with increasing power. Figures 4.16 and 4.17 report the experimental results for constant nominal inlet temperatures of the coolant in the secondary loop. Equivalent trends as those already shown by the previous plots can be observed: the values for $Sh_{0x}/Sc^{1/3}$ tend to decrease with increasing power. Unfortunately, an analysis in terms of Sherwood number Sh_x was not proposed in the two works, which would be useful to analyze the suction phenomena and have a further insight in understanding the aforemen-

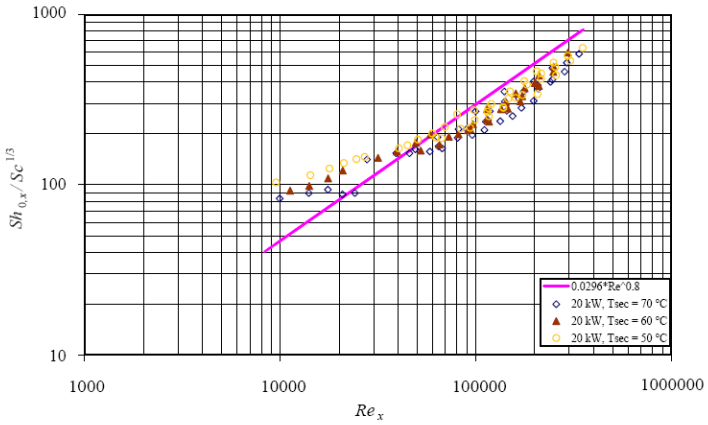

Figure 4.15: Effect of the secondary coolant inlet temperature (high temperature cases) in the prediction of the corrected Sherwood number Sh_{0x} (figure from Konle [109])

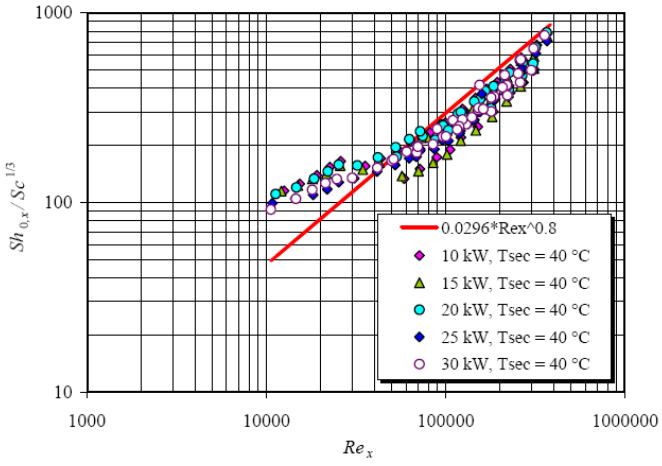

Figure 4.16: Effect of the steam generator power in the prediction of the corrected Sherwood number Sh_{0x} at low secondary coolant temperatures (figure from Mogliani [92])

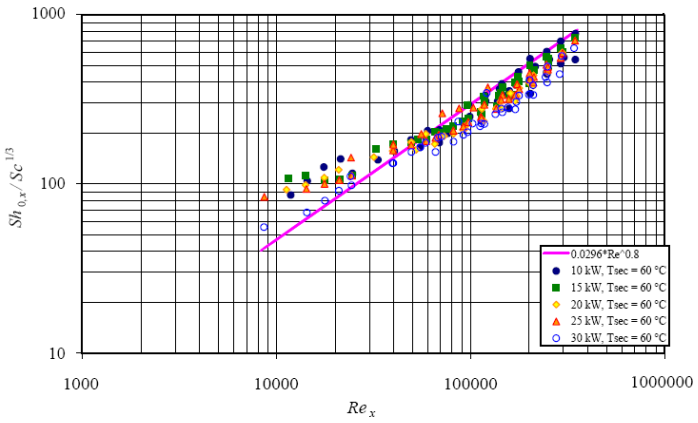

Figure 4.17: Effect of the steam generator power in the prediction of the corrected Sherwood number Sh_{0x} at high secondary coolant temperatures (figure from Konle [109])

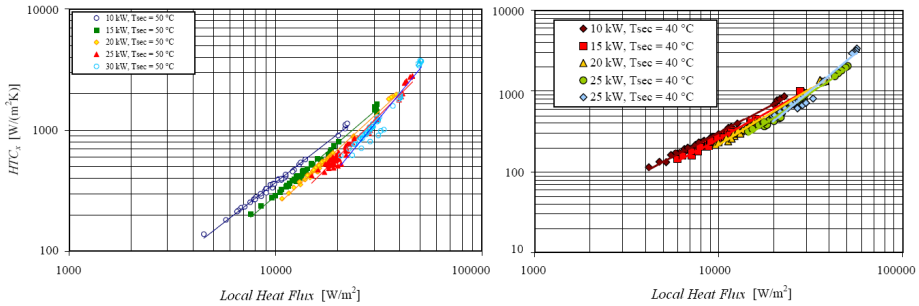

Figure 4.18: Effect of local heat flux and steam generator power on the local heat transfer coefficient (figures from Konle [109] and Mogliani [92])

tioned results. Anyway, the dependence of the overall heat transfer coefficient on the local heat flux was analyzed, pointing out that the heat transfer coefficient increases with increasing local heat flux (see Fig. 4.18) and that, for the same value of the local heat flux, it increases with increasing temperature in the secondary side, particularly at the highest secondary side temperatures (see Fig. 4.19). This conclusion is detailed in Fig. 4.20, where the local heat transfer coefficient is plotted versus the temperature difference between the bulk and the surface of the cooled plate for the case at 20 KW. In Fig. 4.21, the heat transfer coefficient is plotted against the vapor mass fraction for the different steam generator powers, revealing the intrinsic relation between steam generator power and steam mass fraction in bulk. A further analysis detailed that, according to the operating procedure of CONAN, in tests performed at the same operating steam generator power, the steam mass fraction in bulk decreases with increasing velocity whereas the heat transfer coefficient increases (see Fig. 4.22). This is the result of the fact that with a higher velocity the heat transfer coefficient

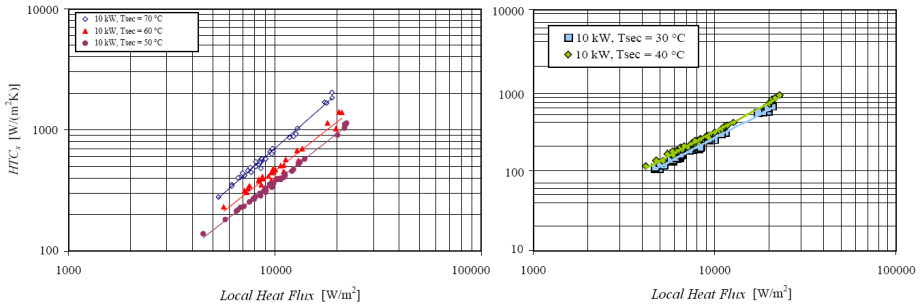

Figure 4.19: Effect of local heat flux and secondary coolant inlet temperature on the local heat transfer coefficient (figures from Konle [109] and Mogliani [92])

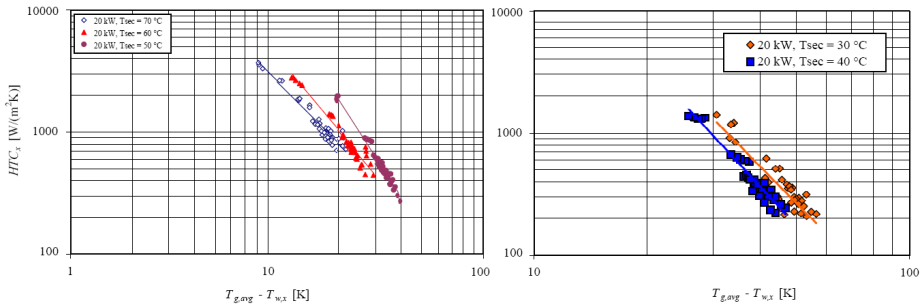

Figure 4.20: Effect of bulk to wall temperature difference and secondary coolant inlet temperature on the local heat transfer coefficient (figures from Konle [109] and Mogliani [92])

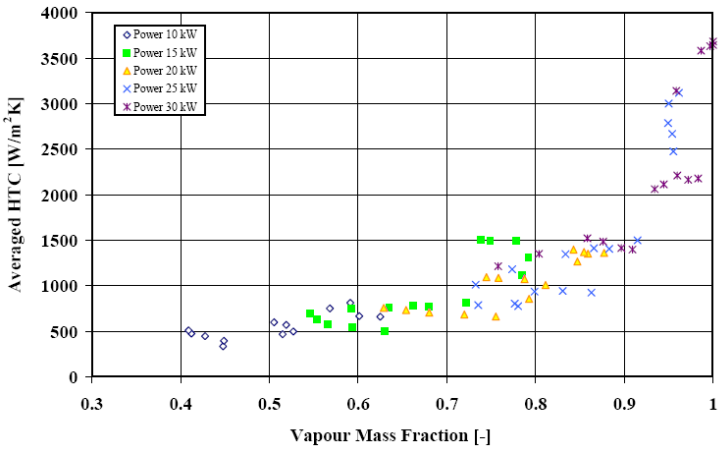

Figure 4.21: Effect of steam mass fraction and steam generator power on the local heat transfer coefficient (figures from Konle [109])

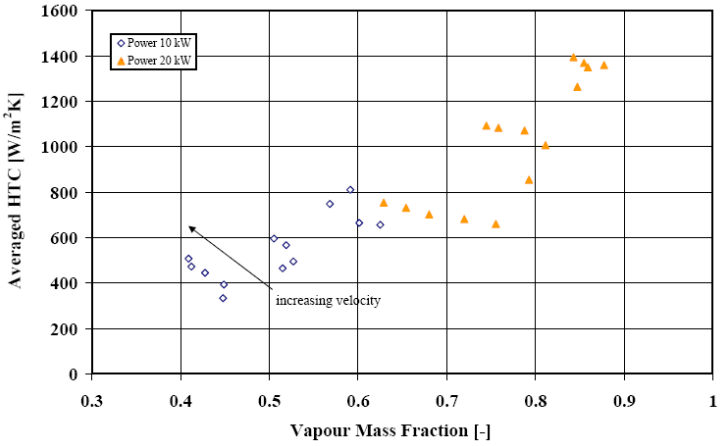

Figure 4.22: Effect of steam mass fraction and mixture velocity on the local heat transfer coefficient (figures from Konle [109])

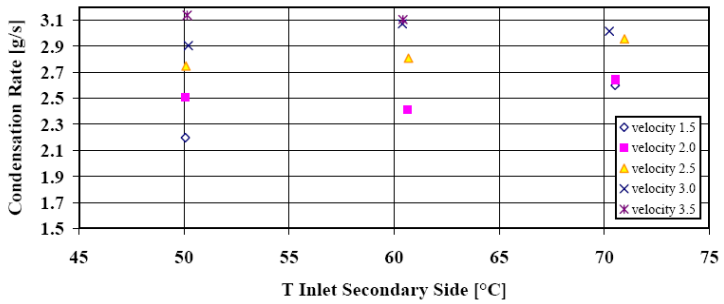

Figure 4.23: Condensation rate as a function of the secondary coolant inlet temperature at the different velocities (figures from Konle [109])

increases and so does the condensation rate (see Fig. 4.23). Thus, due to the open orifice which ensures the atmospheric pressure inside the facility, the system increases the amount of air for obtaining stable conditions. Because of this feature of the system the vapor mass fraction can only be controlled by changing boundary conditions, not directly. This is a keypoint for understanding the operating behavior of the facility. Actually, not all the power released by the steam generator is transferred to the condensing plate. Part of this amount of energy is removed as spurious condensation and sensible heat losses outside the test section of the channel. At the lowest velocities, even if higher steam mass fraction in bulk are experienced, the heat transfer coefficient is reduced and so is the temperature difference between the condensing surface and the mixture. The decrease in heat transfer at the condensing plate is balanced by spurious condensation, promoted also by the higher amount of steam experienced in bulk.

4.3 Revisited analysis of COPAIN and CONAN experimental data

In paragraphs 4.1.3 and 4.2.4, the analyses previously presented on the COPAIN and the CONAN experimental data have been summarized. Further details can be found in the work of Bazin [1] for what concerns the COPAIN facility and Konle [109] and Mogliani [92] for what concerns the CONAN facility. In the frame of this research activity, the experimental data of both facilities have been reviewed and analyzed under a different point of view. Basing on the local processing procedure of COPAIN, a new analysis has been performed, aimed at investigating condensation phenomena in the different convection regimes. In this aim, experimental data have been considered as a function of the local Richardson number, expressing the ratio between buoyancy and inertia forces:

$$Ri_x = \frac{Gr_x}{Re_x^2} \tag{4.28}$$

The experimental Sh_x and Sh_{0x} numbers are compared to correlations available in literature for the different convection regimes.

In the natural convection regime, the local formulation of the McAdams correlation is employed:

$$Nu_x = 0.13\ Gr_x^{1/3} Pr^{1/3} \tag{4.29}$$

The correlation proposed for forced convection, usually referred to as Schlichting's, is obtained by the Reynolds-Colburn analogy, basing on the Schlichting correlation for the friction coefficient:

$$St_x Pr^{2/3} = \frac{Nu_x}{Re_x Pr} Pr^{2/3} = \frac{C_{f,x}}{2} = 0.0296 Re_x^{-0.2} \tag{4.30}$$

Indeed, the Schlichting correlation is accurate for Prandtl and Schmidt numbers higher than 0.6 and smaller than 3000. In the case of COPAIN, tests are performed with a Schmidt number ranging from 0.5 to 0.6, with the smallest values associated to the highest mass transfer rate tests (see Fig. 4.24). To account for smaller Prandtl and Schmidt numbers, a correction is thus proposed to the Schlichting correlation based on the work of Fortier [110], adopted in the analysis of the COPAIN experimental data:

$$Nu_x = f_F(Re_x, Pr)\ 0.0296 Re_x^{0.8} Pr^{1/3} \tag{4.31}$$

where

$$f_F(Re_x, Pr) = \frac{Pr^{2/3}}{0.89 + \left[(B(Pr) - 5)\sqrt{0.0296\ Re_x^{-0.2}}\right] + 8\ 0.0296\ Re_x^{-0.2}} \tag{4.32}$$

with

$$B(Pr) = 2.18\ \ln(Pr) + 5.5\ Pr + 0.5 \tag{4.33}$$

To evaluate the Sherwood number the same coefficient is used, in which the Prandtl number is substituted by the Schmidt number. The modified correlation is applicable in the range of Schmidt and Prandtl numbers between 0.1 and 10

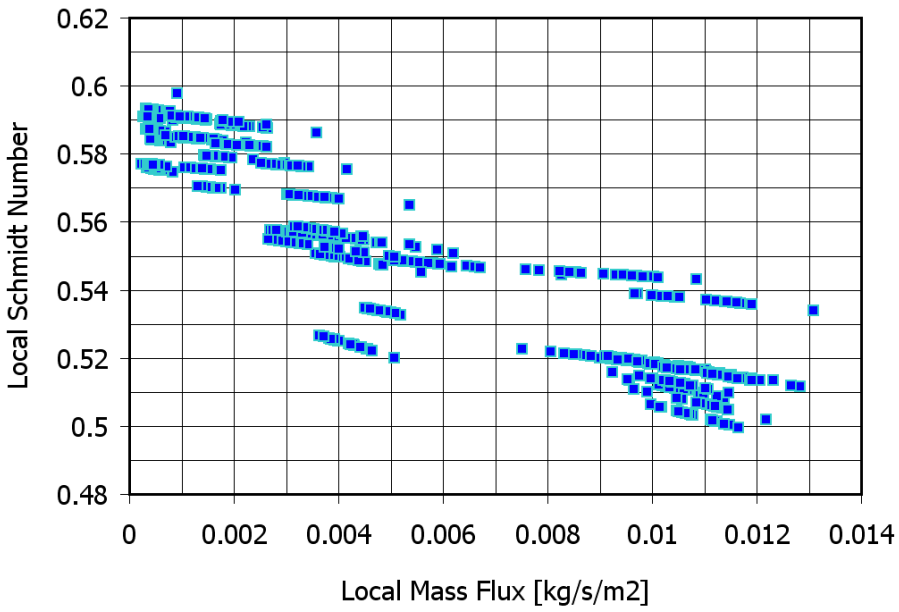

Figure 4.24: Local values of the Schmidt number in the COPAIN tests

and recovers the original Schlichting correlation when these are around 1. In Fig. 4.25, the ratio between the experimental Fortier coefficient f_F is shown for the COPAIN tests, on the basis of the Schmidt number for the mass transfer case and on the basis of the Prandtl number for the pure heat transfer cases. It is remarked that small Prandtl or Schmidt number affects the Nusselt and the Sherwood number prediction (20 % max).

In order to avoid spurious data points, relative to measurements taken near the inlet section and so affected by entrance effects, where heat and mass transfer properties are improved, data have been only considered for the fully developed region, according to the following criterion

$$\begin{array}{llll} Ri_x > 1 \ \& & Gr_x > 2.E+10 & \Rightarrow & accepted \\ Ri_x > 1 \ \& & Gr_x < 2.E+10 & \Rightarrow & discarded \\ Ri_x < 1 \ \& & Re_x > 2.E+6 & \Rightarrow & accepted \\ Ri_x < 1 \ \& & Re_x < 2.E+6 & \Rightarrow & discarded \end{array}$$

4.3.1 Analysis of the COPAIN data of pure heat transfer

Among the several tests performed within COPAIN, a couple of series have been conceived to analyze pure heat transfer phenomena. Different convection regimes have been investigated, proposing different local heat fluxes. In figure 4.26, the Nusselt number is normalized to correlations adopted for forced and natural turbulent convection regimes. Whenever the buoyancy forces overwhelm the inertia force, that is for Richardson numbers in the order of 10 or even more, the McAdams correlation is accurately recovered by the experimental data (red dots). On the other hand, whenever inertia forces predominate,

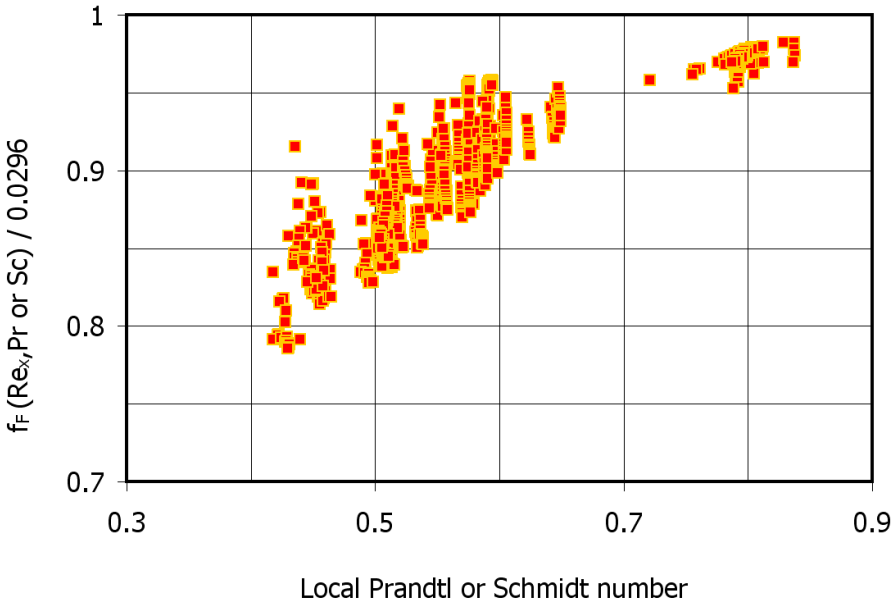

Figure 4.25: Experimental Fortier coefficient to Schlichting coefficient ratio

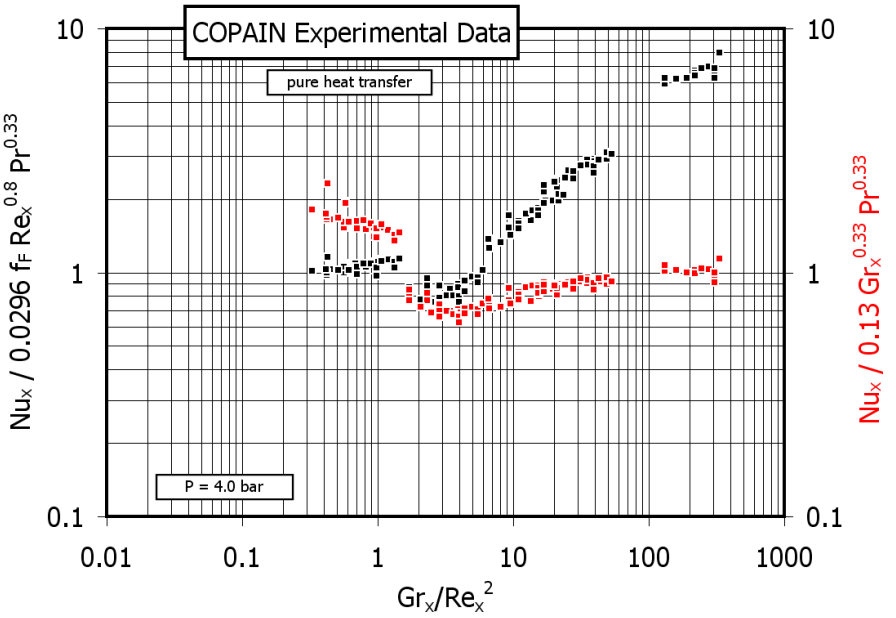

Figure 4.26: Normalized Nusselt number in pure heat transfer tests

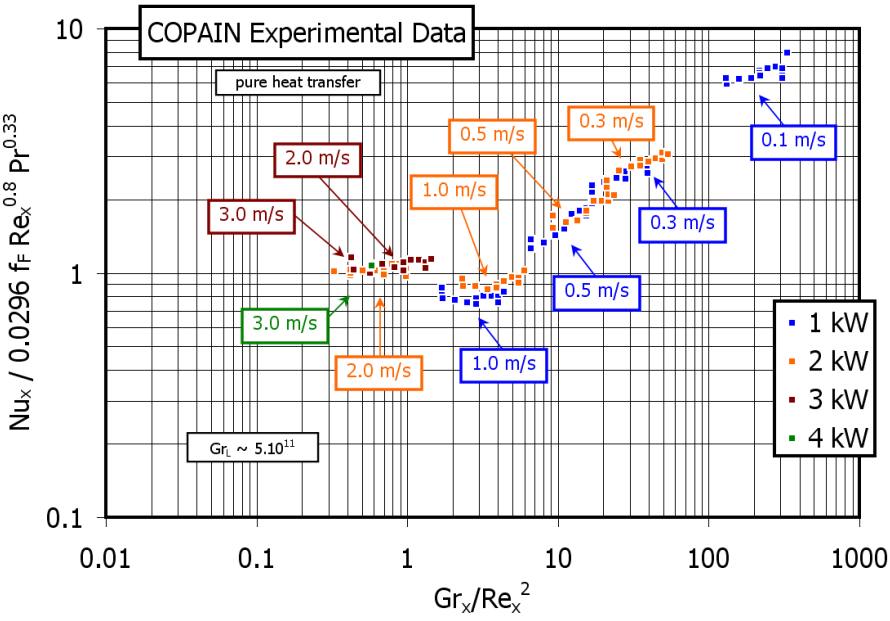

Figure 4.27: Nusselt number in pure heat transfer tests identified by heat transfer rates

for Richardson numbers below 1, experimental data are next to the values predicted by the Schlichting or Fortier correlations, that in the range of Prandtl number next to 0.6 are very similar (black dots). The analysis has also allowed identifying the presence of a mixed convection regime for Richardson numbers approximatively in the range 0.5 to 30. This is characterized by Nusselt numbers decreasing with respect to pure forced or natural convection. Such a behavior is likely to happen in mixed convection regimes where buoyancy forces act in the same direction than inertia forces [111]. In Fig. 4.27, the Nusselt number is reported identified on the basis of the heat flux, reveling an unclear dependence of the Nusselt number on the operating heat flux in the mixed convection region. Unfortunately, experimental data are available for pure heat transfer only at very low heat transfer rates. Further experimental data would be useful to detail the behavior of the phenomenon, with particular attention to mixed convection regimes.

4.3.2 Analysis of the COPAIN data of steam condensation in presence of air

Adopting the analogy between heat and mass transfer, experimental data of pure heat transfer are useful to be compared to Sherwood numbers of the mass transfer tests.

In Fig. 4.28 and Fig. 4.29 the actual Sherwood numbers are respectively compared to the reference correlations for forced convection and natural convection. Nusselt data are also reported (labelled by HT) normalized by the same cor-

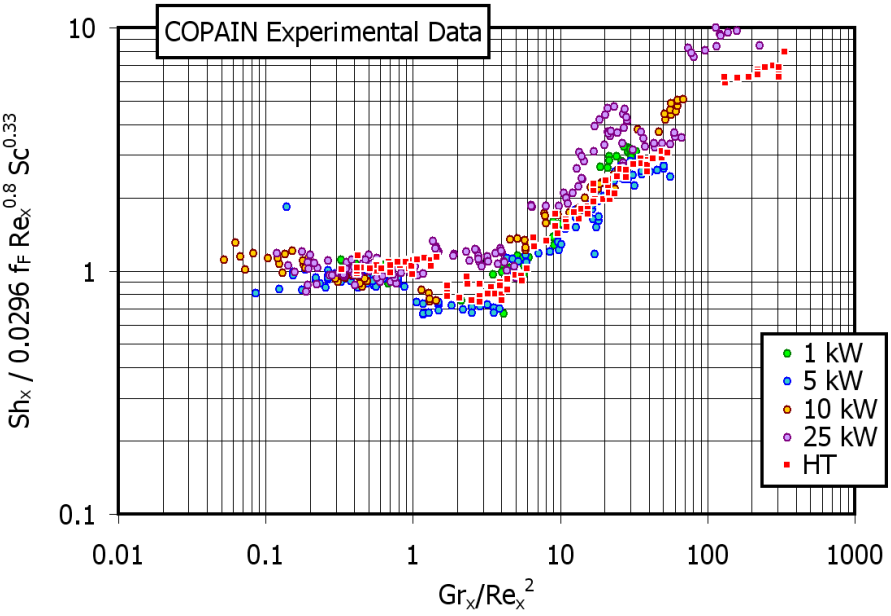

Figure 4.28: Normalized Sherwood number Sh vs. Richarson number (forced convection analysis) at different heat transfer rates

relations, in which the Schmidt number is substituted by the Prandtl number. The evidence of suction effects is shown, which makes the mass transfer and the heat transfer coefficient to increase with respect to the corresponding pure heat transfer cases, mostly in the natural convection cases having the highest heat and mass transfer rates. In Fig. 4.28, the analysis is focused on the forced convection regime; for the highest heat fluxes the effect of suction appears, becoming more and more important for the lowest Richardson numbers and for the highest heat fluxes. Unlike in the previous analyses performed basing on the classical Schlichting correlation [1], the adoption of a formulation capable of accounting for low Schmidt number effects, has allowed to show experimental Sherwood data points to be above the corresponding Nusselt data points, that is the suction effect due to condensation. In Fig. 4.29, the natural convection regime is instead addressed. Suction effects are found to be very important for the highest heat fluxes and so it is also in the mixed convection regime.

To account for suction effects, the Sherwood number is corrected by the Stefan factor. The analogy between heat and mass transfer allows thus comparing the corrected Sherwood number Sh_{0x} to the proposed correlation and the pure heat transfer data. In Fig. 4.30 and Fig. 4.31, Sherwood numbers Sh_{0x} are shown compared respectively to the correlations for forced convection and natural convection. Previous work performed by Konle [109], Mogliani [92] suggested that the Stefan factor may overestimate suction effects, resulting in a too strong correction of the actual Sherwood number. This is also apparent from the present analysis.

For forced convection or natural convection as well, most data points, at

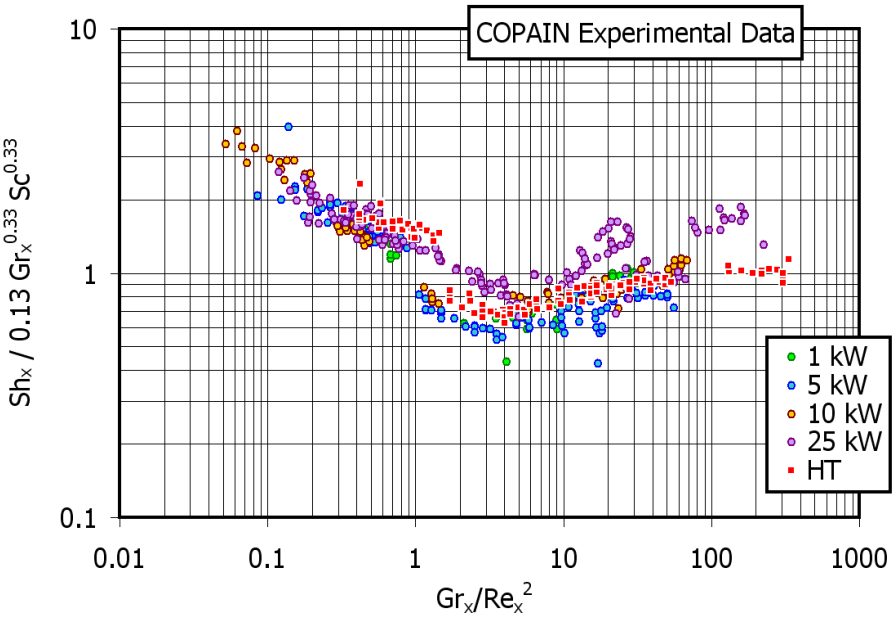

Figure 4.29: Normalized Sherwood number Sh vs. Richarson number (natural convection analysis) at different heat transfer rates

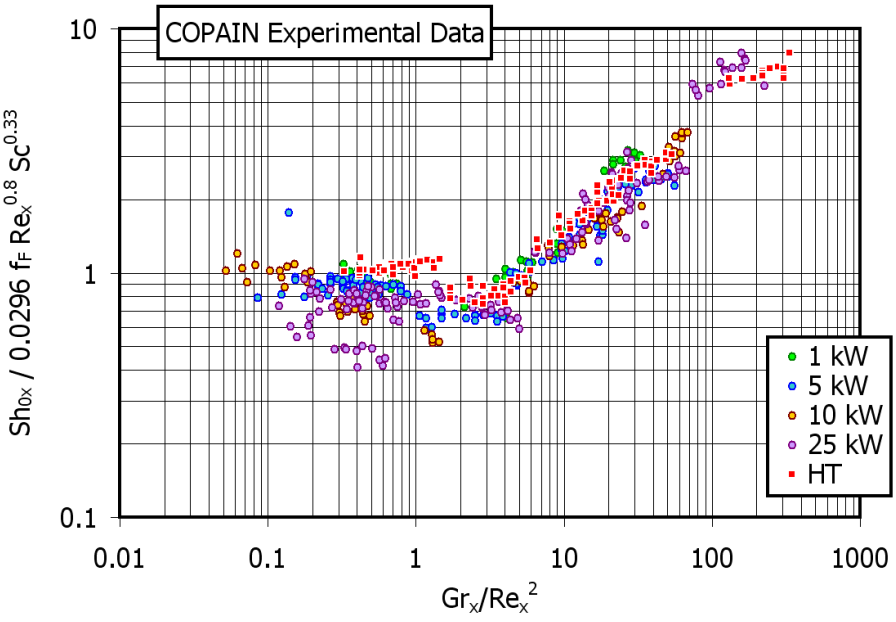

Figure 4.30: Normalized Sh_0 number vs. Richarson number (forced convection analysis) at different heat transfer rates

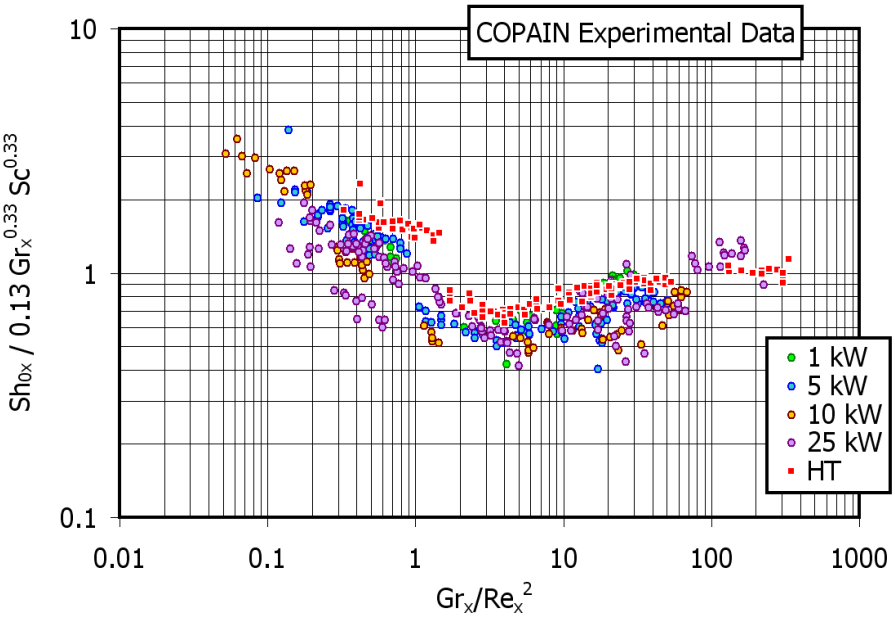

Figure 4.31: Normalized Sh_0 number vs. Richarson number (natural convection analysis) at different heat transfer rates

higher heat fluxes, are clearly below the heat transfer curve (see Fig. 4.30 and 4.31). A limited number of condensation data points are weakly affected by Stefan correction and basically agree with the heat transfer curve. In general, the higher is the Stefan factor, the more overestimated is its prediction of suction effects, as shown in Fig. 4.32 where the ratio between the actual Sherwood number and the proposed correlation is compared to the Stefan factor, for the forced convection cases.

The Stefan factor is obtained based on the hypothesis of constant density and diffusivity in the condensing boundary layer. Indeed, the condensing boundary layer can be characterized by sharp variations of properties, most of all density. The accuracy of the Stefan factor can therefore be affected by this inaccurate assumption. An analysis of the same data, identified on the basis of the non-condensable mass fraction in bulk, allowed drawing further conclusions. In mixtures very rich of steam, suction effects are more visible, most of all in the natural convection regime (see Fig. 4.33). In these cases, the Stefan factor results in a too severe correction of the Sherwood number. Indeed, in the most condensation cases, with the highest heat flux, the mass transfer rate and the steam mass fraction in bulk are monotonically related and the analysis results strictly coupled: the higher is the steam mass fraction in bulk, the higher is the condensation mass flux.

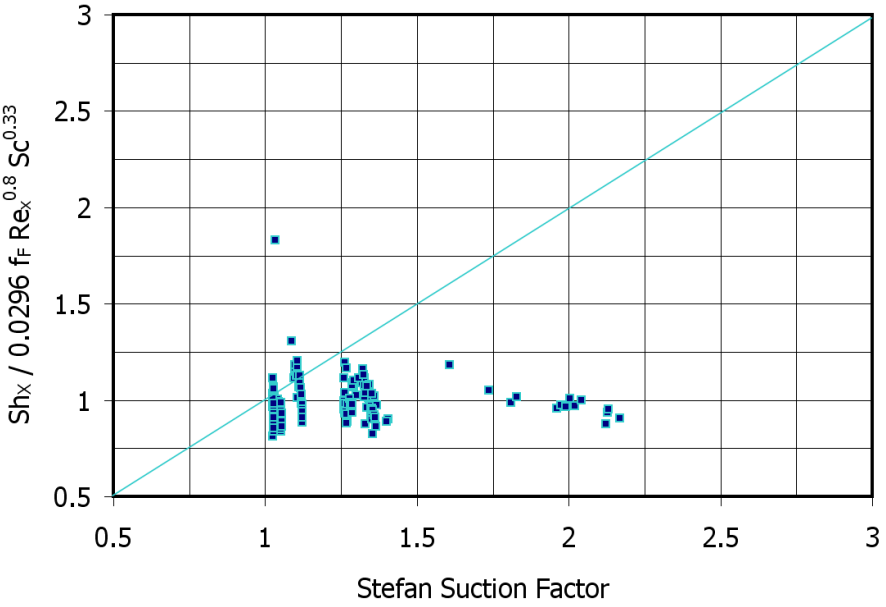

Figure 4.32: Experimental Sherwood to forced convection correlation ratio vs. Stefan Suction Factor in the forced convection cases

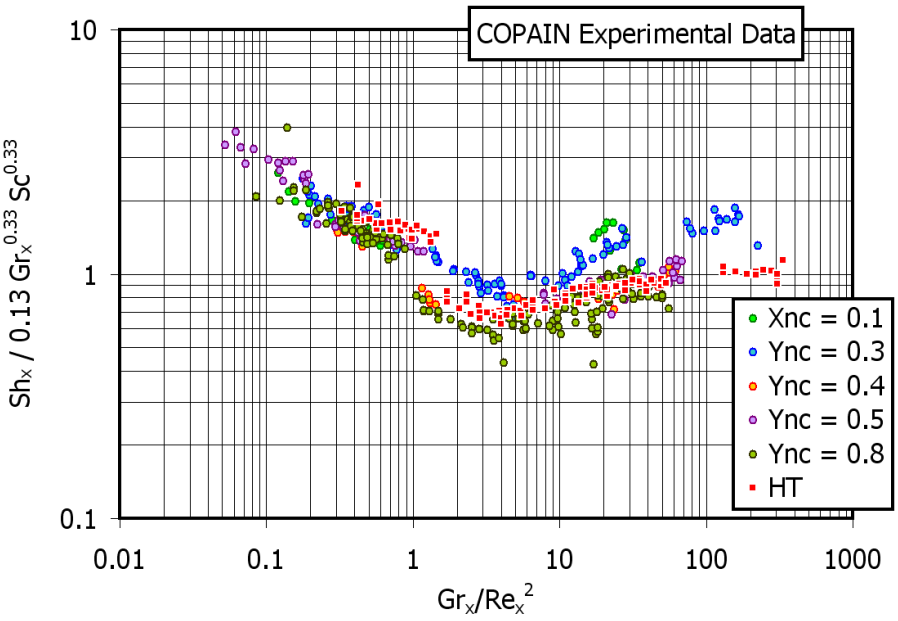

Figure 4.33: Effect of noncondensable gas concentration on the Sherwood number Sh vs. Richarson number

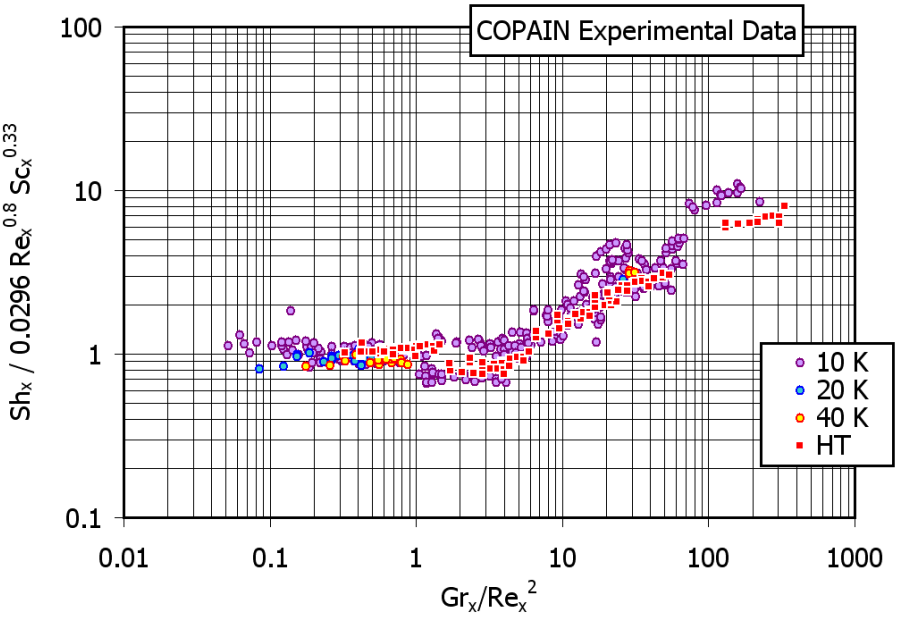

Figure 4.34: Effect of steam superheating on the Sherwood number Sh vs. Richarson number

4.3.3 Superheating and Pressure effects in the COPAIN tests of steam condensation in presence of air

The peculiarity of COPAIN, with respect to CONAN, consists in providing condensation test data in pressurized conditions and at temperature higher than the saturation temperature corresponding to the steam partial pressure in bulk. In the analysis of the experimental data proposed by Bazin [1] it is remarked that superheating increases the sensible heat transfer and the latent heat transfer is unchanged. In Fig. 4.34, the Sherwood number data identified on the basis of the superheating temperature is reported. Superheating is likely not to affect the physics of mass transfer phenomena, except for modifying the properties of the mixture that are intrinsically accounted for in the definition of the nondimensional numbers. In Fig. 4.35, the effects of pressure are analyzed. Test cases at higher pressure are usually associated with higher steam mass fraction in the bulk and thus higher heat and mass fluxes. To refine the analysis on the effect of pressure, tests at the same nominal operating conditions are selected, at different pressures. The results of this analysis are reported in Fig. 4.36, demonstrating that pressure does not affect the local Sherwood number, as remarked in the previous analyses [1].

4.3.4 Analysis of the CONAN data of steam condensation in presence of air

The processing of the CONAN data has been repeated adopting the same procedure adopted for COPAIN. In particular, the difference with respect to the

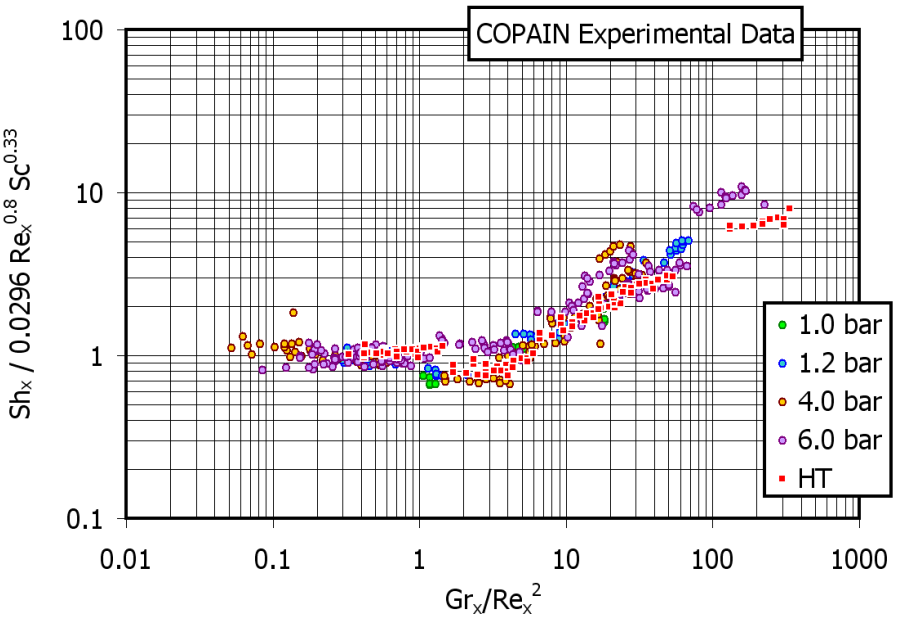

Figure 4.35: Overall effect of pressure on the Sherwood number Sh vs. Richarson number

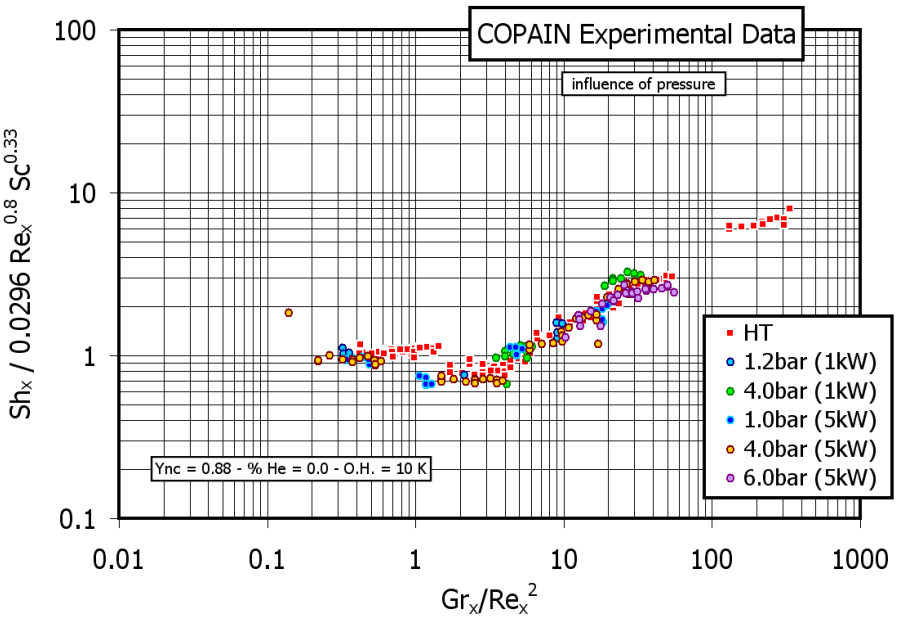

Figure 4.36: Effect of pressure on the Sherwood number Sh vs. Richarson number in separate effect conditions

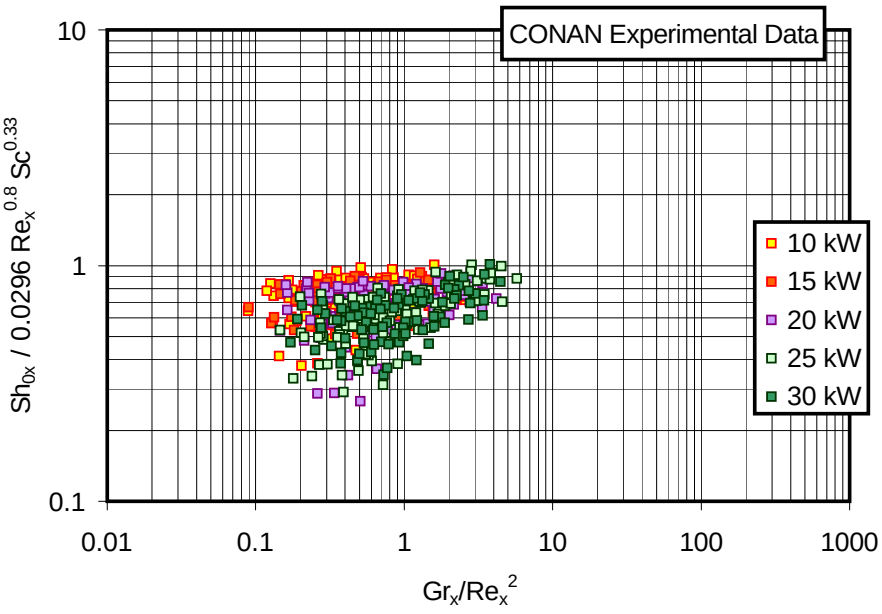

Figure 4.37: Sh_0 number vs. Richardson number at different steam generator powers

previously adopted data processing consists in the way to estimate the sensible heat transfer contribution in the overall heat transfer. In the original CONAN method, the sensible heat transfer was estimated by the Schlichting correlation. In the here adopted method, the ratio between the sensible and the latent heat transfer is estimated via the heat and mass transfer analogy as illustrated in the paragraph 4.1.3. Indeed, the sensible heat transfer consists of a very small percentage of the overall heat transfer and the differences between the two choices was found negligible. As expected, the results of the analyses of Konle [109] and Mogliani [92] have been fully confirmed. In Fig. 4.37, the corrected Sherwood number is reported compared to the Schlichting correlation[3], revealing that the higher is the steam generator power, the lower is the predicted Sh_0 number and therefore confirming the results of the previous analyses reported in paragraph 4.2.4. In Fig. 4.38, the dependence between the local mass flux and the predicted Stefan factor is proposed, showing the general monotone correspondence between these quantities: the higher is the mass flux, the more important suction effects should be expected. This makes the Sherwood number Sh to be higher for the higher heat transfer rates, as shown in Fig. 4.39. From Fig. 4.40 to Fig. 4.44, the same data are identified on the basis of the secondary coolant inlet temperature, confirming the trend.

Another interesting aspect was put in evidence in this analysis. From Fig. 4.45

[3]The new proposal based on the Fortier coefficient has not been adopted in the case of CONAN to make the comparison with previous analyses as clearer as possible. The effects of adopting the new correlation can be quantified in an increasing of Sh and Sh_0 numbers in the order of 10 %. Anyway, qualitative conclusions are confirmed.

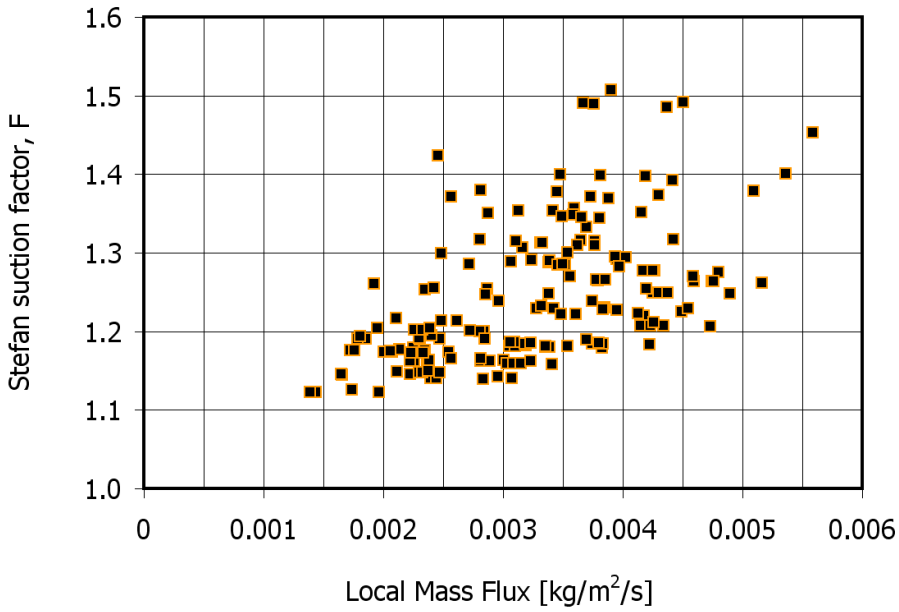

Figure 4.38: Stefan suction factor vs. condensation mass flux

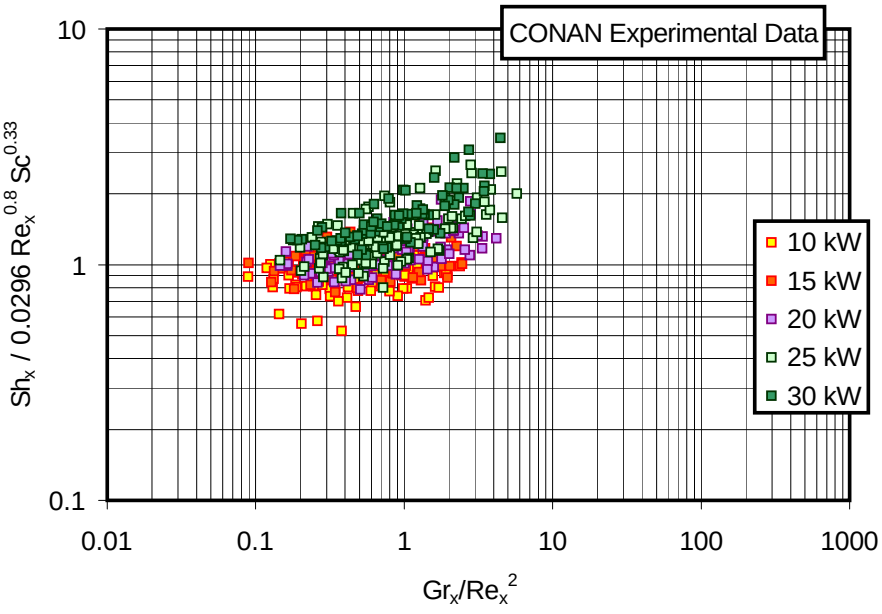

Figure 4.39: *Sh* number vs. Richardson number at different steam generator powers

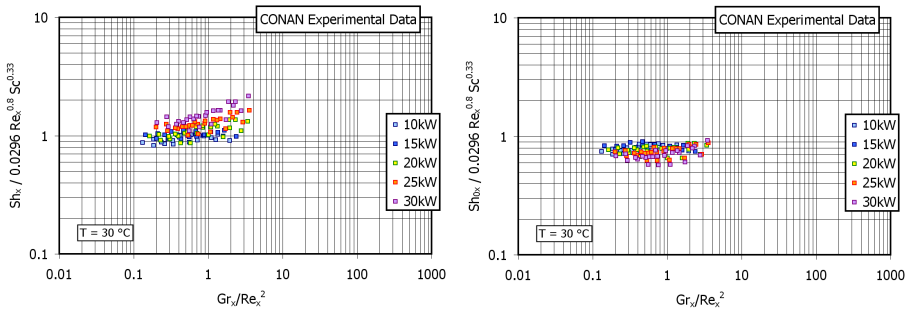

Figure 4.40: Effect of steam generator power on the Sh number in the cases at secondary coolant inlet temperature of 30 $^{\circ}C$

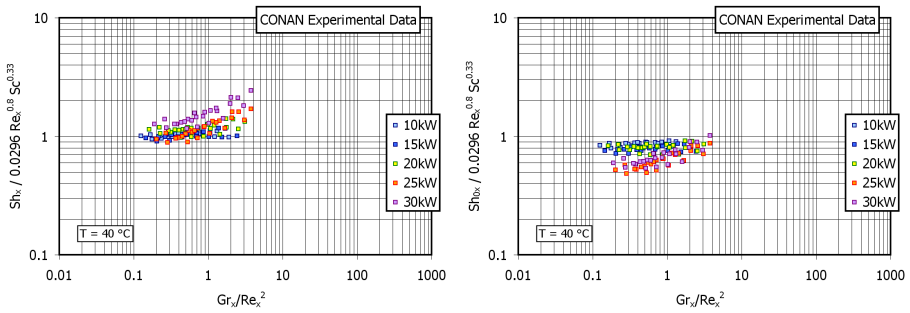

Figure 4.41: Effect of steam generator power on the Sh number in the cases at secondary coolant inlet temperature of 40 $^{\circ}C$

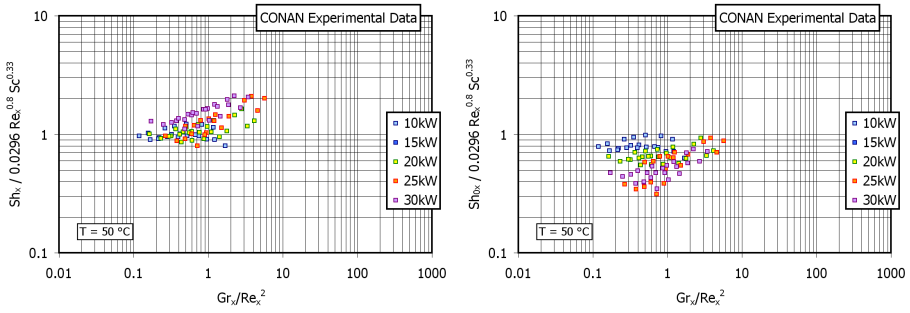

Figure 4.42: Effect of steam generator power on the Sh number in the cases at secondary coolant inlet temperature of 50 $^{\circ}C$

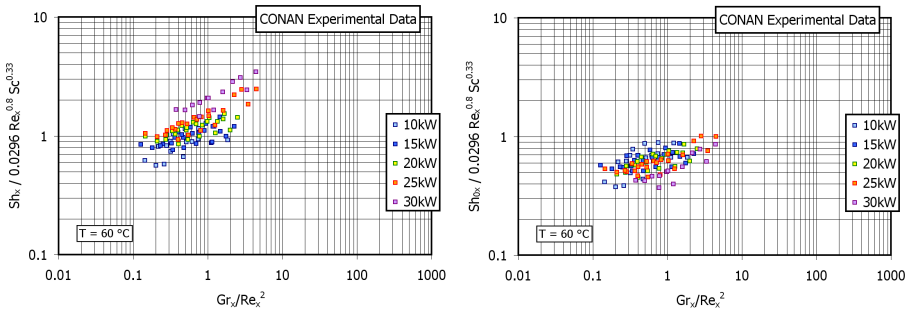

Figure 4.43: Effect of steam generator power on the Sh number in the cases at secondary coolant inlet temperature of 60 $°C$

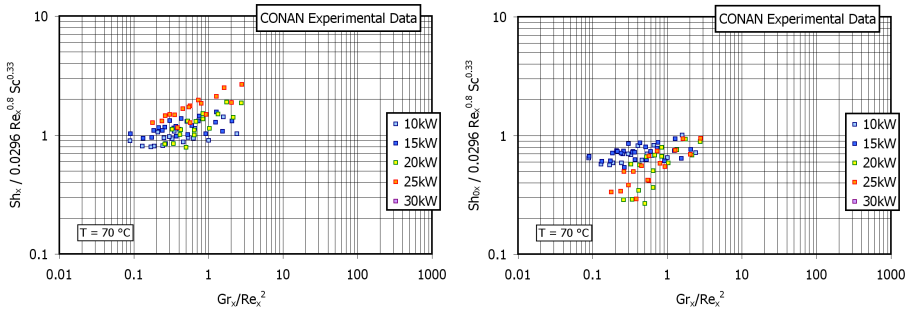

Figure 4.44: Effect of steam generator power on the Sh number in the cases at secondary coolant inlet temperature of 70 $°C$

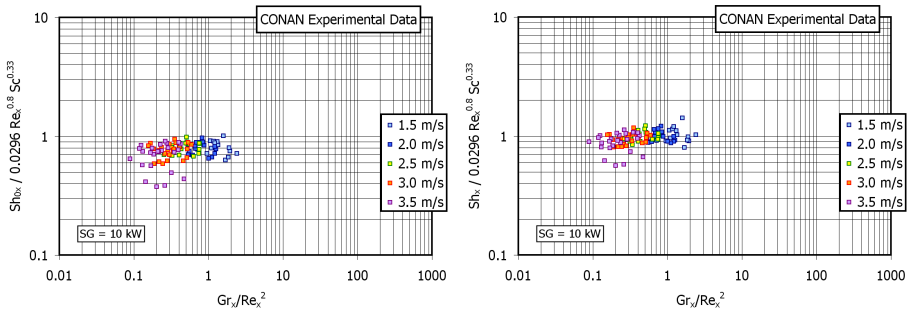

Figure 4.45: Effect of mixture velocity on the Sh number in the cases at steam generator power of 10 kW

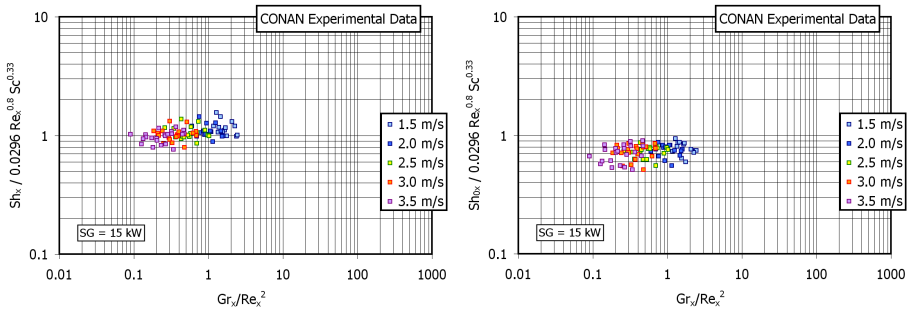

Figure 4.46: Effect of mixture velocity on the Sh number in the cases at steam generator power of 15 kW

to Fig. 4.49, the actual and the corrected Sherwood numbers are compared to the Schlichting correlation for the different steam generator powers, classified on the basis of the inlet mixture velocity. As expected, at a fixed power, datapoints corresponding to highest velocities are the leftmost. On the contrary, datapoints corresponding to the lowest velocities are the rightmost, which are the most likely affected by buoyancy forces. Indeed, at low heat transfer rates, as well as at the highest, the tendency is shown that Sherwood numbers increase for decreasing velocities whenever Richarson numbers approach 1. This is likely to be a mixed convection effect. Indeed, a local analysis of the Sherwood number for some representative cases is proposed in Fig. 4.50 and 4.51 for the lowest velocity test cases. A comparison is proposed for both forced and natural convection conditions, suggesting the mixed nature of the experimental convection regime.

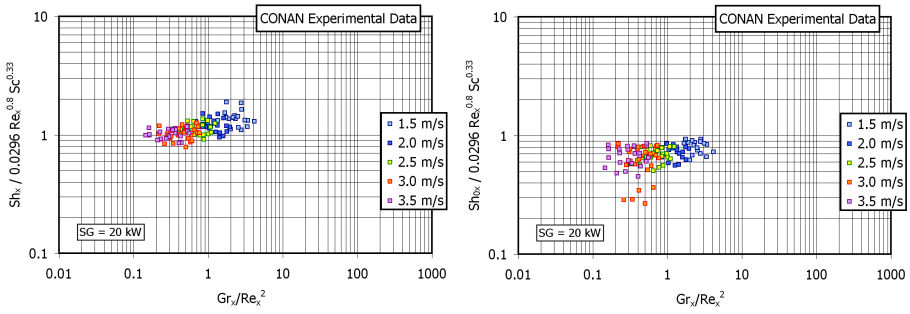

Figure 4.47: Effect of mixture velocity on the Sh number in the cases at steam generator power of 20 kW

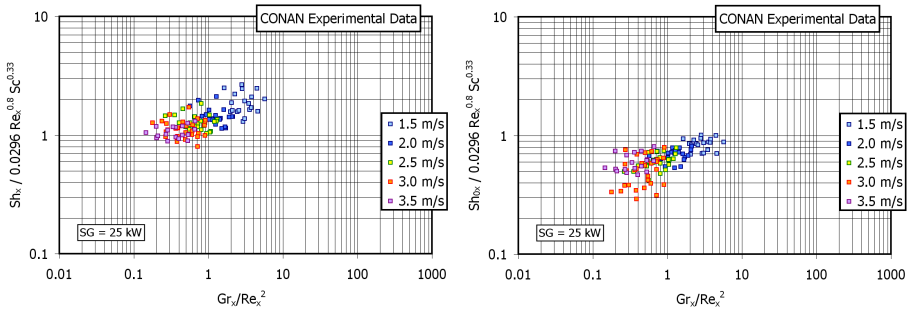

Figure 4.48: Effect of mixture velocity on the Sh number in the cases at steam generator power of 25 kW

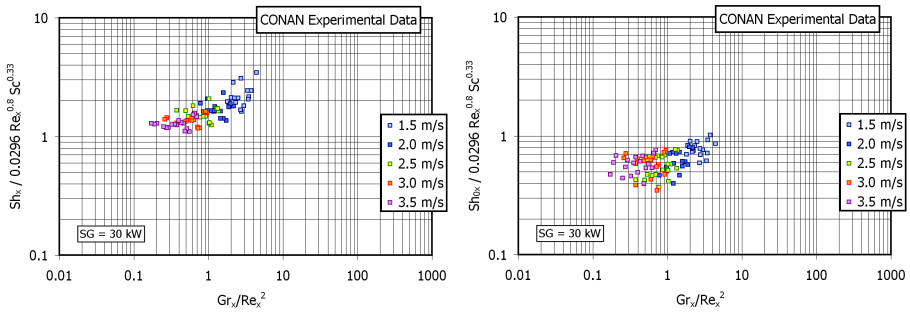

Figure 4.49: Effect of mixture velocity on the Sh number in the cases at steam generator power of 30 kW

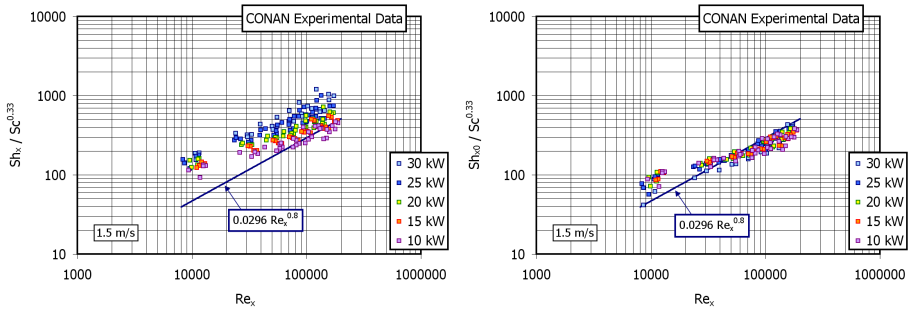

Figure 4.50: Local Sh and $Sh0$ numbers vs. Schlichting correlation in tests having free stream velocity of 1.5 m/s

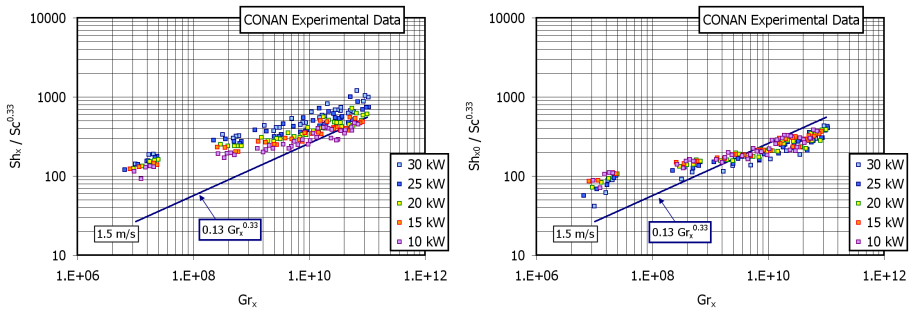

Figure 4.51: Local Sh and $Sh0$ numbers vs. McAdams correlation in tests having free stream velocity of 1.5 m/s

4.4 Concluding remarks

An analysis of the experimental data available by the CONAN and the COPAIN facilities has been performed. The attention was focused on the steam condensation tests in presence of air. A review of the previous analyses performed on the experimental data has also been proposed.

CONAN experimental data were analyzed in detail by Konle [109] and Mogliani [92] concerning the effect of the different operating conditions on the heat transfer coefficient. The influence of the different steam generator powers were analyzed revealing that, considering tests with the same secondary coolant inlet temperature, the higher is the heat and mass transfer rate, the higher is the heat transfer coefficient. On the other hand, the higher is the secondary coolant inlet temperature, the lower is the heat transfer coefficient. Local data were analyzed also proposing a comparison between the experimental local Sherwood number, evaluated on the basis of the local heat flux, and the correlation available in literature for heat transfer and, adopting the heat and mass transfer analogy, for mass transfer. The data suggested that the Stefan factor, accounting for suction effects tends to overestimate suction effects. As remarked, the main assumption at the basis of the evaluation of the Stefan factor is constant density in the condensing boundary layer. Even if the influence of this assumption is not evaluated, this is not the case of steam condensation in presence of air, characterized by sharp variation of density in the proximity of the condensing interface.

COPAIN experimental data were analyzed by Bazin et al. [1], proposing a local and an average approach. A comparison between the local Sherwood number and the Schlichting and McAdams correlations, respectively for forced and natural convection were proposed, identifying the presence of suction effects in the natural convection regime, but not in the forced convection regime. The influence of different degrees of steam superheating was analyzed, revealing that it does not affect the physics of condensation, described by the Sherwood number, and so does not pressure.

A new analysis of the experimental data was proposed in the present work, aimed at improving the understanding of condensation in the different convection regimes. The analysis of the COPAIN data has been repeated adopting a new reference correlation for forced convection conditions, capable of accounting for the low Prandtl and Schmidt numbers experienced in COPAIN in the most condensing cases. The comparison of experimental data with the new correlation allowed putting in evidence the presence of suction phenomena also in the forced convection regime. The results of the previous analysis have been basically confirmed for the natural convection regime. The present analysis has also allowed identifying the presence of mixed convection phenomena, but further experimental data would be required for drawing clearer conclusions. CONAN data have also been analyzed with the new method, confirming the conclusions drawn in the previous works and pointing out interesting buoyancy effects for the lowest velocity test cases, whose presence was also identified on the basis of previous computations [92].

Whatever is the convection regime or the experimental facility, suction effects are experienced to be more and more important for higher and higher mass transfer rates. The Stefan factor usually tends to overestimate these effects, producing a discrepancy between the experimental Sh_0 number and the

reference mass transfer correlations.

The analysis of both CONAN and COPAIN databases has allowed drawing the outline for future required activities, pointing out the interest in understanding suction phenomena. Moreover, the need emerges for a more in-depth understanding of buoyancy effects in the presence of air and also in the presence of helium. Indeed, the effect of noncondensable gases lighter than steam is also a fundamental aspect, whose analysis will be the subject of the forthcoming chapter 5.

Chapter 5

Tests of steam condensation in the presence of both air and helium

In chapter 3, a review of CFD models available for condensation modelling was performed. Basing on the conclusions drawn from the ISP47 and on the different test cases proposed for validating these models, the need emerged for achieving a better understanding of steam condensation phenomena in the presence of non-condensable gases lighter than steam, both under experimental and numerical point of view.

Several facilities have been operated in the past decades, aimed at analyzing how a noncondensable gas lighter than steam influences condensation. Most activities have anyway concerned the study of the thermal-hydraulic phenomenon under a general point of view. To achieve a better understanding of the physical phenomena and to collect high quality experimental data suitable for a more extensive CFD codes validation, separate effect test (SET) facilities were recently operated. The CONAN facility [8], in particular, was mainly operated in forced convection conditions, but also tests having a low free stream velocity were performed in the presence of helium in the aim to investigate mixed and natural convection regimes.

In this chapter, an analysis of the experimental database of CONAN is proposed, concerning the tests in presence of helium. A theoretical analysis of the effects induced by helium is proposed, focusing on the role of buoyancy forces. In CONAN, two different experimental campaigns have been performed to investigate the effect of noncondensable gases lighter than steam, whose results are here analyzed. The first one was carried out addressing the effects of helium in presence of high stream velocities [108]. Tests were performed having mixture velocity of 1.5 m/s up to 3.5 m/s. Three different test series were performed at different steam generator powers. In the frame of this PhD research, a further experimental campaign was carried out aiming at analyzing the behavior of a ternary mixture with helium and low stream velocities. Results of parametrical scoping calculations are also recalled to support the main conclusion of this analysis.

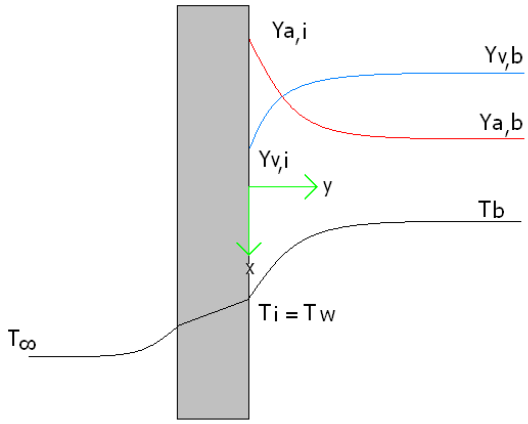

Figure 5.1: Sketch of concentration and temperature profile in a condensing steam-air mixture

5.1 Noncondensable buildup at the condensing interface

Steam condensing over a cold surface causes the noncondensable species to be transported towards the condensation interface. Due to the non permeability of the condensation interface, the noncondensable gases accumulate in its proximity. In air-steam mixture, a stable noncondensable layer is established, having the mass fraction profile qualitatively reported in Fig. 5.1. Due to temperature and to the buildup of air in the proximity of the condensation interface, the steam-air mixture is heavier than in the bulk. Buoyancy forces then come into play, whose influence on the flow field and on the transport processes depends on the free-stream mixture velocity. The dominating contribution between buoyancy and inertia forces can be clarified once their ratio is analyzed, known as the Richarson number

$$Ri = \frac{Gr}{Re^2} \tag{5.1}$$

Natural convection regimes are likely to be experienced when buoyancy forces overwhelm inertia forces, that is for $Ri >> 1$. On the other hand, when $Ri << 1$, inertia forces are predominant and the convection regime is forced. Mixed convection regimes occur when buoyancy and inertia forces have the same order, that is when $Ri \sim 1$. Moreover, the way buoyancy forces influence transport properties in the mixed convection region is twofold. When buoyancy forces and inertia forces are co-current the case is said to be of *buoyancy-aided* mixed convection:

$$(\rho_i - \rho_b)\,\vec{g} \cdot \vec{U} > 0 \tag{5.2}$$

Otherwise, when buoyancy forces and inertia forces are counter-current, the case is said to be of *buoyancy-opposed* mixed convection:

$$(\rho_i - \rho_b)\,\vec{g} \cdot \vec{U} < 0 \tag{5.3}$$

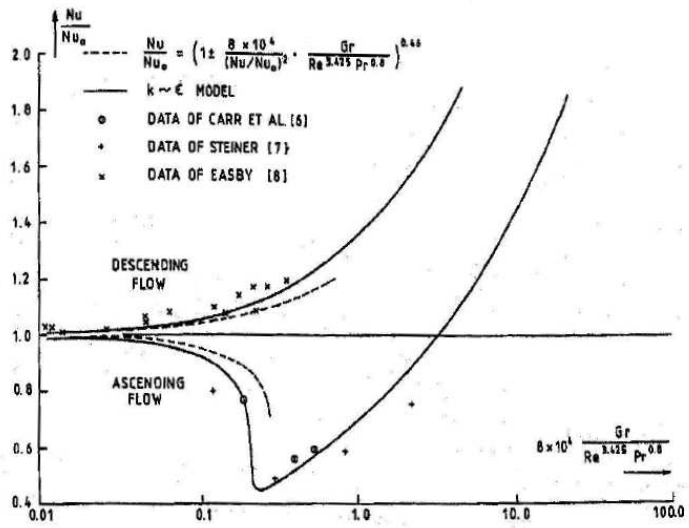

Figure 5.2: Variation of the Nusselt number in heated vertical pipe for *buoyancy-aided* (ASCENDING FLOW) and *buoyancy-opposed* (DESCENDING FLOW) cases (Fig. from Cotton and Jackson [111])

Figures 5.2, 5.3 and 5.4 show the results of studies on mixed convection respectively for a small vertical pipe [111], a rectangular channel [112] and an annular cross section channel [113], proposing the variation of Nusselt number ratio with a proposed buoyancy parameter. As it can be seen, in the *buoyancy-aided* cases, the impairment of heat transfer is predicted with onset of buoyancy influence. The Nusselt number falls to about half the forced convection value. Maximum impairment of heat transfer corresponds to a condition where the turbulence is being produced at a very much reduced rate. With further increase of buoyancy parameter, a progressive recovery of natural convection heat transfer effectiveness is predicted for the *buoyancy-aided* case. For the *buoyancy-opposed* case, when buoyancy forces and inertia forces are counter-current, a systematic enhancement of heat transfer is instead predicted with increase of buoyancy influence.

Despite mixed convection data in square channel more representative of the CONAN and COPAIN phenomenologies are not available in literature, it is clear that buoyancy effects that occur in the presence of condensing air-steam mixtures are *buoyancy-aided* and therefore an impairment is likely to be experienced before buoyancy forces become dominating. This is of course the case of COPAIN, where mixed convection effects can be remarked in analyzing the pure heat transfer tests and the heat and mass transfer ones (see chapter 4).

The regime usually addressed in the CONAN facility is instead forced convection, however, as observed in chapter 4, buoyancy forces could become important for the lowest velocity cases for which mixed convection effects are likely to have an effect. Unfortunately, the analysis of this regime was not a specific target for previous experimental campaigns and available data are not exhaustive for

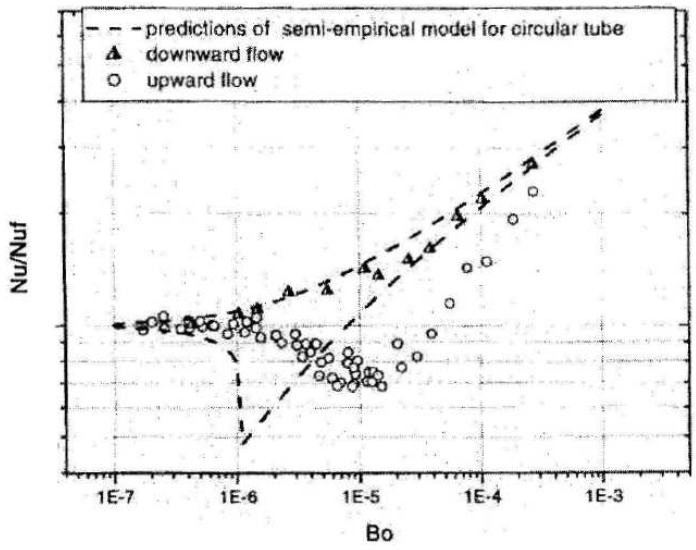

Figure 5.3: Variation of the Nusselt number in a heated square channel for *buoyancy-aided* (UPWARD FLOW) and *buoyancy-opposed* (DOWNWARD FLOW) cases (Fig. from Wang and Jackson [112])

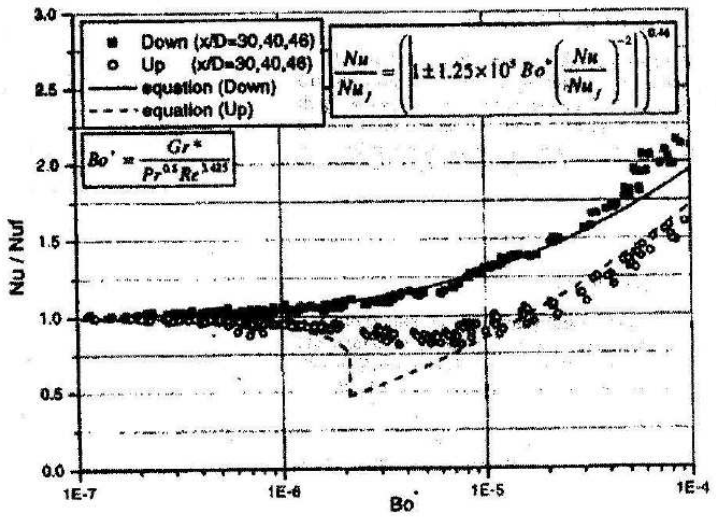

Figure 5.4: Variation of the Nusselt number in an heated annular cross section channel for *buoyancy-aided* (UP) and *buoyancy-opposed* (DOWN) cases (Fig. from Chung et al. [113])

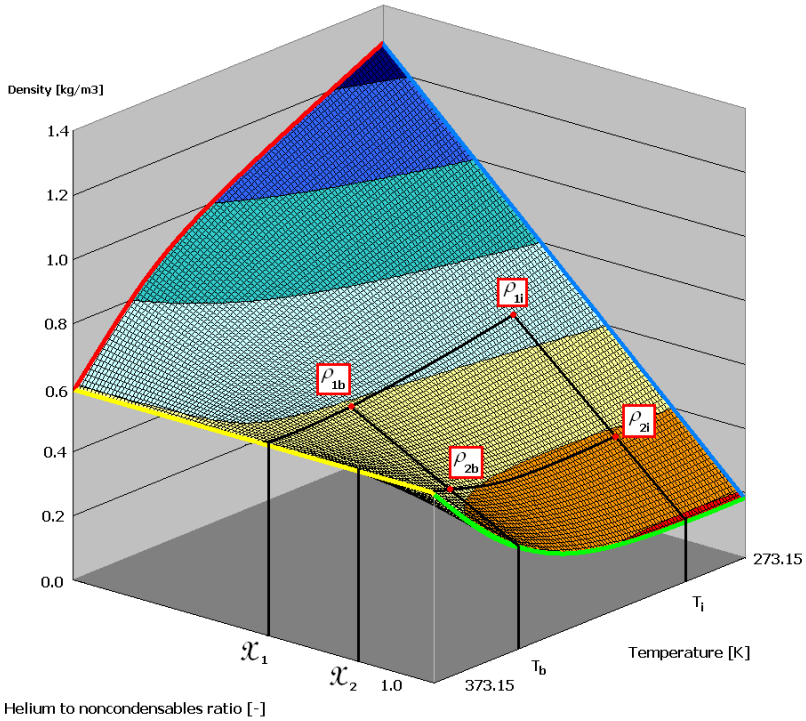

Figure 5.5: Air-steam-helium mixture density as a function of the mixture temperature and the helium-to-noncondensable gas ratio

drawing further conclusions.

When dealing with ternary mixtures, including a lighter than steam noncondensable gas, very interesting phenomena may occur. Indeed, in the presence of helium, the light gas build-up at the interface may reach critical values for which the density difference between the interface and the bulk is annealed and so are buoyancy forces. This condition is defined as *buoyancy reversal*. Further helium addition in bulk may also cause the interface density to be lower than the bulk and the buoyancy effect to be *buoyancy-opposed*. Assuming that the steam is in saturation conditions, the steam partial pressure is defined once the mixture temperature is given. Moreover, if it is also assumed that steam in saturation conditions can be considered as an ideal gas, the steam molar fraction is also known once the absolute pressure and temperature are known. If the noncondensable gas inventory is known, the mixture density is also known. In Fig. 5.5, the air-steam-helium mixture density at atmospheric pressure is shown as a function of the mixture temperature and the helium-to-noncondensable gas ratio χ defined as follows

$$\chi = \frac{X_{he}}{X_{nc}} = \frac{X_{he}}{X_{he} + X_a} \tag{5.4}$$

Let us consider a colder temperature, corresponding to the condensing in-

terface and an hotter temperature, corresponding to bulk conditions. Given the bulk temperature and the helium-to-noncondensable gas ratio, the mixture density is also known in bulk. The knowledge of the helium-to-noncondensable gas ratio at the interface is necessary to know the interface density. Indeed, in turbulent convection, since turbulence diffusion coefficients are dominating with respect to molecular diffusivities, helium and air diffuse in a similar way and the helium-to-noncondensable gas ratio at the interface can be reasonably considered equal to the bulk one[1]. Therefore, the interface density is also known. Depending on the helium-to-noncondensable gas ratio in bulk, two different phenomenologies can be expected (see Tab. 5.1). Let us select two different helium-to-noncondensable gas ratio values. In the first case, corresponding to the lower helium-to-noncondensable gas ratio χ_1 (see Fig. 5.5), the interface density is higher than the bulk density. In the second case χ_2, corresponding to the higher helium-to-noncondensable gas ratio, the interface density is instead lower than the bulk one. Between the two cases, a critical helium-to-noncondensable gas ratio value exists for which *buoyancy reversal* is experienced. This critical value for which the interface and the bulk density are identical is obtained by comparing the interface and the bulk densities

$$\rho_i = \frac{P}{RT_i}\left(M_v\frac{P_{v,sat}(T_i)}{P} + \left(M_{he}\chi_i + M_a\left(1-\chi_i\right)\right)\left(1-\frac{P_{v,sat}(T_i)}{P}\right)\right) \quad (5.5)$$

$$\rho_b = \frac{P}{RT_b}\left(M_v\frac{P_{v,sat}(T_b)}{P} + \left(M_{he}\chi_b + M_a\left(1-\chi_b\right)\right)\left(1-\frac{P_{v,sat}(T_b)}{P}\right)\right) \quad (5.6)$$

The critical helium-to-noncondensable gas ratio χ_{br} is therefore obtained by imposing $\rho_i = \rho_b$. It is

$$\chi_{br} = \frac{M_a - M_v\dfrac{\left(\frac{P_{v,sat}(T_b)}{PT_b} - \frac{P_{v,sat}(T_i)}{PT_i}\right)}{\left(\frac{1}{T_i} - \frac{1}{T_b}\right) + \left(\frac{P_{v,sat}(T_b)}{PT_b} - \frac{P_{v,sat}(T_i)}{PT_i}\right)}}{M_a - M_{he}} \quad \chi \in [0;1] \quad (5.7)$$

$\rho_i - \rho_b$	χ	flow direction	mixed convection regime
> 0	$< \chi_{br}$	*downward*	*buoyancy-aided*
$= 0$	$= \chi_{br}$	*downward*	*buoyancy reversal*
< 0	$> \chi_{br}$	*downward*	*buoyancy-opposed*
> 0	$< \chi_{br}$	*upward*	*buoyancy-opposed*
$= 0$	$= \chi_{br}$	*upward*	*buoyancy reversal*
< 0	$> \chi_{br}$	*upward*	*buoyancy-aided*

Table 5.1: Mixed convection phenomenologies depending on the direction of buoyancy and inertia forces

Each CONAN test can be therefore classified according to the theoretical value of χ_{br}. The χ_{br} is calculated according to Eq. (5.7), basing on the experimental bulk temperature and the interface temperature near the outlet section,

[1]This is also assumed in the analysis of experimental data

Test	χ_b	χ_{br}
P05-T40-V06-H03	0.026	0.617
P05-T40-V06-H34	0.330	0.624
P05-T40-V06-H62	0.610	0.626
P05-T40-V06-H64	0.631	0.627
P05-T40-V06-H65	0.653	0.628
P05-T40-V06-H66	0.667	0.627
P05-T40-V06-H67	0.669	0.629
P05-T40-V06-H69	0.685	0.627
P05-T40-V06-H70	0.704	0.627
P05-T40-V06-H33	0.331	0.622
P05-T40-V06-H39	0.396	0.623
P05-T40-V06-H47	0.469	0.623
P05-T40-V06-H52	0.521	0.623
P05-T40-V06-H55	0.546	0.623
P05-T40-V06-H57	0.574	0.623
P05-T40-V06-H59	0.592	0.623
P05-T40-V06-H62	0.618	0.624
P05-T40-V06-H69	0.690	0.623
P05-T40-V06-H70	0.703	0.622
P05-T40-V06-H75	0.730	0.623
P05-T40-V06-H78	0.780	0.634
P05-T40-V06-H90	0.893	0.643

Table 5.2: Calculated critical helium-to-noncondensable gas ratio in the CONAN steam-air-helium tests

obtained on the basis of the local heat flux and the temperature within the condensing plate. In Tab. 5.2, the helium-to-noncondensable gas ratios in bulk are compared to the theoretical values for which buoyancy reversal occur, estimated for each test by Eq. (5.7). Tests having a helium-to-noncondensable gas ratio in bulk less than the corresponding χ_{br} are likely to present a *buoyancy-aided* character; on the other hand, tests having an helium-to-noncondensable gas ratio greater than χ_{br} are likely to have a *buoyancy-opposed* character. Since bulk and interface temperatures are similar for all tests, the *buoyancy reversal* ratio is similar for all tests, estimated around 62 per cent.

5.1.1 Further comments on the noncondensable buildup at the condensing interface

Instead of assuming that the helium-to-noncondensable gas ratio at the interface is equal to the one in bulk, models can be used to predict the interface composition once the bulk composition is known. Indeed, the detail of the molecular transport become more and more important next to the condensing wall; differences in the diffusion of the light species could therefore be expected. A particular approach was proposed by Peterson [81] for evaluating the interface composition of ternary mixtures on the basis of the bulk composition and the binary diffusion coefficient. Peterson presented a fundamental analysis of

the mass transport with noncondensable species, identifying a simple method to calculate an effective mass diffusion coefficient to be use in his Diffusion Layer Model [79]. Here, the steps of Peterson's reasoning are summarized.

Being the condensing interface impermeable to the n noncondensable species, the interface molar average velocity is given by

$$U^*_{m,i} = X_{v,i} U_{v,i} \tag{5.8}$$

that can be turned as a function of the j-th noncondensable species:

$$U^*_{m,i} = \frac{D_{jv,i}}{X_{j,i}} \frac{dX_j}{dy}\Big|_i = D_{jv,i} \frac{d}{dy} ln(X_j)\Big|_i \tag{5.9}$$

Noting that noncondensable species are stagnant also in the diffusion layer, the molar average velocity in the entire diffusion layer can also be turned as a function of the j-th component gradient:

$$U^*_m = \frac{D_{jv}}{X_j} \frac{dX_j}{dy} = D_{jv} \frac{d}{dy} ln(X_j) \tag{5.10}$$

For one-dimensional flow, mass conservation requires that

$$\frac{d}{dy}(CU^*_m) = C\frac{dU^*_m}{dy} + U^*_m \frac{dC}{dy} = 0 \tag{5.11}$$

Since pressure is constant through the diffusion layer, if it is assumed that the temperature gradients are typically small compared with the absolute temperature, it is also valid to assume that the molar density C is constant. Thus, the continuity equation requires the molar average velocity U^*_m be constant in the diffusion layer. Under these assumptions, by integrating the equation 5.9 for each noncondensable species from the interface through the diffusion layer thickness δ, we finally get n equations of the kind

$$U^*_m = \frac{D_{jv}}{\delta}[ln(X_{j,b}) - ln(X_{j,i})] = \frac{D_{jv}}{\delta} \frac{(X_{j,b} - X_{j,i})}{X_{j,ave}} \tag{5.12}$$

where $X_{j,ave}$ is the logarithmic average molar fraction of the species j in the diffusion layer. Multiplying both sides of the n equations 5.12 by $X_{j,ave}$ and summing over j, the condensation velocity can be rearranged as

$$U^*_m = \left(\frac{X_{nc,ave}}{\sum_{j=1}^{n} (X_{j,ave}/D_{jv})} \right) \frac{1}{\delta} \frac{(X_{nc,b} - X_{nc,i})}{X_{nc,ave}} \tag{5.13}$$

On the other hand, it's easy to note that, for a single noncondensable species

$$U^*_m = \frac{D_{vm}}{\delta} \frac{(X_{nc,b} - X_{nc,i})}{X_{nc,ave}} \tag{5.14}$$

By comparing equation 5.13 and equation 5.14, the idea of Peterson is to define an effective binary diffusion coefficient for the condensing species to be used in multicomponent mixtures.

$$D_{vm} = \frac{X_{nc,ave}}{\sum_{j=1}^{n} (X_{j,ave}/\mathcal{D}_{jv})} \tag{5.15}$$

In the aim to evaluate the effective binary diffusion coefficient and the interface molar fraction, an iterative process is necessary. At the beginning of the iterative process, the same relative proportions are assumed at the interface and in the bulk. For the noncondensable j species, for instance, the first tentative value would be given by:

$$X_{j,i}^{'} = X_{j,b}\frac{X_{nc,i}^{'}}{X_{nc,b}} \tag{5.16}$$

the molar fractions are then updated as follows

$$X_{j,i}^{''} = exp\left[\ln X_{j,b} - \frac{D_{vm}^{'}}{\mathcal{D}_{jv}}\frac{X_{nc,b}}{X_{nc,i}^{'}}\right] \tag{5.17}$$

with

$$D_{vm}^{'} = \frac{X_{nc,ave}}{\sum_{j=1}^{n}(X_{j,ave}/\mathcal{D}_{jv})} \tag{5.18}$$

where the average molar fractions $X_{j,ave}$ $X_{nc,ave}$ have to be intended as the logarithmic mean between the interface and the bulk values and the diffusivity D_{jv} as the diffusivity at the logarithmic mean temperature. The molar fractions are then normalized by means of the following normalization relationship:

$$X_{j,i}^{'} = X_{j,i}^{''}\frac{X_{nc,i}^{'}}{\sum_{j=1}^{n} X_{j,i}} \tag{5.19}$$

The iterations are then repeated a few times until the the convergence is reached on the molar fractions values.

An important result presented in the Peterson theory is embedded in equation :

$$U_m^* = \frac{D_{jv}}{\delta}[\ln(X_{j,b}) - \ln(X_{j,i})] = \frac{D_{jv}}{\delta}\frac{(X_{j,b} - X_{j,i})}{X_{j,ave}} \tag{5.20}$$

Because U_m^* and δ are constant through the diffusion layer, equation 5.20 requires that high-mass-diffusivity species like helium, will have interface molar fraction quite similar to the bulk molar fraction, resulting in an almost flat molar fraction profile through the boundary layer. On the other hand, heavy species like air, will present higher molar fraction gradients.

This conclusion, reported in [81] seems to be in a deep disagreement with the possibility of having *buoyancy reversal* condition in mixtures of steam, air and helium at low velocities. In the aim clarify these aspects, the following remarks are proposed:

- Peterson's one-dimensional diffusion theory is based on the assumption that temperature gradients through the diffusion layer are small compared to the absolute temperature; in the test we proposed, anyway, the temperature experiences a jump of some tens of degrees in the few centimeters of the boundary layer, being the interface temperature not far from 40 $°C$. In this situation molar concentration and then molar average velocity cannot be considered constant.

- Peterson's model does not take into account the free stream velocity of the condensing mixture.

χ_b	$U_{inlet}[m/s]$	flow	χ_i CFD	χ_i Peterson [81]
0.3	0.8	laminar	0.226	0.137
0.3	0.8	turbulent	0.246	0.137
0.3	3.0	laminar	0.226	0.137
0.3	3.0	turbulent	0.258	0.137
0.3	6.0	laminar	0.226	0.137
0.3	6.0	turbulent	0.265	0.137
0.8	0.8	laminar	0.703	0.451
0.8	0.8	turbulent	0.725	0.451
0.8	3.0	laminar	0.704	0.451
0.8	3.0	turbulent	0.747	0.451
0.8	6.0	laminar	0.705	0.451
0.8	6.0	turbulent	0.757	0.451

Table 5.3: Comparison between CFD results and the Peterson model [81] in the prediction of the interface helium-to-noncondensable gas ratio

- When condensation occurs for a steam-helium mixture, the interface molar fractions are basically determined by interface temperature. Indeed, when the temperature difference is large enough, interface density can be remarkably lower than bulk density and, at low stream velocity, buoyancy forces can increase up to cause the near-the-wall velocity field to reverse. When little quantities of air are added to the mixture, the physical behavior of the system shouldn't change but mildly. Local inverse velocity field are then likely to occur even in ternary mixtures of steam, air and helium.

- Peterson's model does not take into account the turbulent diffusivities.

Moreover, scoping calculations in a simple geometry like the one adopted in the benchmark-0 exercise were performed to check the agreement between the Peterson's model [81] and CFD predictions. In the following Tab. 5.3, the results are reported for different cases having interface temperature of 303.15 K and bulk temperature of 363.15 K. Different velocities and different helium-to-noncondensable gas ratios in bulk were analyzed. In particular, the helium-to-noncondensable gas ratio at the interface were compared in a point near the outlet section. Calculations were mainly performed for turbulent flows, adopting the EBD model with the RNG $\kappa - \varepsilon$ turbulence model (see chapter 6) with an appropriate two layer model to deal with the near wall turbulence (see chapter 7). Idealized laminar flows were also checked.

As shown in Tab. 5.3, CFD calculations predict a smaller decrease of the helium concentration at the interface with respect to the Peterson model. The decrease is maximum for the idealized laminar conditions whereas for turbulent flows, the higher is the free stream velocity, the less is the difference between the helium-to-noncondensable gas ratio in bulk and at the interface. However, the impairment of the helium concentration in turbulent flows is expected to be not greater than a few per cents. Even if the interface helium-to-noncondensable gas ratio decreases from the bulk to the interface, owing to the high mobility of helium, the interface density can therefore be lower then the bulk. Indeed,

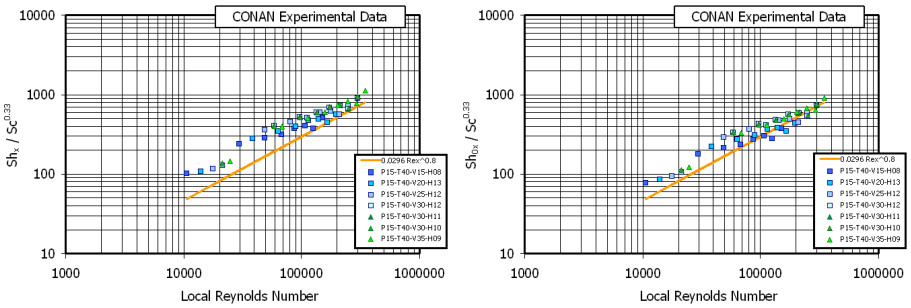

Figure 5.6: Experimental Sherwood Sh_x (left) and corrected Sherwood numbers $Sh_{x,0}$ (right) as a function of the Reynolds number for the P15-T40 series (experimental data of Lioce [108])

also in the case of laminar condensation, *buoyancy-opposed* conditions can be predicted basing on the self-similarity solution of the boundary layer equations, as proposed by Karkoszka [114].

5.2 Condensation tests at high stream velocity

In Table 5.4, the boundary conditions of the different considered tests are summarized for the first experimental campaign of steam-air-helium condensation tests at high free stream velocities.

The effects of helium were investigated in CONAN at different steam generator powers and different velocities. Different helium-to-noncondensable gas ratios were adopted, ranging from traces of helium up to almost pure steam-helium mixtures. An analysis of these data have been proposed by Lioce [108]. Here, experimental data are treated according to the postprocessing method illustrated in chapter 4. In Fig. 5.6, 5.7 and 5.8, a comparison between the local experimental values of the Sherwood number and the already mentioned forced convection correlation of Schlichting [115] is proposed. As observed by Lioce [108], the asymptotic values of the experimental data, corresponding to the highest values of the local Reynolds numbers, are pretty well aligned with the forced convection correlation. The trend of the series P15-T40 is anyway a little different from the trends of the P20-T50 and the P25-T50 series, presenting a wider spread of the experimental data points and a different asymptotic slope. Lioce observed also that, for fully developed flow, the local heat and mass transfer coefficient are not remarkably sensible to the helium concentration. It was also observed that helium affects the near-the-entrance transport phenomena by enhancing the local transfer. The overall condensation rate was also observed to depend on the helium-to-noncondensable gas ratio; for a given velocity, the higher is the helium amount, the higher is the condensation rate. Lioce justified this effect as the result of the increase in the mobility of the steam with helium [108].

In Fig. 5.9, the experimental local Sherwood numbers are reported normalized to the Schlichting correlation for all tests, as function of the local Richardson number. The same analysis is proposed normalizing the experimental Sherwood number by the McAdams correlation for natural convection regimes, in Fig. 5.10.

Test	$\dot{M}_{sec}[kg/s]$	$T_{in,sec}[^{\circ}C]$	$T_{out,sec}[^{\circ}C]$	$U_{inlet}[m/s]$	$T_{avg,ch}[^{\circ}C]$	$T_{wb}[^{\circ}C]$	$T_{db}[^{\circ}C]$	$\dot{M}_{cond}[g/s]$	$Y_{a,in}[-]$	$Y_{he,in}[-]$
P15-T40-V15-H08	1.4540	39.9	41.3	1.50	86.2	86.2	86.5	3.28	0.493	0.006
P15-T40-V20-H13	1.4885	40.5	41.8	2.05	83.4	83.4	83.7	3.33	0.539	0.011
P15-T40-V25-H12	1.4782	39.4	41.1	2.56	82.2	82.3	82.7	3.73	0.567	0.010
P15-T40-V30-H10	1.4542	40.1	41.8	3.08	81.4	81.2	82.1	3.99	0.592	0.009
P15-T40-V30-H11	1.4566	39.4	41.1	3.08	81.4	81.3	82.1	4.08	0.589	0.010
P15-T40-V30-H12	1.4533	39.8	41.5	3.08	81.4	81.4	82.0	4.08	0.585	0.010
P15-T40-V35-H09	1.4534	39.8	41.6	3.57	84.0	81.0	84.7	4.11	0.603	0.008
P20-T50-V15-H08	0.9033	49.8	53.4	1.68	92.1	92.2	92.6	4.65	0.323	0.004
P20-T50-V20-H09	0.9341	49.9	53.1	2.09	91.3	91.3	91.9	4.80	0.350	0.005
P20-T50-V25-H10	0.8878	50.1	53.6	2.58	90.2	90.2	91.0	5.12	0.380	0.006
P20-T50-V30-H08	0.9536	50.2	53.6	3.11	92.0	89.7	92.1	5.26	0.402	0.005
P20-T50-V35-H11	0.9873	50.1	53.5	3.59	92.2	88.4	92.3	5.40	0.431	0.007
P20-T50-V20-H67	1.1075	50.2	52.9	2.02	89.9	89.9	90.5	4.87	0.182	0.051
P20-T50-V25-H66	1.0591	50.0	52.9	2.56	89.3	89.1	89.9	5.01	0.200	0.054
P20-T50-V30-H65	1.0832	49.7	52.7	3.06	89.1	88.2	89.5	5.21	0.223	0.056
P20-T50-V35-H64	1.1264	51.0	53.8	3.57	89.6	87.4	89.7	5.38	0.241	0.059
P25-T50-V20-H71	0.9666	50.3	54.7	2.02	94.3	94.1	95.0	6.77	0.094	0.033
P25-T50-V25-H70	0.9401	50.1	54.8	2.58	94.1	93.3	94.4	7.05	0.115	0.035
P25-T50-V30-H71	0.9732	50.3	54.8	3.12	95.5	92.4	96.0	7.10	0.128	0.041
P25-T50-V35-H74	0.9762	50.4	55.0	3.63	96.5	91.5	97.0	7.35	0.136	0.047
P25-T50-V15-H02	0.9633	50.1	54.7	1.71	97.2	96.9	98.0	6.67	0.158	0.000
P25-T50-V20-H02	0.9370	50.2	55.0	2.13	96.8	96.4	97.5	6.73	0.178	0.001
P25-T50-V25-H03	0.9839	50.1	54.7	2.61	96.5	95.4	96.9	6.96	0.220	0.001
P25-T50-V30-H03	1.0196	50.0	54.4	3.14	97.9	94.3	98.3	7.17	0.261	0.001
P25-T50-V35-H05	1.0422	50.3	54.6	3.63	98.5	93.6	98.9	7.33	0.285	0.002

Table 5.4: Boundary conditions of the CONAN steam-air-helium tests at high free stream velocities

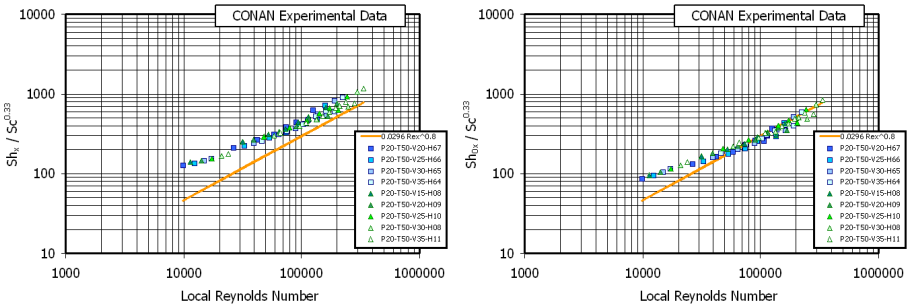

Figure 5.7: Experimental Sherwood Sh_x (left) and corrected Sherwood numbers $Sh_{x,0}$ (right) as a function of the Reynolds number for the P20-T50 series (experimental data of Lioce [108])

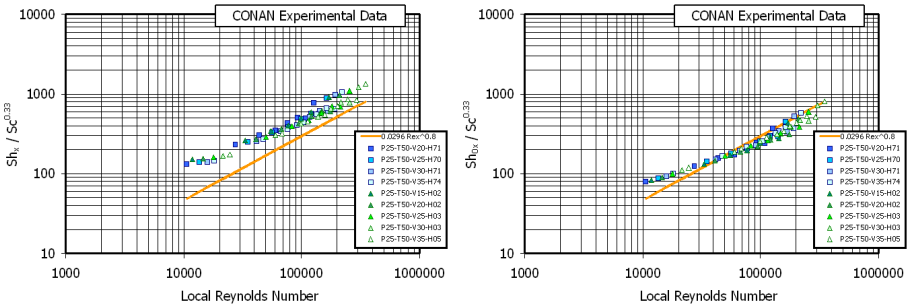

Figure 5.8: Experimental Sherwood Sh_x (left) and corrected Sherwood numbers $Sh_{x,0}$ (right) as a function of the Reynolds number for the P25-T50 series (experimental data of Lioce [108])

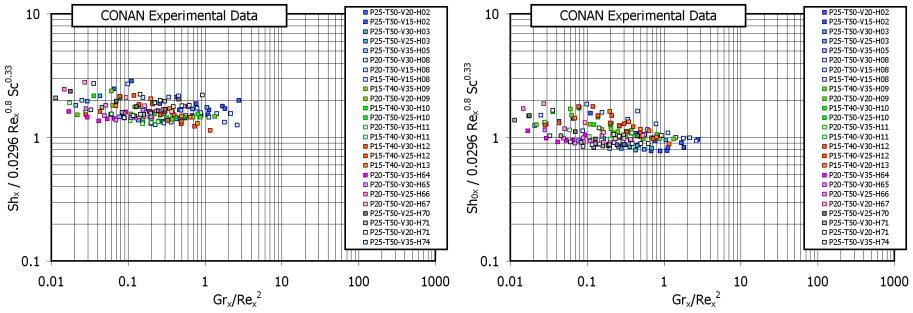

Figure 5.9: Normalized Sherwood number Sh_x (left) and corrected Sherwood number $Sh_{x,0}$ (right) vs. Richardson number (forced convection analysis)

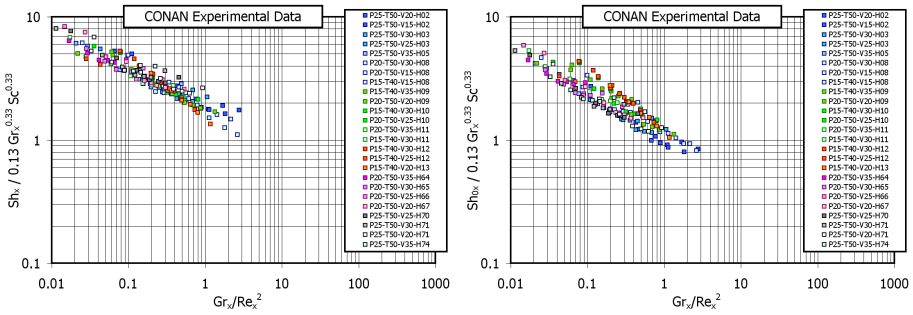

Figure 5.10: Normalized Sherwood number Sh_x (left) and corrected Sherwood number $Sh_{x,0}$ (right) vs. Richardson number (natural convection analysis)

A more in-depth analysis of the experimental Sherwood values is also reported, as proposed in the previous chapter 4. Data can be filtered in order to avoid data points affected by entrance effects, according to the following criteria.

$$\begin{aligned} Ri_x > 1 \;\&\quad Gr_x > 1.E+10 \;&\Rightarrow\quad accepted \\ Ri_x > 1 \;\&\quad Gr_x < 1.E+10 \;&\Rightarrow\quad discarded \\ Ri_x < 1 \;\&\quad Re_x > 1.E+5 \;&\Rightarrow\quad accepted \\ Ri_x < 1 \;\&\quad Re_x < 1.E+5 \;&\Rightarrow\quad discarded \end{aligned}$$

In Fig. 5.11, for all the experimental datapoints, the local Reynolds number is reported as a function of the local Richardson number. On the basis of the aforementioned criteria, four different zones of interest can be identified in the figure. A first zone (1), representative of dominating forced convection, includes datapoints having Richardson number less than one, Reynolds number greater than 10^5 and Grashof number less than 10^{10}. A second zone (2) is representative of points having forced convection character, but influenced by buoyancy forces; these are points having Richardson number less than one, Reynolds number greater than 10^5 and Grashof number greater than 10^{10}. An opposite behavior is associated to datapoint having Richardson number greater than one, Reynolds number greater than 10^5 and Grashof number greater than 10^{10}, for which buoyancy forces are expected to dominate, though influenced by inertia forces. Mixed convection conditions are therefore likely for the second (2)

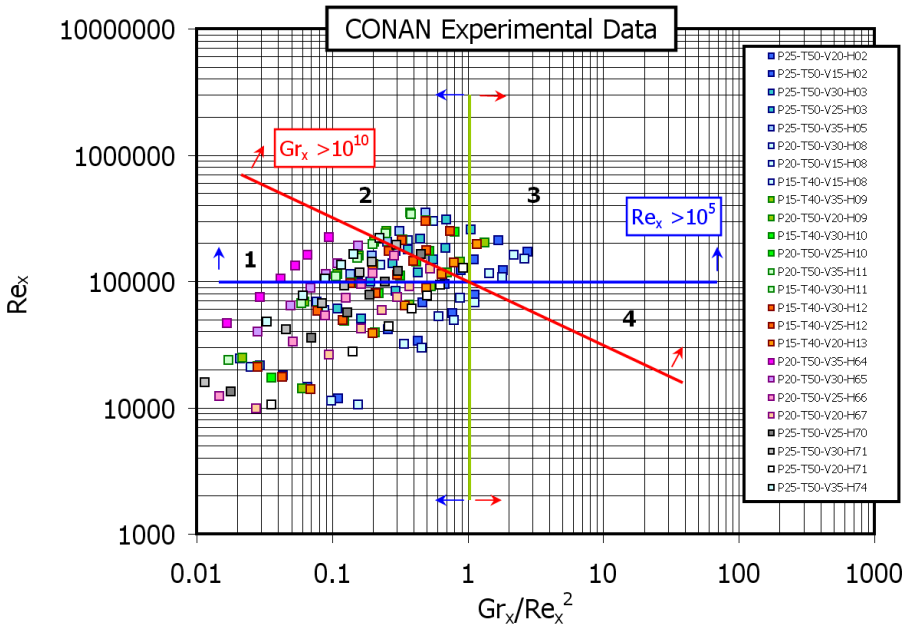

Figure 5.11: Regions of CONAN experimental data at high free stream velocity

and the third zones (3). A fourth zone (4) would include points having a dominant natural convection character; this would include points having Richardson number greater than one, Reynolds number less than 10^5 and Grashof number greater than 10^{10}. No data points are actually available in this zone, as shown in Fig. 5.11. Data having local Reynolds number less than 10^5 and Grashof number less than 10^{10} are considered affected by entrance effects and are discarded. Figures 5.9 and 5.10 are reproposed in Fig. 5.12 and 5.13 for the filtered data.

A further analysis is proposed for data points corresponding to the P20-T50 and the P25-T50 series, having the highest heat transfer rates (see Figs. 5.14 and 5.15). As expected, data corresponding to developed froced flow agree reasonably with the forced convection correlation. In tests having the highest heat transfer rates in particular, the Stefan correction factor accounts very well for the suction effects for the tests with higher helium-to-noncondensable gas ratio, between 60 and 70 percent. Indeed, as remarked in paragraph 5.1, for helium-to-noncondensable gas ratios ranging between 60 and 70 percent, in the proposed CONAN tests, the interface to bulk density difference is quite small. This makes the assumptions at the basis of the Stefan factor to be better satisfied, since constant density is assumed in the boundary layer. The trend of the data points corresponding to the cases having the lowest heat transfer rate is instead less clear.

The following remarks are therefore supported only by the data of the P20-T50 and the P25-T50 series. For these series, a more in depth analysis is proposed discriminating for the different velocities. In Fig. 5.16, adetailed view is proposed of Fig. 5.14 and two different trends for the Sherwood numbers Sh_x are

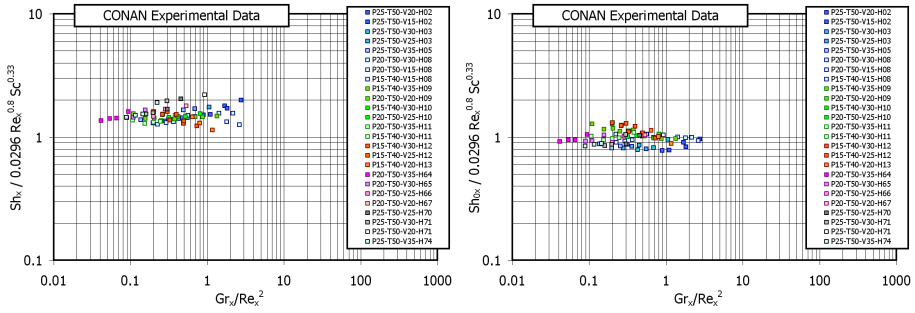

Figure 5.12: Selected values of normalized Sherwood number Sh_x (left) and corrected Sherwood number $Sh_{x,0}$ (right) vs. Richardson number (forced convection analysis)

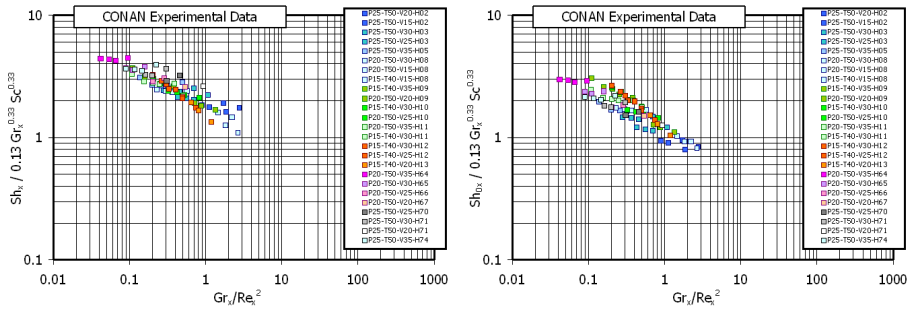

Figure 5.13: Selected values of normalized Sherwood number Sh_x (left) and corrected Sherwood number $Sh_{x,0}$ (right) vs. Richardson number (natural convection analysis)

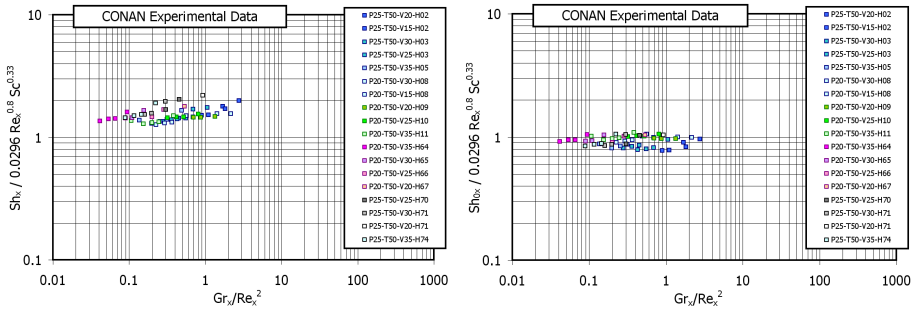

Figure 5.14: P20-T50 and P25-T50 series: selected normalized Sherwood number Sh_x (left) and corrected Sherwood number $Sh_{x,0}$ (right) vs. Richardson number (forced convection analysis)

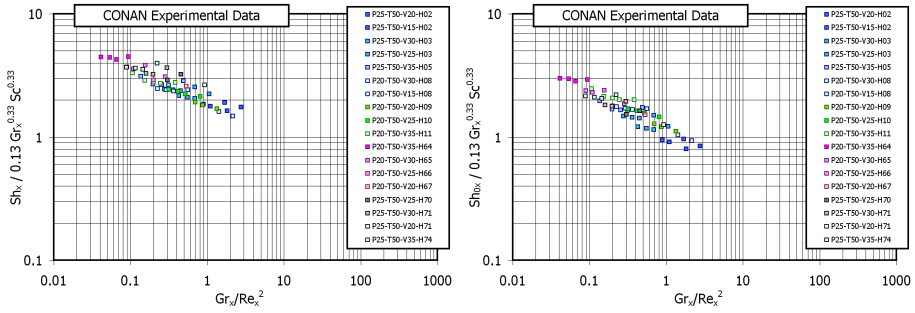

Figure 5.15: P20-T50 and P25-T50 series: selected normalized Sherwood number Sh_x (left) and corrected Sherwood number $Sh_{x,0}$ (right) vs. Richardson number (natural convection analysis)

remarked depending on the helium-to-noncondensable gas ratio. The minimum Richardson number corresponds to datapoints having helium-to-noncondensable gas ratios from 60 to 70 percent. Departing from this condition, likely to be near to the *buoyancy reversal* condition, two different trends are possible: an higher curve corresponds to helium-to-noncondensable gas ratios larger than the critical values; other points lie below the latter, having helium-to-noncondensable gas ratios lower than the critical value. Indeed, the evidence of that can be better detected by analyzing each velocity independently (see Fig. 5.17). In all tests having a free stream velocity of 1.5, 2.0, 3.0 or 3.5 m/s, the effects of helium can be observed, having the same relevance. Indeed, the modification of the Sherwood numbers Sh_x related to the presence of helium are likely to be due to a modification of suction effect. Moreover, these effects are probably related to the *buoyancy reversal* condition. However, buoyancy is less likely to affect these tests. In fact, a further analysis of the local experimental Sherwood numbers $Sh_{x,0}$ shows a pretty well agreement of $Sh_{x,0}$ numbers with the forced convection correlation (see 5.18); the dependence observed for the Sherwood numbers Sh_x is not experienced. Even at the lowest free stream velocities buoyancy effect are reduced with respect to steam-air tests; helium is in fact effective in reducing the density difference between the interface and the bulk, with respect to a pure binary steam-air mixture.

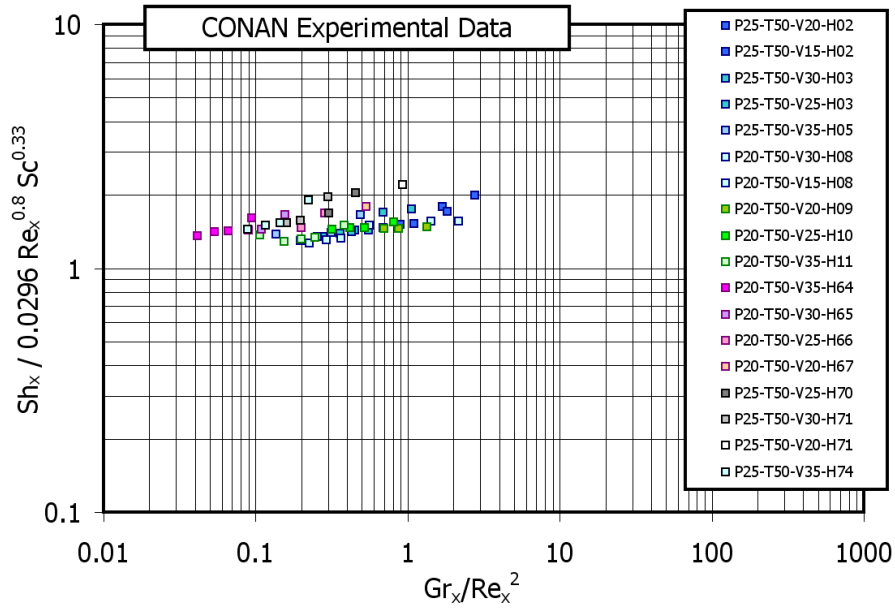

Figure 5.16: P20-T50 and P25-T50 series: selected normalized Sherwood number Sh_x vs. Richardson number (forced convection analysis)

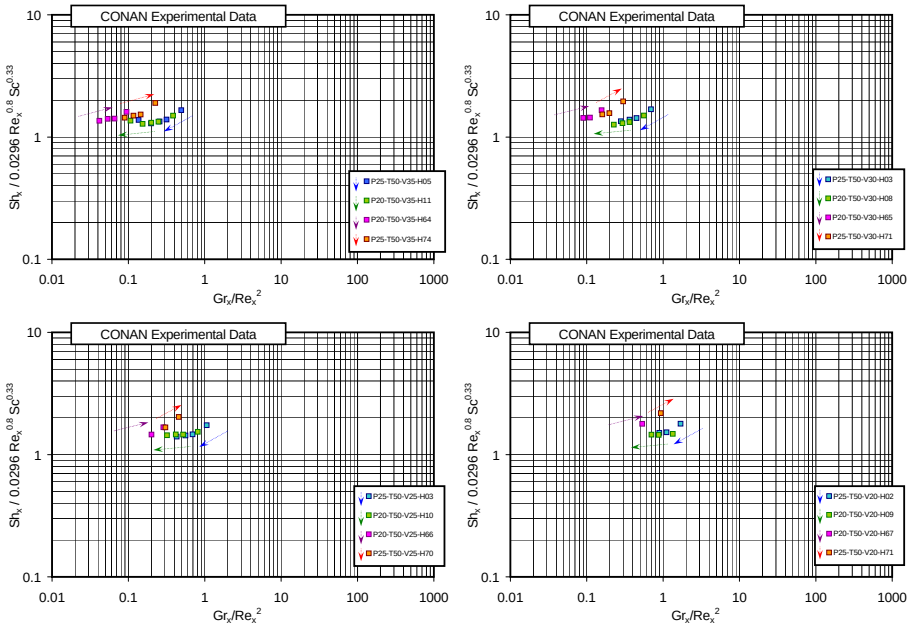

Figure 5.17: P20-T50 and P25-T50 series: selected normalized Sherwood number Sh_x vs. Richardson number (forced convection analysis) for the test cases with free stream velocity of 3.5 m/s (top left), 3.0 m/s (top right), 2.5 m/s (bottom left) and 2.0 m/s (bottom right)

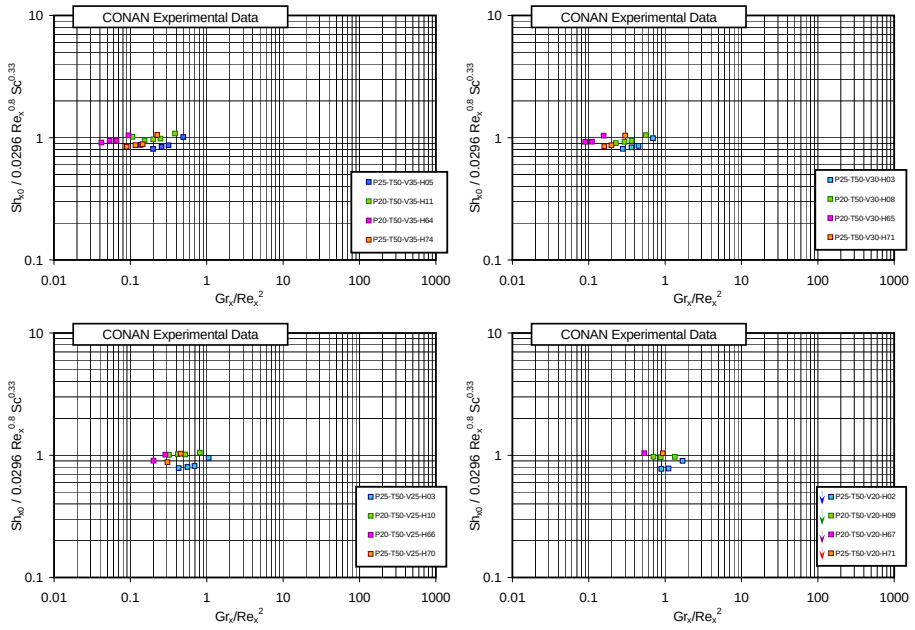

Figure 5.18: P20-T50 and P25-T50 series: selected normalized Sherwood number $Sh_{x,0}$ vs. Richardson number (forced convection analysis) for the test cases with free stream velocity of 3.5 m/s (top left), 3.0 m/s (top right), 2.5 m/s (bottom left) and 2.0 m/s (bottom right)

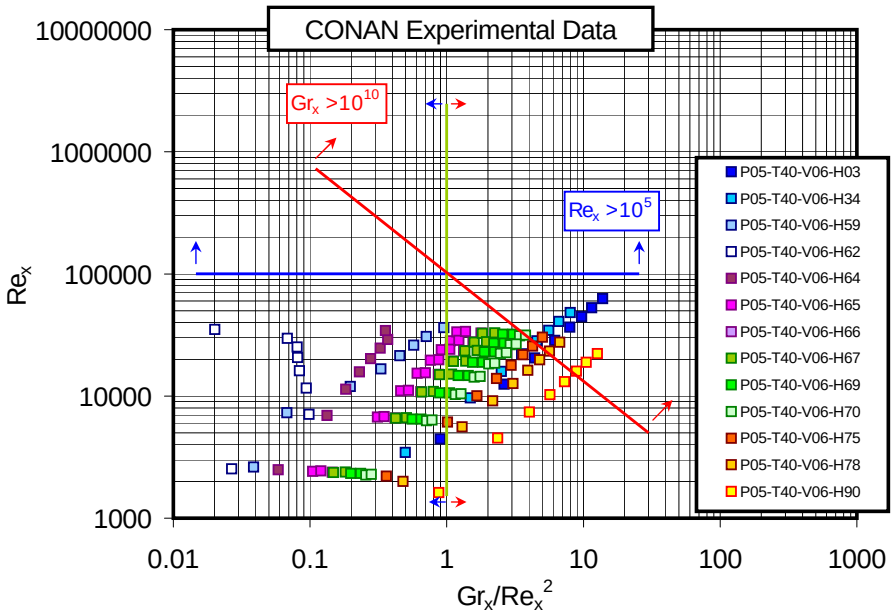

Figure 5.19: Regions of CONAN experimental data at low free stream velocity

5.3 Condensation tests at low stream velocity

In the aim to achieve a more in-depth understanding on the buoyancy effects promoted by helium, tests at lower free stream velocity have been designed and performed in the frame of this doctoral research (see also [116]). Two different test series were carried out having an operating free stream velocity estimated around 0.6 m/s. Boundary conditions of the tests are summarized in Tab. 5.5.

Different helium-to-noncondensable gas ratios were investigated, most of all ranging around the critical value for which buoyancy forces are supposed to vanish. The buoyancy reversal condition is achieved for helium-to-noncondensable gas ratio in the range between 60 and 70 percent.

In figure 5.19, the experimental data points are reported, identified by the corresponding local Reynolds and Richardson numbers. As can be seen, developed flow conditions are generally not reached, with exception of some datapoints corresponding to natural convection conditions. Indeed, as shown in Figs. 5.20 and 5.21, where a comparison with the natural convection correlation of McAdams is proposed, tests characterized by traces of helium (P05-T40-V06-H03) or almost all helium (P05-T40-V06-H90) attain an asymptotic behavior. For these tests, the Sherwood number has in fact a very similar slope to the McAdams correlation. Other tests are mostly characterized by developing flows, as also shown in Figs. 5.22 and 5.23, where the experimental Sherwood numbers are compared to the Schlichting correlation.

The effect of helium can be twofold. Departing from a critical helium-to-noncondensable gas ratio for which the buoyancy forces are annealed, two different phenomenologies can be experienced: *buoyancy-aided* convection occurs

Test	$\dot{M}_{sec}[kg/s]$	$T_{in,sec}[°C]$	$T_{out,sec}[°C]$	$T_{avg,ch}[°C]$	$T_{db}[°C]$	$T_{wb}[°C]$	$\dot{M}_{cond}[g/s]$	$Y_{a,in}[-]$	$Y_{he,in}[-]$
P05-T40-V06-H03	0.7933	39.8	40.7	79.2	79.4	79.6	1.11	0.648	0.002
P05-T40-V06-H34	0.7698	39.9	40.8	77.3	77.5	77.7	1.01	0.571	0.039
P05-T40-V06-H62	0.7232	39.9	40.9	76.6	76.8	77.1	0.95	0.429	0.093
P05-T40-V06-H64	0.7394	39.8	40.7	76.4	76.4	76.8	0.96	0.418	0.099
P05-T40-V06-H65	0.7143	40.0	41.0	76.0	76.3	76.4	1.07	0.405	0.105
P05-T40-V06-H66	0.7093	40.0	41.0	76.2	76.4	76.7	1.04	0.393	0.109
P05-T40-V06-H67	0.7307	39.8	40.8	75.8	76.1	76.3	1.04	0.394	0.110
P05-T40-V06-H69	0.7650	40.0	40.8	76.3	76.5	76.8	1.10	0.377	0.113
P05-T40-V06-H70	0.6929	39.8	40.8	76.2	76.3	76.6	1.10	0.363	0.120
P05-T40-V06-H33	0.7237	40.0	41.1	77.3	77.7	77.7	1.13	0.568	0.039
P05-T40-V06-H39	0.7295	39.8	40.9	77.0	77.3	77.4	1.09	0.543	0.049
P05-T40-V06-H47	0.7142	39.9	41.1	77.0	77.4	77.4	1.07	0.506	0.062
P05-T40-V06-H52	0.7122	40.2	41.3	77.1	77.5	77.5	1.09	0.475	0.071
P05-T40-V06-H55	0.6673	40.0	41.2	77.1	77.4	77.4	1.06	0.461	0.077
P05-T40-V06-H57	0.7221	39.9	41.1	77.1	77.4	77.5	1.09	0.443	0.082
P05-T40-V06-H59	0.6802	39.9	41.1	77.1	77.4	77.4	1.06	0.431	0.087
P05-T40-V06-H62	0.6631	39.8	41.0	76.9	77.2	77.3	1.06	0.416	0.093
P05-T40-V06-H67	0.6664	39.8	41.1	77.3	77.6	77.7	1.02	0.372	0.105
P05-T40-V06-H69	0.7114	39.9	41.1	77.2	77.5	77.5	1.15	0.360	0.111
P05-T40-V06-H70	0.7378	40.0	41.2	77.3	77.7	77.7	1.13	0.346	0.113
P05-T40-V06-H75	0.6647	40.1	41.4	77.1	77.4	77.5	1.32	0.327	0.122
P05-T40-V06-H78	0.7224	40.3	41.5	73.9	74.9	75.0	1.27	0.309	0.152
P05-T40-V06-H90	0.6901	40.5	41.7	71.1	72.9	72.9	1.27	0.190	0.219

Table 5.5: Boundary conditions of the CONAN steam-air-helium tests at low free stream velocities

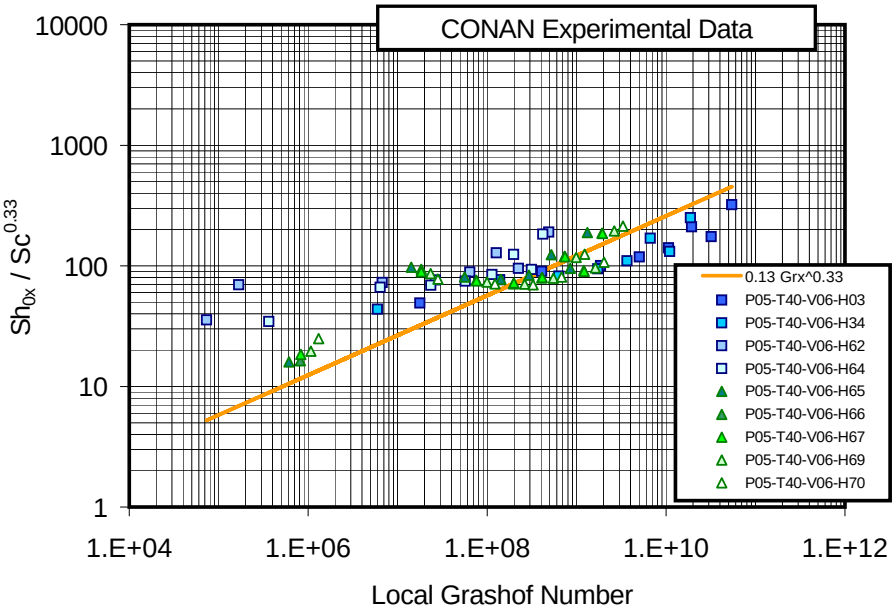

Figure 5.20: Experimental corrected Sherwood numbers $Sh_{x,0}$ (right) for the first low free stream velocity test series, compared to the McAdams correlation

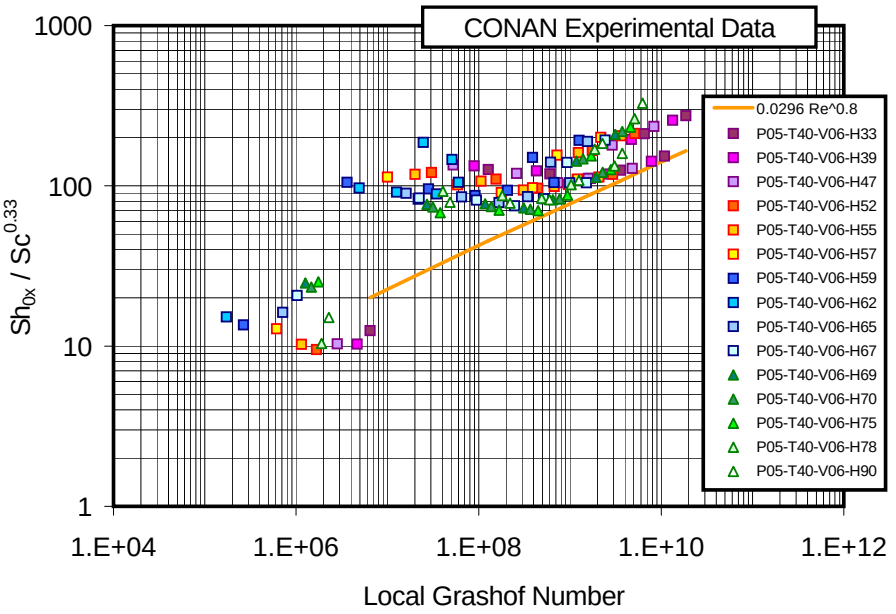

Figure 5.21: Experimental corrected Sherwood numbers $Sh_{x,0}$ (right) for the second low free stream velocity test series, compared to the McAdams correlation

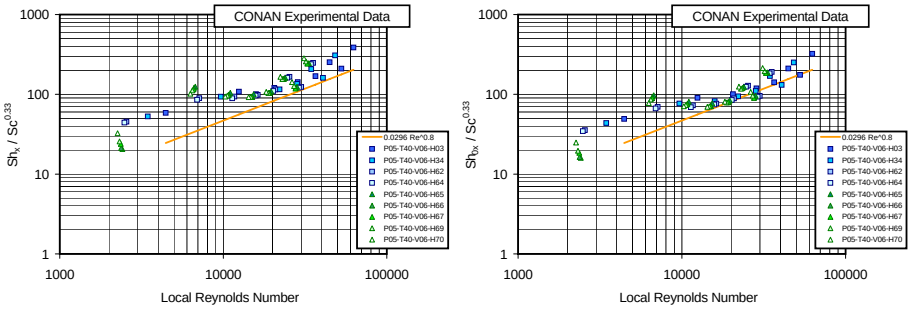

Figure 5.22: Experimental Sherwood Sh_x (left) and corrected Sherwood numbers $Sh_{x,0}$ (right) for the first low free stream velocity test series, compared to the Schlichting correlation

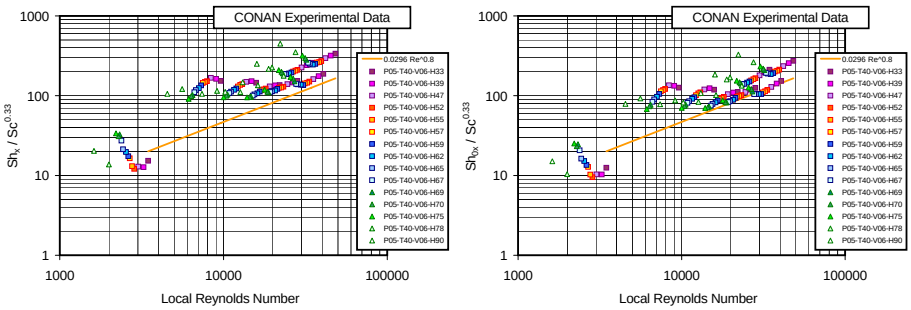

Figure 5.23: Experimental Sherwood Sh_x (left) and corrected Sherwood numbers $Sh_{x,0}$ (right) for the second low free stream velocity test series, compared to the Schlichting correlation

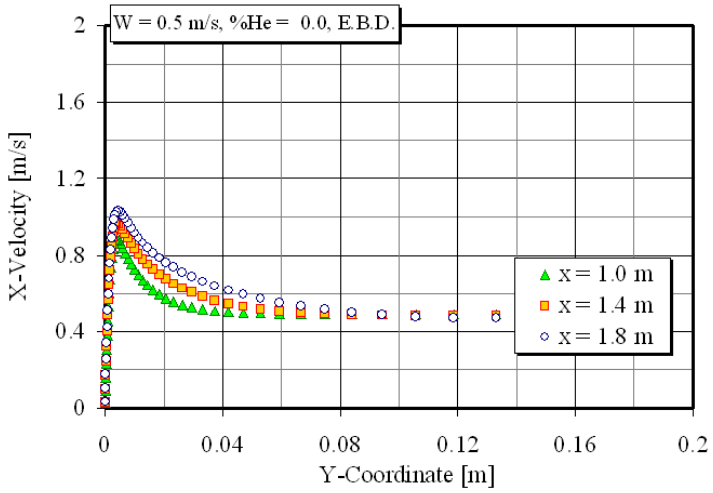

Figure 5.24: Sketch of the velocity profiles in well developed natural convection regime (Fig. from Bucci et al. [18])

when the amount of helium is reduced and therefore the buoyancy force acts in the same direction of inertia forces; on the other hand, when the interface mixture is lighter than the bulk mixture, *buoyancy-opposed* convection is experienced.

The differences between the high velocity tests and the low velocity tests consists in the influence that these buoyancy forces have on the flow field and on the transport processes. Indeed, in the cases of higher free stream velocities, buoyancy forces are not enough important to affect the velocity boundary layer macroscopically. Their effect is more likely to change the turbulence and the transport characteristics in the near-wall region [18].

A reduction of the free stream velocity makes the Richardson number to increase, that is the buoyancy forces are more and more important with respect to inertia forces. If the free stream velocity is small enough, the velocity boundary layer can be strongly affected by buoyancy. In the case of *buoyancy-aided* convection, a sketch of the velocity profile corresponding to a well developed natural convection regime is represented in Fig. 5.24. The figure illustrates the result of a scoping calculation performed with the HMTDM^{EBD} model (see chapter 6) on the computational domain already adopted for the SARnet benchmark-0 calculations, having homogeneous interface temperature of 30 $°C$, inlet temperature of 90 $°C$ and an helium-to-noncondensable gas ratio equal to zero. A velocity peak clearly appears close to the wall, that becomes more important when the distance from the inlet section increases, that is for higher local Richardson numbers. When the helium-to-noncondensable gas ratio is higher than the critical values for which *buoyancy-reversal* occurs, since the local Richardson number is proportional to the distance from the channel inlet section, counter-current buoyancy forces become more and more important, making the velocity profile to be inverted. This critical condition is known as *flow reversal*. According to scoping calculations, helium-to-noncondensable gas ratio around 80 percent

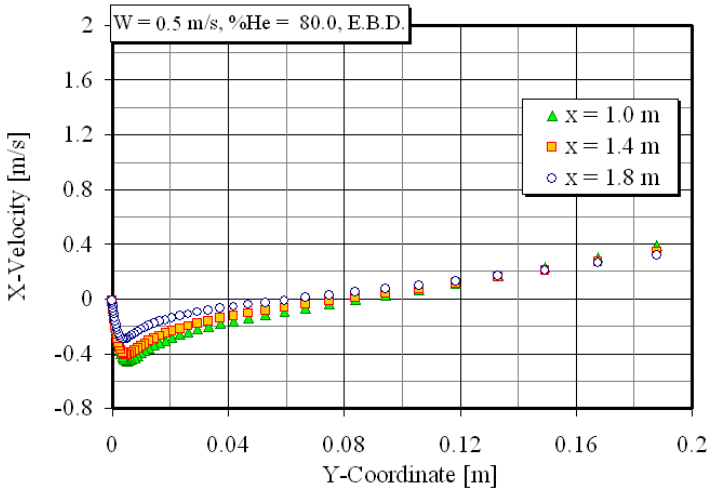

Figure 5.25: Velocity profiles in *flow reversal* conditions (Fig. from Bucci et al. [18])

are enough to make the *flow reversal* condition to be experienced within the CONAN test section in tests having a free stream velocity of about 0.6 m/s, as illustrated in Fig. 5.25. The velocity flow field is macroscopically affected by buoyancy and so are the turbulent transport processes. According to the results of the scoping calculations performed by the RNG $\kappa - \varepsilon$ turbulence model with an appropriate two layer model to deal with the near-wall turbulence (see chapter 7), the turbulence kinetic energy is in fact remarkably modified by the helium-to-noncondensable gas ratio (see Fig. 5.26). Indeed, given the turbulence kinetic energy profile corresponding to the case of steam-air mixture at low velocity, the addition of helium causes the velocity peak to reduce and therefore the turbulence kinetic energy production term to reduce. The minimum of the turbulence kinetic energy peak is reached when the buoyancy reversal condition is reached. Further helium addition makes the buoyancy to be opposed. When the flow reversal conditions are reached, the local velocity inversion makes the shear stress to be much more important than in the *buoyancy-aided* cases and so is the turbulence kinetic energy production. The resulting turbulence kinetic energy is remarkably larger than before, resulting in a strong increase of the transport properties. An analysis in terms of nondimensional turbulence kinetic energy could be also interesting to analyze the displacement of the turbulence kinetic energy peak as a function of the nondimensional distance from the wall, for different helium concentration. Clearly experimental data would be very usefull concerning these effects.

Since, as already remarked, the effect of buoyancy forces is dependent on the distance from the inlet section, an analysis of experimental data is here proposed based on the datapoints near the outlet test section. As shown in Fig. 5.27 (right), *buoyancy reversal* conditions are suspected to occur in tests having a helium to noncondensable ratio around 62 percent. The agreement with the values predicted by Eq. (5.7) and reported in Tab. 5.2 is remarkable.

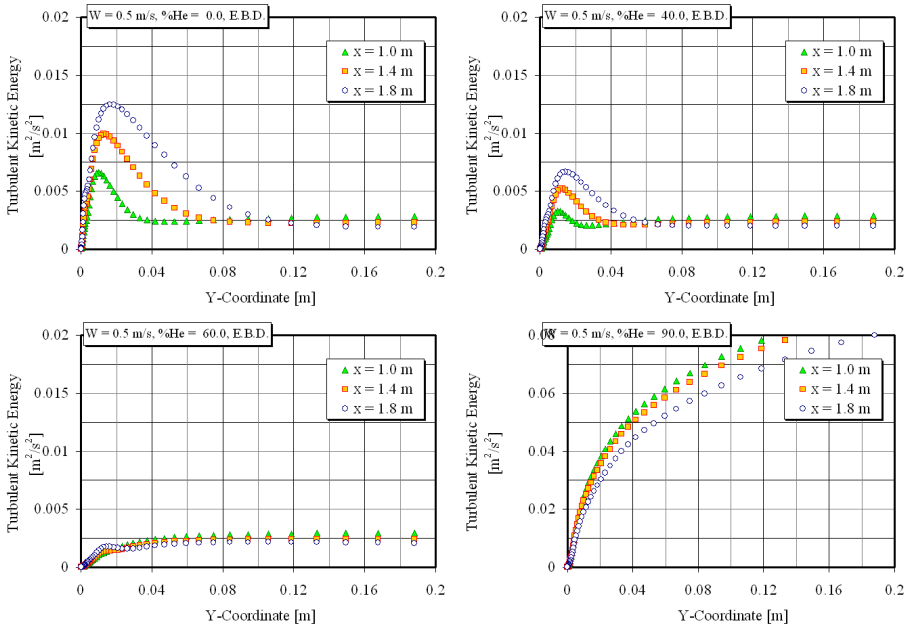

Figure 5.26: Turbulence kinetic energy profiles at different helium-to-noncondensable gas ratio (Fig. from Bucci et al. [18])

Buoyancy-aided and *buoyancy-opposed* regimes are typical respectively of cases having a lower and an higher helium-to-noncondensable gas ratio. In the same Fig. 5.27 (left), the Reynolds number at the outlet is also shown as a function of the helium-to-noncondensable gas ratio, being the viscosity of the mixture increased when helium is added.

In Fig. 5.28, the Sherwood number is reported normalized to the Schlichting correlation as a function of the helium-to-noncondensable gas ratio. As it can be seen, in the *buoyancy-opposed* cases, following *flow reversal*, a sharp increase of the Sherwood number is experienced. The same data can be reported as a function of the local Richardson number, as shown in Fig. 5.29, where colored arrows are reported to highlight the dependence of the datapoints on the helium-to-noncondensable gas ratio. According to Fig. 5.29, the P05-T40-V06-H62 test is observed to have the characteristics of forced convection, even in presence of a relatively low stream velocity, owing to the little buoyancy effects. In fact, this is clearly the test corresponding to the *buoyancy reversal* condition $\chi = \chi_{br}$, for which the buoyancy forces are annealed. The velocity profile is therefore expected to be not far from the one of turbulent forced convection and the Sherwood number to be comparable to the one predicted by Schlichting. However, fully developed flow conditions are not necessarily reached for this test (see Fig. 5.27 left) and therefore the Sherwood number at the end of the channel, represented in Figs. 5.28 and 5.29, is probably affected by entrance effects and is therefore higher then the one it would be experienced for fully developed flow. In Fig. 5.29 the presence of two different branches in the data trend is highlighted for the *buoyancy-aided* and the *buoyancy-opposed* condition. A clearer prospective is obtained by normalizing the Sherwood number to the

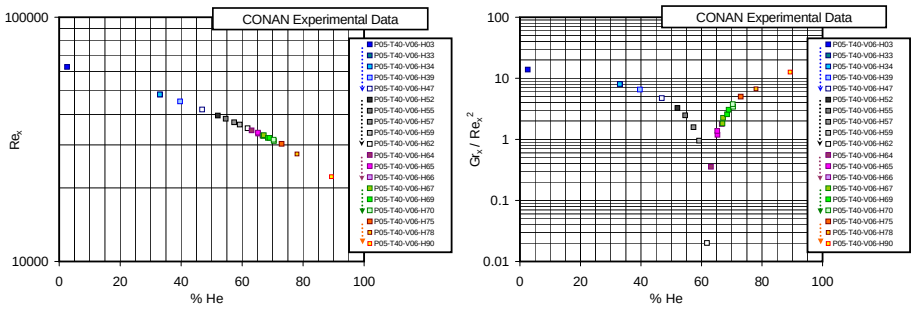

Figure 5.27: Reynolds (left) and Richardson (right) numbers vs. helium-to-noncondensable gas ratio in the low free stream velocity tests (data corresponding to the measurement near the outlet section)

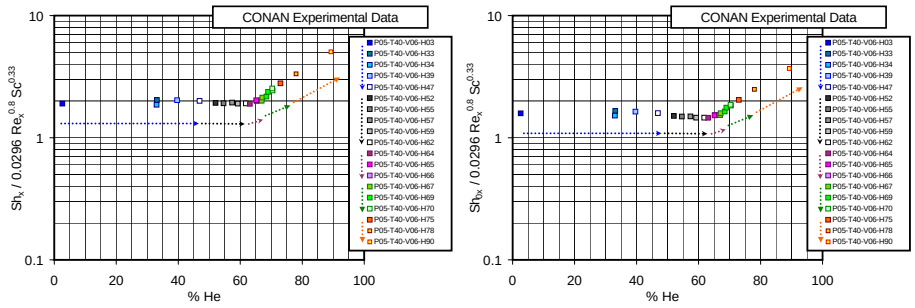

Figure 5.28: Sherwood number Sh_x (left) and corrected Sherwood number $Sh_{x,0}$ (right) normalized on the Schlichting correlation vs. helium-to-noncondensable gas ratio in the low free stream velocity tests (data corresponding to the measurement near the outlet section)

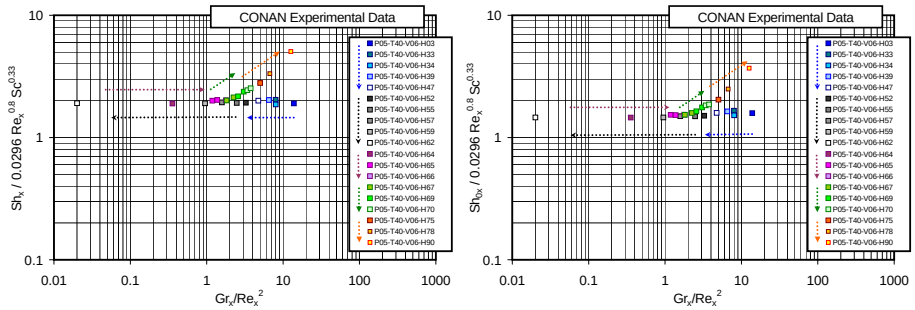

Figure 5.29: Sherwood number Sh_x (left) and corrected Sherwood number $Sh_{x,0}$ (right) normalized on the Schlichting correlation vs. local Richardson number in the low free stream velocity tests (data corresponding to the measurement near the outlet section)

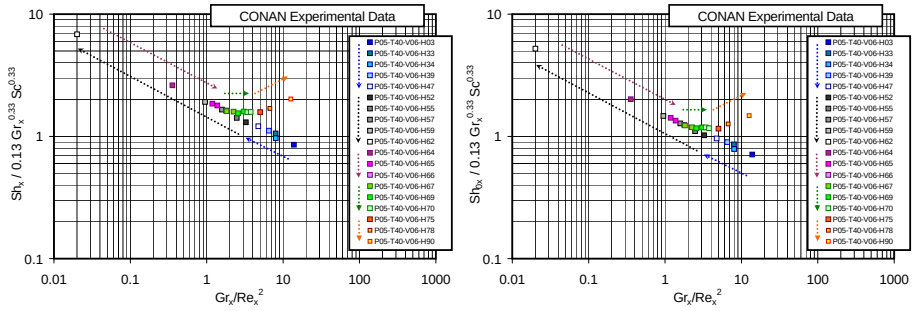

Figure 5.30: Sherwood number Sh_x (left) and corrected Sherwood number $Sh_{x,0}$ (right) normalized to the McAdams correlation vs. local Richardson number in the low free stream velocity tests (data corresponding to the measurement near the outlet section)

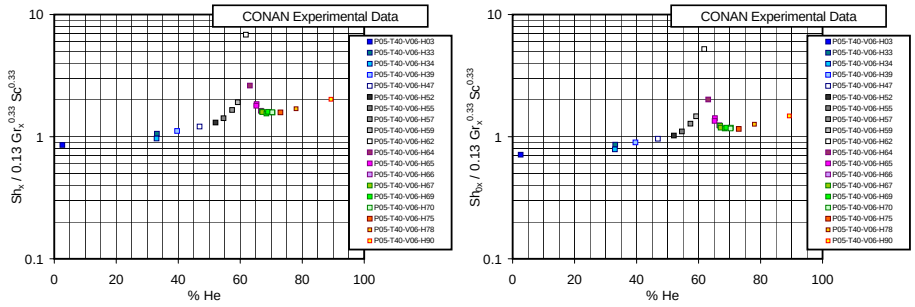

Figure 5.31: Sherwood number Sh_x (left) and corrected Sherwood number $Sh_{x,0}$ (right) normalized to the McAdams correlation vs. helium-to-noncondensable gas ratio in the low free stream velocity tests (data corresponding to the measurement near the outlet section)

McAdams correlation, reported in Fig. 5.30 as a function of the local Richardson number or in Fig. 5.31 as a function of the helium-to-noncondensable gas ratio. As it can be seen, the Sherwood number corresponding to the *buoyancy-opposed* cases are higher than the *buoyancy-aided* cases, confirming the results reported in paragraph 5.1. Unfortunately, local Richardson numbers are not large enough to reach fully developed natural convection conditions for which the *buoyancy-aided* points and the *buoyancy-opposed* points would reach the same asymptotic behavior.

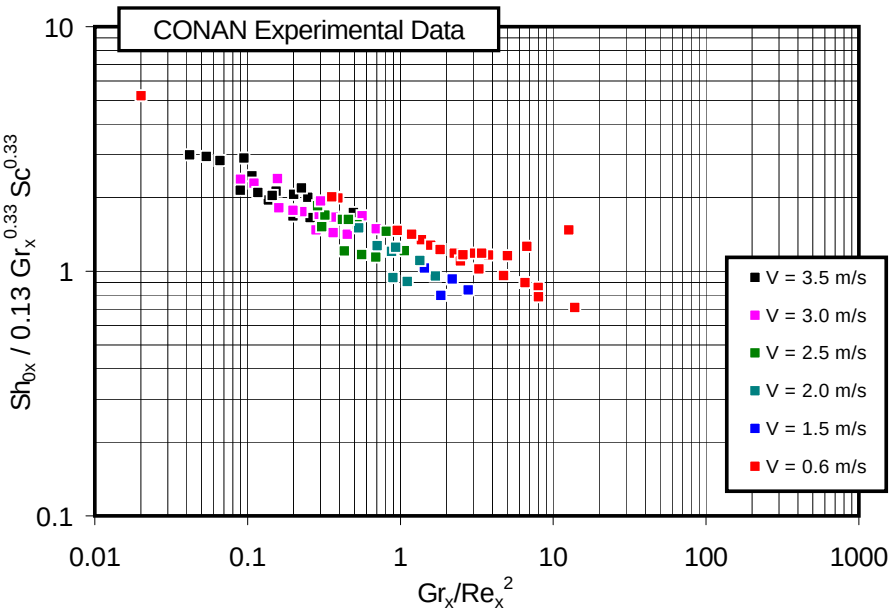

Figure 5.32: CONAN experimental Sherwood number Sh_{0x} normalized to the McAdams correlation, identified by the free stream velocity

In Fig. 5.32, all the CONAN available data points are reported normalized to the McAdams correlation, identified on the basis of the free stream velocity. In Fig. 5.33, the same analysis is proposed, where experimental data points are normalized to the Schlichting correlation for forced convection. As it can be seen, a clear trend is observed for the data points corresponding to Richardson numbers less than unity. Two branches are instead present for the greater values of the Richardson number, the bifurcation occurring around unity. The low stream velocity data are slightly above the free stream velocity data. Actually, as already remarked, these data are expected to overestimate the Sherwood number due to the presence of entrance effects. Fully developed conditions are in fact generally not reached for these points. Finally, in Fig. 5.34, the CONAN and the COPAIN data are compared.

5.4 Concluding remarks

Studies concerning the effect of helium on steam condensation were performed by the separate effect test CONAN and COPAIN facilities. In this chapter, an analysis of the experimental data available has been proposed, aimed at improving the understanding of the effects induced by helium, mostly in terms of buoyancy forces. The forced convection and natural convection regimes are addressed.

Experimental data for fully developed forced convection were analyzed. New data are proposed analyzing cases at low free stream velocity. Even if fully developed flow conditions are not completely attained, interesting effects are

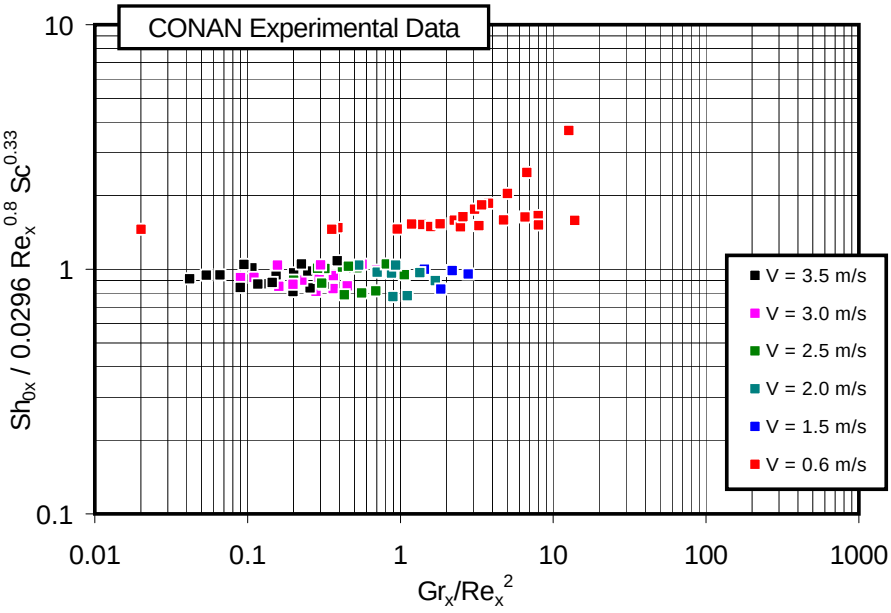

Figure 5.33: CONAN experimental Sherwood number Sh_{0x} normalized to the Schlichting correlation, identified by the free stream velocity

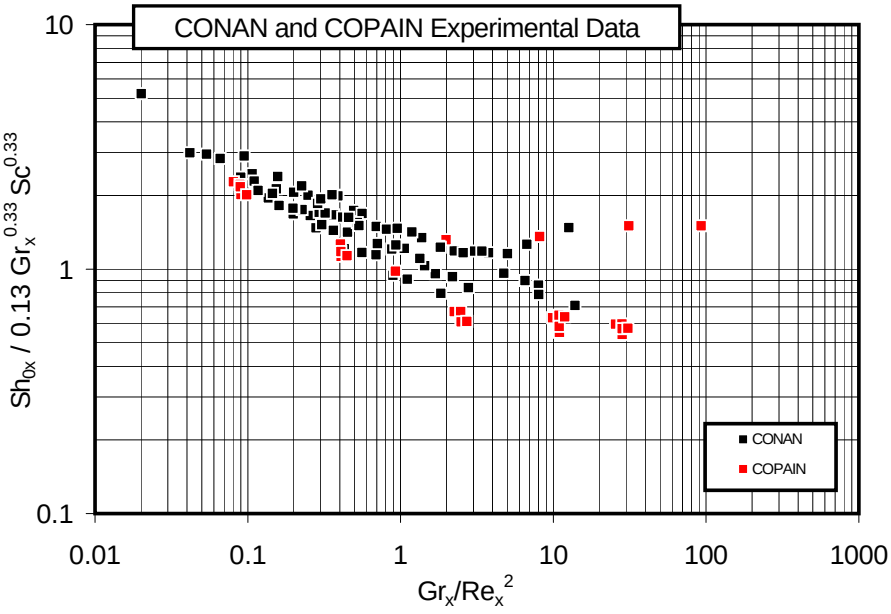

Figure 5.34: CONAN and COPAIN experimental Sherwood number Sh_{0x} normalized to the McAdams correlation

clearly put into evidence, related to the presence of helium.

The mixed convection regime are addressed, for which two different phenomenologies are possible: the *buoyancy-aided* regime occurs when buoyancy forces are co-current with inertia forces. In the case of CONAN, where the condensing mixture circulates downward, *buoyancy-aided* conditions occur when the interface mixture is heavier than the bulk, that is for steam-air mixture or steam-air-helium mixtures having a helium-to-noncondensable gas ratio less than the critical value for which *buoyancy reversal* occurs.

A simple relationship is proposed for estimating the helium-to-noncondensable gas ratio χ_{br} for which *buoyancy reversal* occurs, basing on the assumption that the helium-to-noncondensable gas ratio at the interface and in the bulk are very similar. This is found to be a reasonable assumption in turbulent flows, for which the impairment of the interface helium concentration is minimum with respect to air.

Buoyancy-opposed conditions are experienced when the interface mixture is lighter than in bulk. This condition is typical of steam-air mixtures flowing upward or, in the case of CONAN, of steam-air-helium mixtures having a helium-to-noncondensable gas ratio higher than the one allowing for buoyancy reversal to occur. For low free stream velocity, in *buoyancy-opposed* conditions, *flow reversal* can be also experienced, for which the flow field is inverted with respect to the free stream and the turbulence kinetic energy is remarkably increased.

A comparison with the data provided by the COPAIN facility was also performed. A common trend is clearly observed for both facilities, confirming the previous remarks; indeed, even if experimental uncertainties could obviously affect the measured values[2], the qualitative trend is reasonably well defined and so is the phenomenology related to the presence of a noncondensable gas lighter than steam.

Important effects related to turbulence are put in evidence by scoping calculations. The presence of helium affects the turbulence kinetic energy profiles both in forced and in natural convection. Further experimental and numerical studies would be useful to achieve a better understanding of these effects. Local velocity and turbulence measurements are advisable in this purpose.

The effect of helium is therefore not only studied *per-se*. Different phenomenologies are introduced, like *buoyancy-aided* and *buoyancy-opposed* mixed convection, and *flow reversal*, representing very challenging aspects to be coped with. New experimental data representative of different phenomenologies are therefore proposed, whose interest is fundamental for improving the accuracy and testing the validity of condensation models to be employed in present and future codes, aimed at performing the thermal-hydraulic analysis of the nuclear reactor containment.

[2]Experimental uncertainties will be treated in chapter 8, where a comparison between calculated and experimental data will be proposed

Chapter 6

CFD Models for wall condensation phenomena

This chapter is aimed at analyzing and proposing CFD models for simulating turbulent wall condensation phenomena in multicomponent mixtures. In paragraph 6.1, an overview of the different turbulence modelling strategies is offered. The incompressible and the compressible RANS (*Reynolds Averaged Navier-Stokes*) equations for multicomponent mixtures are presented in paragraphs 6.2 and 6.3. The *Boussinesq* and the *gradient-diffusion* hypotheses are introduced in paragraph 6.4. The effect of turbulence on the diffusion of chemical species is analyzed in detail in paragraph 6.6, proposing two different CFD diffusion models: a simplified model based on the *effective binary diffusivity* approximation and an additional model derived on the basis of the principles of the *irreversible thermodynamics*, as illustrated in chapter 2. Finally, in paragraph 6.7, three different condensation models are proposed, basing on the two main strategies adopted for wall condensation modelling in CFD codes, as illustrated in chapter 3: a fine approach based on the resolution of the concentration, the temperature and the velocity gradients near the condensing wall and a less expensive approach adopting coarser discretization in the proximity of the condensing wall, basing on the heat and mass transfer analogy to estimate the condensation mass transfer rates.

6.1 Modelling of turbulence phenomena in CFD codes

Most flows of interest in the thermal-hydraulic analysis of the reactor containment are turbulent. Turbulent flows are characterized by fluctuating velocities and, as a consequence, fluctuating transported quantities. These fluctuations can involve different length scales and different time scales. A direct numerical simulation (DNS) of such phenomena would require very fine meshes and very small time steps; despite of the increasing power of modern calculators, it is unlikely to be attainable in the next future, at the length scales typical of a nuclear reactor containment. An alternative to this approach consists in solving a modified form of the Navier-Stokes (NS) equations, which were fully detailed

in chapter 2. Two methods are available aimed at treating the NS equations in order to avoid the direct simulation of the small-scale turbulent fluctuations. A first method consists in solving an averaged form of the NS equations, known as RANS (*Reynolds averaged Navier-Stokes*) equations. A second method, known as LES (*large eddy simulations*), consists in filtering the NS equations in the aim to solve the largest turbulence scales and model only the smallest ones. Indeed, whatever is the selected method, additional unknowns are introduced in the governing equations. These are turbulence transport terms that need to be modelled to close the mathematical problem. The RANS based approach, in particular, consists in modeling all the turbulence scale and therefore allows reducing remarkably the computational effort with respect to DNS. The LES method, on the other hand, models only the smallest turbulence scales and can be thus considered as an intermediate approach between DNS and RANS, also in terms of computational cost. Despite of the encouraging improvement of the modern computers performances, the RANS approach is presently the only attainable technique for modelling turbulence phenomena at the scale of a reactor containment.

In the following paragraphs the RANS equations will be detailed for multicomponent incompressible and compressible mixtures. Later, the Boussinesq and the diffusion-gradient hypotheses will be illustrated, aimed at preparing the background for modelling turbulent diffusion phenomena and therefore turbulent condensation.

6.2 The incompressible RANS equations

The RANS equations are obtained by averaging the NS equations, in which the different quantities are decomposed in an average and a fluctuating component: A relatively simple formulation of the RANS is that of incompressible flows having constant density, obtained basing on the Reynolds' averaging method. The same formulation can be applied to flows in which density fluctuations are supposed to be negligible.

According to Reynolds, the average mixture velocity in the mass reference frame defined by Eq. (2.12) is given by a time average and a fluctuating term

$$\vec{U}_m = \langle \vec{U}_m \rangle + \vec{U}'_m \tag{6.1}$$

where the average term is given by

$$\langle \vec{U}_m \rangle = \frac{1}{\triangle t} \int_t^{t+\triangle t} \vec{U}_m dt^* \tag{6.2}$$

and the fluctuating term is therefore defined as

$$\vec{U}'_m = \vec{U}_m - \langle \vec{U}_m \rangle \tag{6.3}$$

Similarly, all scalar quantities can be decomposed as

$$\phi = \langle \phi \rangle + \phi' \tag{6.4}$$

where ϕ can denote every transported quantity. Once the different decomposed quantities are substituted in the most general transport balance equation

$$\frac{\partial \rho\phi}{\partial t} + \nabla \cdot \left(\rho\phi \vec{U}_m \right) = \nabla \cdot \vec{j}_\phi + \rho G_\phi \tag{6.5}$$

and each term is averaged, making use of classical assumption we finally get

$$\frac{\partial \rho\langle\phi\rangle}{\partial t} + \nabla \cdot \left(\rho\langle\phi\rangle\langle\vec{U}_m\rangle\right) = \nabla \cdot \langle\vec{j}_\phi\rangle + \rho\langle G_\phi\rangle - \nabla \cdot \left(\rho\langle\phi'\vec{U}'_m\rangle\right) \tag{6.6}$$

where the density fluctuations were assumed to be zero, according to the hypothesis of incompressible flow. In a non reacting multicomponent mixture, without any volumetric source term of mass, the set of the *incompressible* RANS equations includes:

- the *incompressible* averaged continuity equation

$$\nabla \cdot \langle\vec{U}_m\rangle = 0 \tag{6.7}$$

- the *incompressible* averaged momentum equations

$$\frac{\partial \rho\langle\vec{U}_m\rangle}{\partial t} + \nabla \cdot \left(\rho\langle\vec{U}_m\rangle\langle\vec{U}_m\rangle\right) = \nabla \cdot \left(\langle\vec{\bar{\tau}}\rangle - \langle P\rangle[\mathbb{I}]\right) + \rho\langle\vec{F}\rangle - \nabla \cdot \left(\rho\langle\vec{U}'_m\vec{U}'_m\rangle\right) \tag{6.8}$$

  where the mean shear stress tensor is defined as

$$\langle\vec{\bar{\tau}}\rangle = 2\langle\mu\rangle[\langle\mathbb{S}\rangle] + 2\langle\mu'[\mathbb{S}']\rangle \tag{6.9}$$

  with the mean rate-of-strain tensor defined as

$$[\langle\mathbb{S}\rangle] = \frac{1}{2}[\nabla\langle\vec{U}_m\rangle + \nabla^T\langle\vec{U}_m\rangle] \tag{6.10}$$

  and the fluctuating rate-of-strain tensor as

$$[\mathbb{S}'] = \frac{1}{2}[\nabla\vec{U}'_m + \nabla^T\vec{U}'_m] \tag{6.11}$$

  Equation (6.9) can be simplified by assuming that double correlations with fluctuations of molecular transfer coefficients are negligible; the mean shear stress tensor is therefore given by

$$\langle\vec{\bar{\tau}}\rangle = 2\langle\mu\rangle[\langle\mathbb{S}\rangle] \tag{6.12}$$

- the *incompressible* averaged species balance equations

$$\frac{\partial \rho\langle Y_i\rangle}{\partial t} + \nabla \cdot \left(\rho\langle Y_i\rangle\langle\vec{U}_m\rangle\right) = -\nabla \cdot \langle\vec{j}_i\rangle - \nabla \cdot \left(\rho\langle Y_i'\vec{U}'_m\rangle\right) \tag{6.13}$$

  where the diffusion average mass flux[1] is defined as

$$\langle\vec{j}_i\rangle = -\rho\sum_{k=1}^{n-1}\langle\mathbb{D}_{ik}\rangle\nabla\langle Y_k\rangle - \rho\sum_{k=1}^{n-1}\langle\mathbb{D}'_{ik}\nabla Y'_k\rangle \tag{6.14}$$

  that can be simplified if covariances including fluctuations of molecular transfer coefficients are assumed to be negligible

$$\langle\vec{j}_i\rangle = -\rho\sum_{k=1}^{n-1}\langle\mathbb{D}_{ik}\rangle\nabla\langle Y_k\rangle \tag{6.15}$$

[1] the summation is extended to $n-1$ species since the $\mathbb{D}_{in}$ terms are zero by definition (see paragraph 2.3.4)

- the *incompressible* averaged thermodynamic energy balance equation

$$\frac{\partial \rho\langle\hbar\rangle}{\partial t} + \nabla\cdot\Big(\rho\langle\hbar\rangle\langle\vec{U}_m\rangle\Big) = -\nabla\cdot\langle\dot{\vec{q}}''\rangle + \langle S_h\rangle - \nabla\cdot\Big(\rho\langle\hbar'\vec{U}'_m\rangle\Big) \tag{6.16}$$

where the viscous dissipation terms are neglected. The average heat flux consists of two terms, representing the average thermal conduction and the average interdiffusional convection. The average thermal conduction term is given by

$$-\langle k\nabla T\rangle = -\langle k\rangle\nabla\langle T\rangle - \langle k'\nabla T'\rangle \tag{6.17}$$

whereas the average interdiffusional convection term is given by

$$\begin{aligned}\sum_{i=1}^{n}\langle\vec{j}_i\hbar_i\rangle &= \sum_{i=1}^{n}\Big(\langle\vec{j}_i\rangle\langle\hbar_i\rangle\Big) + \sum_{i=1}^{n}\langle\vec{j}'_i\hbar'_i\rangle \\ &= \sum_{i=1}^{n}\Big(-\rho\sum_{k=1}^{n-1}\langle\mathbb{D}_{ik}\rangle\nabla\langle Y_k\rangle\langle\hbar_i\rangle\Big) + \sum_{i=1}^{n}\Big(-\rho\sum_{k=1}^{n-1}\langle(\mathbb{D}_{ik}\nabla Y_k)'\hbar'_i\rangle\Big)\end{aligned} \tag{6.18}$$

Assuming that covariances including property fluctuations are negligible, the average heat flux can be simplified to

$$\langle\dot{\vec{q}}''\rangle = -\langle k\rangle\nabla\langle T\rangle + \sum_{i=1}^{n}\Big(-\rho\sum_{k=1}^{n-1}\langle\mathbb{D}_{ik}\rangle\nabla\langle Y_k\rangle\langle\hbar_i\rangle\Big) \tag{6.19}$$

In multicomponent mixtures, the mixture enthalpy is given by

$$\hbar = \sum_{i=1}^{n} Y_i\hbar_i = \sum_{i=1}^{n}\left(\langle Y_i\rangle\langle\hbar_i\rangle + Y'_i\langle\hbar_i\rangle + \langle Y_i\rangle\hbar'_i + Y'_i\hbar'_i\right) \tag{6.20}$$

The average enthalpy is therefore given by

$$\langle\hbar\rangle = \sum_{i=1}^{n}\langle Y_i\rangle\langle\hbar_i\rangle + \sum_{i=1}^{n} Y'_i\hbar'_i \sim \sum_{i=1}^{n}\langle Y_i\rangle\langle\hbar_i\rangle \tag{6.21}$$

and the fluctuating enthalpy by

$$\hbar' = \sum_{i=1}^{n}\left(Y'_i\langle\hbar_i\rangle + \langle Y_i\rangle\hbar'_i\right) \tag{6.22}$$

Moreover, if we assumed that the specific heat is a function of only temperature[2], it is

$$\langle\hbar_i\rangle = \hbar_i(T_{ref}) + \int_{T_{ref}}^{\langle T\rangle} Cp_i(T^*)dT^* \tag{6.23}$$

and

$$\hbar'_i = \int_{\langle T\rangle}^{T} Cp_i(T^*)dT^* \approx Cp_i(\langle T\rangle)\ T' \tag{6.24}$$

[2]this is clearly a reasonable assumption for ideal gases

According to Eqs. (6.22) and (6.24), the term $-\nabla \cdot \left(\rho\langle\hbar'\vec{U}'_m\rangle\right)$ can be therefore rewritten as

$$\begin{aligned} -\nabla \cdot \left(\rho\langle\hbar'\vec{U}'_m\rangle\right) &= -\nabla \cdot \left(\sum_{i=1}^{n} \rho\langle\langle\hbar_i\rangle Y'_i\vec{U}'_m\rangle + \sum_{i=1}^{n} \rho\langle Cp_i\rangle\langle Y_i\rangle\langle T'\vec{U}'_m\rangle\right) \\ &= -\nabla \cdot \left(\sum_{i=1}^{n} \rho\langle\hbar_i\rangle\langle Y'_i\vec{U}'_m\rangle + \rho\langle Cp\rangle\langle T'\vec{U}'_m\rangle\right) \end{aligned} \tag{6.25}$$

since it is

$$\langle Cp\rangle = \sum_{i=1}^{n}\langle Cp_i\rangle\langle Y_i\rangle + \sum_{i=1}^{n} Cp'_iY'_i \sim \sum_{i=1}^{n}\langle Cp_i\rangle\langle Y_i\rangle \tag{6.26}$$

Finally, the thermodynamic energy balance equation can be written as

$$\begin{aligned} \frac{\partial\rho\langle\hbar\rangle}{\partial t} + \quad \nabla \cdot \left(\rho\langle\hbar\rangle\langle\vec{U}_m\rangle\right) &= \nabla \cdot \langle k\rangle\nabla\langle T\rangle - \nabla \cdot \left(\sum_{i=1}^{n}\langle\vec{j}_i\rangle\langle\hbar_i\rangle\right) + \langle S_h\rangle \\ -\nabla \cdot \left(\sum_{i=1}^{n}\left(\rho\langle\hbar_i\rangle\langle Y'_i\vec{U}'_m\rangle\right) + \rho\langle Cp\rangle\langle T'\vec{U}'_m\rangle\right) & \end{aligned} \tag{6.27}$$

6.3 The compressible RANS equations

The previous equations are derived for incompressible flows having constant density or flows for which the density fluctuations can be neglected. However, flows of interest for the containment thermal hydraulics can be compressible. In particular, we are interested in density variations induced by fluctuating temperature and species concentrations. Pressure effect will be neglected since in the applications of our interested, the CONAN and the COPAIN tests in particular, the operating pressure is constant. Adopting the Reynolds averaging method for compressible, variable density flows is not appropriate. Another averaging procedure is employed, proposed by Favre [117]. The Favre's averaging method consists on averaging each transported quantity weighted on density. The Favre average velocity is thus given by

$$\widetilde{\vec{U}_m} = \frac{\langle\rho\vec{U}_m\rangle}{\langle\rho\rangle} \tag{6.28}$$

and other transported scalar quantities by

$$\tilde{\phi} = \frac{\langle\rho\phi\rangle}{\langle\rho\rangle} \tag{6.29}$$

The fluctuating term in the Favre average is given by

$$\phi'' = \phi - \tilde{\phi} \tag{6.30}$$

and applies the property

$$\langle \rho \phi^{''} \rangle = 0 \tag{6.31}$$

Adopting the Favre averaging method, the *compressible* RANS equation are obtained:

- the *compressible* averaged continuity equation

$$\frac{\partial \langle \rho \rangle}{\partial t} + \nabla \cdot \left(\langle \rho \rangle \widetilde{\vec{U}_m} \right) = 0 \tag{6.32}$$

- the *compressible* averaged momentum equation

$$\frac{\partial \langle \rho \rangle \widetilde{\vec{U}_m}}{\partial t} + \nabla \cdot \left(\langle \rho \rangle \widetilde{\vec{U}_m} \widetilde{\vec{U}_m} \right) = \nabla \cdot \left(\langle \vec{\bar{\tau}} \rangle - \langle P \rangle [\mathbb{I}] \right) + \langle \rho \rangle \widetilde{\vec{F}} - \nabla \cdot \left(\langle \rho \rangle \widetilde{\vec{U}_m'' \vec{U}_m''} \right) \tag{6.33}$$

with

$$\langle \vec{\bar{\tau}} \rangle = \langle \mu \rangle \left(\nabla \widetilde{\vec{U}_m} + \nabla^T \widetilde{\vec{U}_m} \right) - \frac{2}{3} \langle \mu \rangle \left(\nabla \cdot \widetilde{\vec{U}_m} \right) [\mathbb{I}] \tag{6.34}$$

where it is assumed, as for the incompressible formulation, that the covariances including properties fluctuations are negligible with respect to other terms.

$$\tilde{\nu} \tilde{\phi} \gg \widetilde{\nu'' \phi''} \tag{6.35}$$

- the *compressible* averaged species balance equations

$$\frac{\partial \langle \rho \rangle \tilde{Y}_i}{\partial t} + \nabla \cdot \left(\langle \rho \rangle \tilde{Y}_i \widetilde{\vec{U}_m} \right) = -\nabla \cdot \tilde{\vec{j}}_i - \nabla \cdot \left(\langle \rho \rangle \widetilde{Y_i' \vec{U}_m'} \right) \tag{6.36}$$

where $\tilde{\vec{j}}_i$, once the covariances including fluctuating diffusion coefficient are cancelled, is given by

$$\tilde{\vec{j}}_i = -\sum_{i=1}^{n-1} \langle \rho \rangle \langle \mathbb{D}_{ik} \rangle \nabla \tilde{Y}_k \tag{6.37}$$

- the *compressible* averaged thermodynamic energy balance equation

$$\frac{\partial \langle \rho \rangle \tilde{\hbar}}{\partial t} + \nabla \cdot \left(\langle \rho \rangle \tilde{\hbar} \widetilde{\vec{U}_m} \right) = -\nabla \cdot \langle \dot{\vec{q}}^{''} \rangle + \langle S_h \rangle - \nabla \cdot \left(\langle \rho \rangle \widetilde{\hbar'' \vec{U}_m''} \right) \tag{6.38}$$

where the viscous dissipation terms is neglected. The heat flux $\dot{\vec{q}}^{''}$, under the aforementioned hypothesis concerning the fluctuating properties, can be written as

$$\langle \dot{\vec{q}}^{''} \rangle = -\langle k \rangle \nabla \tilde{T} + \sum_{i=1}^{n} \tilde{\vec{j}}_i \tilde{\hbar}_i \tag{6.39}$$

According to the definition of enthalpy, following the same procedure adopted for the incompressible formulation, the covariance $\langle \rho \rangle \widetilde{\hbar'' \vec{U}_m''}$ can be rewritten as

$$\langle \rho \rangle \widetilde{\hbar'' \vec{U}_m''} = \sum_{i=1}^{n} \langle \rho \rangle \tilde{\hbar}_i \widetilde{Y_i'' \vec{U}_m''} + \langle \rho \rangle \langle Cp \rangle \widetilde{T'' \vec{U}_m''} \tag{6.40}$$

and the thermodynamic energy balance equation is finally given by

$$\begin{aligned}\frac{\partial\langle\rho\rangle\tilde{\hbar}}{\partial t} \quad &+\nabla\cdot\left(\langle\rho\rangle\tilde{\hbar}\widetilde{\vec{U}_m}\right) = \langle k\rangle\nabla\tilde{T} - \sum_{i=1}^{n}\tilde{\vec{j}}_i\tilde{\hbar}_i \\ &-\nabla\cdot\left(\sum_{i=1}^{n}\langle\rho\rangle\tilde{\hbar}_i\widetilde{Y_i''\vec{U}_m''} + \langle\rho\rangle\langle Cp\rangle\widetilde{T''\vec{U}_m''}\right)\end{aligned} \tag{6.41}$$

6.4 The Boussinesq and the gradient-diffusion hypotheses

Both incompressible and compressible RANS equations are very similar to the NS equations. The differences between the averaged and the NS equations consist in additional terms given by the product of the fluctuating transport property and the fluctuating velocity, for each transported quantity. Clearly, the compressible RANS equations reduce to the incompressible ones when density is constant and so we will focus on the compressible RANS equations in the following. The terms $-\rho\langle\vec{U}'_m\vec{U}'_m\rangle$ in incompressible momentum equations or the similar terms $-\langle\rho\rangle\widetilde{\vec{U}''_m\vec{U}''_m}$ in the compressible momentum equations are the so called Reynolds stresses, constituting the Reynolds stress tensor. The Reynolds stress tensor is a symmetric tensor of order two. This means that six further unknowns are introduced in the momentum balance equations that need to be modeled, in principle solving a transport equation for each Reynolds stress. Further turbulence transport terms are introduced for each chemical species and for the energy equation. In a multicomponent system of n chemical species, additional turbulence terms to be modelled with respect to NS equations would be therefore $6+(n-1)+1$. An important simplification of the problem can be anyway achieved by adopting the *Boussinesq* or *turbulent-viscosity hypothesis*. The *Boussinesq hypothesis* consists on assuming that the deviatoric Reynolds stress tensor given by

$$-\langle\rho\rangle\widetilde{\vec{U}''_m\vec{U}''_m} + \frac{2}{3}\langle\rho\rangle\kappa[\mathbb{I}] \tag{6.42}$$

is proportional to the double of the mean-rate-of-strain

$$2\tilde{\mathbb{S}} = \mu_t\left(\nabla\widetilde{\vec{U}_m} + \nabla^T\widetilde{\vec{U}_m}\right) - \frac{2}{3}\mu_t(\nabla\cdot\widetilde{\vec{U}_m})\,[\mathbb{I}] \tag{6.43}$$

via a turbulence viscosity coefficient. The Reynolds stress tensor is therefore given by

$$-\langle\rho\rangle\widetilde{\vec{U}''_m\vec{U}''_m} = \mu_t\left(\nabla\widetilde{\vec{U}_m} + \nabla^T\widetilde{\vec{U}_m}\right) - \frac{2}{3}\left(\langle\rho\rangle\kappa + \mu_t(\nabla\cdot\widetilde{\vec{U}_m})\right)[\mathbb{I}] \tag{6.44}$$

where the turbulence kinetic energy κ has been introduced, defined as half the trace of the Reynolds stress tensor

$$\kappa = \frac{1}{2}\sqrt{u''^{\,2}_m + v''^{\,2}_m + w''^{\,2}_m} \tag{6.45}$$

When Eq. (6.44) is substituted in Eq. (6.33) , the averaged momentum balance equation becomes

$$\begin{aligned}\frac{\partial\langle\rho\rangle\widetilde{\vec{U}_m}}{\partial t}+\nabla\cdot\left(\langle\rho\rangle\widetilde{\vec{U}_m}\widetilde{\vec{U}_m}\right) &= \nabla\cdot\left[(\mu+\mu_t)\left(\nabla\widetilde{\vec{U}_m}+\nabla^T\widetilde{\vec{U}_m}-\frac{2}{3}(\nabla\cdot\widetilde{\vec{U}_m})\,[\mathbb{I}]\right)\right]\\ &\quad -\nabla\left(\langle P\rangle+\frac{2}{3}\langle\rho\rangle\kappa\right)+\langle\rho\rangle\tilde{\vec{F}}\end{aligned} \tag{6.46}$$

In this case, two further unknowns appear, the turbulence kinetic energy and the turbulence viscosity. Turbulence effects are reduced to modelling the appropriate turbulence viscosity term, which is just a property of the flow field. Turbulence models have been developed and validated since a long time, aiming at providing estimation of the turbulence viscosity. The simplest models needed to close the problem of turbulence, allowing the turbulent velocity and the length scales to be independently determined, are the two-equations models. Among these, the family of the $\kappa-\varepsilon$ and the $\kappa-\omega$ models are the most validated, consisting in solving two additional transport equations for the turbulence kinetic energy κ and either the turbulence dissipation rate ϵ or the specific dissipation rate ω. The turbulence viscosity μ_t is therefore computed as a function of the latter, via a constitutive relationship that links μ_t, κ and ϵ or ω. Similarly to the *Boussinesq hypothesis* for the Reynolds stress tensor, another hypothesis can be formulated for the turbulent transport of energy and chemical species. The *gradient-diffusion hypothesis* consists in assuming that the turbulent transport terms are down the mean scalar gradient of the corresponding quantity

$$\langle\rho\rangle\widetilde{Y_i''\vec{U}_m''}=-\frac{\mu_t}{Sc_t}\nabla\tilde{Y}_i=-\langle\rho\rangle\frac{\nu_t}{Sc_t}\nabla\tilde{Y}_i=-\langle\rho\rangle D_t\nabla\tilde{Y}_i \tag{6.47}$$

$$\langle\rho\rangle\langle Cp\rangle\widetilde{T''\vec{U}_m''}=-\frac{\mu_t}{Pr_t}\langle Cp\rangle\nabla\tilde{T}=-\frac{\nu_t\langle\rho\rangle\langle Cp\rangle}{Pr_t}\nabla\tilde{T}=-k_t\nabla\tilde{T} \tag{6.48}$$

The resulting compressible species average balance equations is therefore given by

$$\begin{aligned}\frac{\partial\langle\rho\rangle\tilde{Y}_i}{\partial t}+\nabla\cdot\left(\langle\rho\rangle\tilde{Y}_i\widetilde{\vec{U}_m}\right) &= -\nabla\cdot\left(-\sum_{k=1}^{n-1}\langle\rho\rangle\langle\mathbb{D}_{ik}\rangle\nabla\tilde{Y_k}\right)-\nabla\cdot\left(-\langle\rho\rangle D_t\nabla\tilde{Y}_i\right)\\ &= \nabla\cdot\left(\sum_{k=1}^{n-1}\langle\rho\rangle(\langle\mathbb{D}_{ik}\rangle+D_t\delta_{ik})\nabla\tilde{Y_k}\right)\end{aligned} \tag{6.49}$$

that in matrix form, introduced in chapter 2, can be written as

$$\frac{\partial\langle\rho\rangle\tilde{\mathbf{Y}}}{\partial t}+\nabla\cdot\left(\langle\rho\rangle\tilde{\mathbf{Y}}\widetilde{\vec{U}_m}\right)=\nabla\cdot\left(\langle\rho\rangle\ [\langle\mathbb{D}\rangle+D_t\mathbb{I}]\nabla\tilde{\mathbf{Y}}\right) \tag{6.50}$$

where $\tilde{\mathbf{Y}}$ is the vector of the $\tilde{Y_i}$ mass fractions. The resulting compressible thermodynamic energy balance equations is instead given by

$$\begin{aligned}\frac{\partial\langle\rho\rangle\tilde{\hbar}}{\partial t}+\nabla\cdot\left(\langle\rho\rangle\tilde{\hbar}\widetilde{\vec{U}_m}\right) &= (\langle k\rangle+k_t)\nabla\tilde{T}\\ &+\sum_{i=1}^{n}\left(\sum_{k=1}^{n-1}\langle\rho\rangle(\langle\mathbb{D}_{ik}\rangle+D_t\delta_{ik})\nabla\tilde{Y_k}\right)\tilde{\hbar_i}\end{aligned} \tag{6.51}$$

6.5 Averaged ideal gas equation of state

To complete the set of partial differential equations including the averaged continuity equation, the averaged momentum balance equations, the averaged thermodynamic energy balance equation and the averaged species balance equations, the equation of state (EOS) is here reported.

Let us consider a mixture of ideal gases. The averaged equation of state will be given by:

$$\tilde{\rho}=\sum_{i=1}^{n}\tilde{\rho_i}=\sum_{i=1}^{n}\frac{M_i}{R}\left(\widetilde{\frac{P_i}{T}}\right)=\sum_{i=1}^{n}\frac{M_i}{R}\left(\widetilde{\frac{PX_i}{T}}\right) \tag{6.52}$$

Moreover, if the thermodynamic pressure is assumed to be constant in our systam, as it is the case of CONAN and COPAIN tests, Eq. (6.52) can be further simplified to obtain

$$\tilde{\rho}=\sum_{i=1}^{n}\frac{PM_i}{R}\left(\widetilde{\frac{X_i}{T}}\right) \tag{6.53}$$

that is

$$\tilde{\rho}=\sum_{i=1}^{n}\frac{PM_i}{R}\left(\tilde{X_i}\frac{1}{\tilde{T}}+\left(\widetilde{X_i''\frac{1}{T''}}\right)\right) \tag{6.54}$$

Assuming that the covariant term is negligible with respect to the other term

$$\tilde{X_i}\frac{1}{\tilde{T}}\gg\left(\widetilde{X_i''\frac{1}{T''}}\right) \tag{6.55}$$

It is finally

$$\tilde{\rho}=\sum_{i=1}^{n}\frac{PM_i\tilde{X_i}}{R\tilde{T}} \tag{6.56}$$

Moreover, it is assumed that

$$\tilde{Y_i}=\sum_{i=1}^{n}\left(\widetilde{\frac{M_iX_i}{M}}\right)=\sum_{i=1}^{n}\left(\frac{M_i\tilde{X_i}}{\tilde{M}}+\left(\widetilde{\frac{X_i''M_i}{M''}}\right)\right) \tag{6.57}$$

can be approximated by

$$\tilde{Y_i}=\sum_{i=1}^{n}\frac{M_i\tilde{X_i}}{\tilde{M}} \tag{6.58}$$

6.6 Turbulent diffusion models

The set of equations including Eqs. (6.1), (6.46), (6.49), (6.51) and (6.56) is the final set to be solved. Four unknown can be recognized. Behind the aforementioned turbulence kinetic energy κ and turbulence viscosity μ_t, the turbulent Prandtl Pr_t and Schmidt Sc_t numbers appear. Since turbulence is assumed to affect the transport of all quantities in the same way, turbulent mass and thermal diffusion coefficients, respectively D_t and α_t are usually assumed to be proportional to the turbulence kinematic viscosity ν_t. The proportionality coefficients are the inverse of the turbulent Schmidt and Prandtl numbers that are therefore assumed constants and do not have to be modeled. In this paragraph, the effects of turbulence on the diffusion phenomena are analyzed, assuming that the required turbulence diffusivities are given. The details of turbulence models aimed at determining these quantities will be instead analyzed in chapter 7.

Let us rewrite the compressible RANS balance equation of the i-th chemical species omitting to represent the averaging symbols over the different quantities for the sake of simplicity[3].

$$\frac{\partial \rho Y_i}{\partial t} + \nabla \cdot \left(\rho Y_i \vec{U}_m \right) = \nabla \cdot \left(\sum_{k=1}^{n-1} \rho (\mathbb{D}_{ik} + D_t \delta_{ik}) \nabla Y_k \right) \tag{6.59}$$

In chapter 2, different diffusion models were analyzed. Basing on that analysis, two different typologies of models are presented for modeling diffusion phenomena: those based on the effective binary diffusion approximation and those derived on the basis of the irreversible thermodynamics principles.

6.6.1 The MSD model

In multicomponent mixtures, a generalization of the Fick's law can be proposed, where the multicomponent mass transfer coefficients are provided on the basis of the Maxwell-Stefan equations. This is possible since the Maxwell-Stefan diffusion coefficients in a mixture of ideal gases are proven to be equal to the actual binary diffusion coefficients in a pure binary mixture. As a result of this analysis, fully detailed in chapter 2, a multicomponent diffusion model is proposed, referred to as MSD (*Maxwell-Stefan Diffusion*). According to Eq. (2.153), the $\mathbb{D}_{ik}$ terms of the multicomponent diffusion matrix $[\mathbb{D}]$ are given by

$$[\mathbb{D}] = [A]^{-1}[R] \tag{6.60}$$

with the R_{ii} and the R_{ik} terms given by

$$R_{ii} = \left[M \left(\frac{X_i}{M_n} + \frac{1 - X_i}{M_i} \right) \right] \tag{6.61}$$

$$R_{ik} = \left[X_i M \left(\frac{1}{M_k} - \frac{1}{M_n} \right) \right] \tag{6.62}$$

and the A_{ii} and the A_{ik} terms are given by

$$A_{ii} = -M \left(\frac{X_i}{D_{in} M_n} + \sum_{\substack{k=1 \\ k \neq i}}^{n} \frac{X_k}{D_{ik} M_i} \right) \tag{6.63}$$

[3] and so will be later on

and

$$A_{ik} = X_i M\Big(\frac{1}{D_{ik}M_k} - \frac{1}{D_{in}M_n}\Big) \tag{6.64}$$

As also remarked in paragraph 2.3.4), according to Eq. (6.60), since the terms A_{in} are zero and so are corresponding term of the inverse matrix $[A]^{-1}$, the n-th column of the diffusion matrix is also zero.

The effective diffusion matrix for the MSD model can be therefore rewritten as the sum of the molecular multicomponent diffusion matrix $[\mathbb{D}]$ and the turbulent multicomponent diffusion matrix defined as

$$[\mathbb{D}_t] = D_t[\mathbb{I}] \tag{6.65}$$

The resulting species balance equation in matrix form is given by

$$\frac{\partial \rho \mathbf{Y}}{\partial t} + \nabla \cdot \Big(\rho \mathbf{Y} \vec{U}_m\Big) = \nabla \cdot \left(\rho \, [\mathbb{D} + \mathbb{D}_t] \nabla \mathbf{Y}\right) \tag{6.66}$$

The MSD model involves a tight coupling of all the species balance equations that must be solved at once. The numerical algorithm is therefore relatively expensive.

6.6.2 The EBD model

A simplified model is based on the *effective binary diffusivity* approximation and will be referred to as EBD (*Effective Binary Diffusion*) in the following. The EBD model can be thought of as a particular case of the MSD model where the diffusion coefficient matrix degenerates to a diagonal form whose terms are given by

$$\mathbb{D}_{ik} = D_{im}\delta_{ik} \tag{6.67}$$

and thus, the diffusion mass flux of the i species is simply given by

$$\vec{j_i} = -\rho(D_{im} + D_t)\nabla Y_i \tag{6.68}$$

where

$$D_{im} = \frac{1 - X_i}{\displaystyle\sum_{\substack{k=1 \\ k \neq i}}^{n} \frac{X_k}{D_{ik}}} \tag{6.69}$$

Equation (6.59) can be therefore rewritten as

$$\frac{\partial \rho Y_i}{\partial t} + \nabla \cdot \Big(\rho Y_i \vec{U}_m\Big) = \nabla \cdot \left(\rho (D_{im} + D_t) \nabla Y_i\right) \tag{6.70}$$

or, in the matrix form

$$\frac{\partial \rho \mathbf{Y}}{\partial t} + \nabla \cdot \Big(\rho \mathbf{Y} \vec{U}_m\Big) = \nabla \cdot \left(\rho \, [(D_{im} + D_t)\mathbb{I}] \nabla \mathbf{Y}\right) \tag{6.71}$$

The main feature of the EBD model is that species equations are fully decoupled. This allows a remarkable simplification of the numerical schemes with respect to the MSD model, since species equations can be solved segregated.

6.6.3 Differences and similarities of the EBD and MSD diffusion models

The simpler model EBD is based on the *effective binary diffusivity* approximation and allows a remarkable simplification of the species balance equations that, as observed, can be solved separately. The other model, the MSD, is a full multicomponent mass transfer model; the diffusion mass flux of a species is influenced by concentration gradients of all species. The set of the $n-1$ species balance equations is coupled and species equations cannot be solved as a segregated set. The computational cost is thus increased but, in turn, the accuracy of the modelling is improved. In turbulent flows, however, the turbulent diffusion coefficient can be some orders of magnitude larger than the molecular diffusion coefficients. This makes the effective diffusion matrix of the MSD model to be very similar to the EBD diffusion diagonal matrix

$$\lim_{D_t \to \infty} [\mathbb{D} + \mathbb{D}_t] = D_t[\mathbb{I}] = \lim_{D_t \to \infty} (D_{im} + D_t)[\mathbb{I}] \tag{6.72}$$

This means that for turbulent flows, at least in principle, there are no great advantage in using more sophisticated models, since turbulence is almost everywhere the dominating transport process. On the other hand, when the details of the molecular transport become important, the use of the MSD model is more advisable. In chapter 2 in fact, the main deficiency of the EBD model was mentioned to be, that in multicomponent mixtures the sum of the different diffusion mass fluxes obtained by the EBD model does not allow the mixture continuity equation to be exactly satisfied. When dealing with wall condensation phenomena, these details are important since it is the molecular diffusivity that mainly governs the diffusion processes in the laminar sublayer near the condensing interface. The correct evaluation of molecular diffusivity is therefore a very important task in simulating wall condensation phenomena in presence of air and helium. In this scenario, the MSD model is of course the most accurate model. However, despite of the aforementioned deficiency, the EBD model can also be an appropriate solution. As remarked in chapter 2, at the basis of the EBD model is in fact the assumption that there is a single species diffusing in a almost stagnant mixture, that is the case of vapor condensation in presence of noncondensable gases. Whereas the condensing species has a finite velocity towards the interface, the noncondensable species are reasonably stagnant, owing to the concurring phenomena of counter diffusion and mixture entrainment; as a result, noncondensable species velocity is zero at the condensing interface and is presumably very low in the laminar sublayer. Moreover, the mole fraction of the condensing species is expected to be very low, whereas the gradient can be very strong. The approximation expressed by Eq. (2.164) is thus acceptable.

6.7 Wall condensation models

When dealing with the modelling of wall condensation phenomena in CFD codes, a common approach consists in applying source terms in the cells close to the condensing surface (see chapter 3). Volumetric sinks are assigned to the balance equations, basing on mass transfer rates that can be estimated in different ways. Condensation modelling techniques can be distinguished on the basis

of the required discretization in the near-wall region. Our aim is to develop two different approaches:

- a first, accurate approach relies on the solution of the different gradients in the boundary layer and therefore requires a very fine discretization;
- a second approach is conceived to allow faster calculations with coarser discretization and the estimation of the mass transfer rates is based on the analogy between heat and mass transfer.

6.7.1 General assumptions

Whatever is the adopted diffusion or condensation model, some assumptions are possible, based on theoretical and experimental evidence. Here these assumption are discussed and justified.

- *Zero film thickness*: a first assumption is that the liquid film is negligible and that therefore the phase-change interface can be assumed to coincide with the condensing wall surface. In Fig. 4.4, a picture taken within the COPAIN facility was shown, putting in evidence that, even in the condensing cases having a larger condensation rate, a continuous liquid film of condensate, laminar, turbulent or wavy, is hardly attainable. The presence of liquid droplets or liquid rivulets is instead experienced. Huhtiniemi et Al. [66] investigated the effect of droplets formation over condensing surface, concluding that these play an important role for horizontal downfacing condensing surfaces, but a minor role for vertical walls. This effect was basically attributed to the increasing of turbulence in the condensing mixture, due to droplets pending from the condensing surface under the action of gravity. Beside the aforementioned reasons, there is a common agreement on the fact that the thermal resistance due to liquid film, even if any, is doubtless of negligible importance with respect to the thermal resistance associated to the noncondensables buildup at the interface, at least at sufficiently high noncondensable mass fractions. Independent numerical investigations performed in the frame of the benchmark-0 exercise (see chapter 3), allowed in fact assessing that taking into account liquid film via an appropriate additional thermal resistance produces a very small difference in the prediction of local mass fluxes.
- *No-slip conditions at the condensing interface*: as a consequence of neglecting the liquid film, shear velocity at the interface is imposed equal to zero. The orthogonal velocity is in principle equal to the mixture average velocity of condensation at the interface. The orthogonal mixture velocity is anyway assigned equal to zero at the interface, since the velocity boundary condition is implicitly imposed by the volumetric sinks of mass applied in the cells close to the condensing wall. Indeed, these sinks cause the mixture to be sucked towards the condensing wall with an appropriate velocity, corresponding to the condensation mass transfer flux.
- *Ideal gas behavior*: steam, air and helium are assumed to constitute a mixture of ideal gases. This assumption is doubtless appropriate for noncondensable gases, also considering the range of temperature and pressure of interest. In the case of steam this is also reasonable. Indeed, in the

application of our interest we deal with saturated steam in the CONAN facility or weakly superheated steam in the case of the COPAIN facility. Superheating is generally around 10 K degree, but some tests are performed up to 40 K of superheating. The compressibility factor of steam in the range of the considered application is reasonably close to unity, since the discrepancy with the ideal gas behavior is in the order of few tenths of a percent. Steam can be therefore considered as an ideal gas at a first approximation. Pressure is constant in the different tests; mixture density depends therefore only on the mixture composition and the mixture temperature.

6.7.2 The HMTDM^{EBD} and the HMTDM^{MSD} condensation models

Whatever is the adopted diffusion model, estimating the mass transfer rate is possible on the basis of the interface boundary conditions, provided that the different gradients are accurately predicted. An accurate resolution of the diffusion processes in the near-wall region is therefore required. In this aim, both the accuracy of the molecular transport model and the transport of the turbulence quantities are fundamental aspects. To achieve a good resolution of diffusion phenomena, turbulence models with low-Reynolds capabilities must be used, requiring very fine discretization in the near-wall region. The details and the discretization requirements of these turbulence models will be better detailed in chapter 7.

It is here anticipated that these models require the non dimensional distance of the first cell from the wall y_c^+ being in the order of one or preferably less. This assures the first cell of the computational domain to be located within the viscous layer where the velocity profiles are as linear as possible. To assure that also temperature and concentration profiles are linear, we will also take care of satisfying the conditions

$$y_c^+ Pr < 1 \tag{6.73}$$

and

$$y_c^+ Sc < 1 \tag{6.74}$$

Since in our cases both the Prandtl number and the Schmidt number are less than 1, if $y_c^+ < 1$, the conditions expressed by Eq. 6.73 and Eq. 6.74 are intrinsically satisfied. Due to the zero film thickness approximation, the boundary of the computational domain coincides with the condensing interface, for which the following boundary conditions are applied: the interface temperature and the non permeability conditions of the noncondensable species. Since phase change phenomena occur at saturation conditions, once the interface temperature is known, the corresponding saturation steam pressure is known, and so are the steam partial pressure and the molar fraction at the interface. In particular, if steam is supposed to be an ideal gas at the interface, the molar fraction is given by the ratio between its partial pressure and the total pressure of the system, which is supposed to be uniform all over the volume. The local mass transfer

flux of steam condensation at the condensing interface [4] is thus given by

$$\dot{m}''_{v,i} = \frac{j_{v,i}}{1 - Y_{v,i}} \tag{6.75}$$

where the terms $\dot{m}''_{v,i}$ and $j_{v,i}$ are mass fluxes and diffusion mass fluxes in the direction orthogonal to the condensing interface. These components are supposed to be the only finite components of the mass flux and of the diffusion mass flux vectors of the condensing species. Based on the available diffusion models, two condensation models are available to estimate the diffusion mass flux $j_{v,i}$ at the condensing interface. If the EBD model is adopted to deal with molecular diffusion, in ternary mixtures, the corresponding diffusion mass flux at the interface, where transport phenomena are strictly molecular, will be given by

$$j_{v,i} = -\rho_i D_{vm,i} \frac{Y_{v,c} - Y_{v,i}}{\triangle_c} \tag{6.76}$$

where, according to Eq. (6.69), it is

$$D_{vm,i} = \frac{1 - X_{v,i}}{\dfrac{X_{a,i}}{D_{va,i}} + \dfrac{X_{he,i}}{D_{vhe,i}}} \tag{6.77}$$

The subscript c denotes the center of the first cell beside the condensing interface and $\triangle_c$ is its distance from the condensing wall (see Fig. 6.1). This model will be referred to as HMTDM^{EBD} model. If, on the other hand, the MSD model is adopted to model molecular transport, the corresponding condensation model referred to as HMTDM^{MSD}, will estimate the local condensation diffusion mass flux of steam in ternary mixture as

$$j_{v,i} = -\rho_i \mathbb{D}_{vv} \frac{Y_{v,c} - Y_{v,i}}{\triangle_c} - \rho_i \mathbb{D}_{va} \frac{Y_{a,c} - Y_{a,i}}{\triangle_c} \tag{6.78}$$

where the terms $\mathbb{D}_{vv}$ and $\mathbb{D}_{va}$ of the diffusion matrix are obtained according Eq. (6.60).

6.7.3 The HMTAM condensation models

At the length scales typical of a nuclear reactor containment, a fine resolution of the boundary layer is difficult to be attainable. An alternative approach is thus proposed in similarity with a previous work [96] that allows using a coarser discretization near the condensing wall. This model is implemented coupled with the EBD diffusion model and is based on the analogy between heat and mass transfer. An overview of the model has already been proposed in chapter 3. A more in-depth description is here given. Basing on the analogy between heat and mass transfer, once the effect of suction is taken into account as illustrated in chapter 2, the steam condensation mass flux at a cold interface is given by

$$\dot{m}''_{v,i} = h_{m,0} \ln \frac{Y_{nc,b}}{Y_{nc,i}} = Sh_{0,l} \frac{\rho_{f,l} D_{vm,f,l}}{l} \ln \frac{Y_{nc,b,l}}{Y_{nc,i,l}} \tag{6.79}$$

[4] In the following equations, up to the end of this chapter, the i subscript will refer to interface and not to the i-th species

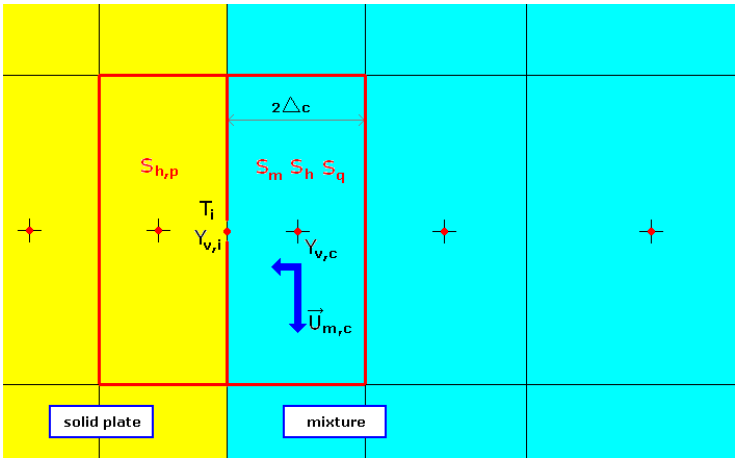

Figure 6.1: Sketch of discretization in the near the condensing wall region

where l is a characteristic length of the geometry and all the properties are defined as *film* properties, that is the average between the interface and the bulk. Actually, when dealing with the CFD implementation of the model there could be ambiguities in the way to define bulk conditions. This is mostly a problem we would be dealing with in complex geometries and in the presence of different flow phenomenologies. In the case of CONAN or COPAIN we are anyway coping with a simplified phenomenology, consisting on a one-directional flow, where the different boundary layers that establish at the different walls of the test section do not interact. This means that it is possible to identify a bulk region in which the velocity and the scalar field are homogeneous and therefore bulk properties can be resumed. Moreover, since boundary layers develop from the inlet section and never affect the central core of the channel cross section, in the case of CONAN and COPAIN bulk conditions can be assumed equal to the inlet conditions. Basing on the corresponding Nusselt number obtained in corresponding pure heat transfer conditions, the $Sh_{0,l}$ number is given by

$$Sh_{0,l} = C_l \; Re_l^a \; Sc_l^b \; Gr_{m,l}^c \tag{6.80}$$

The $Sh_{0,l}$ can be defined as a local or an average quantity. In our case, since the flow field is typical of shear flows, the local Sherwood number is defined on the basis of the distance from the inlet section x

$$Sh_{0,x} = C_x \; Re_x^a \; Sc^b \; Gr_{m,x}^c \tag{6.81}$$

whereas the average Sherwood number is defined based on the total height of the condensing plate L.

$$Sh_{0,L} = C_L \; Re_L^a \; Sc^b \; Gr_{m,L}^c \tag{6.82}$$

Whatever is the flow regime, that is, whatever are the a, b and c coefficients, the relationship that link C_L and C_x, obtained by averaging the $Sh_{0,x}$ number over the length of the condensing plate, is given by

$$C_L = \frac{C_x}{a + 3c} \tag{6.83}$$

Among the different available correlations, we are mostly interested to those concerning turbulent forced and natural convection under a local point of view. For the turbulent forced convection case, the correlation adopted is the Schlichting's [115]

$$Sh_{0,x} = 0.0296\ Re_x^{0.8}\ Sc^{0.33} = 0.0296\Big(\frac{\rho_{f,x}\ u_\infty}{\mu_{f,x}}\Big)^{0.8}\Big(\frac{\nu_{f,x}}{D_{vm,f,x}}\Big)^{0.33} \tag{6.84}$$

The McAdams correlation is adopted for natural convection cases

$$Sh_{0,x} = 0.13\ Gr_{m,x}^{0.33}\ Sc^{0.33} = 0.13\Big(\frac{\rho_{f,x}\ g\ \triangle\rho_x\ x^3}{\mu_{f,x}^2}\Big)^{0.33}\Big(\frac{\nu_{f,x}}{D_{vm,f,x}}\Big)^{0.33} \tag{6.85}$$

where

$$\triangle\rho_x = |\rho_{b,x} - \rho_{i,x}| \tag{6.86}$$

The very advantage of the HMTAM model is the possibility to use it with a coarse discretization. Instead of solving concentration gradients, the mass transfer rates are estimated on the basis of the flow properties. This makes the near-wall turbulence to be dealt with in a simpler way. Wall functions can be applied for the velocity, the temperature and the species equations in the near-wall cells. In the frame of this research, standard logarithmic profiles have been used, owing to their simplicity, even if not adapted to account for blowing or suction phenomena (see chapter 7. Indeed, even if the accuracy of prediction can be affected by this choice, this allows the computational efforts to be drastically reduced.

6.7.4 Volumetric source terms

Once the condensation mass fluxes are obtained by the selected condensation model, the condensation model is implemented in the CFD code by means of appropriate volumetric source terms. Mass sinks are added to the continuity and the steam balance equations, given by

$$S_m = S_v = \frac{\dot{m}''_{v,i}}{2\ \triangle_c} \tag{6.87}$$

where $2\ \triangle_c$ denotes the thickness of the cell where the source is applied, which in our case is twice the distance $\triangle_c$ of the cell center from the condensing wall. The corresponding energy sink is given by

$$S_h = S_m \hbar_{v,i} = \frac{\dot{m}''_{v,i}}{2\ \triangle_c}\hbar_{v,i} \tag{6.88}$$

Heat transfer through the conducting condensing plate, whenever included, is simulated by means of the conjugated heat transfer method. In this aim, energy source terms are applied to the cells of the solid condensing plate, immediately close to the condensation surface

$$S_{h,p} = -S_m \hbar_{v,i}^{lat} = -\frac{\dot{m}''_{v,i}}{2\ \triangle_c}\hbar_{v,i}^{lat} \tag{6.89}$$

Clearly, the energy embedded in the liquid film, given by $S_m \hbar_{h_2o,i}$ is cancelled from the computational domain, as well as the liquid film itself.

As a consequence of applying sinks of mass, the specific momentum of the mixture in those cells is increased. To avoid acceleration of the mixture, appropriate momentum source terms must be applied to the momentum equation, defined by

$$S_q = S_m \vec{U}_{m,c} = \frac{\dot{m}''_{v,i}}{2 \triangle_c} \vec{U}_{m,c} \tag{6.90}$$

where $\vec{U}_{m,c}$ is the velocity of the mixture in the center of the cell where the source terms are applied. Actually, in the HMTDM models, the magnitude of the aforementioned velocity is very small and so are the corresponding momentum source terms. The influence of these source terms in the HMTDM models will be analyzed in chapter 7. An analysis on the influence of these source terms on the HMTAM model was performed in a previous work by the same author [96], assessing that momentum source terms in the direction parallel to the condensing wall are indispensable to avoid the mixture to be accelerated. Cells where mass source terms are applied are in fact sufficiently thick to make the velocity in the center a non negligible fraction of the mixture velocity in bulk.

6.7.5 The Mixture Interface Composition

A fundamental aspect in evaluating the mass transfer fluxes, and then the condensation rates, is the knowledge of the local interface mixture composition. Actually, the steam partial pressure is known once the interface temperature is known, since phase change is supposed to occur in saturation conditions. Since steam is supposed to be an ideal gas, the molar fraction is known given by the ratio between the steam partial pressure and the absolute pressure. It follows that, in binary mixtures the interface composition is determined once the interface temperature is given. In ternary mixtures, on the other hand, the molar fractions of the noncondensable species are not known and the boundary condition to be imposed for the noncondensable species is the non permeability of the condensing interface. However, the knowledge of the mixture interface composition is necessary to estimate interface density, average molecular weight, diffusivity, steam mass fraction and other properties, all depending on the interface mixture composition and therefore calculate the condensation mass flux. In a first instance, the interface composition of noncondensable gases could be assumed to be equal to that in the bulk. However, since helium and air have different molecular diffusivities in steam, the noncondensable composition is expected to vary from bulk to interface. Several other strategies suitable for CFD codes are therefore proposed for evaluating the noncondensable composition at the interface. The thinner is the near-wall cell, the more accurate are these strategies. However, even if they are necessarily more adapted to be used with the HMTDM models, encouraging results where also obtained with the HMTAM model [96, 118].

Proportionality assumption

As a first and simple alternative, the noncondensables interface percentages can be assumed equal to the percentages in the center of the cells next to the

condensing wall:

$$X_{he,i}/(X_{he,i}+X_{a,i}) = X_{he,c}/(X_{he,c}+X_{a,c}) \tag{6.91}$$

The thinner is the first cell close to the condensing wall, the more accurate is this approximation. On the other hand, for large mesh mass transfer models, the left hand term of Eq. (6.91) is expected to be slightly affected by the first cell size.

Analytic condition

The interface molar fluxes of the noncondensable species can be written as follows

$$\dot{n}''_{a,i} = j^*_{a,i} + X_{a,i}\dot{n}''_i \tag{6.92}$$

$$\dot{n}''_{he,i} = j^*_{he,i} + X_{he,i}\dot{n}''_i \tag{6.93}$$

For the non permeability boundary condition at the interface, both molar fluxes of the species in equations (6.92) and (6.93) are zero. The right hand terms of Eqs. (6.92) and (6.93) are then equal to zero. By manipulating them, the following relationship can then be obtained between molar fluxes and interface molar fractions:

$$j^*_{a,i}/X_{a,i} = j^*_{he,i}/X_{he,i} \tag{6.94}$$

Numerical implementation

Even if interface molar fractions can be calculated implicitly, the applicability of an implicit algorithm for containment calculations is undesirable, due to the increasing computational costs. Interface composition and source terms are then treated explicitly. For steady state calculations, this option is completely reasonable and even in transient calculations there are no particular problems if the time step is reasonably small. In the proportionality approximation, interface molar fraction at the step `n`, used to estimate the explicit sources, are evaluated on the basis of the species molar fractions at the previous step `n-1`

$$\left(X_{he,i}/(X_{he,i}+X_{a,i})\right)^{\mathtt{n}} = X^{\mathtt{n-1}}_{he,c}/(X^{\mathtt{n-1}}_{he,c}+X^{\mathtt{n-1}}_{a,c}) \tag{6.95}$$

Similarly, the mass fluxes of Eq. (6.94) are evaluated at the previous iteration or time step and the ratio between the helium and the air molar fraction is therefore given by

$$\left(X_{he,i}/X_{a,i}\right)^{\mathtt{n}} = \left(j^{*,\mathtt{n-1}}_{he,i}/j^{*,\mathtt{n-1}}_{a,i}\right) \tag{6.96}$$

In the frame of this research, both models were tested. For the model with refined near-wall discretization, the same results were obtained by both models and therefore the proportionality assumption has been retained. When dealing with thicker cells, both previous models are expected to be less accurate. No major differences were experienced between the two models; moreover, minor differences in the order of few tenths were observed with respect to the models with refined near-wall discretizations. For the sake of simplicity, the proportionality assumption was thus adopted also for the HMTAM model.

CFD model	Diffusion model	Condensation model	Interface model	Near-wall turbulence
HMTDM^{EBD}	EBD	HMTDM	Proportionality assumption	low-Re treatment
HMTDM^{MSD}	MSD	HMTDM	Proportionality assumption	low-Re treatment
HMTAM	EBD	HMTAM	Proportionality assumption	standard wall function

Table 6.1: Main features of the proposed CFD models

6.8 Concluding remarks

An analysis of the diffusion phenomena in turbulent multicomponent mixture has been performed. The RANS equations have been derived for multicomponent mixtures, focusing on turbulent diffusion and turbulent interdiffusional convection terms. Two different models have been proposed to deal with diffusion phenomena in the presence of turbulence, basing on the molecular transport models analyzed in chapter 2. A first model, named EBD, is based on the effective binary diffusion approximation. A second and more sophisticated model, named MSD, is a full multicomponent model, developed basing on the principles of the irreversible thermodynamics. Three different condensation models have been proposed. Two of them consist in evaluating the near-wall gradients in detail and evaluating the mass transfer rates on the basis of the diffusion mass fluxes. The two models are therefore named HMTDM^{EBD} and the HMTDM^{MSD}, depending on the selected diffusion model. A third model, developed for coarser near-wall discretizations consists in estimating the mass transfer rates on the basis of the heat and mass transfer analogy. The models of the HMTDM family are more sophisticated and are mainly conceived to improve the understanding of condensation phenomena in detail. The HMTAM model, on the other hand, is a fast-running simulation strategy adopting several modelling approximations and therefore more suitable for dealing with full scale geometries. The main features of the different models are summarized in the table 6.1.

Chapter 7

Prediction of transpiration effects in turbulent boundary layers

Turbulence modelling is a keypoint in the modelling of wall condensation phenomena. In chapter 6, the effects of turbulence on the balance equations have been analyzed, focusing on heat transfer and molecular diffusion. In this chapter, different turbulence models will be proposed aimed at estimating the different quantities introduced in the RANS equations for modelling turbulence effects. Different turbulence models are described and analyzed:

- the low-Reynolds $\kappa - \omega$ model of Wilcox [119];
- the low-Reynolds $\kappa - \varepsilon$ models of Abe et al. [120] and Yang and Shih [121];
- the RNG $\kappa - \varepsilon$ model in two variants to deal with the near-wall turbulence: standard wall functions for relatively coarse near-wall discretizations and a two-layer modelling (TLM) approach for fine near-wall discretizations.

Clearly, turbulence models with low-Reynolds capabilities are proposed to be used by the HMTDM models. The $\kappa - \varepsilon$ low-Reynolds models and the $\kappa - \omega$ model of Wilcox with low-Reynolds capabilities consist on solving similar equations for the turbulence kinetic energy, but adopt a very different strategy in the modelling of the dissipation rate. The dissipation of the turbulence kinetic energy ε is modelled in the $\kappa - \varepsilon$ models, whereas the rate of dissipation ω is adopted in the $\kappa - \omega$ model. Different near-wall treatment are therefore selected: the dissipation rate at the interface is usually imposed equal to zero in the $\kappa - \varepsilon$ models; an analytic boundary condition is instead imposed for ω. The two models where thus proposed to asses the capabilities of the different near-wall treatments to deal with transpirating flows. Further details on the models are reported in the following.

The RNG $\kappa - \varepsilon$ with standard wall functions will be used coupled with the HMTAM model. This last approach, adopting CFD for predicting the relevant flow pattern and the heat and mass transfer analogy for representing mass transfer phenomena is a compromise to be accepted for full-scale containment simulations, before more powerful computers will allow an extended

use of completely mechanistic approaches, as those of HTMDM models. However, the HMTDM models represent very powerful tools for achieving a more in-depth understanding of physical phenomena involved in condensation and, nevertheless, for assessing the quantitative consistency of the heat and mass transfer analogy to be employed in the HMTAM model. For these reasons, the need emerges for an in-depth validation of mechanistic diffusion models and low Reynolds turbulence models.

This chapter is therefore aimed at analyzing the capabilities of the aforementioned turbulence models to deal with turbulent transpirating boundary layers. The lack of experimental data concerning the characteristics of turbulence in condensation phenomena is a negative point for the validation of these turbulence models, purposely conceived to deal with different flow phenomenologies than transpirating boundary layers. Thus, to assess the capabilities of the different turbulence models and the different low-Reynolds strategies, a route has been proposed accounting for different phenomena of interest. A first stage allowed analyzing the capabilities of turbulence models to reproduce nondimensional velocity profiles in the presence of pure mass and momentum transfer, basing on the experimental data by Favre [13]. A second stage concerned the analysis of suction effects induced by condensation, in the light of different correlation proposed in literature to quantify its impact on the Sherwood number, the Nusselt number and the friction coefficient.

In the following paragraphs a description of the aforementioned turbulence models is provided. The FLUENT code is used and the capabilities of the low-Reynolds turbulence models and the RNG model with the two-layer near-wall treatment are anlysed in modelling transpiration phenomena. The results of this analysis are reported in the second part of the chapter. The final aim is to propose a turbulence model with low Reynolds capabilities to be further employed coupled with the HMTDM models in the modelling of the actual CONAN and COPAIN tests.

7.1 The $\kappa - \omega$ model

The $\kappa-\omega$ model [119] is an empirical model based on tranport equations for the turbulence kinetic energy κ and the specific dissipation rate ω, representative of the ratio between ε and κ. The transport equations for the turbulence kinetic energy κ and the specific dissipation rate ω are respectively

$$\frac{\partial \rho\kappa}{\partial t} + \nabla \cdot (\rho\kappa\vec{U}_m) = \nabla \cdot ((\mu + \mu_t\sigma_\kappa^*)\nabla\kappa) + \mu_t P - \beta^* f_{\beta^*}\rho\omega\kappa \tag{7.1}$$

$$\frac{\partial \rho\omega}{\partial t} + \nabla \cdot (\rho\omega\vec{U}_m) = \nabla \cdot ((\mu + \mu_t\sigma_\omega^*)\nabla\omega) + \mu_t P\alpha\frac{\omega}{\kappa} - \beta f_\beta\rho\omega^2 \tag{7.2}$$

where σ_κ^* and σ_ω^* are the inverse of the turbulent Prandtl numbers respectively for κ and ω. The turbulent viscosity μ_t is given by:

$$\mu_t = \rho\alpha^*\frac{\kappa}{\omega} \tag{7.3}$$

where α^* is a function of the local turbulent Reynolds number

$$Re_t = \frac{\rho\kappa}{\mu\omega} \tag{7.4}$$

taking into account low-Reynolds-number effects. It is given by:

$$\alpha^* = \alpha^*_\infty \left(\frac{\alpha^*_0 + Re_t/R_\kappa}{1 + Re_t/R_\kappa} \right) \tag{7.5}$$

The production term P is simply given by

$$P = \frac{1}{2} \| \nabla \vec{U}_m + \nabla^T \vec{U}_m \|^2 \tag{7.6}$$

where compressibility effects are neglected. In the ω equation, the production term is linked to a damping function α, similar to α^*:

$$\alpha = \alpha_\infty \frac{1}{\alpha^*} \frac{\alpha_0 + Re_T/R_\omega}{1 + Re_T/R_\omega} \tag{7.7}$$

The dissipation rate of κ requires the knowledge of β^* and f_{β^*}. For incompressible flows, β^* is given by

Constants	Values
α_0	$1/9$
α^*_0	$\beta/3.$
α_∞	$13/25$
α^*_∞	1
β	$9/125$
β^*_∞	$9/100$
R_κ	6.0
R_β	8.0
R_ω	2.95
σ^*_κ	0.5
σ^*_ω	0.5
Pr_t	0.85
Sc_t	0.7

Table 7.1: Constants of the k-ω model

$$\beta^* = \beta^*_\infty \frac{5/18 + (Re_t/R_\beta)^4}{1 + (Re_t/R_\beta)^4} \tag{7.8}$$

The f_{β^*} term is then given by

$$f_{\beta^*} = \frac{1 + 680\ \xi^2_\kappa}{1 + 400\ \xi^2_\kappa} \tag{7.9}$$

where ξ_κ are the cross-diffusion terms given by

$$\xi_\kappa = \frac{1}{\omega^3} \nabla\kappa \cdot \nabla\omega \tag{7.10}$$

When $\xi_\kappa < 0$, f_{β^*} is defined equal 1. In the same way, the dissipation rate of ω requires the knowledge of β and f_β. The f_β introduces a correction term for axisymmetric geometries

$$f_\beta = \frac{1 + 70\ \xi_\omega}{1 + 80\ \xi_\omega} \tag{7.11}$$

Anyway, the vortex stretching parameter ξ_ω is zero for two-dimensional incompressible flows [119] and therefore it is

$$f_\beta = 1. \tag{7.12}$$

Other constants of the model are summarized in Tab. 7.1.

Discretization requirements of the low-Reynolds $\kappa - \omega$ model

The nondimensional distance from the wall of the center of near-wall cell y_c^+ is defined as

$$y_c^+ = \frac{\rho y_c U^*}{\mu} \tag{7.13}$$

where the shear velocity U^* is given by

$$U^* = \sqrt{\frac{\tau_w}{\rho}} = \sqrt{\frac{\mu \frac{\partial u}{\partial y}|_w}{\rho}} \tag{7.14}$$

must be of order one or preferably less. Experiences highlighted that mesh independence is achieved when it approaches

$$y_c^+ \sim 0.4 \tag{7.15}$$

7.2 Low Reynolds $\kappa - \varepsilon$ turbulence models

The low-Reynolds $\kappa - \varepsilon$ models consist of a standard $\kappa - \varepsilon$ model, employing damping functions to join the turbulence variables in the fully turbulent region to the low turbulence Reynolds number region, that in our cases is the near-wall region. The κ tranport equation of the model is direcly derived from the exact κ equation

$$\frac{\partial \rho\kappa}{\partial t} + \nabla \cdot (\rho\kappa \vec{U}_m) = \nabla \cdot \left((\mu + \frac{\mu_t}{\sigma_\kappa}) \nabla\kappa \right) + G_\kappa + G_b - \rho\varepsilon \tag{7.16}$$

where G_κ represents the generation of turbulence kinetic energy due to the mean velocity gradients

$$G_\kappa = \mu_t \frac{1}{2} \| \nabla \vec{U}_m + \nabla^T \vec{U}_m \|^2 \tag{7.17}$$

and G_b is the generation of turbulence kinetic energy due to buoyancy

$$G_b = -\frac{\mu_t}{\rho Pr_t} \, \vec{g} \cdot \nabla\rho \tag{7.18}$$

It is remarked that the density gradients induce a turbulent generation term only if the density gradient component in the direction of the gravity is not zero. The term σ_κ is the turbulent Prandtl number for κ. The ε tranport equation of the model, unlike the model transport equation of κ is not derived from the exact ε equation. The simplified ε equation is instead given by

$$\frac{\partial \rho\varepsilon}{\partial t} + \nabla \cdot (\rho\varepsilon \vec{U}_m) = \nabla \cdot \left((\mu + \frac{\mu_t}{\sigma_\varepsilon}) \nabla\varepsilon \right) + C_{\varepsilon 1} \frac{\varepsilon}{\kappa} G_\kappa - C_{\varepsilon 2} \rho \frac{\varepsilon^2}{\kappa} \tag{7.19}$$

where σ_ε is the turbulent Prandtl number for ε. To account for low Reynolds number effects, appropriate damping functions are introduced. Moreover, the ε equation can be proposed in an alternative formulation, in which we define $\tilde{\varepsilon}$ as

$$\varepsilon = \varepsilon_0 + \tilde{\varepsilon} \tag{7.20}$$

The $\tilde{\varepsilon}$ balance equation is therefore given by

$$\frac{\partial \rho \tilde{\varepsilon}}{\partial t} + \nabla \cdot (\rho \tilde{\varepsilon} \vec{U}_m) = \nabla \cdot \left((\mu + \frac{\mu_t}{\sigma_\varepsilon}) \nabla \tilde{\varepsilon} \right) + C_{\varepsilon 1} \frac{\tilde{\varepsilon}}{\kappa} f_1 G_\kappa - f_2 C_{\varepsilon 2} \rho \frac{\tilde{\varepsilon}^2}{\kappa} \tag{7.21}$$

where f_1 and f_2 are the damping functions respectively for the production of ε and its dissipation. Once κ and $\tilde{\varepsilon}$ are known, the turbulence viscosity is finally given by

$$\mu_t = \rho C_\mu f_\mu \frac{\kappa^2}{\tilde{\varepsilon}} \tag{7.22}$$

where f_μ is the damping function for μ_t.

Several low Reynolds number $\kappa - \varepsilon$ models are available, proposed by different authors. In the frame of this research, a work was performed investigating the behavior of five different low Reynolds models in predicting transpiration phenomena [122]. In this work, two out of these five different low Reynolds number models have been reproposed:

- the model by ABE et al. [120], later on labelled AKN;
- the model by Yang and Shih [121], later on labelled YS;

The damping functions and the constants of the models are summarized respectively in Tabs. 7.2 and 7.3, where the following terms are introduced

$$Re_t = \frac{\kappa^2}{\tilde{\varepsilon}\nu}, \quad Re_y = \frac{\kappa^{1/2} y}{\nu}, \quad y^* = \frac{(\nu \tilde{\varepsilon})^2 y}{\nu} \tag{7.23}$$

.

Model	f_1	f_2	f_μ
YS	1	1	$\left(1 - e^{-1.5 \cdot 10^{-4} Re_y - 5. \cdot 10^{-7} Re_y^3 - 1. \cdot 10^{-10} Re_y^5}\right)^{1/2}$
AKN	1	$\left(1 - 0.3 e^{-(Re_t/6.5)^2}\right) \cdot \left(1 - e^{-y^*/3.1}\right)^2$	$\left(1 + \frac{5}{Re_t^{0.75}} e^{-(Re_t/200)^2}\right) \cdot \left(1 - e^{-y^*/14}\right)^2$

Table 7.2: Summary of low Reynolds number turbulence models damping functions

Model	C_μ	$C_{\varepsilon 1}$	$C_{\varepsilon 2}$	σ_κ	σ_ε	ε_0	E	$\tilde{\varepsilon}$wall B.C.	Pr_t	Sc_t
YS	0.09	1.44	1.92	1.0	1.3	0	$2\nu\nu_t \left(\frac{\partial^2 U_i}{\partial x_j \partial x_k}\right)^2$	$2\nu \left(\frac{\partial \sqrt{\kappa}}{\partial n}\right)^2$	0.85	0.7
AKN	0.09	1.5	1.9	1.4	1.4	0	0	$2\nu \left(\frac{\partial \sqrt{\kappa}}{\partial n}\right)^2$	0.85	0.7

Table 7.3: Summary of constants and near-wall correction functions for the low-Reynolds number turbulence models

Discretization requirements of the low-Reynolds $\kappa - \varepsilon$ model

The nondimensional distance y_c^+ of the center of near-wall cell from the wall must be of order one or preferably less. Experiences highlighted that mesh independence is generally achieved for

$$y_c^+ \sim 0.8 \tag{7.24}$$

for both models.

7.3 The RNG $\kappa - \varepsilon$ turbulence model

The RNG-based $\kappa - \varepsilon$ turbulence model is derived from the Navier-Stokes equations, using a mathematical technique called "renormalization group" (RNG) method [123]. The analytical derivation results in a model with constants different from those of the standard $\kappa - \varepsilon$ model, and additional terms in the transport equations, the R_ε term in particular. Except for the aforementioned differences, the RNG $\kappa - \varepsilon$ equation has a similar form to the standard $\kappa - \varepsilon$ model. The turbulent kinetic energy equation and the dissipation of turbulence kinetic energy equation are:

$$\frac{\partial \rho\kappa}{\partial t} + \nabla \cdot (\rho\kappa \vec{U}_m) = \nabla \cdot (\alpha_\kappa(\mu + \mu_t)\nabla\kappa) + G_\kappa + G_b - \rho\varepsilon \tag{7.25}$$

$$\frac{\partial \rho\varepsilon}{\partial t} + \nabla \cdot (\rho\varepsilon \vec{U}_m) = \nabla \cdot (\alpha_\varepsilon(\mu + \mu_t)\nabla\varepsilon) + C_{\varepsilon 1}\frac{\varepsilon}{\kappa}G_\kappa - C_{\varepsilon 2}\rho\frac{\varepsilon^2}{\kappa} - R_\varepsilon \tag{7.26}$$

where G_κ represents the generation of turbulent kinetic energy due to the mean velocity gradients and G_b is the generation of turbulent kinetic energy due to buoyancy, estimated as proposed in Eqs. (7.17) and (7.18). The terms α_κ and α_ε are the inverse of the effetive Prandtl numbers, computed using the following formula derived analytically by the RNG theory

$$\left|\frac{\alpha - 1.3929}{\alpha_0 - 1.3929}\right|^{0.6321} \left|\frac{\alpha + 2.3929}{\alpha_0 + 2.3929}\right|^{0.3679} = \frac{\mu}{\mu_t + \mu} \tag{7.27}$$

with $\alpha_0 = 1.0$. In the high Reynolds number limit, for $\mu/(\mu_t + \mu) << 1$, is $\alpha_k = \alpha_\varepsilon = 1.393$. The constants $C_{\varepsilon 1}$ and $C_{\varepsilon 2}$ are also derived analytically by the RNG theory

$$C_{\varepsilon 1} = 1.42, \quad C_{\varepsilon 2} = 1.68 \tag{7.28}$$

An additional destruction term of ε is introduced, given by

$$R_\varepsilon = \frac{C_\mu \rho \eta^3 (1 - \eta/\eta_0)}{1 + \beta \eta^3} \frac{\varepsilon^2}{\kappa} \tag{7.29}$$

with

$$\eta \equiv S\kappa/\varepsilon, \quad \eta_0 = 4.38, \quad \beta = 0.012 \tag{7.30}$$

where

$$S = \left(\frac{G_\kappa}{\mu_t} \right)^{1/2} \tag{7.31}$$

In the high Reynolds number limit, the turbulence viscosity is given by

$$\mu_t = \rho C_\mu \frac{\kappa^2}{\varepsilon} \tag{7.32}$$

where $C_\mu = 0.0845$.

A further characteristic of the RNG $\kappa - \varepsilon$ model consists in the way to estimate the turbulence thermal and molecular diffusivities. The RNG $\kappa - \varepsilon$ model proposes a different formulation for the effective thermal conductivity and the effective diffusion coefficient with respect to other models that follow the definition given in chapter 6. In the case of RNG $\kappa - \varepsilon$, it is

$$k + k_t = \frac{C_p(\mu + \mu_t)}{Pr_t} \tag{7.33}$$

$$D_{vm} + D_t = \frac{(\mu + \mu_t)}{\rho Sc_t} \tag{7.34}$$

where Pr_t and Sc_t are defined by

$$\left| \frac{\frac{1}{Pr_t} - 1.3929}{\frac{1}{Pr} - 1.3929} \right|^{0.6321} \left| \frac{\frac{1}{Pr_t} + 2.3929}{\frac{1}{Pr} + 2.3929} \right|^{0.3679} = \frac{\mu}{\mu_t + \mu} \tag{7.35}$$

$$\left| \frac{\frac{1}{Sc_t} - 1.3929}{\frac{1}{Sc} - 1.3929} \right|^{0.6321} \left| \frac{\frac{1}{Sc_t} + 2.3929}{\frac{1}{Sc} + 2.3929} \right|^{0.3679} = \frac{\mu}{\mu_t + \mu} \tag{7.36}$$

Unlike in other models, in the RNG $\kappa - \varepsilon$ model, a modification in the turbulent Prandtl and Schmidt numbers is introduced, where the two numbers are estimated on the basis of both molecular viscosity and turbulence viscosity.

7.3.1 Standard wall functions

When dealing with coarse discretizations in the near-wall region, wall functions are adopted, linking the solution variables at the near-wall cells and the corresponding quantities on the wall. Laws-of-the wall are proposed for the velocity, the temperature and all transported scalar quantities [123]. For the mean velocity, the law-of-the-wall yields

$$\begin{cases} U^* = y^* & y^* < 11.225 \\ U^* = \frac{1}{k} \ln(Ey^*) & y^* > 11.225 \end{cases} \tag{7.37}$$

where

$$U^* \equiv \frac{U_c C_\mu^{1/4} \kappa_c^{1/2}}{\tau_w/\rho} \tag{7.38}$$

$$y^* \equiv \frac{\rho C_\mu^{1/4} \kappa_c^{1/2} y_c}{\mu} \tag{7.39}$$

and the Von Karman constant $k = 0.41$, $E = 9.793$. The term U_c, κ_c, y_c are respectively the shear velocity, the turbulence kinetic energy and the distance from the wall in the center of the near-wall cell. The logarithmic law is valid for $30 < y^* < 300$ and it's employed for $y^* > 11.225$. Below this value, the flow is supposed to be laminar and therefore the laminar stress-strain relationship is adopted. Thanks to the Reynolds analogy between momentum and heat transfer, similar profiles are obtained for temperature, including two different laws: a linear law for the laminar sublayer where thermal conduction is dominant and a logarithmic law for the region dominated by turbulence

$$T^* = \frac{(T_w - T_c)\rho C p C_\mu^{1/4} \kappa_c^{1/2}}{\dot{q}''} = \begin{cases} Pr\ y^* & y^* < y_t^* \\ Pr_t\ \left[\frac{1}{k}\ln(Ey^*) + P_h\right] & y^* > y_t^* \end{cases} \tag{7.40}$$

where

$$P_h = 9.24 \left[\left(\frac{Pr}{Pr_t} \right)^{3/4} - 1 \right] \left[1 + 0.28 e^{-0.007 Pr/Pr_t} \right] \tag{7.41}$$

and y_t^* is the distance corresponding to the intersection of the linear and the logarithmic laws. When dealing with species tranport, similar wall functions are proposed for species

$$Y^* = \frac{(Y_w - Y_c)\rho C p C_\mu^{1/4} \kappa_c^{1/2}}{j_w} = \begin{cases} Sc\ y^* & y^* < y_c^* \\ Sc_t\ \left[\frac{1}{k}\ln(Ey^*) + P_c\right] & y^* > y_c^* \end{cases} \tag{7.42}$$

where

$$P_c = 9.24 \left[\left(\frac{Sc}{Sc_t} \right)^{3/4} - 1 \right] \left[1 + 0.28 e^{-0.007 Sc/Sc_t} \right] \tag{7.43}$$

and y_c^* is similarly to y_t^*, the distance corresponding to the intersection of the linear and the logarithmic laws. As it can be noted, the proposed wall functions do not account for suction effects due to possible interface mass transfer.

Despite the adoption of wall functions, the turbulence kinetic energy transport equations is solved all over the volume, including the near-wall cells and the boundary condition to be imposed for κ is

$$\frac{\partial \kappa}{\partial n}|_{y=0} = 0 \tag{7.44}$$

where n denotes the direction normal to the wall. On the other hand, the boundary condition for the ε equation consists in imposing the ε value in the center of the cells beside the condensing wall. Basing on the equilibrium between the production of the turbulence kinetic energy, G_κ, and its dissipation ε, it is therefore

$$\varepsilon_c = \frac{C_\mu^{3/4} \kappa_c^{3/2}}{\kappa\ y_c} \tag{7.45}$$

Discretization requirements of the RNG $\kappa - \varepsilon$ model with standard wall functions

The nondimensional distance y_c^* of the center of near-wall cell from the wall is required to be in the range

$$60 < y_c^* < 300 \tag{7.46}$$

7.3.2 Two-Layer model

When the need emerges for achieving a fine resolution of the boundary layers, a different approach than standard wall functions is used, requiring a finer discretization of the near-wall region. Standard wall functions in fact are not conceived to deal with transpiration effects, typical of condensation or evaporation. A different approach, based on a two-layer treatment and therefore named TLM (*Two-Layer Model*) is proposed capable to deal with low-Reynolds effects in presence of tranpiration phenomena [123]. In this approach the whole domain is divided into a near wall region and a fully turbulent region. The demarcation of the two regions is established on the basis of the turbulent Reynolds number Re_y, defined as follows:

$$Re_y \equiv \frac{\rho y \sqrt{\kappa}}{\mu} \tag{7.47}$$

where y is the distance from the wall at the cells centers. The RNG $\kappa - \varepsilon$ equations are solved in the fully turbulent region, for $Re_y > Re_y^* = 200$, whereas the one-equation model of Wolfstein is employed in the viscosity-affected near-wall region below the aforementioned value.

The Wolfshtein κ-l low-Reynolds turbulence model

The Wolfshtein's κ-l is a one-equation low-Reynolds turbulence model consisting in solving the κ equation in the same way than the standard $\kappa - \varepsilon$ model

$$\frac{\partial \rho \kappa}{\partial t} + \nabla \cdot (\rho \kappa \vec{U}_m) = \nabla \cdot \left((\mu + \frac{\mu_t}{\sigma_\kappa}) \nabla \kappa \right) + G_\kappa - \rho \varepsilon \tag{7.48}$$

and estimating the the turbulence viscosity in the viscous-affected sublayer by the following relationship

$$\mu_t^{in} = \rho C_\mu l_\mu \sqrt{\kappa} \tag{7.49}$$

where the length scale, accounting for low-Reynolds effects is given by

$$l_\mu = y c_l \left(1 - e^{-Re_y / A_\mu} \right) \tag{7.50}$$

The different constants appearing in the previous equations are

$$c_l = k C_\mu^{-3/4}, \quad A_\mu = 70 \quad C_\mu = 0.09 \tag{7.51}$$

The dissipation rate in the viscosity-affected region is not modelled, but it is calculated by means of the following algebraic relationship

$$\varepsilon = \frac{\kappa^{3/2}}{l_\epsilon} \tag{7.52}$$

where the length scale l_ϵ is given by

$$l_\epsilon = yc_l \left(1 - e^{-Re_y/A_\varepsilon}\right) \tag{7.53}$$

and

$$A_\varepsilon = 2c_l \tag{7.54}$$

Blending function

The turbulence viscosities in the viscosity-affected sublayer, μ_t^{in}, and the fully-turbulent region μ_t^{out} are blended according to the following relationship

$$\mu_t = \lambda_\varepsilon \mu_t^{out} + (1 - \lambda_\varepsilon)\mu_t^{in} \tag{7.55}$$

where the blending parameter λ_ε is defined as

$$\lambda_\varepsilon = \frac{1}{2}\Big[1 + tanh\left(\frac{Re_y - Re_y^*}{A}\right)\Big] \tag{7.56}$$

where Re_y^* is taken equal to 200. The constant A determines the width of the blending function in terms of the turbulence Reynolds number. Selected a $\triangle Re_y$ value where the blending parameter λ_ε is 1 % of its far field value, the constant A will be given by

$$A = \frac{|\triangle Re_y|}{tanh(0.98)} \tag{7.57}$$

The values of ε for the viscosity-affected region are also blended to the bulk values in a similar way as turbulence viscosity.

Discretization requirements of the RNG $\kappa - \varepsilon$ model with TLM

The nondimensional distance y_c^+ of the center of the near-wall cell from the wall must be of order one or preferably less. Experiences highlighted that mesh independence is achieved for

$$y_c^+ \sim 1.0 \tag{7.58}$$

7.4 The experiment of Favre

A first step for analysing the capabilities of turbulence models in representing transpiration phenomena is the experiment of Favre et al. [13]. The Favre's experimental set up consists of a rectangular channel where air is made flowing (see Fig. 7.1). The air flowing in the channel is sucked uniformly via a porous plate. Different tests are performed with different suction parameters

$$A = -\frac{\rho_0 V_0}{\rho_\infty u_\infty} \tag{7.59}$$

where u_∞ is the free-stream velocity in the channel and V_0 is the suction velocity (negative for suction and positive for blowing). Since the facility is operated with pure air and isothermal conditions, it is

$$A = -\frac{V_0}{u_\infty} \tag{7.60}$$

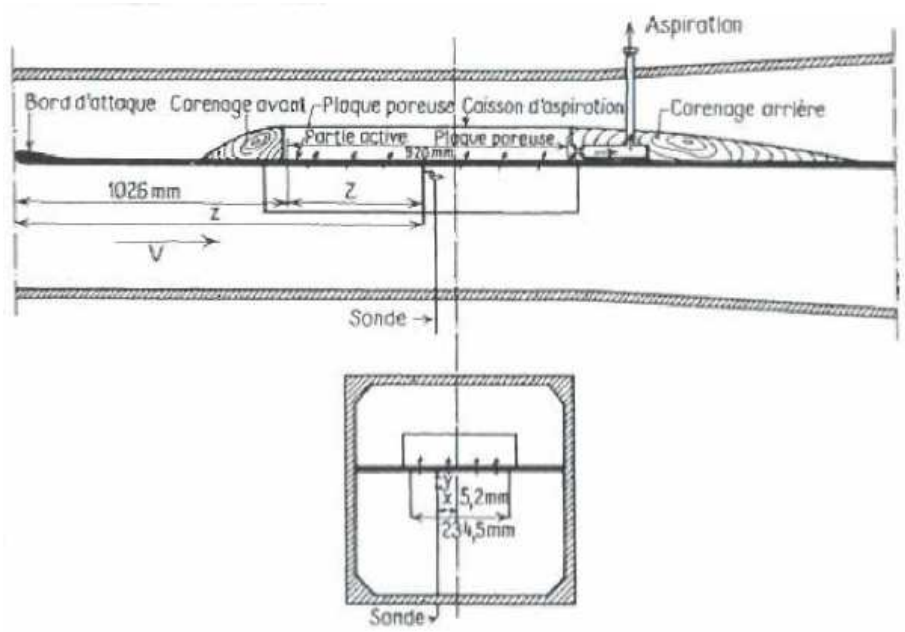

Figure 7.1: Test section of the Favre's facility

Alternatively, the suction parameter can be expressed as the ratio between the suction velocity and the shear velocity U^* introduced by Eq. (7.14). It is

$$A^+ = -\frac{V_0}{U^*} \tag{7.61}$$

The nondimensional local average velocity U^+, defined as

$$U^+ = \frac{u}{U^*} \tag{7.62}$$

is reported in Fig. 7.2 at a distance of 0.4 m from the leading edge of the porous plate as a function of the nondimensional distance from the wall

$$y^+ = \frac{\rho y U^*}{\mu} \tag{7.63}$$

When the facility is operated without suction, the data are in agreement with the Van Driest [124] or the Reichardt [125] profiles (see paragraph 7.5). Indeed, suction causes the velocity boundary to become thinner and the velocity gradient sharper. This causes the shear velocity U^* to increase, causing the nondimensional velocity U^+ to decrease and the nondimensional distance from the wall y^+ to increase. Thus, when suction is applied, the stronger is suction, the lower is the nondimensional velocity profile.

In this research, the different turbulence models with low-Reynolds capabilities were tested. Figures from 7.3 to 7.11 propose a comparison among the different models for different values of A, representative of the conditions of CONAN and COPAIN. As it can be noted, all models give similar results; a

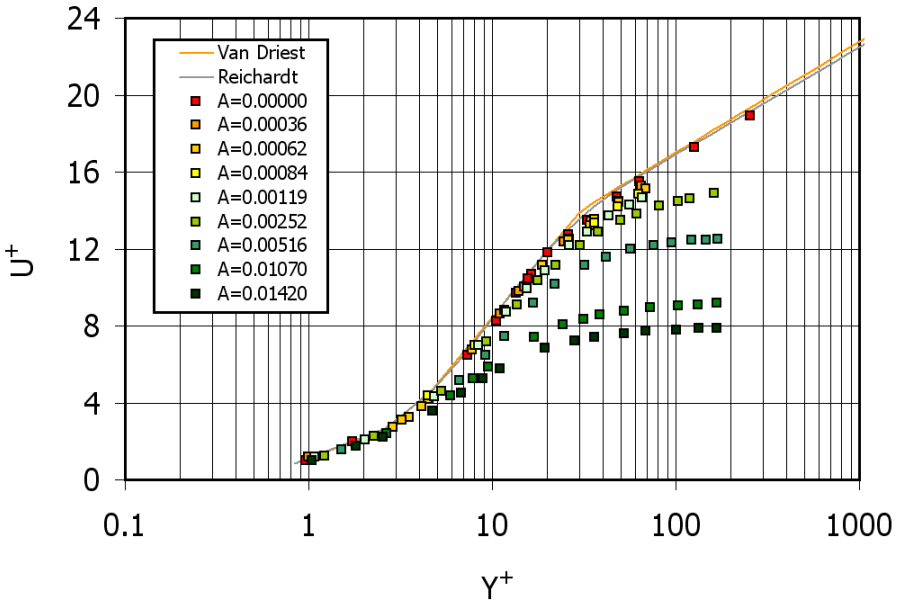

Figure 7.2: Local averaged velocity distributions across the test section in the Favre's tests

very good agreement with experimental data isobserved for the lowest suction parameter, especially in the case of RNG $\kappa - \varepsilon$ with TLM. At the larger suction rates, the prediction is less accurate, but the qualitative trend is well captured by all models. The RNG $\kappa - \varepsilon$ has proven to be the less sensitive to grid refinements in the near-wall region, requiring y^+ to be in the range of unity to achieve grid convergence. This makes also the model to be likely the less expensive, since other models require smaller y^+ and therefore finer meshes.

7.5 Numerical analysis of simultaneous turbulent momentum, heat and mass transfer

The Favre's experiment addressed tranpiration phenomena in presence of a single species and isothermal conditions. A further step has included effects of heat and species transport by considering an idealized problem of steam condensation in presence of air. The validation of the different turbulence models is proposed in front of the available correlation for the Sherwood and the Nusselt number, the friction coefficient, and the different relationship aimed at accounting suction effects on the aforementioned correlations.

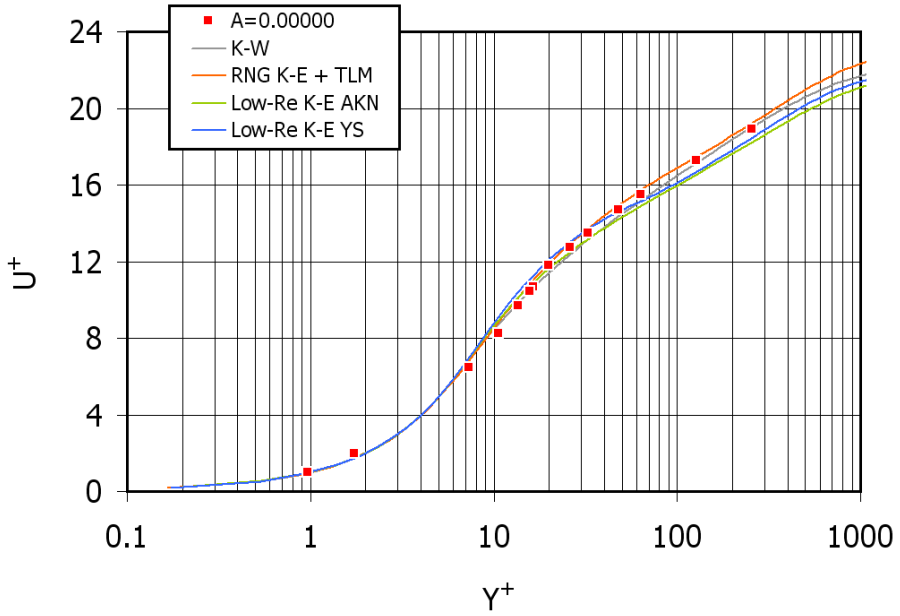

Figure 7.3: Experimental vs. calculated averaged velocily profile for the test case with $A = 0.00000$

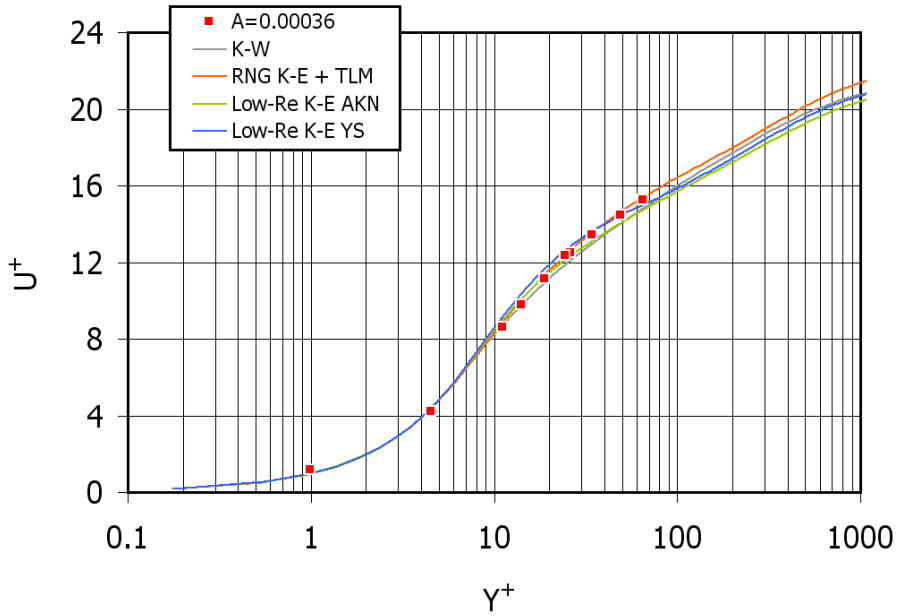

Figure 7.4: Experimental vs. calculated averaged velocily profile for the test case with $A = 0.00036$

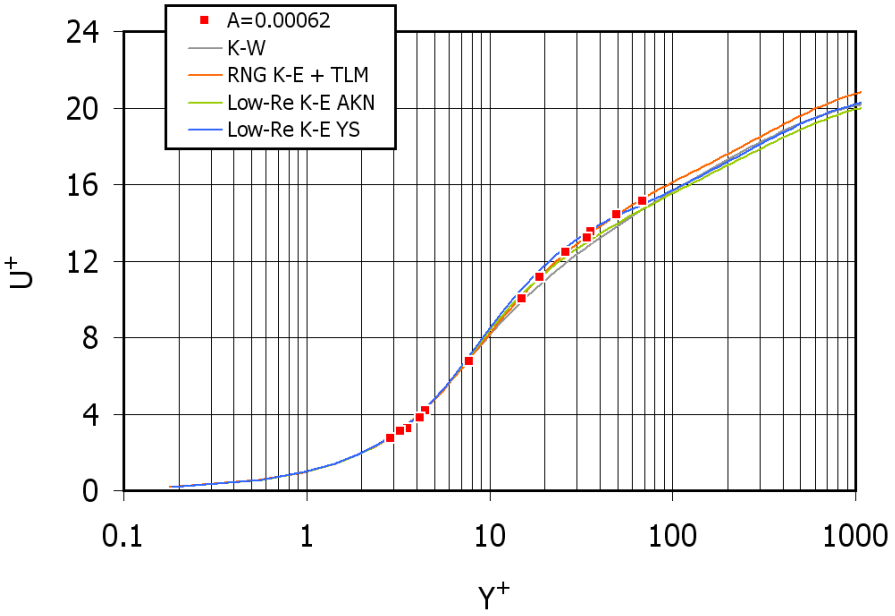

Figure 7.5: Experimental vs. calculated averaged velocily profile for the test case with $A = 0.00062$

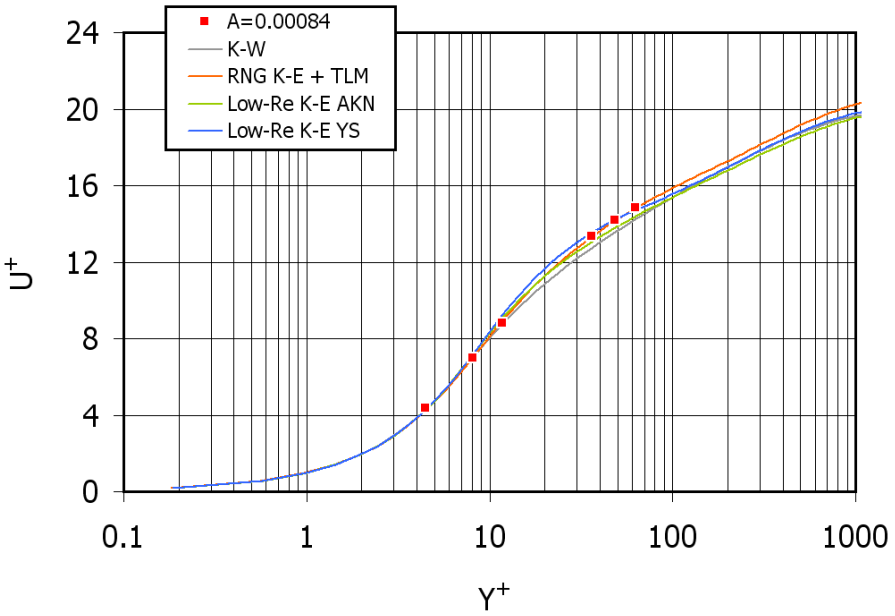

Figure 7.6: Experimental vs. calculated averaged velocily profile for the test case with $A = 0.00084$

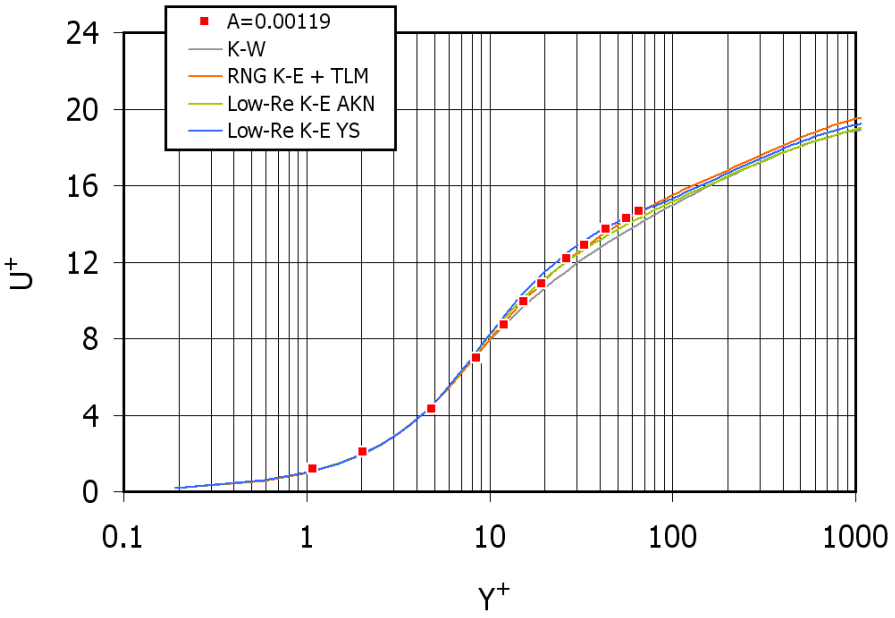

Figure 7.7: Experimental vs. calculated averaged velocily profile for the test case with $A = 0.00119$

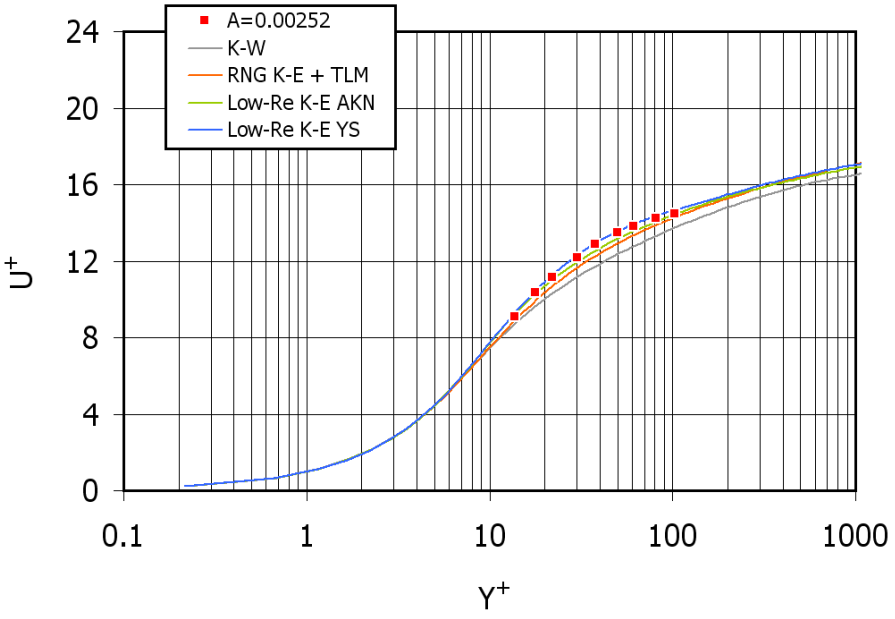

Figure 7.8: Experimental vs. calculated averaged velocily profile for the test case with $A = 0.00252$

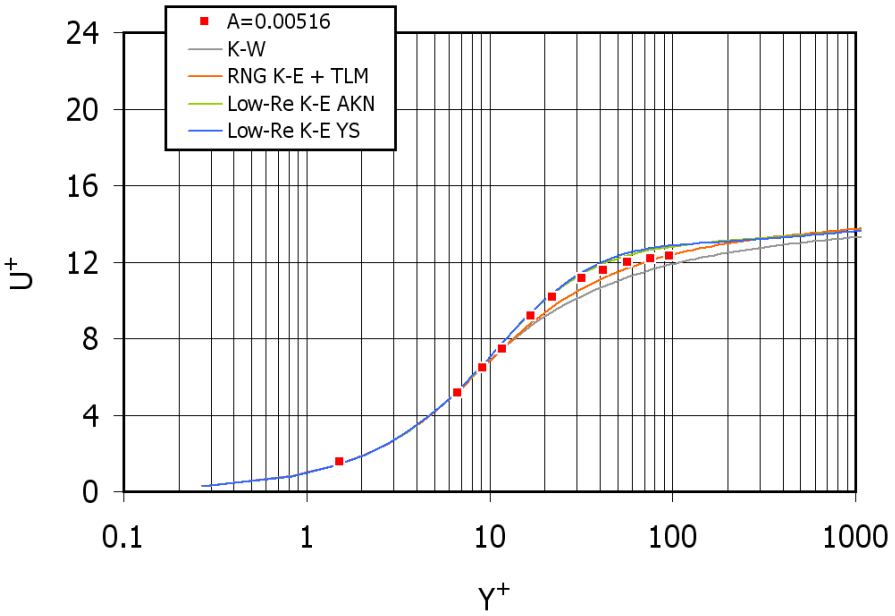

Figure 7.9: Experimental vs. calculated averaged velocily profile for the test case with $A = 0.00516$

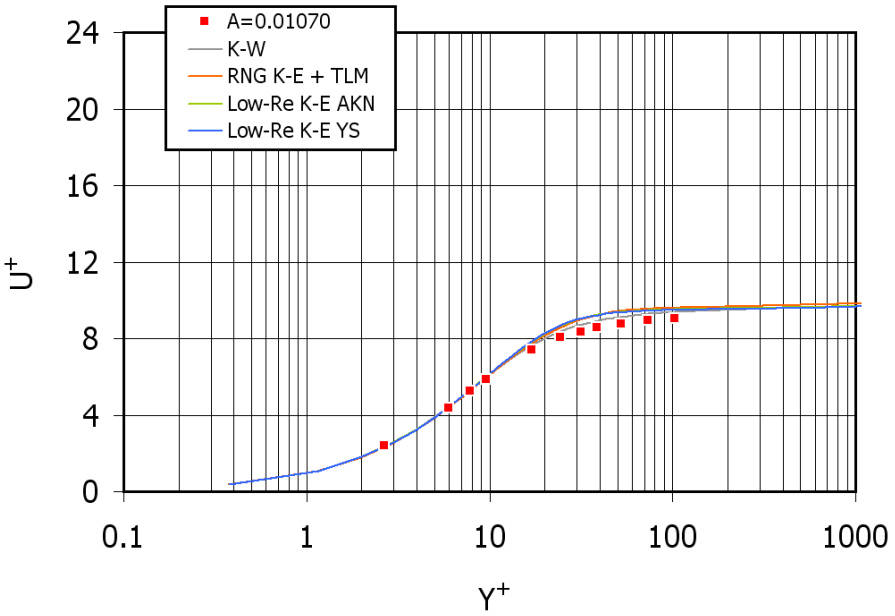

Figure 7.10: Experimental vs. calculated averaged velocily profile for the test case with $A = 0.01070$

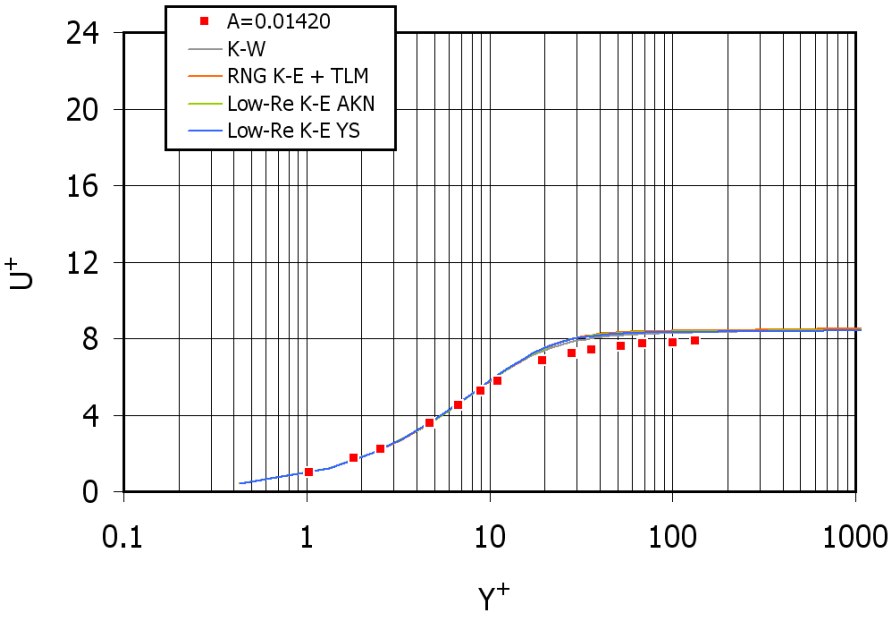

Figure 7.11: Experimental vs. calculated averaged velocily profile for the test case with $A = 0.01420$

Equilibrium boundary layers

As suggested by Kays and Moffat [126, 26][1], there are some simple cases in which a phenomenological analysis of the transpirating boundary layers is meaningful. In laminar boundary layer the concept of velocity-profile similarity leads to a very considerable mathematical simplification and to a whole family of simple mathematical solutions for some particular cases of transpiration and free-stream velocity variations. Albeit a self-similarity cannot be experienced in turbulent boundary layers, Clauser demonstrated that there are some particular families of turbulent non transpirating boundary layers for which an "outer region similarity" exists [127]. For turbulent boundary layers, in fact, it is possible to have an inner region, near the wall, in which turbulent energy production and dissipation are in equilibrium, while an outer region continues to develop. Clauser called these boundary layers, having an outer region similarity and inner region equilibrium, "equilibrium boundary layers", for which the outer region velocity profile plotted in the velocity defect coordinate system is universal

$$\frac{u - u_\infty}{U^*} = f\left(\frac{y}{\delta_c}\right) \tag{7.64}$$

[1] *What are the more fundamental cases that should be tested to provide firm bench-marks and from which the various constants and functions necessary to a more general theory can be derived?* (Kays & Moffat, 1975 [26])

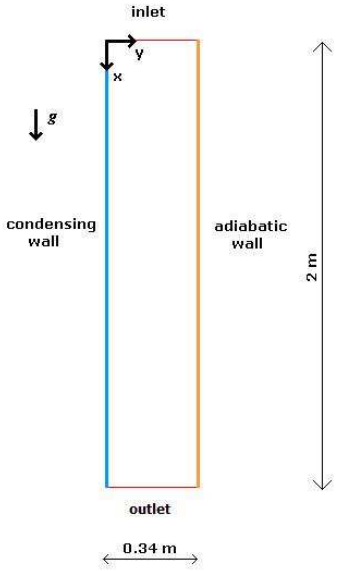

Figure 7.12: Selected geometrical configuration for the numerical analysis (reproduction of Fig. 3.10)

where

$$\delta_c = \int_0^\infty \frac{u - u_\infty}{U^*} dy \tag{7.65}$$

Turbulent boundary layers which form on a constant temperature surface with a constant free-stream velocity have an outer region similarity; moreover, in the presence of mass transfer, both thermal and momentum boundary layers approach an equilibrium state when the transpiration parameter B is constant [126, 26]

$$B = \frac{\rho_i v_i}{\rho_\infty u_\infty (f_{i,0}/2)} = const \tag{7.66}$$

In studying condensation phenomena, such a condition can be simply reached analyzing a rectangular channel case with imposed condensing temperature and non interacting momentum boundary layers. Far from the inlet section of the channel, when the flow is fully developed, the transpiration parameter is expected to be reasonably constant; conditions for an equilibrium boundary layer are then reached.

Selected geometry

The selected geometry consists of a 2D rectangular channel (see Fig. 7.12), representative of the CONAN facility geometry, already adopted in the frame of the benchmark-0 exercise (see chapter 3). The computational domain height is 2.0 m and the width is 0.34 m. The mixture enters the channel in downward flow at the channel top, parallel to gravity. The right vertical wall is adiabatic, while a uniform temperature profile is imposed on the vertical left wall. A pressure

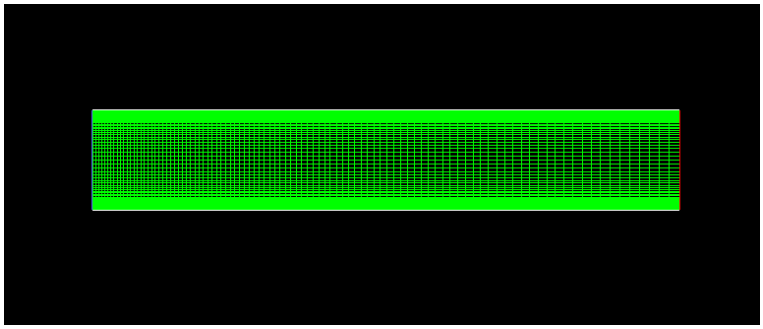

Figure 7.13: Space discretisation of the rectangular channel adopted for the numerical analysis

Test name	U_{inlet} $[m/s]$	T_w $[°C]$	T_{inlet} $[°C]$	$Y_{v,inlet}$ [-]	P $[Pa]$
HT-60-6	6	60.0	90.0	0	101325
HT-30-6	6	30.0	90.0	0	101325
HMT-60-6	6	60.0	90.0	saturation:0.5831	101325
HMT-30-6	6	30.0	90.0	saturation:0.5831	101325

Table 7.4: Selected Boundary Conditions

outlet boundary condition is used at the channel bottom. In the figure 7.13, the space discretisation employed for the simulations is shown. The grid is refined near the inlet section (left side of the figure) and near the lateral walls, according to the requirements of the different turbulence models.

Selected boundary conditions

Forced convection conditions are addressed. Important condensation rates are achieved to better put into evidence the effects of suction. Flat profile for mixture velocity, temperature, turbulence intensity and vapor mass fraction are imposed at the inlet surface. Steam is assumed to be in saturation condition. The temperature on the condensing surface is also assumed uniform. In the table 7.4, the specified boundary conditions are summarized.

7.5.1 Methodology of the heat transfer cases analysis

The capabilities of the model to solve a simple heat transfer case without mass transfer are checked on the basis of common correlations for Nusselt and Stanton numbers, friction coefficient, nondimensional stream velocity and temperature profiles. In forced convection pure heat transfer conditions, the correlation for friction coefficient is the Schlichting's [115]

$$\frac{f_{i,0}}{2} = 0.0296 Re_x^{-0.2} \tag{7.67}$$

On the basis of the momentum and heat transfer analogy, the corresponding Nusselt number can be expressed by:

$$\frac{Nu_x}{Pr^{0.33}} = 0.0296 Re_x^{0.8} \tag{7.68}$$

The Stanton number can be predicted by means of a correlation proposed by Kader [128]:

$$St_x = \frac{Nu_x}{Re_x Pr} = \frac{\sqrt{C_f/2}}{2.12\ln(Re_x C_f) + 12.5Pr^{2/3} + 2.12\ln(Pr) - 7.2} \tag{7.69}$$

Available correlations for nondimensional velocity profiles are the well known Van Driest's [124] and the Reichardt's [125] ones. The calculated U^+ velocity is here compared with the Reichardt's profile defined by the following correlation

$$u^+ = \frac{1}{0.41}\ln[1 + 0.41y^+] + 7.8\left[\left(1 - exp\left(-\frac{y^+}{11}\right)\right) - \frac{y^+}{11}\ exp(-\frac{y^+}{3})\right] \tag{7.70}$$

Nondimensional temperature profile correlations are also proposed by Kader for shear flow conditions [129]. The calculated nondimensional temperature Θ^+, defined as

$$\Theta^+ = (T - T_w)/\Theta^* \tag{7.71}$$

with

$$\Theta^* = \dot{q}^{''}/(Cp\sqrt{\tau_w \rho}) \tag{7.72}$$

is compared with the Kader's Θ^+, given by

$$\Theta^+ = y^+ exp(-\Gamma)Pr + \left[2.12\left([1 + y^+]\frac{2.5(2 - y/\delta_T)}{1 + 4(1 - y/\delta_T)^2}\right) + \beta(Pr)\right] exp(-1/\Gamma) \tag{7.73}$$

with

$$\beta(Pr) = (3.85Pr1/3 - 1.3)^2 + 2.12\ln(Pr) \tag{7.74}$$

$$\Gamma = \frac{0.01(Pry^+)^4}{1 + 5Pr^3 y^+} \tag{7.75}$$

and δ_T is the thickness of the thermal boundary layer.

7.5.2 Methodology of the heat & mass transfer cases analysis

Once the capabilities of the model are tested in predicting pure heat transfer phenomena, the analogous mass transfer cases are addressed. The actual Sherwood number is obtained from calculations as

$$Sh_x = \frac{\dot{m}^{''} x}{\rho_f D_{vm,f}\left(\frac{Y_{v,i} - Y_{v,b}}{1 - Y_{v,i}}\right)} \tag{7.76}$$

The corresponding Sherwood number for low mass transfer rates, as given by the analogy between heat and mass transfer, can be resumed by dividing the previous number by the Stefan suction factor introduced in chapter 2

$$Sh_{0,x} = Sh_x/F \tag{7.77}$$

where

$$F = \frac{\Phi_m}{e^{\Phi_m} - 1} \tag{7.78}$$

and

$$\Phi_m = \frac{\dot{m}_i^{''}}{h_{m,0}} \tag{7.79}$$

Finally, the Sherwood number for low mass transfer rates can be written as

$$Sh_{0,x} = \frac{\dot{m}^{''} x}{\rho_f D_{vm,f} \ln\left(\frac{Y_{nc,b}}{Y_{nc,i}}\right)} \tag{7.80}$$

The calculated Sh_0 number is therefore compared with the Sherwood number evaluated on the basis of the analogy between heat and mass transfer, expressed by the following relationship:

$$\frac{Sh_{0,x}}{Sc^{0.33}} = 0.0296 Re_x^{0.8} \tag{7.81}$$

A good agreement is expected between the two curves in the Reynolds number region corresponding to turbulence (approximately $Re_x > 10^5$), even if the Stefan suction factor F is suspected to be overestimating transpiration effects in case of condensation [122]. Due to transpiration phenomena, the friction coefficient and the Nusselt number are increased with respect to the pure heat transfer case. The agreement between the computational results and the available correlations for correcting the Nusselt number and the friction coefficient in the presence of transpiration phenomena are checked. In particular, the agreement with the Ackermann correction factor [25] is investigated in relation to the Nusselt number via the heat transfer coefficient

$$A_f = \frac{h_s}{h_{s,0}} = \frac{\Phi_t}{e^{\Phi_t} - 1} \tag{7.82}$$

where

$$\Phi_t = \frac{\dot{m}_{v,i}^{''} Cp_{v,i}}{h_{s,0}} \tag{7.83}$$

For friction, a correlation proposed by Kays and Moffat is considered [26]:

$$M_f = \left.\frac{f_i}{f_{i,0}}\right|_{Re_x} = \frac{ln(1+\Phi_v)}{\Phi_v} \tag{7.84}$$

where Φ_v is equal to B defined by equation 7.66.

7.6 Results of the numerical analysis

Two heat transfer cases and the corresponding heat and mass transfer cases have been addressed with the HMTDM^{EBD} model[2] (see table 7.4). Four different turbulence models with low Reynolds capabilities have been tested: the RNG $\kappa-\varepsilon$ with the *Two-Layer Model* (RNG K-E TLM) [123], the Yang-Shih (YS) [121] and the Abe-kondoh-Nagano (AKN) [120] low Re $\kappa-\varepsilon$ models and the Wilcox's $\kappa-\omega$ (K-W) model [119].

[2]The HMTDM^{EBD} and the HMTDM^{MSD} models reduce to the same model for binary mixture

test case	AKN	YS	K-W	RNG K-E TLM
HMT-30-6	0.00959	0.00946	0.00993	0.01039
HMT-60-6	0.00811	0.00779	0.00883	0.00878

Table 7.5: Condensation rate comparison $[kg/s]$

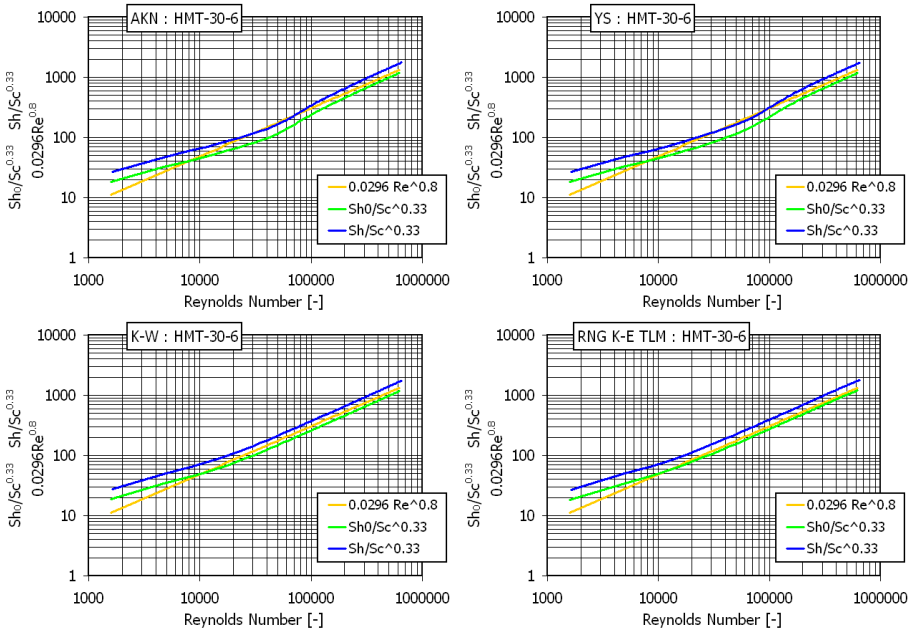

Figure 7.14: Sherwood number in the 30-6 test cases: Abe et al. low Re $\kappa-\varepsilon$ (top-left), Yang-Shih low Re $\kappa-\varepsilon$ (top-right), $\kappa-\omega$ low Re $\kappa-\varepsilon$ (bottom-left) and RNG $\kappa-\varepsilon$ (right) with Two-layer model (bottom-right)

In figures 7.14 and 7.15, the calculated Sherwood number for low mass transfer rates (green line) evaluated by equation 7.76 and divided by the $Sc^{0.33}$ is compared with the Schlichting correlation for forced convection (yellow line) defined by Eq. (7.81). The actual Sherwood number (blue line) is also reported, being the difference between the actual Sherwood number and the Sherwood number for low mass transfer rates representative of the calculated suction effect. As expected, the suction effect has an increasing relevance for higher and higher mass transfer fluxes. The difference between the actual Sherwood number and the corrected one is in fact larger in the HMT-30-6 test case at higher condensation rates (see Tab. 7.5). However, as already observed in a parallel work [122], the widely employed Stefan correction factor is suspected to overestimate the effect of transpiration in condensation, whereas it seems to work more accurately in evaporation. In the fully turbulent region, all turbulence model behave in a very similar way. The obtained differences in the overall condensation rates (see table 7.5) are likely due to the different behavior of the models in the inlet region, due to the different ways of the model in treating the boundary layer transition region. Due to transpiration, the friction coefficient is also modified with respect to the pure heat transfer cases. In the figures from 7.16

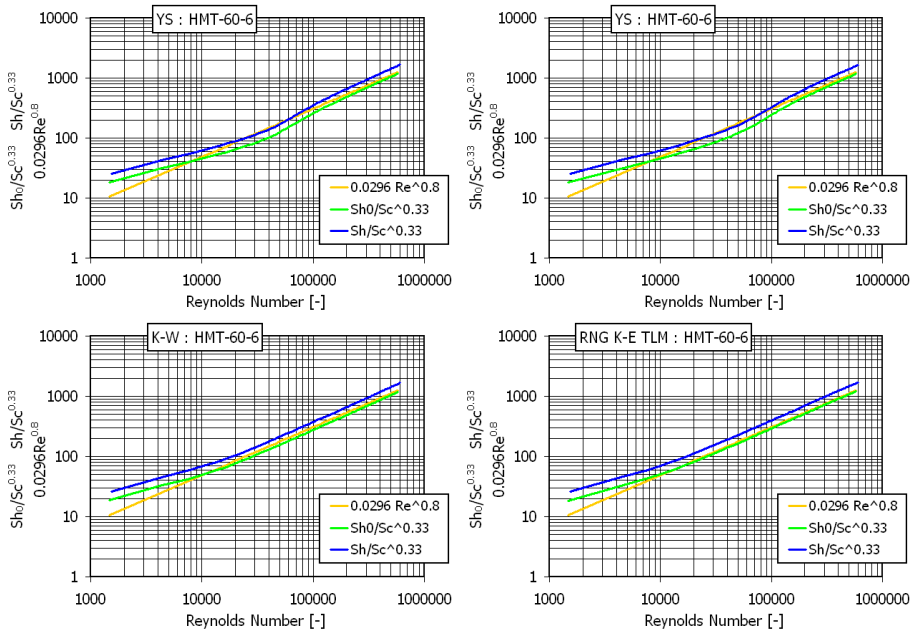

Figure 7.15: Sherwood number in the 60-6 test cases: Abe et al. low Re $\kappa-\varepsilon$ (top-left), Yang-Shih low Re $\kappa-\varepsilon$ (top-right), $\kappa-\omega$ low Re $\kappa-\varepsilon$ (bottom-left) and RNG $\kappa-\varepsilon$ (right) with Two-layer model (bottom-right)

to 7.17, the calculated friction coefficients in the pure heat transfer cases (orange line) are compared with the values predicted by the Schlichting correlation (green line). The computed friction coefficient is also reported for the heat & mass transfer cases (white blue line), compared with the friction coefficient predicted by the Kays and Moffat correction (red line) [26] (see Eq. (7.84)) on the basis of the pure heat transfer friction coefficient and the local condensation mass flux. It is remarkable that, for the two heat transfer cases, the turbulence models are able to fit the Schlichting correlation, but the low Reynolds $\kappa-\varepsilon$ models provide a different slope in the asymptotic region corresponding to high Reynolds number values. Despite of that, for all models, the proposed Kays and Moffat correction factor allows predicting the friction coefficient calculated in the mass transfer cases with a good accuracy. In particular, the accuracy of the RNG $\kappa-\varepsilon$ TLM and the $\kappa-\omega$ model is remarked. The same reasoning concerns also heat transfer; in the following figures from 7.18 to 7.19 are reported the classical turbulent heat transfer correlation for Nusselt number (yellow line), the Nusselt number computed in the pure heat transfer cases (red line), the Nusselt number computed in the mass transfer cases (green line) and the Nusselt number predicted by the Ackermann correction (blue line) [25] (see Eq. (7.82)) on the basis of the pure heat transfer Nusselt number and the local condensation mass flux. It is remarkable that the pure convective Nusselt number is perfectly captured by all models and the Ackermann correction seems to work outstandingly. From figure 7.20 to figure 7.21, a comparison between the calculated Stanton number and the correlation proposed by Kader (see Eq. (7.69)) for pure heat transfer. As a consequence of the good behavior in

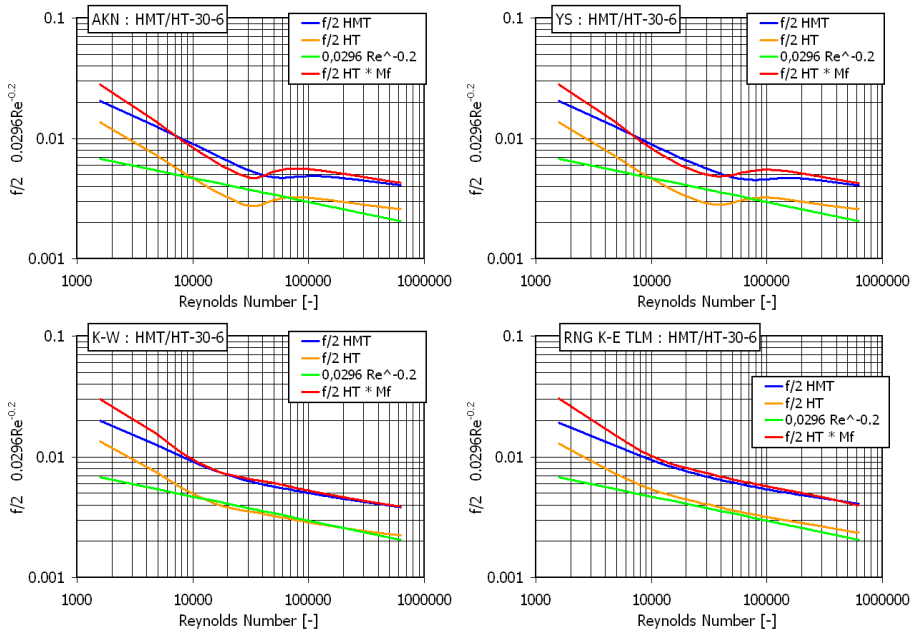

Figure 7.16: Friction coefficient in the 30-6 test cases: Abe et al. low Re $\kappa-\varepsilon$ (top-left), Yang-Shih low Re $\kappa-\varepsilon$ (top-right), $\kappa-\omega$ low Re $\kappa-\varepsilon$ (bottom-left) and RNG $\kappa-\varepsilon$ (right) with Two-layer model (bottom-right)

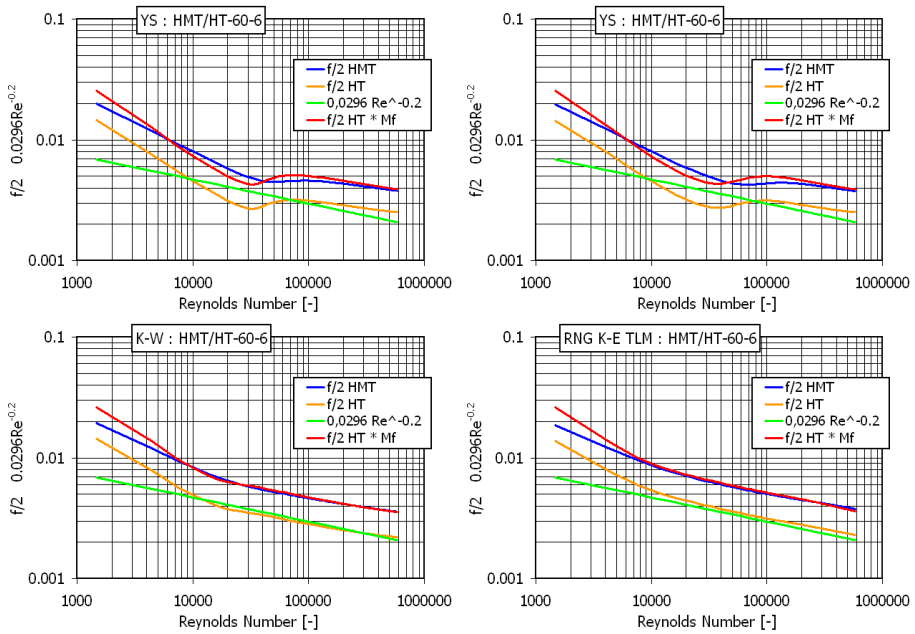

Figure 7.17: Friction coefficient in the 60-6 test cases: Abe et al. low Re $\kappa-\varepsilon$ (top-left), Yang-Shih low Re $\kappa-\varepsilon$ (top-right), $\kappa-\omega$ low Re $\kappa-\varepsilon$ (bottom-left) and RNG $\kappa-\varepsilon$ (right) with Two-layer model (bottom-right)

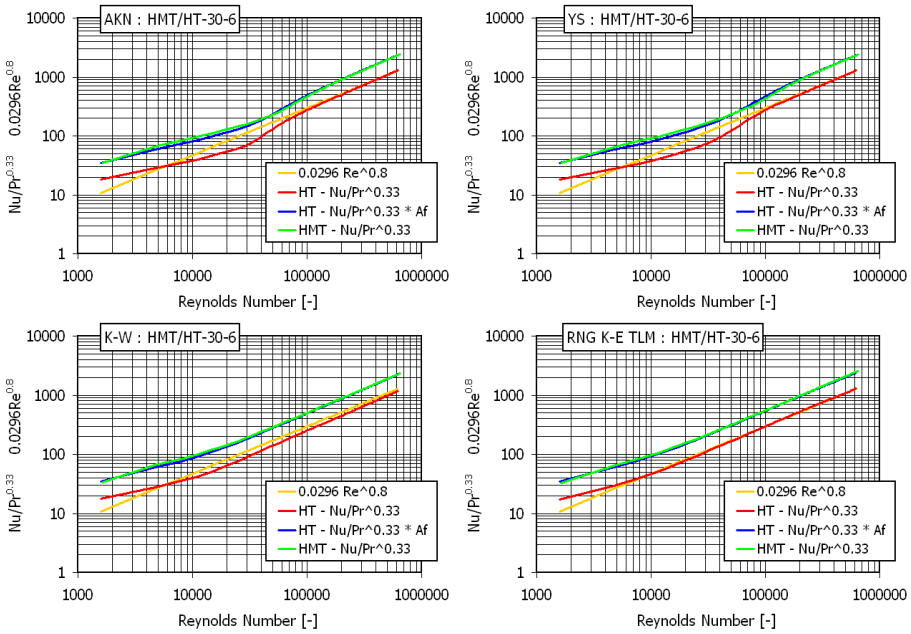

Figure 7.18: Nusselt number in the 30-6 test cases: Abe et al. low Re $\kappa - \varepsilon$ (top-left), Yang-Shih low Re $\kappa - \varepsilon$ (top-right), $\kappa - \omega$ low Re $\kappa - \varepsilon$ (bottom-left) and RNG $\kappa - \varepsilon$ (right) with Two-layer model (bottom-right)

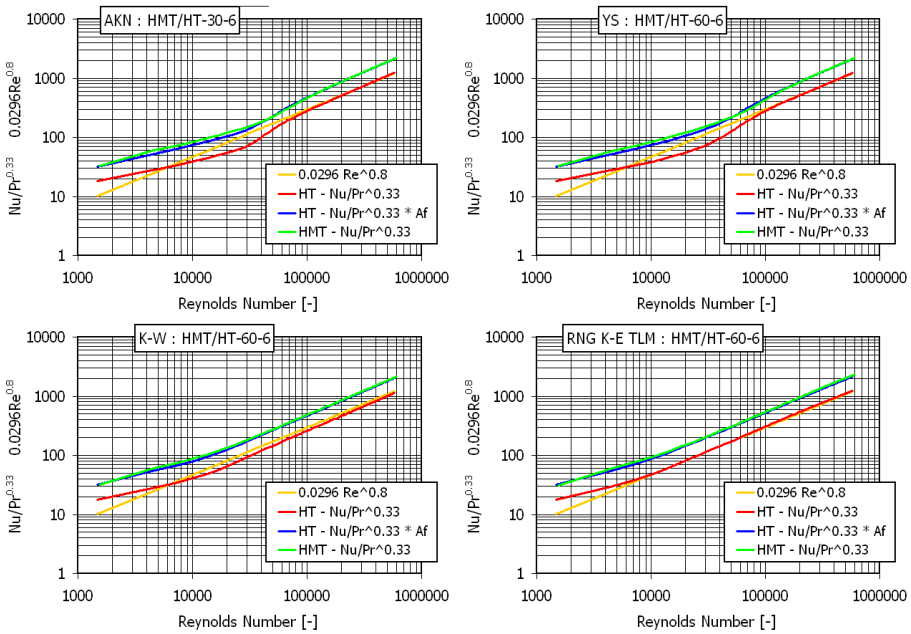

Figure 7.19: Nusselt number in the 60-6 test cases: Abe et al. low Re $\kappa - \varepsilon$ (top-left), Yang-Shih low Re $\kappa - \varepsilon$ (top-right), $\kappa - \omega$ low Re $\kappa - \varepsilon$ (bottom-left) and RNG $\kappa - \varepsilon$ (right) with Two-layer model (bottom-right)

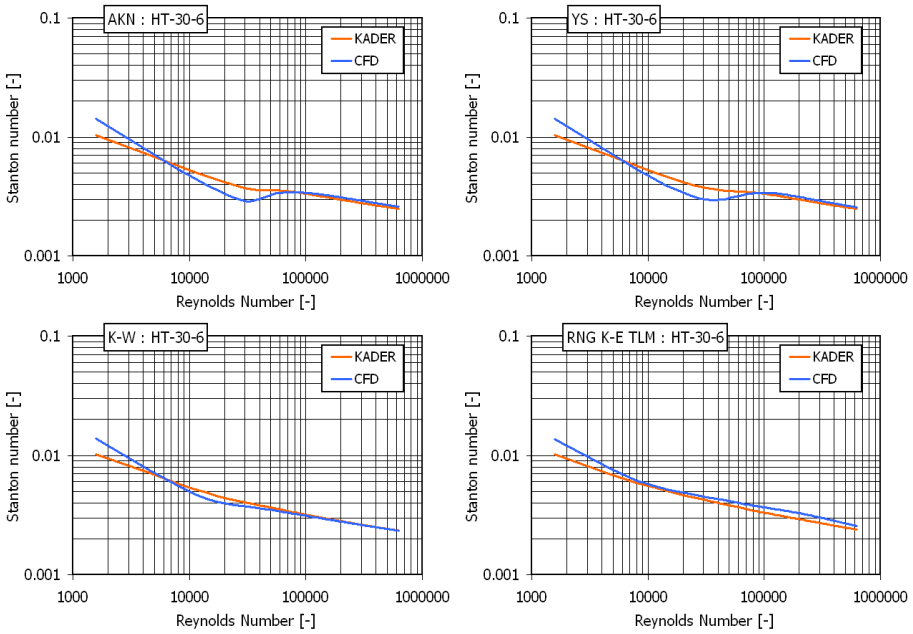

Figure 7.20: Stanton number in the HT-30-6 test case: Abe et al. low $Re\ \kappa-\varepsilon$ (top-left), Yang-Shih low $Re\ \kappa-\varepsilon$ (top-right), $\kappa-\omega$ low $Re\ \kappa-\varepsilon$ (bottom-left) and RNG $\kappa-\varepsilon$ (right) with Two-layer model (bottom-right)

reproducing the Nusselt number, the calculated Stanton number shows a good agreement with the proposed correlation in the heat transfer cases; obviously, the Stanton number is affected by transpiration effect in the same way as the Nusselt number.

The effect of transpiration on the different coefficients and nondimensional numbers are shown in figure 7.22 and 7.23, where the different nondimensional numbers and the friction coefficent are reported normalized by the corresponding pure heat trnafer values. Whereas the Stefan suction factor is constant (since the interface temperature is constant and so is the mixture interface composition in binary mixtures), the Ackermann and the Kays and Moffat coefficients, as well as the ratio between the pure heat transfer and the heat and mass transfer Stanton numbers vary along the channel length according to the mass transfer rate. In particular, the turbulence models behave differently in the first part of the channel. According to the analogy between momentum, heat and mass transfer, the different transpiration factors trends are similar in the fully developed flow region of the channel. A remarkably higher Ackermann factor is experienced in all cases, probably due to mixture composition differences between the heat transfer cases and the mass transfer ones.

The figures 7.24 and 7.25, on one side, and 7.26 and 7.27, on the other, show respectively the velocity and the temperature nondimensional profiles near the channel exit ($x = 1.8$ m). In the heat transfer cases, the agreement between the calculated nondimensional profiles and the Reichardt and Van Driest wall functions is very good with the RNG $\kappa-\varepsilon$ model, while some differences are

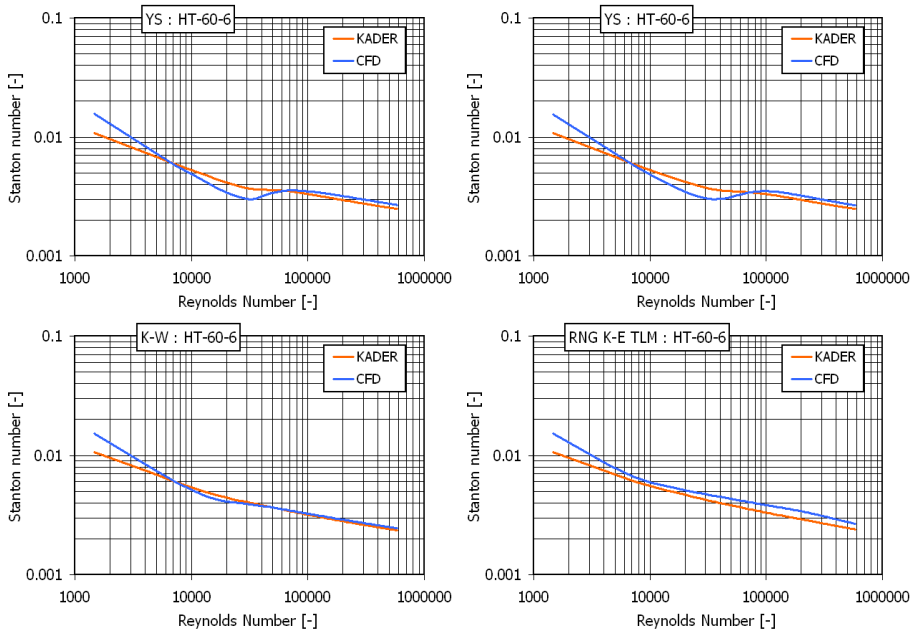

Figure 7.21: Stanton number in the HT-60-6 test case: Abe et al. low Re $\kappa-\varepsilon$ (top-left), Yang-Shih low Re $\kappa-\varepsilon$ (top-right), $\kappa-\omega$ low Re $\kappa-\varepsilon$ (bottom-left) and RNG $\kappa-\varepsilon$ (right) with Two-layer model (bottom-right)

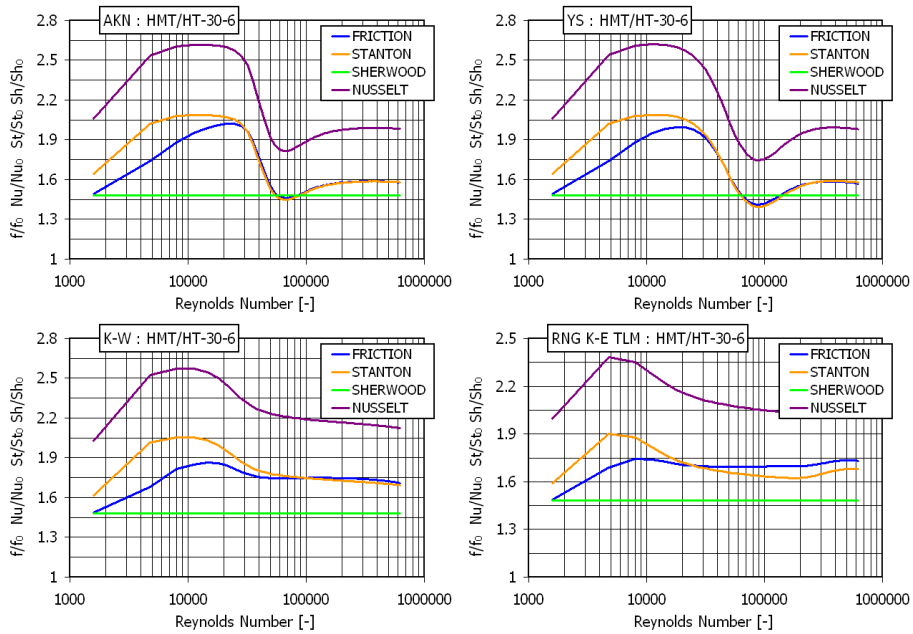

Figure 7.22: Transpiration factors in the 30-6 test cases: Abe et al. low Re $\kappa-\varepsilon$ (top-left), Yang-Shih low Re $\kappa-\varepsilon$ (top-right), $\kappa-\omega$ low Re $\kappa-\varepsilon$ (bottom-left) and RNG $\kappa-\varepsilon$ (right) with Two-layer model (bottom-right)

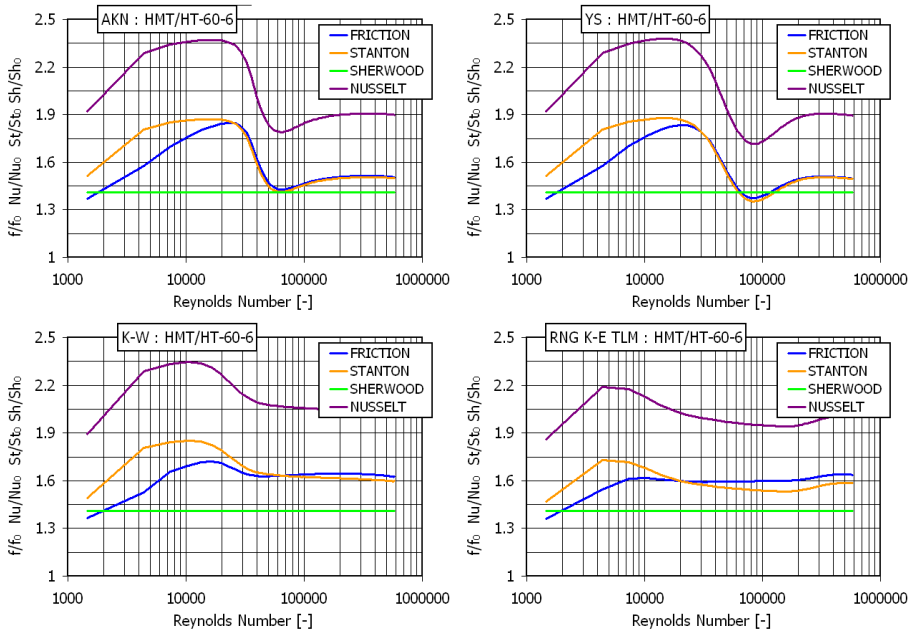

Figure 7.23: Transpiration factors in the 60-6 test cases: Abe et al. low Re $\kappa-\varepsilon$ (top-left), Yang-Shih low Re $\kappa-\varepsilon$ (top-right), $\kappa-\omega$ low Re $\kappa-\varepsilon$ (bottom-left) and RNG $\kappa-\varepsilon$ (right) with Two-layer model (bottom-right)

experienced with the low Reynolds $\kappa-\varepsilon$ models and the $\kappa-\omega$ model[3]. In the mass transfer case, the nondimensional velocity profiles are well below the proposed functions; in fact, as mentioned in paragraph 7.4, the velocity boundary layer is thinner when higher mass transfer fluxes are achieved, but, for the same reason, the friction coefficient is also increased. Since the friction coefficient increases, it follows that the shear velocity U^* is increased. The nondimensional velocity U^+ is thus decreased. The profiles of the nondimensional velocity for the mass transfer cases are therefore below those of the pure heat transfer cases, confirming the results of Favre. In Favre's experiences anyway the transpiration factors defined by equation 7.59 are constant. In condensation tests, due to species gradients, the density is not constant but, in the presence of air and steam for instance, it decreases monotonically from the interface to the bulk. As a consequence, the suction factor defined by Eq. (7.59) also decreases from the interface to the bulk. Indeed, in the figures from 7.24 to 7.25 it can be observed that, according to the previous remarks, the computed nondimensional transpiration velocities, defined by 7.61, are next to $A^+ = 0.053$ in the near wall region, whereas they are next to $A^+ = 0.023$ in the bulk region. Differences in the profiles for the heat transfer cases are experienced in the outer turbulent region of the boundary layer, but not in the laminar sublayer (See figures 7.26 and 7.27). Following the same reasoning as for nondimensional velocities, due to the in-

[3]The calculated nondimensional velocity profiles are traced normalized with respect to the shear velocity at the condensing surface and the nondimensional distance from the condensing surface. Points corresponding to the boundary layer near the adiabatic vertical wall (right side) are therefore not meaningful

creasing convective heat transfer flux, the Θ^+ decreases. Therefore, despite the temperature boundary layer is thinner, the nondimensional temperature profiles are well below those of the pure heat transfer cases.

7.6.1 Effect of fluid properties

In the previous Figs. 7.22 and 7.23, the predicted ratio between the nondimensional numbers in the mass transfer cases and the corresponding pure heat transfer cases were reported for the cases specified in the table 7.4. In these figures, a common trend of the different curves was remarked in the Reynolds number region corresponding to fully developed turbulent flow. However, the effective values of the different correction factor are quite different; the Nusselt correction factors in particular are considerably higher than the others. Actually, a steam-air mixture is flowing through the channel in the mass transfer cases, while only air is employed in the pure heat transfer calculations. The fluid properties are therefore supposed to influence the aforementioned effects.

In this section, a comparison is proposed between a mass transfer case and a pure heat transfer case obtained with the same air-steam mixture, in which the condensation source terms are numerically zeroed. Figures from 7.28 to 7.30 the Sherwood number, the Nusselt number and the friction coefficient are reported. In Fig. 7.31, a comparison among the different correction factors is proposed, in which it is shown that these vary in a narrower range for the fully turbulent flows with respect to the previous results for the analogous cases (see figure 7.23). Mixture composition is therefore likely to cause the experienced higher Nusselt values in the reference cases.

7.6.2 Momentum sources effect

In chapter 6, a description of the condensation models has been reported including the momentum source terms. The HMTDM models assign source terms of momentum in the cells in which the mass source terms are applied, only for the velocity component parallel to the condensing surface. Momentum sources for the velocity component orthogonal to the condensing surface are not usually applied. In the two following sections, the modelling is performed respectively neglecting or including both momentum sources, aiming at analysing the sensitivity of the solution on these terms.

No momentum sources

When no momentum source terms are applied, an higher stream velocity component is expected in the cells beside the condensing wall, since the specific momentum is increased. In these cells, due to the increased local velocity, the calculated friction coefficient is also increased, resulting higher than the one of the reference model (see Fig. 7.32). Due to the increasing friction coefficient, despite of the higher velocities in the first cells, the nondimensional velocity profile lies below the one calculated for the reference model (see figure 7.33). Similar effects are observed for the nondimensional temperature (see Fig. 7.34). On the other hand, the predicted Sh_0 and Nu are very similar to the reference model case (see figures 7.35 and 7.36). In figure 7.37, a comparison between the different nondimensional numbers is reported between the investigated case and

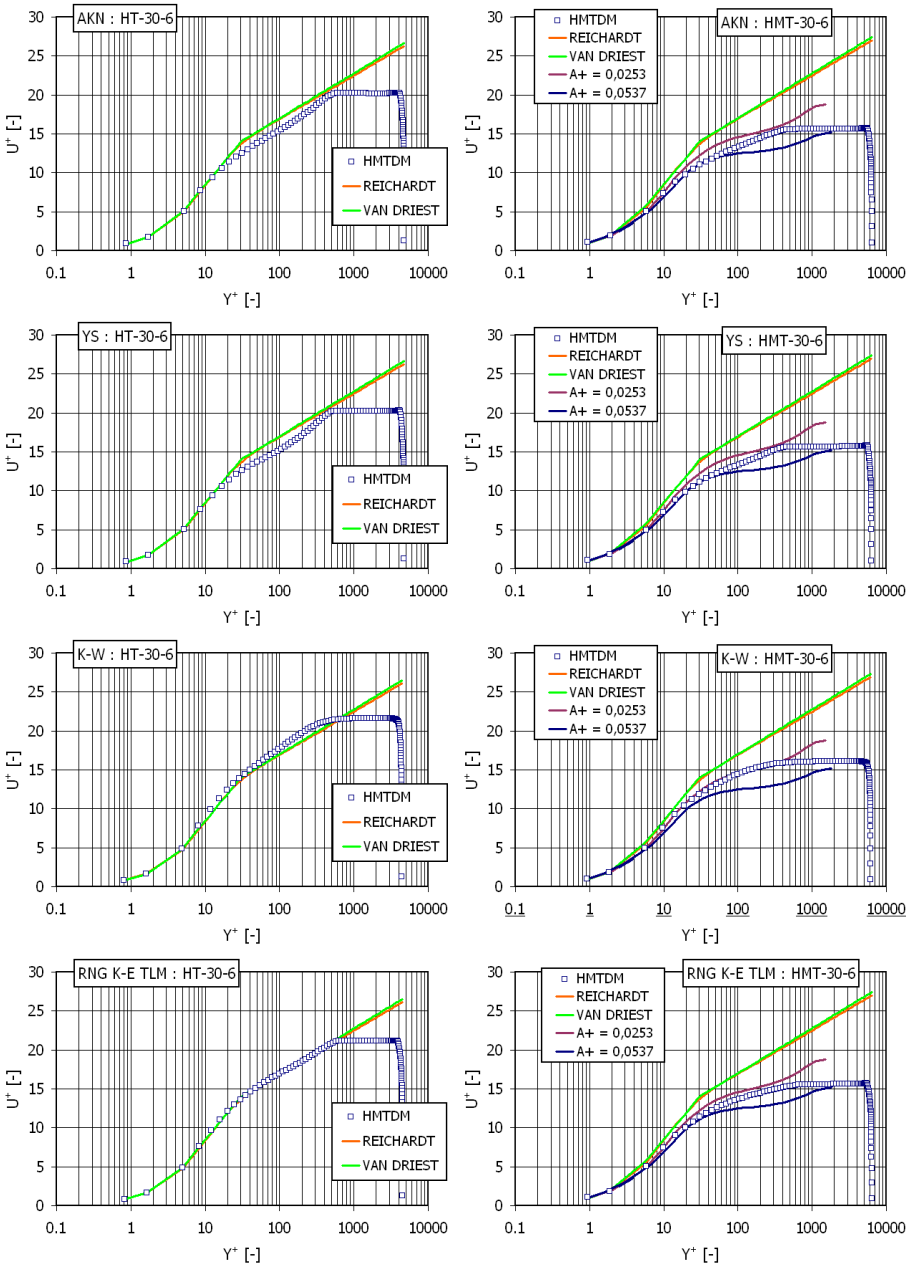

Figure 7.24: Nondimensional velocity in the 30-6 test cases: pure heat transfer cases (left figures) and heat & mass transfer cases (right figures)

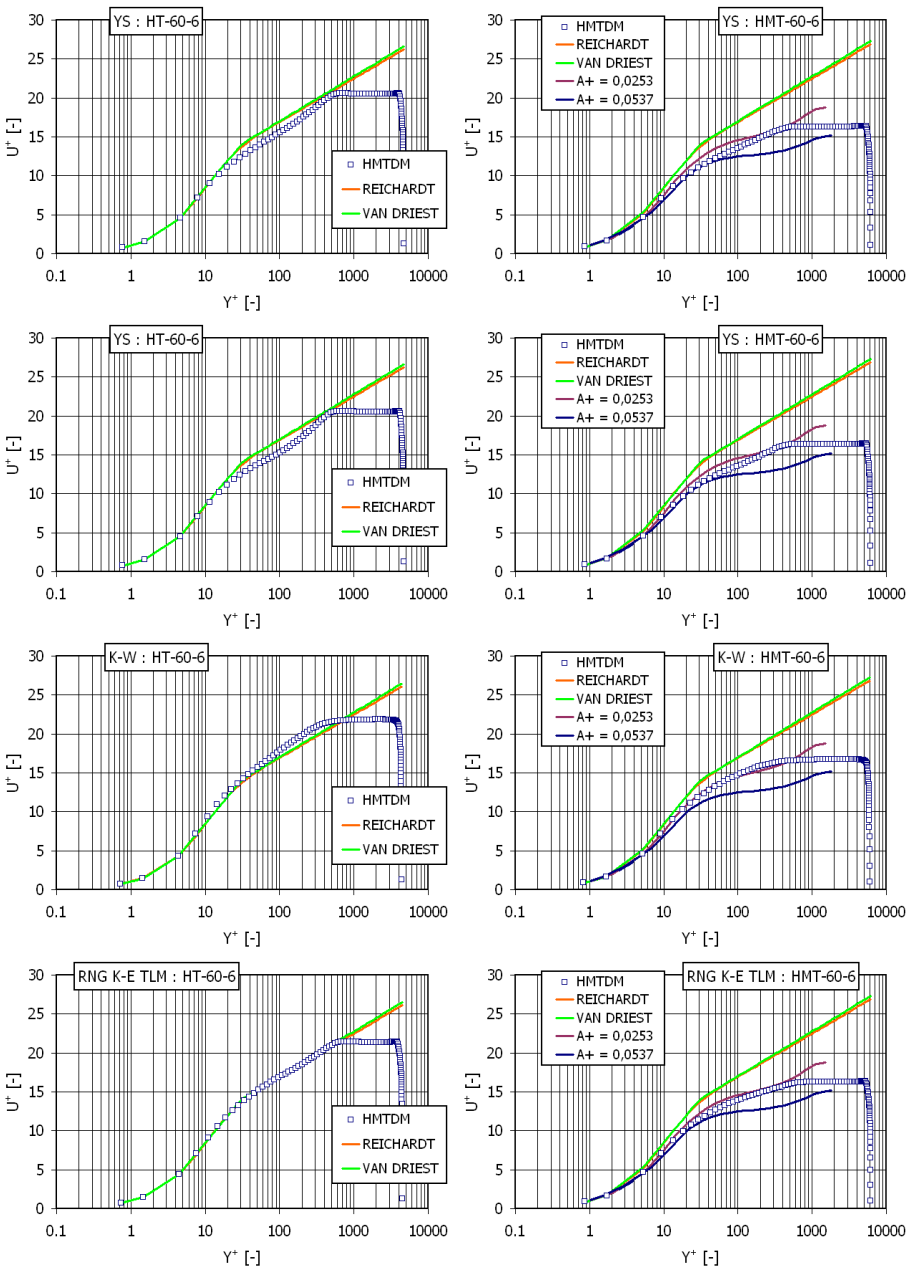

Figure 7.25: Nondimensional velocity in the 60-6 test cases: pure heat transfer cases (left figures) and heat & mass transfer cases (right figures)

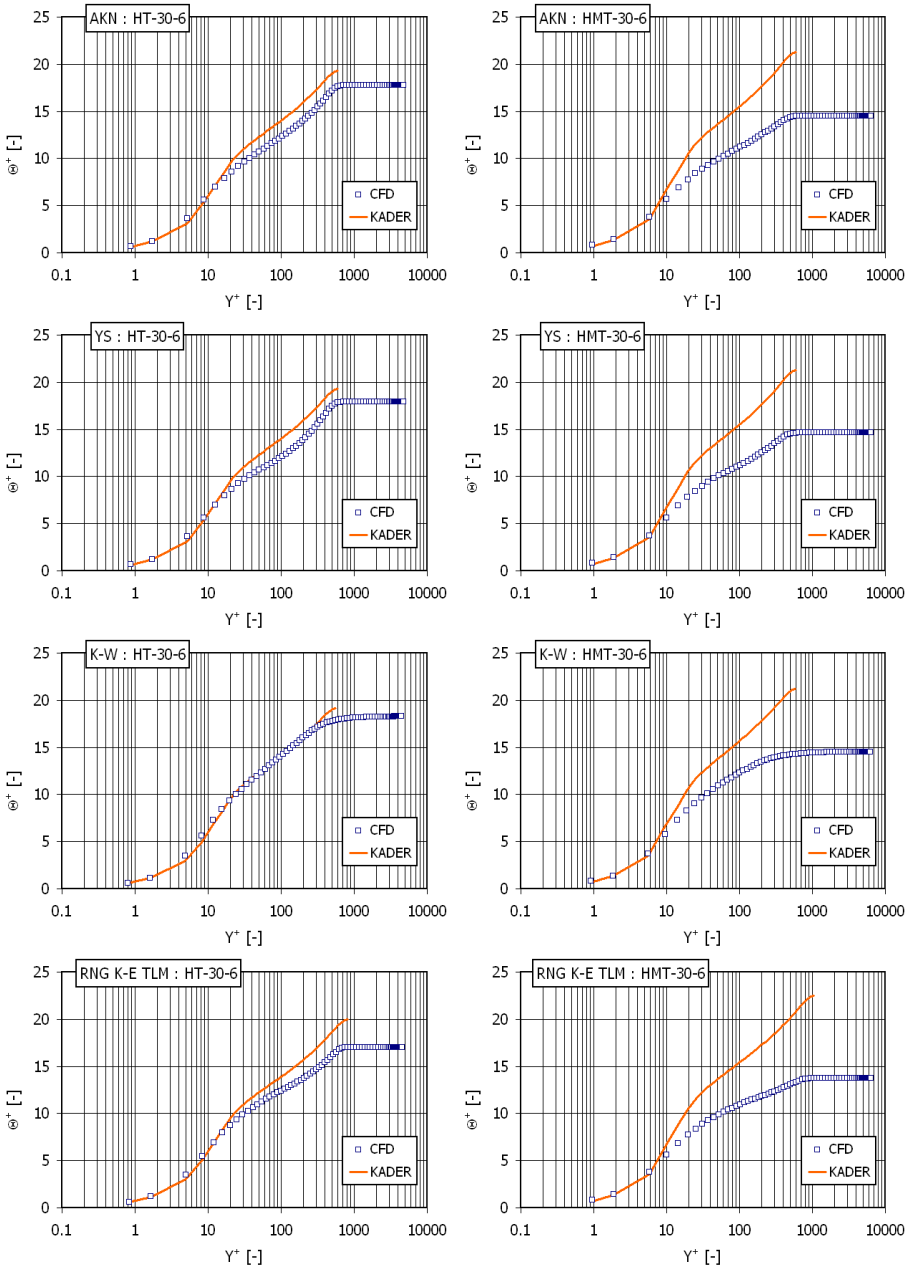

Figure 7.26: Nondimensional temperature in the 30-6 test cases: pure heat transfer cases (left figures) and heat & mass transfer cases (right figures)

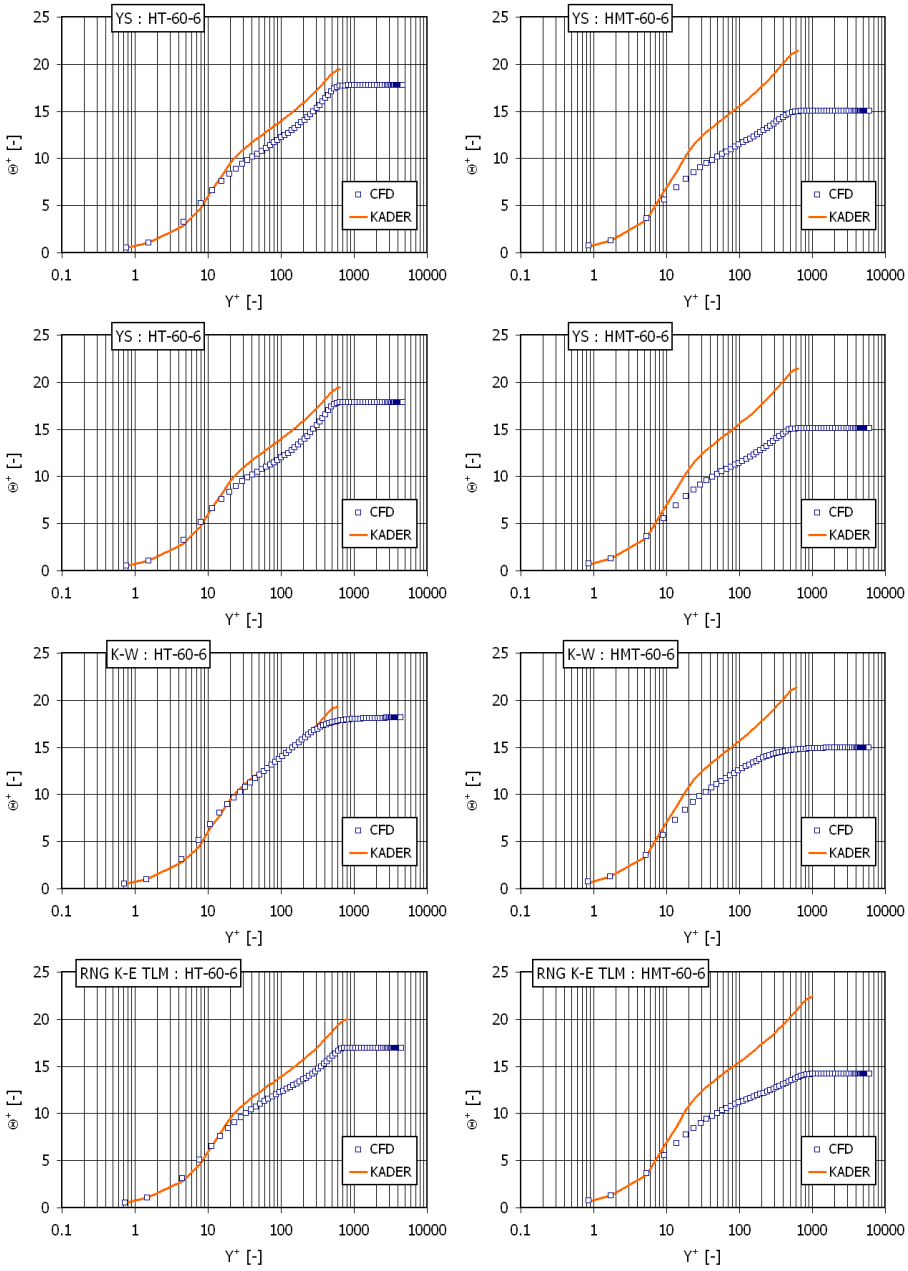

Figure 7.27: Nondimensional temperature in the 60-6 test cases: pure heat transfer cases (left figures) and heat & mass transfer cases (right figures)

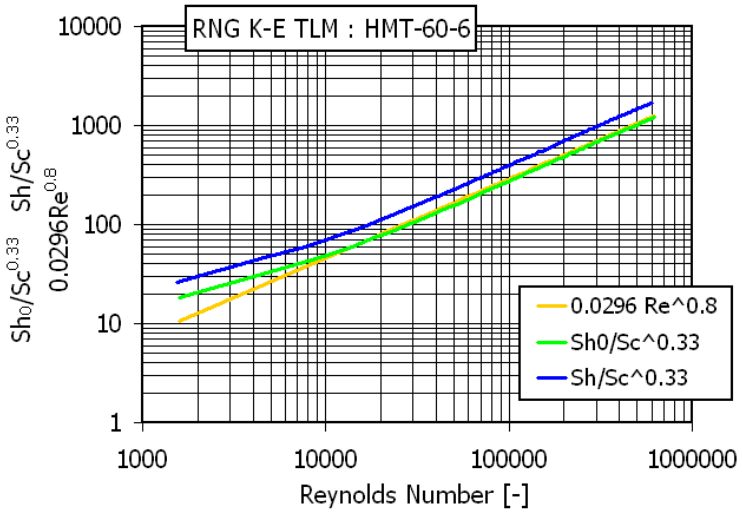

Figure 7.28: Sherwood number in the 60-6 test cases (HT case is run with same mixture composition than HMT-60-6, deactivating the condensation model): RNG $\kappa - \varepsilon$ turbulence models

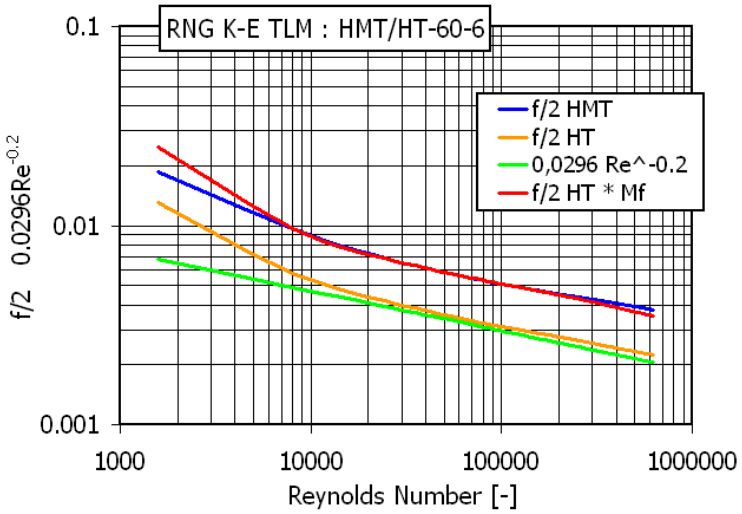

Figure 7.29: Friction Coefficient in the 60-6 test cases (HT case is run with same mixture composition than HMT-60-6, deactivating the condensation model): RNG $\kappa - \varepsilon$ (right) turbulence models

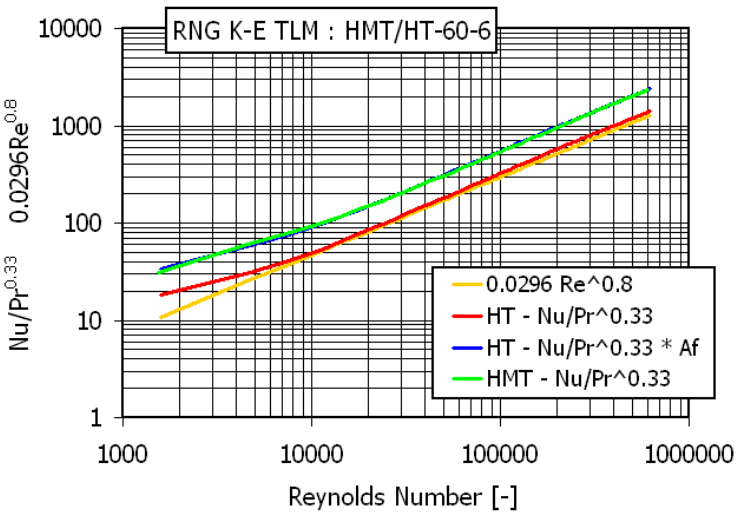

Figure 7.30: Nusselt number in the 60-6 test cases (HT case is run with same mixture composition than HMT-60-6, deactivating the condensation model): RNG $\kappa - \varepsilon$ (right) turbulence models

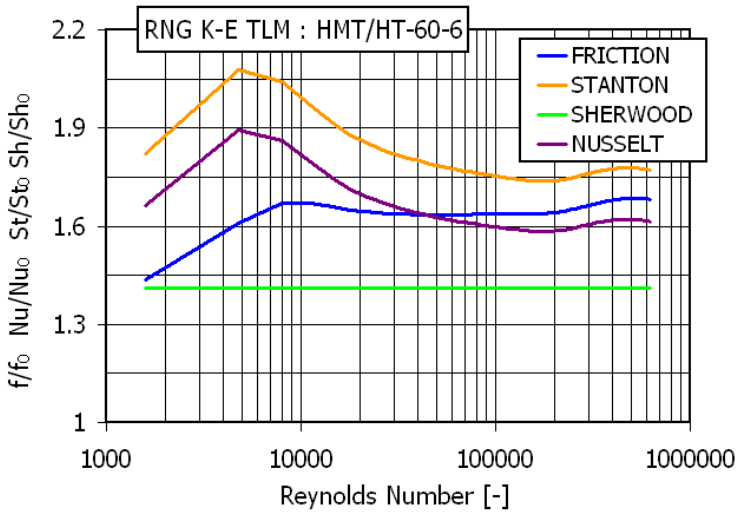

Figure 7.31: Transpiration Factors in the 60-6 test cases (HT case is run with same mixture composition than HMT-60-6, deactivating the condensation model): RNG $\kappa - \varepsilon$ (right) turbulence models

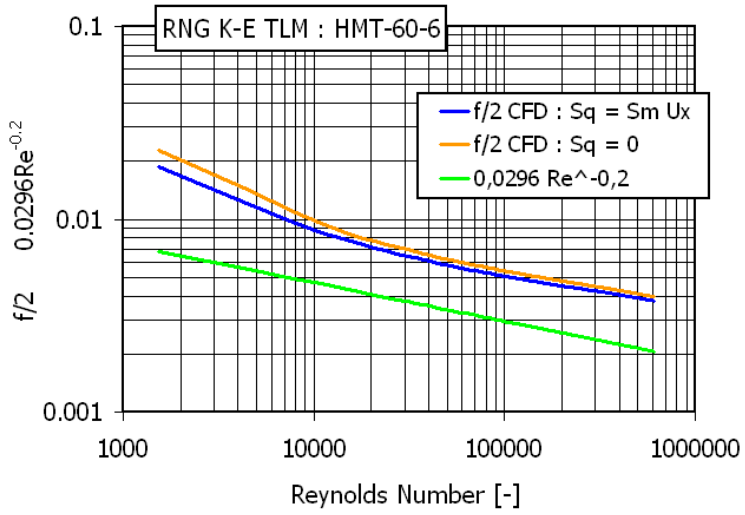

Figure 7.32: Friction coefficient in the 60-6 test cases (Effects of Momentum source on the Friction Coefficient: HMTDM vs. HMTDM without Momentum source terms)

the reference case. Being the Sherwood number very similar in the two cases, the calculated ratio between the two suction factors equals one very strictly. The Stanton ratio, representative also of the Nusselt ratio, is also more and less equal one. A remarkable difference is experienced for friction coefficients, being this one lower in the reference case than in the case in which the velocity source terms are neglected.

Momentum sources for both velocity directions

The effect of including both momentum sources is also addressed. A further momentum source for the velocity component orthogonal to the condensing wall is added to the reference model, given by the product of the source term of mass and the mixture velocity in the center of the cell, corresponding to the Stefan velocity of the mixture at the condensing interface. Since the actual steam velocity at interface is very small, a very small effect is experienced. Results are shown in figures from 7.38 to 7.43.

The nondimensional numbers, as well as the nondimensional profiles are strictly similar. No meaningful difference can then be noted with respect to the reference model. The source terms in direction orthogonal to the condensing wall can be therefore omitted.

7.7 Concluding remarks

In the aim to model turbulent condensation phenomena, several turbulence models have been analyzed. Four different models with low Reynolds number capabilities were considerd: the models of Yang and Shih, the model of Abe et al., the low Reynolds variant of the $\kappa - \omega$ model of Wilcox and the RNG $\kappa - \varepsilon$

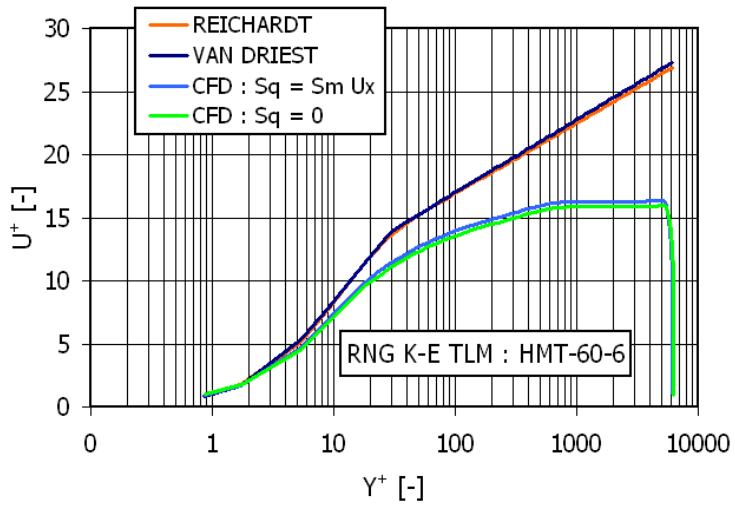

Figure 7.33: Sherwood number in the 60-6 test cases (Effects of Momentum source on the U^+ profile: HMTDM vs. HMTDM without Momentum source terms)

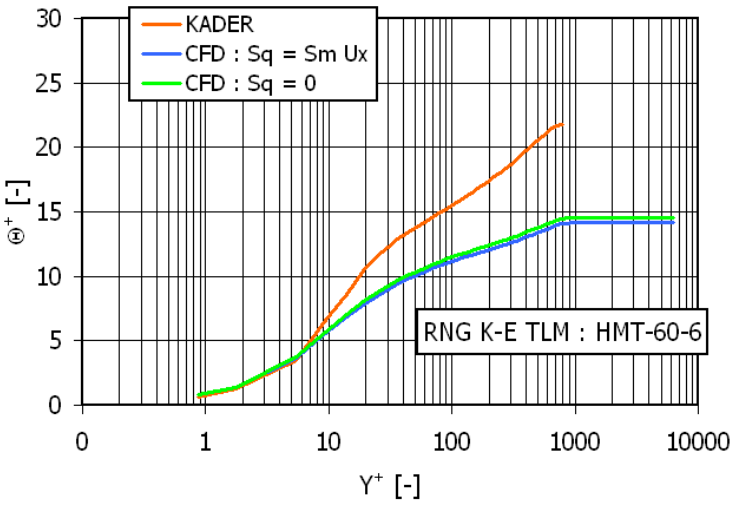

Figure 7.34: Sherwood number in the 60-6 test cases (Effects of Momentum source on the Θ^+ profile: HMTDM vs. HMTDM without Momentum source terms)

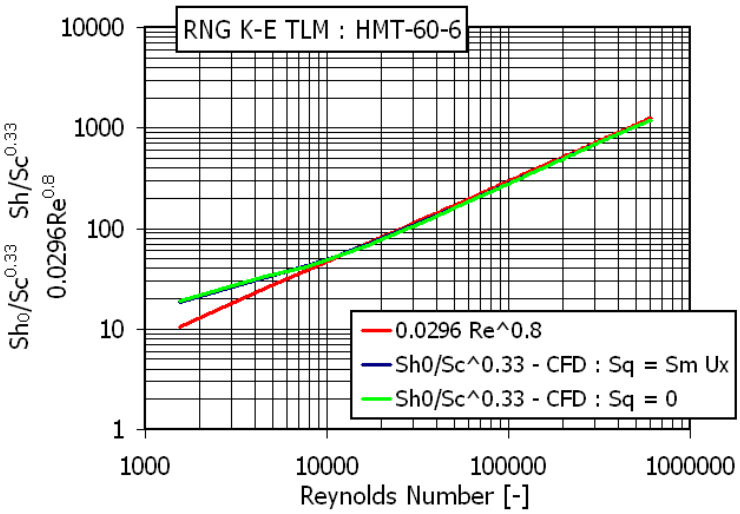

Figure 7.35: Sherwood number in the 60-6 test cases (Effects of Momentum source on the Sherwood Number: HMTDM vs. HMTDM without Momentum source terms

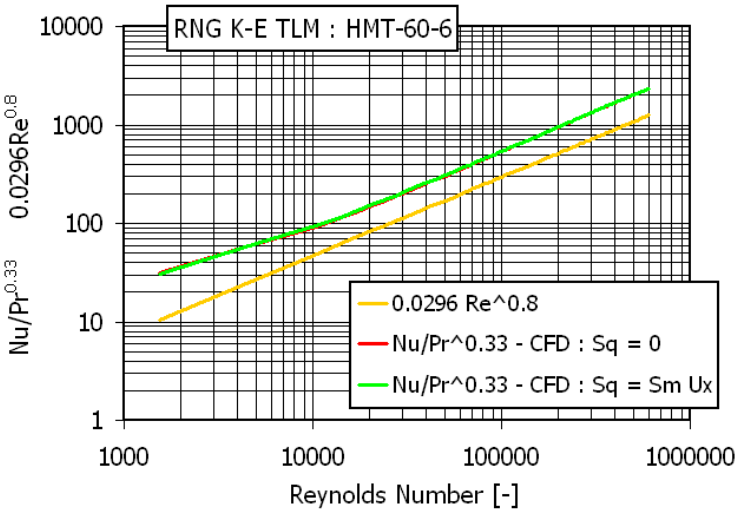

Figure 7.36: Nusselt number in the 60-6 test cases (Effects of Momentum source on the Nusselt Number: HMTDM vs. HMTDM without Momentum source terms)

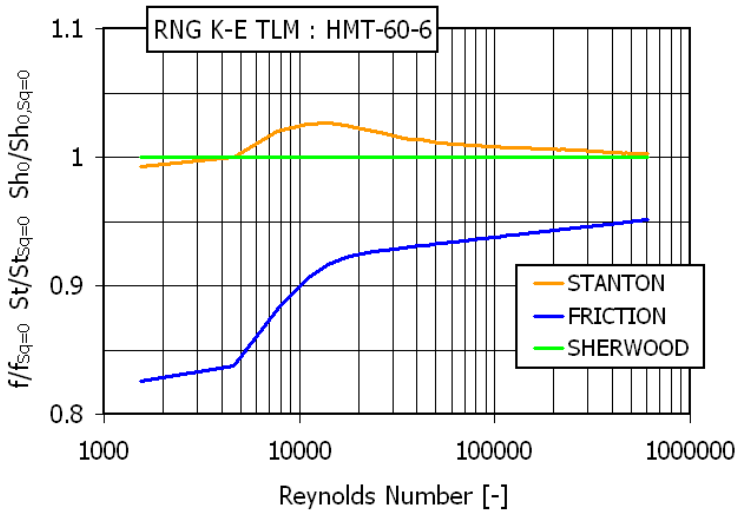

Figure 7.37: Nondimensional numbers ratio in the 60-6 test cases (Effects of Momentum source on the Transpiration Factors: HMTDM vs. HMTDM without Momentum source terms)

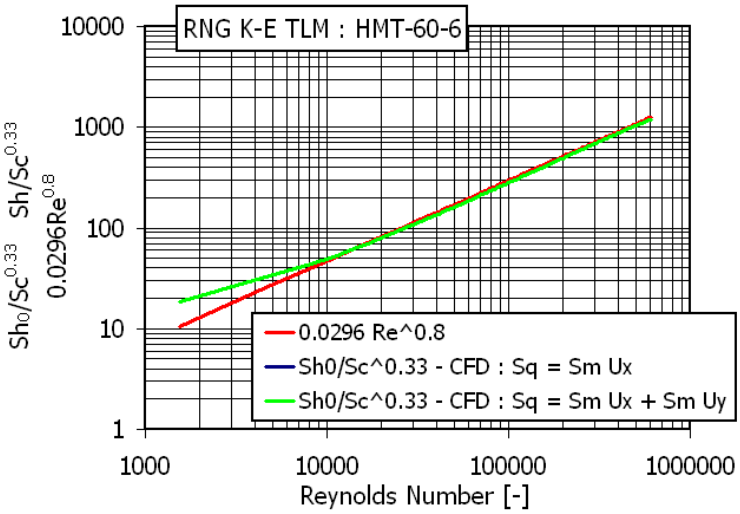

Figure 7.38: Sherwood number in the 60-6 test cases (Effects of Momentum source on the Sherwood Number: HMTDM vs. HMTDM with both Momentum source terms

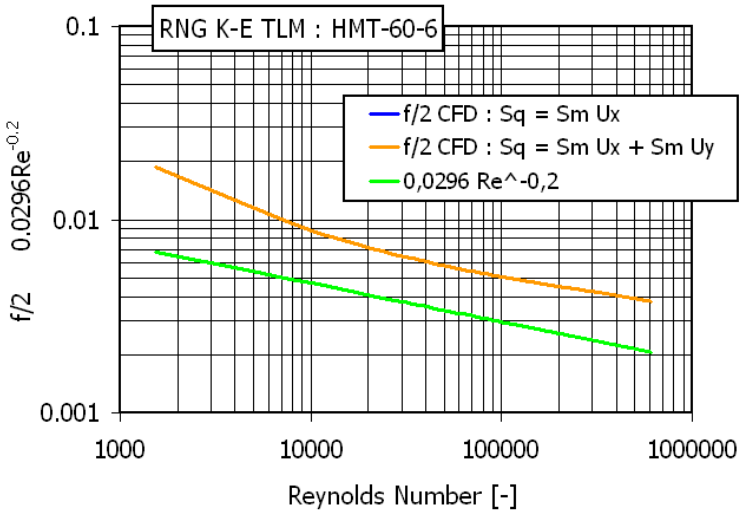

Figure 7.39: Sherwood number in the 60-6 test cases (Effects of Momentum source on the Friction Coefficient: HMTDM vs. HMTDM with both Momentum source terms

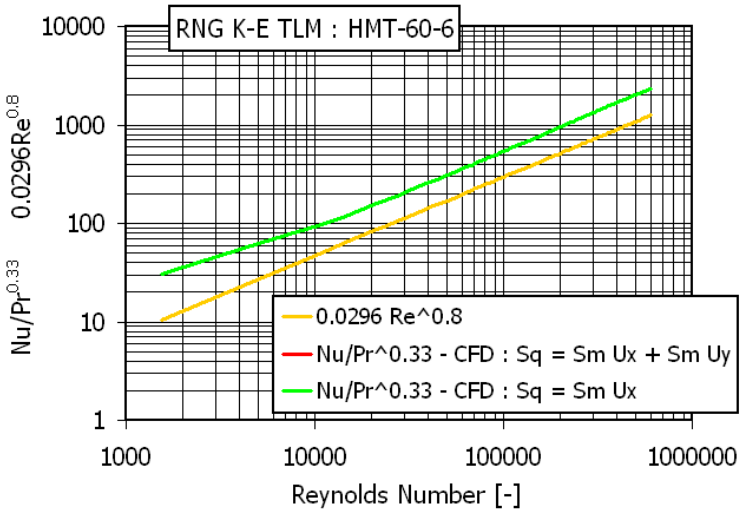

Figure 7.40: Sherwood number in the 60-6 test cases (Effects of Momentum source on the Nusselt Number: HMTDM vs. HMTDM with both Momentum source terms

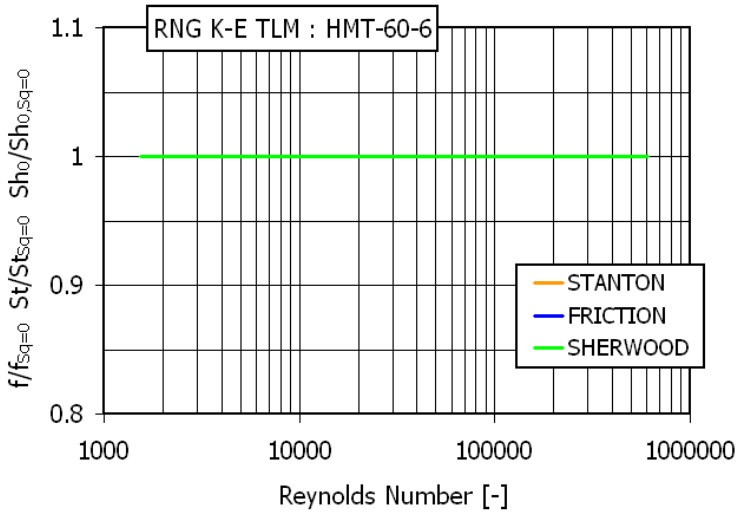

Figure 7.41: Sherwood number in the 60-6 test cases (Effects of Momentum source on the Transpiration Factors: HMTDM vs. HMTDM with both Momentum source terms

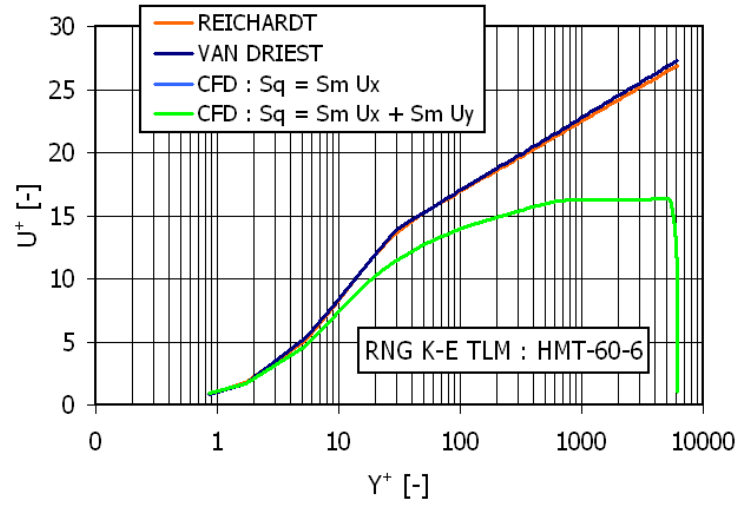

Figure 7.42: Sherwood number in the 60-6 test cases (Effects of Momentum source on the U^+ profile: HMTDM vs. HMTDM with both Momentum source terms

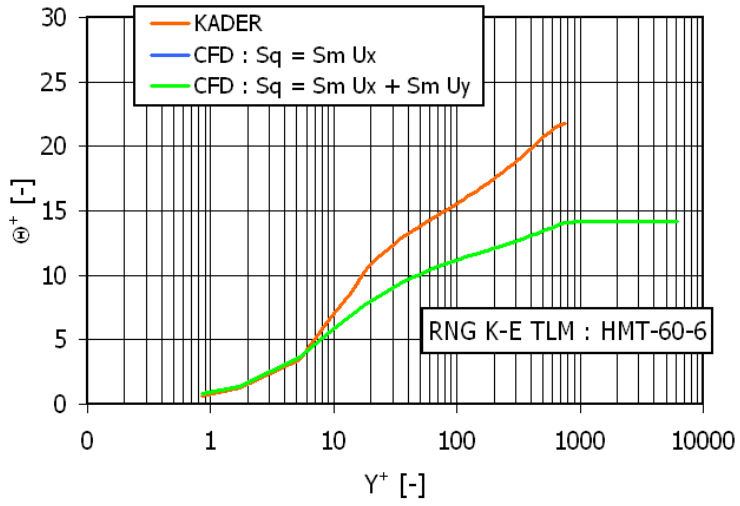

Figure 7.43: Sherwood number in the 60-6 test cases (Effects of Momentum source on the Θ^+ profile: HMTDM vs. HMTDM with both Momentum source terms

model with a two-layer model for the near-wall region. These models are appropriate to be used with a HMTDM condensation model: indeed, both turbulence and condensation models requires a very fine near-wall spatial discretization. The HMTAM model, aiming at performing fast-running large scale simulations is instead conceived to allow using coarser near-wall discretization. The RNG $\kappa - \varepsilon$ turbulence model based with standard wall function is proposed to deal with turbulence, coupled with the HMTAM model.

The HMTDM models represent a powerful tool for achieving a more in-depth understanding of physical phenomena involved in condensation and, nevertheless, for assessing the quantitative consistency of the heat and mass transfer analogy to be employed in the HMTAM model. For these reasons, the need emerges for an in-depth validation of mechanistic diffusion models and low-Reynolds turbulence models. To assess the capabilities of the different turbulence models and the different low-Reynolds strategies, a route has been therefore proposed for validation accounting for different phenomena of interest.

A first stage allowed analysing the capabilities of turbulence models in reproducing nondimensional velocity profiles in the presence of pure mass and momentum transfer, basing on the experimental data by Favre [13]. All turbulence models demonstrated a satisfactory behavior. The RNG $\kappa - \varepsilon$ with TLM is particularly accurate, at least in the cases with lower suction parameters. Moreover, the model has proven to be the less sensitive to grid refinement in the near-wall region, requiring y^+ around one to achieve grid convergence.

A second stage concerned the anaysis of suction effects induced by condensation, in the light of different correlations proposed in literature to quantify its impact on the Sherwood number, the Nusselt number and the friction coefficient. The capabilities of the turbulence models have been addressed for pure heat transfer cases in recovering the various correlations available in literature for the main nondimensional numbers and nondimensional profiles. Then, the

differences due to the presence of transpiration effects in the mass transfer cases have been investigated. The capabilities of the common available correlations in predicting the transpiration correction factors have been addressed. The RNG $\kappa - \varepsilon$ model with TLM has shown the best overall behavior.

The effect of the momentum source terms have also been investigated with respect to the reference mass transfer model. The performed analysis has shown that, for correctly evaluating the mass transfer effect on the different boundary layers, and mostly friction, the presence of a momentum source term linked to the mass source term is necessary for the velocity component parallel to the condensing surface. Moreover, the presence of a momentum source for the velocity component orthogonal to the condensing surface is not strictly necessary and has the disavantage to increase the computational effort.

Basing on the results of the proposed route for validation, but also in the light of the extensive validation already performed with the RNG $\kappa - \varepsilon$ model with TLM in simulating wall mass transfer phenomena [91, 130, 8, 92, 93, 122], this model will be later on employed for performing the analysis of steam condensation tests.

The modelling of the CONAN and the COPAIN experiences will be therefore addressed with the HMTDM^{EBD} and the HMTDM^{EBD} condensation models coupled with the RNG $\kappa - \varepsilon$ model with TLM. The capabilities of the fast-running HMTAM model coupled with a simple RNG $\kappa - \varepsilon$ model and standard wall function will be also addressed.

The analysis of these numerical test cases has allowed making important reflections on the nature of turbulence phenomena in transpirating flows, on their modelling and on the needs for a future development of the models.

It is first of all remarked that standard versions where used, without performing any possible tuning of the different constants that appear in the models. Moreover, constant turbulence Prandtl and Schmidt numbers where adopted with the exception of the RNG $\kappa - \varepsilon$, where the turbulent Prandtl and the Schmidt number are estimated on the basis of the turbulence viscosity and the local molecular viscosity.

Basing on the results obtained by this analysis, we could conclude that, at least in forced convection, transpiration effects are first order phenomena and that low-Reynolds models can account for these effects, provided that these are used correctly. In particular, turbulence production terms associated to mean velocity gradients are the responsible in capturing the modification induced by transpiration on the generation of turbulence kinetic energy and, as a consequence on the nondimensional velocity profiles. These hypotheses, unfortunately, cannot be fully confirmed experimentally, due to the lack of experimental data concerning the characteristic of boundary layers in the presence of momentum and mass transfer or condensation phenomena.

In the aim to achieve a further improvement of turbulence models, different steps are therefore suggested. In a first instance, momentum and mass transfer cases, like the Favre's, could be performed to investigate the behavior of the nondimensional turbulence kinetic energy κ^+, the nondimensional turbulence kinetic energy production P+ and the nondimensional turbulence kinetic energy dissipation ε^+. By analyzing the modification of the turbulence kinetic energy peak and the nondimensional dissipation rate profile, a clearer perspective could be in fact achieved on the effects of transpiration and on which terms are due to account for these effects. In a second instance, condensation

experiments should be perfomed in a SET facility, like CONAN or COPAIN, permitting local measurements of velocity, temperature and concentration in the boundary layer, paying particular attention to the non-intrusivity of the selected measurement techniques. This would allow analyzing the behavior of the nondimensional temperature T^+ and nondimensional concentration ϕ^+ profiles, contributing also remarkably to the development of wall functions dedicated to wall condensation. A new perspective is in fact suggested, once these data would be available, to develop wall functions accounting for simultaneous momentum heat and mass transfer, which could be used with relatively coarse spatial discretizations, without penalyzing the accuracy of predictions.

Chapter 8

Computational results and discussion

In this chapter, the modelling of the CONAN and COPAIN condensation tests in presence of steam-air and steam-air-helium mixtures is addressed. Three different models have been used: the HMTDM^{EBD}, the HMTDM^{MSD} and the HMTAM models. The selected turbulence model is the RNG $\kappa - \varepsilon$; the near-wall turbulence is dealt with by an appropriate two-layer treatment in the HMTDM models, whereas standard logarithmic wall functions are adopted with the HMTAM model. A detailed description of condensation and turbulence models was proposed respectively in chapter 6 and 7.

In the first part of this chapter, results are reported concerning the modelling of steam-air tests. The CONAN and the COPAIN tests are modelled with the HMTDM^{EBD} and the HMTAM model, since the HMTDM^{EBD} and HMTDM^{MSD} reduce to the same model when binary mixtures are addressed, as shown in a parallel work [18]. The condensation tests in presence of helium are instead addressed with the three models and the results are reported in the second part of this chapter.

Steam condensation tests in presence of air have been performed within the CONAN facility, mainly concerning the forced convection regime. Natural convection and mixed convection conditions have been addressed with the COPAIN facility. Different operating pressures and steam superheating were also addressed. Condensation tests in presence of helium were performed within the CONAN and the COPAIN facility, addressing natural and forced convection regimes. In the frame of this Phd thesis, experimental tests addressing low free stream velocity conditions have been performed within the CONAN facility, aimed at achieving a better understanding of the local phenomena promoted in presence of helium.

A route for the validation of the models is therefore proposed consisting on the following paths:

- modelling of the steam-air CONAN test in forced convection regime;
- modelling of the steam-air COPAIN tests in forced, natural and mixed convection regimes, at several operating pressure and with steam in superheated conditions;

- modelling of the steam-air-helium CONAN tests;
- modelling of the steam-air-helium COPAIN tests.

In the following paragraphs the results of the CFD modelling are reported compared to the experimental data. A detailed comparison with local experimental data is proposed for the HMTDM models adopting a refined discretization. The analysis is proposed cast in terms of local Sherwood number for the CONAN tests, whereas local heat fluxes are preferred for COPAIN tests. The behavior of the HMTAM model is instead analyzed macroscopically.

The overall condensation rates calculated by the three models are compared to the experimental ones. The discrepancy between calculated and experimental values is analyzed under different points of view. In particular, the accuracy of the calculations is investigated against different parameters, like the steam mass fraction, the helium-to-noncondensable gas ratio, the average Richardson number or the ratio between the overall condensation rate and the inlet mass flow rate.

8.1 Modelling steam-air condensation tests within the CONAN facility

Steam condensation tests in the presence of air were performed within the CONAN facility, mainly concerning forced convection regimes. The modelling of the CONAN steam-air tests by the HMTDM^{EBD} model was performed by Dannoelh [131] and Mogliani [92]. The main results of these studies are reported and discussed in this paragraph, compared to the results obtained with the HMTAM model, implemented as detailed in chapter 6.

8.1.1 Steam-air CONAN tests: results by the HMTDM model

The HMTDM model, originally developed for modelling the evaporation of falling liquid film [91, 130], was also applied in the modelling of steam-air condensation tests [8, 92]. Dannoelh [131] and Mogliani [92] applied the model to the database of the CONAN tests of steam condensation in the presence of air. Here, the results of these simulations are summarized in terms of overall condensation rates and local heat transfer rates.

The geometrical discretization adopted by Mogliani [92] is shown in Fig. 8.1. According to the requirements of the selected turbulence model, the grid was optimized to achieve the near-wall nondimensional distance from the wall y_c^+ to be less than one (see chapter 7).

Velocity, mixture composition and temperature are imposed at the inlet section of the channel. On the secondary side of the condensing plate, it is imposed the heat transfer coefficient with the coolant and the free stream temperature profile of the coolant itself. This is assumed linear, varying from the cold leg temperature of the secondary coolant circuit and the hot leg temperature. The conjugated heat transfer approach is adopted to model the heat transfer from the steam-air mixture to the aluminum plate over which condensation occurs. Other surfaces are assumed to be adiabatic. A pressure-outlet condition is imposed in the outlet section. The complete set of boundary conditions are reported in appendix A.

The comparison between the experimental condensation rates and the condensation rates predicted by the HMTDM model is reported in Fig. 8.2. According to the figure, the HMTDM models allows predicting the nominal condensation rate with an accuracy of $\pm 20\%$, mostly ranging around $\pm 15\%$ of the experimental condensation rates, whose uncertainty is in the order of $\pm 1\%$.

From Fig. 8.3 to Fig. 8.6, the comparison between the calculated and the experimental local heat fluxes is proposed for test cases having a low secondary side coolant temperature. In particular, data corresponding to tests having 2.5 m/s of free stream velocity are reported in Figs. 8.3 and 8.4, respectively for test cases having a secondary side nominal coolant temperature of 30 $^\circ C$ and 40 $^\circ C$. Different free stream velocity conditions are analyzed in Fig. 8.5 and 8.6, corresponding to tests having respectively a free stream velocity of 3.0 m/s and 3.5 m/s and a secondary side coolant temperature of 40 $^\circ C$. The calculated local heat fluxes are in agreement with the experimental values in the fully developed flow region, depending on the local Reynolds number values[1]. Local

[1]Turbulent forced convection fully developed flow is assumed attained for $Re_x > 10^5$

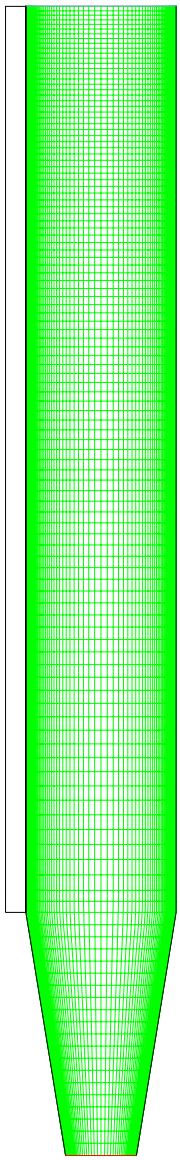

Figure 8.1: Spatial discretization used with the HMTDM model (Fig. from Mogliani [92])

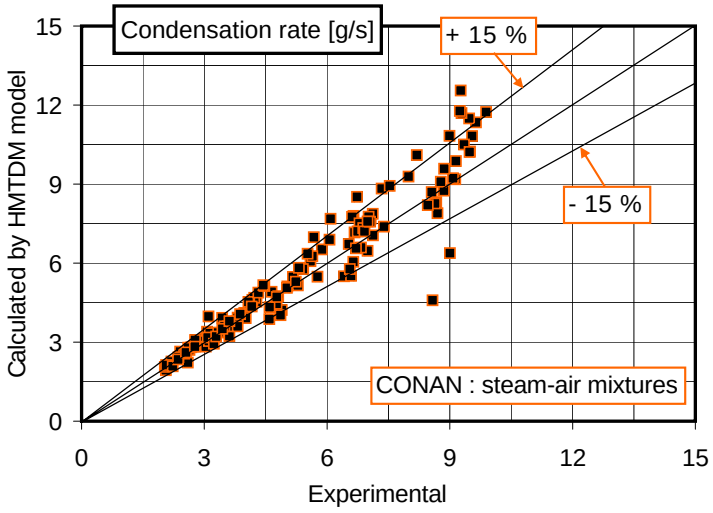

Figure 8.2: Overall condensation rate in the CONAN steam-air tests: Prediction by the HMTDM model vs. experimental data (data from Mogliani [92])

heat fluxes near the inlet section are generally underestimated, probably due to the difficulties of the selected turbulence model, the RNG κ-ε model with TLM (two-layer model), to deal with developing flow conditions. Moreover, the local heat flux near the inlet section could be also sensitive to the grid refinement in the stream direction, which was not checked. The uncertainty on the measured heat flux is in the order of ± 700 W, that is a few percent of the heat transferred to the condensing plate in the cases at the highest nominal steam generator powers ($\pm 2\%$ at 35 kW) and $\pm 7\%$ at the lowest nominal steam generator powers (10 kW).

Calculated velocity profiles are also reported to better describe the effect of suction on the boundary layers. In Figs. 8.7 and 8.8, the velocity profiles predicted for a high free stream velocity case and a low free stream velocity case are reported. Indeed, the effect of suction is shown, since the left boundary layer, corresponding to the condensing wall is thinner than the right one, corresponding to the adiabatic wall. Buoyancy effects on the velocity profile are predicted in the tests having a lower free stream velocity, confirming the remarks drawn in the analysis of experimental data (see chapter 4).

In the aim to achieve a better understanding of the overall behavior of the model, the Figs. 8.9 and 8.10 show the discrepancy of the condensation rate calculated by the model with respect to the experimental one, defined by

$$\delta = 100 \frac{CR_{MODEL} - CR_{EXP}}{CR_{EXP}} \tag{8.1}$$

respectively as a function of the ratio between the experimental overall condensation rate and the inlet mass flow rate (labelled IMFR in the following figures) and the inlet steam mass fraction. The ratio between the experiemntal overall condensation rate and the inlet mass flow rate is defined very similar to the transpiration factor A defined by Eq. (7.59) in the analysis of the Favre's

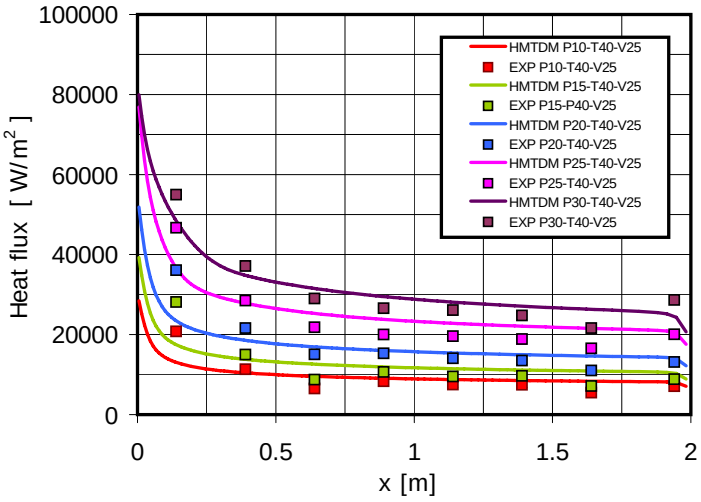

Figure 8.3: Comparison between experimental and calculated heat flux profiles in cases at secondary side coolant temperature of $40°C$ and free stream velocity of 2.5 m/s (data from Mogliani [92])

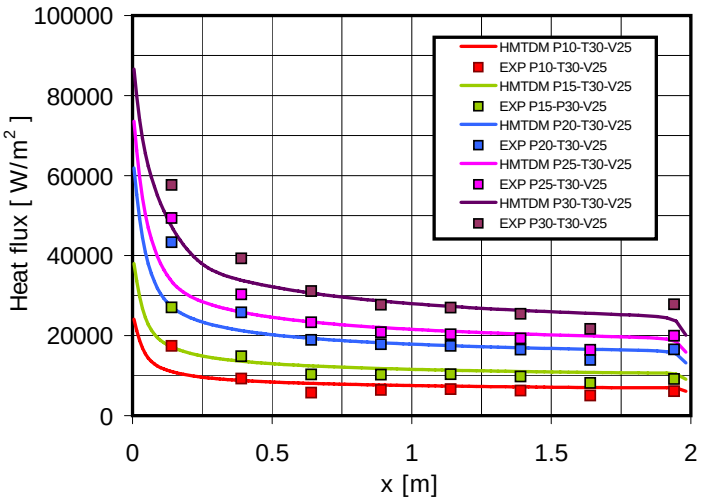

Figure 8.4: Comparison between experimental and calculated heat flux profiles in cases at secondary side coolant temperature of $30°C$ and free stream velocity of 2.5 m/s (data from Mogliani [92])

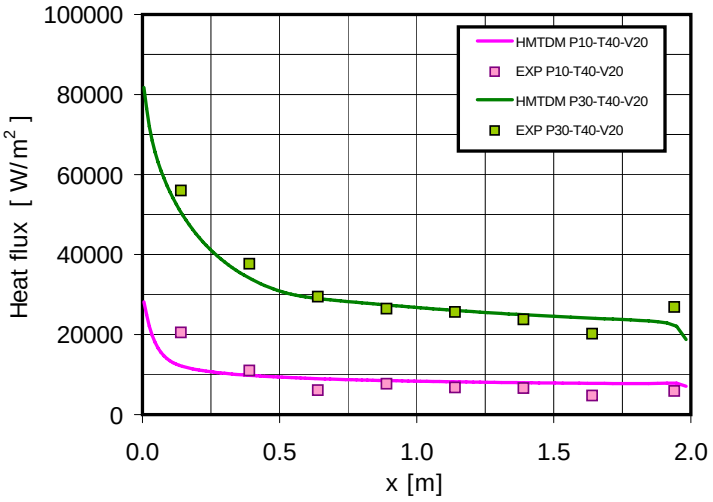

Figure 8.5: Comparison between experimental and calculated heat flux profiles in cases at secondary side coolant temperature of $40°C$ and free stream velocity of 2.0 m/s (data from Mogliani [92])

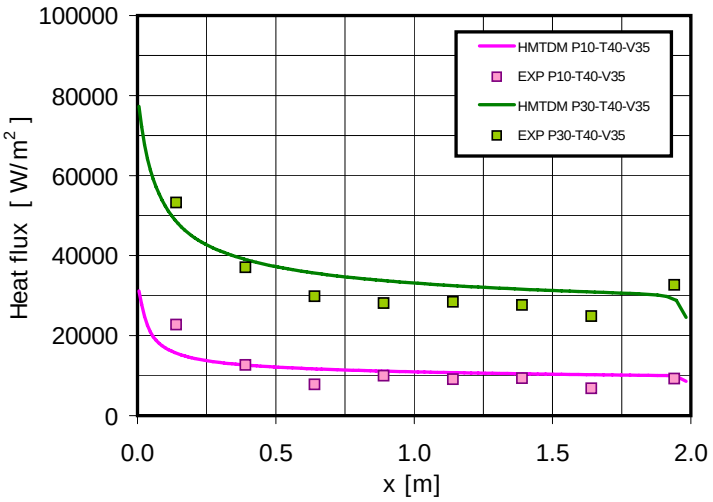

Figure 8.6: Comparison between experimental and calculated heat flux profiles in cases at secondary side coolant temperature of $40°C$ and free stream velocity of 3.5 m/s (data from Mogliani [92])

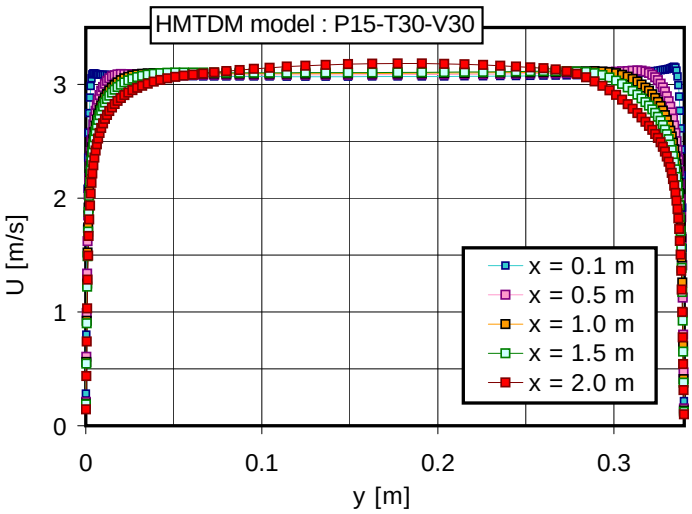

Figure 8.7: Comparison of predicted velocity profiles for a high free stream velocity case (data from Mogliani [92])

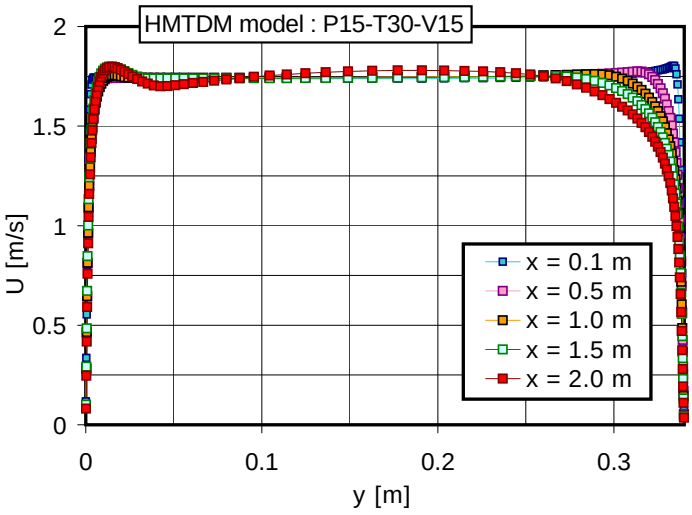

Figure 8.8: Comparison of predicted velocity profiles for a low free stream velocity case (data from Mogliani [92])

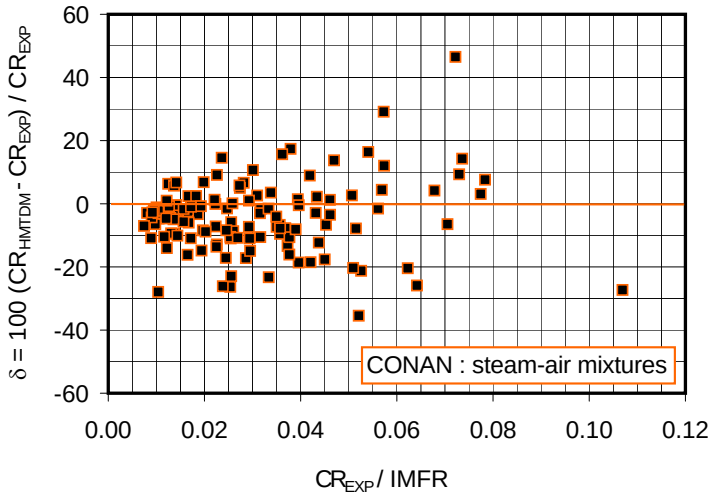

Figure 8.9: Discrepancy between the condensation rate calculated by the HMTDM model and the experimental overall condensation rate vs. the ratio between the experimental overall condensation rate and the inlet mass flow rate (IMFR) in the steam-air tests within CONAN

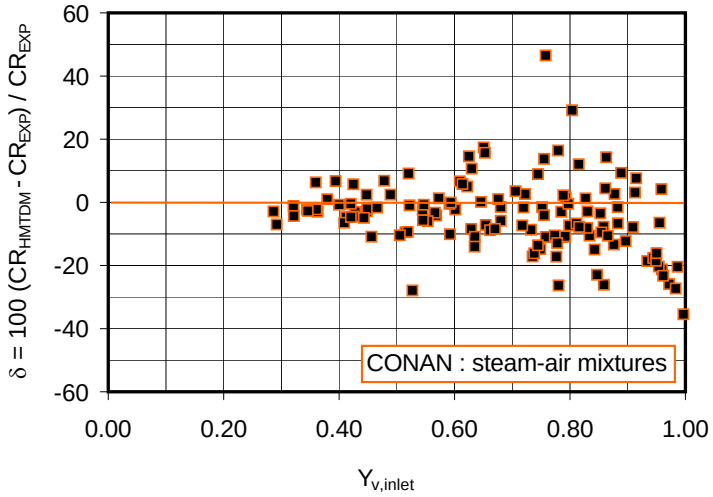

Figure 8.10: Discrepancy between the condensation rate calculated by the HMTDM model and the experimental overall condensation rate vs. the inlet steam mass fraction

experiences (see paragraph 7.4):

$$A = -\frac{\rho_0 V_0}{\rho_\infty u_\infty} \tag{8.2}$$

This ratio is representative of the intensity of the suction effects expected in the tests. As it can be seen in Fig. 8.9, for higher values of the ratio, the discrepancy of the calculated condensation rates with respect to the experimental ones seems to be more important. A clear trend is observed in Fig. 8.10, where the discrepancy is reported as a function of the inlet steam mass fraction. The model seems to be less accurate for mixtures rich of steam.

8.1.2 Steam-air CONAN tests: results by the HMTAM model

The first version of the HMTAM model was conceived to predict condensation phenomena in forced convection or natural convection conditions [96]. The natural convection version was applied to the modelling of the ISP47 tests within the TOSQAN [118] and the MISTRA facilities [96]. The forced convection model was instead applied to the modelling of the steam-air forced convection tests performed within CONAN [96]. In this section, the results obtained by the HMTAM model are reported, concerning the experimental database of steam condensation in the presence of air available by the CONAN facility. A comparison with experimental data is proposed, together with a comparison with the HMTDM model.

Unlike in the HMTDM model, a coarse discretization can be used, as shown in Fig. 8.11. The thickness of the cells beside the condensing wall is here taken of 2 cm, according to the requirement of the standard logarithmic wall functions that require $60 < y^* < 300$ (see chapter 7). The same boundary conditions are used as adopting the HMTDM model.

In Fig. 8.12, the comparison between the calculated and the experimental overall condensation rates is proposed. Calculated values are mostly included in a range of $\pm 15\%$ of the experimental values. The discrepancy of the calculated values with respect to the experimental ones, evaluated according to Eq. (8.1), is shown in Figs. 8.13 and 8.14, respectively as a function of the ratio between the experimental overall condensation rate and the inlet mass flow rate (IMFR) and the inlet steam mass fraction. The overall behavior of the model is very similar to the HMTDM model, but the predicted condensation rates are usually slightly lower than the HMTDM model, as shown in Fig. 8.15.

The reason for the overall condensation rate predicted by the HMTAM model to be lower than the HMTDM model can be clarified by analyzing Fig. 8.16. Indeed, whereas the asymptotic values of the local heat flux predicted by the HMTAM model are slightly higher than the values predicted by the HMTDM model, in the near-inlet region, entrance effects predicted by the HMTAM model are less pronounced then the HMTDM model, probably resulting in a reduced overall mass transfer rate. This is likely to be due to the space discretization adopted with the HMTAM model, which is not conceived to capture entrance effects in detail. In the asymptotic region, the HMTAM model predicts the heat flux to be slightly higher than the HMTDM. This is likely to be due to the Stefan factor, introduced to account for suction effects at high mass transfer rates. Since this, as remarked in chapter 4 and chapter 7, is suspected to overestimate suction effects, the resulting mass fluxes and therefore the resulting local heat fluxes are higher than those predicted by the HMTDM models, whose agreement with the experimental data is remarkable.

A pure numerical comparison between the velocity profiles predicted by the two models is also proposed in Fig. 8.17. The stream velocity in the near-wall cells calculated by the HMTAM depends on the selected wall functions. Since standard wall functions are used, not due to deal with transpiration phenomena, the velocity resulting in the first cell is slightly lower than the velocity obtained with the HMTDM model. The overall behavior of the HMTAM model is anyway very satisfactory.

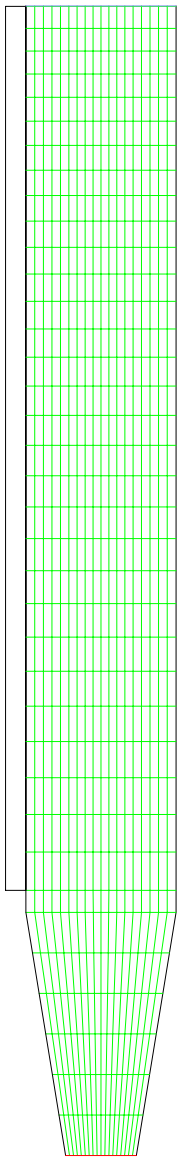

Figure 8.11: Space discretization used with the HMTAM model (Fig. from Bucci [96])

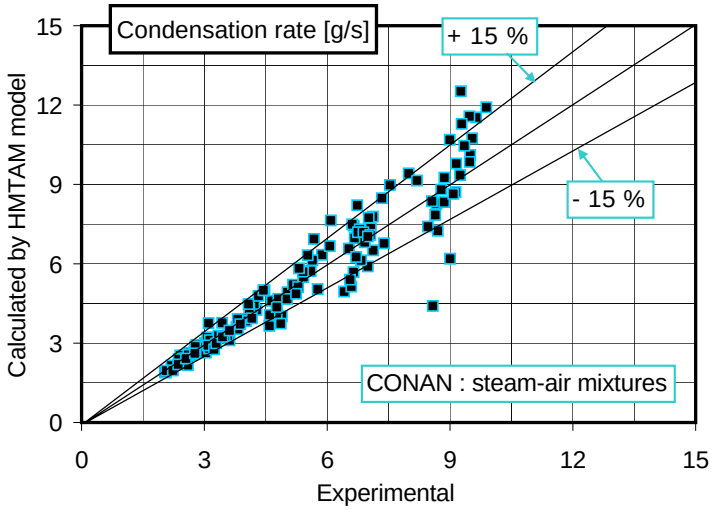

Figure 8.12: Overall condensation rate in the CONAN steam-air tests: Prediction by the HMTAM model vs. experimental data (data from Bucci [96])

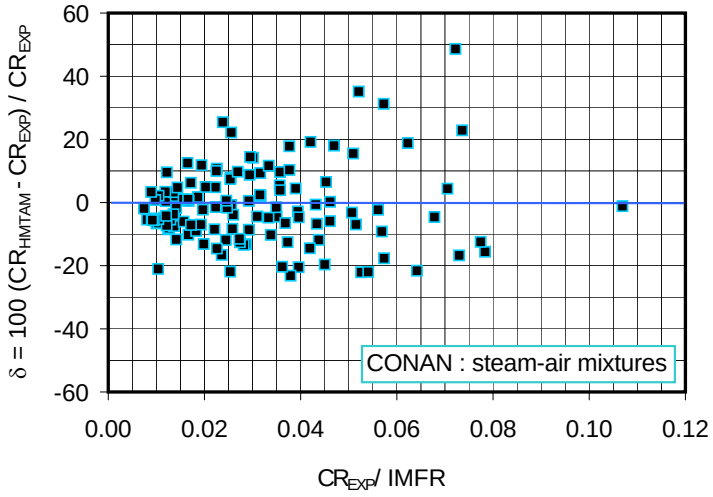

Figure 8.13: Discrepancy between the condensation rate calculated by the HMTAM model and the experimental overall condensation rate vs. the ratio between the experimental overall condensation rate and the inlet mass flow rate (IMFR) in the steam-air tests within CONAN

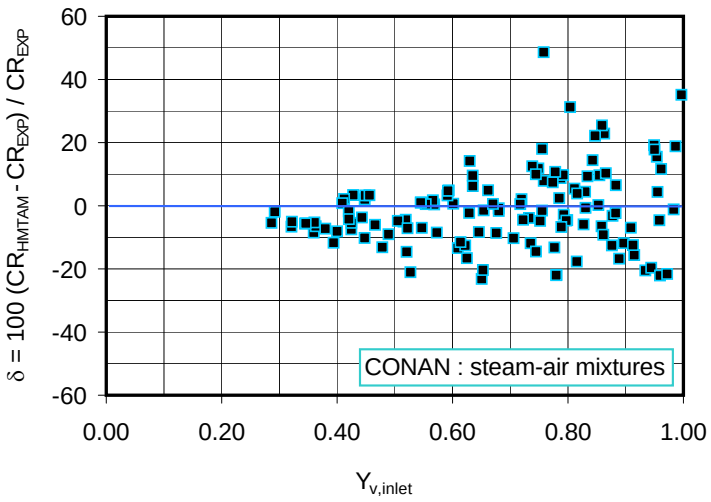

Figure 8.14: Discrepancy between the condensation rate calculated by the HMTAM model and the experimental overall condensation rate vs. the inlet steam mass fraction

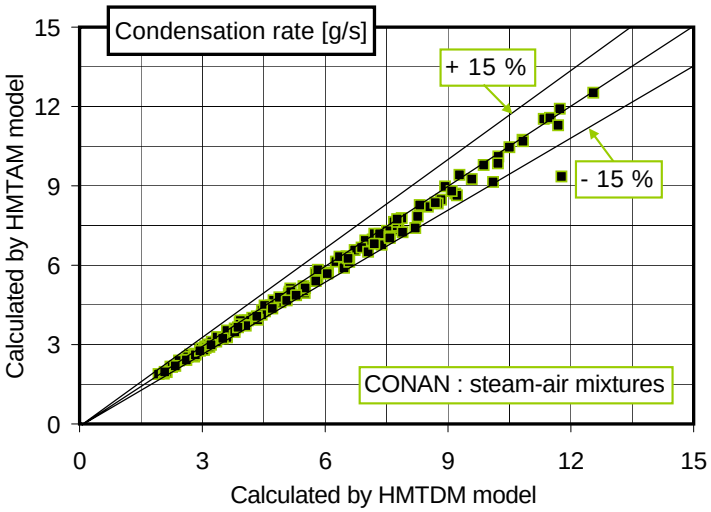

Figure 8.15: Overall condensation rate in the CONAN steam-air tests: Prediction by the HMTAM model vs. prediction by the HMTDM model (data from Bucci [96])

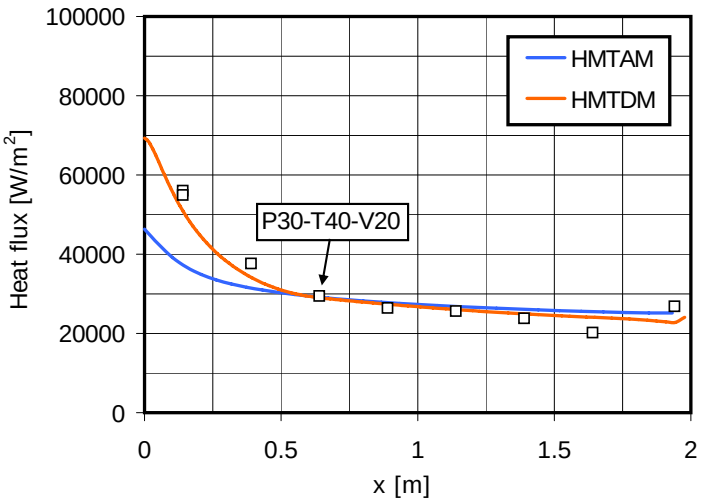

Figure 8.16: Comparison between the calculated and the experimental local heat flux profile in the CONAN P30-T40-V20 test (data from Bucci [96] and Mogliani [92])

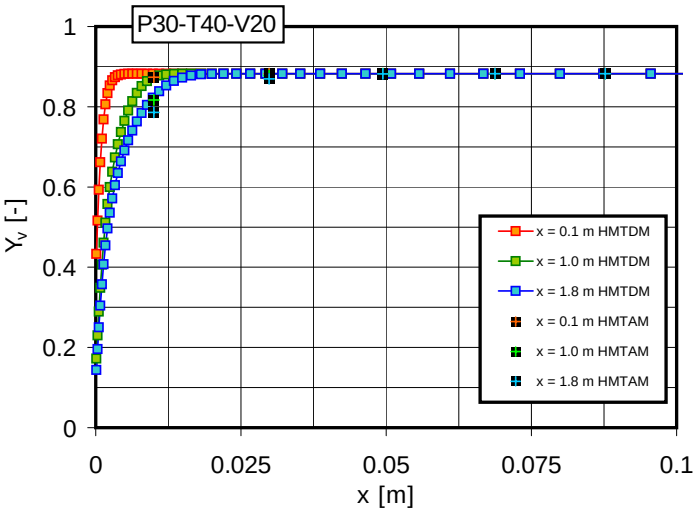

Figure 8.17: Comparison between the local velocity profile predicted by the HMTDM and the HMTAM models in the CONAN P30-T40-V20 test (data from Bucci [96] and Mogliani [92])

8.2 Modelling steam-air condensation tests within the COPAIN facility

The modelling of the pure heat transfer and the condensation tests performed within the COPAIN facility has been performed in the frame of this doctoral research, aimed at investigating the capabilities of the models in addressing natural and mixed convection conditions. Moreover, forced convection tests have also been modelled, aimed at enriching the validation matrix of the model by further test cases addressing different pressure conditions and with superheated steam.

8.2.1 Steam-air COPAIN tests: results by the HMTDM model

The optimized space discretization adopted in the modelling of the COPAIN tests is shown in figures 8.18. According to the requirements of the turbulence model, the nondimensional distance from the wall of the near-wall cells y_c^+ is strictly less than 1. Indeed, since the Prandtl and the Schmidt numbers are less than 1, the conditions $y_c^+ Pr < 1$ and $y_c^+ Sc < 1$ (see chapter 6) are intrinsically satisfied. The independence of the solution from the refinement in the longitudinal direction was also checked near the inlet section.

In Fig. 8.19, a comparison between the experimental average heat flux and the average heat flux predicted by the HMTDM model is proposed. Computed heat fluxes are generally included within $\pm 15\%$ of the experimental values, which is estimated with an uncertainty of $\pm 6\%$. Similarly, the calculated condensation rates and the experimental condensation rates deduced from the average heat transfer fluxes on the basis of the heat and mass transfer analogy are compared in Fig. 8.20.

By analyzing the discrepancy between the calculated condensation rate and the experimental value, two main tendencies can be identified. As can be seen in Fig. 8.21, the model tends to overestimate condensation for low Richardson numbers, and viceversa it tends to underestimate at the highest values of the Richardson number. Test cases having a dominant forced convection character are therefore overestimated, whereas cases having a natural convection character are underestimated. Moreover, as shown in Fig. 8.22, the lower is the average heat flux, that is the lower is the condensation rate, the wider is the discrepancy between the calculated and the experimental values; obviously, experimental uncertainties on the boundary conditions play a major role in the modeling of tests characterized by a low heat and mass transfer rate.

In Figs. 8.23 and 8.24, the discrepancy of the condensation rates calculated by the model with respect to the ones derived from the heat transfer measurements is shown, respectively as a function of the ratio between the experimental overall condensation rate and the inlet mass flow rate and the inlet steam mass fraction. As it can be seen in Fig. 8.23, in the steam-air COPAIN tests, the ratios between the condensation rates and the inlet mass flow rates available by COPAIN tests are lower those available by the CONAN tests (see Fig. 8.9).

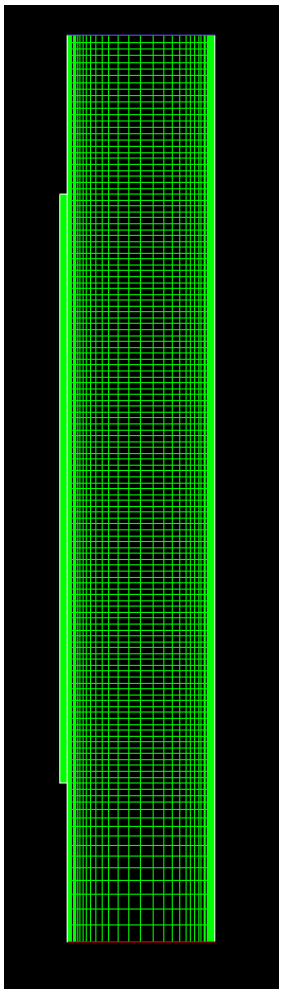

Figure 8.18: Space discretization of COPAIN used with the HMTDM model

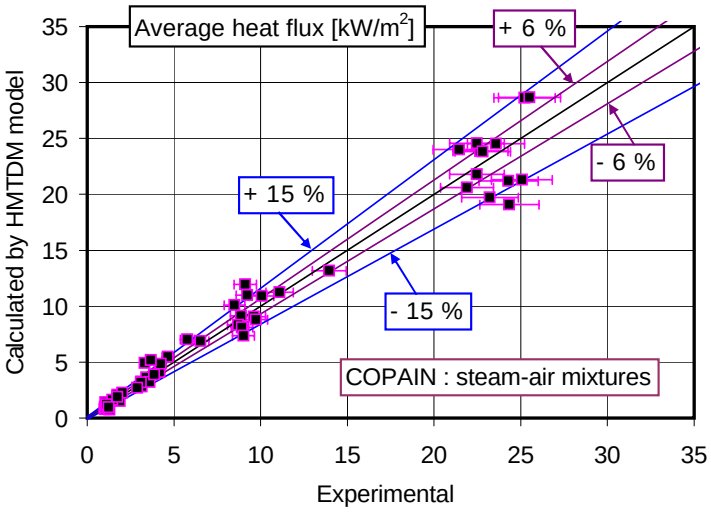

Figure 8.19: Average heat transfer rate in the COPAIN steam-air tests: Prediction by the HMTDM model vs. experimental data

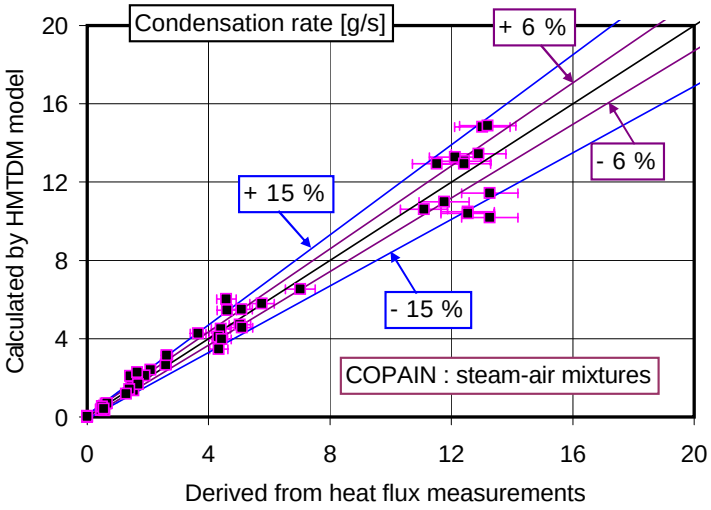

Figure 8.20: Overall condensation rate in the COPAIN steam-air tests: Prediction by the HMTDM model vs. experimental value derived from heat flux measurements

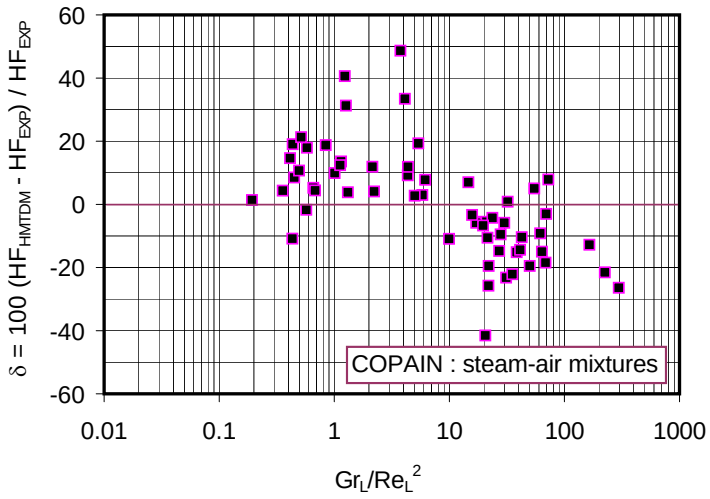

Figure 8.21: Discrepancy between the average heat flux calculated by the HMTDM model and the experimental average heat flux vs. the average Richardson number in the steam-air tests within COPAIN

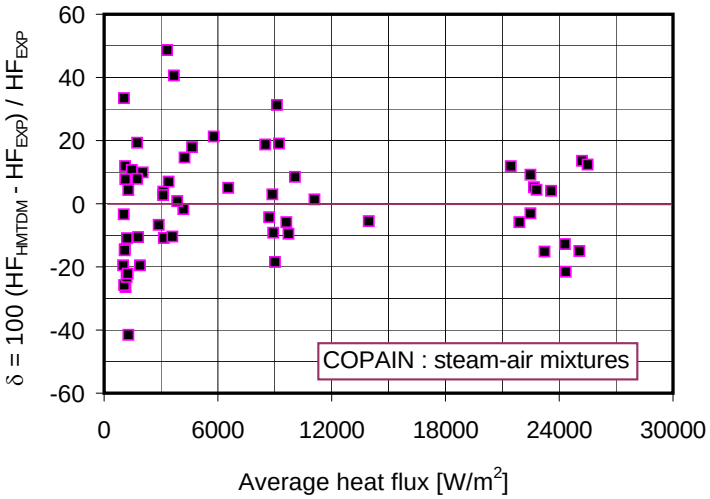

Figure 8.22: Discrepancy between the average heat flux rate calculated by the HMTDM model and the experimental average heat flux vs. the average heat flux in the steam-air tests within COPAIN

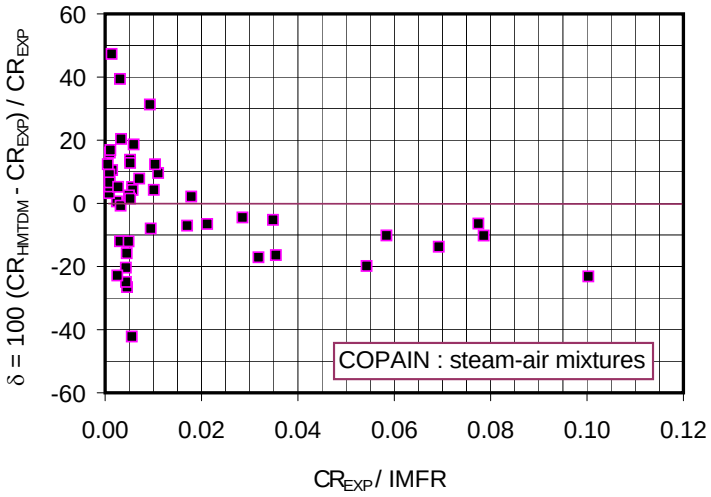

Figure 8.23: Discrepancy between the condensation rate calculated by the HMTDM model and the experimental overall condensation rate derived from heat transfer measurements vs. the ratio between the experimental overall condensation rate and the inlet mass flow rate (IMFR) in the steam-air tests within COPAIN

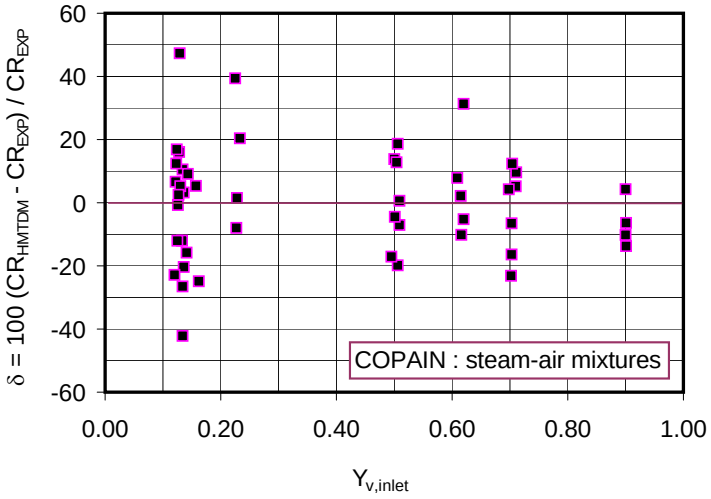

Figure 8.24: Discrepancy between the condensation rate calculated by the HMTDM model and the experimental overall condensation rate derived from heat transfer measurements vs. the inlet steam mass fraction in the steam-air tests within COPAIN

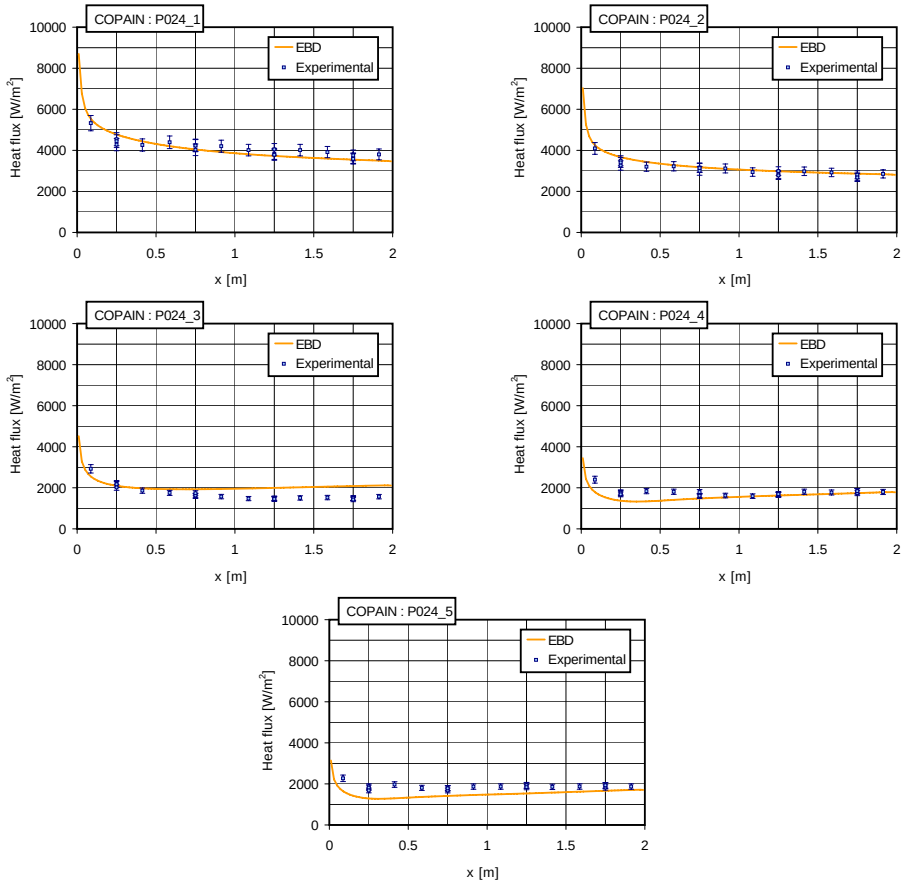

Figure 8.25: Axial heat flux profiles in the P024 COPAIN tests (pure heat transfer, $P = 6bar$): calculated values vs. experimental data

An extensive comparison between the calculated and the experimental local heat fluxes is proposed from Fig. 8.25 to Fig. 8.41. As can be seen, calculated local heat fluxes are generally included in the range of uncertainty given for the measured heat fluxes. The series P024 and P029 in particular (see respectively Figs. 8.25 and 8.30) address pure heat transfer cases. Other series address condensation in different operating conditions. In particular, the series P027, P028, P040 and P042 (see respectively Figs. 8.28, 8.29, 8.38 and 8.39) were performed at the pressure of 6 bar. Steam superheating is usually 10 $°C$. However, the series P036 included also tests having a superheating of 40$°C$. The test P025, P038, P039 and P043 (see respectively Figs. 8.26, 8.36, 8.37 and 8.40) were performed at the pressure of 4 bar. The test P043 was performed having almost all steam. The test P044 is instead performed at atmospheric pressure and a large amount of noncondensable gases, similar to the CONAN tests.

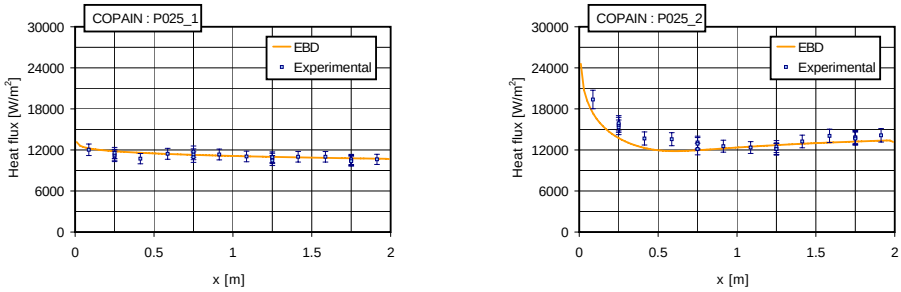

Figure 8.26: Axial heat flux profiles in the P025 COPAIN tests (condensation, $P = 4bar$, $\triangle T_{sh} = 10°C$): calculated values vs. experimental data

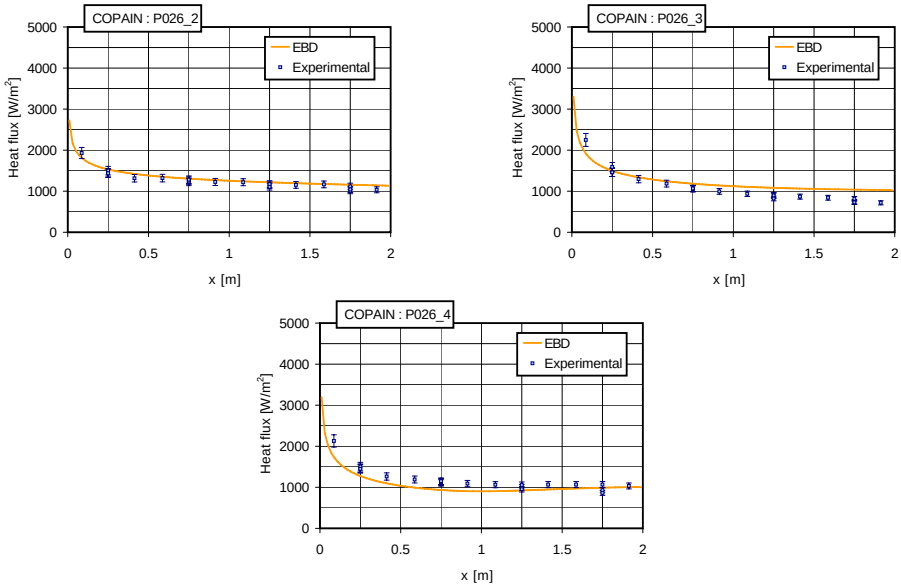

Figure 8.27: Axial heat flux profiles in the P026 COPAIN tests (condensation, $P = 1bar$, $\triangle T_{sh} = 10°C$): calculated values vs. experimental data

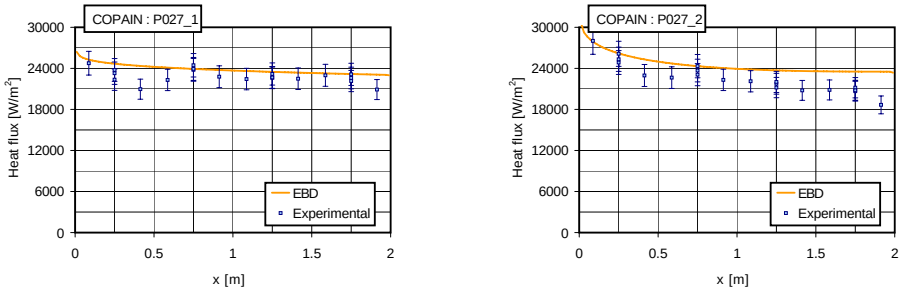

Figure 8.28: Axial heat flux profiles in the P027 COPAIN tests (condensation, $P = 6bar$, $\triangle T_{sh} = 10°C$): calculated values vs. experimental data

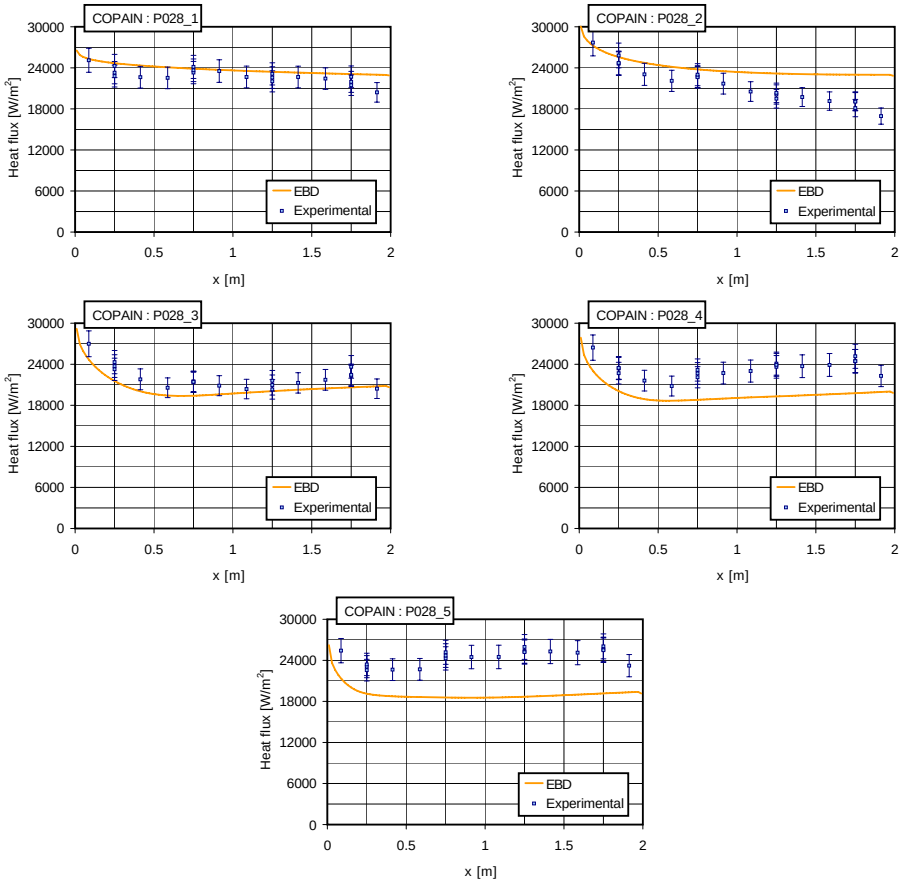

Figure 8.29: Axial heat flux profiles in the P028 COPAIN tests (condensation, $P = 6bar$, $\triangle T_{sh} = 10°C$): calculated values vs. experimental data

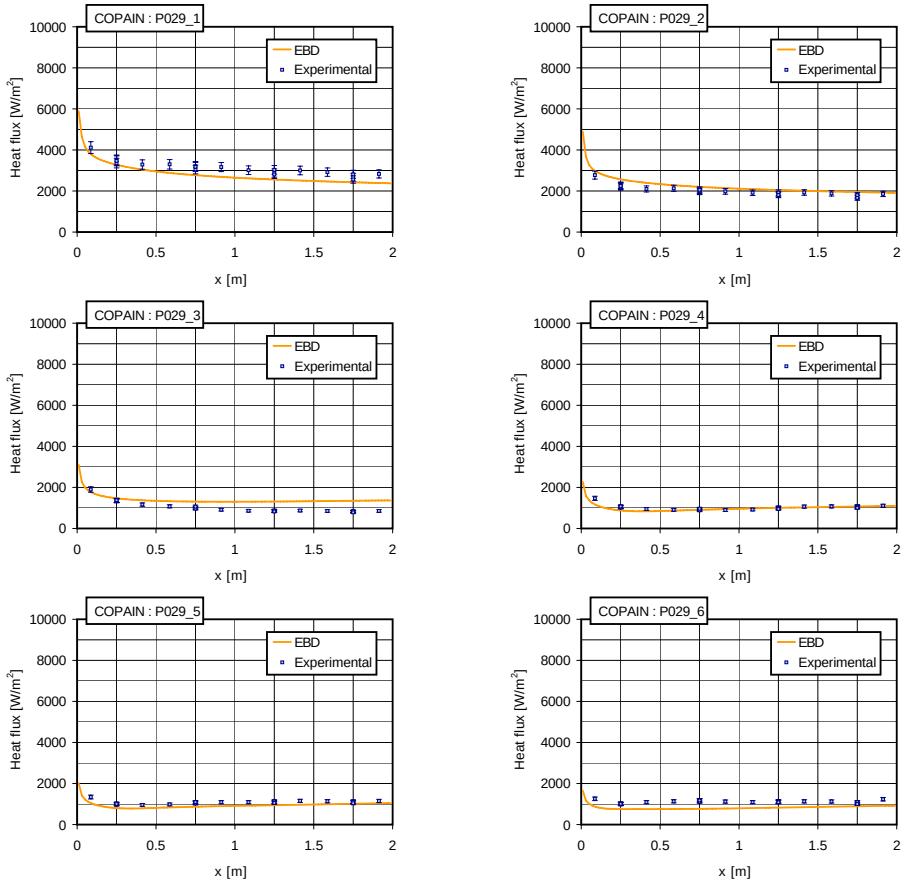

Figure 8.30: Axial heat flux profiles in the P029 COPAIN tests (pure heat transfer, $P = 4bar$): calculated values vs. experimental data

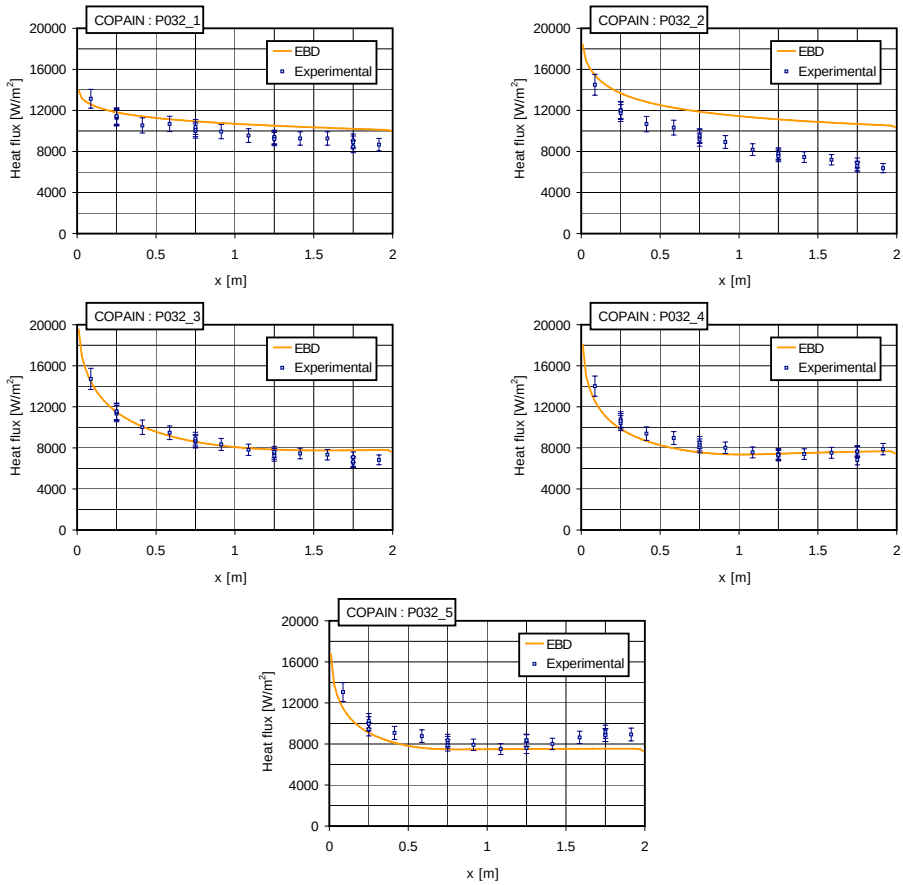

Figure 8.31: Axial heat flux profiles in the P032 COPAIN tests (condensation, $P = 1bar$, $\triangle T_{sh} = 10°C$): calculated values vs. experimental data

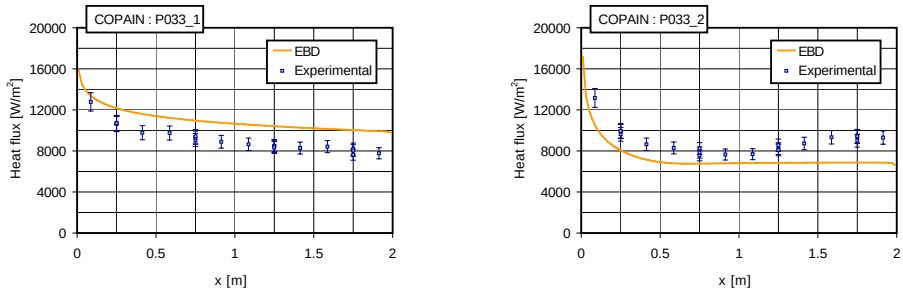

Figure 8.32: Axial heat flux profiles in the P033 COPAIN tests (condensation, $P = 1bar$, $\triangle T_{sh} = 10°C$): calculated values vs. experimental data

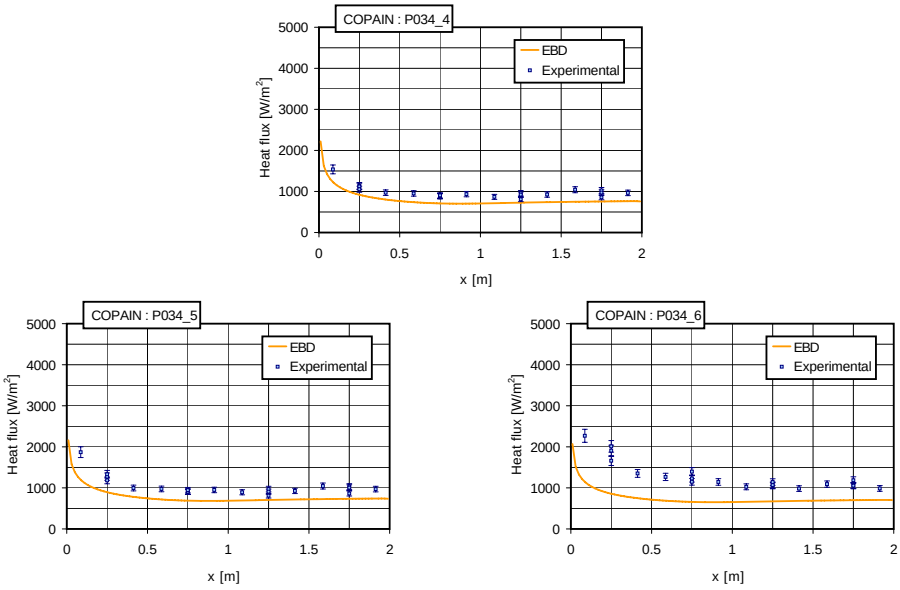

Figure 8.33: Axial heat flux profiles in the P034 COPAIN tests (condensation, $P = 1bar$, $\triangle T_{sh} = 10°C$): calculated values vs. experimental data

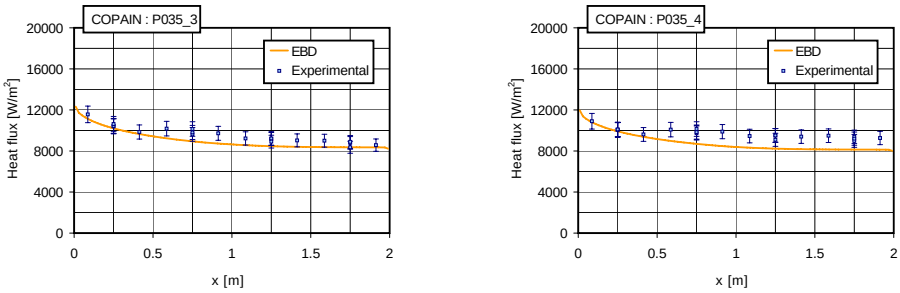

Figure 8.34: Axial heat flux profiles in the P035 COPAIN tests (condensation, $P = 1bar$, $\triangle T_{sh} = 10°C$): calculated values vs. experimental data

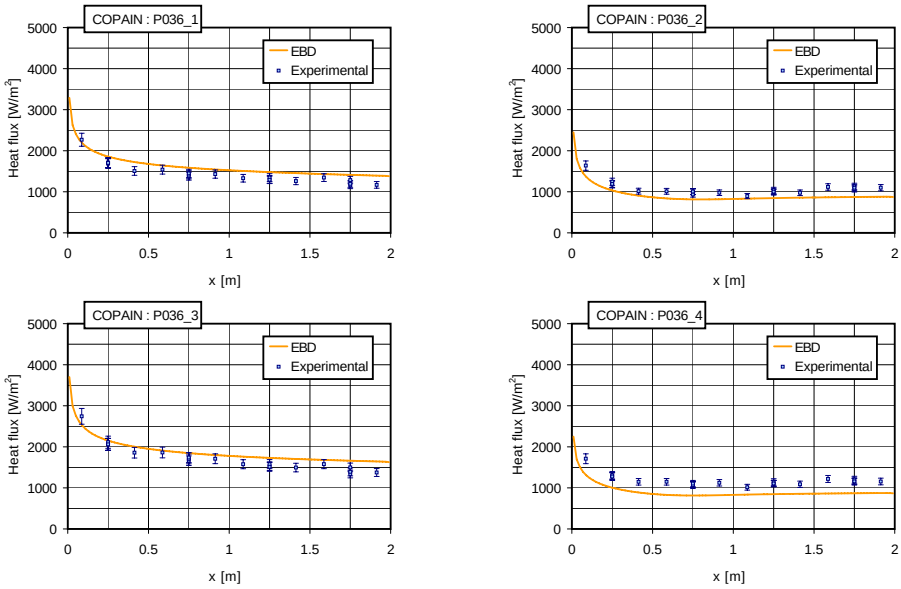

Figure 8.35: Axial heat flux profiles in the P036 COPAIN tests (condensation, $P = 1bar$, $\triangle T_{sh} = 20°C$ in the P036_1 and P036_2 tests and $\triangle T_{sh} = 40°C$ in the P036_3 and P036_4 tests): calculated values vs. experimental data

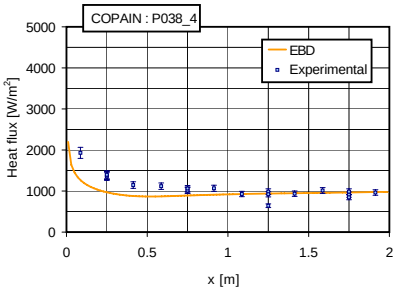

Figure 8.36: Axial heat flux profiles in the P038 COPAIN tests (condensation, $P = 4bar$, $\triangle T_{sh} = 10°C$): calculated values vs. experimental data

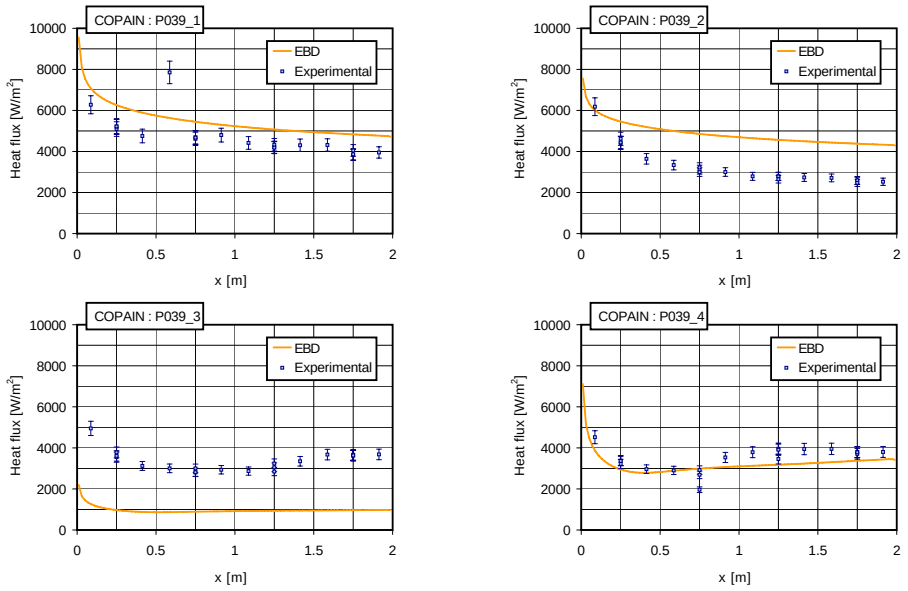

Figure 8.37: Axial heat flux profiles in the P039 COPAIN tests (condensation, $P = 4bar$, $\triangle T_{sh} = 10°C$): calculated values vs. experimental data

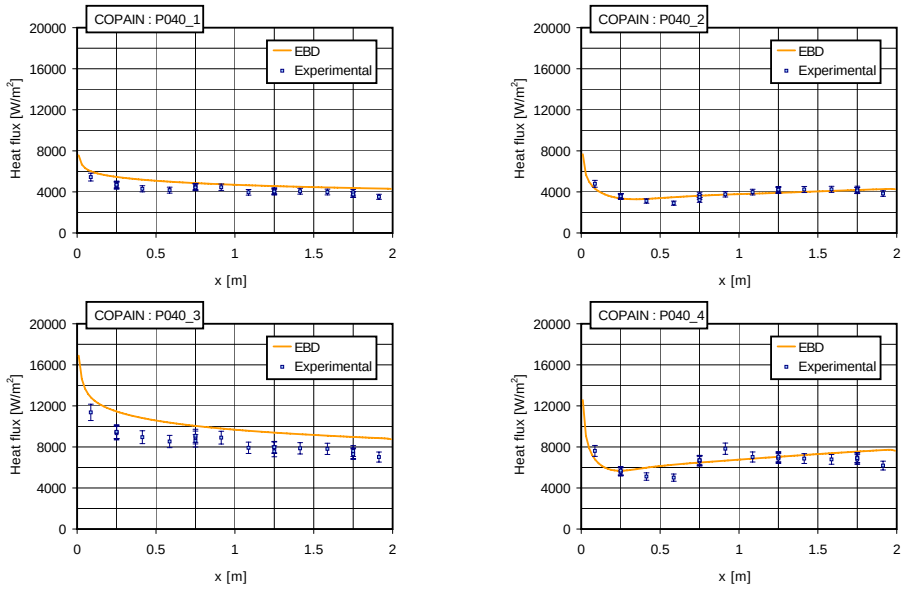

Figure 8.38: Axial heat flux profiles in the P040 COPAIN tests (condensation, $P = 6bar$, $\triangle T_{sh} = 10°C$): calculated values vs. experimental data

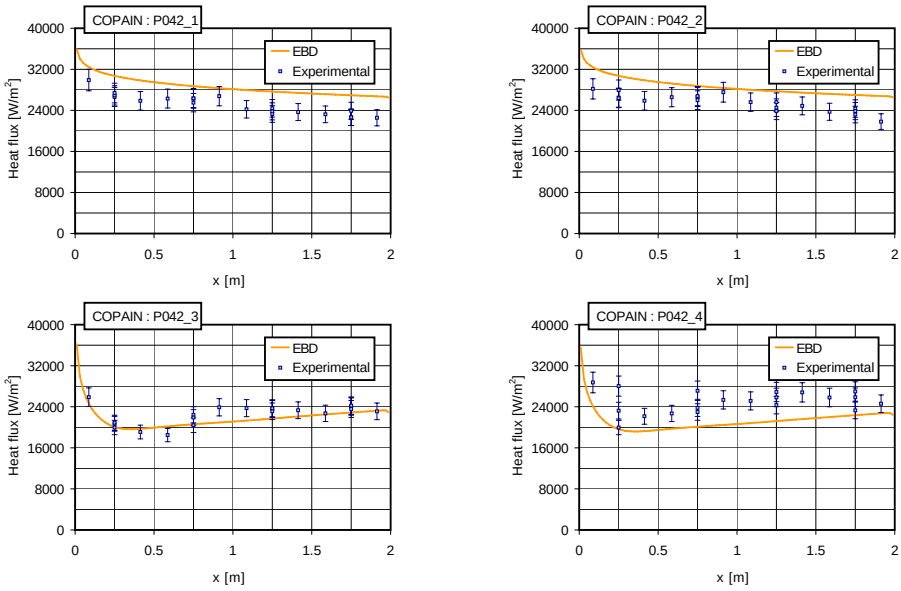

Figure 8.39: Axial heat flux profiles in the P042 COPAIN tests (condensation, $P = 6bar$, $\triangle T_{sh} = 10°C$): calculated values vs. experimental data

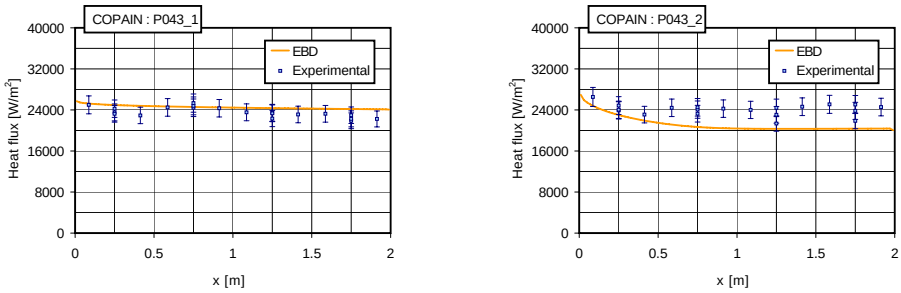

Figure 8.40: Axial heat flux profiles in the P043 COPAIN tests (condensation, $P = 4bar$, $\triangle T_{sh} = 10°C$): calculated values vs. experimental data

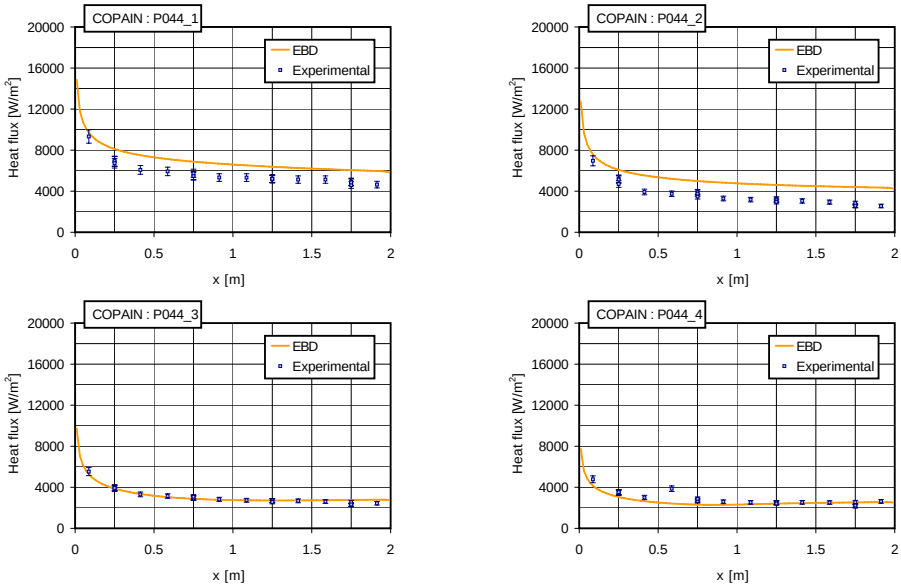

Figure 8.41: Axial heat flux profiles in the P044 COPAIN tests (condensation, $P = 1bar$, $\triangle T_{sh} = 10°C$): calculated values vs. experimental data

An additional series of steam-air experimental tests was carried out in COPAIN aiming at gathering experimental data in the turbulent boundary layer. Further details on these tests are available in [132]. Measures of temperature and concentration were performed, aiming at validating turbulence and mass transfer models. Measurements were carried out according to the experimental procedure described in chapter 4, by an appropriate device conceived to allow simultaneous measures of temperature and concentration, and therefore the saturation temperature of the steam. In Fig. 8.45, the calculated temperature profiles are compared to the measured temperatures for the test P064. As can be seen, the experimental temperature boundary layer seems remarkably thicker than the calculated one. Moreover, the temperature boundary layer thickness is remarkably larger than the one expected for pure turbulent heat transfer. The thickness of the momentum boundary layer δ in pure heat transfer condition is in fact classically given by [107]

$$\delta = 0.37 x Re_x^{-1/5} \tag{8.3}$$

Adopting the analogy between heat and momentum transfer, the thickness of the thermal boundary layer is given by

$$\delta_T = \delta / Pr^{0.33} \tag{8.4}$$

In the test P064, for which the average heat transfer flux is small (1 kW), the condensation mass flux is supposed to be small enough that boundary layer thickness is affected only weakly by condensation and therefore the theoretical thickness estimated by Eq. (8.4) should be comparable with the experimental and the calculated values. Experimental data show a boundary layer thickness higher than the theoretical value for pure heat transfer conditions, whereas calculated temperature profile are in agreement with the theoretical thickness.

As remarked in chapter 4, an open issue concerns the non invasivity of these measurements. The velocity of suction at the entrance of the sampling line adopted for concentration measurements ranges from 0.02 m/s to 0.1 m/s [1]. These values are very high with respect to the velocity scales characteristic of condensation that are of order 0.01 m/s for the cases having the most important condensation rates. Suction effects due to condensation are expected to be annealed by the suction in the sampling line that may cause the boundary layers to thicken; the condensing boundary layers could be therefore changed and they could become even thicker than in the pure heat transfer case. For the same test, air mass fraction profiles are also reported in the near-wall region, compared with the results of simulations. Since the condensation rate is quite small for the test P064, the thickness of the concentration boundary layer can be roughly estimated by the analogy between heat and mass transfer, for which the species boundary layer at low mass transfer rates is

$$\delta_{Y,0} = \delta / Sc^{0.33} \tag{8.5}$$

Indeed, the theoretical values predicted by Eq. 8.5 are in excellent agreement with the calculated values, as shown in Fig. 8.43.

In the case having larger heat transfer rates, as expected, the calculated profiles are thinner than the theoretical values. As it can be seen in Figs. 8.44 and 8.45 for the P070 test or in Figs. 8.46 and 8.47 for the P073 test, suction

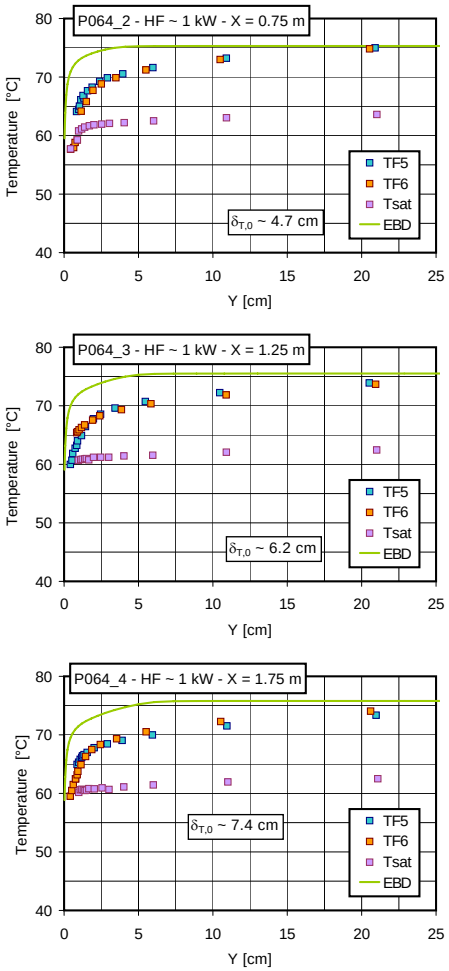

Figure 8.42: Temperature profiles in the P064 COPAIN tests: calculated values vs. experimental data

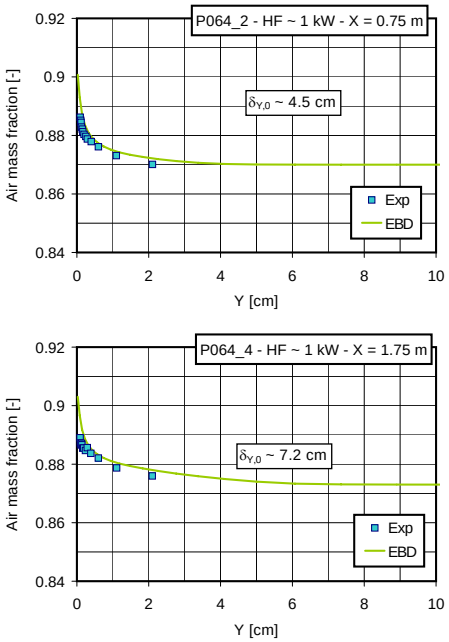

Figure 8.43: Air mass fraction profiles in the P064 COPAIN tests: calculated values vs. experimental data

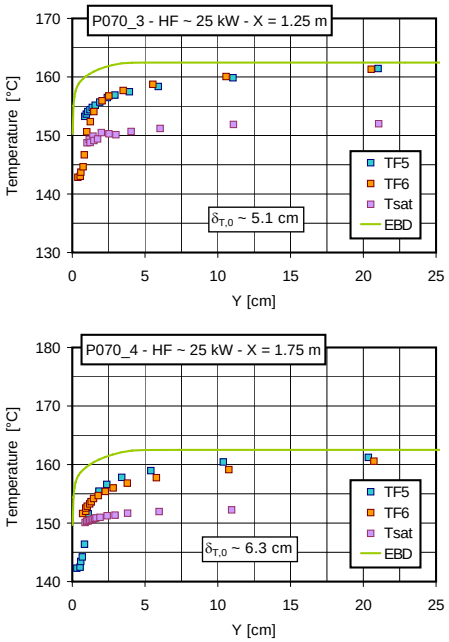

Figure 8.44: Temperature profiles in the P070 COPAIN tests: calculated values vs. experimental data

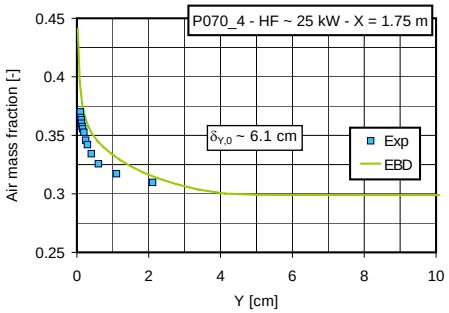

Figure 8.45: Air mass fraction profiles in the P070 COPAIN tests: calculated values vs. experimental data

effects are pointed out by calculations but also by experimental air mass fraction profiles, whose agreement with calculated profiles is remarkable.

Another important aspect to be addressed concerning the local measurements of COPAIN is the difference experienced in some tests between the TF5 and the TF6 temperature. This discrepancy, observed in Fig. 8.46 is likely to be due to the wetting that may occur to thermocouples when, at the beginning of the measurement procedure, they are almost in contact with the condensing wall. Indeed, water rivulets or droplets may wet one of the two thermocouples. As a consequence, the wet thermocouple measures a lower value than the dry ones, due to the evaporation process of water occurring on that.

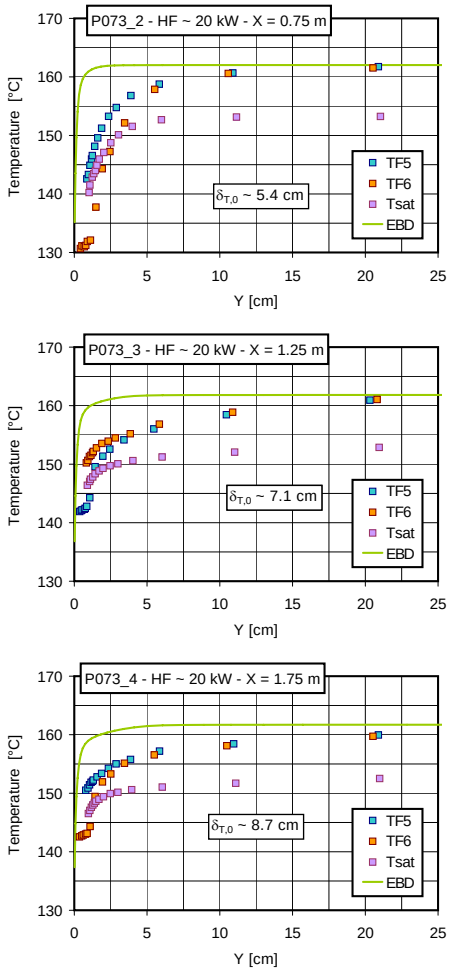

Figure 8.46: Temperature profiles in the P073 COPAIN tests: calculated values vs. experimental data

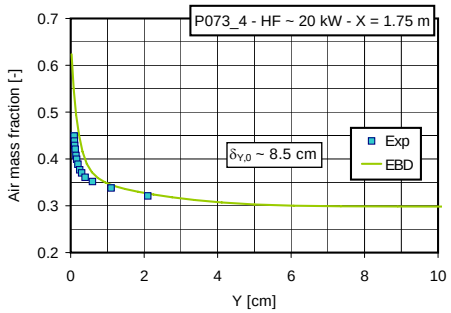

Figure 8.47: Air mass fraction profiles in the P073 COPAIN tests: calculated values vs. experimental data

8.2.2 Steam-air COPAIN tests: results by the HMTAM model

The HMTAM model has been applied to the modelling of the steam-air COPAIN tests. The important task to be addressed by the heat and mass transfer analogy is the modelling of the different convection regimes addressed in COPAIN by proposing a local correlation capable to deal with forced, natural and mixed convection regimes.

The simplest correlations proposed for mixed convection flows in free volumes are those given by

$$Sh_{0,x}^{n} = |Sh_{0,x,CF}^{n} \pm Sh_{0,x,CN}^{n}| \tag{8.6}$$

that combines the Sherwood number for forced convection regime and that for natural convection regimes [107]. The Schlichting correlation is adopted to estimated the Sherwood number in forced convection conditions, whereas the McAdams correlation is adopted for the natural convection Sherwood number:

- Schlichting pure forced convection correlation

$$Sh_{0,x} = 0.0296 Re_{x}^{0.8} Sc^{0.33} \tag{8.7}$$

- McAdams pure natural convection correlation

$$Sh_{0,x} = 0.13 Gr_{x}^{0.33} Sc^{0.33} \tag{8.8}$$

Though this is a role of thumb, for turbulent flows, the sign + is used for *buoyancy-opposed* convection and the sign − for *buoyancy-aided* convection for which the impairment of the heat and mass transfer coefficient in the mixed convection regime is expected. According to Incropera [107], the exponent n has been chosen equal 3. Clearly, the proposed correlation attains the pure forced convection or natural convection correlations when the dominating convection regime is well defined.

In chapter 5 it was observed that, for steam-air condensation tests, the only mixed convection regime possible within COPAIN is the *buoyancy-aided*. The buoyancy-aided correlation having the − sign has been therefore used and the comparison between the calculated and the experimental condensation rates derived from the experimental average heat fluxes on the basis of the heat and mass transfer analogy is shown in Fig. 8.48. The agreement with experimental data is really satisfactory, for all the convection regimes. In Figs. 8.49 and 8.50, the discrepancy between the calculated and the experimental condensation rate is shown, respectively as a function of the average Richardson number and the ratio between the experimental overall condensation rate and the inlet mass flow rate (IMFR). As it can be seen, in most cases, whatever is the regime or the condensation rate, the discrepancy is generally limited to ±15%.

The adoption of a mixed convection correlation, even if very simple, is a fundamental aspect for capturing the experimental overall condensation rate. Indeed, another possible and very simple choice would be to take the maximum Sherwood value between the one predicted by the local forced convection correlation and the one predicted by the local natural convection correlation.

$$Sh_{0,x} = max\left[Sh_{0,x,CF}; Sh_{0,x,CN}\right] \tag{8.9}$$

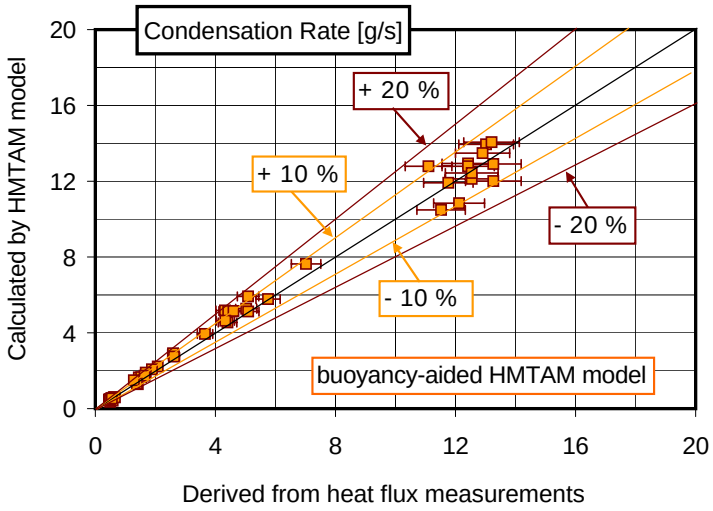

Figure 8.48: Overall condensation rate in the COPAIN steam-air tests: Prediction by the *buoyancy-aided* HMTAM model vs. experimental value derived from the experimental average heat flux

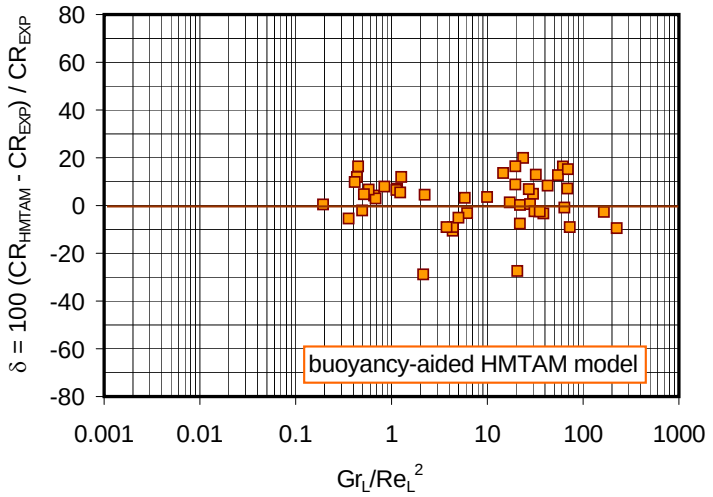

Figure 8.49: Discrepancy between the condensation rate calculated by the *buoyancy-aided* HMTAM model and the experimental value derived from the experimental average heat flux vs. average Richardson number in the steam-air tests within COPAIN

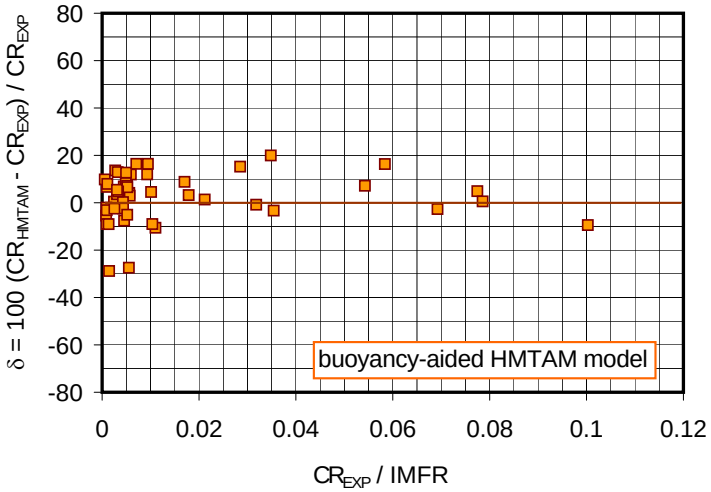

Figure 8.50: Discrepancy between the condensation rate calculated by the *buoyancy-aided* HMTAM model and the experimental value derived from the experimental average heat flux vs. the ratio between the experimental overall condensation rate and the inlet mass flow rate (IMFR) in the steam-air tests within COPAIN

The comparison between the experimental condensation rates and those obtained by adopting Eq. (8.9) is shown in Fig. 8.51. In Figs. 8.52 and 8.53, the discrepancy between the calculated and the experimental condensation rates is reported, respectively as a function of the average Richardson number and the ratio between the experimental overall condensation rate and the inlet mass flow rate (IMFR). As can be seen, the accuracy of the model is poor in the range of the average Richardson numbers between 1 and 10, for which buoyancy effects are more important. Indeed, as it can be seen in Fig. 8.54, the buoyancy-aided correlation proposed in Eq. (8.6) and the formulation expressed by Eq. (8.9) are very similar in situations dominated either by forced convection or by natural convection. A remarkable difference is instead experienced in the mixed convection range, for which the second formulation results less appropriate.

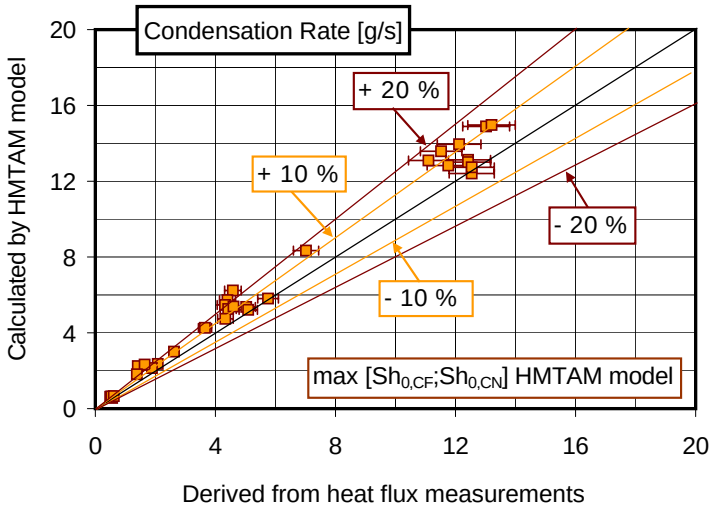

Figure 8.51: Overall condensation rate in the COPAIN steam-air tests: Prediction by the HMTAM model adopting Eq. (8.9) vs. experimental value derived from the experimental average heat flux

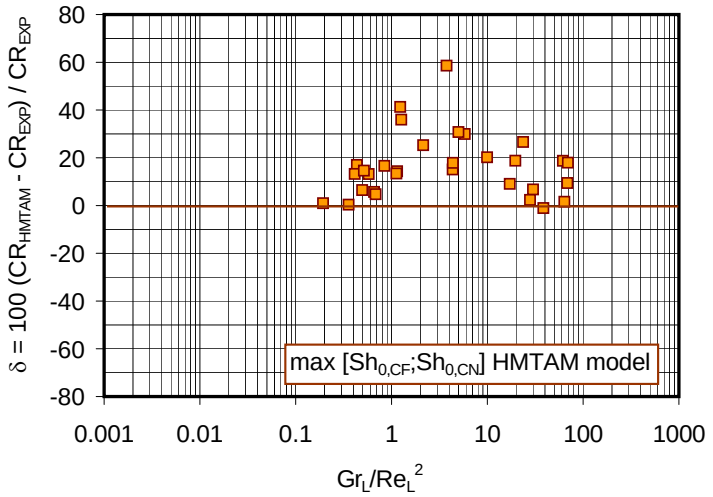

Figure 8.52: Discrepancy between the condensation rate calculated by the HMTAM model adopting Eq. (8.9) and the experimental value derived from the experimental average heat flux vs. average Richardson number in the steam-air tests within COPAIN

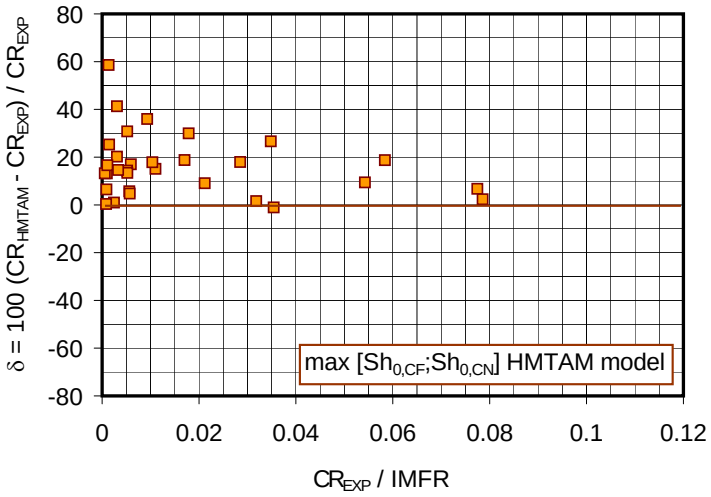

Figure 8.53: Discrepancy between the condensation rate calculated by the HMTAM model adopting Eq. (8.9) and the experimental value derived from the experimental average heat flux vs. the ratio between the experimental overall condensation rate and the inlet mass flow rate (IMFR) in the steam-air tests within COPAIN

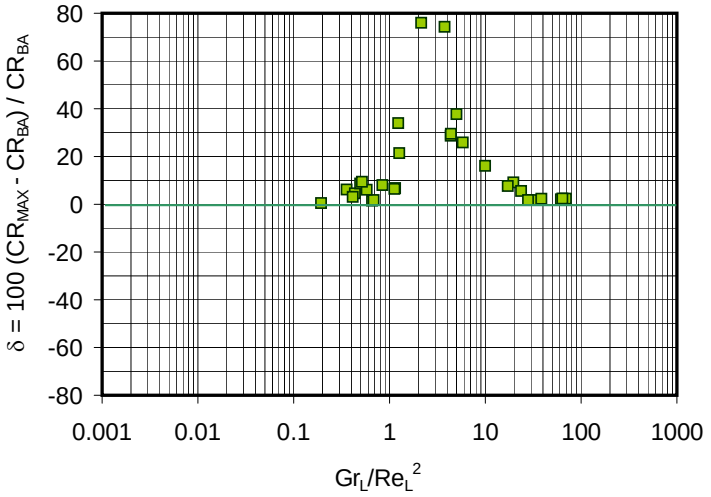

Figure 8.54: Discrepancy between the condensation rate calculated by the HMTAM model adopting Eq. (8.9) and the condensation rate calculated by the *buoyancy-aided* HMTAM model vs. average Richardson number in the steam-air tests within COPAIN

8.3 Modelling steam-air-helium condensation tests within the CONAN facility

In this paragraph, the results of the steam-air-helium condensation tests performed within CONAN is presented. In the first part, the cases at high free stream velocity are addressed by the HMTDM models. Later, the cases at low free stream velocity are addressed by the same models[2]. Finally, the results obtained by the HMTAM model for both phenomenologies are reported and discussed.

8.3.1 Modelling steam-air-helium CONAN tests at high free stream velocity by HMTDM models

The modelling of the steam-air-helium tests within CONAN was performed by both HMTDM models. The complete set of boundary conditions is reported in Tab. 5.4. The comparison with local experimental data is cast in terms of local Sherwood numbers. Calculated and experimental values are compared from Fig. 8.55 to Fig. 8.79, where the classical Schlichting correlation for forced convection is also reported. As it can be seen, forced convection regimes are mostly predicted for all free stream velocities. The performances of the two different diffusion models, the HMTDM^{EBD} (left figures) and the HMTDM^{MSD} (right figures) are very similar: a very good agreement is observed in the asymptotic region where fully developed flow is expected.

In Fig. 8.80, a comparison between the local experimental and calculated Sherwood numbers is proposed at a distance of 1.94 m from the inlet section, corresponding to the last available measurement point in the test section. Data from the different tests are reported as a function of the helium-to-noncondensable gas ratio defined in chapter 5. As it can be seen, experimental and calculated values to the Schlichting correlation are reasonably in the order of unity. This means that, whatever is the helium concentration, forced convection conditions are likely to be experienced in test performed at high free stream velocities. When the Sherwood numbers are considered instead of the ones corrected to account for suction, a clear dependence from helium is instead experienced, as shown in Fig. 8.81. The actual Sherwood number decreases for increasing helium-to-noncondensable gas ratio, when the helium concentration is small. On the other hand, when the helium concentration is large, an increase in the helium-to-noncondensable gas ratio implies an increase in the actual Sherwood number. These effects are likely to be due to mixture properties modifications induced by helium, but the demarcation between the two behavior is not clear. Unfortunately, extensive experimental data are not available in this range and more detailed conclusions are difficult to be drawn.

[2] As reported in chapter 4, tests are labeled as follows:

Paa-Tbb-Vcc-Hee

- aa : steam generator power in kW;
- bb : secondary coolant temperature at the inlet of the cooling channel [$^{\circ}C$];
- cc : inlet velocity in decimal of m/s;
- ee : molar fractions of helium in the noncondensable gas.

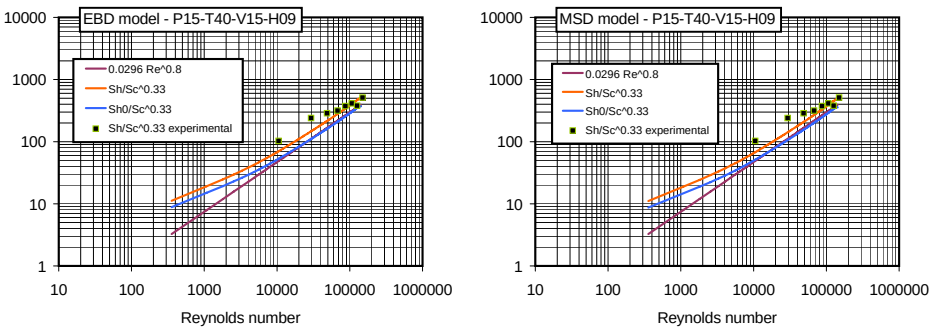

Figure 8.55: Calculated vs. experimental Sherwood number in the P15-T40-V15-H09 test by the HMTDM^{EBD} model (left) and the HMTDM^{MSD} model (right)

In the first part of the channel, next to the inlet cross section, calculated Sherwood numbers are lower than experimental. In this region, condensation phenomena are therefore underestimated. This effect, remarked in all test cases, corresponds to a region in which momentum, temperature and species boundary layers are developing. Albeit grid convergence is tested in longitudinal direction, capabilities of turbulence models are tested only for fully developed conditions, whereas transitional flows like those that may be experienced in the first part of the CONAN test section have not been addressed.

Calculated and experimental overall condensation rates are finally compared in Fig. 8.82. As it can be seen, both the HMTDM models, for which predicted condensation rates are very similar, tend to underestimate the experimental value. This is probably due to entrance effects, that are more important in presence of helium with respect to the steam-air tests. Moreover, these effects seem to be more and more important at the lower heat trnasfer rates. Indeed, it is remarked that in test cases at the lowest steam generator power (15 kW), the transient behavior of the experimental Sherwood numbers differs qualitatively from the predicted values and from the other series at 20 and 25 kW. Experimental Sherwood numbers are in fact remarkably higher in the developing region than those predicted by both models. As a consequence, a larger underestimation of the overall condensation rate is observed for these tests. In Fig. 8.83, the discrepancy between the calculated and the experimental condensation rates are reported as a function of the helium-to-noncondensable gas ratio. The tests of the P15-T40 series are those having the higher discrepancy with experimental data, as it can be seen in Fig. 8.84, where the data points corresponding to this series are omitted.

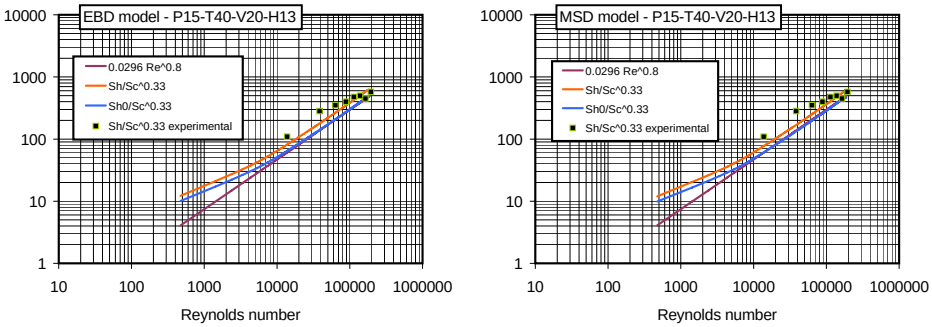

Figure 8.56: Calculated vs. experimental Sherwood number in the P15-T40-V20-H13 test by the HMTDM^{EBD} model (left) and the HMTDM^{MSD} model (right)

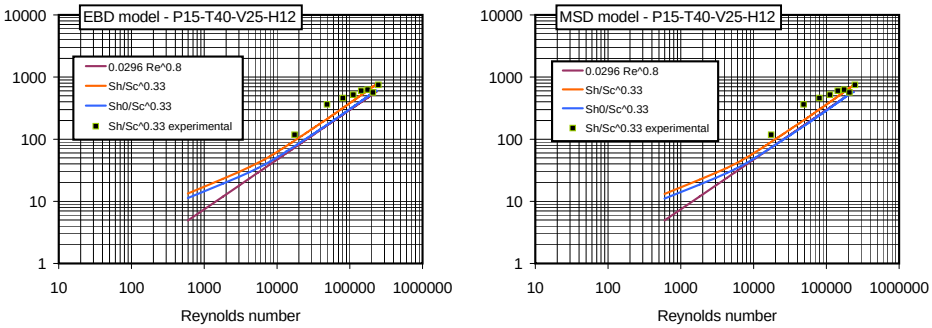

Figure 8.57: Calculated vs. experimental Sherwood number in the P15-T40-V25-H12 test by the HMTDM^{EBD} model (left) and the HMTDM^{MSD} model (right)

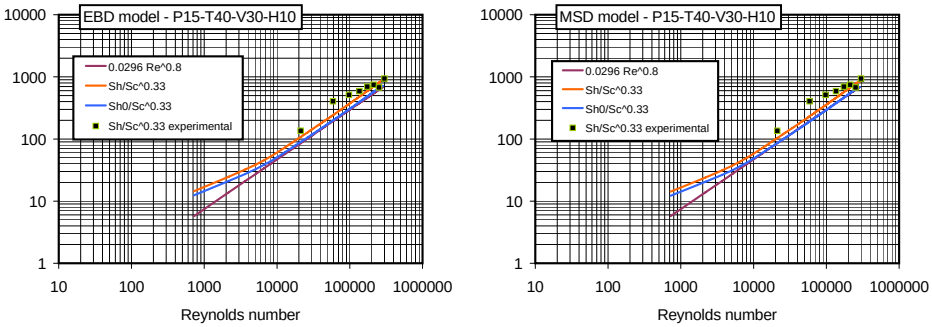

Figure 8.58: Calculated vs. experimental Sherwood number in the P15-T40-V30-H10 test by the HMTDM^{EBD} model (left) and the HMTDM^{MSD} model (right)

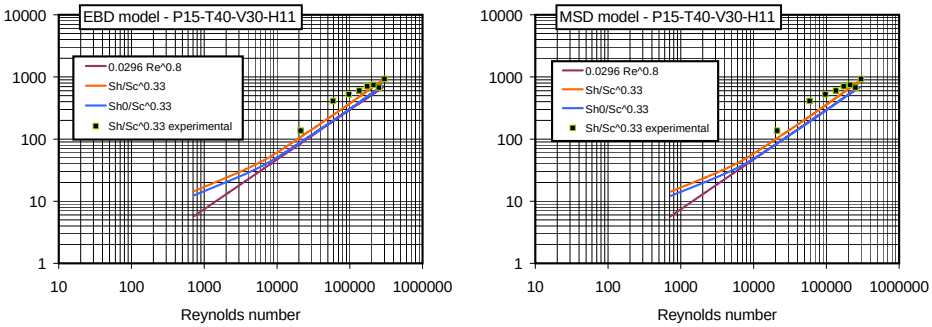

Figure 8.59: Calculated vs. experimental Sherwood number in the P15-T40-V30-H11 test by the HMTDM^{EBD} model (left) and the HMTDM^{MSD} model (right)

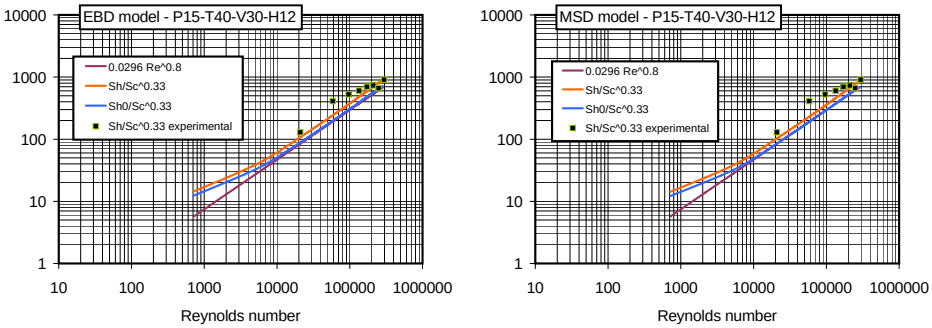

Figure 8.60: Calculated vs. experimental Sherwood number in the P15-T40-V30-H12 test by the HMTDM^{EBD} model (left) and the HMTDM^{MSD} model (right)

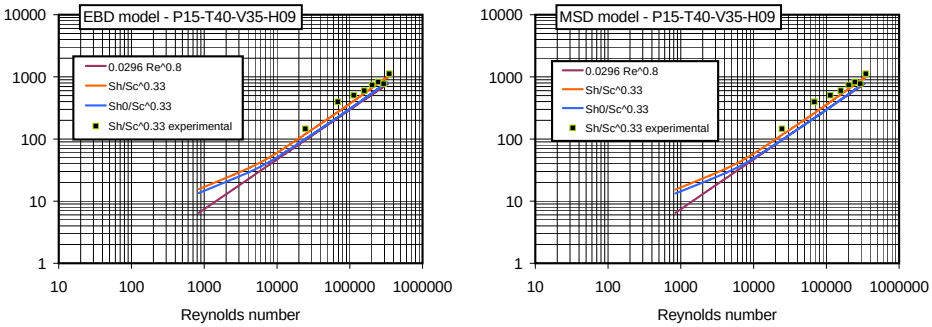

Figure 8.61: Calculated vs. experimental Sherwood number in the P15-T40-V35-H09 test by the HMTDM^{EBD} model (left) and the HMTDM^{MSD} model (right)

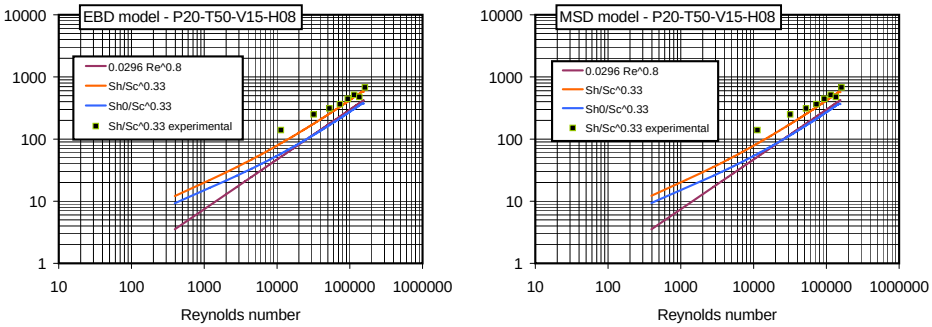

Figure 8.62: Calculated vs. experimental Sherwood number in the P20-T50-V15-H08 test by the HMTDM^{EBD} model (left) and the HMTDM^{MSD} model (right)

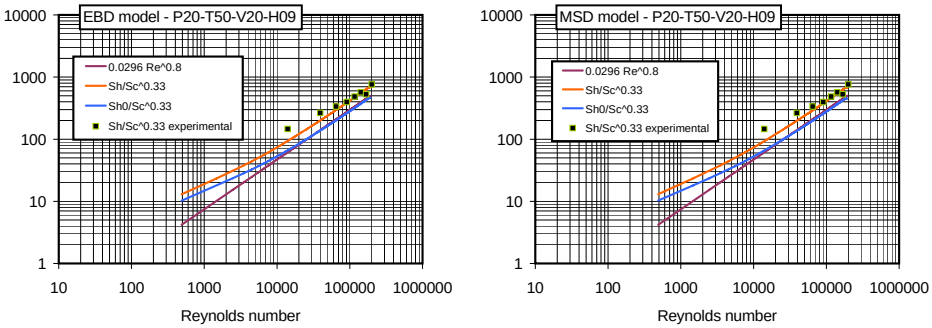

Figure 8.63: Calculated vs. experimental Sherwood number in the P20-T50-V20-H09 test by the HMTDM^{EBD} model (left) and the HMTDM^{MSD} model (right)

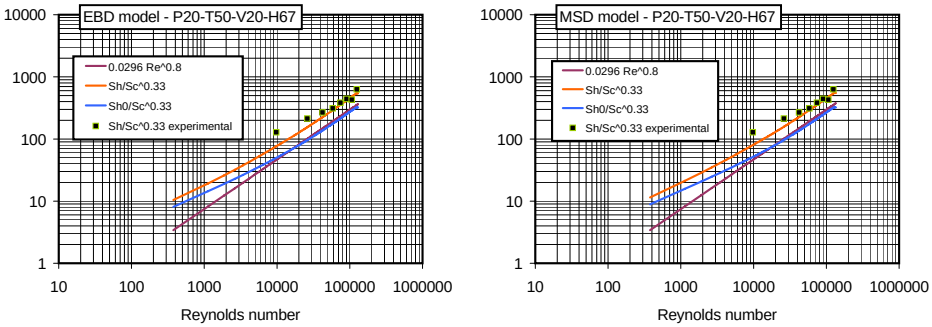

Figure 8.64: Calculated vs. experimental Sherwood number in the P20-T50-V20-H67 test by the HMTDM^{EBD} model (left) and the HMTDM^{MSD} model (right)

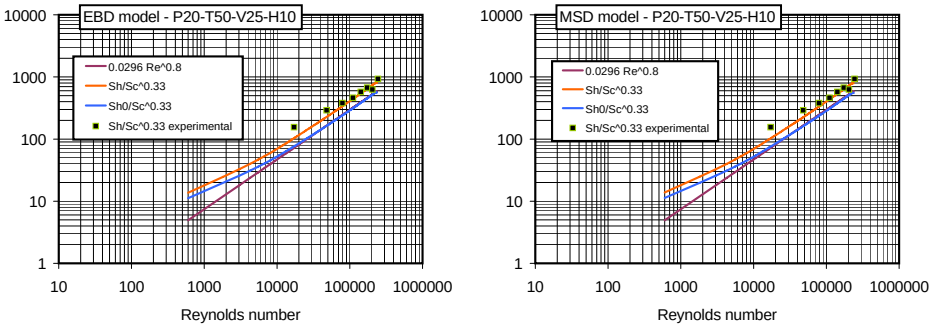

Figure 8.65: Calculated vs. experimental Sherwood number in the P20-T50-V25-H10 test by the HMTDM^{EBD} model (left) and the HMTDM^{MSD} model (right)

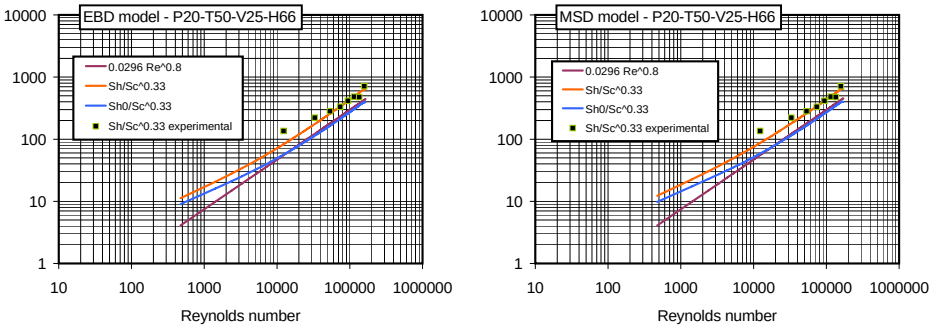

Figure 8.66: Calculated vs. experimental Sherwood number in the P20-T50-V25-H66 test by the HMTDM^{EBD} model (left) and the HMTDM^{MSD} model (right)

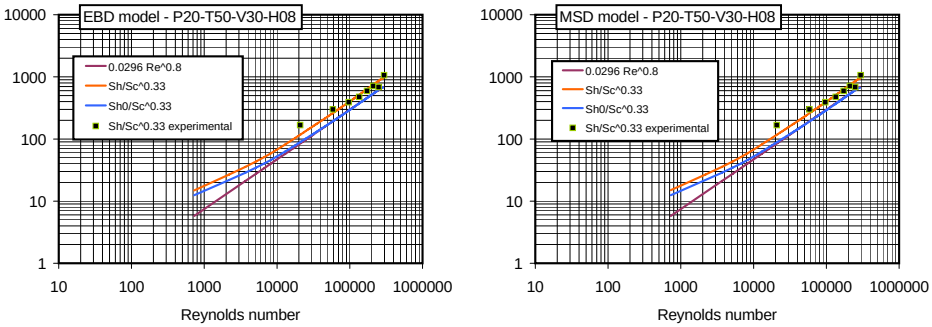

Figure 8.67: Calculated vs. experimental Sherwood number in the P20-T50-V30-H08 test by the HMTDM^{EBD} model (left) and the HMTDM^{MSD} model (right)

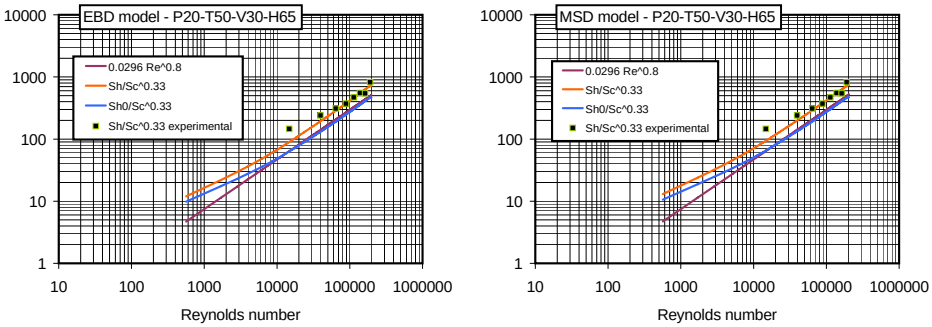

Figure 8.68: Calculated vs. experimental Sherwood number in the P20-T50-V30-H65 test by the HMTDM^{EBD} model (left) and the HMTDM^{MSD} model (right)

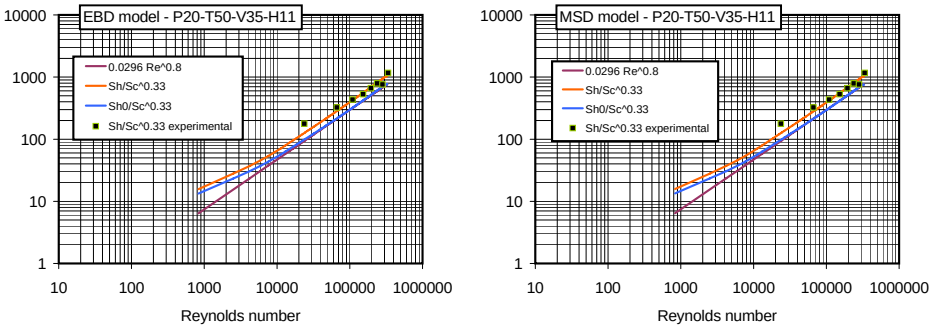

Figure 8.69: Calculated vs. experimental Sherwood number in the P20-T50-V35-H11 test by the HMTDM^{EBD} model (left) and the HMTDM^{MSD} model (right)

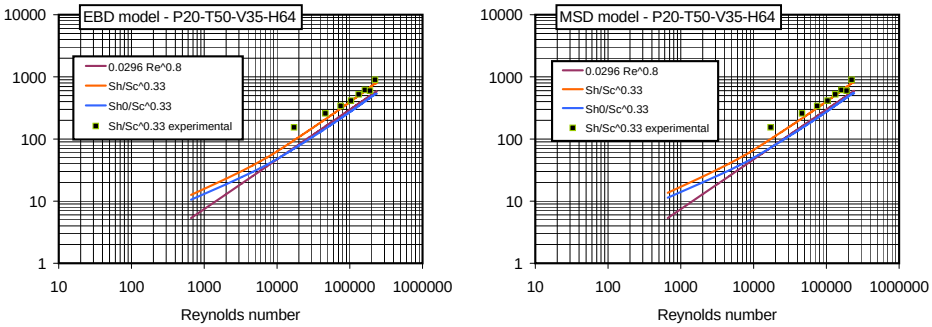

Figure 8.70: Calculated vs. experimental Sherwood number in the P20-T50-V35-H64 test by the HMTDM^{EBD} model (left) and the HMTDM^{MSD} model (right)

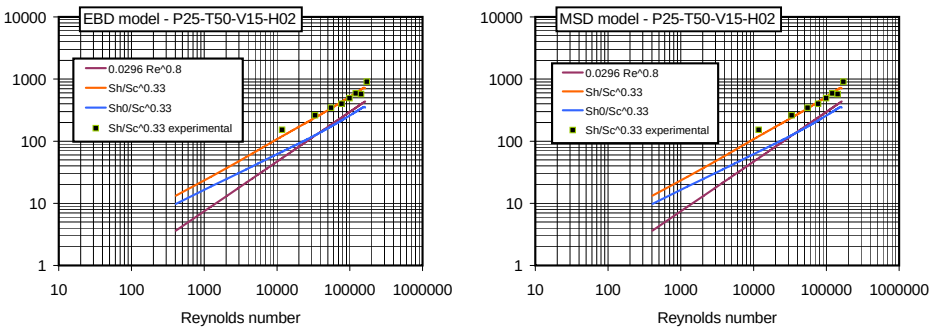

Figure 8.71: Calculated vs. experimental Sherwood number in the P25-T50-V15-H02 test by the HMTDM^{EBD} model (left) and the HMTDM^{MSD} model (right)

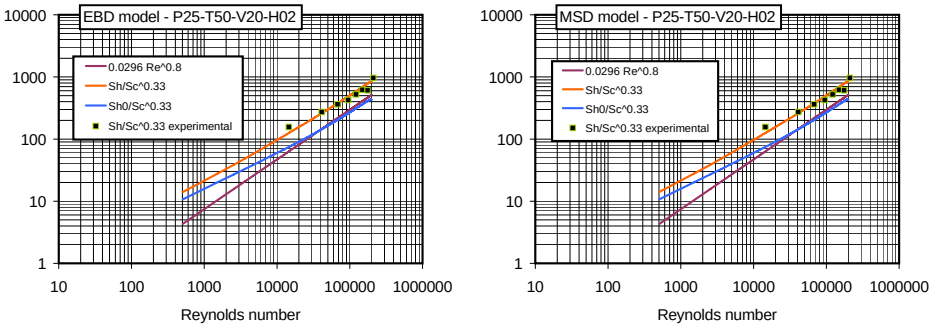

Figure 8.72: Calculated vs. experimental Sherwood number in the P25-T50-V20-H02 test by the HMTDM^{EBD} model (left) and the HMTDM^{MSD} model (right)

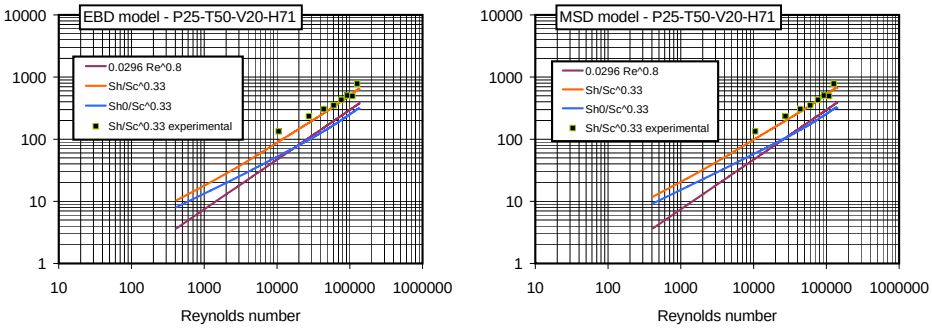

Figure 8.73: Calculated vs. experimental Sherwood number in the P25-T50-V20-H71 test by the HMTDM^{EBD} model (left) and the HMTDM^{MSD} model (right)

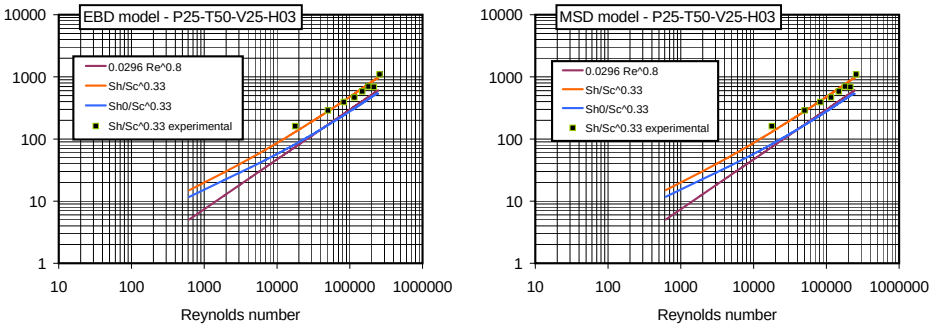

Figure 8.74: Calculated vs. experimental Sherwood number in the P25-T50-V25-H03 test by the HMTDM^{EBD} model (left) and the HMTDM^{MSD} model (right)

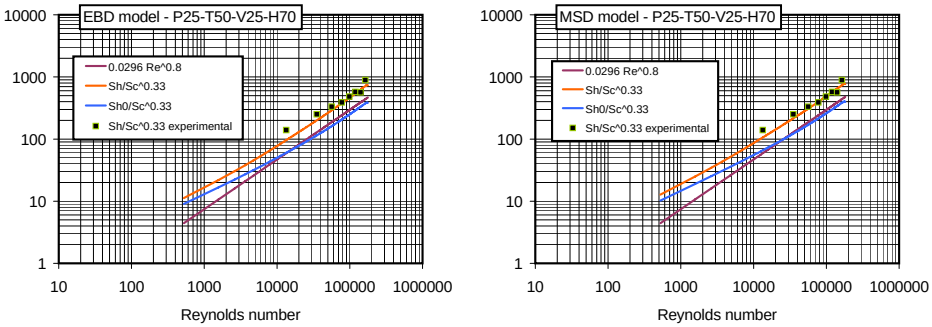

Figure 8.75: Calculated vs. experimental Sherwood number in the P25-T50-V25-H70 test by the HMTDM^{EBD} model (left) and the HMTDM^{MSD} model (right)

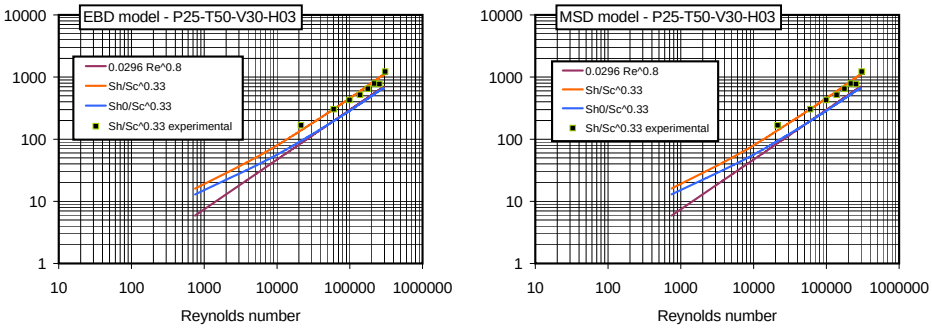

Figure 8.76: Calculated vs. experimental Sherwood number in the P25-T50-V30-H03 test by the HMTDM^{EBD} model (left) and the HMTDM^{MSD} model (right)

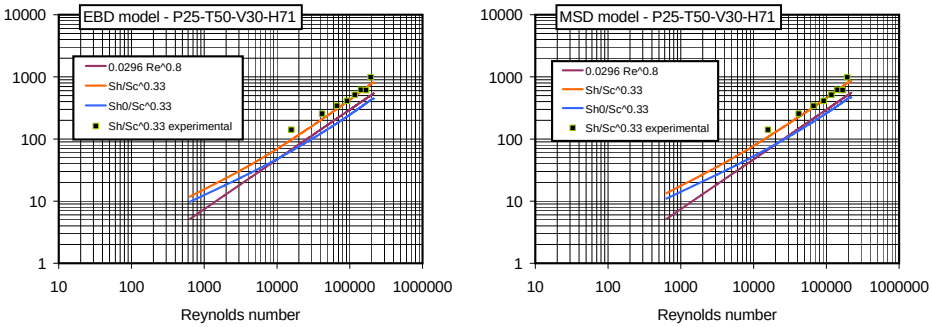

Figure 8.77: Calculated vs. experimental Sherwood number in the P25-T50-V30-H71 test by the HMTDM^{EBD} model (left) and the HMTDM^{MSD} model (right)

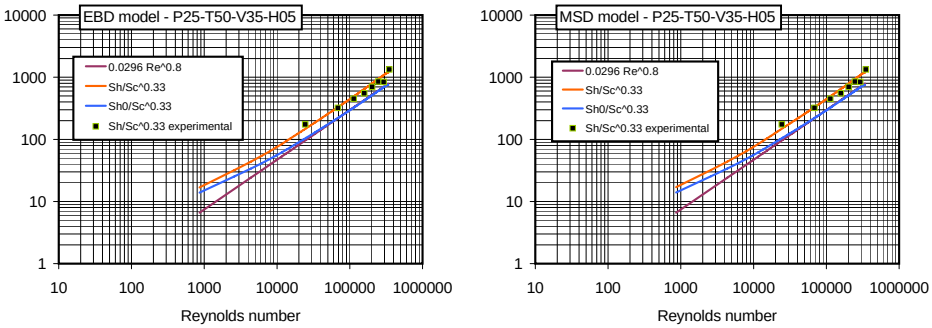

Figure 8.78: Calculated vs. experimental Sherwood number in the P25-T50-V35-H05 test by the HMTDM^{EBD} model (left) and the HMTDM^{MSD} model (right)

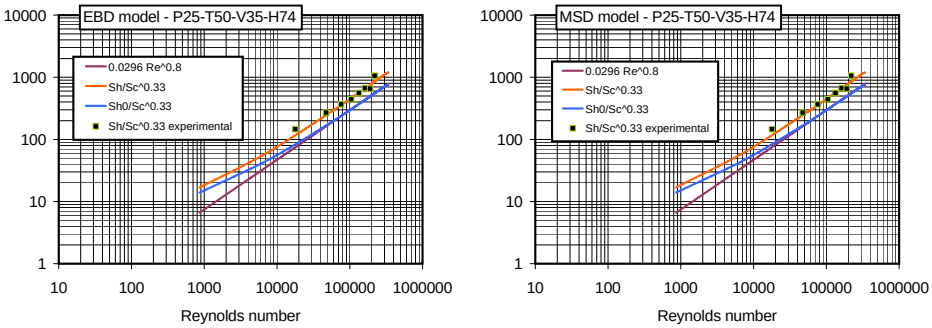

Figure 8.79: Calculated vs. experimental Sherwood number in the P25-T50-V35-H74 test by the HMTDM^{EBD} model (left) and the HMTDM^{MSD} model (right)

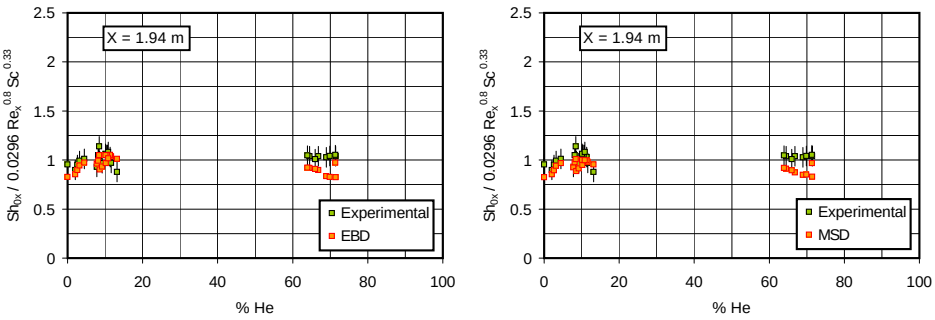

Figure 8.80: Calculated vs. experimental Sherwood number Sh_{0x}, normalized to the Schlichting correlation as a function of the helium-to-noncondensable gas ratio at the distance of 1.94 m from the inlet section

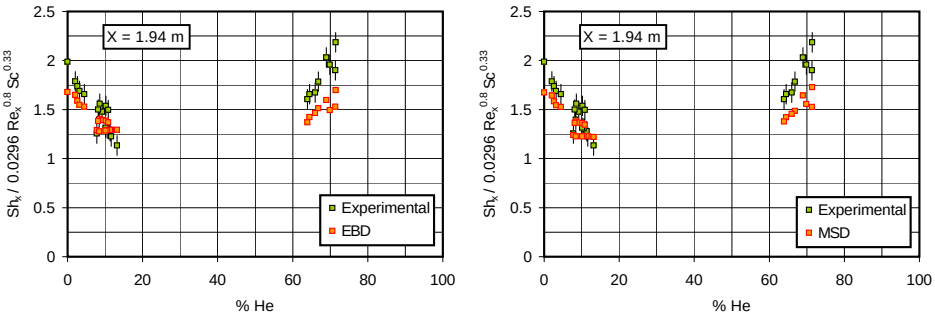

Figure 8.81: Calculated vs. experimental Sherwood number Sh_x, normalized to the Schlichting correlation as a function of the helium-to-noncondensable gas ratio at the distance of 1.94 m from the inlet section

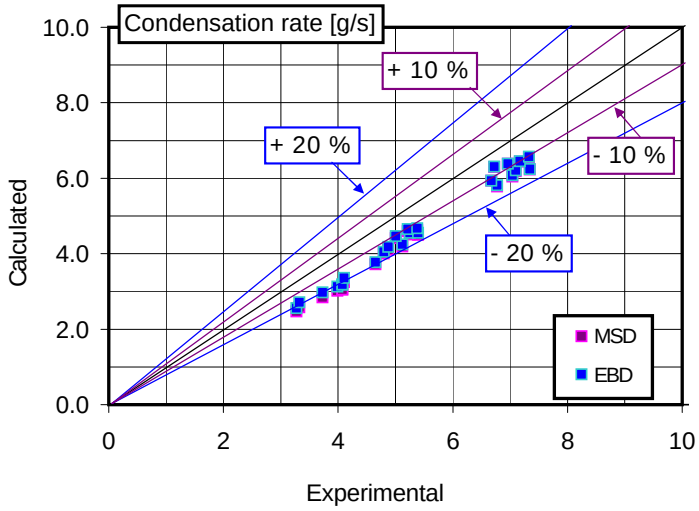

Figure 8.82: Overall condensation rate in the CONAN steam-air-helium tests at high free stream velocity: Prediction by the HMTDM models vs. experimental data

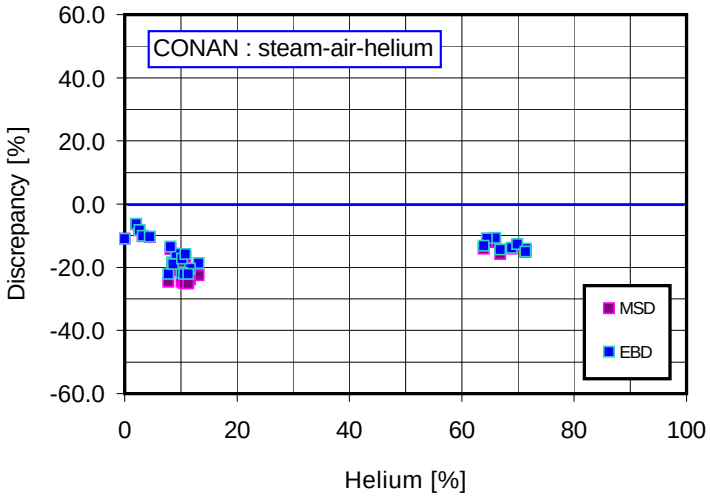

Figure 8.83: Discrepancy between the condensation rate calculated by the HMTDM models and the experimental overall condensation rate vs. the helium-to-noncondensable gas ratio in the test series within CONAN

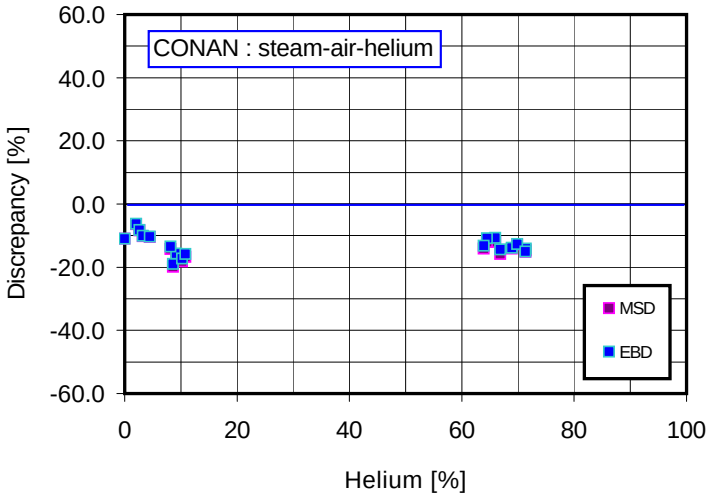

Figure 8.84: Discrepancy between the condensation rate calculated by the HMTDM models and the experimental overall condensation rate vs. the helium-to-noncondensable gas ratio in the P20-T50 and P25-T50 test series with helium within CONAN

8.3.2 Modelling steam-air-helium CONAN tests at low free stream velocity by HMTDM models

The CONAN tests at low free stream velocities have also been addressed by both the HMTDM^{EBD} and the HMTDM^{MSD} models. The complete set of boundary conditions is reported in Tab. 5.5.

From Fig. 8.85 to Fig. 8.103, the local experimental Sherwood numbers are compared to those predicted by both models as a function of the local Reynolds number. Profiles are reported for the different tests in order of growing helium-to-noncondensable gas ratios, departing from a test having a very small percentage of helium for which the interface mixture is heavier than the bulk and the flow is essentially driven by buoyancy. As it can be seen in Fig. 8.85, corresponding to a pure steam-air case at low free-stream velocity, experimental Sherwood numbers near the outlet section of the channel are characterized by a different slope than forced convection. Indeed, near the outlet section, buoyancy effects due to air are dominating effects and the expected convection regime is natural convection. Both models allow capturing the expected growth of the Sherwood number in the last part of the channel, but their behavior in the flow development region is quite different from the experimental. Experimental data point out the presence of strong entrance effects related to the presence of helium.

The experimental trend corresponding to datapoints near the outlet section is clearer. Despite a fully developed regime is hardly reached, as also remarked in chapter 5, the dependence of the asymptotic Sherwood numbers on the helium to noncondensable ratio suggest the presence of interesting effects. As shown in Fig. 8.104 and 8.105, where the Sherwood number Sh_x and the corrected Sherwood number Sh_{0x} are reported for all tests as a function of the helium to noncondensable ratio, the presence of a minimum corresponding to the so called *buoyancy reversal* condition is experienced for the datapoints nearest to the outlet section. Both experimental and calculated Sherwood numbers show this phenomenon, but CFD models predict the minimum of the Sherwood number shifted towards higher helium to noncondensable ratios. The same analysis is also reported in Figs. 8.106 and 8.107, corresponding to measurements at a distance respectively of 1.39 and 1.14 m from the inlet section. As can be easily noted, whatever is the distance from the inlet section, the presence of a minimum for the same helium to noncondensable ratio is experienced, but the dependence of the Sherwood number on the helium to noncondensable ratio is less evident. As it can be seen from Fig. 8.85 to Fig. 8.94, the asymptotic slope of the Sherwood number profiles decreases when the helium to noncondensable ratio increases, up to the critical value for which *buoyancy reversal* occurs. Indeed, departing from natural convection conditions typical of steam-air mixtures, the reduction of the buoyancy forces due to the presence of helium makes the interface to bulk density difference to decrease. Similarly, the mass transfer coefficient decrease and, as a consequence, also the Sherwood number.

When the *buoyancy reversal* conditions occur, for the critical helium-to-noncondensable gas ratio for which the interface to bulk density difference is zero, the asymptotic slope of the Sherwood profile is well parallel to the Schlichting correlation. The buoyancy forces are in fact annealed and the convection regime is essentially ruled by inertia forces (see Fig. 8.94).

For helium to noncondensable ratio higher than the critical value for which

buoyancy reversal occurs, the asymptotic slope of the Sherwood number increases when helium is added (see from Fig. 8.95 to Fig. 8.103). *Buoyancy-opposed* mixed convection conditions are expected, which make the Sherwood number to increase. When buoyancy forces are very important, the *flow reversal* can occur, which make the Sherwood number increasing remarkably in the last part of the channel. Indeed, *flow reversal* conditions are possibly experienced within the CONAN test section for the tests having the highest helium-to-noncondensable gas ratios.

In Fig. 8.108 calculated velocity profiles are reported, reproducing the aforementioned *flow reversal* phenomenon in the test having helium-to-noncondensable gas ratio of 90 percent for both models. The *flow reversal* is anticipated by the HMTDM^{EBD} model, for which an inversion of the flow field is predicted also in the case having the 78 per cent of helium. Unfortunately, detailed local velocity measurements are not available, which would allow proving the presence of *flow reversal* experimentally. In Fig. 8.109, the velocity profiles predicted by the MSD models are reported for the P05-T40-V06-H90 test, in the proximity of the point where *flow reversal* occurs. As can be seen in the zoomed figure, the longitudinal spatial discretization seems to be refined enough to capture the local phenomenon in detail. To check the sensitivity of the flow reversal point to the grid refinement, the space discretization was refined in the longitudinal direction of a factor 2. In Fig. 8.110, the longitudinal velocity at the center of the cells near the condensing wall is reported as a function of the distance from the inlet section. Major differences are not observed. Grid refinement causes the flow reversal to be slightly anticipated with respect to the reference space discretization, as can be seen in the zoom proposed in Fig. 8.110.

Finally, a comparison between calculated and experimental overall condensation rate is proposed in Fig. 8.111. Despite of the difficulties in reproducing entrance effects and the experimental uncertainty in the value of the free stream velocity, a good agreement is remarked; the calculated condensation rate are generally included in a range of $\pm$ 10 per cent of the experimental values. Both HMTDM models give similar results. For helium-to-noncondensable gas ratio less than the critical value for which *buoyancy reversal* occurs, the discrepancy with the experimental data is very small, mostly for the EBD model (see Fig. 8.112). For helium-to-noncondensable gas ratios greater than the *buoyancy reversal* value, coherently with the behavior of the local Sherwood number profiles (see from Fig. 8.95 to Fig. 8.103) both models tend to underestimate the overall condensation rate.

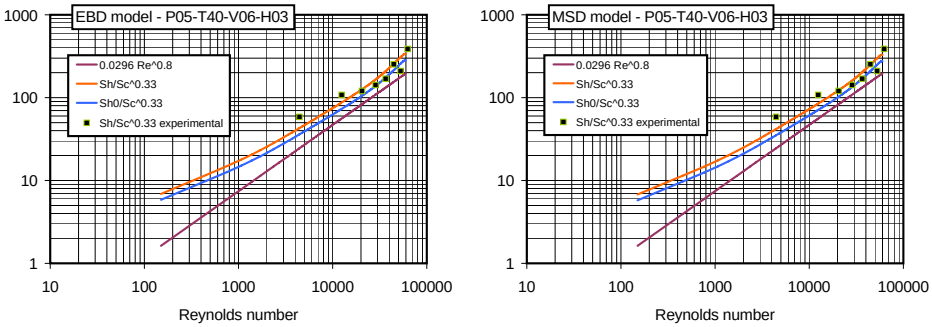

Figure 8.85: Calculated vs. experimental Sherwood number in the P05-T40-V06-H03 test by the HMTDM^{EBD} model (left) and the HMTDM^{MSD} model (right)

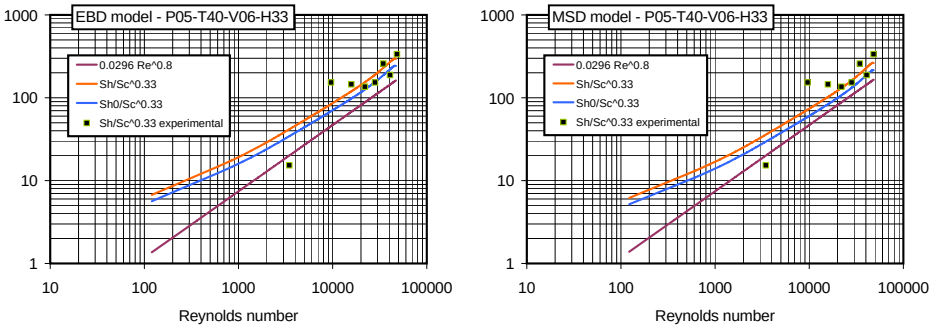

Figure 8.86: Calculated vs. experimental Sherwood number in the P05-T40-V06-H33 test by the HMTDM^{EBD} model (left) and the HMTDM^{MSD} model (right)

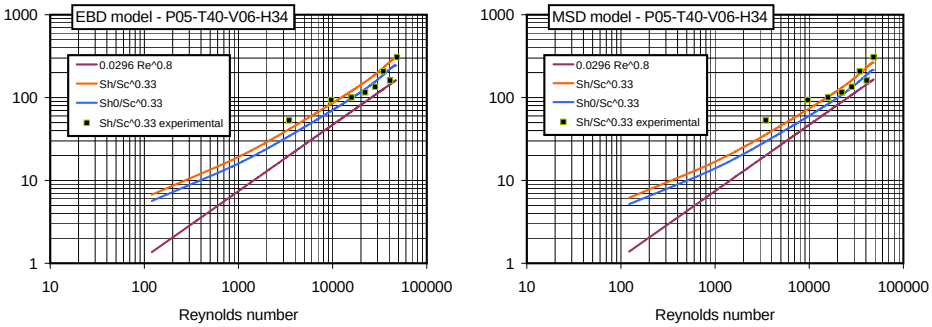

Figure 8.87: Calculated vs. experimental Sherwood number in the P05-T40-V06-H34 test by the HMTDM^{EBD} model (left) and the HMTDM^{MSD} model (right)

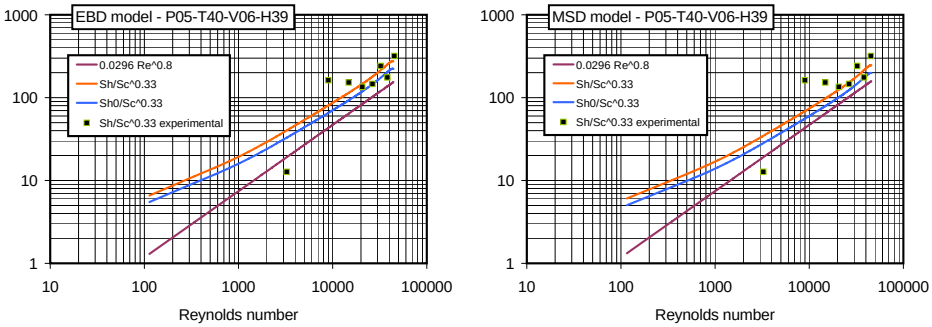

Figure 8.88: Calculated vs. experimental Sherwood number in the P05-T40-V06-H39 test by the HMTDM^{EBD} model (left) and the HMTDM^{MSD} model (right)

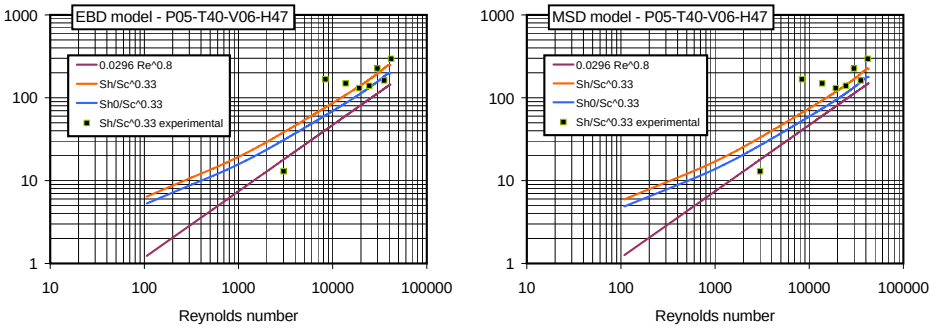

Figure 8.89: Calculated vs. experimental Sherwood number in the P05-T40-V06-H47 test by the HMTDM^{EBD} model (left) and the HMTDM^{MSD} model (right)

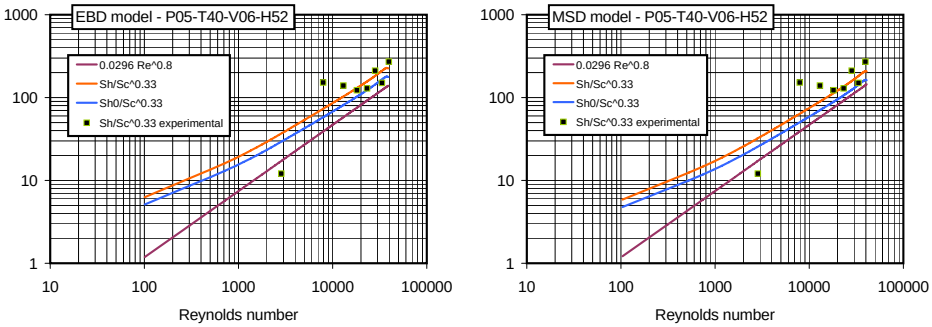

Figure 8.90: Calculated vs. experimental Sherwood number in the P05-T40-V06-H52 test by the HMTDM^{EBD} model (left) and the HMTDM^{MSD} model (right)

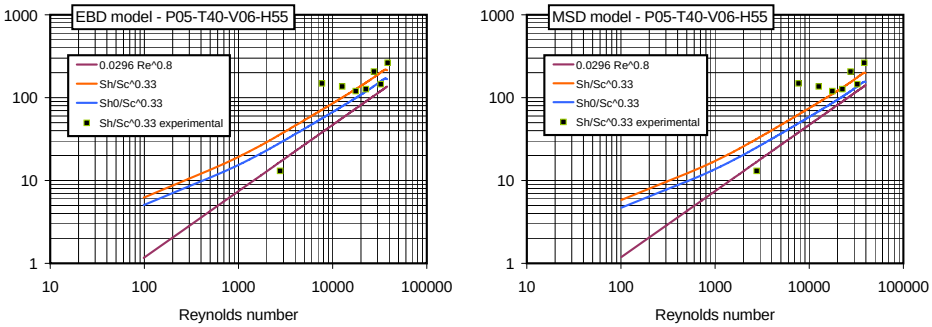

Figure 8.91: Calculated vs. experimental Sherwood number in the P05-T40-V06-H55 test by the HMTDM^{EBD} model (left) and the HMTDM^{MSD} model (right)

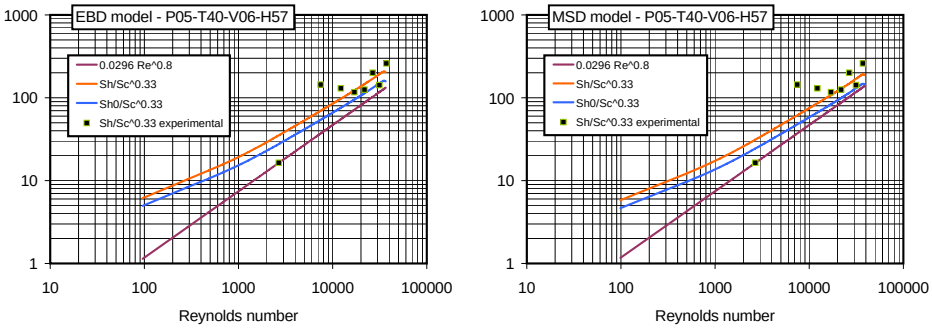

Figure 8.92: Calculated vs. experimental Sherwood number in the P05-T40-V06-H57 test by the HMTDM^{EBD} model (left) and the HMTDM^{MSD} model (right)

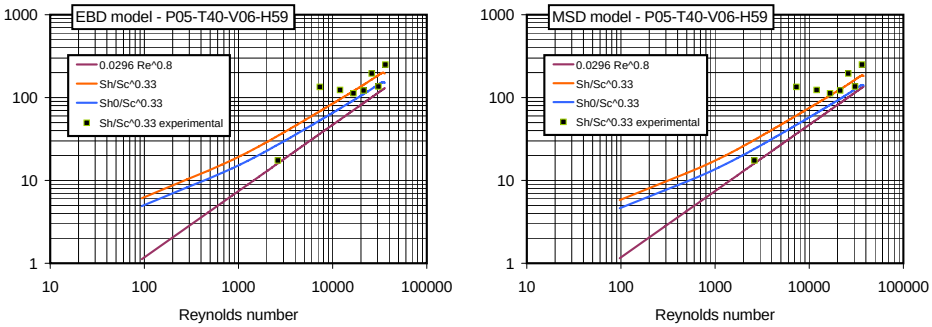

Figure 8.93: Calculated vs. experimental Sherwood number in the P05-T40-V06-H59 test by the HMTDM^{EBD} model (left) and the HMTDM^{MSD} model (right)

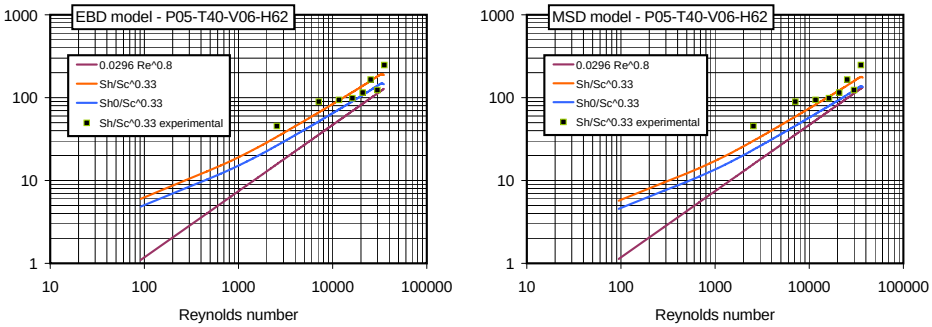

Figure 8.94: Calculated vs. experimental Sherwood number in the P05-T40-V06-H62 test by the HMTDM^{EBD} model (left) and the HMTDM^{MSD} model (right)

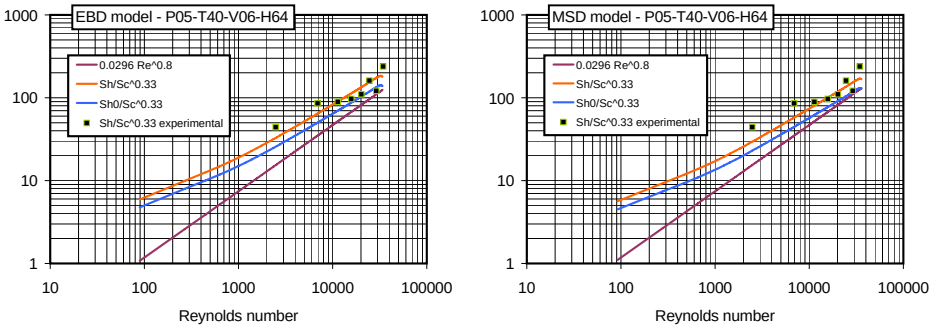

Figure 8.95: Calculated vs. experimental Sherwood number in the P05-T40-V06-H64 test by the HMTDM^{EBD} model (left) and the HMTDM^{MSD} model (right)

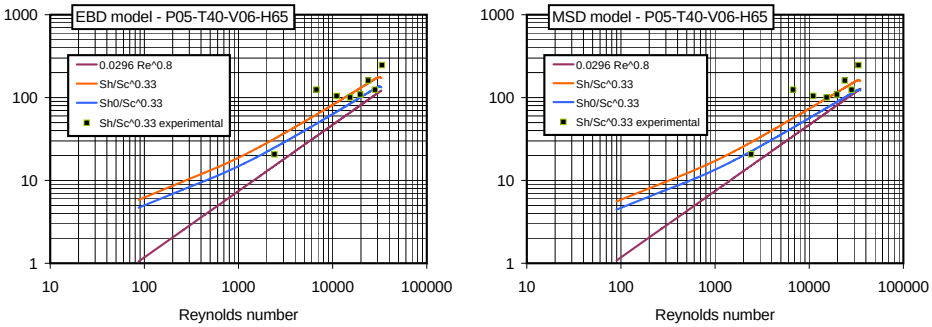

Figure 8.96: Calculated vs. experimental Sherwood number in the P05-T40-V06-H65 test by the HMTDM^{EBD} model (left) and the HMTDM^{MSD} model (right)

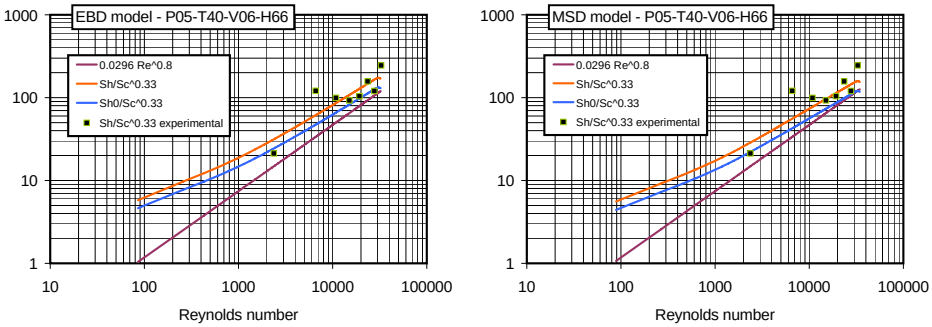

Figure 8.97: Calculated vs. experimental Sherwood number in the P05-T40-V06-H66 test by the HMTDM^{EBD} model (left) and the HMTDM^{MSD} model (right)

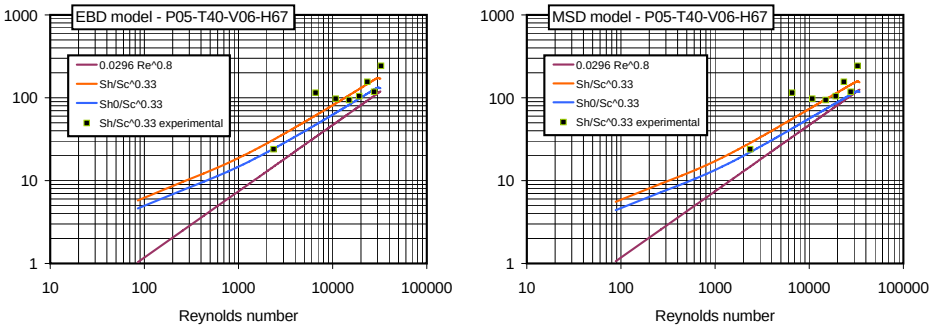

Figure 8.98: Calculated vs. experimental Sherwood number in the P05-T40-V06-H67 test by the HMTDM^{EBD} model (left) and the HMTDM^{MSD} model (right)

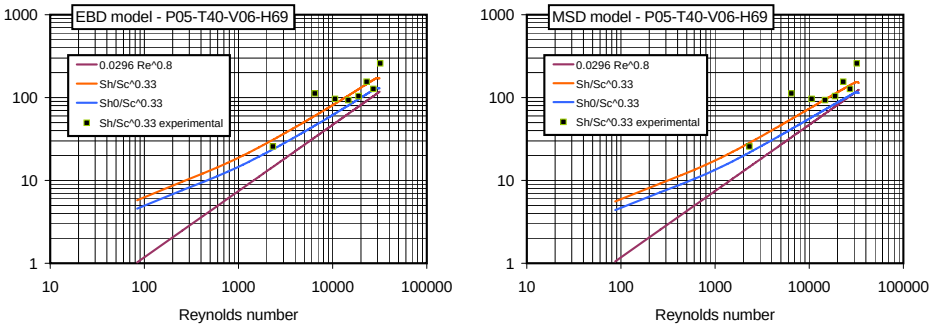

Figure 8.99: Calculated vs. experimental Sherwood number in the P05-T40-V06-H69 test by the HMTDM^{EBD} model (left) and the HMTDM^{MSD} model (right)

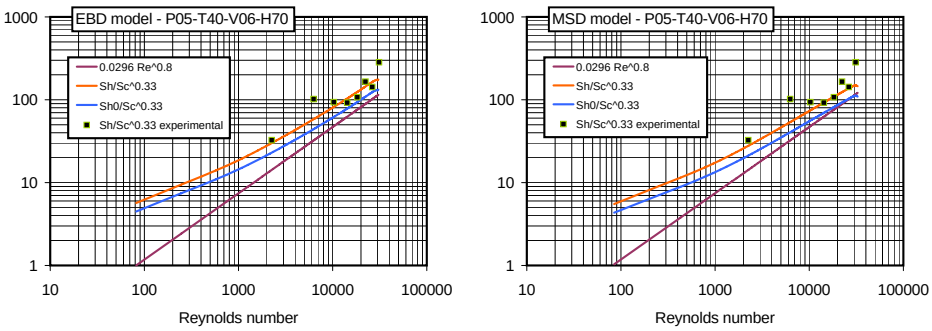

Figure 8.100: Calculated vs. experimental Sherwood number in the P05-T40-V06-H70 test by the HMTDM^{EBD} model (left) and the HMTDM^{MSD} model (right)

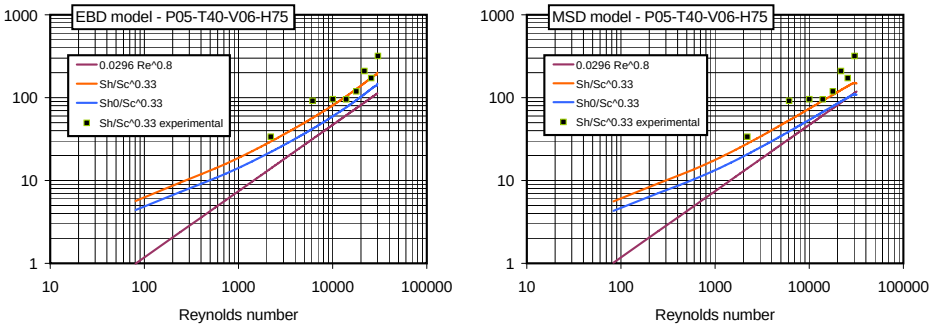

Figure 8.101: Calculated vs. experimental Sherwood number in the P05-T40-V06-H75 test by the HMTDM^{EBD} model (left) and the HMTDM^{MSD} model (right)

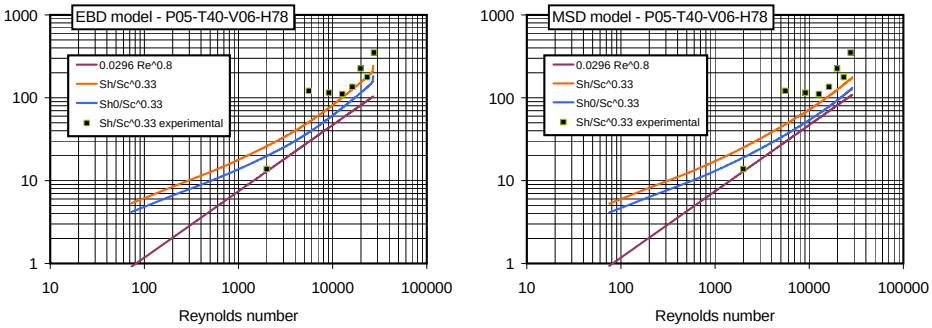

Figure 8.102: Calculated vs. experimental Sherwood number in the P05-T40-V06-H78 test by the HMTDM^{EBD} model (left) and the HMTDM^{MSD} model (right)

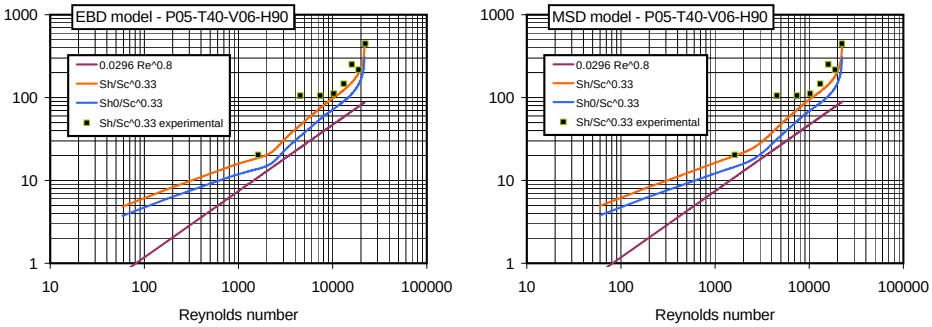

Figure 8.103: Calculated vs. experimental Sherwood number in the P05-T40-V06-H90 test by the HMTDM^{EBD} model (left) and the HMTDM^{MSD} model (right)

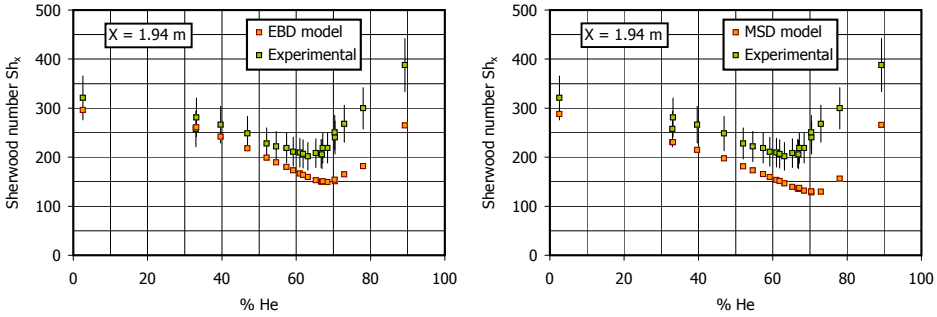

Figure 8.104: Calculated vs. experimental Sherwood number Sh_x as a function of the helium-to-noncondensable gas ratio at the distance of 1.94 m from the inlet section

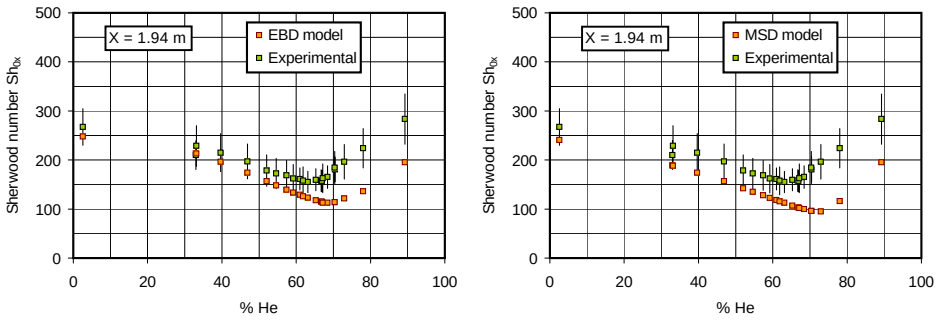

Figure 8.105: Calculated vs. experimental Sherwood number Sh_{0x} as a function of the helium-to-noncondensable gas ratio at the distance of 1.94 m from the inlet section

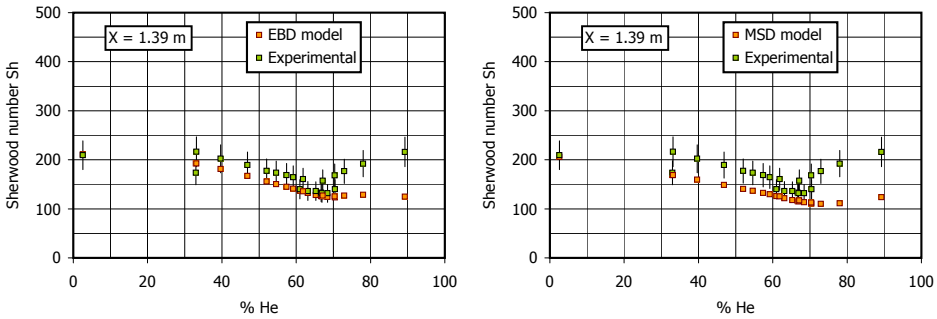

Figure 8.106: Calculated vs. experimental Sherwood number Sh_x as a function of the helium-to-noncondensable gas ratio at the distance of 1.39 m from the inlet section

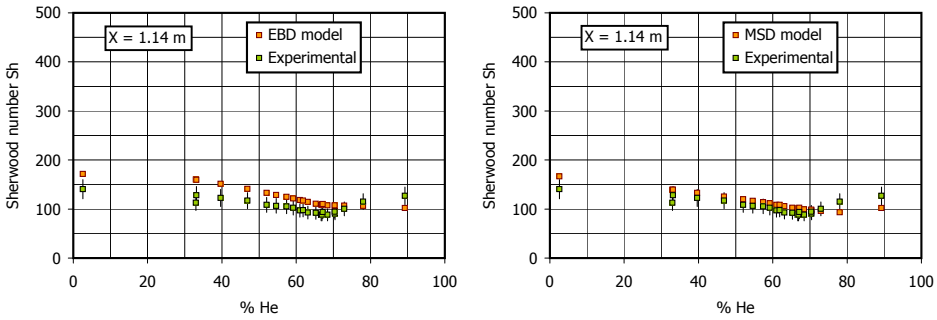

Figure 8.107: Calculated vs. experimental Sherwood number Sh_x as a function of the helium-to-noncondensable gas ratio at the distance of 1.14 m from the inlet section

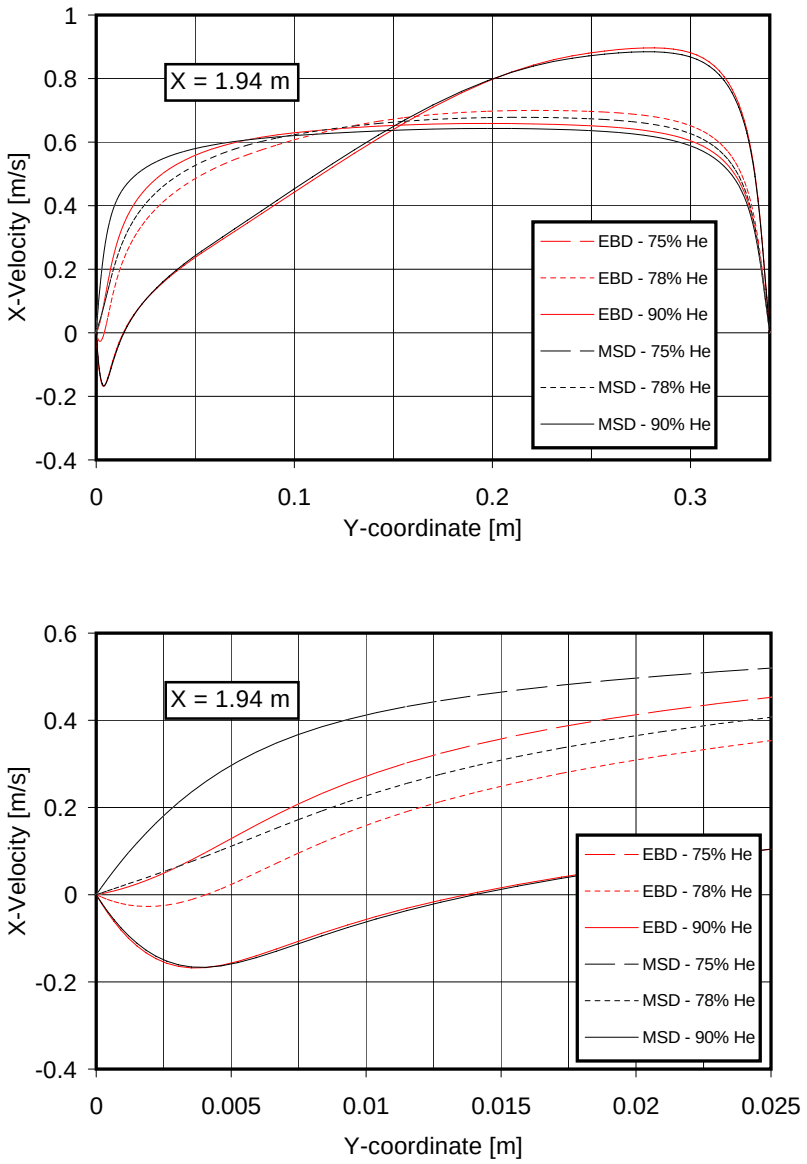

Figure 8.108: Calculated longitudinal velocity profiles in the P05-T40-V06-H75, P05-T40-V06-H78 and P05-T40-V06-H90 test (near-wall velocity profiles are zoomed in the bottom figure)

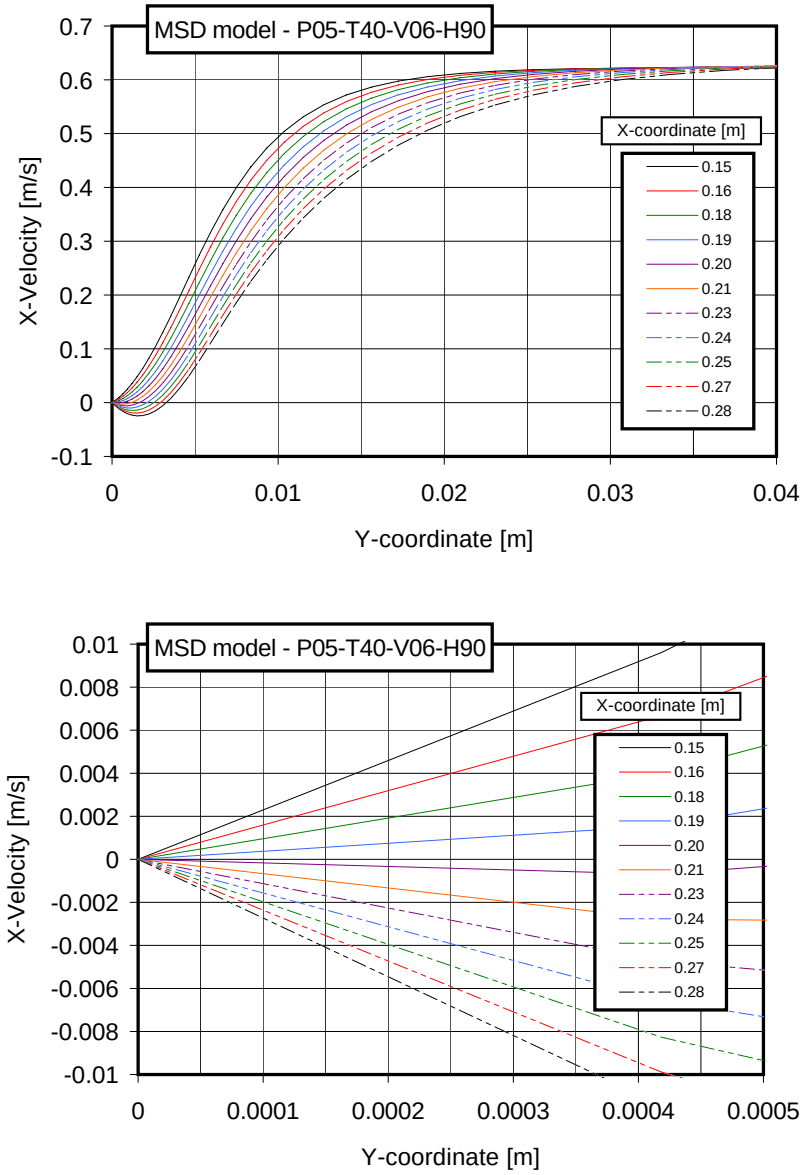

Figure 8.109: Calculated longitudinal velocity profiles near the *flow reversal* point in the P05-T40-V06-H90 test at different distance from the inlet section (near-wall velocity profiles are zoomed in the bottom figure)

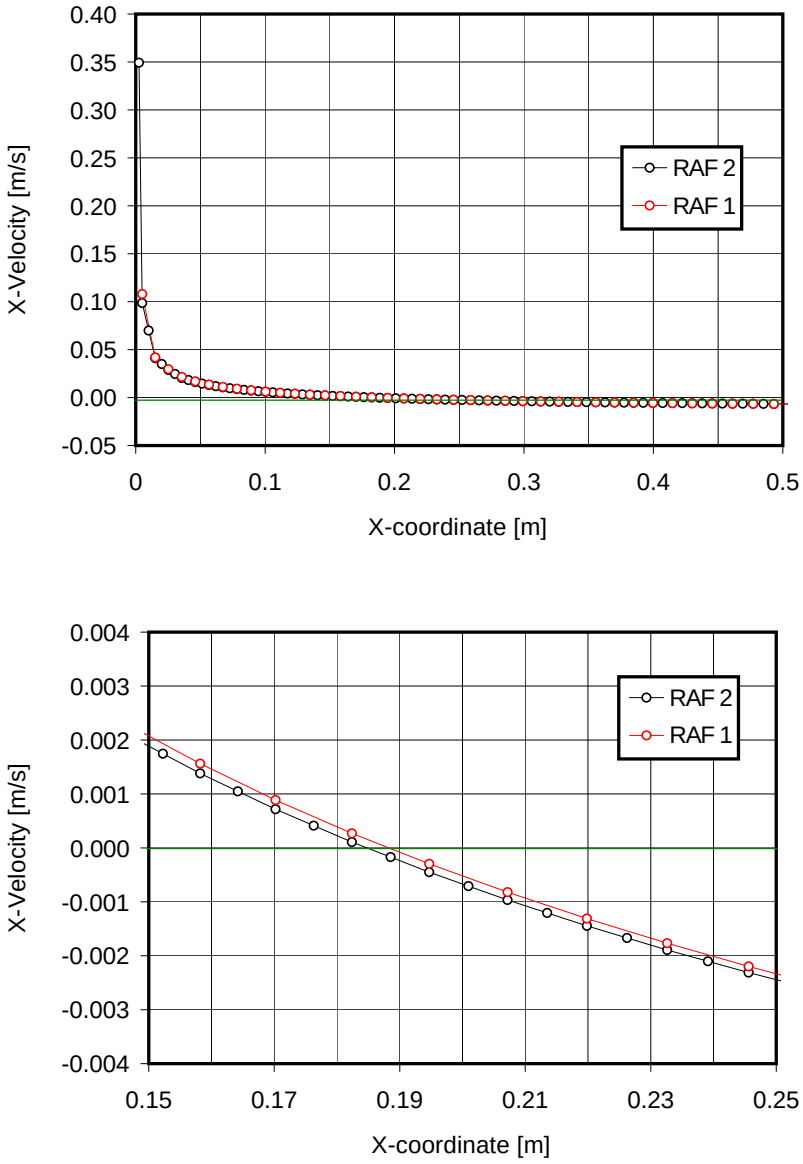

Figure 8.110: Calculated near-wall longitudinal velocities in the P05-T40-V06-H90 test, obtained by the reference longitudinal discretization (RAF 1) and the refined discretization (RAF 2) (velocities near the *flow reversal* point are zoomed in the bottom figure)

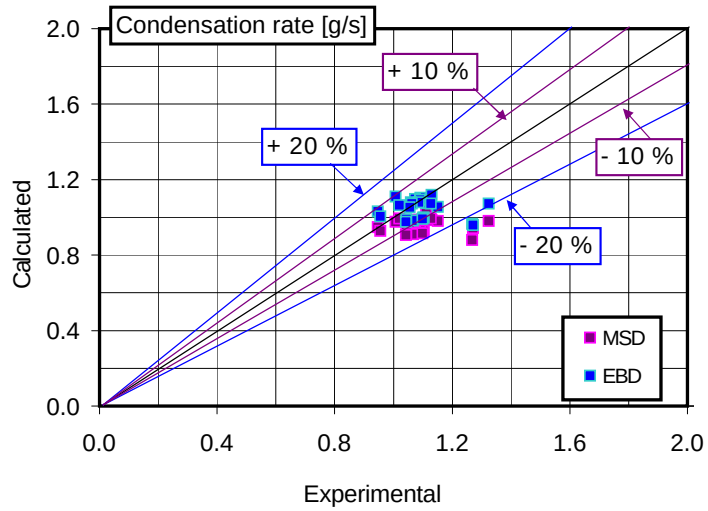

Figure 8.111: Overall condensation rate in the CONAN steam-air-helium tests at low free stream velocity: Prediction by the HMTDM models vs. experimental data

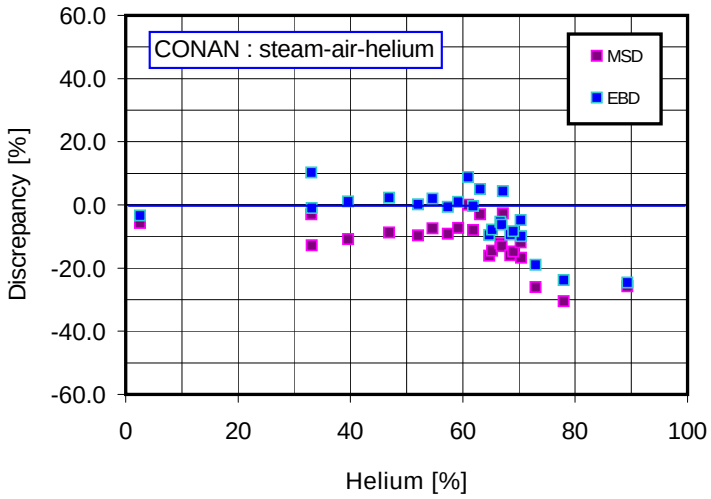

Figure 8.112: Discrepancy between the condensation rate calculated by the HMTDM models and the experimental overall condensation rate vs. the helium-to-noncondensable gas ratio in the CONAN steam-air-helium tests at low free stream velocity

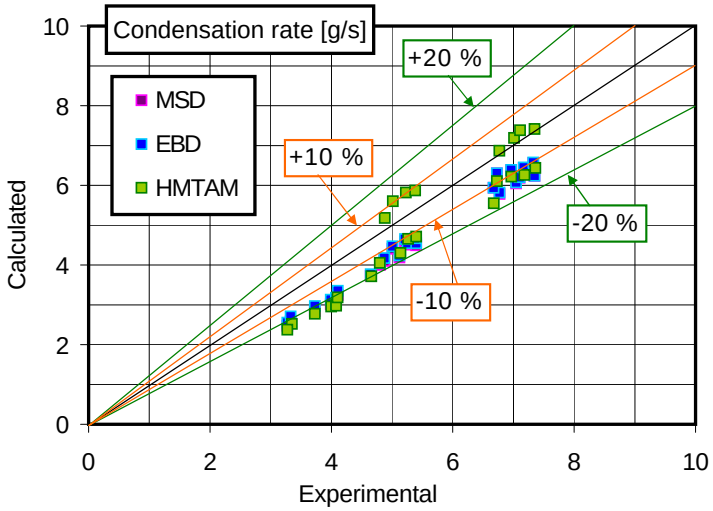

Figure 8.113: Overall condensation rate in the CONAN steam-air-helium tests at high free stream velocity: prediction by the HMTAM model vs. experimental data

8.3.3 Modelling steam-air-helium CONAN tests by the HMTAM model

The HMTAM model was successfully applied to the modelling of steam-air tests in forced convection conditions. Results of calculations were reported in paragraph 8.1.2. The modelling of steam-air-helium tests is here addressed. Firstly, the capability of the model to deal with forced convection conditions in the presence of helium are analyzed. Then, tests cases having lower free stream velocities are addressed, aimed at analyzing the capabilities of the model to deal with different convection regimes induced by the presence of helium. Basing on the analysis of experimental data presented in chapter 5, the steam-air-helium CONAN tests at high free stream velocity have been modelled by the HMTAM model, adopting the Schlichting forced convection correlation.

In Fig. 8.113, a comparison between the calculated and the experimental condensation rate is proposed. The results obtained by the HMTDM models are also reported. The condensation rate predicted by the heat and mass transfer analogy are very similar to those predicted by the other models, with the exception of the test having the highest helium-to-noncondensable gas ratios, where the HMTAM model predicts a remarkably larger condensation rate; the discrepancy between the calculated and the experimental condensation rates of the three models, calculated according to Eq. (8.1), is reported in Fig. 8.114 as a function of the helium-to-noncondensable gas ratio and the ratio between the experimental overall condensation rate and the inlet mass flow rate (IMFR). In Fig. 8.115, the discrepancy of the three models in instead reported as a function of the inlet velocity. As it can be seen, the accuracy of the HMTAM model is not affected by the inlet velocity.

In Fig. 8.116 and Fig. 8.117, the local heat fluxes respectively for a case

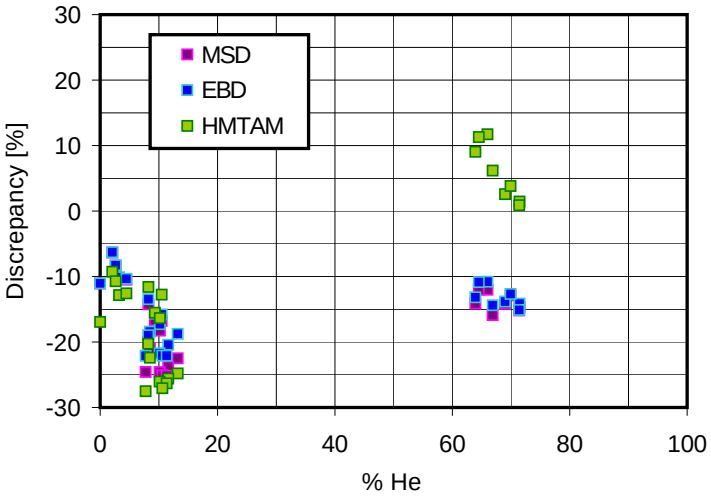

Figure 8.114: Discrepancy between the condensation rate calculated by the HMTAM model and the experimental overall condensation rate vs. the helium-to-noncondensable gas ratio in the steam-air-helium tests at high free stream velocity within CONAN

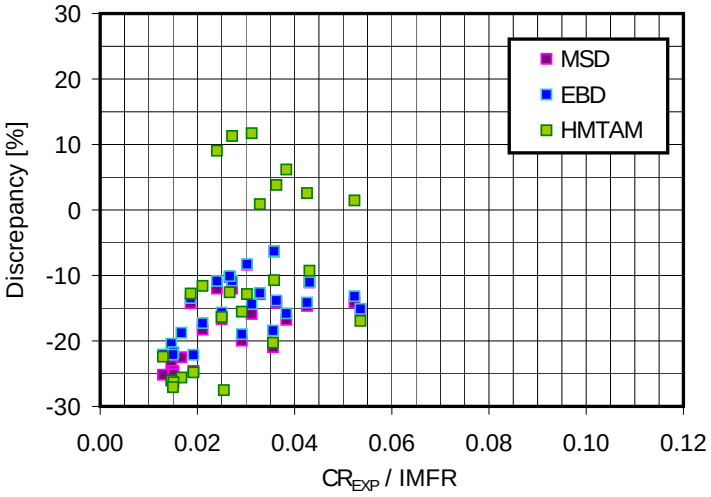

Figure 8.115: Discrepancy between the condensation rate calculated by the HMTAM model and the experimental overall condensation rate vs. the ratio between the experimental overall condensation rate and the inlet mass flow rate (IMFR) in the steam-air-helium tests at high free stream velocity within CONAN

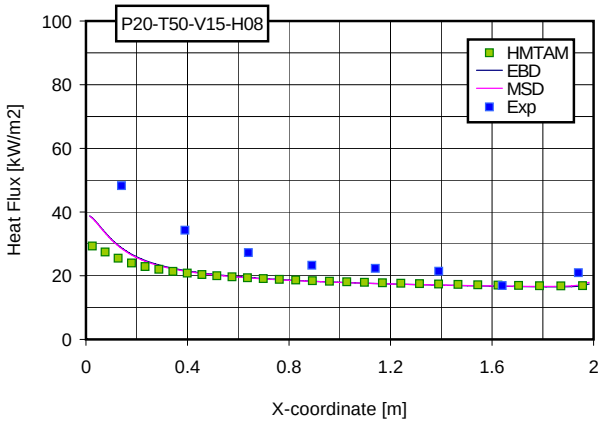

Figure 8.116: Local heat flux in the P20-T50-V15-H08 CONAN test: comparison of the three models

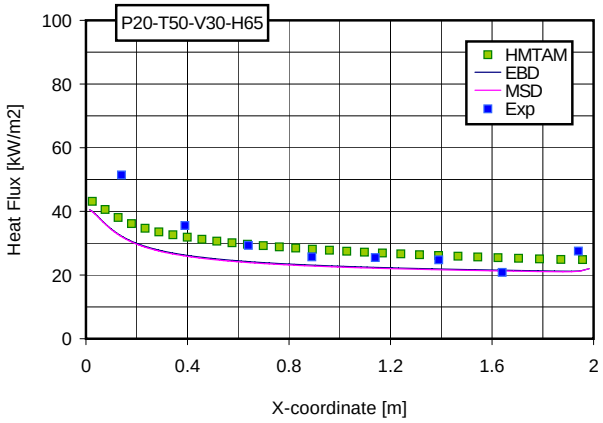

Figure 8.117: Local heat flux in the P20-T50-V30-H65 CONAN test: comparison of the three models

having a low helium-to-noncondensable gas ratio (P20-T50-V15-H08) and high helium-to-noncondensable gas ratio (P20-T50-V30-H65) are shown. The three models are compared. In the first case, an excellent agreement is observed in the fully developed flow region. The HMTAM model underestimates the local heat flux is the near-inlet region, resulting in a slightly reduced overall condensation rate (see also Fig. 8.114). In the case having the higher helium concentration, the local heat flux predicted by the HMTAM model is higher than the ones by HTMDM models. Actually, the reason for this difference is not clear on the basis of the numerical analyses and the collected experimental data.

The modelling of the steam-air-helium tests was performed by the HMTAM model by adopting the mixed convection correlation proposed in Eq. (8.6) and here reported

$$Sh^n_{0,x} = |Sh^n_{0,x,CF} \pm Sh^n_{0,x,CN}| \tag{8.10}$$

As usual, the Schlichting and the McAdams correlations are used respectively for the forced and the natural convection regime.

According to the results of the analysis of experimental data (see chapter 5), the $-$ sign is adopted for those cases having the helium-to-noncondensable gas ratio in bulk less the the critical value of 62 %. For this value the Grashof number is in fact zeroed. For those tests having a higher helium concentration, the $+$ sign is instead adopted.

In Fig. 8.118, a comparison between the calculated and the experimental condensation rates is proposed. Calculated condensation rates are also reported for the HMTDM models. A slight underestimation of the HMTAM model is observed with respect to the HMTDM models. However, the effects related to the helium-to-noncondensable gas ratio are pretty well captured by HMTAM (see Fig. 8.119). The reason for the underestimation of the model are addressed by analyzing the local heat flux profile. In Fig. 8.120, the HMTDM models and the HMTAM model are compared. As it can be seen, the difference between the more accurate diffusion based models and the HMTAM model are mainly concentrated in the near-inlet region where the adoption of a mass transfer correlation for fully developed flow clearly reduces the mass transfer. Moreover, the refinement of the mesh in the longitudinal direction can play a role, since the HMTAM model makes use of a coarser discretization.

In Fig. 8.121, the P05-T50-V06-H90 test is addressed. This is the test having the highest helium-to-noncondensable gas ratio, for which both HMTDM models predict the *flow reversal* phenomenon. As it can be observed, the local heat fluxes calculated by the HMTDM models and the HMTAM model agree very well in the intermediate region of the test section. Near the inlet section, as usual, the HMTAM model underestimates the heat and mass transfer. The local heat flux is also underestimated near the outlet section; the presence of flow reversal phenomenon is in fact qualitatively captured by the HMTAM model, but not quantitatively. In Fig. 8.122, the velocity profiles are reported for the P05-T50-V06-H75, the P05-T50-V06-H78 and the P05-T50-V06-H90 tests; despite the inversion of the velocity profile is predicted by the HMTAM model, an accurate prediction of the velocity boundary layer is clearly out of the possibilities of the standard wall functions adopted to deal with the near-wall turbulence.

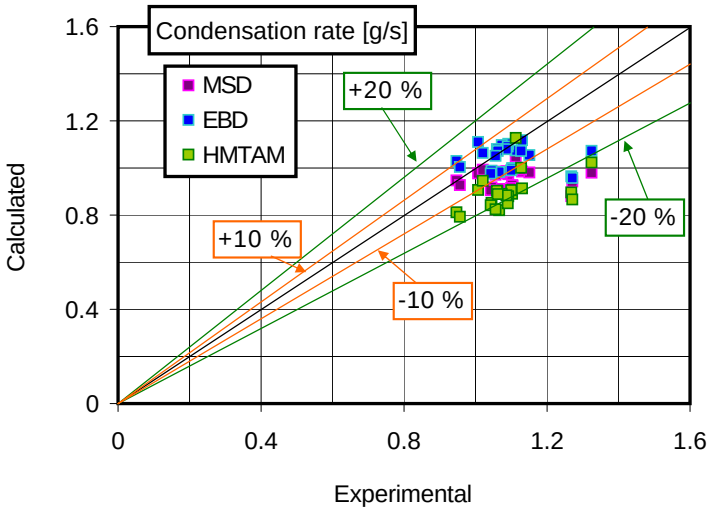

Figure 8.118: Overall condensation rate in the CONAN steam-air-helium tests at low free stream velocity: prediction by the HMTAM model vs. experimental data

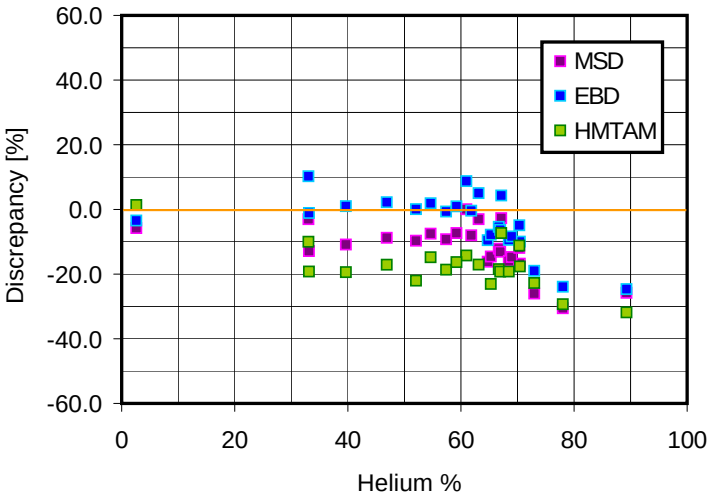

Figure 8.119: Discrepancy between the condensation rate calculated by the HMTAM model and the experimental overall condensation rate vs. the helium-to-noncondensable gas ratio in the steam-air-helium tests at low free stream velocity within CONAN

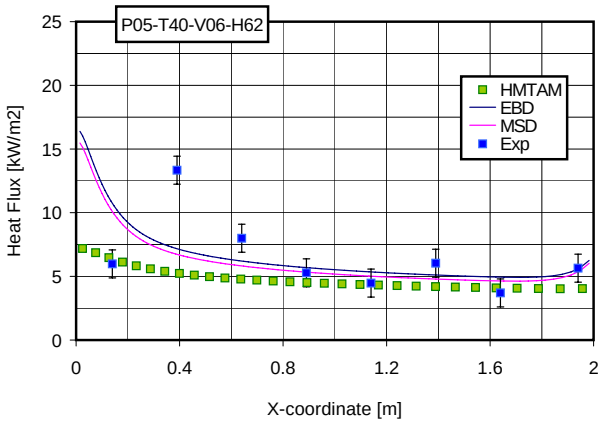

Figure 8.120: Local heat flux in the P20-T50-V06-H62 CONAN test: comparison of the three models

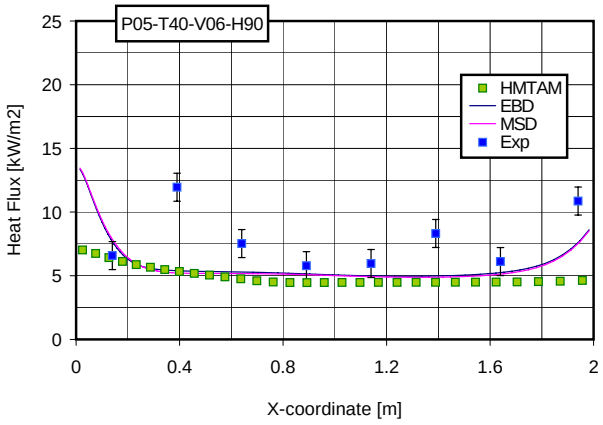

Figure 8.121: Local heat flux in the P20-T50-V06-H90 CONAN test: comparison of the three models

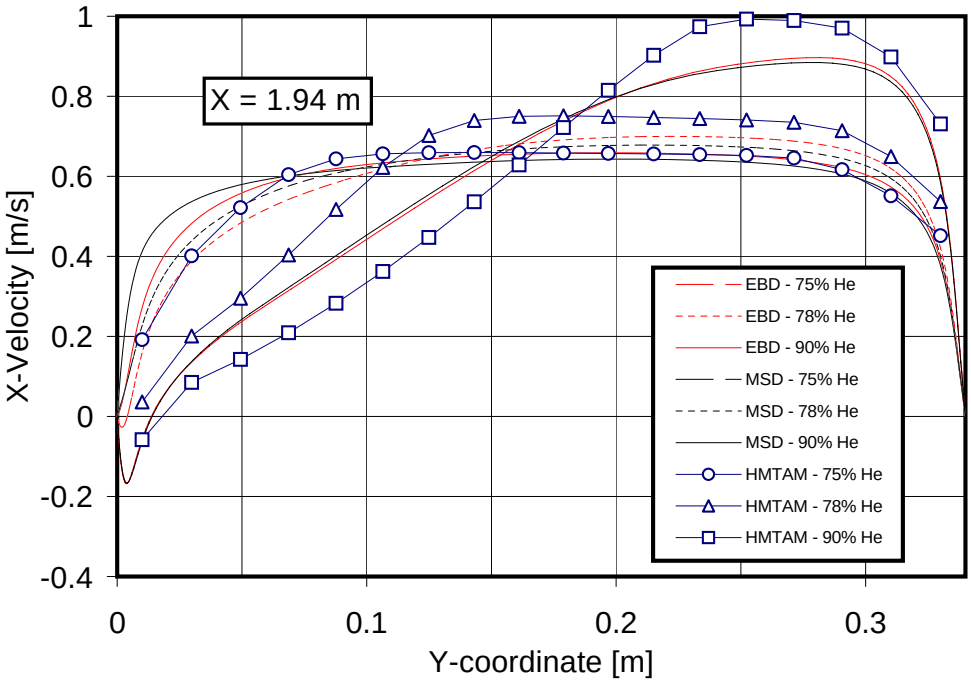

Figure 8.122: Comparison between the velocity profiles predicted by the EBD, the MSD and the HMTAM models near the outlet section ($X = 1.94m$) in the P05-T50-V06-H75, the P05-T50-V06-H78 and the P05-T50-V06-H90 tests with CONAN

8.4 Modelling steam-air-helium condensation tests within the COPAIN facility

8.4.1 Modelling steam-air-helium COPAIN tests with the HMTDM models

The HMTDM^{EBD} and the HMTDM^{MSD} were proven to give very similar results in the modelling of CONAN tests in the presence of helium. Here, the modelling of the steam-air-helium COPAIN tests is therefore proposed performed only by the HMTDM^{EBD} model. A comparison with experimental data is reported based on the local heat fluxes, the average heat transfer rates and the average condensation rates.

Tests are proposed at different powers, different velocities and different helium-to-noncondensable ratios. From Fig. 8.123 to Fig. 8.127, the comparison between the experimental and the calculated local heat fluxes is proposed. In Fig. 8.123 in particular, the P045 tests having a low helium-to-noncondensable ratio are analyzed. Different helium-to-noncondensable gas ratios are addressed in tests P046 (see Fig. 8.124) and P049 (see Fig. 8.127), having respectively the 40 percent and the totality of helium among the noncondensable gases. The effect of pressure is investigated in tests P047 (see Fig. 8.125) and P048 (see Fig. 8.126), having a nominal operating pressure of 6 bars. As it can be seen, the comparison between the predicted and the calculated local heat flux show the tendency of the CFD model to overestimate the heat fluxes and, as a consequence, the overall condensation rates in tests having the highest inlet velocities and therefore a more pronounced forced convection character. On the other hand, heat fluxes and condensation rates are slightly underestimated in tests having a low free stream velocity.

In Fig. 8.130, the discrepancy between the calculated average heat fluxes and the experimental values is reported, reproposing the same tendency observed for the steam-air cases and supporting the conclusions drawn on the basis of the local heat flux comparisons.

Further remarks are suggested concerning the local trends of the experimental and calculated heat fluxes. Despite of CONAN, where local Sherwood numbers were shown strongly affected by entrance and development effects, COPAIN data seem less sensitive, since the spatial profiles of the local heat flux are quite regular. An exception concerns tests P047 and P048 at high pressure for which a bump of the local heat flux profile is observed after the inlet region. In tests P049, flow reversal conditions are expected according to the HMTDM^{EBD} model, for test having the lowest free stream velocities (tests P049_3, P049_4 and P049_5, see Fig. 8.127).

In Figs. 8.128 and 8.129, calculated and experimental average heat fluxes and condensation rates derived from the average heat fluxes on the basis of the heat and mass transfer analogy are reported. A good agreement is experienced for test cases having important transfer rates; for these tests the discrepancy between experimental and calculated values is mostly within $\pm 20\%$. In Fig. 8.131, the discrepancy between the calculated and the experimental heat flux is reported as a function of the average heat flux. Indeed, it is clearly shown that the discrepancy is more pronounced at the lowest heat transfer rates, for which the experimental uncertainties on the boundary conditions are expected to play

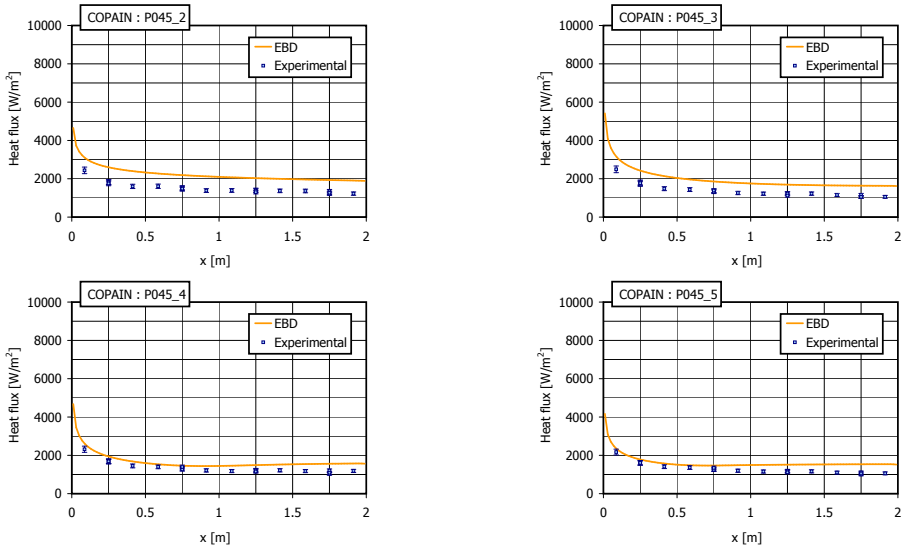

Figure 8.123: Axial heat flux profiles in the P45 COPAIN tests ($P = 1bar$,$\chi = 0.1$): calculated values vs. experimental data

an important role.

The effect of pressure is also analyzed. In Fig. 8.134, the discrepancy between the calculated and the experimental condensation rates is reported as a function of the operating pressure. As it is shown, for both air-steam and air-steam-helium tests, the EBD model is capable to deal with the different pressures; major differences are not observed with data at atmospherical pressure, for which the model was already tested.

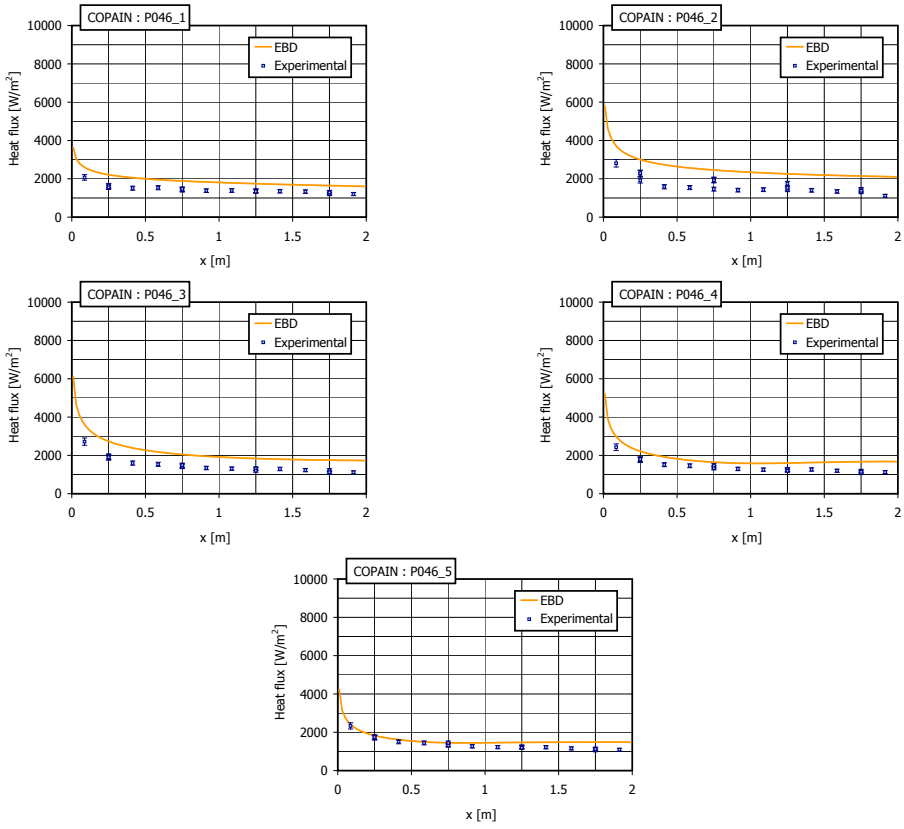

Figure 8.124: Axial heat flux profiles in the P46 COPAIN tests ($P = 1bar$,$\chi = 0.4$): calculated values vs. experimental data

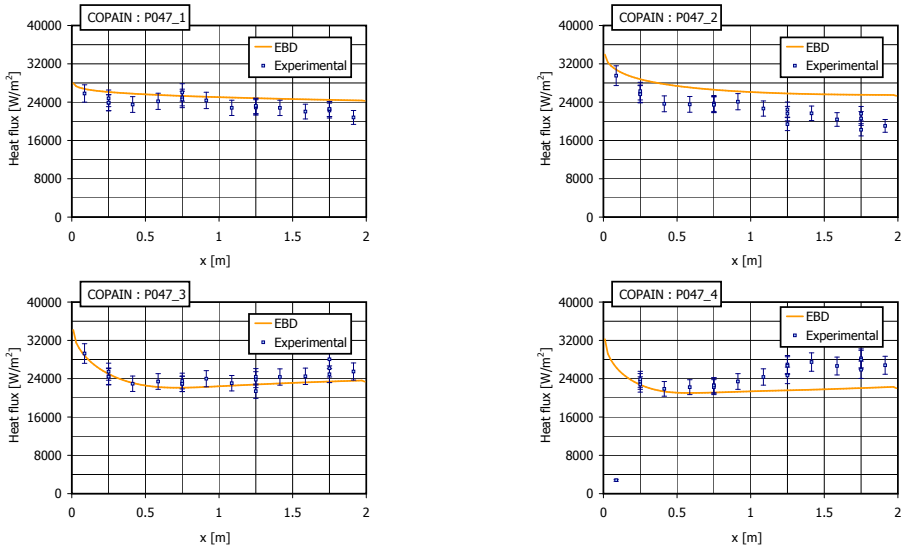

Figure 8.125: Axial heat flux profiles in the P47 COPAIN tests ($P = 6bar$,$\chi = 0.1$): calculated values vs. experimental data

In Figs. 8.132 and 8.133, the discrepancy of the condensation rates calculated by the model with respect to the ones derived from the heat transfer measurements is shown, respectively as a function of the ratio between the experimental overall condensation rate and the inlet mass flow rate and the inlet steam mass fraction.

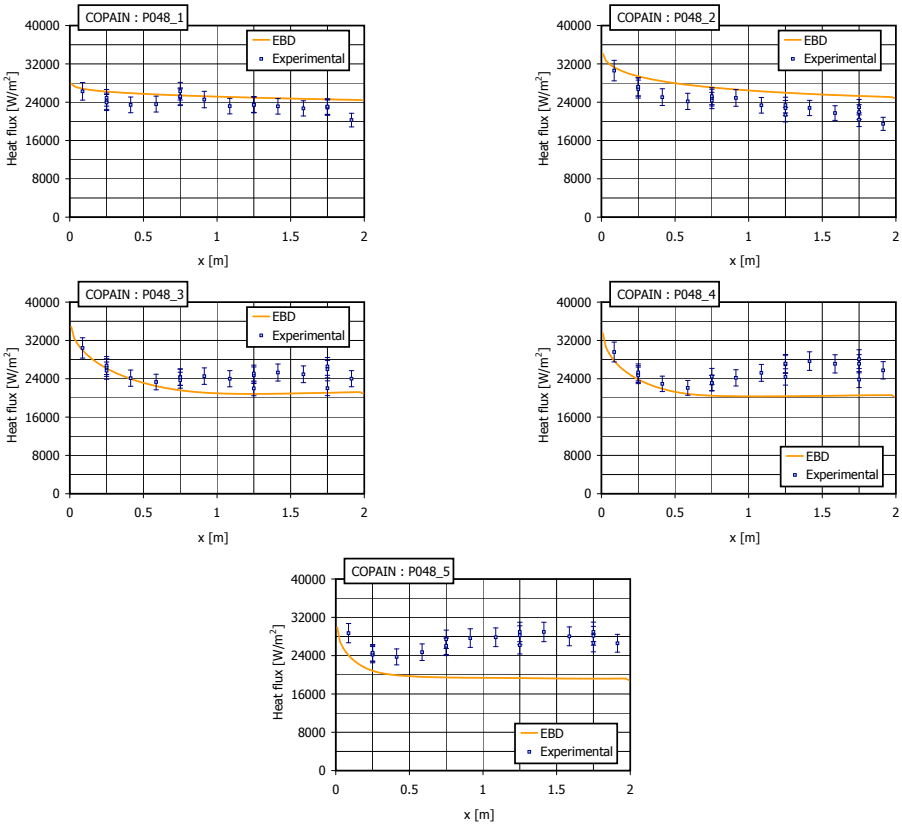

Figure 8.126: Axial heat flux profiles in the P48 COPAIN tests ($P = 6bar$,$\chi = 0.4$): calculated values vs. experimental data

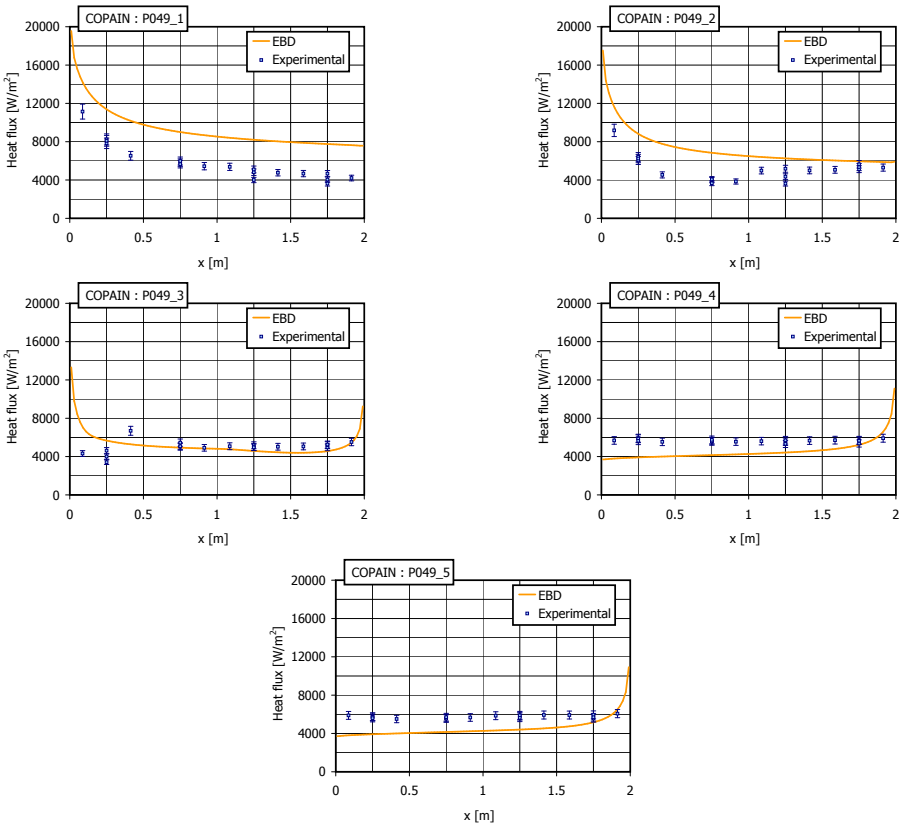

Figure 8.127: Axial heat flux profiles in the P49 COPAIN tests ($P = 6bar$,$\chi = 1.0$): calculated values vs. experimental data

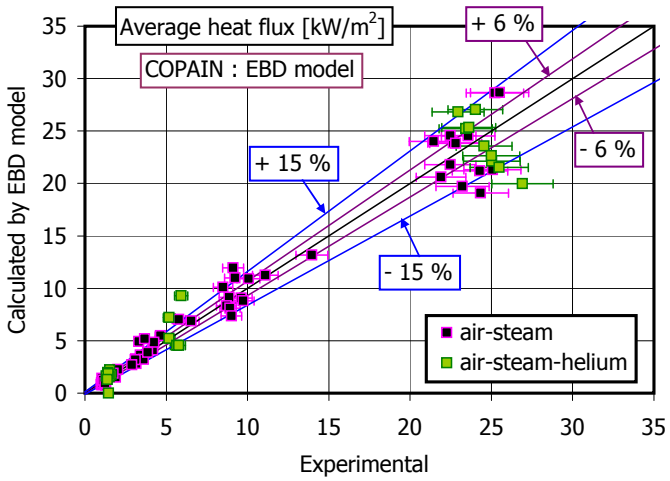

Figure 8.128: Average heat transfer rate in the COPAIN steam-air-helium tests: Prediction by the EBD model vs. experimental data

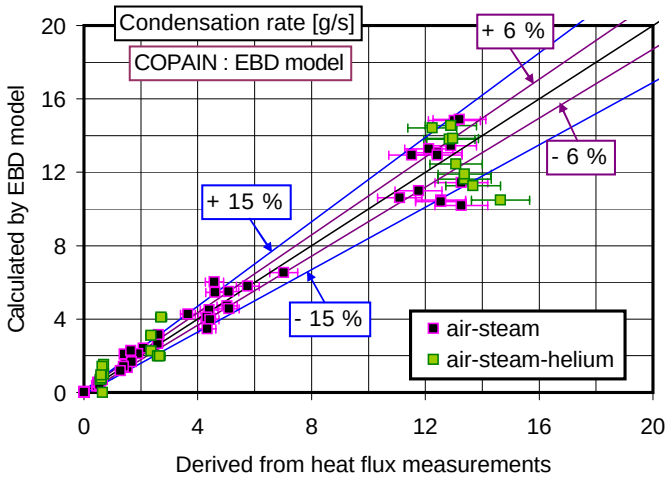

Figure 8.129: Overall condensation rate in the COPAIN steam-air-helium tests: Prediction by the EBD model vs. experimental value derived from heat flux measurements

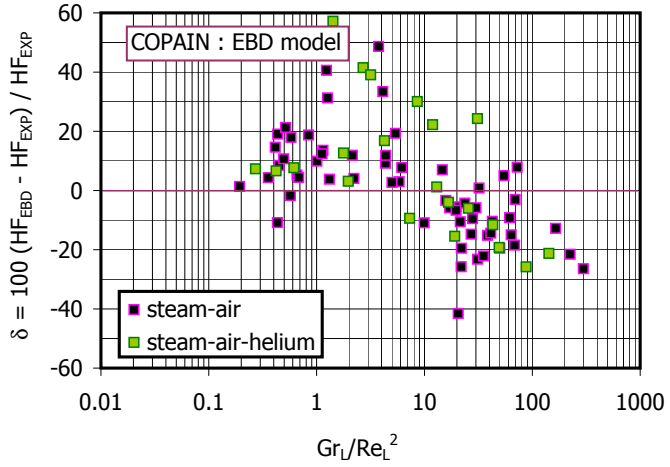

Figure 8.130: Discrepancy between the average heat flux calculated by the EBD model and the experimental value vs. average Richardson number in the steam-air-helium tests within COPAIN

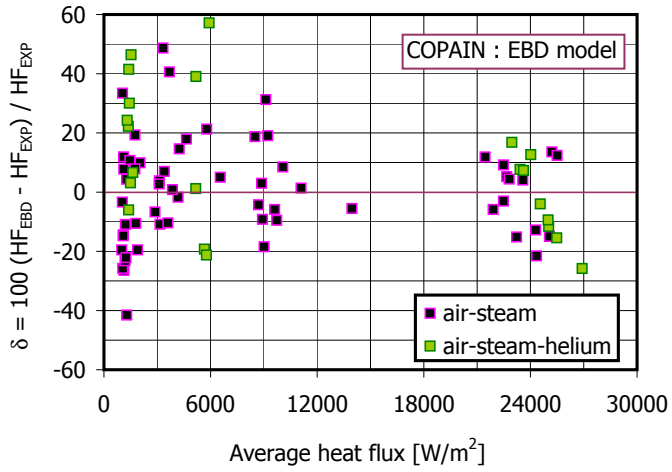

Figure 8.131: Discrepancy between the average heat flux calculated by the EBD model and the experimental value vs. the experimental value in the steam-air-helium tests within COPAIN

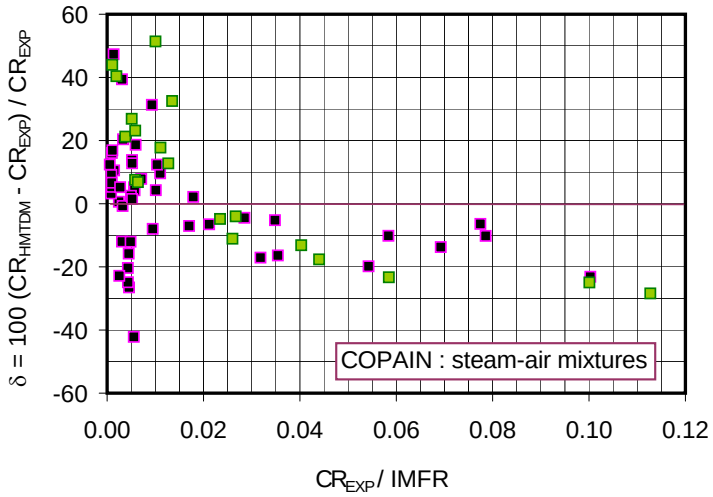

Figure 8.132: Discrepancy between the condensation rate calculated by the HMTDM model and the experimental overall condensation rate derived from heat transfer measurements vs. the ratio between the experimental overall condensation rate and the inlet mass flow rate (IMFR) in the steam-air-helium tests within COPAIN

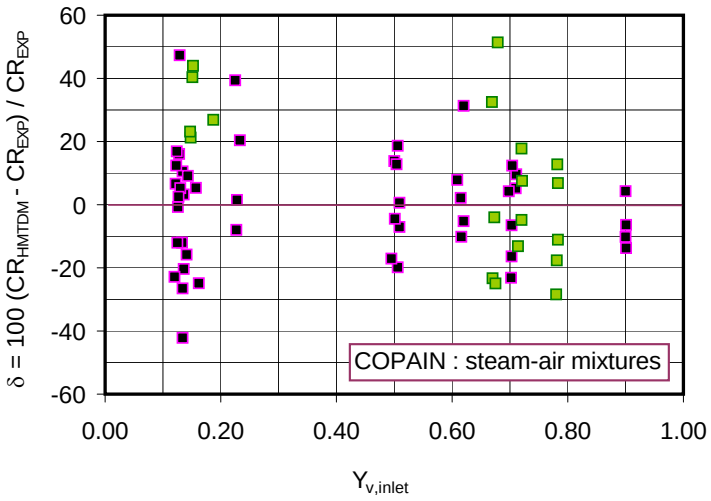

Figure 8.133: Discrepancy between the condensation rate calculated by the HMTDM model and the experimental overall condensation rate derived from heat transfer measurements vs. the inlet steam mass fraction in the steam-air-helium tests within COPAIN

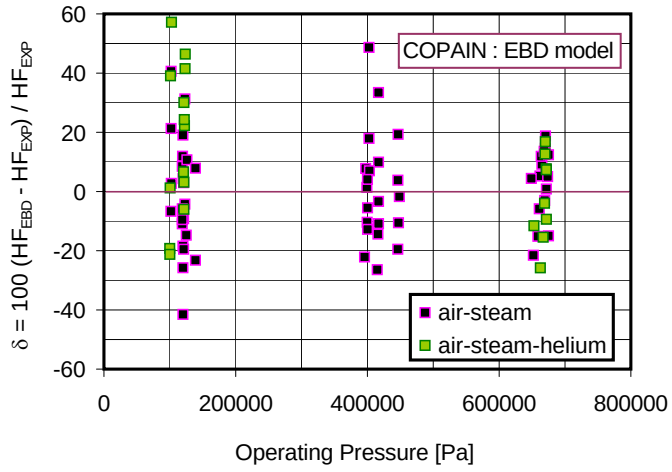

Figure 8.134: Discrepancy between the average heat flux calculated by the EBD model and the experimental value vs. operating pressure in the steam-air-helium tests within COPAIN

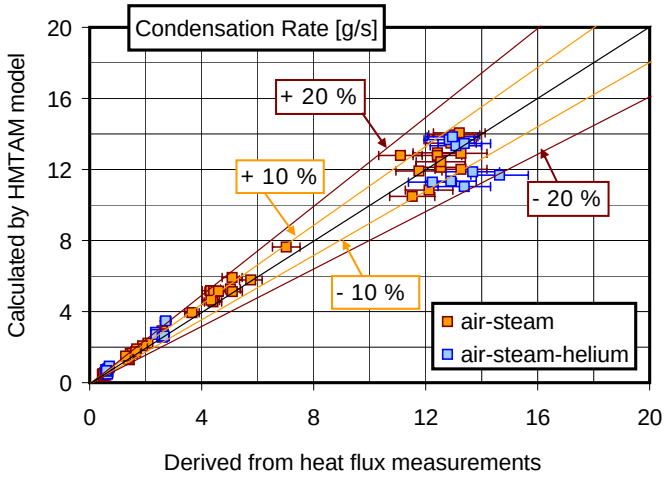

Figure 8.135: Comparison between the condensation rates calculated by the HMTAM model and the experimental values derived from heat flux measurements in the COPAIN tests

8.4.2 Modelling steam-air-helium COPAIN tests with the HMTAM model

An analysis of the COPAIN steam-air-helium tests has been carried out by the HMTAM model. The same mixed convection correlation adopted in modelling of the steam-air-helium tests within CONAN was used, defined by Eq. (8.6) and here reproposed:

$$Sh^n_{0,x} = |Sh^n_{0,x,CF} \pm Sh^n_{0,x,CN}| \tag{8.11}$$

Three different helium-to-noncondensable gas ratios were addressed experimentally: 10, 40 and 100 %. Depending on the helium-to-noncondensable gas ratio, the sign was selected. Only tests having all helium are expected to present a *buoyancy-opposed* mixed convection character. The buoyancy-opposed correlation (having the + sign is therefore used for the tests of the P049 series. Other tests are modelled by the *buoyancy-aided* correlation (having the − sign). A comparison between the condensation rates calculated by the HMTAM model and the experimental values derived from the heat flux measurements is shown in Fig. 8.135, where both the steam-air and the steam-air-helium tests are reported. As it can be seen, the results are mostly included in the range of ±20 % of the experimental values.

Major differences in the accuracy of the model are not evident with respect to steam-air tests. In Fig. 8.136, the discrepancy between calculated and experimental values is reported as a function of the Richardson number. As it is observed, forced, natural and mixed convection regimes are predicted with the same order of accuracy. In Fig. 8.137, the discrepancy between the calculated and the experimental values is reported as a function of the helium-to-noncondensable gas ratio. In Fig. 8.138, the same data are analyzed as a function of the ratio between the experimental overall condensation rate and the inlet mass flow rate (IMFR).

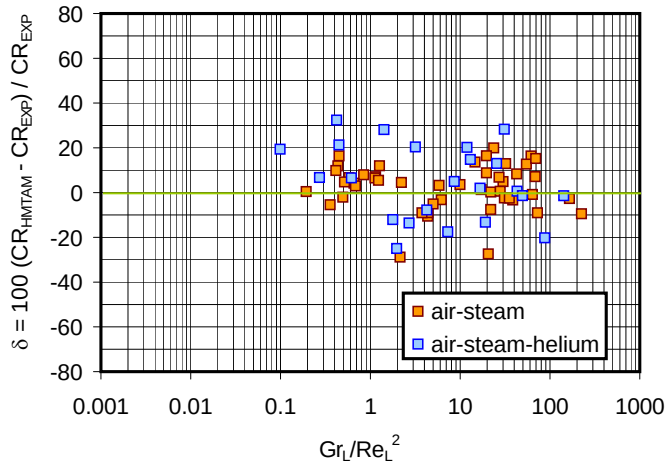

Figure 8.136: Discrepancy between the condensation rate calculated by the HMTAM model and the experimental value derived from heat transfer measurements vs. average Richardson number in the steam-air and steam-air-helium tests within COPAIN

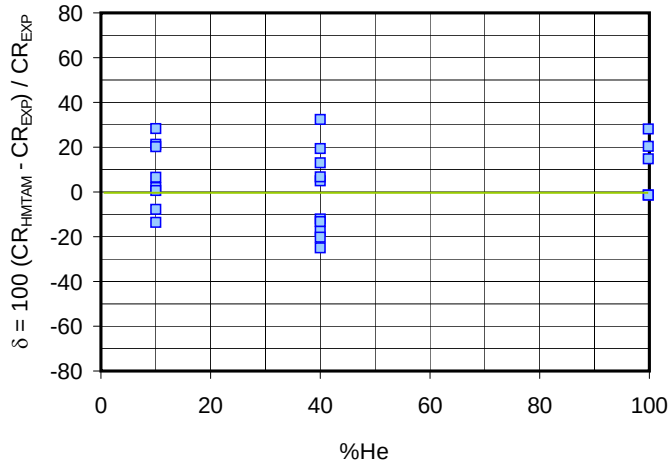

Figure 8.137: Discrepancy between the condensation rate calculated by the HMTAM model and the experimental value derived from heat transfer measurements vs. the helium-to-noncondensable gas ratio in the steam-air-helium tests within COPAIN

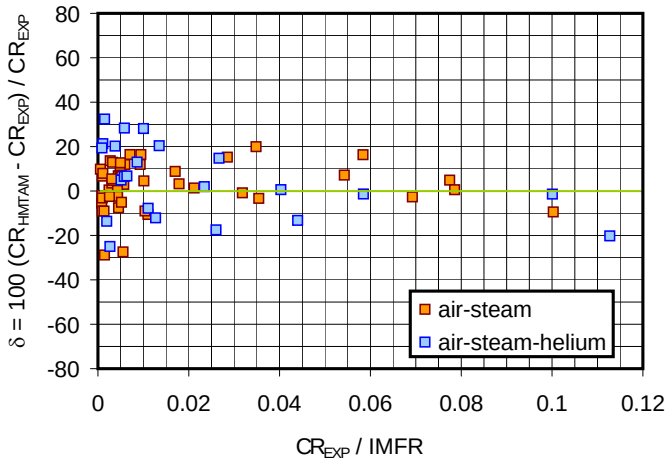

Figure 8.138: Discrepancy between the condensation rate calculated by the HMTAM model and the experimental value derived from heat transfer measurements vs. the ratio between the experimental overall condensation rate and the inlet mass flow rate (IMFR) in the steam-air and steam-air-helium tests within COPAIN

The capability of the HMTAM model to deal with different operating pressure is also tested. In Fig. 8.139, the discrepancy between the calculated and the experimental condensation rates is reported as a function of the operating pressure. Data corresponding to the EBD model are also reported. As it is shown, for both air-steam and air-steam-helium tests, the effects induced by pressure are accounted for by the HMTAM model; major differences are not observed with the EBD model. As already remarked in the steam-air-helium CONAN tests, flow reversal phenomena can occur when the free stream velocity is sufficiently low. In Fig. 8.140, the velocity profiles predicted by the EBD and the HMTAM model in the P049_5 test are reported, suggesting both the presence of the flow reversal phenomenon.

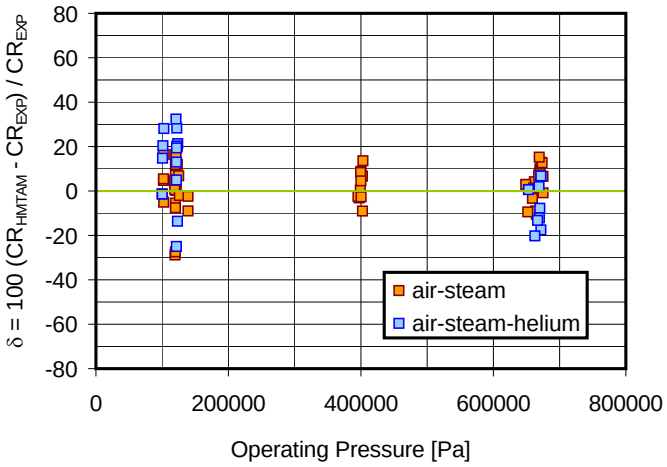

Figure 8.139: Discrepancy between the condensation rate calculated by the HMTAM model and the experimental value derived from heat transfer measurements vs. operating pressure in the steam-air and steam-air-helium tests within COPAIN

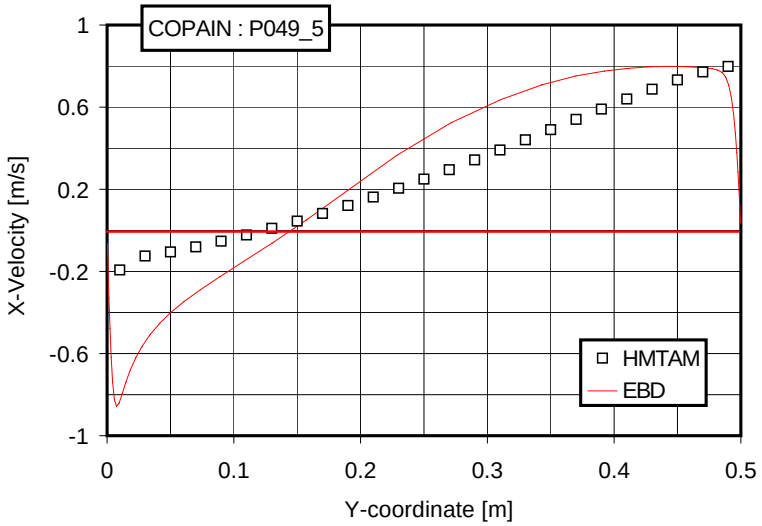

Figure 8.140: Comparison between the velocity profiles predicted by the EBD and the HMTAM model near the outlet section in the P049_5 test within COPAIN

8.5 Concluding remarks

The HMTDM^{EBD} model was originally developed at the University of Pisa for modelling the evaporation of falling liquid film [91, 130]. Later, it was applied to the modelling of the steam-air CONAN condensation tests [8, 92, 131, 92]. Mogliani also used the model to perform parametrical scoping calculations aimed at investigating suction effects in the presence of helium [92]. On the other hand, the original version of the HMTAM model was developed and applied to the modelling of the steam-air coondensation CONAN condensation tests in forced convection regime [96]. Moreover, the ISP47 tests performed within TOSQAN [118] and MISTRA [96] were also addressed by adopting a natural convection correlation to estimate the mass transfer rates on the basis of the heat and mass transfer analogy.

In the frame of this PhD research, these models have been improved to deal with different phenomenologies than those investigated earlier.

An additional version of the HMTDM models was proposed, developed basing on the principles of the irreversible thermodynamics and named HMTDM^{MSD}. The MSD model is a full multicomponent diffusion matrix model that allows the mixture and the species continuity equations to be all intrinsically satisfied. On the contrary, the EBD model, based on the approximation of effective binary diffusion does not assure the species continuity equations of all species to be satisfied, as shown in chapter 2. In the MSD model, the species balance equations are solved in coupled form, whereas the EBD model allows solving the species balance equations in segregated form; in this last case, computational efforts can be therefore remarkably reduced.

The HMTAM model was also modified to deal with different convection regimes and most of all, to deal with the transition between the forced and the natural convection regimes that may occur in CONAN and COPAIN tests in presence of low free stream velocities. Basing on the analysis of experimental data, correlations for buoyancy-aided and buoyancy-opposed regimes were treated differently.

The whole database available by CONAN and COPAIN was addressed. Further important aspects were investigated aiming at testing and proving the capabilities of the models:

- the capabilities of the models to account for steam superheating and pressure were checked by modelling the steam-air and the steam-air-helium tests performed within COPAIN;
- *buoyancy-aided* mixed convection regimes and natural convection regimes were addressed by modelling the steam-air tests performed within COPAIN;
- the effects related to the presence of helium were analyzed in forced convection conditions by addressing the steam-air-helium tests at high free stream velocities performed within CONAN;
- steam-air-helium test at low free stream velocities were also addressed by modelling CONAN tests.

On the basis of the results obtained by the different models, the strength

and the weak points of the different models are discussed in the following. The perspectives for the future development of the models are also discussed.

8.5.1 The HMTDM models

Detailed mechanistic models are very important to support the understanding of physical phenomena and the development of fast running and less detailed models aimed at coping with large scale geometries, like the HMTAM model. In this aim, the development of the HMTDM models and the analysis of their results was very successful.

Diffusion based models were proven to give very good results in steam-air forced convection condensation. The local and the overall behavior of the models was proven very satisfactory in the analysis of steam-air buoyancy-aided mixed convection and natural convection. Important pending questions concerning measured temperature profiles within COPAIN were also clarified thanks to the HMTDM model and theoretical considerations. In particular, the invasivity of the measurement technique is suspected.

Very important aspects appear from the analysis of steam-air-helium condensation tests. In particular, when forced convection conditions are addressed, as in the case of the high free stream velocity CONAN test, both models were proven to behave very similar. Moreover the agreement with local experimental data was also remarkable. The difference with the experimental data in terms of overall condensation rate can be mainly attributed to the difficulties of the turbulence model to account for entrance effects in the presence of helium.

Very interesting results were obtained by analyzing simultaneously the experimental data and the results of the modelling in the steam-air-helium test at low free-stream velocity. *Buoyancy reversal* and *flow reversal* phenomena are clearly confirmed by experimental data and by CFD analyses. The EBD and the MSD model are both capable of predicting such phenomena.

Minor differences are anyway observed between the two models. In particular, the EBD model predict the buoyancy reversal to occur at a slightly lower helium concentration than the MSD model. Experimental data suggest that the onset of *buoyancy reversal* occurs for an helium to noncondensable ratio less than those predicted by both HMTDM models.

Since minor differences are experienced between the two HMTDM models, COPAIN tests were only addressed by the EBD model. Steam superheating and pressure are adequately accounted for by the model. *Flow reversal* conditions are predicted for the cases having the highest helium-to-noncondensable gas ratios and low free stream velocities.

Basing on the analysis of the modelling results, the adequacy of the simplified EBD model is assessed against the prediction of the MSD model.

Two pending aspects need to be solved in the future; on one hand, a more accurate reproduction of local entrance effects should be achieved. This should be achieved for both steam-air and steam-air-helium mixtures, since helium was observed to influence remarkably the mass transfer near the inlet section; on the other hand, the need is felt for achieving a better understanding of turbulent transport processes in the mixed and natural convection regimes, either in the presence of steam-air and in the presence of steam-air-helium mixture.

This second aspect is identified as a fundamental point to achieve a significant improvement in the understanding of the physical phenomena and in the

modelling of condensation.

The modelling of turbulence phenomena in the different convection regimes is in fact a key point. Indeed, turbulence models were tested for transpirating boundary layers in the forced convection regime. Unfortunately, local velocity and turbulence data representative of mixed or natural convection regimes are not available. Local experimental data in the presence of helium are also not available.

The way helium influences turbulent transport processes is not completely understood. Helium is first of all responsible of the modification induced in the shear stress turbulence production, since velocity gradients are modified by buoyancy forces. This effect is normally accounted for by turbulence production terms available in the different turbulence models (see chapter 7). However, other aspects can play a role that are not usually taken into account. In a first instance, we are interested to those effects that, in the case of either steam-air or steam-air-helium mixtures, can be induced by the density gradients that establish across the turbulent boundary layer. These effects are not accounted for by buoyancy simple gradient turbulence production terms that account only for density gradients along the gravity direction:

$$G_b = -\vec{g} \cdot \frac{\mu_t}{\rho Pr_t} \nabla \rho \tag{8.12}$$

Clearly, the need for dedicated experimental data is felt in the aim to better understand the physics of *buoyancy-aided* and *buoyancy-opposed* mixed convection regimes. In particular, local experimental data of velocity and turbulence would be advisable for the following phenomenologies:

- natural convection condensation in the presence of air;
- *buoyancy-aided* mixed convection condensation in the presence of air;
- *buoyancy-aided* mixed convection condensation in the presence of air and helium, with the helium-to-noncondensable gas ratio less than the critical value for which *buoyancy reversal* occur
- *buoyancy-aided* mixed convection condensation in the presence of air and helium with the helium-to-noncondensable gas ratio greater than the critical value for which *buoyancy reversal* occur, before during and after the transition to *flow reversal*.

8.5.2 The HMTAM model

Models based on the heat and mass transfer analogy are usually conceived to be applied in the modelling of large scale facilities or full scale containment geometries. These models are usually based on natural convection correlations, since natural convection is the expected dominating convection regime in the reactor containment during the course of a loss of coolant accident. However, a renewed interest emerged towards these convection regimes, mostly in the aim to analyze coupled effects and integral effect tests performed within large scale facilities. Different phenomenologies can be experienced within large scale facilities, mostly in the presence of compartments and impinging flows as in the

case of the M8 MISTRA test [133]. Moreover, local phenomena in the nuclear reactor containment can also be interested by forced or mixed convection.

The HMTAM model, originally developed at the University of Pisa to deal with pure turbulent natural convection condensation [96, 118] and pure forced convection condensation [96], was subjected to a deep modification in the frame of this PhD research. Simple mixed convection correlations were introduced to check the capabilities of the model to deal with different convection regimes. Basing on the analysis of the experimental data available by CONAN and COPAIN, a simple correlation was introduced aimed at testing the response of the model when *buoyancy-aided* and *buoyancy-opposed* mixed convection effects are qualitatively taken into account.

Forced convection steam condensation in the presence of air and also in the presence of air and helium are remarkably well predicted by the model. Differences with the experimental data and with the prediction of the HMTDM models are reduced to the near-inlet region and affect only slightly the accuracy in the prediction of the overall condensation rates. Indeed, entrance effects are out of reach for this kind of models.

A remarkable improvement was also obtained in the mixed and natural convection regimes. It is the case of the COPAIN tests performed in the presence of air. In the mixed convection regime, the results obtained by the model adopting the *buoyancy-aided* mixed convection correlation are particularly improved with respect to those obtained by a correlation not accounting for the impairment of the mass transfer coefficient. Buoyancy-opposed mixed convection effects are also reproduced by the model in the presence of helium. The buoyancy reversal phenomena are correctly modelled. The flow reversal phenomenon is also qualitatively predicted.

Whatever is the mixture or the convection regime, the model was proven reasonably able to deal with steam superheating and different pressures.

The results obtained by the HMTAM model are clearly encouraging. Towards a better understanding and an improvement in the modelling capabilities, a more detailed experimental analysis of mixed convection regimes would be advisable. The experimental data available by CONAN and COPAIN have allowed drawing important remarks on the qualitative aspects of mixed convection, but they were not purposely conceived to investigate these effects. It is therefore advisable that further dedicated and well tailored experimental campaigns will be carried out in the future researches in order to provide precious informations about these phenomena. Clearly, HMTAM models will also benefit of the development of the more detailed HMTDM models in dealing with these phenomenologies.

Chapter 9

Some considerations on the suitability of helium as a substitute for hydrogen

Most facilities aimed at studying hydrogen safety aspects, either in the nuclear or in the conventional fields make often use of helium as a substitute for hydrogen. This choice is mainly due to practical and safety reasons. Helium is the ideal substitute for hydrogen, since it has low molecular weight, with the advantage to be not flammable.

The aim of this chapter is to investigate to what extent helium can be considered a suitable substitute for hydrogen. In particular, steam condensation phenomena are addressed, in the presence of air and of a third noncondensable gas lighter than steam.

After performing a critical review of the physical properties of the two species, which are also compared to the properties of water vapor and air, theoretical and computational analyses are performed. Forced and natural convection regimes are investigated. For both regimes, criteria are proposed for the design of experiments of steam condensation representative of actual steam-air-hydrogen mixtures.

One of the main aspects we may be concerned with when designing experiments of steam condensation in the presence of helium is how to achieve the same local mass flux as in the presence of hydrogen. In the natural convection regime, we can be also interested to determine the density difference between the condensing interface and the bulk, in the aim to identify the concentrations at which the *buoyancy reversal* and *flow reversal* conditions are expected.

Gas	M (g/mol)	T_f (K)	T_v (K)	T_c (K)	P_c (MPa)	ρ_c (kg/m^3)
Air	28.966	59.75	78.90	132.60	3.900	957.8
H_2	2.016	13.84	20.27	32.98	1.293	30.1
He	4.003	2.15	4.30	5.19	0.227	69.6
H_2O	18.0153	273.15	373.12	647.10	22.064	322.0

Table 9.1: Main gas properties (c, critical; f, fusion; v, vaporization)

9.1 A comparison of physical properties

[1] In the range of temperatures and pressures of interest for the thermal-hydraulic analysis of the nuclear reactor containment, during and after the course of a LOCA, air, hydrogen and helium can be clearly considered as ideal gases (see Tab. 9.1). When dealing with condensation, steam is assumed in saturation conditions at the condensing wall, whereas superheating conditions can be observed in bulk. In a first instance, superheated and saturated steam can be also considered as ideal gases. The ideal gas equation of state is therefore considered applicable to the four gases, as well as to the mixtures of our interest: steam-air-helium and steam-air-hydrogen mixtures. As a first immediate consequence, since the helium molecular weight is twice that of hydrogen, the hydrogen density is half the helium density at the same temperature and pressure conditions.

In the following, the physical properties influencing momentum, heat and mass transfer processes are analyzed; the specific heat, the dynamic viscosity and the thermal conductivity of the different chemical species are reported respectively in Fig. 9.1, Fig. 9.2 and Fig. 9.3. For steam, hydrogen and helium the selected reference data are those available by the NIST [135]. For air, the data of Lemmon and Jacobsen [136, 137] are selected; air is considered as a dry mixture of fluids including nitrogen, oxygen and argon and neglecting carbon dioxide and other elements present in traces. According to the results of these studies, air is treated as a single gas species. In appendix C, different polynomial correlations are proposed, developed based on the reference data for the aforementioned properties.

As it can be seen in Fig. 9.1, hydrogen has almost three times the specific heat of helium all over the range of temperature of interest. On the other hand, the hydrogen viscosity is about half the helium viscosity (see Fig. 9.2). Hydrogen thermal conductivity is a little greater than that of helium (see Fig. 9.3).

Triangular diagrams are a useful way of representing mixture properties, where the three sides represent each one a gas molar fraction, as shown in Fig. 9.4. Steam molar fraction grows from left to right, as reported in Fig. 9.6. The iso light-to-noncondensable ratio *loci* are instead shown in Fig. 9.5.

If steam is assumed in saturation conditions, once the mixture pressure is fixed, the mixture temperature can be found as a function of steam molar fraction. Since the absolute pressure and the steam molar fraction are imposed in every point of the triangular diagram, the partial pressure of the steam is also assigned. The saturation temperature (see Fig. 9.7) is therefore obtained as a function of the steam partial pressure (proposed correlations are reported in appendix C). In Fig. 9.7, the temperature of the mixture of saturated steam is

[1] This section partially summarizes the studies performed in cooperation with Mitia Turrin and Enrico Deri [134], who are sincerely acknowledged for their precious contribution

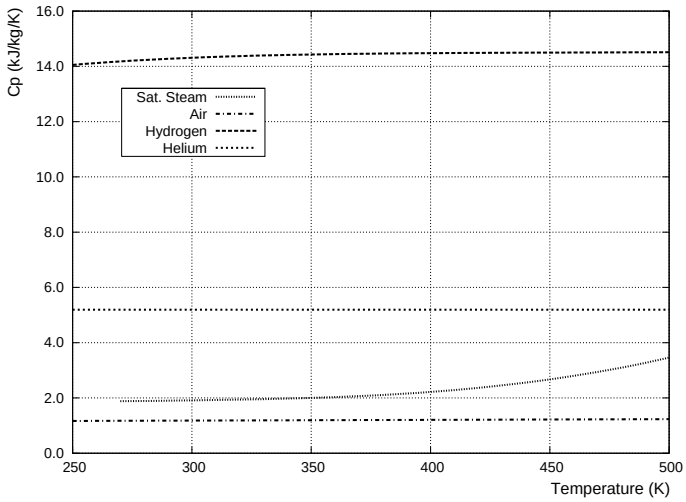

Figure 9.1: Isobaric Specific Heat for air, steam, hydrogen and helium at 0.1 MPa.

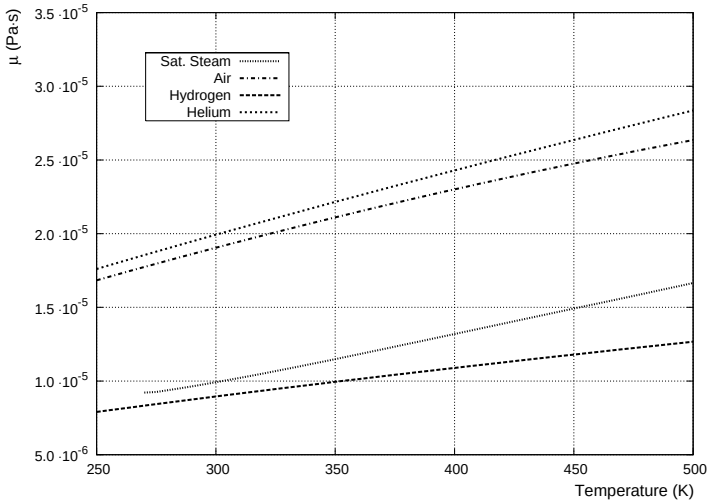

Figure 9.2: Dynamic Viscosity of air, steam, hydrogen and helium at 0.1 MPa.

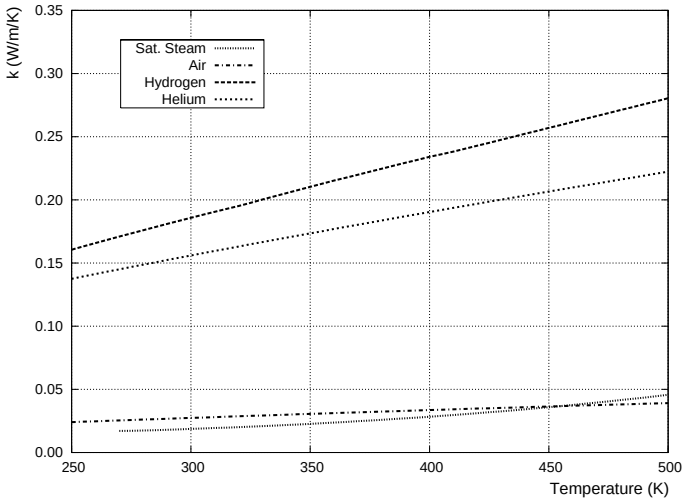

Figure 9.3: Thermal Conductivity of air, steam, hydrogen and helium at 0.1 MPa.

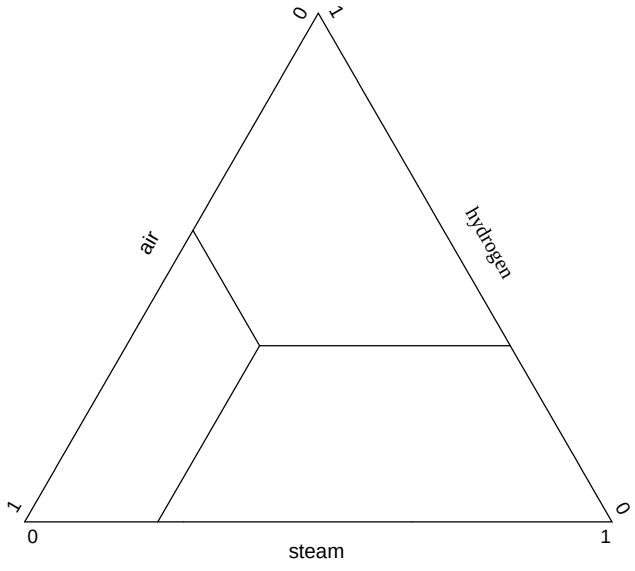

Figure 9.4: Molar fractions in triangular diagrams

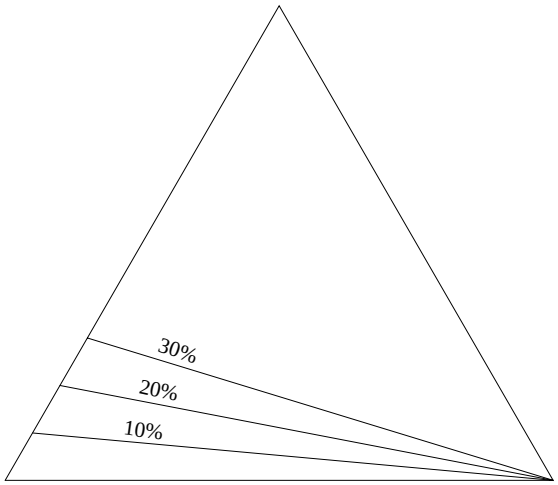

Figure 9.5: Iso-*light-to-noncondensable gas ratio* locus. The steam concentration grows from 0 at left to 1 at right

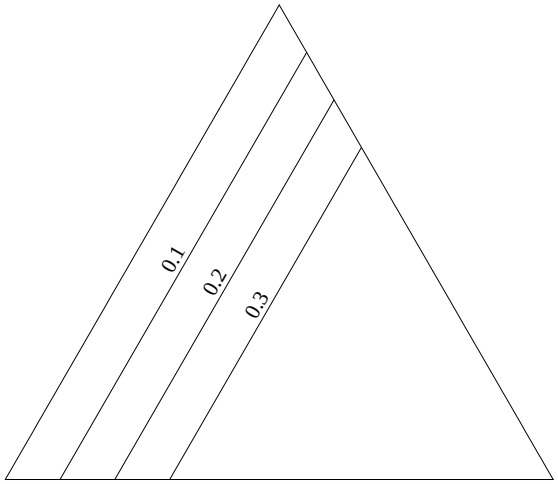

Figure 9.6: Steam iso-molar fraction locus. The $LG\%$ grows in each line from bottom to top

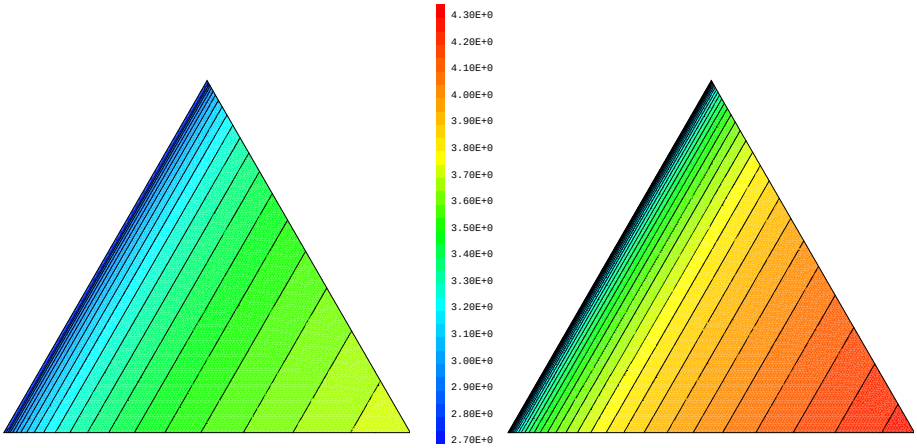

Figure 9.7: Temperature [K] in a mixture of saturated steam at 0.1 MPa (left) and 0.5 MPa (right)

reported as a function of the steam molar fraction for the pressure of 1 and 5 bar. Clearly, the higher is the absolute pressure, the higher is the saturation temperature at the same steam molar fractions.

In the following section, the physical properties of the mixtures will be discussed. Each property depends on the molar fraction of the different components but also intrinsically by the mixture temperature, imposed as reported in Fig. 9.7 as a function of saturated steam molar fraction.

9.1.1 Specific heat of the mixture

The most common way to estimate the specific heat of a mixture is the mass fraction weighted average of the specific heats of the different species

$$C_p = \sum_{i=1}^{n} \frac{X_i M_i C_{p_i}}{\overline{M}} = \sum_{i=1}^{n} Y_i C_{p_i} \tag{9.1}$$

In Fig. 9.8 and Fig. 9.9, the specific heat at 1 and 5 bar are reported respectively for air-steam-hydrogen and air-steam-helium mixtures. In ideal gases, the specific heat is not remarkably affected by pressure or temperature. For both mixtures, the differences between the two cases at different pressures, and therefore also different saturation temperatures, are in fact small. On the other hand, a remarkable difference is observed between the two mixtures. Clearly, since hydrogen has a very large specific heat, almost three times than helium, the higher is the light gas concentration, the larger is the difference between the two mixtures.

9.1.2 Dynamic viscosity of the mixture

In literature, various correlations are proposed to calculate the viscosity of multicomponent mixtures. Wilke proposed in particular a method valid for mixtures

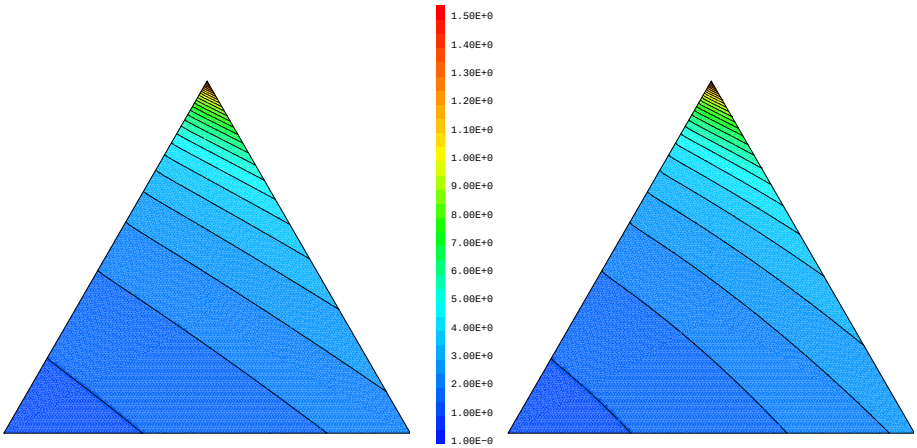

Figure 9.8: Specific heat [kJ/kg/K] in a steam-air-hydrogen mixture at 0.1 MPa (left) and 0.5 MPa (right)

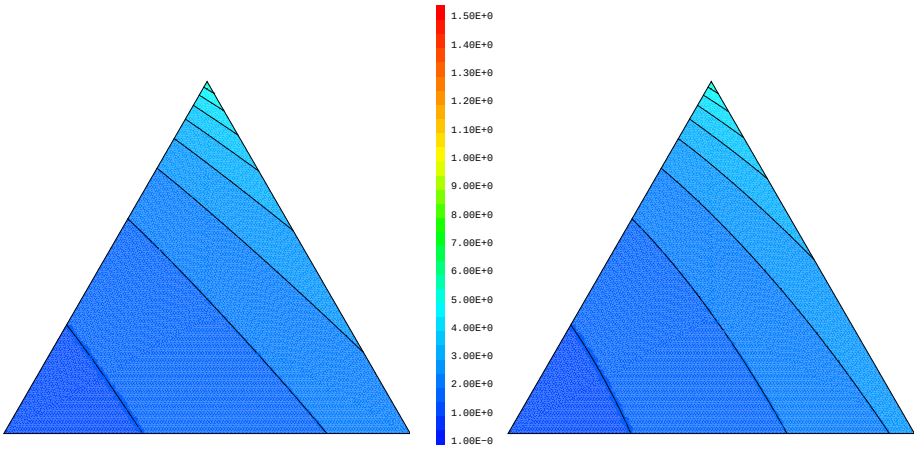

Figure 9.9: Specific heat [kJ/kg/K] in a steam-air-helium mixture at 0.1 MPa (left) and 0.5 MPa (right)

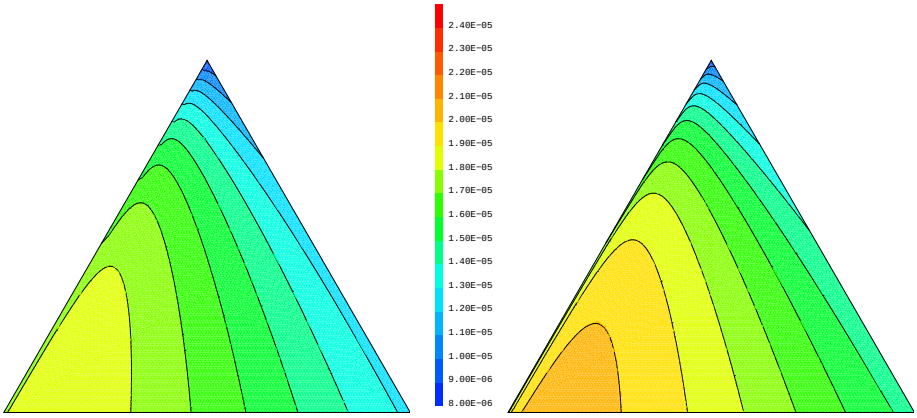

Figure 9.10: Dynamic viscosity [Pa.s] in a steam-air-hydrogen mixture at 0.1 MPa (left) and 0.5 MPa (right)

of non polar fluids[2], based on the molar fractions X_i, the molecular weights M_i, the dynamic viscosities μ_i of each single gas and the Φ_{ij} coefficients evaluated with equation 9.3 [24]:

$$\mu = \sum_{i=1}^{n} \frac{X_i \mu_i}{\sum_{j=1}^{n} X_j \Phi_{ij}} \tag{9.2}$$

where

$$\Phi_{ij} = \frac{\left[1 + \left(\frac{\mu_i}{\mu_j}\right)^{\frac{1}{2}} \left(\frac{M_j}{M_i}\right)^{\frac{1}{4}}\right]^2}{\left[8\left(1 + \frac{M_i}{M_j}\right)\right]^{\frac{1}{2}}} \tag{9.3}$$

In Fig. 9.10 and Fig. 9.11 the mixture viscosities are reported respectively for steam-air-hydrogen and steam-air-helium mixtures. The viscosities of the single species depend on the mixture temperature (see Fig. 9.2), and therefore for the cases at the pressure of 5 bar, for which the mixture temperature (corresponding to the steam saturation temperature) is higher, the mixture viscosities are higher than in the cases at 1 bar. Moreover, it is observed that, since helium viscosity is higher than the other species, the mixture viscosity is higher in the steam-air-helium mixture than in the presence of hydrogen. It is also remarked that the maximum value is not achieved for pure helium mixtures (see Fig. 9.11), but for intermediate concentrations of helium. This important result is achieved by the adoption of the Wilke's law. Molar or mass weighted average correlation would not allow this characteristic of mixture viscosity to be reproduced.

9.1.3 Thermal conductivity of the mixture

The methods for evaluating the thermal conductivity of a mixture of gases are the same as for viscosity; also in this case, the most reliable correlation is the

[2]Steam-air-helium and steam-air-hydrogen mixtures can be considered mixtures of non polar fluids, since only water vapor is polar and do not interact with other gases, air, hydrogen or helium, that are no polar

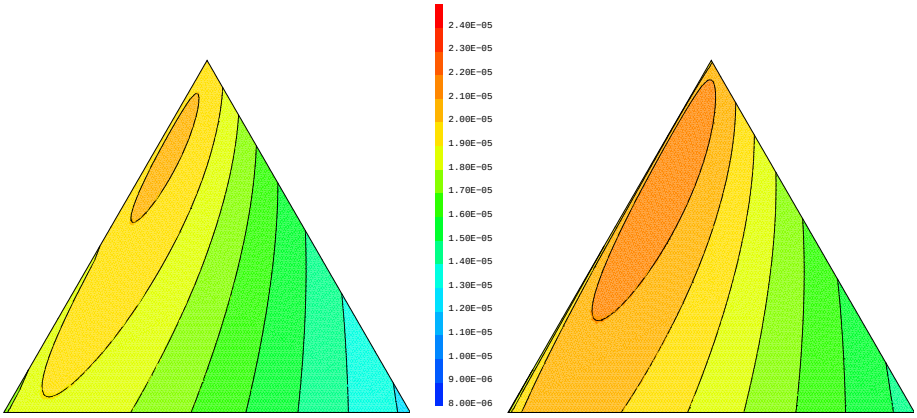

Figure 9.11: Dynamic viscosity [Pa.s] in a steam-air-helium mixture at 0.1 MPa (left) and 0.5 MPa (right)

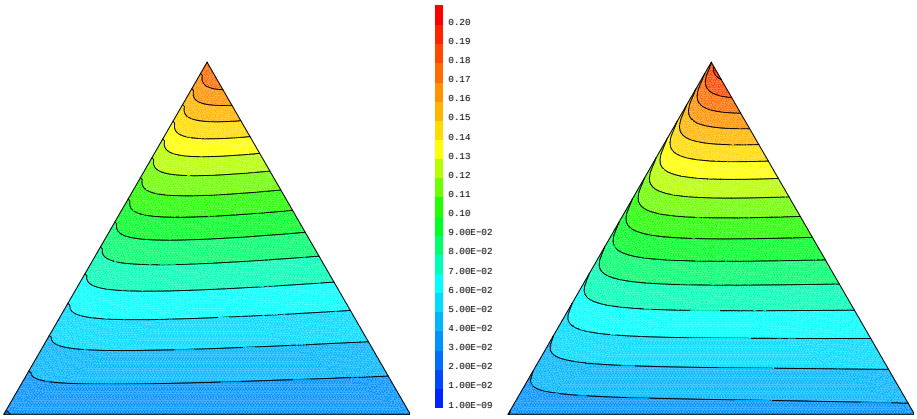

Figure 9.12: Thermal conductivity [W/m/K] in a steam-air-hydrogen mixture at 0.1 MPa (left) and 0.5 MPa (right)

one proposed by Wilke:

$$k = \sum_{i=1}^{n} \frac{X_i k_i}{\sum_{j=1}^{n} X_j \Phi_{ij}} \tag{9.4}$$

where the Φ_{ij} terms are again calculated by Eq. (9.3). The mixture conductivities given by the Wilke's formulation are shown in figures 9.12 and 9.13. The differences between the two gas mixtures are considerable in the region rich of the light gas, but less important than for other properties: in Fig. 9.3, in fact, we could observe that the gap between the thermal conductivity of hydrogen and helium is relatively small.

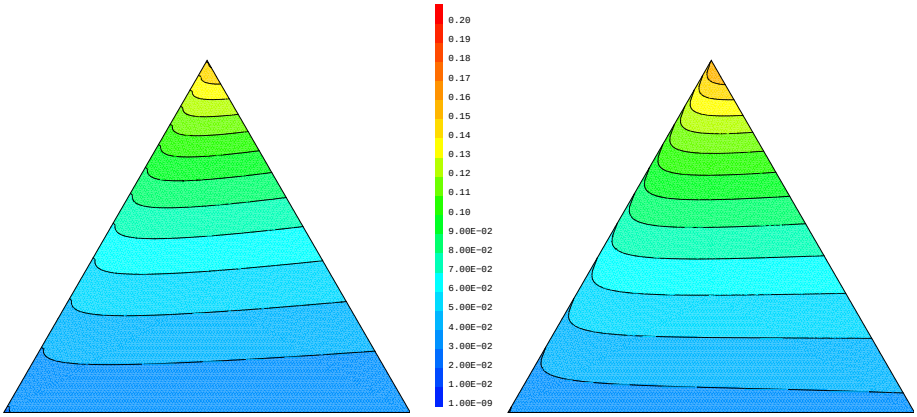

Figure 9.13: Thermal conductivity [W/m/K] in a steam-air-helium mixture at 0.1 MPa (left) and 0.5 MPa (right)

Mixture	$10^5 \cdot A$	s	S (K)	T Range (K)
$Steam - Air$	0.187	2.072	0	250-450
	2.75	1.632	0	450-550
$Steam - H_2$	2.33	1.849	0	250-550
$Steam - He$	3.85	1.750	0	250-550
$Air - H_2$	3.64	1.750	0	250-550
$Air - He$	3.78	1.729	0	250-550

Table 9.2: Experimental Marrero-Mason's coefficients.

9.1.4 Steam diffusion coefficient in the mixture

For a pure binary mixture, the knowledge of the diffusion mass flux of the two species a and b is linked to the evaluation of the diffusion coefficient D_{ab} and their gradient (see chapter 2). It's well remarked that available experimental data suggest the independence of the binary diffusion coefficient on molar fractions [21]. In particular, Marrero and Mason [138, 139] proposed a correlation not dependent on molar fractions, in the form:

$$\ln\left(pD_{12}\right) = \ln A + s \ln T - \frac{S}{T} \tag{9.5}$$

where A, s and S are empiric coefficients, reported in Tab. 9.2. In Eq. (9.5), the pressure is expressed in atm, the temperature in K and the diffusion coefficient in cm^2/s. The Marrero and Mason's studies did not address steam-hydrogen and steam-helium binary mixtures: for those mixtures, the corresponding parameters in Tab. 9.2, are thus recovered adopting the Chapman formulation [140], turned out to obtain a formulation like Eq. (9.5). For the gas mixtures of interest the S coefficient is zero; this allows simplifying Eq. 9.5 to the following form:

$$D_{12} = \frac{AT^s}{p} \tag{9.6}$$

The direct dependence of the diffusion coefficient on the mixture absolute

pressure is remarked. Indeed, pressure plays an important role in the evaluation of the diffusion coefficients in binary and multicomponent mixtures.

The Marrero-Mason formulation and the relative coefficients are however obtained based on experiments at equimolar compositions (50 % of the first species and 50 % of the second species). Marrero and Mason proposed a correction coefficient to evaluate the influence of non equimolar composition in binary mixtures. The corrected coefficient D_{12} is expressed as the product of the calculated diffusion coefficient and the correction parameter Δ

$$D_{12} = D_{12}\,(1 + \Delta_{12}) \tag{9.7}$$

with Δ_{12} given by

$$\Delta_{12} \approx \zeta(6C_{12}^{*} - 5)^2 \frac{aX_1}{1 + bX_1} \tag{9.8}$$

where X_1 is the molar fraction of the heavy component and C_{12}^{*} is the collision integrals ratio, which can be calculated from the Lennard-Jones potential, and depends only on the temperature and the value of the characteristic Lennard-Jones energy ϵ. Moreover, ζ, a and b are tabulated coefficients.
The influence of the mixture composition on the value of D_{12} is anyway evaluated to be less than 5% [138, 139] and will be neglected in the following analysis.

When dealing with multicomponent mixtures, the difficult task to cope with is the evaluation of the diffusion coefficients in the mixture. In this aim the effective binary diffusion approximation is adopted as proposed in chapter 2, which was proven to allow predictions very similar to those of the more accurate full multicomponent diffusion matrix model:

$$\frac{1}{D_{im}} = \frac{1}{1 - X_i} \sum_{j \neq i}^{n} \frac{X_j}{D_{ij}} \tag{9.9}$$

In ternary mixtures of steam, air and a third noncondensable gas l, the effective diffusion coefficients of steam is thus evaluated by

$$D_{vm} = \left[\frac{1}{1 - X_v} \left(\frac{X_a}{D_{va}} + \frac{X_l}{D_{vl}} \right) \right]^{-1} \tag{9.10}$$

In Fig. 9.14 and Fig. 9.15, the diffusion coefficients of steam are reported respectively in steam-air-hydrogen and steam-air-helium mixtures. As it can be seen, hydrogen and helium improves the mobility of steam in a very similar way. According to Eq. (9.6), the diffusion coefficient is expected to be inversely proportional to pressure. Indeed, the diffusion coefficients in the cases at 5 bar are remarkably lower than at 1 bar.

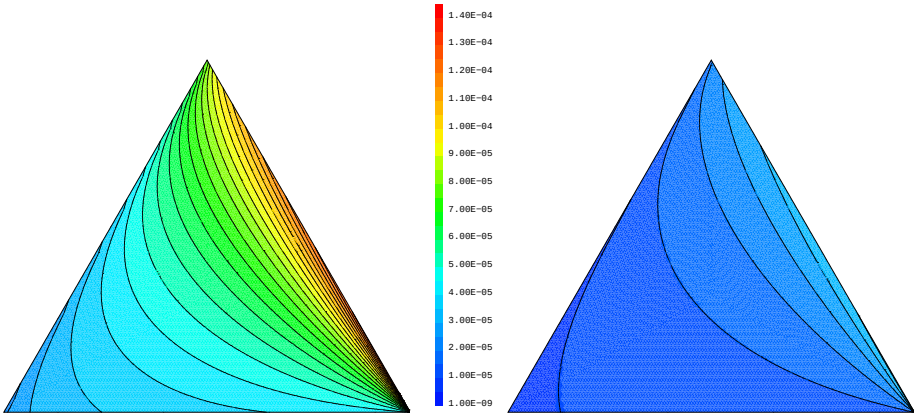

Figure 9.14: Steam effective binary diffusion coefficient [m^2/s] in a steam-air-hydrogen mixture at 0.1 MPa (left) and 0.5 MPa (right)

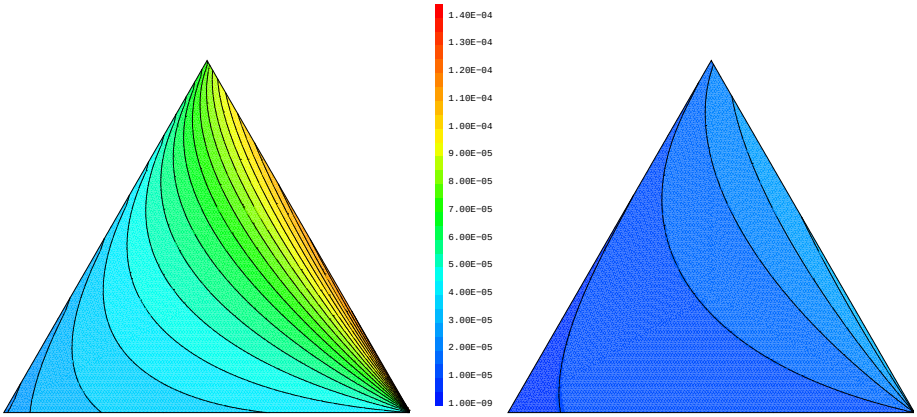

Figure 9.15: Steam effective binary diffusion coefficient [m^2/s] in a steam-air-helium mixture at 0.1 MPa (left) and 0.5 MPa (right)

9.2 Forced convection conditions

Computational tools are useful in supporting the design of experiments. In this aim, detailed models, like the HMTDM ones are very powerful. However, theoretical considerations are also very important, which can be later confirmed by detailed CFD analyses. In this aim, the heat and mass transfer analogy, whose consistency can be also proven against the prediction of the HMTDM models, can provide a relevant information on the boundary conditions to be addressed, before performing dedicated parametrical scoping calculations.

The forced convection regime is investigated in this paragraph via the heat and mass transfer analogy. In particular, the formulation proposed by Bird is adopted [14], which is cast in terms of molar fractions. The differences between the molar formulation of the heat and mass transfer analogy [14] and the corresponding formulation cast in terms of mass fractions are discussed by Ambrosini et al. [52], where a relationship is also proposed to correlate the local mass fluxes predicted by the two approaches.

The conclusions drawn on the basis of theoretical considerations are supported by computations performed with the MSD model. The attention is clearly focused on fully developed flow conditions.

We are mostly interested to establish which are the modifications induced in the mass transfer fluxes when hydrogen is substituted by helium.

Let us consider a geometry representative of the CONAN or the COPAIN facility, similar to the one proposed in the frame of the benchmark-0 exercises (see chapter 3). Inlet conditions are:

- inlet temperature;
- inlet velocity;
- inlet light-to-noncondensable gas ratio;
- inlet steam mass fraction;
- inlet turbulence intensity (2 %).

Other boundary conditions are: the condensing wall temperature, which is supposed uniform all over the condensing plate; adiabatic non-condensing walls; a pressure outlet condition at the outlet section.

Since steam is assumed at saturation conditions, the steam partial pressure at the inlet is known. Moreover, if it is also assumed an ideal gas behavior, the steam inlet molar fraction is known. As a consequence, since the light-to-noncondensable gas ratio is given, the light gas and the air molar fraction are also known. Since steam is in saturation conditions at the condensing interface, the interfacial steam molar fraction is known as well. In a first approximation, according to the results of the experimental analysis and to the results of numerical analyses described in chapter 5, the interface light-to-noncondensable gas ratio is supposed equal to the bulk one. This is a rough approximation but it will be retained only for purpose of simplification. The interface mixture composition is thus known.

The local mass flux predicted by the heat and mass transfer analogy [14] is given by

$$\dot{m}''_{v,i} = M_v Sh_{0,x} \frac{CD_{vm}}{x} \ln \frac{X_{nc,b}}{X_{nc,i}} \tag{9.11}$$

According to the heat and mass transfer analogy, the Sherwood number $Sh_{0,x}$ is expressed as a function of the Reynolds and the Schmidt numbers.

$$Sh_{0,x} = ARe_x^B Sc^E \tag{9.12}$$

The mass flux can be thus rewritten as

$$\dot{m}''_{v,i} = M_v \frac{CD_{vm}}{x} \ln \frac{X_{nc,b}}{X_{nc,i}} ARe_x^B Sc^E \tag{9.13}$$

$$\dot{m}''_{v,i} = M_v \frac{CD_{vm}}{x} \ln \frac{X_{nc,b}}{X_{nc,i}} A \left(\frac{\rho U_\infty x}{\mu} \right)^B \left(\frac{\mu}{\rho D_{vm}} \right)^E \tag{9.14}$$

Now, we isolate the terms that are supposed not to depend on the nature of the selected light gas. These terms are:

- the steam molecular weight M_v;
- the mixture molar concentration C. It is in fact

$$C = \frac{P}{RT} \tag{9.15}$$

  where the different terms do not depend on the nature of the light gas;
- the characteristic length x;
- the constant A;
- the free stream velocity U_∞.

The Eq. (9.14) can be thus rewritten as:

$$\dot{m}''_{v,i} = \left(M_v \frac{P}{RTx} \ln \frac{X_{nc,b}}{X_{nc,i}} AU_\infty^B x^B \right) \left(D_{vm}^{1-E} \rho^{B-E} \mu^{E-B} \right) \tag{9.16}$$

The differences between hydrogen and helium are therefore related to the mixture density, the mixture viscosity and the molecular diffusion coefficient of steam in the mixture. The ratio between the local mass flux obtained in the presence of helium and the one obtained in the presence of hydrogen can be therefore expressed by

$$\frac{\dot{m}''_{v,i}(He)}{\dot{m}''_{v,i}(H_2)} = \left(\frac{D_{vm}(He)}{D_{vm}(H_2)} \right)^{1-E} \left(\frac{\rho(He)}{\rho(H_2)} \right)^{B-E} \left(\frac{\mu(He)}{\mu(H_2)} \right)^{E-B} \tag{9.17}$$

According to the Schlichting correlation, in turbulent forced convection conditions, it is $B = 4/5$ and $E = 1/3$. Eq. 9.17) can be finally written as

$$\frac{\dot{m}''_{v,i}(H_2)}{\dot{m}''_{v,i}(He)} = \left(\frac{D_{vm}(H_2)}{D_{vm}(He)} \right)^{2/3} \left(\frac{\rho(H_2)}{\rho(He)} \right)^{7/15} \left(\frac{\mu(H_2)}{\mu(He)} \right)^{-7/15} \tag{9.18}$$

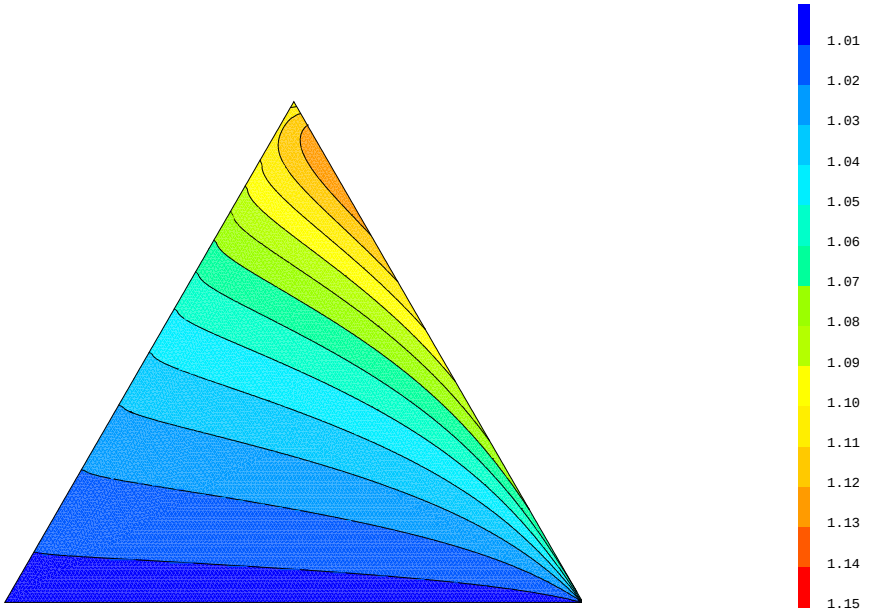

Figure 9.16: Theoretical steam-air-hydrogen to steam-air-helium mass flux ratio predicted by Eq. (9.18) at 0.1 MPa)

where all properties must be taken at the film temperature, that is the average temperature between the bulk and the interface [107]:

$$T_f = \frac{T_i + T_b}{2} \tag{9.19}$$

In Fig. 9.16, the ratio between the mass flux predicted by Eq. (9.18) for steam-air-hydrogen mixtures and the mass flux predicted for steam-air-helium mixtures is reported. The larger differences are observed in the presence of large concentration of the light gas. The expected maximum difference is about 13 %. For small concentrations of the light gas, the differences are reduced to few percentages. In Fig. 9.17, the ratio between the mass flux predicted for steam-air-hydrogen mixtures and the mass flux predicted for steam-air-helium mixtures is reported for condensation cases having bulk temperature of $90°C$ and interface temperatures of $30°C$, as a function of the light-to-noncondensable ratio. If it is assumed that the light-to-noncondensable gas ratio does not change remarkably between the bulk and the interface, that is the case of fully developed turbulent flows (see chapter 5), the ratio between the mass fluxes in the presence of hydrogen and those in the presence of helium is immediately defined once the bulk temperature, the inlet temperature and the light-to-noncondensable gas ratio are known.

A CFD analysis has been carried out aimed at supporting the results proposed by the theoretical analysis. The same geometry adopted for the benchmark-0 exercise was used (see chapter 3). Mixture inlet velocity was chosen 6.0 m/s. Different light-to-noncondensable gas ratios where selected. In the same Fig. 9.17, the mass flux ratios predicted by the HMTDM^{MSD} model are also

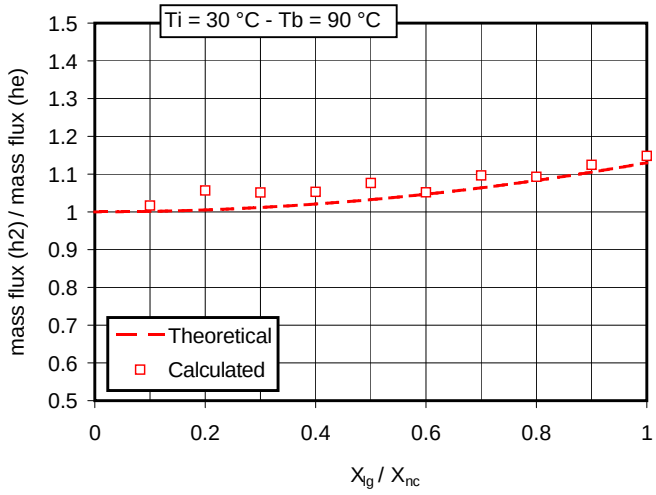

Figure 9.17: Comparison between theoretical and calculated (HMTDM^{MSD}) steam-air-hydrogen to steam-air-helium mass flux ratio for a case having bulk temperature of $90°C$ and interface temperature of $30°C$

reported. The local value of the calculated mass fluxes is taken near the outlet section of the computational domain, where the flow field is expected to be pretty well developed. As it can be seen, in forced convection conditions, a very good agreement is observed between the theoretical and the CFD model results.

9.3 Natural convection conditions

Natural convection regimes are investigated in this paragraph. Two aspects are addressed in particular; we are first of all interested to analyze what happens when traces of the light gas are introduced in the mixture, that is, which way buoyancy forces associated to air are affected by the presence of light gases; on the other hand, the effects of helium or hydrogen are analyzed when the two gases are the dominating noncondensable species, for light-to-noncondensable gas ratios greater than the critical value for which the buoyancy reversal is expected to occur.

When dealing with natural convection conditions, the Sherwood number $Sh_{0,x}$ is expressed as function of the local Grashof and Schmidt numbers.

$$Sh_{0,x} = AGr_x^B Sc^E \tag{9.20}$$

In turbulent natural convection in particular, the McAdams correlation is adopted having $A = 0.13$, $B = 1/3$ and $E = B = 1/3$. According to Eq. (9.11), the local mass flux in turbulent natural convection conditions can be thus written as

$$\dot{m}''_{v,i} = M_v \frac{CD_{vm}}{x} \ln \frac{X_{nc,b}}{X_{nc,i}} AGr_x^B Sc^B \tag{9.21}$$

and therefore

$$\dot{m}''_{v,i} = M_v \frac{CD_{vm}}{x} \ln \frac{X_{nc,b}}{X_{nc,i}} A \left(\frac{x^3 \rho g \triangle \rho}{\mu^2} \right)^B \left(\frac{\mu}{\rho D_{vm}} \right)^B \tag{9.22}$$

Once the terms that do not depend on the nature of the light gas are isolated, the local mass flux can be written as

$$\dot{m}''_{v,i} = \left(\frac{M_v C}{x} \ln \frac{X_{nc,b}}{X_{nc,i}} A g^B x^{3B} \right) D_{vm}^{1-B} \mu^{-B} \left(\triangle \rho \right)^B \tag{9.23}$$

The differences between hydrogen and helium are therefore related to the mixture density and mixture viscosity and the molecular diffusion coefficient of steam in the mixture. The ratio between the local mass flux obtained in the presence of helium and the one obtained in the presence of hydrogen can be expressed by

$$\frac{\dot{m}''_{v,i}(He)}{\dot{m}''_{v,i}(H_2)} = \left(\frac{D_{vm}(He)}{D_{vm}(H_2)} \right)^{1-B} \left(\frac{\mu(He)}{\mu(H_2)} \right)^{-B} \left(\frac{\triangle \rho(He)}{\triangle \rho(H_2)} \right)^B \tag{9.24}$$

Two terms can be identified. A first term depends on the film temperature and the corresponding film properties

$$\left(\frac{D_{vm}(He)}{D_{vm}(H_2)} \right)^{1-B} \left(\frac{\mu(He)}{\mu(H_2)} \right)^{-B} \tag{9.25}$$

This term will be later on labelled as *film property ratio*. A second term depends on the interface and the bulk temperature, via the densities

$$\left(\frac{\triangle \rho(He)}{\triangle \rho(H_2)} \right)^B \tag{9.26}$$

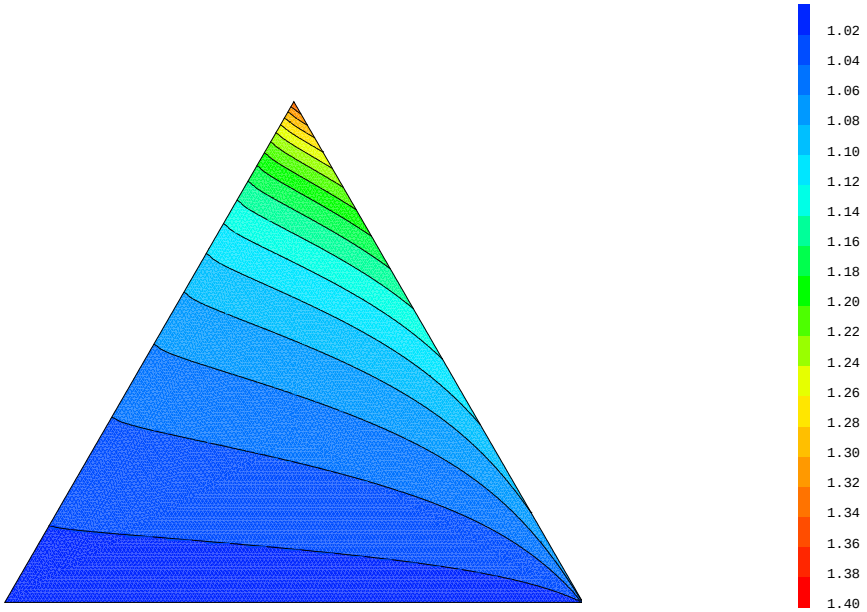

Figure 9.18: Contours of the *film property ratio* calculated by Eq. (9.25)

The *film property ratio* is shown in Fig. 9.18. As it can be seen, the differences between the two mixtures are limited to some percents in the region poor of the light noncondensable gas. In the region rich of the light gas, the differences increase up to 35 %. Amidst the two region, the buoyancy reversal phenomenon is expected to occur.

This point is better clarified by analyzing Fig. 9.19, where the density ratio terms are reported calculated by Eq. (9.26). The density differences between the bulk and the interface are also reported in the aim to identify the critical light-to-noncondensable gas ratios at the *buoyancy reversal* conditions, for which the density difference between the bulk and the interface is zeroed. As it can be seen, in all cases, a region can be identified where the density ratio is almost constant; for light-to-noncondensable gas ratios less than the hydrogen or helium critical concentrations, where the buoyancy forces due to air are expected to be still dominating, the density ratio is always around one. On the other hand, when the light-to-noncondensable ratio is greater then the critical values, the density ratio is a few percents higher than one, but pretty well constant. These two region are separated by a narrow region in which the buoyancy reversal phenomenon is expected to occur for both hydrogen and helium mixtures. As it can be seen in Fig. 9.19, the critical hydrogen-to-noncondensable gas ratio is lower than the critical helium-to-noncondensable gas ratio; fixed the bulk temperature at $90°C$, the lower is the interface temperature the larger is this difference. Moreover, ranging from an interface temperature of $10°C$ up to a temperature of $80°C$, the critical light-to-noncondensable gas ratio decrease from approximatively 0.65 to 0.5 for helium and from 0.6 to 0.5 for hydrogen.

The comparison between steam-air-hydrogen and steam-air helium mixtures

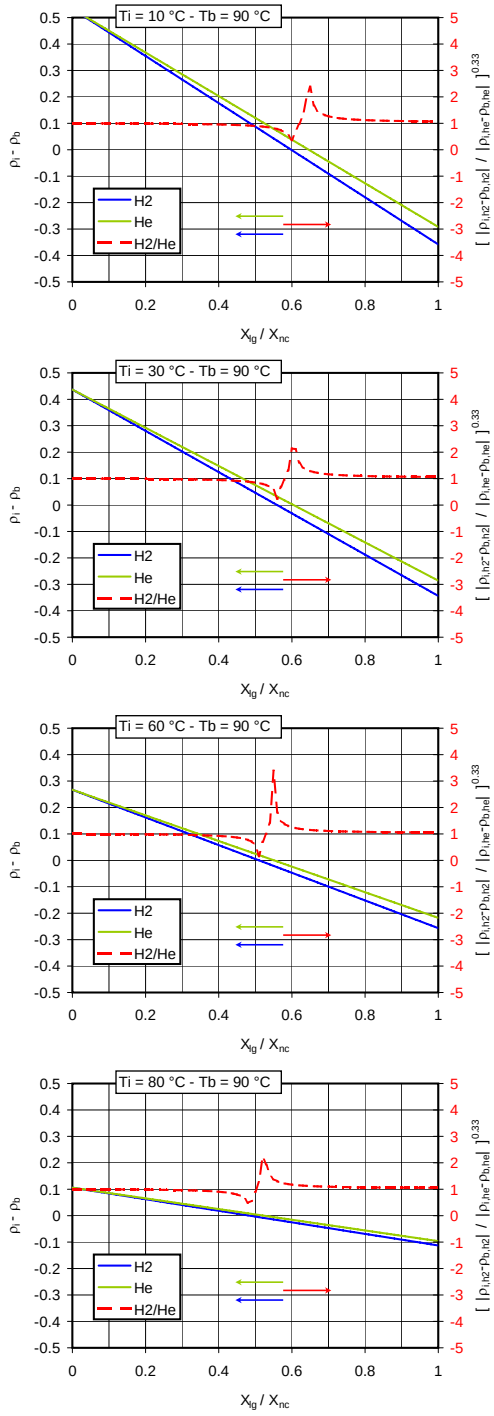

Figure 9.19: Density difference ratio, calculated by Eq. 9.26 (singularity peaks corresponding to *buoyancy reversal* conditions for the two mixtures are not reported)

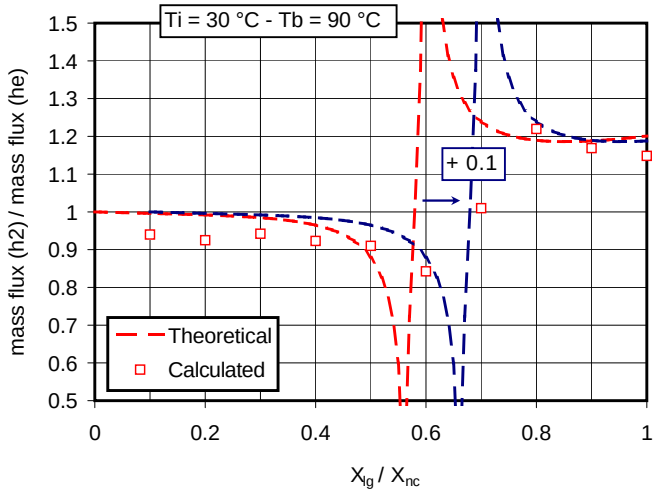

Figure 9.20: Comparison between theoretical and calculated (HMTDM^{MSD}) steam-air-hydrogen to steam-air-helium mass flux ratio for a case having bulk temperature of 90°C and interface temperature of 30°C

is therefore possible by analyzing simultaneously the differences in the film properties and the density differences between the bulk and the interface. Here, a case is considered having an interface temperature of 30°C, a bulk temperature of 90°C and therefore a film temperature of 60°C for which the film properties are estimated. The inlet velocity is fixed at 0.5 m/s. Several light-to-noncondensable gas ratios are considered. In Fig. 9.20, the mass flux ratios predicted by the theoretical model based on the heat and mass transfer analogy (red dashed line) and those predicted by the HMTDM^{MSD} model are compared. As in the forced convection cases, computed values are taken near the outlet section of the computational domain; even if fully developed flow conditions are not attained, the behavior of both mixtures is clearly identified. In particular, the theoretical and the computational models are qualitatively in agreement in the region having low and very high light-to-noncondensable gas ratios. It is also observed that, as also remarked in the modelling of the CONAN test at low free stream velocity in the presence of helium, the critical value of the light-to-noncondensable gas ratio for which buoyancy reversal occurs is slightly overestimated by the CFD model. In the Fig. 9.20, the curve obtained by the theoretical model (red dashed line), which was proven to agree with helium experimental data (see chapter 5), is also reported translated of a quantity corresponding to a concentration of the light gas ten percent higher than the actual value (blue dashed line). Indeed, the agreement between the two models will be improved by accounting for this last difference. As also remarked in chapter 8, several factors can contribute to this discrepancy caused by the CFD model; turbulence modelling is the first.

9.4 Concluding remarks

This chapter aimed at investigating to what extent helium can be considered a suitable substitute for hydrogen. Steam condensation in the presence of helium or hydrogen was addressed in forced and natural convection conditions.

After performing a critical review of the physical properties of the two species, aa analytical and computational analysis was presented. Basing on the heat and mass transfer analogy, two simple criteria were derived for the forced and the natural convection. A comparison between the theoretical criteria and the predictions obtained by the HMTDM^{MSD} model was also proposed.

In forced convection, the similarities between air-steam-helium and air-steam-hydrogen mixtures can be related to the physical properties of the film. For equimolar mixtures, having the same molar fraction of helium or hydrogen, the difference in terms of local mass flux are limited to few percents. The maximum difference is expected for mixtures rich of the light noncondensable species, where the maximum difference is attained, around 15 per cent.

Basing on the results of this analytical and computational analysis, steam condensation mass fluxes in the presence of hydrogen in forced convection conditions are appropriately scaled if mixtures of helium having the same molar fraction as hydrogen are considered.

In natural convection, the similarities between the two mixtures cannot be related only to the film properties. Indeed, interface and bulk densities also play a role, since the driving force of condensation is correlated to the density difference between the bulk and the interface. Film, interface and bulk properties are therefore necessary to establish a criterion of similarity between steam-air-helium and steam-air-hydrogen mixtures. According to the results of the theoretical and the HMTDM^{MSD} model, equimolar mixture of hydrogen and helium are due to give very similar mass flux profiles for low or very high values of the light-to-noncondensable gas ratios, corresponding to well defined situations of natural convection where the density gradient is respectively negative (interface poor of helium) and positive (interface rich of helium). The differences between the two mixtures in terms of condensation rates are anyway enhanced (up to 35 %) in mixtures rich of the light gas, for which *flow reversal* is also expected.

Buoyancy reversal conditions are predicted by both the analytical and the CFD models to occur for hydrogen-to-noncondensable gas ratio lower the ones expected for steam-air-helium mixtures.

Chapter 10

Conclusions

Steam condensation phenomena in the presence of noncondensable gases lighter than steam have been studied under the theoretical, the experimental and the numerical point of view.

An in depth analysis of the experimental data available by the CONAN and the COPAIN separate effect test facilities was performed. Further experiments were carried out within the CONAN facility to cover a wider range of phenomenologies related to the presence of lighter than steam noncondensable gases. The main findings of these analyses are reported in paragraph 10.1.

According to the theoretical analysis of diffusion phenomena in multicomponent mixtures, two different diffusion models have been proposed: a first model (EBD) is based on the binary diffusivity approximation; the second model (MSD) is a full multicomponent diffusion matrix model, developed based on the principles of the irreversible thermodynamics. Three different CFD models have been developed for the modelling wall condensation phenomena. Two of them consist in evaluating the near-wall gradients in detail and estimating the mass transfer rates on the basis of the interface diffusion mass fluxes. The two models are named HMTDM^{EBD} and the HMTDM^{MSD}, depending on the selected diffusion model. A third model, referred to as HMTAM, is developed for relatively coarse near-wall discretizations and consists in estimating the mass transfer rates on the basis of the heat and mass transfer analogy.

The validation of the turbulence and the condensation models has included different stages. The main findings of these analyses are reported respectively in the paragraphs 10.2 and 10.3.

The suitability of helium as a substitute for hydrogen was investigated theoretically and numerically. The main findings of this analysis are reported in the paragraphs 10.4.

Finally, conclusions are drawn and recommendations for future studies are proposed.

10.1 Analysis of the experimental data available by CONAN and COPAIN

The analysis of the experimental data of steam condensation in the presence of air available by the CONAN and the COPAIN facilities has been performed

in this research, aimed at improving the understanding of condensation in the different convection regimes. The results of the previous analyses were also revisited. In this regard, the main findings are summarized in the following:

- the presence of suction effects was clearly identified in the previous analyses of the COPAIN tests, but only for the natural convection regime; in this work, an alternative correlation for forced convection conditions has been investigated, capable to account for low Prandtl and Schmidt numbers experienced in tests of forced convection; on the basis of the new correlation, suction phenomena are also observed in forced convection tests;
- the presence of mixed convection phenomena has been identified in some COPAIN tests where buoyancy and inertia forces are comparable; pure heat transfer cases and heat and mass transfer cases are both likely to be affected by buoyancy forces; basing on the available data, it was not possible to quantify these effects; the need emerged for a more in-depth understanding of buoyancy effects in the presence of air;
- the conclusions drawn in the previous analyses of the CONAN data were confirmed; buoyancy effects were also confirmed for the lowest velocity cases, whose presence was also identified on the basis of previous computations.
- suction effects are experienced to be more and more important for higher and higher mass transfer rates; the Stefan factor seems to overestimate these effects;

The analysis of the experimental data of steam condensation in the presence of air and helium available by the CONAN facility has also been performed, aimed at improving the understanding of the effects induced by helium, mostly in terms of buoyancy forces. Forced convection and natural convection regimes were addressed. Experimental data for fully developed forced convection were analyzed. New data were proposed analyzing cases at low free stream velocities. Even if fully developed flow conditions were not completely attained, interesting effects have been clearly highlighted, related to the presence of helium. The main findings are summarized in the following list:

- in contrast with the work by Peterson [81], situations may occur where the helium concentration at the interface is significantly different from the one in bulk. simple scoping CFD calculations proved that in a more realistic configuration than the one assumed at the basis of the Peterson model, the light noncondensable species can accumulate at the interface, as well as air does; as shown by the same scoping calculations, in turbulent flows, the helium-to-noncondensable gas ratio at the interface can be not very different from the one in the bulk. indeed, for certain helium concentration in bulk, it could happen that the interface density is lower than the bulk density; this situation is referred to as *buoyancy reversal* and it is expected in some CONAN and COPAIN tests in the presence of large quantities of helium;
- a simple theoretical relationship has been proposed for estimating the helium-to-noncondensable gas ratio χ_{br} for which *buoyancy reversal* occurs; the agreement between the predicted and the experimental values is excellent;

- *buoyancy-aided* mixed convection conditions occur in COPAIN and CONAN tests with steam-air mixture or steam-air-helium mixtures having a helium-to-noncondensable gas ratio less than the critical value for which *buoyancy reversal* occurs; *buoyancy-opposed* conditions are experienced for larger quantities of helium;

- for low free stream velocity, in *buoyancy-opposed* conditions, *flow reversal* conditions can be also experienced, for which the flow field near the condensing wall is locally inverted with respect to the free stream;

- the conclusions drawn on the basis of the CONAN data are also confirmed by the COPAIN tests at higher pressure and with superheated steam: a common trend is clearly observed for both facilities, confirming the presence of the aforementioned phenomenologies.

10.2 Prediction of transpiration effects in turbulent boundary layers

The bahavior of four different models with low Reynolds number capabilities was checked in the analysis of turbulent transpirating boundary layers: the models of Yang and Shih [121], the model of Abe et al. [120], the low Reynolds variant of the $\kappa - \omega$ model of Wilcox [119] and the RNG $\kappa - \varepsilon$ model with a two-layer model (TLM) for the near-wall region [123] were tested.

The capabilities of turbulence models in reproducing nondimensional velocity profiles in the presence of pure mass and momentum transfer, basing on the experimental data by Favre [13] were formerly checked. On the basis of the results obtained it was possible to conclude that:

- all turbulence models demonstrated a satisfactory behavior;

- turbulence production terms associated to mean velocity gradients are likely to be the responsible in capturing the modification induced by transpiration on the generation of turbulence kinetic energy and, as a consequence, on the nondimensional velocity profiles;

- the RNG $\kappa - \varepsilon$ with TLM is enough accurate for this kind of problems, at least in the cases with lower suction parameters; the model was also ascertained to be the less sensitive to grid refinements in the near-wall region, requiring y^+ around one to achieve reasonable grid convergence;

A numerical analysis of suction effects induced by condensation was therefore performed The consistency between the calculations and the common available correlations for predicting momentum, heat and mass transfer coefficients was checked. The coherence between calculations and the proposed transpiration correction factors accounting for suction effects was also tested. Concerning this analysis, it can be remarked that:

- the tendency of the Stefan factor to overestimate the effect of suction on the Sherwood number is confirmed;

- the coherence between the Ackerman correction factor accounting for suction effects on the heat transfer coefficient and the calculations by the different models is really satisfactory;
- modification of the friction coefficient induced by suction are predicted by all CFD models, coherently with the correction factor proposed by Kays and Moffat [126, 26];
- the RNG $\kappa - \varepsilon$ model with TLM had the best overall performance.

The effect of the momentum source terms have also been investigated. The analysis has shown that:

- the presence of a momentum source term for the velocity component parallel to the condensing surface is necessary for evaluating correctly the mass transfer effects on the different boundary layers, and mostly friction;
- the presence of a momentum source for the velocity component orthogonal to the condensing surface is not strictly necessary and has the disavantage to increase the computational effort.

10.3 Modelling of the CONAN and COPAIN tests

The modelling of the CONAN and the COPAIN experiences has been addressed with the HMTDM^{EBD} and the HMTDM^{EBD} condensation models coupled with the RNG $\kappa - \varepsilon$ model with TLM. The capabilities of the fast-running HMTAM model coupled with a simple RNG $\kappa - \varepsilon$ model and standard wall function were also addressed. In addition to the operating conditions for which the models were already validated, additional capabilities were tested for both steam-air and steam-air-helium mixtures. In particular, the following aspects were tested:

- steam superheating and pressure in the presence of air, by modelling the steam-air tests performed within COPAIN;
- *buoyancy-aided* mixed convection regimes and natural convection regimes, by modelling the steam-air tests performed within COPAIN;
- condensation of steam in the presence of helium in forced convection conditions, by modelling the steam-air-helium tests at high free stream velocities performed within CONAN;
- condensation of steam in the presence of helium in natural convection conditions, by modelling the steam-air-helium tests at low free stream velocities performed within CONAN;
- steam superheating and pressure in the presence of helium, by modelling the steam-air-helium COPAIN tests.

Important conclusions can be drawn based on the results obtained by the modelling of these tests:

- whatever is the convection regime or the mixture composition, steam superheating and pressure are intrinsically accounted for by the HMTDM and the HMTAM model, whose accuracy is not affected by them;
- the HMTDM^{EBD} and the HMTDM^{MSD} behave in a very similar way in forced convection conditions and the agreement with local experimental data is also remarkable; the difference with the experimental data in terms of overall condensation rate can be mainly attributed to the difficulties of the turbulence model to account for entrance effects; minor differences are observed between the two models in the CONAN tests at low free stream velocity; in particular, the EBD model predict the *buoyancy reversal* to occur at a slightly lower helium concentration than the MSD model; basing on the analysis of the modelling results, the adequacy of the simplified EBD model is assessed against the prediction of the MSD model and the experimental data;
- *Buoyancy reversal* and *flow reversal* phenomena in the steam-air-helium tests within CONAN are clearly confirmed by experimental data and by CFD analyses; both the EBD and the MSD model predict these phenomena;
- important issues concerning the measuremets of temperature profile close to the wall within COPAIN were clarified thanks to the analysis performed with the HMTDM models and theoretical considerations; on the basis of these results, the invasivity of the temperature measurements is suspected;
- forced convection steam condensation in steam-air and steam-air-helium mixtures are remarkably well predicted by the HMTAM model; differences with the experimental data and with the predictions of the HMTDM models are reduced to the near-inlet region, whose interest is limited in large scale geometries, and affect only slightly the accuracy in the prediction of the overall condensation rates;
- a remarkable improvement was also obtained in the mixed and natural convection regimes by the introduction of two different correlations for *buoyancy-aided* and *buoyancy-opposed* mixed convection; in COPAIN tests performed in the presence of air, the results are particularly improved with respect to those obtained by a correlation not accounting for the impairment of the mass transfer coefficient; a good agreement was also observed for the steam-air-helium tests where the helium concentration is very large and *buoyancy opposed* convection conditions are expected;
- *buoyancy reversal* phenomena are predicted by the HMTAM model for large concentrations of the light noncondensable gas; the flow reversal phenomenon is also qualitatively predicted.

10.4 Suitability of helium as a substitute for hydrogen

An analytical and computational analysis was presented comparing steam-air-helium and steam-air-hydrogen mixtures. Basing on the heat and mass transfer

analogy, simple comparison methodologies were derived for forced and natural convection. A comparison between the theoretical results and the predictions obtained by the HMTDM^{MSD} model was also proposed.

Basing on the results of this analysis, in forced convection conditions, steam condensation mass fluxes in the presence of hydrogen or helium are very similar for mixtures having the same molar fraction of the light gases.

In natural convection conditions, equimolar mixture of hydrogen and helium are expected to give very similar mass flux for low or very high values of the light-to-noncondensable gas ratios, corresponding to well defined situations of natural convection where the density gradient is respectively negative (interface poor of helium) and positive (interface rich of helium).

Buoyancy reversal conditions are predicted by both the analytical and the CFD models to occur for hydrogen-to-noncondensable gas ratio lower the ones expected for steam-air-helium mixtures.

10.5 Future perspectives

The synergy between experimental and computational analyses has always been a keypoint for achieving a real improvement in the understanding of physical phenomena and in their modelling.

It was not by chance that, in the frame of this research, interesting effects related to the presence of lighter than steam noncondensable gases have been highlighted simultaneously by experiments and computations. Further exploitation of this synergic use of experiments and computations seems advisable.

A fundamental point to achieve a significant improvement in the understanding and in modelling condensation phenomena is the understanding of the role of turbulence in transport processes. In this aim, the need is felt for filling the lack of experimental data.

Two important aspects are identified to be investigated:

- a more in-depth analysis of the turbulent boundary layer should be achieved for forced, natural and mixed convection; pure heat transfer tests and steam-air condensation tests are appropriate for this analysis;
- the modifications of the turbulent transport processes induced by helium should also be analyzed in detail in forced and natural convection regimes. In particular, interesting effects are expected for low free stream velocities and the presence of the *flow reversal* phenomenon.

Moreover, in the design of experiments of steam condensation in the presence of air and helium, particular attention should be payed concerning the following aspects:

- entrance effects were observed to be significantly affected by the presence of helium. A denser instrumentation would be advisable near the inlet section region to achieve a better understanding of them;
- in the CONAN tests at low free stream velocity, fully developed flow condition were not completely reached. The need for further experimental data in fully developed flow conditions is felt. In this aim, longer condensing plates could be used;

- in the presence of flow reversal phenomena, the velocity profile in the free stream can be significantly modified. Therefore, interaction phenomena between the momentum boundary layer near the condensing wall and the one near the adiabatic wall (opposite side) should be appropriately checked.

Whatever is the phenomenon to be investigated, in-depth analyses are required, for which advanced measurement techniques are necessary. In particular, it is of major interest that accurate and non intrusive measurements of the velocity, the temperature and the concentration profiles in the condensing boundary layers will be available in different fully developed convection regimes and also in the presence of transition phenomena as the *flow reversal*.

Indeed, for an improved understanding of the phenomena, it is fundamental that the detail of nondimensional velocity U^+, nondimensional temperature T^+ and nondimensional concentration ϕ^+ profiles will be available. Nevertheless, it is also recommended that turbulence nondimensional quantities, like the nondimensional turbulence kinetic energy κ^+, the nondimensional turbulence kinetic energy production P^+ and the nondimensional turbulence kinetic energy dissipation ε^+ will be known.

This is also a fundamental aspect for the development of appropriate wall functions capable to cope with transpirating flows. Indeed, this last approach is considered very promising for the modelling of condensation phenomena in large scale geometries, since it should reduce the problems typical of the heat and mass transfer analogy: in large scale geometries it is in fact not clear how to chose a mass transfer correlation and how to define bulk properties. The development of this approach is therefore suggested, which can be preliminary based on the prediction of the HMTDM models, until detailed experimental data will not be available. Nevertheless, DNS analyses can also provide a relevant information in the absence of detailed measurement of the turbulence structures.

Appendix A: CONAN steam-air test matrix

Test	$\dot{M}_{sec}[kg/s]$	$T_{in,sec}[K]$	$T_{out,sec}[K]$	$T_{inlet}[K]$	$U_{inlet}[m/s]$	$\dot{M}_{cond}[g/s]$	$Y_{a,in}[-]$
P10-T70-V15	1.000	343.7	345.2	365.3	1.36	2.598	0.375
P10-T70-V20	1.001	343.7	345.2	364.6	2.04	2.640	0.399
P10-T70-V25	0.999	344.1	345.9	364.7	2.55	2.955	0.409
P10-T70-V30	1.001	343.4	345.2	365.1	3.03	3.014	0.432
P10-T60-V20	0.964	333.8	335.3	360.8	2.04	2.411	0.485
P10-T60-V25	0.966	333.8	335.6	361.2	2.50	2.807	0.481
P10-T60-V30	0.968	333.5	335.5	362.0	3.06	3.070	0.495
P10-T60-V35	0.970	333.6	335.6	365.5	3.53	3.103	0.473
P10-T50-V17	0.977	323.2	324.7	357.8	1.75	2.197	0.552
P10-T50-V20	0.984	323.2	324.9	357.7	2.05	2.507	0.551
P10-T50-V25	0.985	323.2	325.1	357.0	2.55	2.747	0.572
P10-T50-V30	0.991	323.4	325.3	356.8	3.03	2.904	0.588
P10-T50-V35	0.988	323.3	325.4	357.1	3.50	3.137	0.591
P15-T50-V17	0.992	323.5	325.9	364.5	1.48	3.616	0.370
P15-T50-V20	0.991	323.5	326.0	363.5	2.06	3.786	0.406
P15-T50-V25	0.991	323.3	325.9	362.9	2.55	3.979	0.434
P15-T50-V30	0.991	323.9	326.7	362.8	3.04	4.275	0.446
P15-T50-V35	0.991	323.8	326.7	362.8	3.51	4.645	0.455
P20-T50-V15	0.995	323.2	326.5	368.0	1.37	4.893	0.245
P20-T50-V20	0.994	323.2	326.6	367.2	2.05	5.029	0.280
P20-T50-V25	0.994	323.3	326.7	366.6	2.57	5.168	0.320
P20-T50-V30	0.996	323.2	326.8	366.3	3.04	5.420	0.346
P20-T50-V35	0.997	323.1	326.7	365.9	3.53	5.599	0.371
P25-T50-V35	0.993	323.6	328.1	368.9	3.55	7.066	0.268
P30-T50-V35	0.970	325.0	330.9	372.1	3.58	9.494	0.142
P30-T50-V30	0.965	323.8	329.9	372.6	3.01	9.350	0.103
P30-T50-V25	0.962	323.7	329.7	372.4	2.52	9.153	0.091
P30-T50-V20	0.960	323.6	329.4	372.3	2.13	9.003	0.196
P30-T50-V15	0.958	323.3	328.7	372.1	1.58	8.581	0.242
P30-T60-V35	0.969	333.1	339.1	373.5	3.58	9.888	0.066
P30-T60-V30	0.969	333.6	339.6	373.3	3.08	9.639	0.056
P30-T60-V25	0.969	333.7	339.6	372.9	2.61	9.475	0.040
P30-T60-V20	0.969	333.6	339.4	373.0	2.10	9.285	0.028
P30-T60-V15	0.968	333.7	339.5	372.9	1.26	9.246	0.017

Test	$\dot{M}_{sec}[kg/s]$	$T_{in,sec}[K]$	$T_{out,sec}[K]$	$T_{inlet}[K]$	$U_{inlet}[m/s]$	$\dot{M}_{cond}[g/s]$	$Y_{a,in}[-]$
P30-T70-V35	0.970	343.9	349.9	375.2	3.59	9.857	0.000
P30-T70-V30	0.970	344.0	349.7	374.6	3.10	9.433	0.000
P30-T70-V25	0.968	343.8	349.5	374.2	2.62	9.265	0.003
P30-T70-V20	0.969	343.9	349.3	373.6	2.11	8.994	0.014
P30-T70-V15	0.972	343.2	348.6	373.4	1.85	8.672	0.042
P20-T60-V30	0.928	333.7	337.7	369.2	3.05	5.874	0.242
P20-T60-V25	0.928	334.4	338.3	369.3	2.57	5.641	0.212
P20-T60-V20	0.928	334.1	337.8	369.5	2.05	5.408	0.189
P20-T60-V15	0.931	333.7	337.0	368.9	1.63	4.808	0.207
P20-T70-V35	0.969	343.4	347.2	373.5	3.56	6.089	0.141
P20-T70-V30	0.970	343.1	346.6	372.4	3.07	5.677	0.153
P20-T70-V25	0.969	342.8	346.2	370.6	2.57	5.525	0.157
P20-T70-V20	0.969	342.3	345.6	370.3	2.05	5.313	0.146
P20-T70-V15	0.970	342.2	345.5	370.7	1.45	5.289	0.123
P25-T60-V35	0.902	333.0	337.3	370.2	3.57	6.796	0.226
P25-T60-V30	0.905	334.1	338.8	371.1	3.08	7.118	0.166
P25-T60-V25	0.910	334.3	339.0	371.3	2.59	7.017	0.134
P25-T60-V20	0.911	334.3	339.0	371.3	2.08	6.750	0.117
P25-T60-V15	0.900	333.6	338.6	371.6	1.26	6.993	0.085
P25-T70-V15	0.890	343.6	348.1	372.3	1.41	6.886	0.045
P25-T70-V20	0.891	342.7	347.6	372.3	2.08	7.338	0.046
P25-T70-V25	0.892	343.8	348.8	372.6	2.58	7.533	0.051
P25-T70-V30	0.847	343.9	349.3	373.0	3.06	7.992	0.050
P25-T70-V35	0.835	343.9	349.6	373.6	3.56	8.193	0.039
P15-T60-V35	0.681	333.6	337.0	365.8	3.54	4.178	0.408
P15-T60-V30	0.684	333.7	337.4	366.6	3.06	4.219	0.365
P15-T60-V25	0.678	333.7	337.4	366.5	2.55	4.098	0.338
P15-T60-V20	0.678	333.7	337.2	367.0	2.05	3.981	0.320
P15-T60-V15	0.674	333.7	337.4	367.6	1.68	4.015	0.278
P15-T70-V15	0.657	342.4	345.8	368.7	1.61	3.815	0.215
P15-T70-V20	0.656	343.4	347.0	368.8	2.03	4.080	0.208
P15-T70-V25	0.654	343.9	347.7	368.6	2.55	4.323	0.222
P15-T70-V30	0.652	342.3	346.5	368.1	3.02	4.468	0.251
P15-T70-V35	0.648	343.8	347.7	368.5	3.52	4.442	0.262
P20-T60-V35	0.927	333.7	337.8	369.7	3.55	6.064	0.256

Test	$\dot{M}_{sec}[kg/s]$	$T_{in,sec}[K]$	$T_{out,sec}[K]$	$T_{inlet}[K]$	$U_{inlet}[m/s]$	$\dot{M}_{cond}[g/s]$	$Y_{a,in}[-]$
P10-T30-V15	1.305	303.4	304.6	352.9	1.74	2.060	0.641
P10-T30-V20	1.303	303.3	304.4	350.8	2.08	2.036	0.679
P10-T30-V25	1.304	303.6	304.7	348.7	2.57	2.070	0.714
P10-T30-V30	1.302	303.5	304.9	351.6	3.06	2.683	0.678
P10-T30-V35	1.306	302.9	304.2	349.8	3.53	2.607	0.708
P15-T30-V15	1.312	302.8	304.5	358.6	1.74	3.038	0.522
P15-T30-V20	1.313	302.7	304.5	357.5	2.08	3.115	0.552
P15-T30-V25	1.312	302.7	304.5	356.7	2.60	3.344	0.580
P15-T30-V30	1.309	303.0	304.9	355.9	3.07	3.573	0.600
P15-T30-V35	1.306	303.5	305.3	353.6	3.53	3.495	0.637
P20-T30-V15	1.305	302.6	305.3	364.8	1.60	4.865	0.350
P20-T30-V20	1.306	303.0	305.7	363.6	2.06	4.767	0.391
P20-T30-V25	1.308	303.9	306.9	364.6	2.59	5.768	0.378
P20-T30-V30	1.312	302.6	304.7	357.2	3.07	3.819	0.575
P20-T30-V35	1.314	303.0	305.2	357.5	3.55	4.162	0.575
P25-T30-V15	1.296	304.6	308.3	368.2	1.62	6.589	0.220
P25-T30-V20	1.295	304.4	308.0	367.4	2.07	6.644	0.255
P25-T30-V25	1.296	304.2	307.9	366.9	2.60	6.830	0.294
P25-T30-V30	1.298	304.1	307.9	366.4	3.08	7.122	0.324
P25-T30-V35	1.298	303.9	307.8	365.8	3.57	7.389	0.354
P30-T30-V15	1.296	308.6	313.2	370.9	1.67	8.700	0.111
P30-T30-V20	1.296	308.2	312.8	370.6	2.10	8.640	0.139
P30-T30-V25	1.296	307.9	312.6	370.2	2.62	8.857	0.173
P30-T30-V30	1.295	307.5	312.3	369.8	3.10	9.136	0.203
P30-T30-V35	1.296	306.9	311.5	368.9	3.59	9.081	0.248
P10-T40-V15	1.772	313.0	313.9	354.5	1.70	2.230	0.606
P10-T40-V20	1.773	312.9	313.9	353.7	2.07	2.363	0.620
P10-T40-V25	1.780	313.5	314.5	353.0	2.58	2.553	0.639
P10-T40-V30	1.778	312.3	313.5	352.5	3.05	2.768	0.656
P10-T40-V35	1.778	312.5	313.7	352.9	3.52	3.086	0.654
P15-T40-V15	1.786	312.3	313.6	360.3	1.66	3.236	0.480
P15-T40-V20	1.786	312.3	313.6	359.1	2.06	3.290	0.511
P15-T40-V25	1.786	312.1	313.5	358.5	2.48	3.443	0.534
P15-T40-V30	1.785	312.2	313.6	357.9	2.97	3.612	0.557
P15-T40-V35	1.784	312.3	313.8	357.4	3.54	3.879	0.580

Test	$\dot{M}_{sec}[kg/s]$	$T_{in,sec}[K]$	$T_{out,sec}[K]$	$T_{inlet}[K]$	$U_{inlet}[m/s]$	$\dot{M}_{cond}[g/s]$	$Y_{a,in}[-]$
P20-T40-V15	1.769	313.1	314.9	364.7	1.58	4.589	0.347
P20-T40-V20	1.769	313.1	315.0	363.6	2.06	4.595	0.386
P20-T40-V25	1.770	313.1	315.0	362.7	2.59	4.770	0.427
P20-T40-V30	1.770	313.0	315.0	362.1	3.08	5.021	0.453
P20-T40-V35	1.769	313.5	315.6	361.4	3.55	5.239	0.478
P25-T40-V15	1.582	312.6	315.5	369.0	1.55	6.559	0.185
P25-T40-V20	1.650	312.6	315.4	368.6	2.07	6.708	0.211
P25-T40-V25	1.650	312.6	315.4	368.5	2.61	6.917	0.245
P25-T40-V30	1.650	312.6	315.5	368.6	3.13	7.053	0.283
P25-T40-V35	1.692	312.6	315.3	368.3	3.62	6.993	0.330
P30-T40-V15	1.280	316.3	320.9	371.1	1.54	8.462	0.087
P30-T40-V20	1.280	315.5	320.1	370.9	2.13	8.559	0.117
P30-T40-V25	1.284	315.4	320.1	370.6	2.63	8.784	0.147
P30-T40-V30	1.287	315.6	320.3	370.5	3.11	8.862	0.170
P30-T40-V35	1.287	315.8	320.7	370.4	3.60	9.482	0.184

Appendix C: Physical properties

Steam saturation temperature

$$T_{sat} = 213.656 + 240.5 \cdot {P_v}^{0.181508}$$

Steam saturation pressure

$$P_{v,sat} = e^{26.04750 - 5350.430/T - 3108.420/T^2} \quad 273.18K < T \leq 290K$$

$$P_{v,sat} = e^{23.00652 - 3601.131/T - 25472.13/T^2} \quad 290K < T \leq 475K$$

$$P_{v,sat} = e^{23.64100 - 4212.030/T - 107784.0/T^2} \quad 475K < T \leq 550K$$

Specific heats

Species	C_p (kJ/kg/K)
Air	$1.03437 - 2.12720 \cdot 10^{-4}\ T + 4.07314 \cdot 10^{-7}\ T^2$
H_2	$10.1889 + 2.80060 \cdot 10^{-2}\ T - 6.07974 \cdot 10^{-5}\ T^2 + 4.41246 \cdot 10^{-8}\ T^3$
He	5.19283
Steam	$-4.30484 + 5.64991 \cdot 10^{-2}\ T - 1.75247 \cdot 10^{-4}\ T^2 + 1.86832 \cdot 10^{-7}\ T^3$

Dynamic viscosities

Species	μ (Pa · s)
Air	$2.02910 \cdot 10^{-6} + 6.21004 \cdot 10^{-8}\ T - 2.40179 \cdot 10^{-11}\ T^2$
H_2	$2.15245 \cdot 10^{-6} + 2.50715 \cdot 10^{-8}\ T - 8.05458 \cdot 10^{-12}\ T^2$
He	$5.03696 \cdot 10^{-6} + 5.40569 \cdot 10^{-8}\ T - 1.47908 \cdot 10^{-11}\ T^2$
Steam	$1.75670 \cdot 10^{-6} + 2.33785 \cdot 10^{-8}\ T + 1.29077 \cdot 10^{-11}\ T^2$

Thermal condictivities

Species	K (W/m/K)
Air	$3.89745 \cdot 10^{-3} + 7.86562 \cdot 10^{-5}\ T - 1.67164 \cdot 10^{-8}\ T^2$
H_2	$3.48164 \cdot 10^{-2} + 5.21077 \cdot 10^{-4}\ T - 5.84187 \cdot 10^{-8}\ T^2$
He	$3.77293 \cdot 10^{-2} + 4.31873 \cdot 10^{-4}\ T - 1.24738 \cdot 10^{-7}\ T^2$
Steam	$-5.18738 \cdot 10^{-3} + 1.52267 \cdot 10^{-4}\ T - 4.54796 \cdot 10^{-7}\ T^2 + 7.08550 \cdot 10^{-10}\ T^3$

Molecular diffusivities

See Eq. (9.6) and Tab. 9.2.

List of Figures

List of Tables

Bibliography

[1] W. Bazin and P. Castelli. COPAIN: Rapport d'essai. Technical Report 85, CEA/DEN/DTP/SETEX/LETS, 1999.

[2] J.M. Delhaye, M. Giot, and M.L. Rietmuller. *Thermodynamics of two-phase systems for industrial design and nuclear engineering.* McGrawHill, 1981.

[3] C. Sawyer. thermal-hydraulic challenges for the SBWR. In *Proceeding of the NURETH 5 conference*, volume 1, pages 21–24, Salt Lake, USA, 1992.

[4] M.D. Kennedy, F.E. Peters, M.D. Carelli, and A.T. Poeczynski. Advanced PWR passive containment cooling system testing. In *Proceeding of the ARS'94 Int. Top. Meet. on Advanced Reactor Safety*, volume 1, pages 249–256, 1994.

[5] E. Studer, J.P. Magnaud, F. Dabbene, and I. Tkatschenko. International standard problem on containment thermal-hydraulics ISP47, step 1 - results from the mistra exercise. *Nuclear Engineering and Design*, 237:536–551, 2007.

[6] K. Fischer, A.K. Rastogi, T. Braun, T. Drath, A. Lyubar, and S. Schwarz. Containment code comparison exercise on experiment ThAI TH7. In *Proceeding of the NURETH 10 conference*, Seoul, South Korea, October, 5-9 2003.

[7] J. Malet, E. Porcheron, P. Cornet, P. Brun, O. Norvez, B. Menet, and L. Thause. ISP-47, specification of the calculations - international standard problem on containment thermal- hydraulics, step1: TOSQAN-MISTRA. Technical Report 44, IRSN/DPEA/SERAC/LPMAC, 2002.

[8] W. Ambrosini, N. Forgione, and F. Oriolo. Experimental and CFD analysis on condensation heat transfer in a square cross section channel. In *Proceeding of the NURETH 11 conference*, Pope's Palace Conference Center, Avignon, France, October 2-6 2005.

[9] E. Deri, M. Bucci, E. Studer, and D. Abdo. Analitycal and computational analysis of turbulent buoyant jets in the containment atmosphere. In *Proceeding of the ICONE 16 conference*, Orlando, Florida, May 11-15 2008.

[10] J. Travis, G. Necker, and P. Royl. Recent developments for GASFLOW-2. In *Proceeding of the NURETH 10 conference*, Seoul, Korea, October 5-11 2003.

[11] H. J. Allelein, K. Fischer, J. Vendel, J. Malet, E. Studer, S. Schwarz, M. Houkema, H. Paillre, and A. Bentaib. International standard problem ISP-47 on containment thermal-hydraulics. Technical Report 10, OECD/NEA/CSNI, 2007.

[12] O. Auban, R. Zboray, and D. Paladino. Investigation of large-scale mixing and stratification phenomena related to LWR containment studies in the PANDA facility. *Nuclear Engineering and Design*, 237:409–419, 2007.

[13] A. Favre, R. Dumas, E. Verollet, and M. Coantic. Couche limite turbulente sur paroi poreuse avec aspiration. *Journal de mècanique*, 5(1):3–28, Mars 1966.

[14] Lightfoot Bird, Steward. *Transport phenomena*. Wiley, 1965.

[15] R. Taylor and R. Kristhna. *Multicomponent mass transfer*. Wiley, 1993.

[16] J.H. Lienhard. *A heat transfer textbook*. Prentice Hall, 1987.

[17] B.E. Poling, J.H. Prausnitz, and J.P. O'Connell. *The properties of gases and liquid*. McGraw Hill, 2000.

[18] M. Bucci ans E.Studer and J.P. Magnaud. Theoretical and numerical analysis of condensation phenomena in multicomponent mixture. Technical report, CEA/DEN-DANS/DM2S/SFME/LTMF RT/07-046/A, 2007.

[19] G.A.J. Jaumann. Closed system of physical and chemical differential laws. *Wien. Akad. Sitzungsberichte*, 120(2a):385–530, 1911.

[20] C.F. Curtiss and R.B. Bird. Multicomponent diffusion. *Ind. Eng. Chem. Res.*, 38:2515–2522, 1999.

[21] C.F. Curtis and J.O. Hirschfelder. Transport properties of multicomponent gas mixtures. *The Journal of Chemical Physics*, 17:550–555, 1949.

[22] C.F. Curtis. Symmetric gaseous diffusion coefficients. *The Journal of Chemical Physics*, 49:2917–2919, 1968.

[23] H.J. Merk. *Mass-transfer in laminar boundary layers by forced convection*. PhD thesis, Technische Universiteit Delft, 1957.

[24] C.R. Wilke. A viscosity equation for gas mixtures. *The Journal of Chemical Physics*, 18:517–519, February 1950.

[25] G. Ackerman. Wäemeübertregung und molekulare stoffübertragung in gleichen feld bei grosser temperatur und partialdruckdifferenzen. *ForscHft. Ver. Dt. Ing.*, 382:1–16, 1937.

[26] W.M. Kays and R.J. Moffat. The behavior of transpired turbulent boundary layers. *Studies in convection, theory, measurements and applications*, 1:223–319, 1975.

[27] W. Nusselt. Die oberflachenkondensation des wasserdampfes. *Z. Ver. Deutsch. Ing.*, 60:541–569, 1916.

[28] W. M. Rohsenow, J.H. Webber, and A.T. Ling. Effect of vapor velocity on laminar and turbulent film condensation. *Trans. of ASME*, 78:1637–1643, 1956.

[29] W.M. Rohsenow. Heat transfer and temperature distribution in laminar film condensation. *Trans. of ASME*, 78:1645, 1956.

[30] E.M. Sparrow and J.L. Gregg. A boundary-layer treatment of laminar film condensation. *Journal of Heat Transfer*, 81:13, 1959.

[31] J.C.Y. Koh, E.M. Sparrow, and J.P. Hartnett. The two phase boundary layer in laminar film condensation. *Int. J. Heat Mass Transfer*, 2:69–82, 1961.

[32] R.D. Cess. Laminar film condensation on a flat plate in the absence of a body force. *Z. Angew. Math. Phys.*, 11:426–433, 1960.

[33] J.C.Y. Koh. Film condensation in a forced-convection boundary layer flow. *Int. J. Heat Mass Transfer*, 5:941–954, 1962.

[34] P.M. Chung. Film condensation with and without body force in a boundary layer flow of vapor over a flat plate. Technical note D-790, NASA, 1961.

[35] I.G. Shekriladze and V.I. Gomelauri. Theoretical study of laminar film condensation of flowing vapor. *Int. J. Heat Mass Transfer*, 9:581–591, 1966.

[36] H.R. Jacobs. An integral treatment of combined body force and forced convection film condensation. *Int. J. Heat Mass Transfer*, 9:637–648, 1966.

[37] D.F. Othmer. The condensation of steam. *Industrial & Engineering Chemistry*, 21(6):576, June 1929.

[38] E.M. Sparrow and S.H. Lin. Condensation heat transfer in the presence of a noncondensable gas. *Journal of Heat Transfer*, pages 430–436, August 1964.

[39] W.J. Minkowycz and E.M. Sparrow. Condensation heat transfer in the presence of noncondensables, interfacial resistance, superheating, variable properties and diffusion. *Int. J. Heat Mass Transfer*, 9:1125–1144, 1966.

[40] E.M. Sparrow, W.J. Minkowycz, and M. Saddy. Forced convection condensation in the presence of noncondensables and interfacial resistance. *Int. J. Heat Mass Transfer*, 10:1829–1845, 1967.

[41] W.J. Minkowycz and E.M. Sparrow. The effect of superheating on condensation heat transfer in a forced convection boundary layer. *Int. J. Heat Mass Transfer*, 12:147–154, 1969.

[42] T. Fujii and H. Uehara. Laminar filmwise condensation on a vertical surface. *Int. J. Heat Mass Transfer*, 15:217–233, 1972.

[43] F.S. Felicione and R.A. Seban. Laminar film condensation of a vapor containing a soluble, noncondensing gas. *Int. J. Heat Mass Transfer*, 16:1601–1610, 1973.

[44] H.K. Al-Diwany and J.W. Rose. Free convection film condensation of steam in the presence of non-condensing gases. *Int. J. Heat Mass Transfer*, 16:1359–1369, 1973.

[45] V.E. Denny and V.J. Jusionis. Effects of noncondensable gas and forced flow on laminar film condensation. *Int. J. Heat Mass Transfer*, 15:315–326, 1972.

[46] W.P. Jones and U. Renz. Condensation from a turbulent stream onto a vertical surface. *Int. J. Heat Mass Transfer*, 17:1019–1028, 1974.

[47] H. Dallmeyer. Stoff- und wärmeübertragung bei der kondensation eines dampfes aus einem gemisch mit einem nichtkondensierenden gas in laminarer und turbulenter str:omungsgrenzschicht. *ForscHft. Ver. Dt. Ing.*, 539:4–24, 1970.

[48] O. Reynolds. On the extent and action of the heating surface of steam boilers. In *Proc. Manchester Lit. Phil. Soc.*, volume 8, 1874.

[49] A.P. Colburn. A method for correlating forced convection heat transfer and a comparison with fluid friction. *Transaction of AIChE*, 29:174–210, 1933.

[50] T.H. Chilton and A.P. Colburn. Evaporation of water into a laminar stream of air and superheated steam. *Ind. Eng. Chem.*, 26:373–380, 1934.

[51] T.H. Chilton and A.P. Colburn. Mass transfer absorption coefficients prediction from data on heat transfer and fluid friction. *Ind. Eng. Chem.*, 26(11):1183–1187, 1934.

[52] W. Ambrosini, N. Forgione, A. Manfredini, and F. Oriolo. On the various form of the heat and mass transfer analogy: discussion and application to condensation experiments. *Nuclear Engineering and Design*, 236:1013–1027, 2006.

[53] D.B. Spalding. A standard formulation of the steady convective mass transfer problem. *Int. J. Heat Mass Transfer*, 1:192–207, 1960.

[54] J.H. Lienhard. *A heat transfer textbook*. Prentice Hall, Englewood Cliffs, 1987.

[55] R. Bird, W.E. Steward, and E.N. Lightfoot. *Transport phenomena*. Wiley, New york, 1960.

[56] F. Kreith. *Principi di trasmissione del calore*. Liguori Editore, Napoli, 1974.

[57] J.G. Collier. *Convective boiling and condensation*. McGraw-Hill, 1972.

[58] D. Butterworth and G.F. Hewitt. *Two-phase flow and heat transfer*. Oxford University Press, Oxford, 1977.

[59] H. Uchida, A. Oyama, and Y. Togo. Evaluation of post-incident cooling system of LWR's. In *Proc. Int. Conf. Peaceful Uses of Atomic energy*, volume 13, pages 93–102, 1965.

[60] T. Tagami. Interim report on safety assesment and facilities enstablishment project for june 1965. June 1965.

[61] J. Green and K. Almenas. An overview of the primary parameters and methods for determining condensation heat transfer to containment structures. *Nuclear Safety*, 37(1):26–47, 1996.

[62] P.F. Peterson. Theoretical basis for the uchida correlation for condensation in reactor containments. *Nuclear Engineering and Design*, 162:301–306, 1996.

[63] A.A. Dehbi. *The effects of noncondensable gases on steam condensation under turbulent natural convection conditions*. PhD thesis, Dept. of Nuclear Engineering, Massachusetts Institute of Technology, Canbridge, January 1991.

[64] A.A. Dehbi, M. Golay, and M.S. Kazimi. Condensation experiments in steam-air and steam-air-helium mixtures under turbulent natural convection. In *Proceeding of National Heat Transfer Conference*, pages 19–28, Minneapolis, USA, 1991.

[65] I.K. Huhtiniemi. *Condensation in the presence of a noncondensable gas: the effect of surface orientation*. PhD thesis, University of Winsconsin, 1991.

[66] I.K. Huhtiniemi and M.L. Corradini. Condensation in the presence of noncondensable gases. *Nuclear Engineering and Design*, 141:429–446, 1993.

[67] A. Pernsteiner, I.K. Huhtiniemi, and M.L. Corradini. Condensation in presence of noncondensable gases: effect of helium. In *Proceeding of the NURETH 6 conference*, 1993.

[68] M.H. Anderson, L.E. Herranz, and M.L. Corradini. Experimental analysis of heat transfer within the AP600 containment under postulated accident conditions. *Nuclear Engineering and Design*, 185:153–172, 1998.

[69] K.M. Vierow and V.E. Schrock. An experimental investigation of the effect of air on steam condensation under turbulent natural convection, part.1 - heat transfer. In *Proceeding of Int. Conf. on Multiphase Flow*, Tsukuba, Japan, September 1991.

[70] D.G. Ogg. Vertical downflow condensation heat transfer in gas-steam mixtures. Master's thesis, Dept. of Nuclear Engineering, University of California, Berkeley, January 1991.

[71] M. Siddique. *The effects of noncondensable gases on steam condensation under forced convection conditions*. PhD thesis, Dept. of Nuclear Engineering, Massachusetts Institute of Technology, Canbridge, January 1991.

[72] M. Siddique, M. Golay, and M.S. Kazimi. Local heat transfer coefficients for forced convection condensation of steam in a vertical tube in the presence of a noncondensable gas. *Nuclear Technology*, 102:386–401, 1993.

[73] T. Kageyama. Application of the diffusion layer theory to vertical downflow condensation. Master's thesis, Dept. of Nuclear Engineering, University of California, Berkeley, January 1991.

[74] S.Z. Kuhn, V.E. Schrock, and P.F. Peterson. An investigation of condensation from steam-gas mixtures flowing downward inside a vertical tube. In *Proceeding of the NURETH 7 conference*, September 1995.

[75] S.Z. Kuhn, V.E. Schrock, and P.F. Peterson. An investigation of condensation from steam-gas mixtures flowing downward inside a vertical tube. *Nuclear Engineering and Design*, 177:53–69, 1997.

[76] C. Lin. CONTEMPT4/MOD5: an improvement to CONTEMPT4/MOD4 multicompartment containment system analysis-program for ice containment analysis. Technical report.

[77] M.L. Corradini. Turbulent condensation on a cold wall in the presence of a noncondensable gas. *Heat Transfer and Fluid Flow*, 64:186–195, February 1984.

[78] M.H. Kim and M.L. Corradini. Modeling of condensation heat transfer in a reactor containment. *Nuclear Engineering and Design*, 118:193–212, 1990.

[79] P.F. Peterson, V.E. Schrock, and T. Kageyama. Diffusion layer theory for turbulent vapor condensation with noncondensable gases. *Journal of Heat Transfer*, 115:998–1003, November 1993.

[80] T. Kageyama, P.F. Peterson, and V.E. Schrock. Diffusion layer modeling for condensation in vertical tubes with noncondensable gases. *Nuclear Engineering and Design*, 141:289–302, 1993.

[81] P.F. Peterson. Diffusion layer modeling for condensation with multicomponent noncondensable gases. *Journal of Heat Transfer*, 122:716–720, November 2000.

[82] L.E. Herranz, J.L. Muñoz-Cobo, and G. Verdú. Heat transfer in the vertical tubes of the passive containment cooling system of the simplified boiling water reactor. *Nuclear Engineering and Design*, 178:29–44, 1997.

[83] L.E. Herranz, M.H. Anderson, and M.L. Corradini. A diffusion layer theory for steam condensation within the AP600 containment. *Nuclear Engineering and Design*, 183:133–150, 1998.

[84] W. Ambrosini, M. Bucci, N. Forgione, F. Oriolo, S. Paci, J.P. Magnaud, E. Studer, E. Reinecke, St. Kelm, W. Jahn, J. Travis, H. Wilkening, M. Heitsch, I. Kljenak, M. Babic, M. Houkema, D.C. Visser, L. Vyskocil, P. Kostka, and R. Huhtanen. Comparison and analysis of the condensation benchmark results. In *The 3rd European Review Meeting on Severe Accident Researc (ERMSAR-2008)*, Nesseber, Vigo hotel, Bulgary, 23-25 September 2008.

[85] L. Blumenfeld and H. Paillère. CFD simulation of mixed convection and condensation in a reactor containmetn: the MICOCO benchmark. In *Proceeding of the NURETH 10 conference*, Seoul, South Korea, October, 5-9 2003.

[86] M. Schwarz, G. Hache, and P. von der Hardt. PHEBUS FP: a severe accident research programme for current and advanced light water reactors. *Nuclear Engineering and Design*, 187:47–69, 1999.

[87] M. Bucci, E. Studer, and J.P. Magnaud. A numerical analysis of simultaneous momentum, heat and mass transfer. Technical report, CEA/DEN-DANS/DM2S/SFME/LTMF RT/07-043/A, 2007.

[88] W. Ambrosini, N. Forgione, A. Manfredini, and F. Oriolo. Prediction of heat and mass transferin innovative nuclear reactors. In *Proc. of the Third International Conference on nuclear Option in Countries with Small and Medium Electricity Grids*, Dubrovnik, Croatia, June 19-22 2000.

[89] W. Ambrosini, M. Bucci, N. Forgione, F. Oriolo, S. Paci, H. Paillère, and E. Studer. CFD models for predicting condensation in nuclear reactor containments within the SARnet network of excellence. Technical report, SARnet Report SARNET-CONT-P02, 2006.

[90] M. Houkema, N.B. Siccama, J.A. Lycklama à Nijeholt, and E.M.J. Komen. Validation of the CFX4 CFD code for containment thermal-hydraulics. *Nuclear Engineering and Design*, 238:590–599, 2008.

[91] W. Ambrosini, N. Forgione, D. Mazzini, F. Oriolo, and S. He. CFD analysis of evaporation cooling experimental tests. In *Proceeding of the ICONE 9 conference*, Nice, France, April 6-12 2001.

[92] S. Mogliani. Analisi teorica e sperimentale della condensazione in presenza di gas incondensabili. Master's thesis, University of Pisa, 2005.

[93] N. Forgione and S. Paci. Computational analysis of vapor condensation in presence of air in the TOSQAN facility. In *Proceeding of the NURETH 11 conference*, Pope's Palace Conference Center, Avignon, France, October 2-6 2005.

[94] L. Viskocil and J. Macek. Condensation model for CFD code FLUENT. Technical report, NRI Rez, 2004.

[95] R. Huhtanen and J. Niemi. Simulation of condensation on MISTRA facility using FLUENT. Technical report, Research Report PRO1/P1030/05, 2006.

[96] M. Bucci. Sviluppo di modelli di CFD per lo studio della condensazione nel sistema di contenimento di LWRs. Master's thesis, University of Pisa, 2005.

[97] E. Deri. Development of condensation models in CAST3M and TONUS and qualification against experimental data. Master's thesis, University of Pisa, 2006.

[98] I. Kljenak, M. Babic, B. Mavko, and I. Bajsic. Modeling of containment atmosphere mixing and stratification experiment using a CFD approach. In *Proceedings of the ICONE 13 conference*, Bejing, China, May, 16-20 2005.

[99] I. Kljenak, M. Babic, and B. Mavko. Modeling of atmosphere mixing and stratification in the TOSQAN experimental facility with the CFX code. In *Proceeding of the NURETH 11 conference*, Pope's Palace Conference Center, Avignon, France, October 2-6 2005.

[100] M. Babic, I. Kljenak, and B. Mavko. Simulation of atmosphere mixing and stratification in the thai experimetnal facility with a CFD code. In *Int. Conf. on Nuclear energy for the new Europe*, Bled, Slovenia, September, 5-8 2005.

[101] I. Kljenak, M. Babic, B. Mavko, and I. Baisic. Modeling of containment atmosphere mixing and stratification experiment using a CFD approach. *Nuclear Engineering and Design*, 236:1682–1692, 2006.

[102] H. Terasaka and A. Makita. Numerical analysis of the phebus containment thermal-hydraulics. *J. Nuc. Sci. Technol.*, 34(7):666–678, 1997.

[103] J.M. Martin-Valdepeñas, M.A. Jimenez, F. Martin-Fuertes, and J.A. Fernandez-Benitez. Comparison of film condensation models in presence of non-condensable gases implemented in a CFD code. *Heat Mass Transfer*, 41:961–976, 2005.

[104] J.M. Martin-Valdepeñas, M.A. Jimenez, F. Martin-Fuertes, and J.A. Fernandez-Benitez. Improvements in a CFD code for analysis of hydrogen behavior within containments. *Nuclear Engineering and Design*, 237:627–647, 2007.

[105] J. Stefan. Versuche über die verdampfung. *Sber. Akad. Wiss. Wien.*, 68:385–423, 1873.

[106] W. Ambrosini, M. Bucci, N. Forgione, F. Oriolo, S. Paci, H. Paillère, and E. Studer. Results of the SARnet condensation benchmark-0. Technical report, University of Pisa, DIMNP006(2007), 2006.

[107] Incropera. *Fundamentals of heat transfer.* Wiley, 1965.

[108] D. Lioce. Prove sperimentali di condensazione di miscele ternarie di aria-elio-vapore e qualifica mediante un codice di CFD. Master's thesis, University of Pisa, 2006.

[109] H.J. Konle. Experimental study on condensation onto a flat plate in the presence of noncondensable gases. Master's thesis, University of Pisa, 2004.

[110] A. Fortier. *Mécaniqhe des fluides et transferts de chaleur et de masse par convection.* Masson, 1975.

[111] M.A. Cotton and J.D. Jackson. Vertical tube air flows in turbulent mixed convection regime calculated using a low reynolds number κ-ε model. *Int. J. Heat Mass Transfer*, 33(2):275–286, 1990.

[112] J.L.J. Wang and J.D. Jackson. Mixed convection heat transfer to air flowing upwards through a vertical plane passage: Part 3. *Trans ICHemE.*, 80:252–260, 2002.

[113] JB.J. Chung, W.S. Kim, C. Talbot, and J.D. Jackson. Variable property mixed convection heat transfer to air flowing through a vertical apssage of annular cross section. *Trans ICHemE.*, 80:239–245, 2002.

[114] K. Karkoszka. *Mechanistic modelling of water vapour condensation in presence of noncondensable gases.* PhD thesis, KTH, Stockholm, 2007.

[115] H. Schlichting. *Boundary layer theory.* McGraw Hill, 1981.

[116] F. Poli. Prove sperimentali sulla condensazione a film di miscele ternarie aria-elio-vapore e qualifica dei dati mediante un codice di CFD. Master's thesis, University of Pisa, 2007.

[117] P. Chassaing, R.A. Antonia, E. Anselmet, L. Joly, and S. Sarkar. *Variable density fluid turbulence.* Kluver Academic Publishers, 2002.

[118] M. Bucci, W. Ambrosini, N. Forgione, F. Oriolo, and S. Paci. Validation of a CFD condensation model based on the heat and mass transfer analogy by TOSQAN facility ISP47 test. In *Proceeding of the ICONE 14 conference*, Miami, Florida, July 17-20 2006.

[119] D.C. Wilcox. *Turbulence modelling for CFD.* DCW Industries, La Cañada, California, 2000.

[120] K. Abe, T. Kondoh, and Y. Nagano. A new turbulence model for predicting fluid flow and heat transfer in separating and reattaching flows - i flow field calculations. *Int. J. Heat Mass Transfer*, 37:139–151, 1994.

[121] Z. Yang and T.H. Shih. New time scale based κ-ε model for near wall turbulence. *AIAA Journal*, 31:1191–1198, 1993.

[122] M. Bucci, M. Sharabi, W. Ambrosini, N. Forgione, F. Oriolo, and S. He. Prediction of tranpiration effects on heat and mass transfer by different turbulence models. *Nuclear Engineering and Design*, 238:958–974, 2008.

[123] Fluent Inc., Centerra Resource Park, Lebanon, NH. *Fluent 6.2 user guide*, 2003.

[124] D.B. Spalding. A single formula for the law of the wall. *Journal of Applied Mechanics*, pages 445–458, September 1961.

[125] H. Reichardt. Vollständige darstellung der turbulenten geschwindigkeitsverteilung in glatten leitungen. *Z. angew. Math. Mech.*, 31(7):208–219, July 1951.

[126] W.M. Kays. Heat transfer to the transpired turbulent boundary layer. *Int. J. Heat Mass Transfer*, 15:1023–1044, 1972.

[127] F.H. Clauser. Turbulent boundary layers in adverse pressure gradients. *J. of Aero. Sci.*, 29, 1954.

[128] B.A. Kader and A.M. Yaglom. Heat and mass transfer law for fully turbulent flows. *Int. J. Heat Mass Transfer*, 15:2329–2351, 1972.

[129] B.A. Kader. Temperature and concentration profiles in a fully turbulent boundary layer. *Int. J. Heat Mass Transfer*, 29(9):1541–1544, 1972.

[130] W. Ambrosini, N. Forgione, D. Mazzini, and F. Oriolo. Computational study on evaporative film cooling in a vertical channel. *Heat Tansfer Eng.*, 23(5):25–35, 2002.

[131] C. Dannohl. Computational analysis of experimental tests concerning condensation in the presence of noncondensable gases. Master's thesis, University of Pisa, 2004.

[132] W. Bazin and P. Castelli. Validation d'un modele de condensation sur la base des resultats experimentaux COPAIN. Technical Report 102, CEA/DEN/DTP/SETEX/LETS, 2000.

[133] M. Bucci. Analysis of the M8 MISTRA test with the TONUS code. Technical report, CEA/DEN-DANS/DM2S/SFME/LTMF RT/07-047/A, 2007.

[134] M. Turrin, M. Bucci, and E. Deri. Review of chemical and physical properties of air, steam, helium and hydrogen mixtures. Technical report, CEA/DEN-DANS/DM2S/SFME/LTMF RT/08-016/A, 2008.

[135] E.W. Lemmon, M.O. McLinden, and D.G. Friend. Thermophysical properties of fluid systems. Technical Report in NIST Chemistry WebBook, NIST Standard Reference Database Number 69, Eds. P.J. Linstrom and W.G. Mallard, National Institute of Standards and Technology (http://webbook.nist.gov), Gaithersburg MD, 20899, June 2005.

[136] E.W. Lemmon and R.T. Jacobsen. A generalized model for the thermodynamic properties of mixtures. *International Journal of Thermophysics*, 20:825–835, 1999.

[137] E.W. Lemmon and R.T. Jacobsen. Viscosity and thermal conductivity equations for nitrogen, oxygen, argon, and air. *International Journal of Thermophysics*, 25:21–69, 2004.

[138] T.R. Marrero and E.A. Mason. Gaseous diffusion coefficients. *Journal Physical Chemistry Reference Data*, 1:3–118, 1972.

[139] T.R. Marrero and E.A. Mason. Correlation and prediction of gaseous diffusion coefficients. *AIChE Journal*, 19:498–503, 1973.

[140] B.E. Poling, J.M. Prausnitz, and J.P. O'Connell. *The properties of gases and liquids*. McGraw-Hill, 5 edition, 2001.